Rotordynamic Instability Problems in High-Performance Turbomachinery 1990

Proceedings of a workshop held at
Texas A&M University
College Station, Texas
May 21–23, 1990

NASA

Rotordynamic Instability Problems in High-Performance Turbomachinery 1990

NASA

PREFACE

From the first symposium, where little information was available, to the present symposium, continued progress has been made toward an understanding of rotordynamic instability problems. The proceedings of these symposiums are reported in the following NASA documents:

- 1980 Proceedings, NASA CP-2133
- 1982 Proceedings, NASA CP-2250
- 1984 Proceedings, NASA CP-2338
- 1986 Proceedings, NASA CP-2443
- 1988 Proceedings, NASA CP-2409
- 1990 Proceedings, NASA CP-3122

This proceedings continues to report field experience along with laboratory experiments and the theory of seals, but it also includes works on dampers, bearings, and controls. These topics are necessary since they are interrelated with current and future seals - such as damper seals, smart seals, feedback controls, and eccentric floating ring seals, as well as theoretical contributions of bearing flows that are, in essence, eccentric seals with modified boundary conditions.

Without wishing to slight any of the contributions, we call your attention to the following papers:

(1) Sykes and Holmes begin the difficult task of delineating the effects of manufacturing (assembly) tolerance on the vibration of rotor-damper assemblies.

(2) Nordmann and Weiser form a partitioned computational fluid dynamics (CFD) model for labyrinth seals somewhat similar to multigriding, without the complexity, and to cellular automatons, without the behavior logic.

(3) Childs, Ramsey, and Baskharone combine CFD modeling with laboratory results to design swirl brakes, and they predict and verify the performance of these swirl brakes.

(4) Muszynska and Bently provide relations, comparisons, and results for force- and displacement-excited rotors.

(5) San Andres provides several robust numerical solutions to hydrodynamic problems in bearings and dampers.

We are confident that you will find the papers presented in this proceedings to be of interest. Please read them carefully and form your own impressions.

These workshops have been organized to continue addressing problems of rotordynamic instabilities by gathering those persons with immediate interest, experience, and knowledge of this subject and providing a forum for information exchange of both past stability problems and present research and development efforts. The intent of the workshop organizers and sponsors is

that the workshop and these proceedings provide a continuity of effort and an impetus for an understanding and resolution of these problems.

Chairmen:

Jorgen L. Nikolajsen,
Dara Childs, and
John Vance
Turbomachinery Laboratory
Texas A&M University

Robert C. Hendricks
NASA Lewis Research Center

CONTENTS

Session I - Field Experiences

Session II - Dampers

Session III - Seals

Session IV – General

Session V - Identification

Session VI - Bearings

INVESTIGATION AND CONTROL OF ROTORDYNAMIC INSTABILITY IN TYPICAL LARGE TURBOGENERATORS

Lu Songyuan
Thermal Power Engineering Research Institute
Xian, People's Republic of China

This paper describes the investigation and results of recent studies to solve oil whip in typical large turbogenerators. It includes the following:

(1) Calculations are given of the instability speeds and system damping of rotor-bearing systems. The polynomial-transfer matrix method which was developed by the author during the last few years is used in the calculations.

(2) Vibration measurements and data indicate the stability of these units.

(3) Research reveals that the cause of the instability lies in the three-bole offset bearings.

(4) Work was done to solve these problems, and industry tests were performed on one of these abnormal systems.

INTRODUCTION

Since 1970, many 200 MW-130/355/535 turbogenerator systems have been in operation in China, and these units have gradually become the main fossil fuel power generating units. Unfortunately, oil whip takes place occasionally in some of these systems (about 13 percent of the total number).

This paper describes the investigation and results of recent studies to solve this rotordynamic instability problem.

TYPE OF UNITS AND BEARINGS

Figure 1 shows the rotor-bearing system investigated. It consists primarily of HP, IP, and LP sections and a generator. The turbomachinery has a total weight of 50,400 kgf and an overall length of 18,823 mm. The generator rotor weight is about 42,000 kgf and its length is 8000 mm.

The rotors are supported by seven three-pocket bearings (TPB) which possess three axial grooves. However, each land contains a spiral pocket, creating the convergent film shape shown in Fig. 2. The principal parameters of these TPB are given in Table 1.

CALCULATION ANALYSIS OF THE INSTABILITY

Calculation of the Stiffness and Damping Coefficients of the Bearing

Four stiffness coefficients $K_{xx}, K_{xy}, K_{yx}, K_{yy}$ and four damping coefficients $C_{xx}, C_{xy}, C_{yx}, C_{yy}$ representing the dynamic character of the bearing were obtained by solving the Reynold's equation (1) with the finite difference and finite element methods.

$$\frac{\partial}{\partial x}\left(\frac{1}{Kx} \cdot \frac{h^3}{12\mu} \cdot \frac{\partial p}{\partial x}\right) + \frac{\partial}{\partial z}\left(\frac{1}{Kz} \cdot \frac{h^3}{12\mu} \cdot \frac{\partial p}{\partial z}\right) = \frac{u}{2} - \frac{\partial h}{\partial x} + \frac{\partial h}{\partial t} \qquad (1)$$

where

x circumferential coordinate in the direction of rotation

z axial coordinate

μ dynamic viscosity of oil

p pressure

u tangential velocity of the journal surface

K_x, K_z turbulence coefficients

Considering that the actual flow state is between laminar and turbulent flow, and to compare the results, the calculation was carried out on the basis of three flow states:

   (1) Laminar flow
       For this condition, $K_x = K_z = 1$

   (2) Turbulent flow
       According to Ng–Pan's law, $K_x = 1 + 0.00113R_h^{0.9}$
       and $K_z = 1 + 0.00036R_h^{0.96}$

   (3) Laminar–turbulent mixed state flow

In the calculation of this state, first the Reynold's numbers R_h at each point on the net of the bearing surface were evaluated to determine the parameters of each point, then correct turbulence coefficients were selected.

Calculation of the Instability of the Rotor–Bearing System

In the calculation process, the following two methods are employed:

$K_{eq} - \gamma_{st}$ method. – Usually, the equivalent stiffness K_{eq} of the oil film and the whirl rate γ_{st} (where $\gamma_{st} = \omega/\Omega_{st}$, ω, whirl frequency; Ω_{st}, the threshold speed) can be used to analyze instability. K_{eq} and γ_{st} are, respectively,

$$K_{eq} = \frac{K_{xx}C_{xx} + K_{yy}C_{yy} - K_{xy}C_{yx} - K_{yx}C_{xy}}{C_{xx} + C_{yy}} \tag{2}$$

$$\gamma_{st}^2 = \frac{(K_{eq} - K_{xx})(K_{eq} - K_{yy}) - K_{xy}K_{yx}}{C_{xx}C_{yy} - C_{xy}C_{yx}} \tag{3}$$

They are the function of the bearing load coefficient ζ

$$\zeta = \frac{W\psi^2}{\mu u L} \tag{4}$$

where

W   load acting on bearing

ψ clearance ratio

L   length of bearing

The threshold speed of the elastic rotor with a single disk is therefore

$$\Omega_{st} = \frac{\omega_o^2 m}{2K_{eq}\frac{\mu L}{\phi^3}} + \omega_o \sqrt{\left(\frac{m\omega_o}{2K_{eq}\frac{\mu L}{\phi^3}}\right)^2 + \frac{1}{\gamma_{st}^2}} \tag{5}$$

where ω_o is the natural frequency of the shaft supported by two stiff pedestals.

Transfer Matrix–Polynomial Method (TMPM) (Ref. 1)

This method uses the block matrices for transferring the sequence of calculations along the rotor. The characteristic polynomial can be directly obtained, then all complex eigenvalues are solved with the Bairstow–Newton approach. In the eigenroot $S = \lambda + i\omega$, λ is the system damping. Meanwhile, according to λ, the logarithmic decrement δ corresponding to various speeds can be obtained. It is clear that the stability state of the systems is known immediately on the basis of the value δ or λ.

A program based on the previously mentioned transfer matrix polynomial algorithm was developed by the author during the last few years. The first half of this program employs new recurrence expressions, equations (6) and (7):

$$L_i = U_{i-1}L_{i-1} + W_i M_i \tag{6}$$

$$M_i = U_{i-1}M_{i-1} + R_{i-1}L_{i-1} \tag{7}$$

The second half of the program applies the polynomial algorithm. The size of the new transfer matrices is one-fourth of those used in the Murphy and Vance's

3

method (Ref. 2); therefore, the CPU time and the storage required are greatly reduced.

<center>NUMERICAL RESULTS (Ref. 3)</center>

The results of calculating the threshold speeds Ω_{st} of 200 MW units by the $K_{eq} - \gamma_{st}$ method for the laminar state are presented in Table 2. As shown in this table, the Ω_{st} of bearings 6 and 7 is the lowest, only 3557.6 r/min, and it is merely 1.19 times the working speed 3000 r/min. The next lowest value is the Ω_{st} of bearing 3, 3911.9 r/min.

The Ω_{st} of bearings 6 and 7, as determined by TMPM for the same state, are also listed in Table 2. It should be noted that the results from these two algorithms are almost identical.

A diagram of the damped natural frequencies for the laminar state of the oil film resulting from TMPM is shown in Fig. 3. With the rotor speed as the abscissa and the damped natural frequency as the ordinate, a number of the modes are shown in this figure. The parameter values on the curves give the logarithmic decrement δ.

In Fig. 3, it is noted that the δ of the first forward whirl changed from a positive value to a negative value when the rotor speed reached 3601.5 r/min, then the generator rotor began to become unstable. This frequency is rather lower than the first natural frequency of the generator supported by the stiff pedestal and is consistent with the measured value of the first critical speed.

Again, it should be noted in Fig. 3 that the value of δ for the generator rotor is only 0.08 at the working speed of 3000 r/min and is much less than the one recommended by current standards (Ref. 4).

Table 3 shows the variation of δ with the bearing dimensionless load $\bar{P}$ and the oil inlet temperature T_{in} for the laminar-turbulent mixed state. At nominal working parameters (i.e., at $\bar{P} = 1$ and $T_{in} = 42$ °C), Ω_{st} is 3004.3 r/min. When T_{in} increases to 48 °C, Ω_{st} can also increase to 4593.8 r/min. The reduction of the bearing load can also sharply decrease Ω_{st}. A more common cause of bearing load variation is the differential thermal growth of the bearing pedestals. Besides showing that the stability of the 200 MW generator units is inferior at the nominal speed, an analysis of the calculated results of Table 3 shows that the stability can easily deteriorate with $\bar{P}$ and T_{in}.

The damped natural frequencies of the HP, IP, and LP sections of the turbomachinery rotor-bearing system are shown in Fig. 4, whereas Table 4 presents the δ values of the second forward whirl of these three rotors at 2700, 3000, and 3300 r/min, respectively. From Fig. 4, it can be seen that the stability of all of the rotors, except the LP rotor, are poor.

To thoroughly investigate this kind of turbogenerator and to better examine the calculation program from an engineering viewpoint, a comparative calculation was made between these 200 MW units and a 250 MW unit known for its good stability. The numerical results for this 250 MW unit are listed in

Table 4. It further demonstrates that the 200 MW units are much less stable than the 250 MW units (Ref. 5).

MEASUREMENT AND FIELD DIAGNOSIS TEST ON THE INSTABILITY

VIBRATION OF 200 MW TURBOGENERATORS

Because of the instability of the 200 MW units, a series of measurements and tests in the field were performed to diagnose and determine the cause of violent vibrations that occurred in some of these units, severely affecting normal work as well as safety.

The results of the measurements and tests follow:

(1) The large vibrations that sometimes occurred in some 200 MW units was oil whip. In all of these cases, it is clear that the whip originated in bearings 6 and 7, and then expanded to the turbomachinery causing the whole rotor-bearing system to vibrate violently.

(2) Meanwhile, it was found that the dominant frequency of the generator vibration was 18-19 Hz, which is approximately the first natural frequency of this rotor under actual operating conditions. The maximum vibration amplitude of these two bearings could reach 0.6-0.8 mm (p-p) during whip.

(3) The oil temperature in the bearings is of vital importance to stability during the operation. Oil whip can be temporarily avoided by increasing the oil inlet temperature. Consequently, before whip was completely eliminated in these defective units, some defective units could be operated reluctantly by raising the oil inlet temperature to 48-50 °C for several months, even a year.

(4) Spectrum analysis on some of the 200 MW units with higher oil inlet temperatures indicated that, except for units with whip, a subsynchronous component whose frequency ranged from 18-19 Hz at bearings 6 and 7 or half running speed at bearing 3 exist in most units, though these subsynchronous vibration values are small and there was not typical instability, i.e., whip or obvious oil whirl. Figure 5 shows the spectrum of shaft vibration of bearing 6 at 3000 r/min in this unit (Ref. 6).

IMPROVEMENT OF THE UNITS ON SITE

So far, all of the calculations and measurements have fully demonstrated the poor stability of the 200 MW turbogenerators. Consequently, three main measures were taken to improve these systems:

(1) Modify the geometric parameters of the TPB, e.g., decrease the effective length of the bearing.

(2) Re-adjust the vertical height of the bearings and make the center of bearing 6 higher than bearing 5 by 0.05-0.1 mm in the stopped condition to compensate for the rise of the center of bearing 5 during operation.

5

(3) Use bearings with good stability instead of the TPB.

For some defective units, actions (1) and (2) have been effective, but for a few units, the situation did not take a favorable turn.

It is obvious that the former bearings at least bearings 6 and 7, should be replaced by high-stability ones.

The new design adopted the elliptic bearings shown in Fig. 5. A detailed calculation of the logarithmic decrement δ shows that this improved rotor-bearing system will be much better than for previous systems of stable TPB units. From Table 3, it can be seen that at working speed, the new value is about three times the previous value of 0.08. It is also noted that δ is still 0.213 at the maximum calculation speed 4000 r/min, and this means that the threshold speed of the new rotor-bearing system has gone beyond 4000 r/min.

TEST AND RESULTS OF IMPROVING A UNIT BY REPLACING THE BEARINGS

Bearings were replaced in a unit with severe whip at Xu Zhou Power Plant to solve instability and to test the elliptic bearing on site.

Since they were put into operation at the end of 1985, this unmodified system has experienced whip 39 times. Lastly, the oil inlet temperature has to be maintained above 48 °C to avoid the emergence of whip. Figure 6 gives a typical whip spectrum of this unit at an operation speed of 3000 r/min and an oil inlet temperature of 48 °C (Ref. 7). After failures in modifying the design parameters of the TPB and in readjusting the centers of the bearings, it was finally decided to replace bearings 3 and 7 with the elliptic ones.

The test of the unit with the new bearings was to verify the stability and to determine general vibration characteristics. The test was carried out under the following two special severe working conditions:

(1) The oil inlet temperature was decreased slowly from 48 to 35 °C, which is below the normal value by 5 °C.

(2) The speed of the unit rose to 3300 r/min, then the trip occurred.

During the whole test period, the unit operated smoothly under several working conditions from startup to full power 200 MW, and no whip was encountered.

From Figs. 7 and 8 (Ref. 8), it can be seen that the predominant frequency coincided with the operating speed of the turbine. Between the speeds of 2700 and 3300 r/min, the maximum amplitude of the 18.75 Hz component was only 0.7 μm and is considerably smaller than the amplitude shown in Fig. 5. It is, therefore, of interest to note that whip has no longer occurred and that instability is considered to be completely solved. In addition, the test proves the following properties of this new bearing rotor system:

6

- From the Bode figure, it is seen that there is no resonance peak at bearings 6 and 7 in connection with the second critical speed of the generator rotor from 2600 to 3250 r/min.

- The unbalance response of the rotors mounted in the new bearings is normal and its influence coefficients are approximately the same as those in the previous TPB units. The maximum amplitude of each bearing is less than 0.05 mm when the rotor passes various critical speeds.

- Other operating parameters – for example power loss, temperature of bearing surface, and amount of oil flow – are normal, too.

CONCLUSIONS

The TMPM used to calculate the 200 MW units is a valuable analytical tool. The resulting logarithmic decrement can be effectively employed to evaluate the stability of large turbogenerators. The CPU time of the corresponding program is faster than other ones.

The detailed calculation and measurement revealed that the stability of the 200 MW units is inferior and is not satisfactory for operation. In addition, investigation indicated that the main reason for poor performance is the TPB which has poor stability properties with middle to heavy bearing loads.

Adoption of elliptic bearings for 200 MW units is a valid measure for eliminating whip in these units. Meanwhile, elliptic bearings do not produce side effects on other general properties.

A thorough investigation is needed to choose the optimum parameters for elliptic bearings under various working conditions.

REFERENCES

1. Lu Songyuan, "A Method for Calculating Damped Critical Speeds and Stability of Rotor-Bearing Systems." ASME Paper No. 85-DET-116.

2. B.T. Murphy and J.M. Vance, "An Improved Method for Calculating Critical Speeds and Rotordynamic Stability of Turbomachinery." Journal of Eng. for Power, Trans. ASME, Vol. 105, July 1983.

3. Lu Songyuan, "Analysis on Stability of Rotor-Bearing System of 200 MW Turbogenerator Units." Thermal Power Eng. Research Institute, No. 87248, 1987.

4. S.B. Malanoski, "Rotor-Bearing system Design Audit." The 4th Turbomachinery Symposium, 1975.

5. Lu Songyuan and Wu Rongqing, "Calculation Analysis on a 250 MW Turbogenerator and Comparison With 200 MW Units." Thermal Power Eng. Research Institute and Xian College of Technology, No. 87219, 1987.

6. Lu Songyuan and Shi Weixin, "Measurement and Investigation on Instability of some 200 MW Turbogenerators in Field." Thermal Power Eng. Research Institute, No. 87248, 1987.

7. Gao Wei and Li Yong, "The Vibration Test of No. 6 Unit at Xu Zhou Power Plant." Nian Jing University, 1988.

8. Lu Songyuan and Quan Jun, "The Test of Replace of Bearings at No. 6 Unit at Xu Zhou Power Plant." Thermal Power Generation, No. 6, 1989.
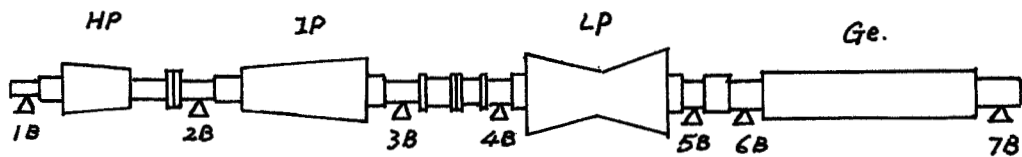
Fig.1   Schematic Diagram of Rotor-Bearing System of 200 MW Turbogenerator
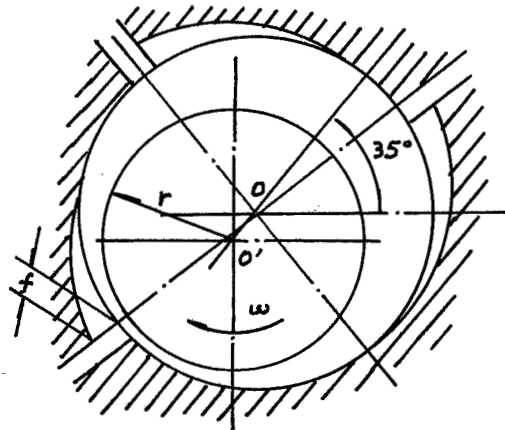
Fig.2   Schematic of the Three-Pocket Bearing

8

cps

700
600 .64 .78 .78 .79 .81
500 .05 .21 .18 .12 .49
400 .49 .52 .55 .58 .61
300 .11 .15 .19 .22 .24

200 .17 .24 .29 .33 .36
.79 .84 .89 .91 .94

100
90
80 .38 .40 .45 .49 .51
70
60 1.48 6.30 1.09 0.87 0.67
50
40 Synchronous 15.70
30 12.17 12.90 12.60 13.20
15.30 13.80
.15 .19 .20 .12 .23
20 .45 .8 Unstable .21

10
9
8 25.84
7
6
5 30.53
4

3

2

1800 2400 3000 3600 4200
rpm

Fig.3 Damped natural frequencies of 200MW generator
in three-pocket bearings

9
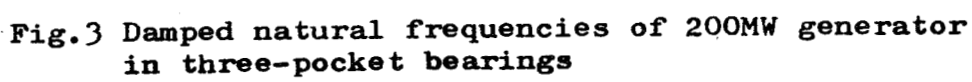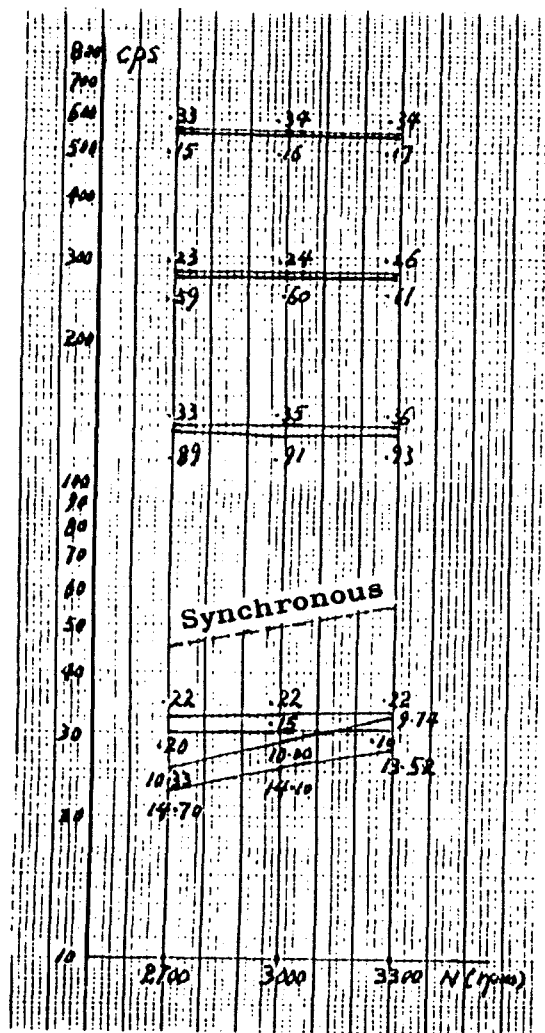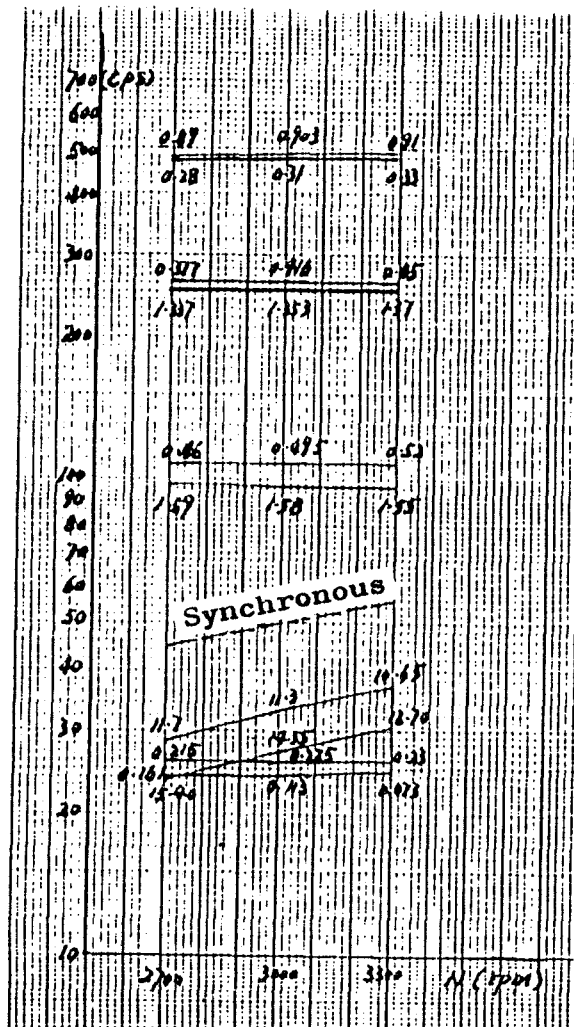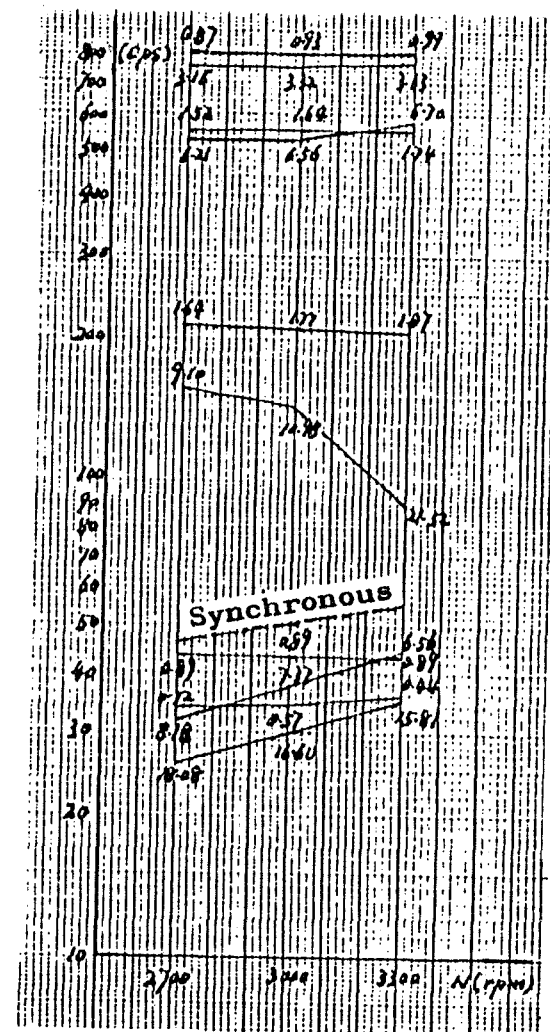
(a) HP rotor   (b) IP rotor   (c) LP rotor

Fig.4   Damped natural frequencies of 200MW turbomachinery
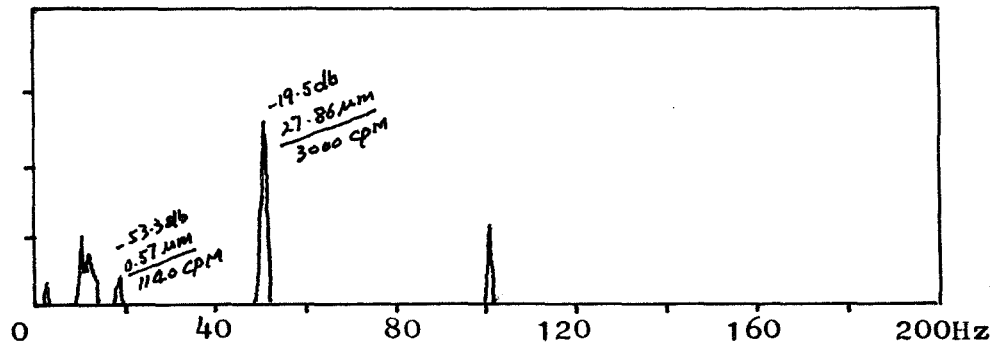
Fig.5 Frequency Spectrum of horizontal vibration of No.6
bearing of a 200MW unit at full load, 3000r/min,
Dec. 12,1985
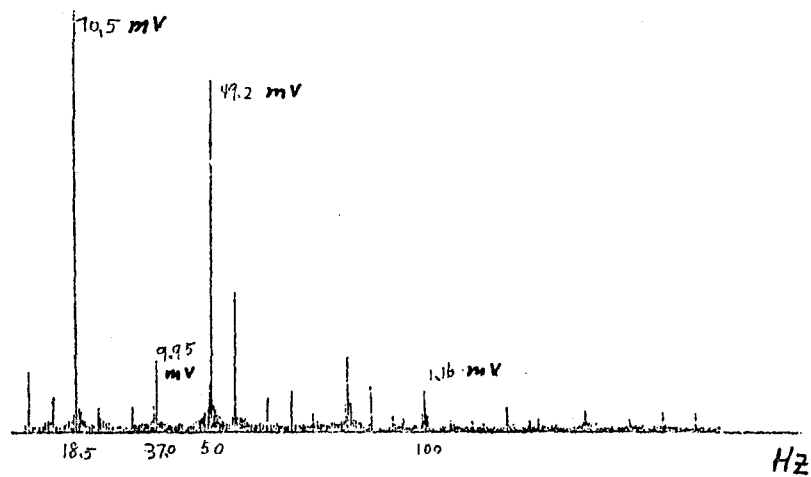
Fig.6 Typical spectrum during the whip at No.6 bearing
of No.6 unit of Xu Zhou Power Plant before the
replacing TPB (7)

11
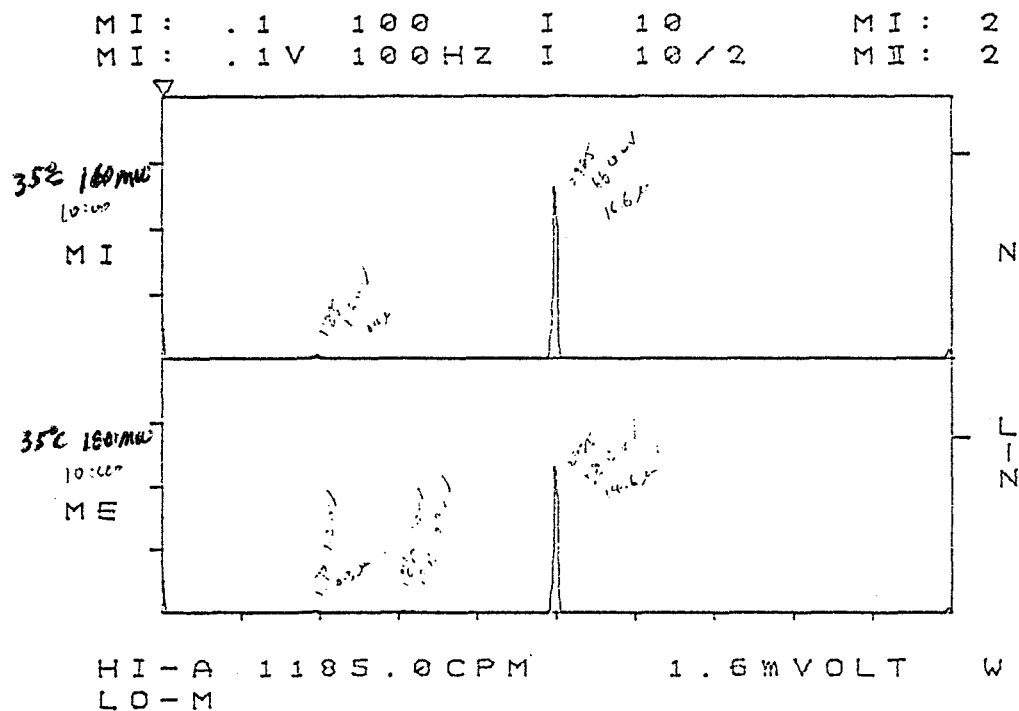
Fig.7 Frequency spectrum of vertical vibration of No.6
bearing of No.6 unit in new elliptic bearings of
Xu Zhou Power Plant, power output: 160 and 180MW,
oil inlet temperature: 35°C
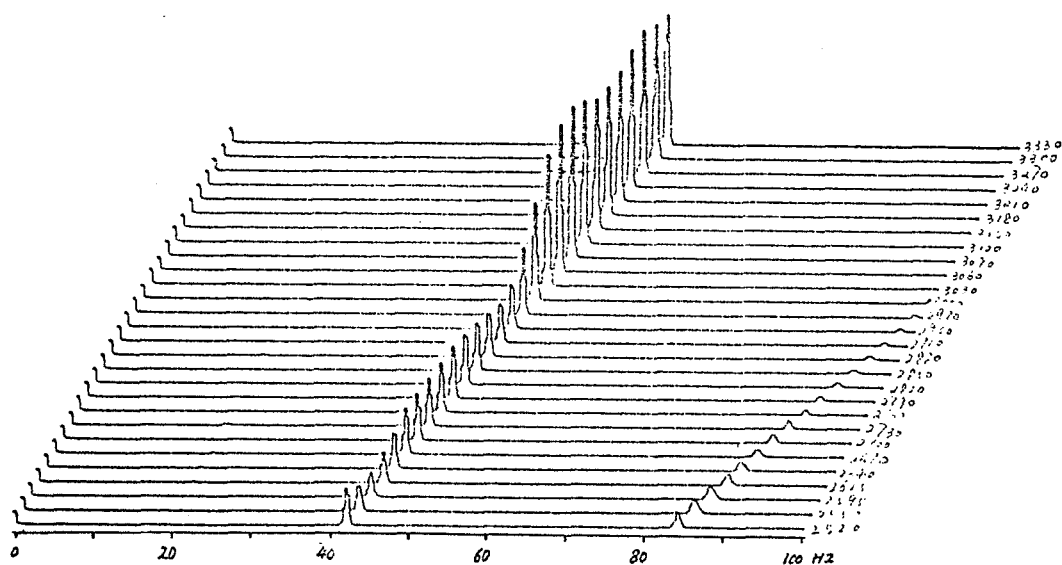
Fig.8 Spectrum cascade of vertical vibration of No.6 bearing
of No.6 unit in new elliptic bearing of Xu Zhou Power
Plant, speed from 2520 r/min to 3330 r/min, Lin..

12

Tab. 1 TP Bearing data of 200MW turbogenerators

No. of bearing		1	2	3	4	5	6 and 7
Diameter D(mm)		250	300	360	360	360	420
Ratio L/D		0.8	0.8	0.75	0.75	0.75	0.7619
Load W (Kgf)		3900	13900	12237	10040	8923	21400
Specific pressure	P_a	7.652E5	1.893E6	1.235E6	1.013E6	9.006E5	1.565E6
P_m	Kgf/Cm	7.8	19.3	12.59	10.33	9.18	15.95

Table 2 Calculation results of threshold speeds Ω_{st} of units (r/min)

Calculation condition			No. of bearings					
			1	2	3	4	5	6,7
200MW unit	$K_{eq}-\gamma_{st}$, Single disc Laminary		4220.8	4487.8	3911.9	4353.2	4206.0	3557.6
	TMP, Multidisc, Lami.							3601.5
	TMP, Multidisc Laminary-turbulence	$T_{in}=42°C$						3004.3
		$T_{in}=48°C$						4593.8
250MW unit	TMP, Multidisc Turbulence							5527.0

Table 3 The calculation results of the threshold speeds
of TPB units versus dimemsionless load of bearing
and oil inlet temperature

Dimensionless load of bearing		100%		90%		80%		70%	
T_{in}	T_m*	Ω_{st}	ε_o**	Ω_{st}	ε_o	Ω_{st}	ε_o	Ω_{st}	ε_o
48°C	60°C	4593.8	0.571	3620.7	0.543	3018.3	0.515	2651.4	0.478
42°C	55°C	3004.3	0.536	2458.9	0.510	2228.3	0.479	2171.3	0.443

* T_m: the average temperature in oil film of bearing

** ε_o: eccentricity ratio

Table 4 The logarithmic decrement δ of 200MW unit
with TPB and 250MW unit with elliptic bearing

	Speed (r/min)	HP	IP	LP	Speed (r/min)	Ge.
200MW unit	2700	0.2001	0.1613	0.7217	2400	0.15
250MW unit		0.708		0.465		0.47
200MW unit	3000	0.1477	0.1131	0.5717	3000	0.08
250MW unit		0.679		0.354		0.25
200MW unit	3300	0.1041	0.0729	0.4411	3600	0.00011
250MW unit		0.654		0.264		0.15

Table 5 The elliptic bearing parameters

No. of bearing	3,4 and 5	6 and 7
Diameter D(mm)	360	420
Assembled clearance	0.0015	0.0015
Elliptic ratio	0.55	0.55
Length/D (L/D)	0.75	0.7619

Table 6 The logarithmic decrement δ of 200MW
unit with new elliptic bearing of
generator rotor

Speed (r/min)	δ	whirl frequency (Hz)
3000	0.217	16.00
3200	0.202	16.11
3400	0.218	16.34
3600	0.128	16.44
3800	0.287	15.62
4000	0.213	16.01

FIELD TELEMETRY OF BLADE-ROTOR COUPLED TORSIONAL VIBRATION AT MATUURA POWER STATION NO. 1 UNIT

Kuniyoshi Isii and Hideaki Murakami
Thermal Power Department
Kyushu Electric Power Co., Inc.
2-1-82, Watanabedouri, Chuo-ku, Fukuoka-shi
Fukuoka-ken, Japan, 810

Yasuhiko Otawara and Akira Okabe
Steam Turbine Design Section
Thermal Power Plant Design Department
Hitachi Works, Hitachi Ltd.
3-1-1, Saiwai-cho, Hitachi-shi
Ibaraki-ken, Japan, 317

At Matuura Power Station No.1 Unit, which is the 700MW coal fired plant of Kyushu Electric Corporation that started commercial operation on June 30, 1989, field telemetry of the last-stage bucket of the steam turbine is executed just after the first steaming in order to verify the blade-rotor (HP, 1P, 2LP's, and Generator) coupled torsional vibration frequency, which is predicted to be near twice the line frequency. ' The measured frequency is different from the double synchronous frequency, and the steam turbine's reliable operation for the negative sequence current is confirmed. This paper reports the analytical procedure for prediction of coupled vibration incorporated with a single rotor test of blade-rotor coupled vibration at the manufacturer's factory. It also compares the predicted value and the measured results.

1 INTRODUCTION

The effect of torsional excitation in a turbine generator system from the power line is an old but still ongoing topic because of the growing size of electrical networks and larger unit capacity. The electric disturbances which cause torsional excitation of the turbine generator include line accidents such as short circuits and faulty synchronization. Since the mid 1970's, these matters have been widely discussed. A turbine generator was generally modeled as a lumped-mass and spring system. Dynamic simulations of the grid system and shaft system were executed in order to estimate the shaft torque. Stresses in the main journal bearings and coupling were analyzed by using the simulation results. (Ref.1) Finally, fatigue strength was evaluated for shaft life expectancy due to the power line transient.

At the same time, the technology to monitor the torsional frequency of main shaft modes has developed. Generally, toothed gears are machined on each rotor to detect the phase differences between rotors by using a magnet pick-up. The differences in shaft twisting during operation were analyzed using FFT (Fast Fourier Transform) in order to find natural frequencies, mode shapes, and modal damping.

These discussions have focused on the principle lower torsional vibration modes of the rotor system. From the late 1970's, examinations of higher torsional frequency modes coupled with long buckets of low pressure turbines have been reported. The so-called umbrella modes are blade-disk coupled vibration. Since all blades mounted on a disk vibrate in the same direction and the disk vibrates with a zero nodal diameter in the case of an umbrella mode of blade-disk vibration, this mode is hardly excited by steam flow but can be excited by torsional excitation due to negative sequence currents from the power line. (Figure 1) This frequency is a higher torsional mode, and approaches different from the mere shaft system torsional analysis are required in order to accurately estimate the higher torsional modes, because this problem is in the boundary between the blade-disk coupled vibration problem and the rotor torsional vibration problem.

In this paper, the analytical method will be reviewed and estimation of input data for the calculation of a blade-rotor coupled system will be made by measuring the
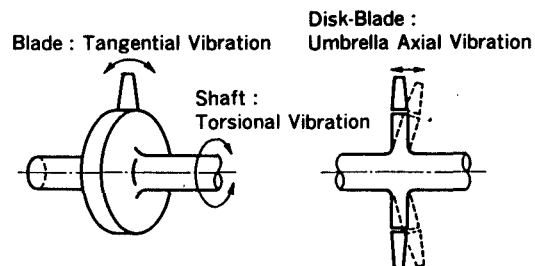
Figure 1 Blade-disk-rotor coupled vibration

umbrella mode of blade vibration coupled with a double-flow low pressure rotor of a 700MW steam turbine during manufacture. Then field telemetry of the last-stage buckets of a 700MW steam turbine at the Matuura P.S. was executed in order to verify the predicted values. The measured results were tabulated and compared with the calculated value.

2 MODELING FOR ANALYSIS

In a coupled shaft-blade system of a turbine generator shaft set, the shaft system and blade system correspond to a main system and to a subsystem, respectively. The main shaft system is more flexible than this subsystem. For example, The first torsional frequency of the shaft system is about 7 to 20Hz compared to the lowest umbrella frequency of blades which is about 50 to 150Hz. Therefore, the coupled model is obtained by combining the standard FEM beam model of the shaft main system with additional branches of a spring-mass model derived from the blade subsystem. A coupled model of the entire system is thus obtained. These additonal branches are actually simple added nodal points with a mass connected to the boss of the shaft by a spring, one for each eigen mode of the blade system.

In case of long blade vibration, two kinds of umbrella modes are generally considered for double synchronous resonance as shown as in Figure 2. The equation of motion can be expressed in the following formula. (Ref.2)

$$\begin{pmatrix} M_1 & & & \\ & m_2+\Delta m & & \\ & & m_{eq1} & \\ & & & m_{eq2} \end{pmatrix} \begin{pmatrix} \ddot{X}_1 \\ \ddot{x}_2 \\ \ddot{x}_{31}{}^* \\ \ddot{x}_{32}{}^* \end{pmatrix} + \begin{pmatrix} K_1 & 0 & 0 \\ \odot k_{eq1} & \odot k_{eq2} & -k_{eq1} & -k_{eq2} \\ 0 & -k_{eq1} & k_{eq1} & 0 \\ 0 & -k_{eq2} & 0 & k_{eq2} \end{pmatrix} \begin{pmatrix} X_1 \\ x_2 \\ x_{31}{}^* \\ x_{32}{}^* \end{pmatrix} = 0$$

where

$m_{eq1} = a_1^2 \phi_1{}^t M_3 \phi_1 =$ equivalent mass of 1st mode
$m_{eq2} = a_2^2 \phi_2{}^t M_3 \phi_2 =$ equivalent mass of 2nd mode
$k_{eq1} = \omega_1^2 m_{eq1} =$ equivalent spring of 1st mode
$k_{eq2} = \omega_2^2 m_{eq2} =$ equivalent spring of 2nd mode
$a_1 = 1^t M_3 \phi_1 / \phi_1{}^t M_3 \phi_1 =$ 1st coupling factor
$a_2 = 1^t M_3 \phi_2 / \phi_2{}^t M_3 \phi_2 =$ 2nd coupling factor
$\odot$ denotes super imposing operation in FEM

Nomenclature is as follows:

X_1 : Absolute disp. vector of the main system
x_2 : Absolute disp. of a bonding point
$x_{31}{}^*$: Absolute disp. vector of 1st equivalent mass
$x_{32}{}^*$: Absolute disp. vector of 2nd equivalent mass
M_1 : Mass matrices of the main system (shaft)
m_2 : Mass of a bonding point
Δm : Residual mass attached to a bonding point
M_3 : Mass matrices of the blade subsystem
ϕ_1 : 1st eigen umbrella mode of an uncoupled blade subsystem
ϕ_2 : 2nd eigen umbrella mode of an uncoupled blade subsystem
ω_1 : Natural frequency of the 1st eigen mode of an uncoupled blade subsystem
ω_2 : Natural frequency of the 2nd eigen mode of an uncoupled blade subsystem

3 COUPLED VIBRATION CALCULATION

3.1 Turbine Plant Description

The Matuura Power Station is a coal fired 700MW power station. Its major specifications are shown in Table 1.

The steam turbine is a tandem-compound type with four cylinders (high pressure turbine, intermediate pressure turbine, two double-flow low pressure turbine, as shown in Picture 1.)

The last-stage buckets of the low pressure turbine
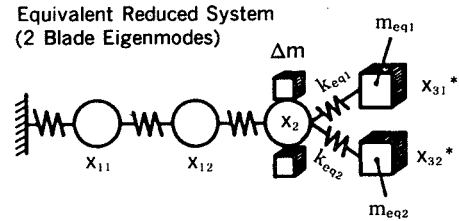
Figure 2 Equivalent Reduced Model (2 Blade Modes)

Table 1

Characteristic Rated		700,000kW
Boiler	Evaporation Quantity	2,300Ton/Hr
	Fuel	Coal
	Stack Height	200m
Turbine	Main Steam Pressure	246kg/cm²
	Main Steam Temperature	538°C deg
	Reheat Steam Temperature	566°C deg
Generator	Speed	3600rpm
	Capacity	778,000kVA
	Voltage	25kV
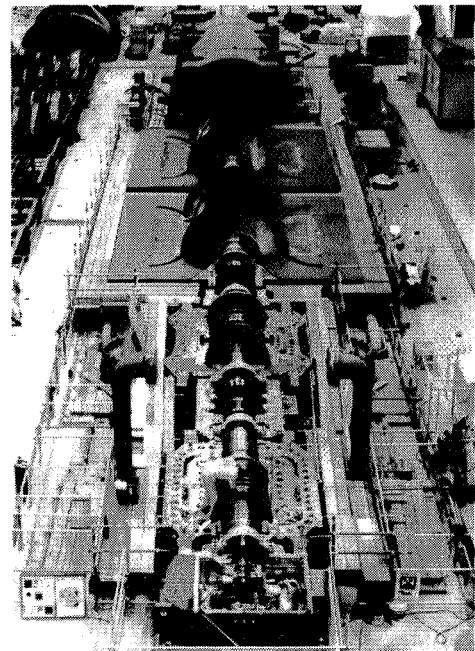
Picture 1 700MW Steam Turbine View

16

are 33. 5 inches in length, and all blades are continuously connected with loose covers and sleeves for 360 degrees. This construction has very good structural damping and good vibration suppression characteristics for the steam force. The almost 20 years experience with this bucket design has shown its very high reliability.

3.2 Modal quantity calculation of the blade

Due to the pretwisted blade configuration, eigen modes vibrate in tangential and axial directions of the umbrella figure. The two modal masses and modes can be calculated by the differential mesh model of buckets incorporating the cover, sleeve, and dovetail configurations. The details of this procedure were reported by Matsusita et al. (Ref. 3)After the eigenvalue problems of the last stage (L-0) and the last minus one (L-1) stage are solved independently, the two eigen modes, called the tangential and axial modes, are reduced to the equivalent additional masses, as shown in Figure 3.

Concerning the L-0 blade, the equivalent masses of the tangential and axial modes comprise 46.1% and 46.3% of the polar moment of the total inertia of the blades, respectively. The residual polar moment of inertia, 7.6%, is attached to the boss of the last stage (L-0). In the same way, the L-1 stage is reduced, as shown in Figure 4.

3.3 Single LP rotor test

In order to calculate the coupled torsional frequency, it is necessary to first determine the uncoupled umbrella frequency of the blades. In the factory balancing pit, the LP rotor with blade vibration measuring equipment was excited by a torsional shaker during operation. Figure 5 shows the eigen frequency of the coupled umbrella mode of last-stage buckets near 120HZ. Since the measured result is a coupled frequency, the uncoupled frequency can be determined to match the measured results with the calculated result. Table 2 compares the calculated uncoupled umbrella frequency and the corrected uncoupled umbrella frequency. Table 3 shows the umbrella frequency coupled with the single LP rotor and the measured coupled frequency. Although the L-0 tangential umbrella mode has only one mode, the coupled mode with the single rotor splits into two modes.

Figure 6 shows the mode configuration of a single rotor
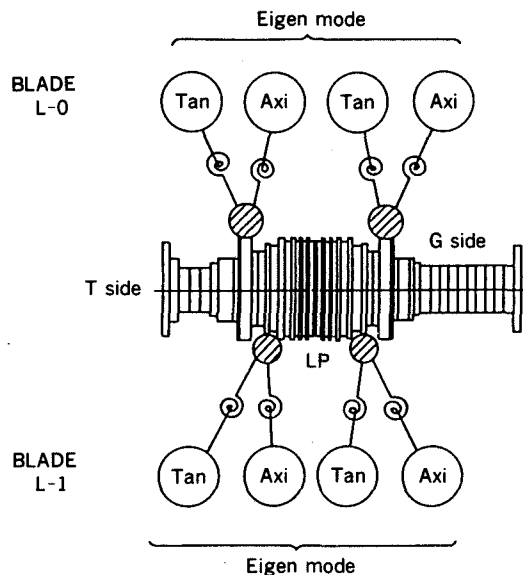
Figure 3 Coupled Model of LP turbine
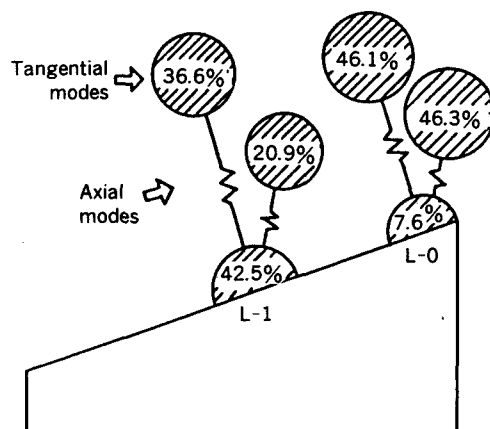
Figure 4 Equivalent Mass Distribution
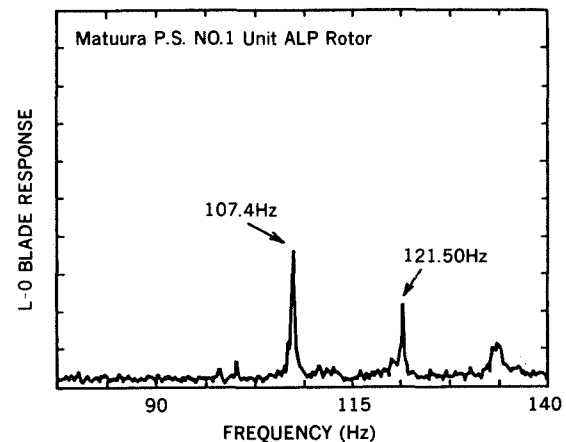
Figure 5 Single rotor umbrella frequency

Table 2 Uncoupled umbrella frequency near 120Hz
(L-0 Tangential mode)

Calculated frequency	118.37Hz
Corrected frequency	116.40Hz

Table 3 Coupled umbrella frequency near 120Hz

Calculated frequency*	Measured frequency
107.40Hz	107.40Hz
121.57Hz	121.50Hz

*) Calculation is based on the corrected uncoupled frequency (116.4Hz)

17

coupled with last-stage blades near 120Hz. In this figure, split modes correspond with the opposite twisting modes of the LP rotor and the blades, where both the turbine (T) and generator (G) side blades twist in the same direction. During the single rotor test, the resonance stress was measured by exciting the torsional exciter. Picture 2 shows the torsional exciter and how it was connected to the LP rotor. Picture 3 shows the LP rotor in the test pit. The measured blade stress is about 1kg/mm² per 5% negative sequence equivalent torque. This means that the stress due to torsional excitation is sufficiently lower than the material fatigue strength.

3.4 Coupled frequency analysis of the rotor train

Based on the single rotor test, the blade-rotor coupled torsional frequency of all rotors connected in a system was analyzed. The shaft system can be modeled by FEM and the blade subsystem can be added using the single rotor test result.

Figure 7 shows the calculated modes and frequencies of blade-rotor coupled vibration near 120Hz. These results are very similar to the single rotor test, because the modes are chiefly related to the L-0 blades and LP rotor stiffness.

The above results also show that there exist two similar modes for each coupled-split result, because there exists two LP rotors (ALP and BLP). Since the 120Hz nearest coupled mode (Mode No.8) is the ALP and L-0 coupled frequency, it was decided to execute a single rotor test for the ALP rotor.

4 FIELD MEASUREMENT OF COUPLED VIBRATION

4.1 Measuring method

In order to verify the coupled frequency under field

CALC. FREQ. 107.40 (Hz)

CALC. FREQ. 121.57 (Hz)
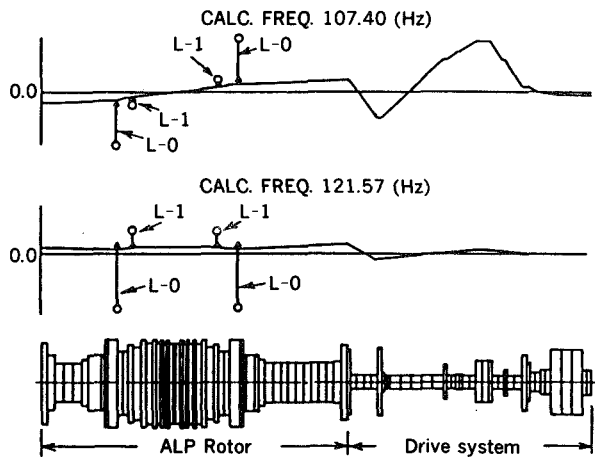
Figure 6 Mode configuration
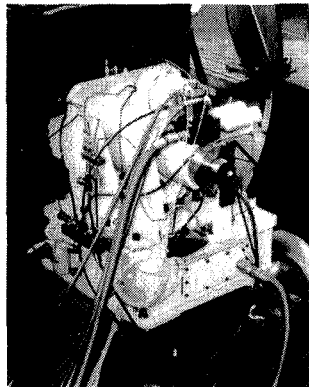
Picture 2 Torsional Exciter
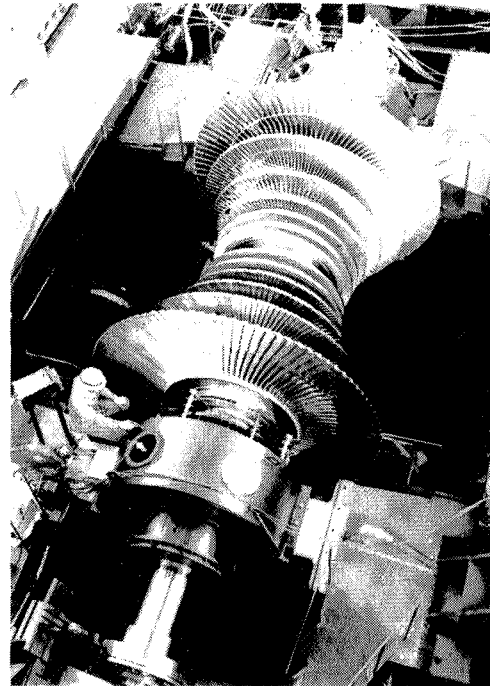
Picture 3 Single LP rotor test view

MODE NO.6 CALC. FREQ. 107.81 (Hz)

MODE NO.7 CALC. FREQ. 108.94 (Hz)

MODE NO.8 CALC. FREQ. 121.67 (Hz)

MODE NO.9 CALC. FREQ. 121.97 (Hz)
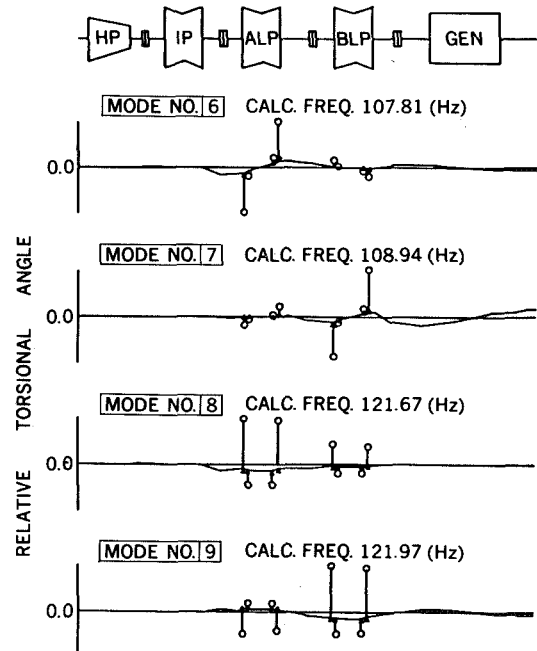
Figure 7 Blade-Shaft Coupled Torsional Modes

18

conditions, it was decided to measure blade-rotor coupled vibration. Since the mode near the double synchronous frequency is the L-0 blade umbrella mode coupled with the shaft system, strain gauges to measure vibration were attached to the L-0 blades of both a ALP rotor and a BLP rotor. The output of the strain gauges was transmitted by a frequency modulation (FM) telemetry system to a receiving antenna. Figure 8 depicts the telemetry system. Picture 4 shows a transmitter and a receiving antenna under preparation. The transmitter and batteries were set in a balance weight slot of the last stage disk. The receiving antenna was set in a bearing cone of the LP casing.

The test was executed just after initial steaming, considering strain gauge life under a steam flow. Under a no load condition, the turbine was slowly sped up and down near 60Hz and the shaft system was excited from a generator by a one phase grounding circuit at the high voltage side of the main transformer. Figure 9 shows the excitation circuit. The breaker between the main tranformer and the line was open. The measured signal was recorded and analyzed by FFT.

4.2 Field test results

Field test results are shown in Figures 10 and 11 for the ALP rotor and the BLP rotor, respectively. The resonance point with double synchronous frequency nearest to 120Hz is 124.2Hz in the ALP rotor. This frequency is far from twice the expected line frequency variation of 58.5~60.5Hz (117Hz~121Hz).

The eigen frequencies of coupled umbrella modes are tabulated in Table 4. These measured values are also compared with the calculated values. Since the calculated values were incorporated in the single rotor test of the ALP rotor, the differences between the measured values and the analyzed results are smaller for modes dominated by the ALP rotor than those of the BLP rotor. From these results and the single rotor test results, it is necessary to confirm
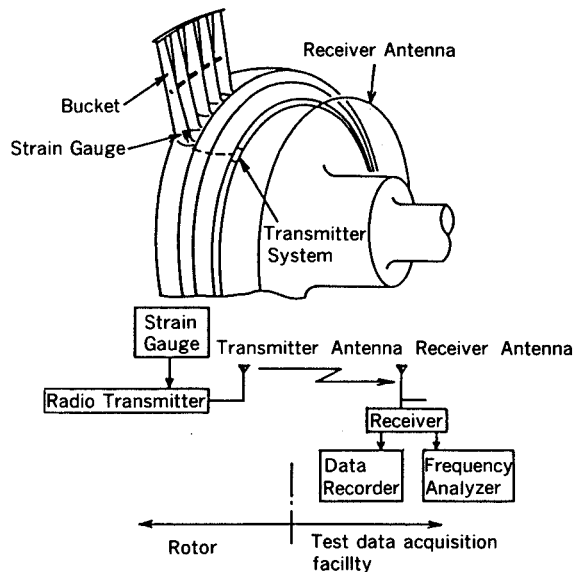
Figure 8 Telemetry System

Figure 9 Excitation Circuit

Picture 4 Telemetry Equipment
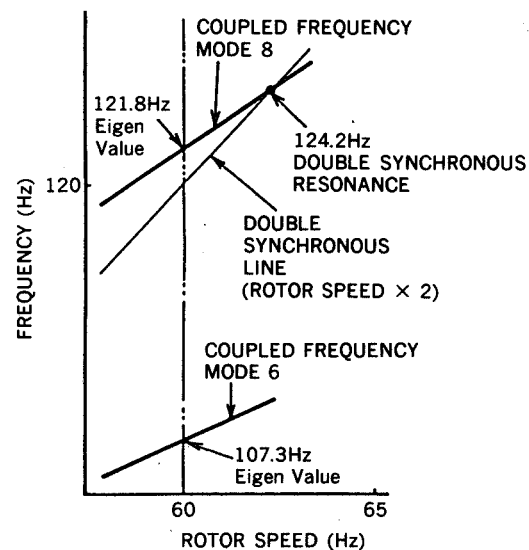
Figure 10 ALP rotor test results

the umbrella frequency and equivalent spring of blades in order to get better accuracy. The input data for blades are one set, but four coupled modes are certain to be very accurate. This means that this analytical procedure (quasi-modal reduction technique) can be applied to estimate the shaft coupled umbrella frequency of an actual turbine shaft.
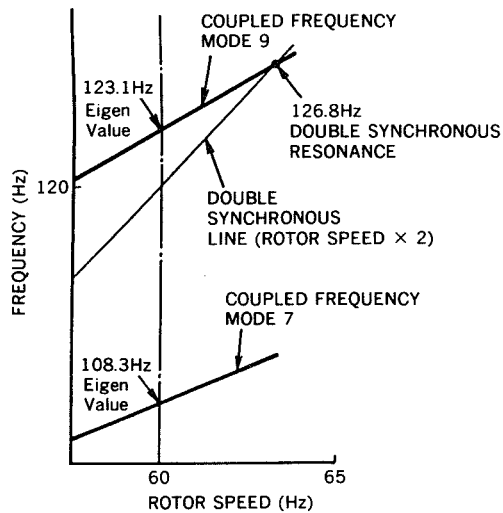
Figure 11 BLP rotor test results

Table 4 Eigen frequencies of test results

Mode	Measured	Calculated	Difference
			Out-of-phase
ALP	107.3Hz	107.81Hz	0.51Hz
BLP	108.3Hz	108.94Hz	0.64Hz
			In-phase
ALP	121.8Hz	121.67Hz	0.13Hz
BLP	123.1Hz	121.97Hz	1.13Hz

4.3 Evaluation at a rated load

The test was executed under a no load condition. Table 5 shows a temperature comparison between the test condition and a rated load condition. The changes in rigidity of the rotor due to this temperature change effect are about 3% for a HP turbine, 4.5% for an IP turbine, and 1.5% for a LP turbine. Since the coupled umbrella modes are mainly dominated by the L-0 buckets and the LP turbine, the change in coupled frequencies is small, as shown in Table 6. Especially, the coupled modes near 120Hz do not change, because these two modes are basically the blade umbrella mode.

Table 5 Temperature condition

	Test condition	Rated load
HP TB. Inlet	397.5°C deg	538.0°C deg
HP TB. Exhaust	218.6°C deg	296.9°C deg
IP TB. Inlet	390.5°C deg	566.0°C deg
IP TB. Exhaust	218.8°C deg	337.8°C deg
LP TB. Exhaust	35.1°C deg	33.0°C deg

Table 6 Frequency change under a rated load

Mode	Measured under no load	Expected change under rated condition
Out-of-phase		
ALP	107.3Hz	−0.2Hz
BLP	108.3Hz	−0.1Hz
In-phase		
ALP	121.8Hz	0.0Hz
BLP	123.1Hz	0.0Hz

5 CONCLUSION

The quasi-modal reduction technique and FEM model were used to construct an analytical model for the blade-rotor coupled torsional vibration of a steam turbine generator of the Matuura Power Station. A single rotor test was executed in order to evaluate umbrella vibration characteristics. Based on the single rotor test results and the quasi-modal procedure, the total rotor system was analyzed to predict coupled torsional frequencies. Finally, field measurement of the vibration of the last-stage buckets was made which confirmed that the double synchronous resonance is 124.2Hz, meaning that the machine can be safely operated. The measured eigen values are very close to the predicted value. The single rotor test and this analytical procedure thus proved to be a valid technique to estimate coupled torsional vibration.

6 ACKNOWLEDGEMENT

The authors would like to express their thanks to the engineers of Matuura Power Station of Kyushu Electric Power C., Inc., and field test crews of Hitachi Ltd..

7 REFERENCES

[1] Watanabe, T., et al. : Influence of High-speed Reclosing on Turbine Generators and the Shaft System, Hitachi Review, Vol.27, No.1, PP.33-38 (1978)

[2] Okabe, A., et al. : COUPLED VIBRATION ANALYSIS: TORSIONAL VIBRATION OF TURBINE-GENERATOR-BLADE COUPLED SYSTEM, THE 1989 ASME DESIGN TECHNICAL CONFERENCES-12th BIENNIAL CONFERENCE ON MECHANICAL VIBRATION AND NOISE, Vol. 18-1, PP.135-140 (1989)

[3] Matsushita, O., et al : Torsional Vibration Analysis of Turbine-Generator-Blade Coupled System, Proc. Am. Power Conf. Vol 41 (1989) (to be published)

THE EFFECTS OF MANUFACTURING TOLERANCES ON THE VIBRATION OF AERO-ENGINE ROTOR-DAMPER ASSEMBLIES*

J.E.H. Sykes and R. Holmes
Department of Mechanical Engineering
University of Southampton
Southampton, England

A range of rotor assemblies incorporating one and two squeeze-film dampers with various static misalignments is investigated. Waterfall diagrams are constructed which demonstrate the effects of such misalignment and damper support flexibility on the nature and severity of subsynchronous resonance and jump phenomena. Vibration signatures of similar rotor-bearing assemblies are shown to contrast strongly due to different accumulations of tolerances during manufacture, fitting and operation.

21

Notation

Notation	Description	Unit
A_1	SFD1 Bearing Factor, $\pi.\mu.R_1(l_1/c_1)^3 f^2/b\sqrt{(k_2.I)}$	-
A_2	SFD2 Bearing Factor, $\pi.\mu.R_2(l_2/c_2)^3 b/\sqrt{(k_2.I)}$	-
a,b	Rig Dimensions	m
c	SFD Radial Clearance	m
d	Rig Dimension	m
e	SFD Eccentricity	m
E_0	SFD Static Eccentricity Ratio	-
f	Rig Dimension	m
G	SFD Groove Depth	m
G_w	SFD Groove Width	m
I	Rotor Moment of Inertia per land	kg.m^2
$\underline{k}$	Flexible Bearing Support Stiffness per land	N/m
$\underline{k_1}$	Non-Dimensional Stiffness per land, $k_1.f^2/(I.w^2)$	-
k_2	Non-Dimensional Stiffness per land, $k_2.b^2/(I.w^2) = (w/w_n)^{-2}$	-
l	SFD Land Width	m
N	Number of Lands per SFD	-
P1	SFD Radial Film Force per land	N
P2	SFD Tangential Film Force per land	N
P_c	Rotor Mass Unbalance Force per land	N
Psup	SFD Oil Supply Pressure	N/m^2,psi
Q_{c2}	Non-Dimensional Unbalance Force, $P_c.a.b/(I.c_2.w^2)$	-
Q_s	Non-Dimensional Static Force, $m.g.d.b/(I.c_2.w^2)$	-
R	SFD Mean Radius	m
t	Time	s
w	Rotor Rotational Speed	rad/s
w_n	Rotor-Bearing Assembly First Bounce Vibration Mode Frequency (Configurations 1a,b)	rad/s
Z	Dummy parameter	-
α	SFD Journal Attitude Angle	rad
$\pounds$	SFD1 non-dimensional preload (gravity offset), $\{[m.g.d./(b.k_2)] + c_2\}.f/(b.c_1)$	-
$\in$	Eccentricity Ratio, e/c	-
μ	Oil Dynamic Viscosity	Ns/m^2
$\cdot$	Derivative with repect to time, t	1/s
$'$	Derivative with respect to Non-Dimensional Time, w.t	1/rad
$^-$	Non-Dimensional Quantity	
$_1$	After a parameter denotes SFD1	
$_2$	After a parameter denotes SFD2	

Abbreviations

Abreviation	Description
c/min	Cycles Per Minute
EO	Engine Order
DOF	Degree(s) of Freedom
FFT	Fast Fourier Transform
RRG	Rotor Relative to Ground
SERC	Science & Engineering Research Council
SFD	Squeeze-Film Damper

INTRODUCTION

The major source of aero-engine rotor vibration is the state of rotor balance which can alter progressively during service and sharply as a result of minor damage. Even with well balanced rotors sudden unexpected non-linear vibration phenomena, such as jumps and subharmonic resonances, can occur. The most prolific sources of non-linearity are the squeeze-film dampers which surround some of the bearings.

The squeeze-film damper, SFD has been applied in a wide range of rotor-bearing assemblies to attenuate resonant vibration and to combat rotor instability. The ever increasing demand for high performance indicates that rotor vibration isolation utilising squeeze-film dampers will remain a prominent feature of future turbomachinery designs.

SFD response characteristics and non-linear jump phenomena have been demonstrated by numerous workers. White (Ref 1) cited jumps in a vertical rotor rig and Simandiri et al (Ref 2) studied jumps on an idealised, horizontal rotor, single SFD rig, aligned to exhibit synchronous circular orbits. Holmes et al (Ref 3) obtained jump phenomena with a horizontal rotor rig involving a rigidly housed SFD, carrying appreciable rotor weight. Actual engine tests have demonstrated jump phenomena, such as observed by Gunter et al (Ref 4).

The operation of a SFD is least beneficial when subharmonic resonances, sometimes dominating the synchronous response, develop in conditions of light damping. Subharmonics of orders up to four were cited by Nikolajsen et al (Ref 5) from a flexible rotor rig. Gunter et al (Ref 4) carried out numerical time marching to observe the transient analysis of a rotor which indicated some half engine order subharmonic resonance in its SFD orbits.

The explanation of such jump phenomena and subharmonic resonances observed in engines employing multiple shaft, multiple SFD assemblies is difficult. Previous simulation of such phenomena on simplified test rigs has met with limited success. Consequently, existing literature has failed to address this problem comprehensively. Appreciation of the relationship between the basic components of assemblies and their potential for introducing misalignment between SFDs provides an insight into the complex responses observed in practice.

THE TEST FACILITY

Aero-engine rotor operating speeds are often above one or more rigid body modes and below any significant flexural mode. Because of this damping can be successfully introduced in the bearing supports to attenuate vibration induced by unbalance.

To create a realistic configuration a three-bearing rigid rotor assembly incorporating the essential features of a small aero-engine was utilised, Fig 1. This test rig was used to investigate the operation of the SFD's, 1, at two of its three rolling-element bearings, 2. The self alignment capability of the bearing, 3, constituted a pivot about which an antisymmetric, or conical mode of vibration occurred when the rotor, 4, was acted upon by a force arising from rotation of the unbalance mass, 5.

23

Flexible bars, 6, simulated pedestal flexibility and were mounted into heavy foundation blocks, 7, which represented ground. Comparisons between different rig configurations (Table 1) allowed the influence of individual assembly components and in-service assembly misalignment conditions to be analysed. Fig 2 gives a schematic diagram of a SFD and relevant dimensions are given in Appendix 1.

Tests were carried out employing four unbalance masses. Values of the unbalance parameter, Q_{c2} ranged from 0.245 to 0.733, or 25g to 75g mass, respectively and rotor speed from 900 to 4860 c/min. Oil supply pressures were varied between 2 psi and 24 psi when one SFD was active and up to 15 psi with two SFDs active. The tests were analysed by studying the SFD orbit magnitudes and the phase angles between SFD eccentricity vectors and the unbalance. The rotor speed was represented as a frequency ratio, by dividing by the first bounce mode frequency of configuration 1a (Table 1), namely 32.4 Hz. Rotor displacements relative to ground and relative to the SFD2 housing were sampled by a spectrum analyser, utilising the Hanning time window.

The transient response of the rig, when stationary, to impulses from a soft hammer enabled its static natural frequencies to be determined.

Responses for configurations 1a through to 2b demonstrated a lowest natural frequency at 32.4 Hz, in both the horizontal (x) and the vertical (y) directions. Higher natural frequencies were 200 Hz or more. Configurations 3a and 3b gave a lowest natural frequency at 34.8 Hz in the x direction and 36.8 Hz in the y direction, indicating a degree of anisotropy.

THEORETICAL CONSIDERATIONS

The theoretical analysis assumed the following;

1. The Reynolds Equation and the Short Bearing approximation apply.
2. The rotor remains rigid.
3. The flexible bars contribute a constant, linear radial stiffness to the system.

The rotor-bearing assembly was modelled as a dynamic system, Fig 3, with the relevant equations summarised in Appendix 2.

Simpson's numerical integration procedure was employed to derive film force predictions at each step of a Runge-Kutta computation scheme. Following work by Feng and Hahn (Ref 6) a cavitation pressure, Pmin of absolute zero (-14.7 psi gauge) was adopted.

The results of prime interest were the displacement orbit size and phase with respect to unbalance, to be compared with the experimentally observed rig behaviour.

Software development provided waterfall diagrams and, with a frequency resolution of 1.0 Hz, have provided sufficient spectral information at reasonable mainframe speeds and data storage requirements. Attention was given to the case with unbalance, Q_{c2} equal to 0.611 as this illustrated all the non-linear phenomena encountered during testing.

24

TABLE 1   Test Rig Configurations

Test Rig Configuration	Static Set Up		Simple Representative Rig Diagram
	E_{o1}	E_{o2}	
1a	0.0	-	ROTOR SFD1 PIVOT k_2
1b	0.4,0.8	-	
2a	0.0,0.5	1.0	ROTOR SFD1 SFD2 PIVOT k_2
2b	1.0	0.0	
3a	1.0	1.0	ROTOR SFD1 SFD2 PIVOT k_1 k_2
3b	0.0	1.0	

EXPERIMENTAL & THEORETICAL RESULTS

The motion of the rotor in configuration 1a was 'well behaved' for reasonably low unbalance factors (Fig 4a), being attenuated by the damper action of SFD1. When the unbalance factor was above a certain level then SFD1, even with increased supply pressure, had difficulty in maintaining an acceptable, damped response and jump phenomena became a feature. This response could take the form of a high vibration level persisting through unity frequency ratio without any jump down. Alternatively, the high response could be abruptly reduced by a jump down to some lower vibration level. Increasing oil pressure reduced the peak eccentricity and the size of the accompanying phase jump to some degree. The orbits were almost circular in shape.

At speeds higher than the minimum jump frequency, any persistently large rotor excursions were quite stable and an impact delivered to the rotor by a soft hammer could not induce a jump down. After inversion at high speed, subsynchronous response occurred at a frequency equal to the natural frequency, Fig 5a. All of the above observations were supported by theoretical predictions (Fig 4b and Fig 5b).

With rig configuration 1b the effect of increasing the static eccentricity, E_{o1} in SFD1 was to generally increase the damping. For E_{o1} 0.8 configuration 1b produced a jump down with increasing speed when the unbalance factor, Q_{c2}, was only 0.490 (Fig 6a) and strong subharmonic resonance developed at the higher speeds. This is clearly demonstrated in the bottom right experimental orbit (w/w_n = 2.253) of Fig 6c. Again

theoretical predictions supported the experimental findings (Figs 6b and 6d).

The experimental results for configuration 2a showed that the rig response was acceptably low for reasonably small unbalance factors, being attenuated by the damper actions of SFD1 and SFD2. Increasing oil pressure required an increase in the unbalance at which bistable operation occurred, introducing jumps. Subsynchronous activity persisted at speeds above twice the first bounce mode frequency (Fig 7a), and higher order vibrations were present over most of the speed range. Again theoretical predictions (Fig 7b) supported the experimental results.

The effect of introducing a static eccentricity, E_{01} of 0.5, to configuration 2a was to change the experimental jump characteristics and the nonsynchronous frequency response, Fig 8a. A jump up and a jump down were observed above the first bounce mode frequency. Half engine orders of large amplitude were present at rotor speeds around 2.5 times the first non-rotating bounce frequency. Theoretical predictions (Fig 8b) again show good agreement.

Experimental results revealed that the change in static misalignment conditions from configuration 2a, constituting configuration 2b, removed the high synchronous amplitudes associated with the first bounce frequency, leaving an apparently well damped response. However, with high unbalances and above the first bounce frequency, a sudden jump up in vibration amplitude with increasing speed was demonstrated, Fig 9a. This speed decreased as unbalance was increased. Corresponding theoretical results are given in Fig 9b.

The most significant result from configurations 3a and 3b was that rotor excursions were much larger than previously experienced, Fig 10. Jump phenomena were still in evidence but below the static natural frequency of the assembly. 'Safe' operation at speeds above the first bounce mode was achievable for all but the highest unbalance. The major effect of statically offloading, or centralising SFD1, configuration 3b, was to appreciably reduce the subsynchronous and higher engine order activity. Configuration 3a exhibited some significant 1/2 EO at just higher than the jump speed. This subharmonic was absent from the corresponding response in configuration 3b.

NON-LINEAR PHENOMENA

The jump up with decreasing speed or jump down with increasing speed above the first bounce mode frequency corresponds to the classical non-linear 'hardening spring' response. The difference in the two speeds is the effective range of the bistable region. Equally, a jump up with increasing speed might be attributed to a non-linear 'softening spring' effect.

In addition there is experimental evidence (Ref 3) that sudden venting of the SFD from atmosphere changes the effective cavitation conditions, and could promote jump up. Oil-film pressure measurements taken for configuration 2b indicated that the minimum pressure rose after jump up on run up. A limited hysteresis in the rotor speeds, of about 4 Hz at most, was noted between the jump up on run up and the jump down on run down.

26

Subharmonic resonances of half engine order have been demonstrated both experimentally and theoretically. Non-synchronous activity at 3/2 EO, 5/2 EO and 7/2 EO accompanied these subharmonics.

A statically centred SFD in configurations 1a and 2a gave rise to weak subsynchronous resonance at the static natural frequency, Figs 5 and 7. Static eccentricity applied to the same SFD increased its non-linearity and excited strong half engine order subharmonics, this time corresponding to the dynamic natural frequency, determined by the stiffnesses of both the static components and the SFD's, Figs 6 and 8.

PRACTICAL IMPLICATIONS ARISING FROM THE RESULTS

Jump phenomena can lead to high transmitted forces and sudden changes in engine vibration. Non-synchronous response causes fluctuating rotor stresses in flexible shafts. It also leads to subharmonic resonances, sometimes larger than the resonances developed by unbalance.

The present research has demonstrated the ability of a range of rotor-bearing assemblies, incorporating unsealed SFDs, to exhibit a number of undesirable non-linear phenomena.

Aero-engine rotor assemblies employ one or more SFD's per rotor, each within a bearing pedestal characterised by a certain stiffness. A degree of misalignment in three-bearing assemblies is inevitable due to the 'stack up' of tolerances and the effects of high speed manoeuvres of military aircraft may serve to further affect the bearing alignments.

Most assemblies employ sealed SFD's to improve damping capacity and strong jump phenomena are not always a problem. However, there have been many reported instances and results emanating from this research indicate the physical mechanisms which promote such phenomena.

Holmes and Dogan's work (Ref 3) indicated that a jump up on run up can exist when a rotor is supported by a rigidly housed SFD and high vibration amplitudes can prevent higher speeds being attained. The same SFD, when mounted flexibly can respond without a jump up but non-synchronous rotor centre orbits can be introduced at speeds around the assembly's natural frequency. Low vibration levels can, however, be achieved at speeds above the natural frequency.

Based on the present research, assemblies with a single SFD, centred by a flexible rotor support, are likely to exhibit jumps only when the unbalance is relatively high, probably outside acceptable contractual limits. These jumps are analogous to the classical non-linear hardening spring response and arise from the stiffness property of a cavitated squeeze-film which increases with speed. On the other hand, the same assemblies with the SFD statically off-centred are likely to demonstrate that low unbalance, possibly within contractual limits, can excite jumps and strong subharmonic resonance.

Some assemblies incorporate two SFD's with very different housing supports, for example, one rigidly housed and the other flexibly housed. With the former statically centred and the latter carrying the rotor weight the

27

response might well be governed by the former, the latter having little influence. Jump phenomena will occur around the first bounce mode frequency. At high speed, after jump down, satisfactory operation should be possible with low amplitude subsynchronous activity at the bounce mode frequency. Raising the housing of the rigidly-supported SFD will result in subharmonic resonance possibly dominating the synchronous response and degrading the vibration performance within the operating range.

By raising the rigidly mounted SFD housing further still, until it carries the static rotor weight and such that the flexibly supported SFD is centred, safe operation can only be guaranteed up to a certain speed, at which a strong jump up can be expected. On running down, the vibration will jump down at a lower speed. A static eccentricity applied to the flexibly-supported SFD may alleviate the jump or increase the speed at which it takes place due to some of the rotor weight being supported dynamically by this flexibly supported SFD.

The flexible supporting of both SFDs with similar support stiffnesses should give rise to desirable operation for all but a small speed range around the first bounce mode. It may be that jumps and subharmonic resonance at these speeds could be eliminated by additional damping from SFD sealing without degrading the performance within the rest of the speed range. Centralising one of the SFDs has the effect of reducing the subharmonic resonance at speeds around the first bounce mode.

The presence of half engine order subharmonic resonance dominating the synchronous response at speeds well above the bounce frequency would suggest that one of the SFDs was not supported flexibly enough and was neither fully eccentric, nor concentric in its housing. If, in another case, strong jumps up on acceleration were encountered at speeds well above the bounce mode, then it might be caused by a SFD housing support being too rigid for it to safely carry the rotor weight. Improvements might be achieved by off-loading the 'rigidly' housed SFD, softening its support or both.

CONCLUSIONS

The rig configurations have demonstrated a range of non-linear responses associated with aero-engine rotor-bearing assemblies and there is pleasing similarity between the experimental and theoretical responses. The experimental dependence of jump phenomena and subharmonic resonances upon SFD misalignment and housing support has been clearly illustrated in the theoretical results.

This work has provided an insight into the mechanism of SFD phenomena and the practical implications arising from these findings should be useful in the design of rotor-bearing assemblies.

REFERENCES

1.   WHITE D.C., Squeeze Film Journal Bearings, PhD Thesis, University of Cambridge, 1970.
2.   SIMANDIRI S. & HAHN E.J., Experimental Evaluation of the Predicted

Behaviour of Squeeze-Film-Bearing-Supported Rigid Rotors, IMechE,
J Mech Eng Science, Feb 1976, pp 109-117.

3. HOLMES,R. & DOGAN M., Investigation of a Rotor Bearing Assembly
Incorpoating a Squeeze-Film Damper Bearing, IMechE, J Mech Eng
Science, 1982, Vol 24, No 3, pp 129-137.

4. GUNTER E.J., BARRETT L.E. & ALLAIRE P.E., Design of Nonlinear Squeeze-
Film Dampers for Aircraft Engines, Trans ASME, J Lubric
Technology, 1977, pp 57-64.

5. NIKOLAJSEN J.L. & HOLMES R., Investigation of Squeeze-Film Isolators
for the Vibration Control of a Flexible Rotor, IMechE, J Mech Eng
Science, 1979, Vol 21, No 4, pp 247-252.

6. FENG N.S. & HAHN E.J., Effects of Gas Entrainment on Squeeze Film
Damper Performance, Trans ASME, J Tribology, 1987, Vol 109, pp
149-154.

APPENDICES

APPENDIX 1   SFD Geometry & Other Rig Parameters

SFD1 Damper Geometry

c_1	= 0.000254	(m)	$(l/c)_1$ = 44.2		(-)
$(l/R)_1$	= 0.144	(-)	G_1	= 0.002	(m)
Gw_1	= 0.004	(m)	N_1	= 2	(-)

SFD2 Damper Geometry

c_2	= 0.000216	(m)	$(l/c)_2$ = 41.6		(-)
$(l/R)_2$	= 0.132	(m)	G_2	= 0.002	(m)
Gw_2	= 0.004	(m)	N_2	= 2	(-)

Rig Parameters

a	= 1.019	(m)	b	= 0.9716	(m)
d	= 0.5434	(m)	f	= 0.5968	(m)
l	= 11.5	(kg.m² per land)	k_1	= 0.505	(MN/m per land)
k_2	= 0.505	(MN/m per land)	w_n	= 203.58	(rad/s)
μ	= 6.0	(cP average)			

APPENDIX 2   Equations of Motion

Equations of motion can be developed by taking moments about the pivot
bearing, referring to Figs 3a,b and c. Equations describing the rotor
motion at the SFD2 journal in a cartesian (x,y) coordinate system can be
written, non-dimensionally, as

Configurations 1a,b (Table 1)

$$y_2'' = Q_{c2}.\sin(w.t) - (\bar{k_2}.\mathcal{E}_1.\sin(\alpha_1))(c_1/c_2)(b/f)$$
$$- (c_1/c_2)(b/f)(\bar{P1_1}.\sin(\alpha_1) + \bar{P2_1}.\cos(\alpha_1)) - Q_s$$

$$x_2'' = Q_{c2}.\cos(w.t) - (\bar{k_2}.\mathcal{E}_1.\cos(\alpha_1))(c_1/c_2)(b/f)$$
$$- (c_1/c_2)(b/f)(\bar{P1_1}.\cos(\alpha_1) - \bar{P2_1}.\sin(\alpha_1))$$

Configurations 2a,b and 3a,b

$$y_2" = Q_{c2}.\sin(w.t) - (\overline{P1}_2.\sin(\alpha_2) + \overline{P2}_2.\cos(\alpha_2))$$

$$- (c_1/c_2)(b/f)(\overline{P1}_1.\sin(\alpha_1) + \overline{P2}_1.\cos(\alpha_1)) - Q_s$$

$$x_2" = Q_{c2}.\cos(w.t) - (\overline{P1}_2.\cos(\alpha_2) - \overline{P2}_2.\sin(\alpha_2))$$

$$- (c_1/c_2)(b/f)(\overline{P1}_1.\cos(\alpha_1) - \overline{P2}_1.\sin(\alpha_1))$$

where $\overline{P1,2}_2 = P1,2_2.b^2/(I.c_2.w^2)$

$\overline{P1,2}_1 = P1,2_1.f^2/(I.c_1.w^2)$

and $y_2", x_2" = \overset{..}{y_2}, \overset{..}{x_2}/(c_2.w^2)$

Variation in the SFD static misalignment conditions is achieved by employing the term $\mathcal{E}$. Thus, converting the cartesian rotor motion at SFD2 relative to ground to the SFD1 polar motion for configurations 2a and 2b;

where $Z = (f.c_2/b.c_1)$

$$\mathcal{E}y_1 = Z.\overline{y_2} - E_{o1} + \mathcal{E} \qquad \mathcal{E}y_1' = Z.y_2'$$

$$\mathcal{E}x_1 = Z.\overline{x_2} \qquad\qquad \mathcal{E}x_1' = Z.x_2'$$

$$\mathcal{E}_1 = (\mathcal{E}x_1^2 + \mathcal{E}y_1^2)^{1/2}$$

$$\alpha_1 = \arctan(\mathcal{E}y_1/\mathcal{E}x_1)$$

$$\mathcal{E}_1' = (\mathcal{E}x_1.\mathcal{E}x_1' + \mathcal{E}y_1.\mathcal{E}y_1')/\mathcal{E}_1$$

$$\alpha_1' = (\mathcal{E}x_1.\mathcal{E}y_1' - \mathcal{E}y_1.\mathcal{E}x_1')/\mathcal{E}_1^2$$

It has been shown (Ref 3) that the SFD housing mass of the test facility for a series SFD and spring configuration has little influence on the rotor dynamics. Thus, neglecting the SFD2 housing mass the force prevailing in the spring, k_2 must equal and oppose the resultant SFD2 film force. Therefore, we can conclude that, for Configurations 2a,b and 3a,b,

$$\overline{k_2}(\overline{y_2} - \mathcal{E}_2.\sin(\alpha_2)) = \overline{P1}_2.\sin(\alpha_2) + \overline{P2}_2.\cos(\alpha_2)$$

$$\overline{k_2}(\overline{x_2} - \mathcal{E}_2.\cos(\alpha_2)) = \overline{P1}_2.\cos(\alpha_2) - \overline{P2}_2.\sin(\alpha_2)$$

and, similarly, for Configurations 3a,b only,

$$\overline{k_1}(\overline{y_1} - \mathcal{E}_1.\sin(\alpha_1)) = \overline{P1}_1.\sin(\alpha_1) + \overline{P2}_1.\cos(\alpha_1)$$

$$\overline{k_1}(\overline{x_1} - \mathcal{E}_1.\cos(\alpha_1)) = \overline{P1}_1.\cos(\alpha_1) - \overline{P2}_1.\sin(\alpha_1)$$

where $\overline{x_1} = \overline{x_2}(c_2/c_1)(f/b)$

$\overline{y_1} = \overline{y_2}(c_2/c_1)(f/b)$
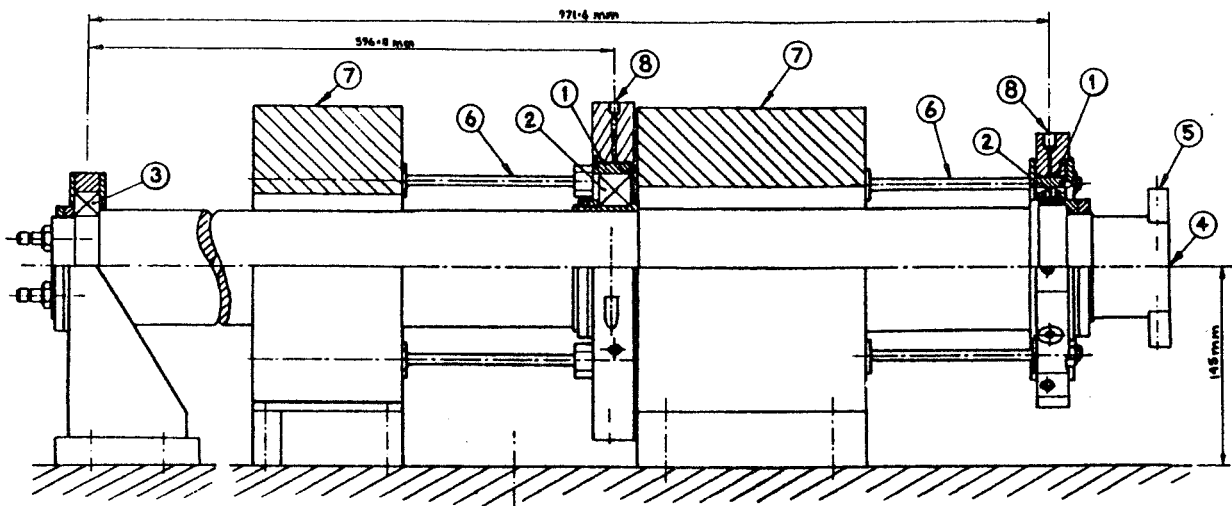
1	Squeeze-Film Damper	5	Unbalance Mass
2	Rolling Element Bearing	6	Flexible Bar
3	Self Aligning Bearing	7	Foundation Block
4	Rotor	8	Oil Supply Port

Fig 1   Details of Fully Assembled Experimental Rig
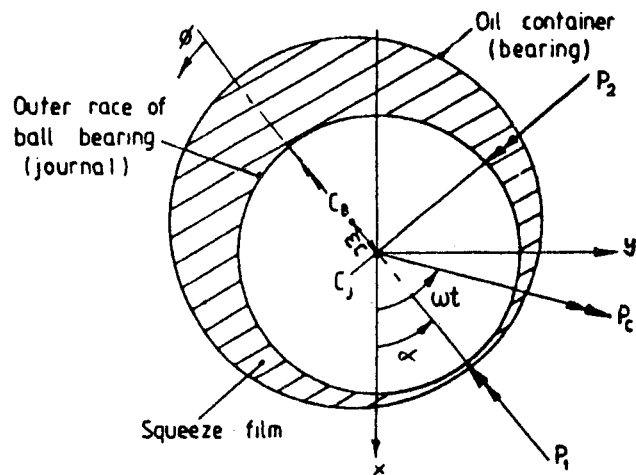
Fig 2   The Squeeze-Film Damper
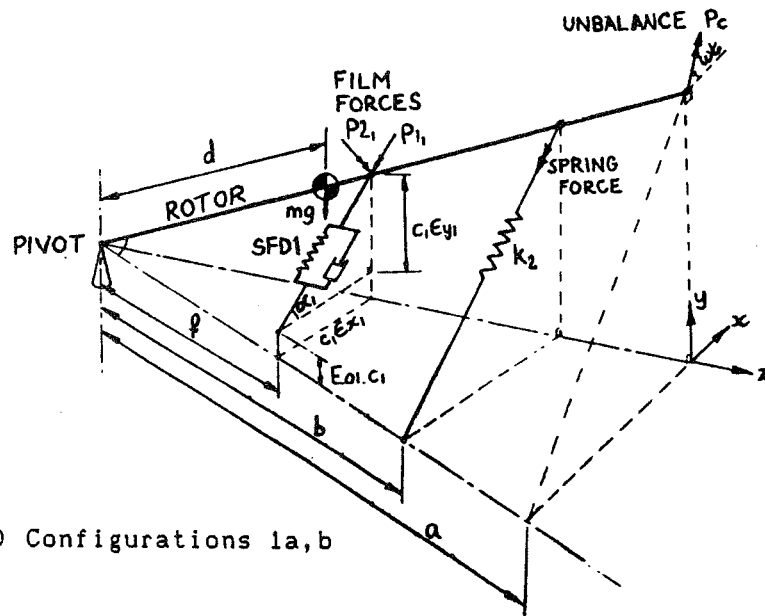
(a) Configurations 1a,b

(b) Configurations 2a,b

(c) Configurations 3a,b

Fig 3   Rig Model Diagrams
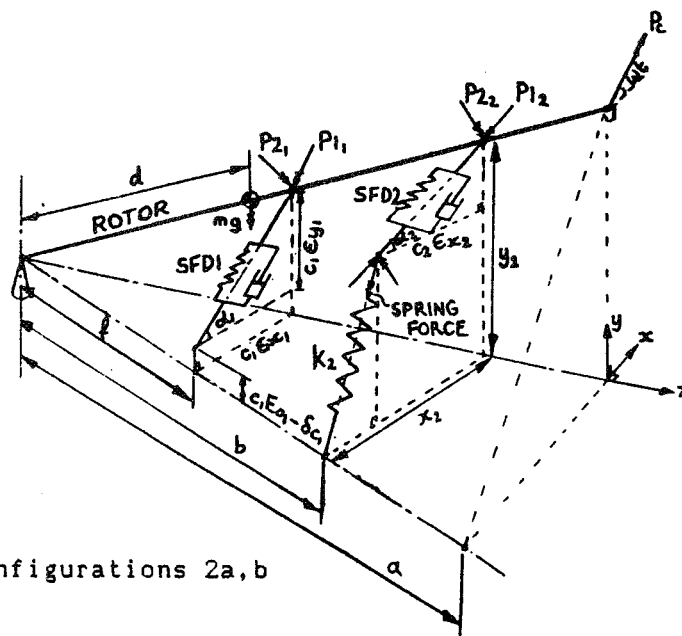
Fig 4a

SQUEEZE-FILM DAMPER SFD1   (0.5mm Groove Depth)

EXPERIMENTAL RESULTS

	△		▽		✕	
A =	0.2132E	-1	0.2132E	-1	0.2132E	-1
Qc2=	0.7332E	0	0.4901E	0	0.2450E	0
Eo =	0.0000E	0	0.0000E	0	0.0000E	0
Psup=	0.2000E	1	0.2000E	1	0.2000E	1	(psi)
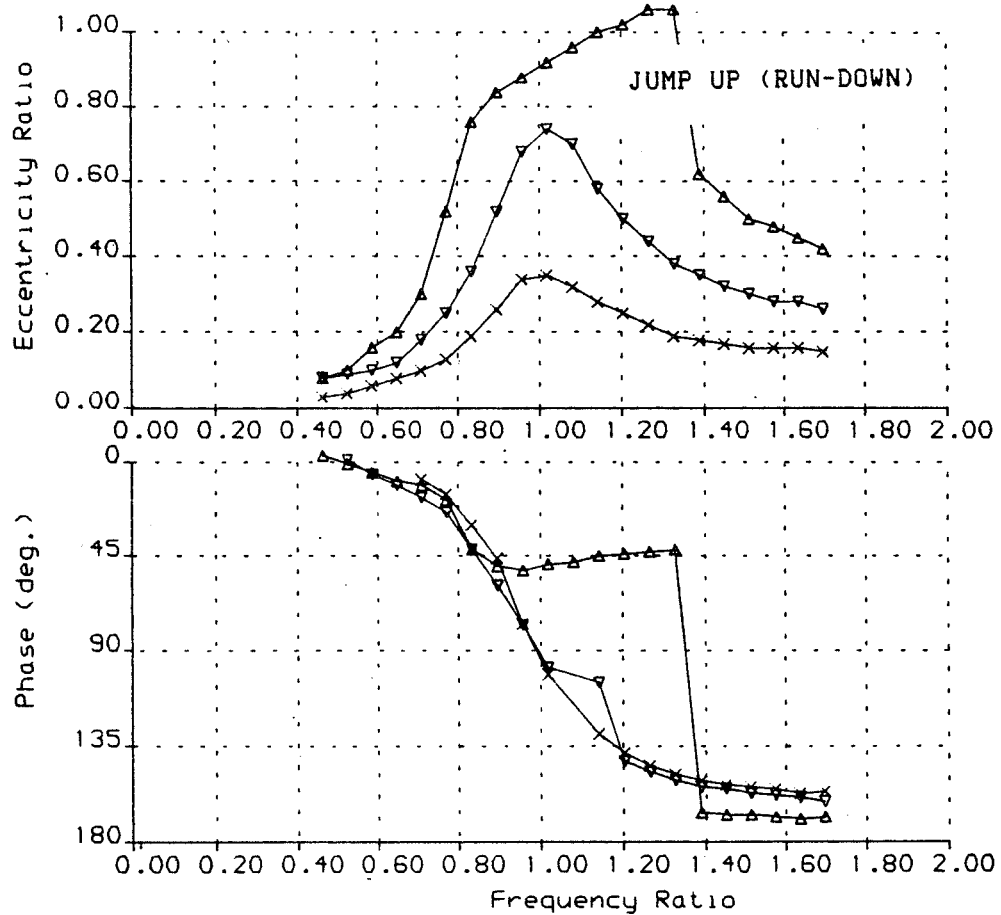
ROTOR-BEARING ASSEMBLY RESPONSE TO UNBALANCE
SQUEEZE-FILM DAMPER RESEARCH   Rig Config. 1a

34

Fig 4b

SQUEEZE-FILM DAMPER SFD1

THEORETICAL NUMERICAL SOLUTION

	Δ	▽	×	▢
A =	0.2132E -1	0.2132E -1	0.2132E -1	0.2132E -1
Qc2=	0.7332E 0	0.6107E 0	0.4901E 0	0.2450E 0
Eo =	0.0000E 0	0.0000E 0	0.0000E 0	0.0000E 0
Psup=	0.2000E 1	0.2000E 1	0.2000E 1	0.2000E 1 (psi
Pmin=	-.1470E 2	-.1470E 2	-.1470E 2	-.1470E 2 (psi
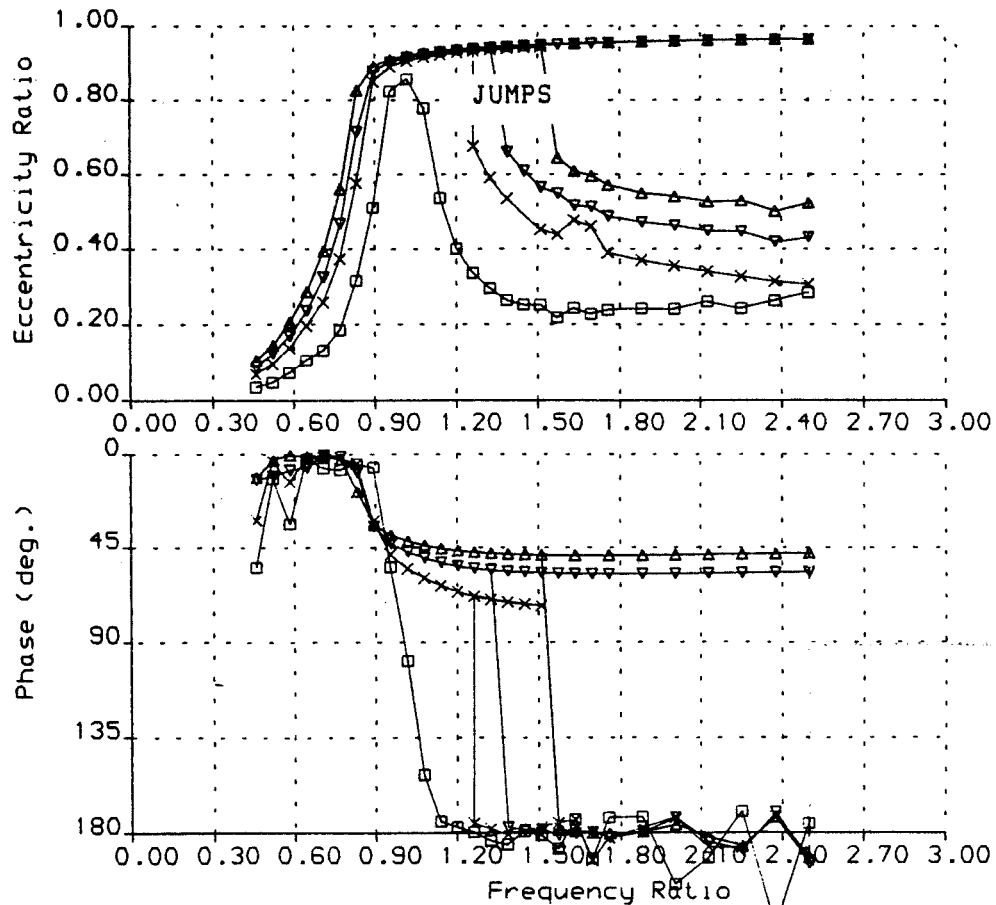
JUMPS

ROTOR-BEARING ASSEMBLY RESPONSE TO UNBALANCE
SQUEEZE-FILM DAMPER RESEARCH   Rig Config. 1a

35
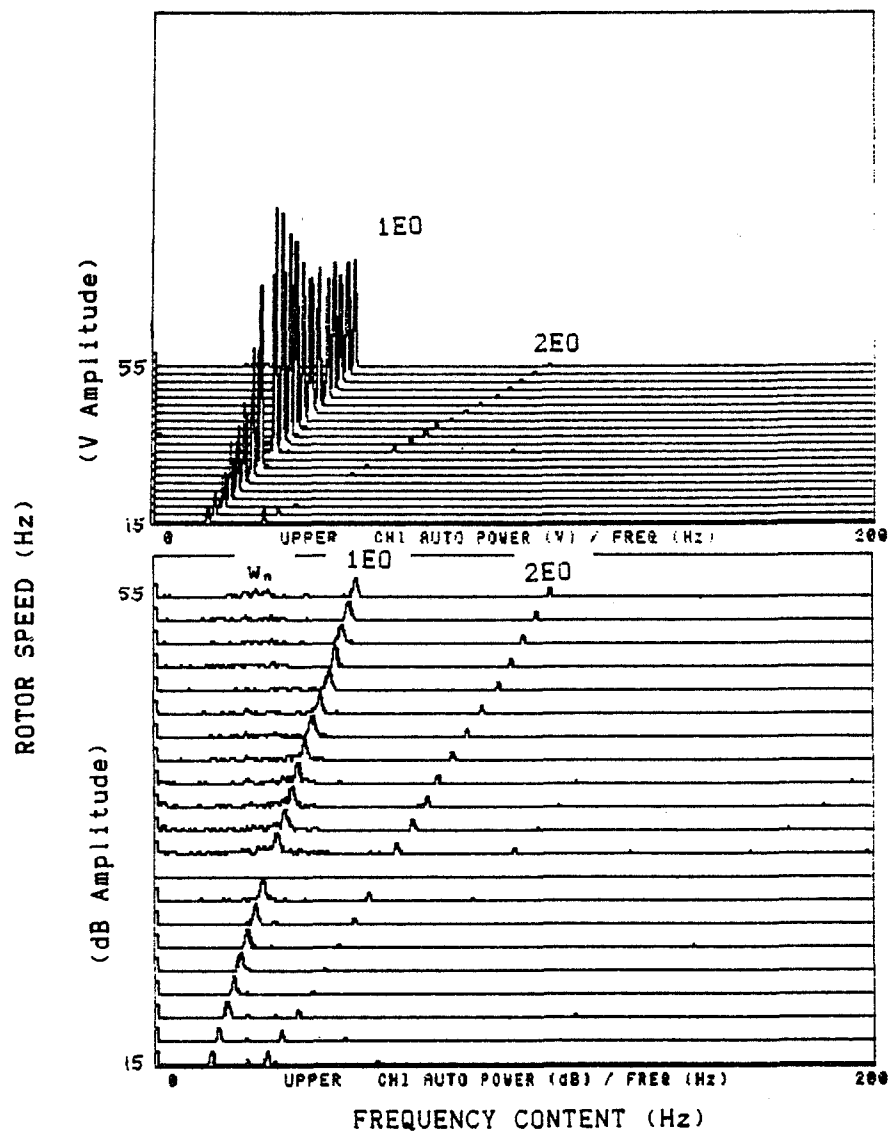
Experimental Waterfall Diagram

(a)

Configuration 1a (Q_{c2}=0.490, Psup=2psi)

Fig 5

$$
\begin{aligned}
A &= 0.213200E-1 \\
Qc2 &= 0.490097E\ 0 \\
Eo &= 0.000000E\ 0 \\
Psup &= 0.200000E\ 1\ (psi) \\
Pmin &= -0.147000E\ 2\ (psi)
\end{aligned}
$$
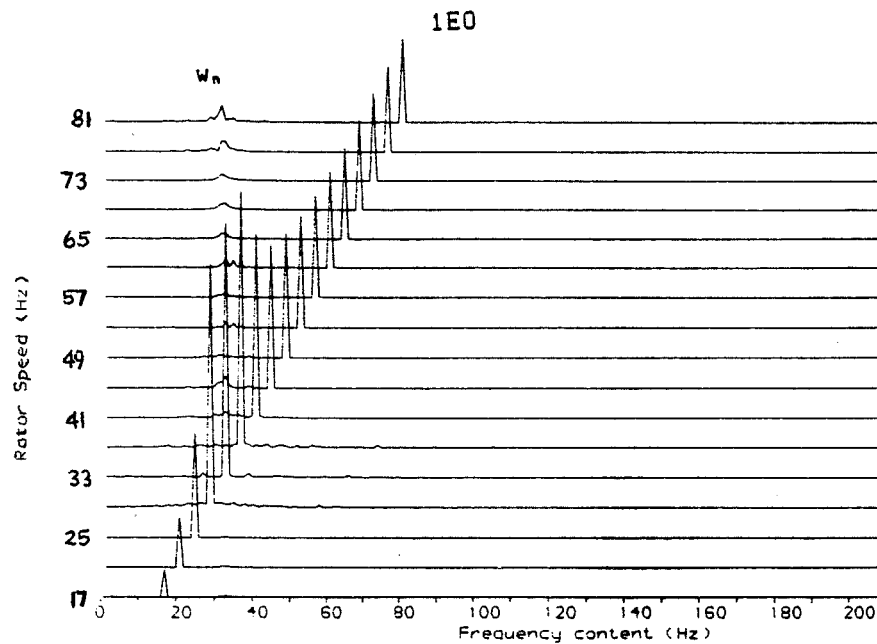
PREDICTED WATERFALL DIAGRAM
SQUEEZE-FILM DAMPER RESEARCH: Rotor-Bearing Response

(Linear Amplitude)

Theoretical Waterfall Diagram

(b)

ROTOR SPEED (Hz)

(V Amplitude)

1EO

2EO

73

17

UPPER   CH1 AUTO POWER (V) / FREQ (Hz)   200

1/2EO __ 1EO __ 3/2EO

73

(dB Amplitude)

17

UPPER   CH1 AUTO POWER (dB) / FREQ (Hz)   200

FREQUENCY CONTENT (Hz)

Experimental Waterfall Diagram

(a)

A   =   0.213200E -1

Q_{c2} =   0.490097E 0

E_0 =   0.800000E 0

P_{sup} =   0.200000E 1 (psi)

P_{min} = -0.147000E 2 (psi)

1EO

1/2EO

3/2EO   2EO

81

73

65

Rotor Speed (Hz)

57

49

41

33

25

17

0   20   40   60   80   100   120   140   160   180   200

Frequency content (Hz)

PREDICTED WATERFALL DIAGRAM
SQUEEZE-FILM DAMPER RESEARCH: Rotor-Bearing Response

(Linear Amplitude)

Theoretical Waterfall Diagram

(b)
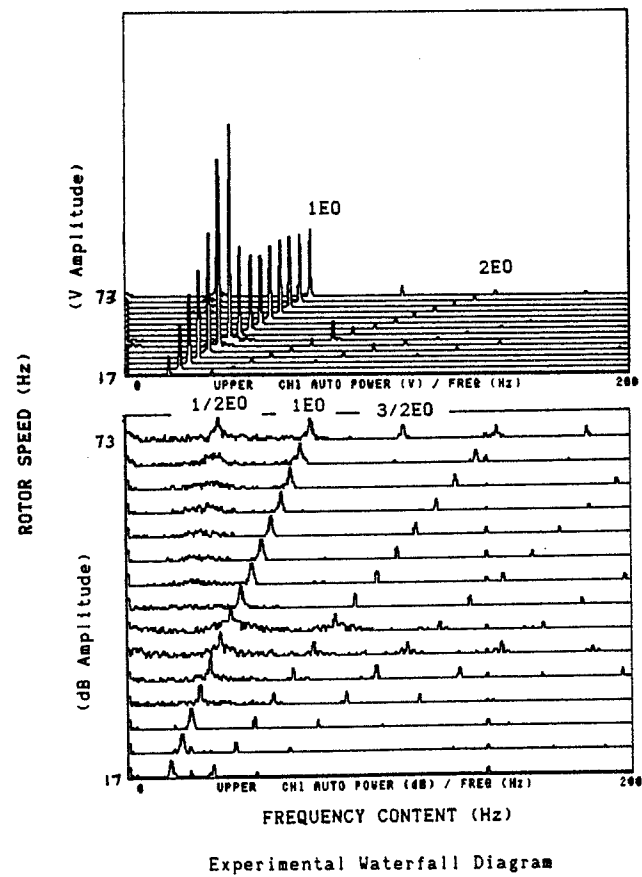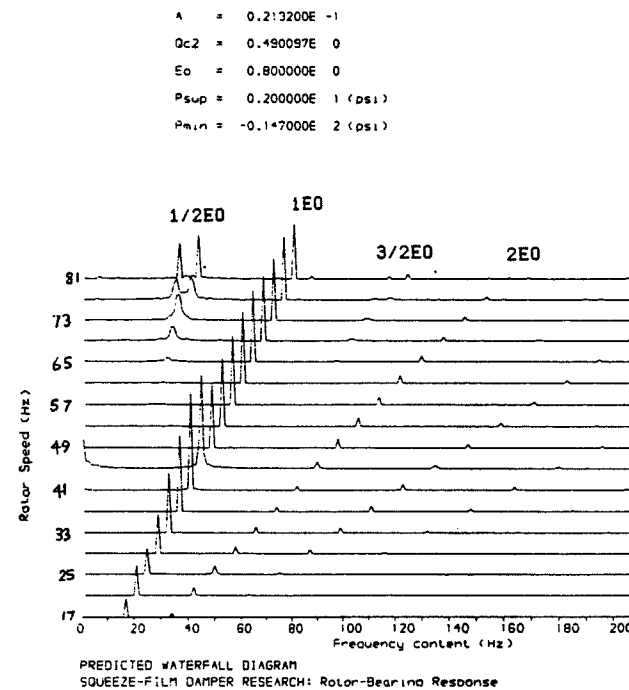
Configuration 1b (Q_{c2}=0.490, Psup=2psi, E_{01}=0.8)

Fig 6
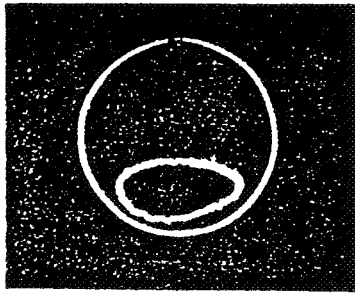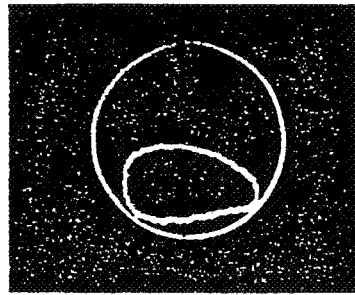
29 Hz (W/Wn = 0.895)   33 Hz (W/Wn = 1.019)   41 Hz (W/Wn = 1.265)
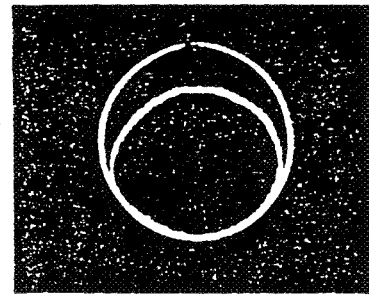
ROTOR SPEED
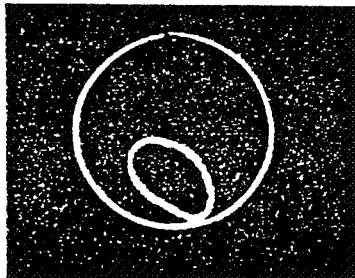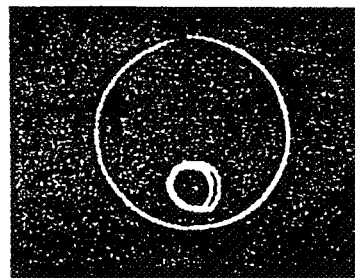
43 Hz (W/Wn = 1.327)   65 Hz (W/Wn = 2.006)   73 Hz (W/Wn = 2.253)
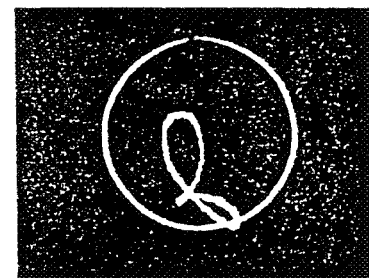
(c) SFD1 EXPERIMENTAL ORBITS (Configuration 1b, Qc2 = 0.490, Psup = 2psi, Eo1 = 0.8)
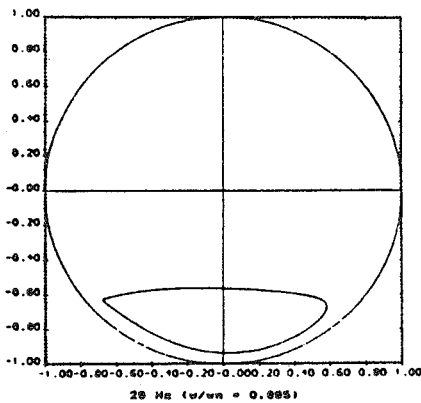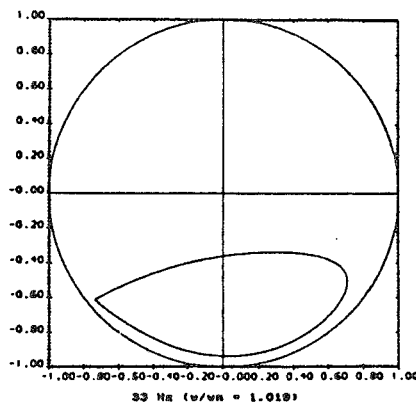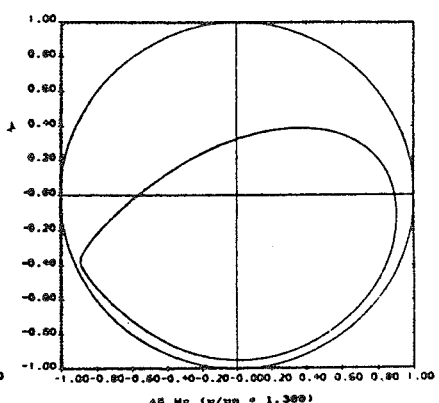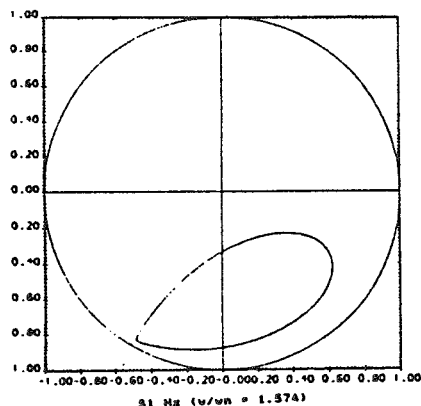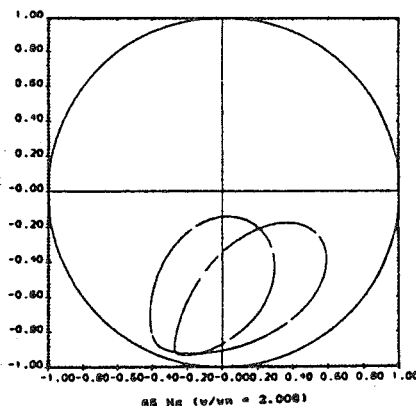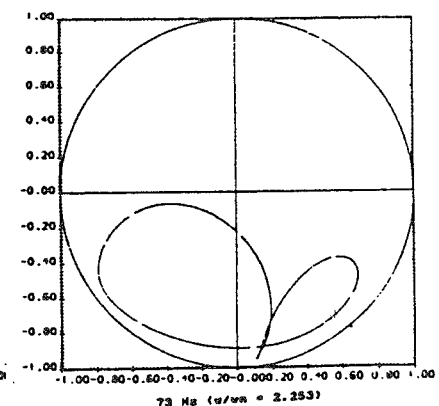
(d) SFD1 THEORETICAL ORBITS (Configuration 1b, Q_{c2}=0.490, Psup=2psi, Eo_1=0.8)

39

Experimental Waterfall Diagram

41

A   = 0.213200E -1
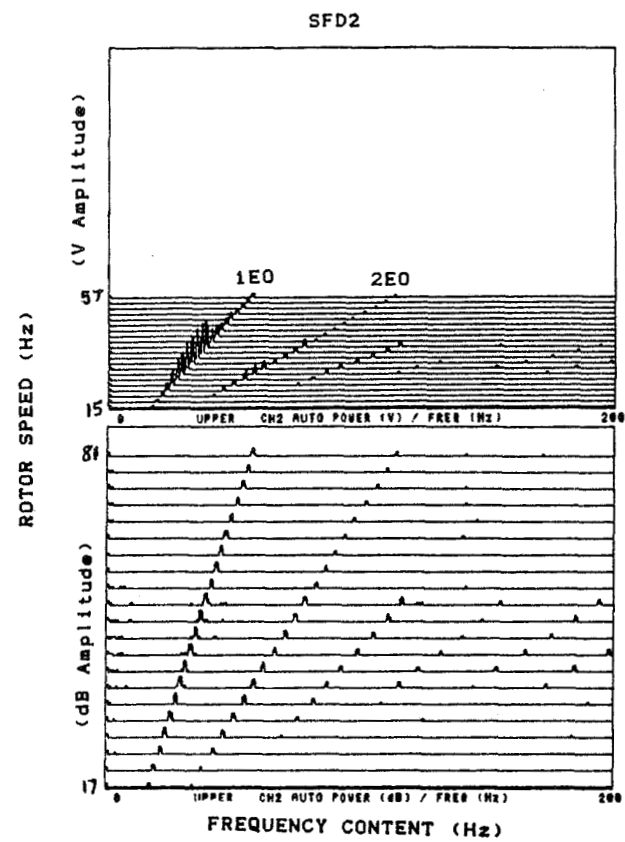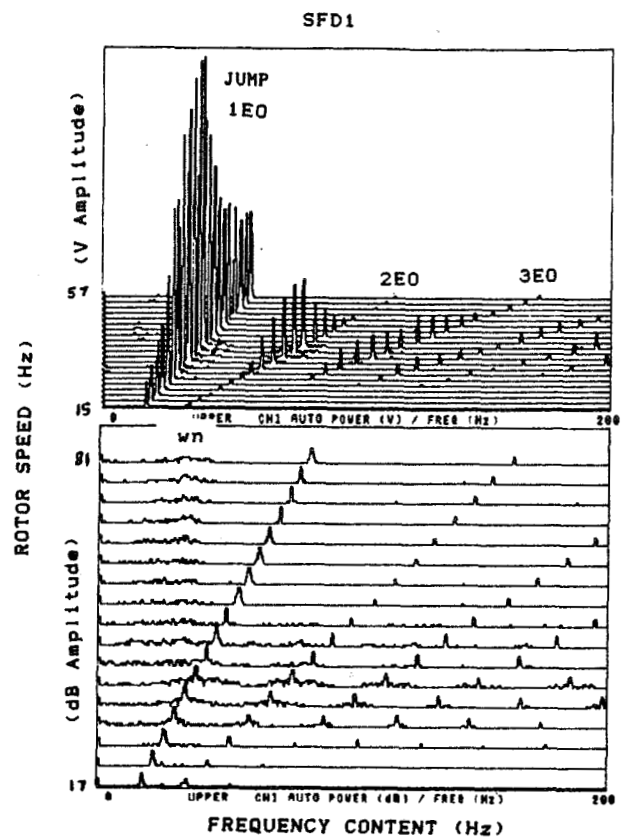
Qc2   = 0.610707E 0

Eo   = 0.000000E 0

Psup = 0.200000E 1 (psi)
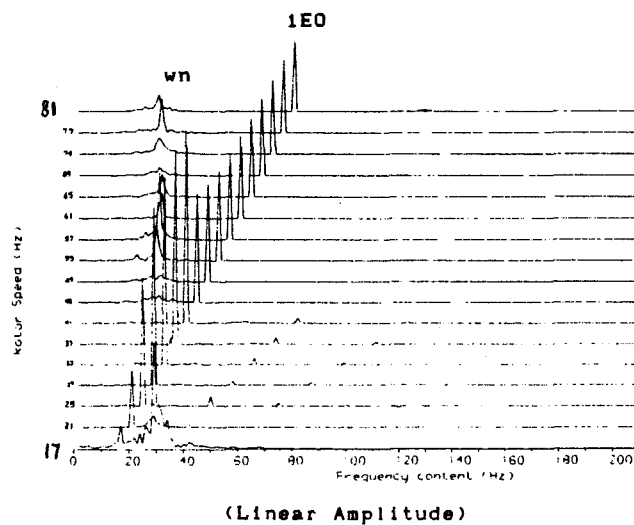
Pmin = -0.147000E 2 (psi)

A   = 0.401000E -1

Qc2   = 0.610707E 0

Eo   = 0.100000E 1

Psup = 0.200000E 1 (psi)
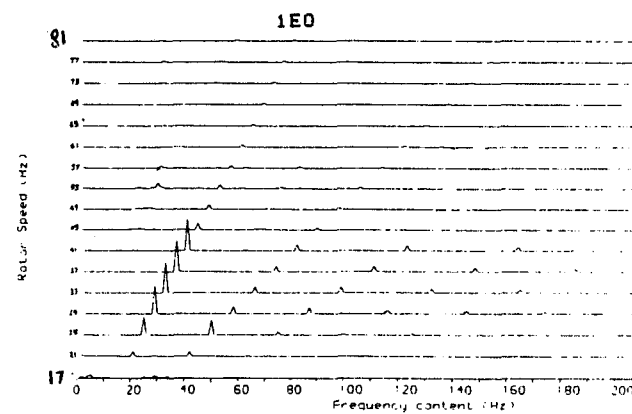
Pmin = -0.147000E 2 (psi)

1EO

wn

1EO

(Linear Amplitude)

(Linear Amplitude)

SFD1

(b)

SFD2

Theoretical Waterfall Diagram

Configuration 2a (Q_{c2}=0.611, Psup=2psi, E_{o1}=0.0)

Fig 7

SFD1

SFD2

JUMP

JUMP

1EO

2EO

(V Amplitude)

67

15

ROTOR SPEED (Hz)

UPPER CH1 **** OWER (V) / ERER (H1)

1/2EO   1EO   3/2EO

81

17

(dB Amplitude)

UPPER CH1 AUTO POWER (dB) / FRER (Hz)

FREQUENCY CONTENT (Hz)

1EO

2EO

(V Amplitude)

57

15

ROTOR SPEED (Hz)

UPPER CH2 AUTO POWER (V) / FREG (Hz)

81

17

(dB Amplitude)

UPPER CH2 AUTO POWER (dB) / FREG (Hz)

FREQUENCY CONTENT (Hz)

(a)

Experimental Waterfall Diagram

(Linear Amplitude)   (Linear Amplitude)

SFD1   (b)   SFD2
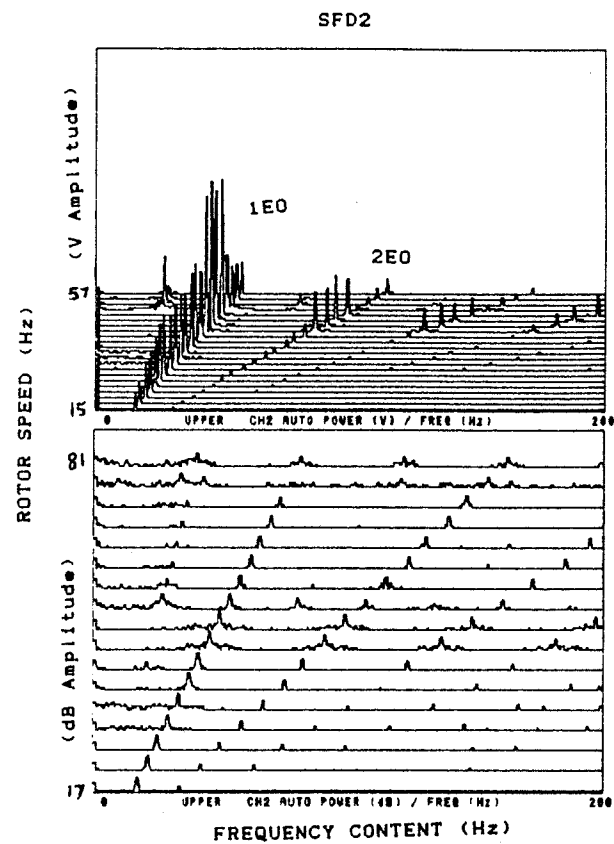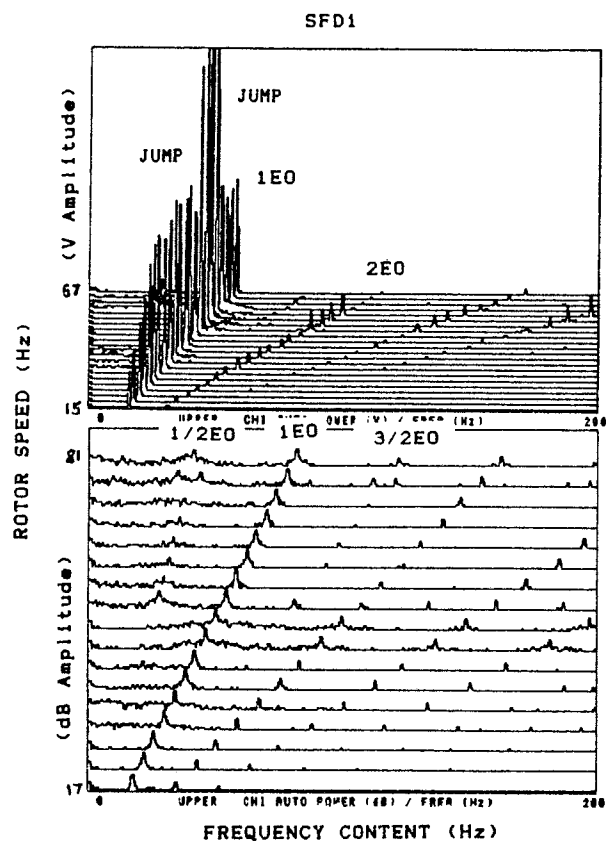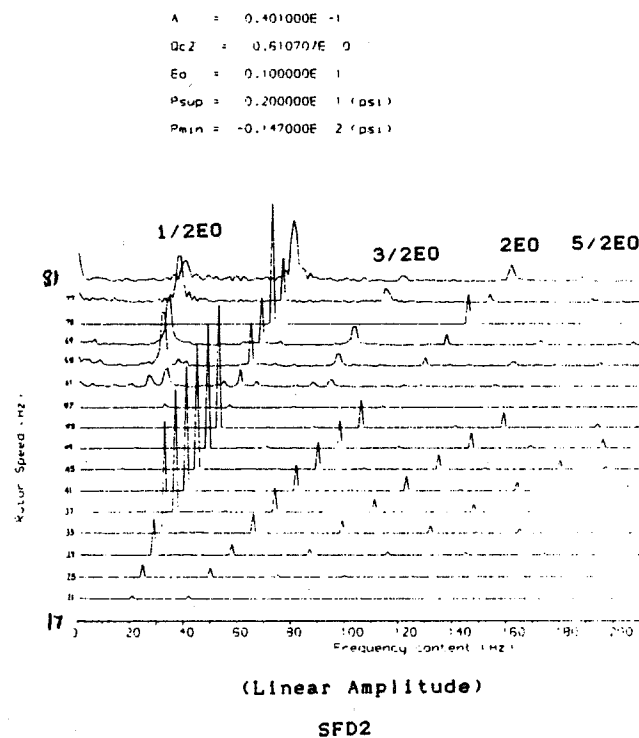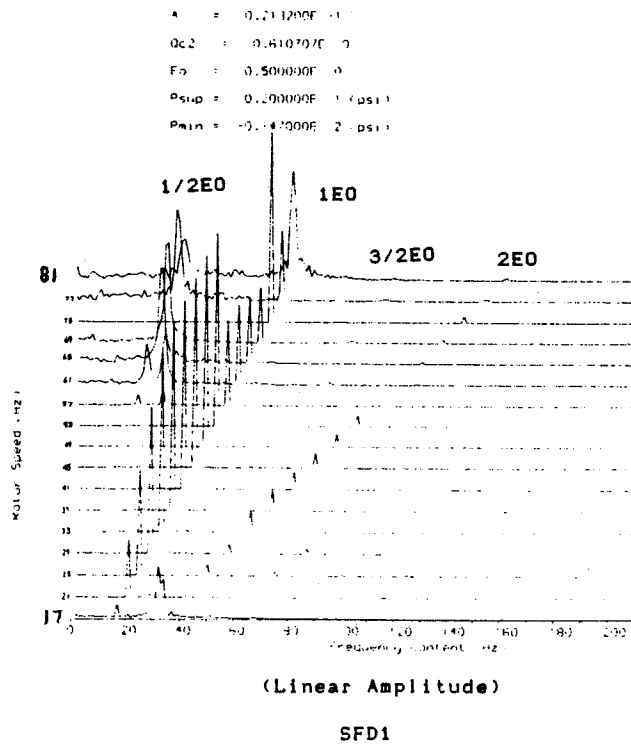
Theoretical Waterfall Diagram

Configuration 2a (Q_{c2}=0.611, Psup=2psi, E_{01}=0.5)

Fig 8

43

SFD1

SFD2

JUMP

1EO

1EO

2EO

2EO   3EO

3EO

ROTOR SPEED (Hz)

57

15

57

15

(V Amplitude)

(dB Amplitude)

57

15

UPPER   CH1 AUTO POWER (V) / FREQ (Hz)

200

UPPER   CH1 AUTO POWER (dB) / FREQ (Hz)

200

FREQUENCY CONTENT (Hz)

ROTOR SPEED (Hz)

57

15

57

15

(V Amplitude)

(dB Amplitude)

UPPER   CH2 AUTO POWER (V) / FREQ (Hz)

200

UPPER   CH2 AUTO POWER (dB) / FREQ (Hz)

200

FREQUENCY CONTENT (Hz)

(a)

Experimental Waterfall Diagram

44

45

A   =   0.213200E -1

Qc2   =   0.610707E 0

Eo   =   0.224030E 1

Psup =   0.150000E   2 (psi)

Pmin =   -0.147000E   2 (psi)

A   =   0.401000E -1

Qc2   =   0.610707E 0

Eo   =   0.100000E   1

Psup =   0.150000E   2 (psi)

Pmin =   -0.147000E   2 (psi)

JUMP   1EO

2EO

1EO

2EO

(Linear Amplitude)

(Linear Amplitude)

SFD1

SFD2

(b)

Theoretical Waterfall Diagram

Configuration 2b (Qc₂=0.611, Psup=2psi)

Fig 9

1E0

JUMP

2E0

3E0

Eo1 =1.0
Eo2 =1.0
Qc2 =0.733
Psup= 2psi

27
31

15
0   UPPER   CH2 AUTO POWER (V) / FREQ (HZ)   200

R
O
T
O
R

S
P
E
E
D

(Hz)

Eo1 =1.0
Eo2 =1.0
Qc2 =0.490
Psup= 2psi

57

15
0   UPPER   CH2 AUTO POWER (V) / FREQ (HZ)   200

Eo1 =1.0
Eo2 =1.0
Qc2 =0.245
Psup= 2psi

57

15
0   UPPER   CH2 AUTO POWER (V) / FREQ (HZ)   200

FREQUENCY CONTENT Hz (V Amplitude)

Rotor Displacement Relative to Ground at SFD2
Configuration 3a

Experimental Waterfall Diagram (Q_{c2}=0.611, Psup=2psi)

Fig 10

46

R
O
T
O
R

S
P
E
E
D

(Hz)
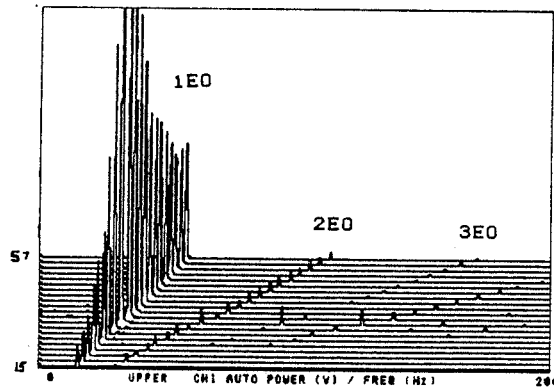
Eo1 =0.0
Eo1 =1.0
Qc2 =0.611
Psup= 2psi
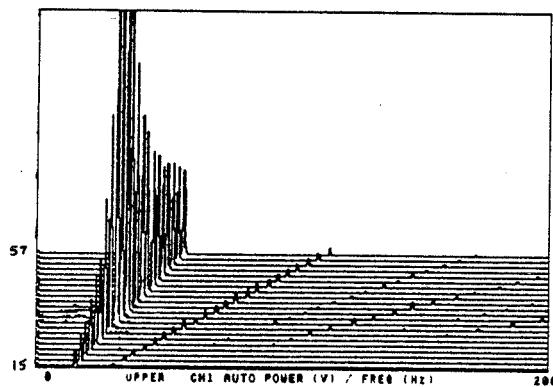
Eo1 =0.0
Eo2 =1.0
Qc2 =0.490
Psup= 2psi

SFD1 FREQUENCY CONTENT Hz (V Amplitude)

Rotor Displacement Relative to Ground at SFD2
Configuration 3b

THE STABILITY OF THE STEADY STATE AND BISTABLE RESPONSE OF A FLEXIBLE ROTOR SUPPORTED ON SQUEEZE FILM DAMPERS*

Meng Guang
The Vibration Research Council
Northwestern Polytechnical University
Xian, China

In this paper, the stability of the steady state circular response and the bistable response of a flexible rotor—centralised squeeze film damper (shortened as SFD) system is analysed, and the system's characteristics of accelerating or decelerating through the bistable region are investigated. It is found that there are two unstable regions for the circular response. The larger the unbalance parameter and the smaller the bearing parameter and external damping, the easier it is to cause an unstable circular response. In addition, the larger mass ratio and the smaller stiffness ratio will decrease the threshold rotating speed of instability. Although in some cases, the system's circular response is unstable, the system is still stable and has stable nonsynchronous response.

It is also found that only when the initial rotating speed is ahead of the bistable region can the bistable response be produced when the system is accelerating through the bistable region. The small solution of the bistable response is more stable than the large one.

NOMENCLATURE

a	= angle acceleration
B	= bearing parameter $(=\mu RL^3/m_B\omega_c c^3)$, where R is the bearing radius, L is land length of SFD, and μ is the absolute viscosity of the lubricant
c	= radial clearance of SFD
c_d	= external damping coefficient
e_u	= unbalance eccentricity
k_a	= retainer spring stiffness
k_s	= shaft stiffness
K	= stiffness ratio $(=k_a/k_s)$
m_B, m_D	= mass lumped at bearing station and rotor mid-span
m_u	= unbalance mass for experiment
n	= rotating speed in RPM
U	= unbalance parameter $(=e_u/c)$

PRECEDING PAGE BLANK NOT FILMED

```
x,y; r,t  = Cartesian and polar coordinates
X,Y       = x/c, y/c
Z         = X+iY
Z̄         = conjugation of Z
α         = mass ratio (=m_B/m_D)
ε_B, ε_D  = eccentricity ratio of journal or disk (=e_B/c or e_D/c), where
            e_B and e_D are eccentricities
β         = damping ratio (=c_d/2m_D ω_c)
Γ         = a/ω_c^2
φ_B, φ_D  = attitude angles
ω         = rotor rotating speed
ω_c       = pin-pin critical speed (=(k_s/m_D)^{1/2}
Ω         = speed ratio (=ω/ω_c)
τ         = ωt for steady state response and ω_c t for transient response
(˙)       = d/dt
(')       = d/dτ
```

Subscripts

```
(B)       = bearing journal
(D)       = disk
(o)       = steady state condition
(x), (y)  = direction subscripts
```

INTRODUCTION

A well designed squeeze film damper (SFD) is a good isolator and damper in rotating machinery and can increase the system's stability. But poorly designed SFD may destabilize the rotor system, so the stability analyses of rotors supported on SFD's have received more attention (Ref. 1 and Ref. 2). The bistable response which is induced by the nonlinear fluid film forces will cause a large vibration amplitude that is harmful to the rotor system. Since the high nonlinearity of the fluid film force makes the mathematical analysis very difficult, most stability analyses of the rotor-SFD system are limited to the case of steady state circular response of the centralised SFD system (Ref. 3 and Ref. 4). Whether the system is unstable when its circular response is unstable is still an undiscussed problem. As the system is nonlinear, it may have a stable response other than the circular response. Furthermore, it is not clear what the properties are when the rotor system accelerates through the bistable region, and the influences of the system parameters on the system's stability have not been thoroughly analysed. As these problems are very important for designing good SFD, they are worth investigating.

EIGEN-MATRIX FOR STABILITY ANALYSIS

For the flexible rotor supported on the centralised SFD shown in Fig. 1, the nondimensional equations of motion can be derived by taking the same assumptions adopted in Ref. 5:

Bearing journal:

$$Z_B'' + \frac{1}{2\alpha\Omega^2}[(1+K)Z_B - Z_D] = \frac{2B}{\Omega}F \qquad (1)$$

$$Z_D'' + \frac{2\beta}{\Omega}Z_D' + \frac{1}{\Omega^2}(Z_D - Z_B) = Ue^{i\tau} \qquad (2)$$

where $F = f_x + if_y$ is the dimensionless fluid film force.
In the assumptions of the short bearing and π-film, there are (ref. 6)

$$\begin{cases} f_x = -\dfrac{1}{(X_B^2 + Y_B^2)^{1/2}}[X_B(\epsilon_B\phi_B'I_1 + \epsilon_B'I_2) - Y_B(\epsilon_B\phi_B'I_3 + \epsilon_B'I_1)] \\ f_y = -\dfrac{1}{(X_B^2 + Y_B^2)^{1/2}}[Y_B(\epsilon_B\phi_B'I_1 + \epsilon_B'I_2) + X_B(\epsilon_B\phi_B'I_3 + \epsilon_B'I_1)] \end{cases} \qquad (3)$$

where

$$I_1 = \int_{\Theta_1}^{\Theta_1 + \pi} \frac{\sin\Theta\cos\Theta}{(1+\epsilon_B\cos\Theta)^3}d\Theta, \quad I_2 = \int_{\Theta_1}^{\Theta_1 + \pi} \frac{\cos^2\Theta}{(1+\epsilon_B\cos\Theta)^3}d\Theta, \quad I_3 = \int_{\Theta_1}^{\Theta_1 + \pi} \frac{\sin^2\Theta}{(1+\epsilon_B\cos\Theta)^3}d\Theta$$

$$\Theta_1 = \arctan[-\epsilon_B'/(\epsilon_B\phi_B')], \quad \epsilon_B = (X_B^2 + Y_B^2)^{1/2}, \quad \phi_B = \arctan(Y_B/X_B)$$

For the steady state circular response, there are

$$Z_{B0} = \epsilon_o e^{i\phi_o}, \quad \epsilon_o = const, \quad \phi_o = \tau - \phi_1, \quad \phi_1 = const \text{ and } Z_{B0} = iZ_{B0}$$

Linearizing the nonlinear fluid film force about the steady state circular response Z_{B0} with the Taylor series, we get (Ref. 6)

$$F = F_0 + A_1Z_2 + (B_1 + iC_1)e^{2i\phi_o}\bar{Z}_2 + A_2Z_2' + (B_2 + iC_2)e^{2i\phi_o}\bar{Z}_2' \qquad (4)$$

where, $Z_2 = Z_B - Z_{B0}$. The linearizing coefficients are

$$\begin{cases} F_0 = (K_0 + iC_0)Z_{B0} \\ A_1 = \dfrac{(3+\epsilon_o^2)\epsilon_o}{(1-\epsilon_o^2)^3}, \quad B_1 = \dfrac{(5\epsilon_o^2-1)\epsilon_o}{(1-\epsilon_o^2)^3}, \quad C_1 = \dfrac{3\pi\epsilon_o^2}{2(1-\epsilon_o^2)^{5/2}} \\ A_2 = \dfrac{\pi(2+\epsilon_o^2)}{4(1-\epsilon_o^2)^{5/2}}, \quad B_2 = \dfrac{3\pi\epsilon_o^2}{4(1-\epsilon_o^2)^{5/2}}, \quad C_2 = \dfrac{2\epsilon_o^2}{2(1-\epsilon_o^2)^2} \end{cases} \qquad (5)$$

51

and

$$K_0 = \frac{2\epsilon_0}{(1-\epsilon_0^2)^2} \quad , \quad C_0 = \frac{\pi}{2(1-\epsilon_0^2)^{3/2}}$$

As ϵ_0=const, $\phi_0 = \tau - \phi_1$, ϕ_1=const, it can be seen that these coefficients are periodic functions of time, the period being π.

In Eq. (1) and Eq. (2), note $Z_1 = Z_D - Z_{DO}$, $Z_2 = Z_B - Z_{BO}$, we can get the perturbed equations of motion about the steady state response $Z_{BO} = \epsilon_0 e^{i\phi_0}$ and $Z_{DO} = \epsilon_{DO} e^{i\phi_{DO}}$ (approximated to the first order term):

$$\begin{cases} Z_1'' + \frac{2\beta}{\Omega} Z_1' + \frac{1}{\Omega^2}(Z_1 - Z_2) = 0 \\ Z_2'' + \frac{1}{2\alpha\Omega^2}[(1+K)Z_2 - Z_1] = -\frac{2B}{\Omega}[A_1 Z_2 + (B_1 + iC_1)e^{2i\phi_0}\overline{Z}_2 + A_2 Z_2' \\ \quad + (B_2 + iC_2)e^{2i\phi_0}\overline{Z}_2'] = 0 \end{cases} \quad (6)$$

Thus, the perturbed equations of motion of the system about its circular response are in the form of the Hill equation with periodic coefficients.

Now $U_1 = p_1 + ip_2$, $U_2 = p_3 + ip_4$, and make the transformation of

$$Z_1 = U_1 e^{i\phi_0}, \qquad Z_2 = U_2 e^{i\phi_0} \qquad (7)$$

that is, analysing the problem in the coordinate rotating synchronously with the rotor shaft, we have

$$Z_1 = U_1 e^{i\phi_0}, \quad Z_1' = (U_1' + iU_1)e^{i\phi_0}, \quad Z_1'' = (U_1'' + 2iU_1' - U_1)e^{i\phi_0} \qquad (8)$$

There are similar results for Z_2. Substituting Eq. (7) and Eq. (8) into Eq. (6) and separating the real and imaginary parts, we get

$$P'' + DP' + SP = 0 \qquad (9)$$

where $P = (p_1, p_2, p_3, p_4)^T$, and the damping matrix D and stiffness matrix S are

$$D=\begin{bmatrix} \dfrac{2\beta}{\Omega} & -2 & 0 & 0 \\[2mm] 2 & \dfrac{2\beta}{\Omega} & 0 & 0 \\[2mm] 0 & 0 & \dfrac{2B}{\Omega}(A_2+B_2) & \dfrac{2B}{\Omega}C_2-2 \\[2mm] 0 & 0 & \dfrac{2B}{\Omega}C_2+2 & \dfrac{2B}{\Omega}(A_2-B_2) \end{bmatrix}$$

$$S=\begin{bmatrix} \dfrac{1}{\Omega^2}-1 & -\dfrac{2\beta}{\Omega} & 0 & 0 \\[3mm] \dfrac{2\beta}{\Omega} & \dfrac{1}{\Omega^2}-1 & 0 & 0 \\[3mm] -\dfrac{1}{2\alpha\Omega} & 0 & \dfrac{1+K}{2\alpha\Omega^2}-1+\dfrac{2B}{\Omega}(A_1+B_1+C_2) & -\dfrac{2B}{\Omega}(A_2+B_2-C_1) \\[3mm] 0 & -\dfrac{1}{2\alpha\Omega} & \dfrac{2B}{\Omega}(A_2-B_2+C_1) & \dfrac{1+K}{2\alpha\Omega^2}-1+\dfrac{2B}{\Omega}(A_1-B_1-C_2) \end{bmatrix}$$

Substituting Eq. (5) into Eq. (9) and noting $R=(r_1,r_2,\dots,r_8)^T$ $=(p_1,p_1',p_2,p_2',p_3,p_3',p_4,p_4')^T$, Eq. (9) can be transferred to the first order form:

$$\frac{dR}{d\tau} = HR \tag{10}$$

Note

$$C_{rr}= \frac{\pi(1+2\epsilon_0^2)}{2(1-\epsilon_0^2)^{5/2}},\quad C_r =\frac{2\epsilon_0}{(1-\epsilon_0^2)^2},\quad C_{sr}=\frac{2\epsilon_0}{(1-\epsilon_0^2)^2},\quad C_{ss}=\frac{\pi}{2(1-\epsilon_0^2)^{3/2}}$$

$$K_{rr}= \frac{4\epsilon_0(1+\epsilon_0^2)}{(1-\epsilon_0^2)^3},\quad K_{rs}=-\frac{\pi}{2(1-\epsilon_0^2)^{3/2}},\quad K_{sr}=\frac{\pi(1+2\epsilon_0^2)}{2(1-\epsilon_0^2)^{5/2}},\quad K_{ss}=\frac{2\epsilon_0}{(1-\epsilon_0^2)^2}$$

These are the same eight fluid film force coefficients commonly used for SFD in the polar coordinate (Ref. 4); then the coefficients matrix H is

$$H=\begin{bmatrix} 0 & 1 & 0 & 0 & 0 & 0 & 0 & 0 \\ 1-\dfrac{1}{\Omega^2} & -\dfrac{2\beta}{\Omega} & \dfrac{2\beta}{\Omega} & 2 & \dfrac{1}{\Omega^2} & 0 & 0 & 0 \\ 0 & 0 & 0 & 1 & 0 & 0 & 0 & 0 \\ -\dfrac{2\beta}{\Omega} & -2 & 1-\dfrac{1}{\Omega^2} & -\dfrac{2\beta}{\Omega} & 0 & 0 & \dfrac{1}{\Omega} & 0 \\ 0 & 0 & 0 & 0 & 0 & 1 & 0 & 0 \\ \dfrac{1}{2\alpha\Omega^2} & 0 & 0 & 0 & 1-\dfrac{1+K}{2\alpha\Omega^2}-\dfrac{2B}{\Omega}K_{rr} & -\dfrac{2B}{\Omega}C_{rr} & -\dfrac{2B}{\Omega}K_{rs} & 2-\dfrac{2B}{\Omega}C_{rs} \\ 0 & 0 & 0 & 0 & 0 & 0 & 0 & 1 \\ 0 & 0 & \dfrac{1}{2\alpha\Omega^2} & 0 & -\dfrac{2B}{\Omega}K_{sr} & -2-\dfrac{2B}{\Omega}C_{sr} & 1-\dfrac{1+K}{2\alpha\Omega^2}-\dfrac{2B}{\Omega}K_{ss} & -\dfrac{2B}{\Omega}C_{ss} \end{bmatrix} \tag{11}$$

The stability of the system's steady state circular response can be determined by the eigenvalue of matrix H. The steady state responses Z_{BO} and Z_{DO} of Eq. (1) and Eq. (2) are asymptotically stable when all the eigenvalues of H have negative real parts, and they are unstable if only one eigenvalue of H has a positive real part.

NUMERICAL ANALYSIS OF STABILITY

The eigenvalues of matrix H are solved with the QR method, and the stability of the system's steady state circular response is analysed. From numerical results we find that, for both $\Omega<1$ and $\Omega>1$, there are two unstable regions. The unstable region generally begins before the peak point of response and finishes after the peak point (see Fig. 2). In most cases, the larger the unbalance parameter U, and the smaller the bearing parameter B and the external damping ratio β, the easier it is to produce the unstable response. Furthermore, the larger the mass ratio α and the smaller the stiffness ratio K, the lower the threshold rotating speed of instability - perhaps because the larger α and smaller K may reduce the critical speed of the system. No instability is found in the region of $\Omega<1$ and $\varepsilon_O<0.5$.

The middle solution of the bistable response is always unstable, while the small solution is always stable. For the bistable response of the isolated bifurcation form, the large solution is generally stable (see Fig. 3), but it may be unstable when the bistable region is large (see Fig. 4). For the bistable response of the Duffing form

54

when $\Omega<1$ (although in most cases the large solution is stable) it may become unstable in some cases (see Fig. 2). When $\Omega>1$, the large solution is unstable in most cases (see Fig. 2 and Fig. 3).

In order to find the reason for this instability, Eq. (1) and Eq. (2) are directly solved with the Runge-Kutta method in the unstable region. It is found that in most cases, the instability is caused by the nonsynchronous response. That is to say, within the unstable region, although the circular response is unstable, the system is still stable and has a stable, nonsynchronous response. For the example of Fig. 3, when $\Omega=2.0$, the circular response is unstable, but the system has a stable 1/3 subharmonic response at the same time (see Fig. 5).

Besides the nonsynchronous response, the lack of a steady state response is another reason for instability. In only a few cases, the system is very unstable, and the response is divergent.

The above results explain the reason why the bistable response is seldom found in practical rotor systems, although it is common in theoretical analyses.

From the numerical results it is also found that the instability can be avoided by selecting reasonable system parameters, especially for the instability in $\Omega<1$.

It is worth paying special attention to the fact that the nonsynchronous response also occurs frequently in centralised SFD, both in the regions of $\Omega<1$ and $\Omega>1$ although the nonsynchronous response may be more prevalent in the uncentralised SFD. The nonsynchronous response should be avoided as it will cause alternating fatigue to the rotor system.

TRANSIENT CHARACTERISTICS WHEN THIS SYSTEM IS ACCELERATING THROUGH THE BISTABLE REGION AND STABLE DEGREE OF BISTABLE RESPONSE

We have analysed the stability of bistable response. But what is the bistable jumping process, and what is its relationship with the initial rotating speed? Furthermore, the large and small solutions of the bistable response are both stable in most cases, but which is more stable? So the transient response of the system accelerating through a bistable region is analysed in the following.

Supposing that the accelerating motion of the flexible rotor---centralised SFD system has a constant acceleration, that is, $\phi''=$ const $= a$, then the dimensionless equations of motion can be written as

$$\begin{cases} Z_D''+2\beta Z_D'+Z_D-Z_B=U\phi'^2 e^{i\phi}-iU\Gamma e^{i\phi} \\ Z_B''+\dfrac{1}{2\alpha}[(1+K)Z_B-Z_D]=2BF \\ \phi''=\Gamma, \quad \phi'=\Gamma\tau+\Omega_0, \quad \phi=\Gamma\tau^2/2+\Omega_0\tau+\phi_0 \end{cases} \qquad (12)$$

where τ is now denoted as $\tau=\omega_c t$ and Ω_0 is the initial speed ratio.

By solving Eq. (12) numerically, we find that, for different initial rotating speeds at the beginning of acceleration, the response routes when passing through the bistable region are different. If we note the beginning and finishing speed ratio of the Duffing bistable

response as Ω_s and Ω_e (see Fig. 6), then the response will take the route of L1 when $\Omega_0 < \Omega_s$, and a bistable response occurs (see Fig. 7). But the response after jumping down will not completely take the route of the steady state response, it goes to steady state after a period of oscillation. During the period of oscillation, a nonsynchronous response appears in some cases. When the initial speed ratio $\Omega_0 > \Omega_s$, only for very suitable initial response conditions can the response take the large solution and cause bistable jumping. In most cases, the response will take the route of L2; that is, the small solution is the practical one and no bistable jumping occurs. If $\Omega_0 < \Omega_s$, but stops accelerating when $\Omega_s < \phi\Omega_e$, then the bistable jumping down will occur in most cases, and when the acceleration is continued, the response will take the route of L2. Therefore, the response will take the route of L3 for the whole process.

From the above analysis, it can be seen that the small solution of the bistable response is more stable than the large one. In decelerating, the response takes the route of L4. It is easy to see that the jumping phenomenon of deceleration is not obvious and sudden as that of acceleration, and the faster the deceleration, the smaller the jumping amplitude.

EXPERIMENTAL ANALYSIS

In this experiment, a symmetric rotor is used which has a diameter of 32 mm and a length of 889 mm, with a 10.325 kg disk assembled in its mid-span. The SFD is fabricated with two load lands, a circumferential groove for the oil supply, and no seals. The first rigid critical speed of the rotor shaft is about 5500 RPM, the absolute viscosity of the lubricant at 18 °C is about $\mu = 8.05 \times 10^{-8}$ kgs/cm.

The rotor and journal vibrations in the horizontal and vertical directions are measured and recorded by a TEAC-R50C type recorder and then processed with an SM-2100B signal analyser. This gives us the magnitudes of vibration, the oscillation orbits, and the power spectrum charts of the response.

Figure 8 is the stable nonsynchronous response of 1/2 the subharmonic. Although theoretical analyses show that, in this case, the steady state circular response of the system is unstable, the system is still stable.

Figure 9 shows a stable synchronous (almost circular) response and theoretical analyses also indicate that the circular response is stable.

Figure 10 shows the experimental results of a bistable jumping down when system is accelerating through the bistable region. It can be seen that the middle solution of the bistable response is unstable, as shown in the orbit figure.

CONCLUSIONS

1. The perturbed equations of motion of a flexible rotor supported on SFD about its circular response are of the form of Hill equations with periodic coefficients, and there are two unstable regions for the system's circular response separately in $\Omega < 1$ and $\Omega > 1$. In most cases,

the larger the unbalance parameter and the smaller the bearing parameter and external damping, the easier it is to produce instability. Furthermore, larger mass ratio and small stiffness ratio will decrease the threshold rotating speed of instability.

2. Although the steady state circular response is unstable, the system is still stable in most cases and has a stable nonsynchronous response. In many cases, especially when $\Omega>1$, the large solution of bistable response is also unstable, and then bistable jumping will not occur. This explains why the bistable response is seldom observed in practical rotor systems. Thus further work on bistable response is not worth pursuing.

3. Whether the bistable jumping occurs or not is largely related to the initial rotating speed where acceleration begins. Only when the initial speed is ahead of the bistable region can the bistable jumping be caused. The small solution of the bistable response is more stable than the large one.

REFERENCES

[1] Tonneson, J.; Lund, J.W., "Some Experiments on Instability of Rotor Supported in Fluid Film Bearing," Trans. of ASME. J. of Mechanical Design, Vol. 100, No. 1, 1978, pp. 147-155.

[2] Yan Litang, "The Bistable Characteristics of Rigid Rotor Supported on Squeeze Film Dampers," Proc. of Fourth Conf. on Structure, Strength and Vibration, 1987, China, pp. 76-78.

[3] Rabinowitz, M.D.; Hahn, E.J., "Stability of Squeeze Film Damper Supported Flexible Rotors," ASME paper 77-GT-51.

[4] White, D.C., "The Dynamics of a Rigid Rotor Supported on Squeeze Film Bearings," Proc. Inst. mech. Engs. Vol. 186, 1972, pp. 213-219, Conf. on Vibration in Rotating System.

[5] Meng Guang; Xue Zhongging, "Investigation on Steady State Response and its Nonlinear Characteristics of Flexible Rotor--Squeeze Film Damper System," ASME paper 85-DET-141.

[6] Meng Guang; Xue Zhongging, "Some Theoretical Analyses on Flexible Rotor--Squeeze Film Damper Bearings System and Fluid Film Forces," Proc. of the Intl. Conf. on Rotordynamics, Sept. 1986, Tokyo, pp. 511-516.
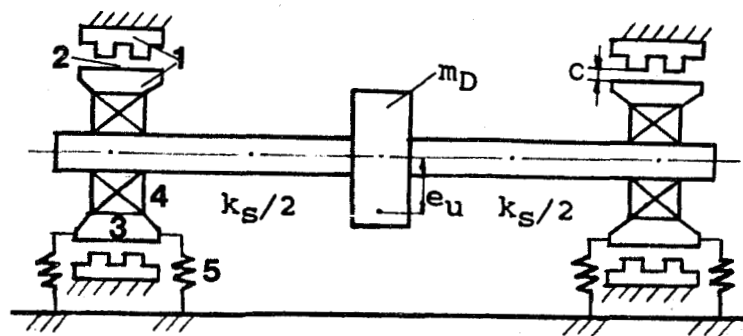
1. squeeze film damper 2. squeeze oil film
3. outer race constrained not to rotate
4. ball bearing   5. centralising spring

Fig.1 Schematic diagram of a flexible rotor
      with squeeze film damper
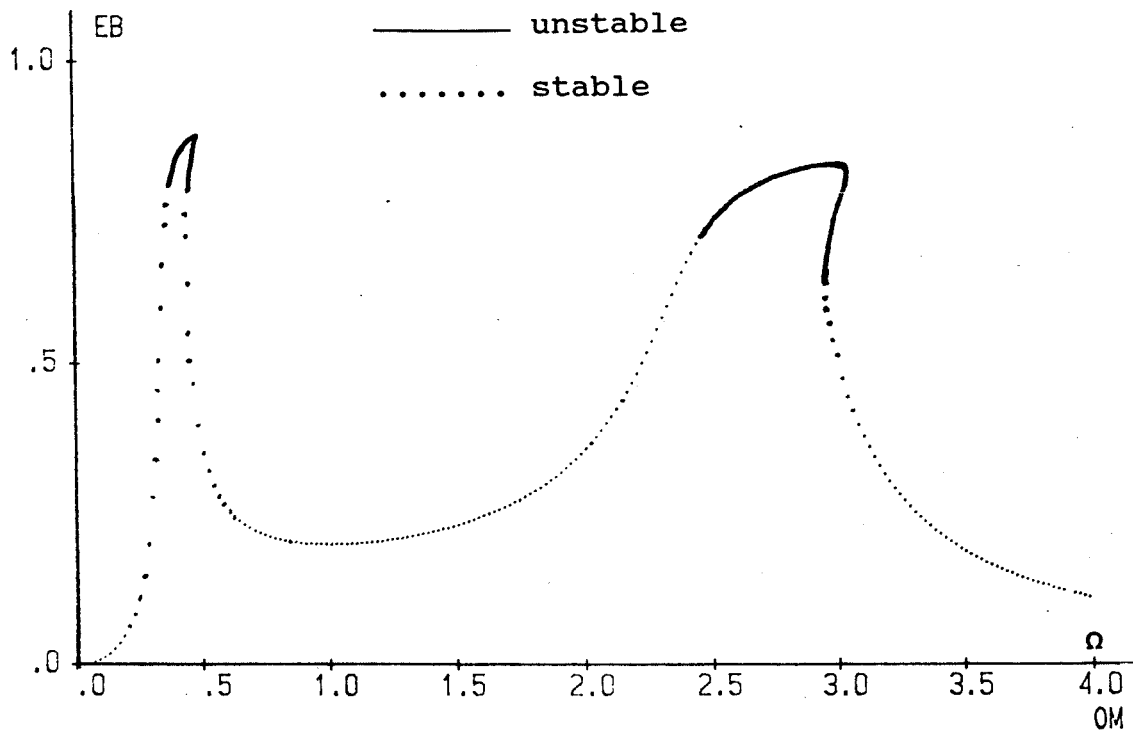
Fig.2 Stability analysis of system's circular response
(U=0.2, β=0.0005, α=0.1, B=0.025, K=0.2)
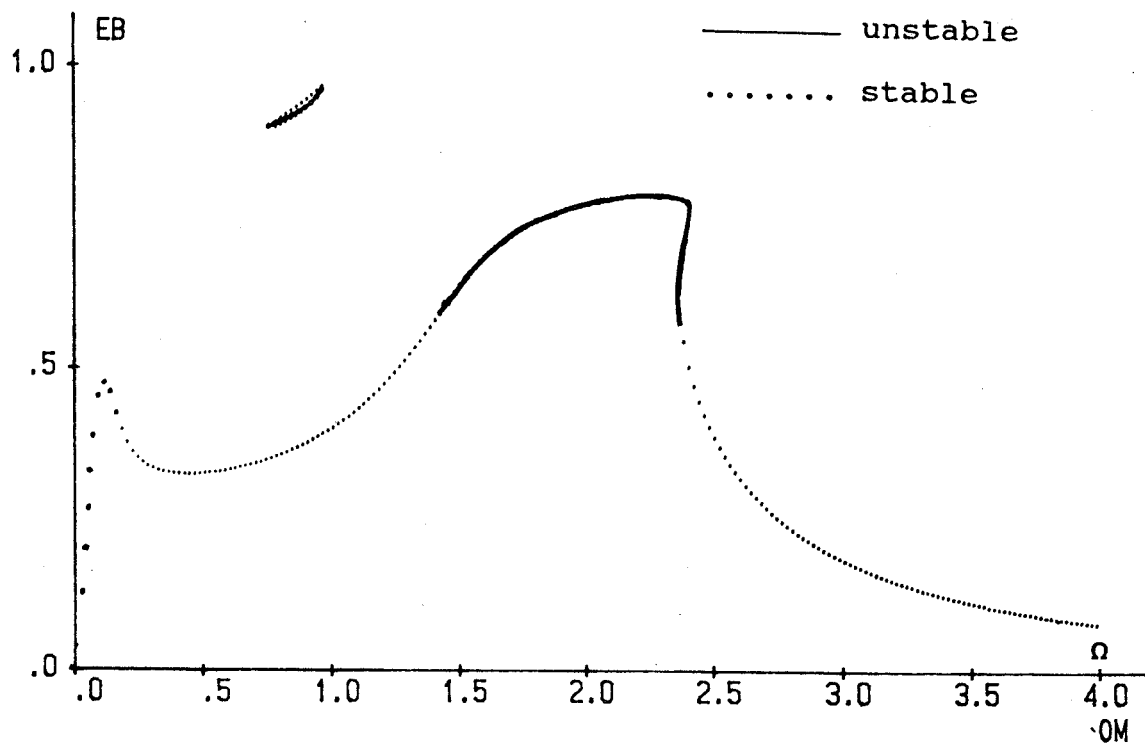
Fig.3 Stability analysis of system's circular response
(U=0.4, β=0.005, α=0.2, B=0.05, K=0.01)
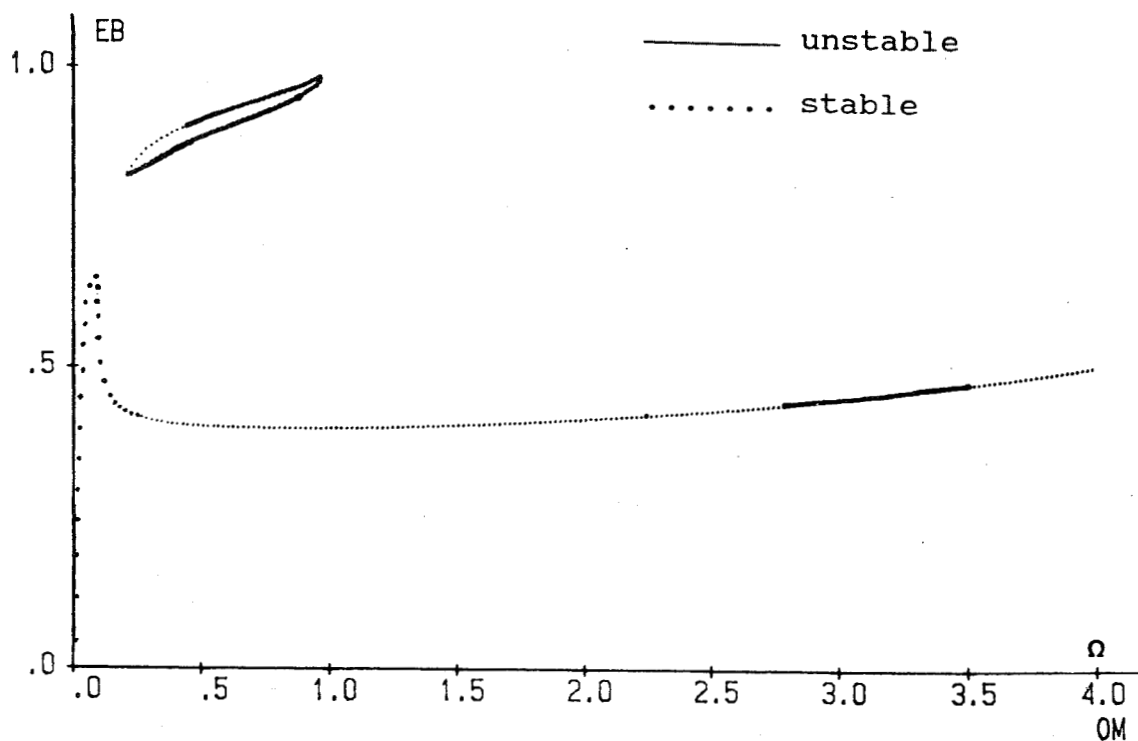
Fig.4 Stability of isolated bistable response
(U=0.4, β=0.0005, α=0.01, B=0.3, K=0.001)
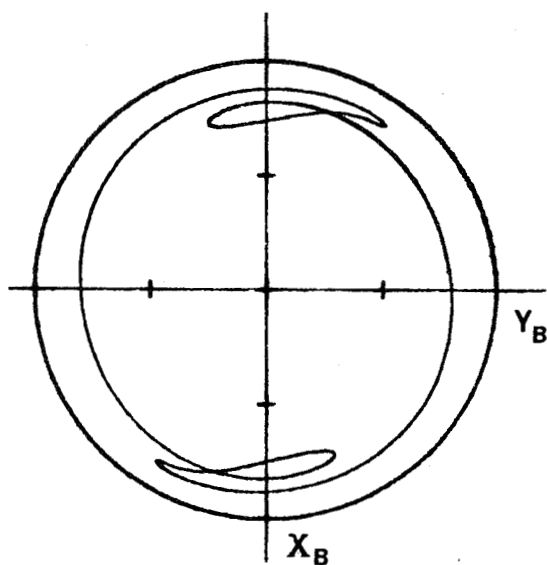
Fig.5 Nonsynchronous response in unstable region (U=0.4, β=0.005, α=0.2, B=0.05, K=0.01, Ω=2.0)
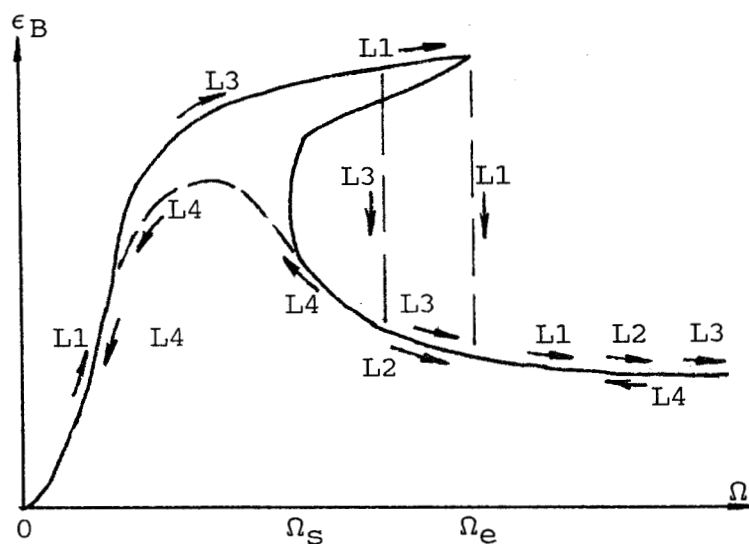
Fig.6 Schematic diagram of the influence of initial rotating speed on bistable jumping
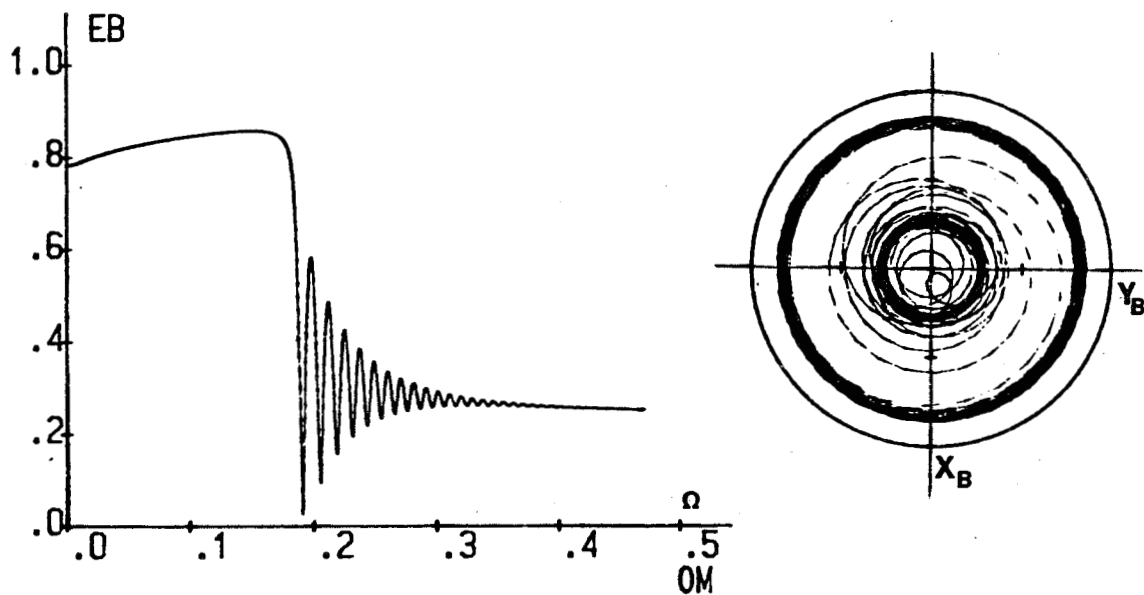
Fig.7 Bistable jumping response of accelerating through
bistable region (U=0.25, β=0.0005, α=0.1, B=0.05,
K=0.2, Ω_0=0.42, Γ=0.0005)
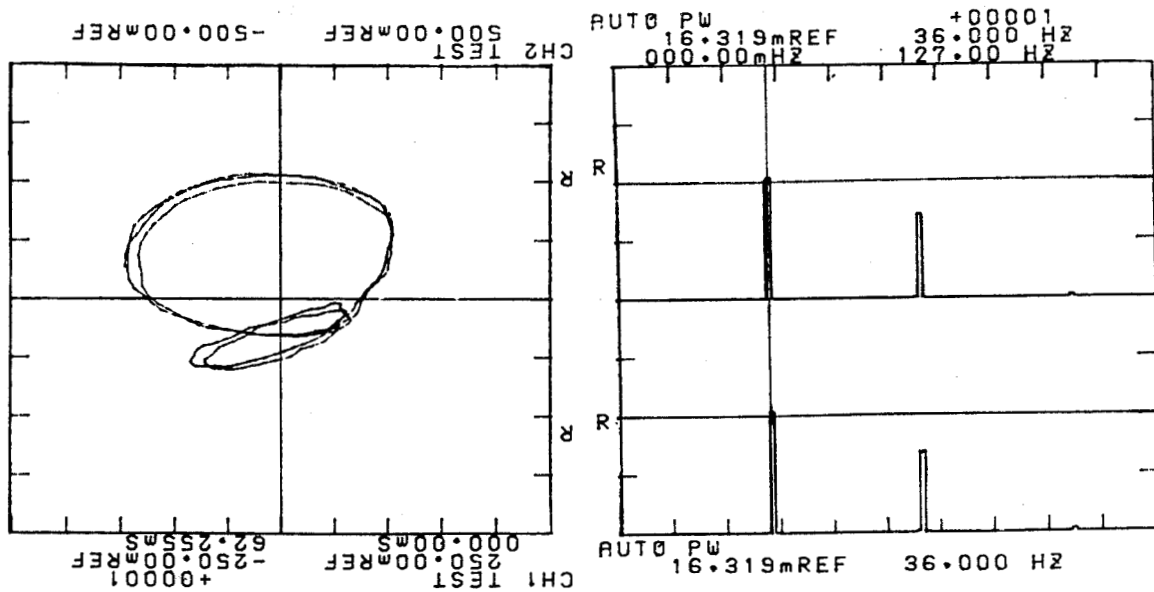
Fig.8 System's 1/2 subharmonic response by experiment
(L=1.2cm, c/R=0.5%, m_u=10.5g, n=4320rpm)

CH1 TEST   +00001
    1·0000 REF   -1·0000 REF
    000·00mS   124·75mS

R

R

CH2 TEST
    1·0000 REF   -1·0000 REF
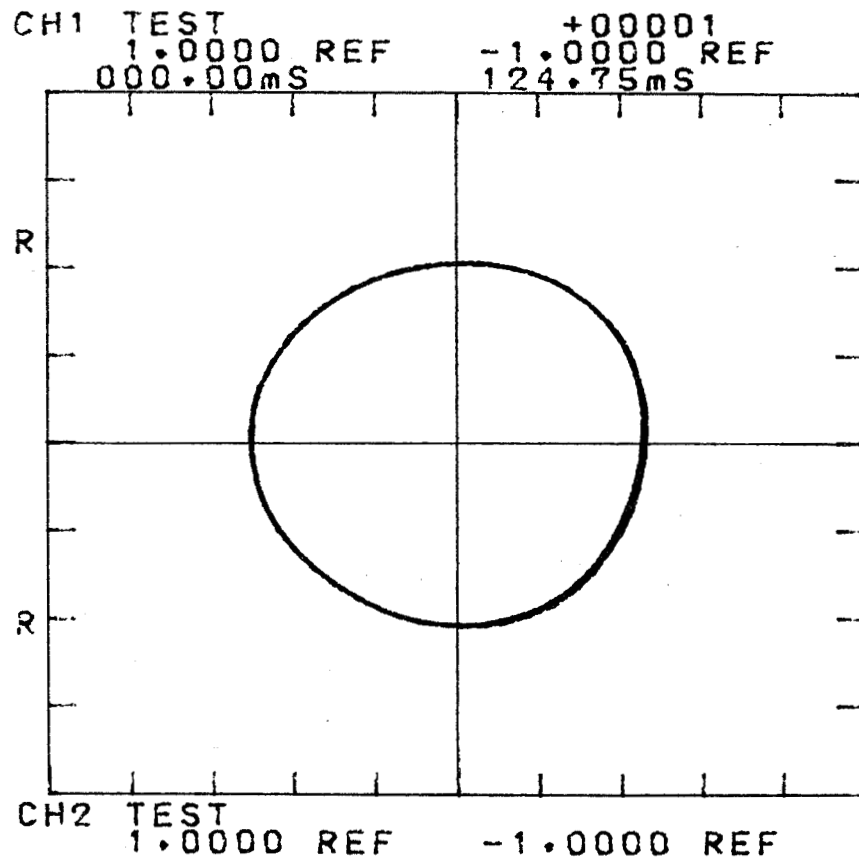
Fig.9 System's synchronous response by experiment
(L=1.6cm, c/R=0.1%, m_u=7.6g, n=5280rpm)
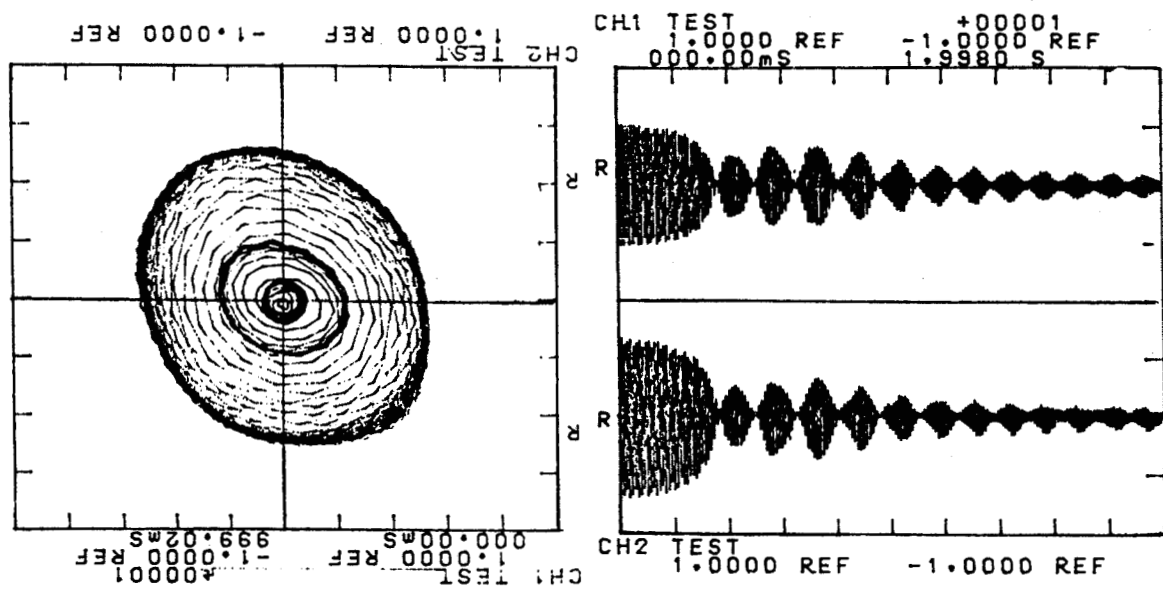
Fig.10 System's bistable response by experiment
(L=1.2cm, c/R=0.1%, m_u=4.6g, n=5430rpm)

STABILITY OF INTERSHAFT SQUEEZE FILM DAMPERS

A. El-Shafei
University of South Florida
Tampa, Florida 33620, U.S.A.

Intershaft squeeze film dampers have been investigated for damping of dual rotor aircraft jet engines. Initial investigations indicated that the intershaft dampers would attenuate the amplitude of the engine vibration and decrease the force transmitted through the intershaft bearing, thereby increasing its life. Also it was thought that the intershaft damper would enhance the stability of the rotor-bearing system. Unfortunately, it was determined both theoretically and experimentally that the intershaft squeeze film damper was unstable above the engine's first critical speed. In this paper, a stability analysis of rotors incorporating intershaft squeeze film dampers is performed. A rotor model consisting of two Jeffcott rotors with two intershaft squeeze film dampers is investigated. Examining the system characteristic equation for the conditions at which the roots indicate an ever growing unstable motion, result in the stability conditions. The cause of the instability is identified as the rotation of the oil in the damper clearance. The oil rotation adds energy to the forward whirl of the rotor system above the critical speed and thus causes the instability. Below the critical speed the oil film removes energy from the forward rotor whirl. It is also shown that the backward whirl of the rotor system is always stable. Several proposed configurations of intershaft squeeze film dampers are discussed, and it is shown that the intershaft dampers are stable supercritically only with a configuration in which the oil film does not rotate.

INTRODUCTION

The ability of a squeeze film damper to attenuate the amplitudes of engine vibration and to decrease the dynamic forces transmitted to the frame of gas turbine engines, make it an attractive rotor support. In a single spool application, the squeeze film damper consists of an oil film in an annulus surrounding a rolling element bearing whose outer race is constrained from rotating, usually by a squirrel cage. Thus the spinning of the rotor does not reach the oil, and only when the rotor whirls does the oil film act to damp the motion.

In some applications it may be necessary to use intershaft differential rolling element bearings in a two-spool engine configuration. The use of the intershaft bearing reduces the rub between the two rotors, decreases the shaft deflections, and eliminates the static support structure in the aerodynamic flow path. Thus the engine's performance, efficiency and reliability are improved. But the intershaft bearing may carry a large load, thus decreasing the life of the bearing (ref. 1), and will also provide a direct path for the transmission of vibration between the inner and outer rotors.

Hibner et. al., in reference 2, proposed using a squeeze film damper in an intershaft configuration to decrease both the intershaft bearing loading and the vibration of the engine. They proposed a damper configuration in which the oil film rotates at the speed of the inner (LP) rotor. They found out that, for their specific engine, by using the intershaft squeeze film damper, the intershaft bearing loads could be reduced to less than half the level achieved by the incorporation of squeeze film dampers on the other bearings of the rotor system. Furthermore, the cyclic stresses on the bearing supports and the engine mount structure were also substantially reduced (ref. 2). However, they also found out that the engine became unstable above its first critical speed. They were able to demonstrate both theoretically and experimentally that this instability is due to the intershaft squeeze film damper. To control this instability,

they had to increase the engine's critical speed, and they proposed adding a spring in parallel to the damper to achieve this goal (ref. 3).

Courage (ref. 4) did an experimental study of an intershaft squeeze film damper which was quite similar to that of Hibner *et. al.* (ref. 2,3), i.e. the oil film rotated at the speed of the inner (LP) rotor. He mentioned that another possible damper configuration would be one in which the oil film rotates at the speed of the outer (HP) rotor. His experimental rig was also unstable above the first critical speed. He suggested, as a solution to the instability problem, a damper configuration in which there are two squeeze films, one rotating at the speed of the inner (LP) rotor, and one rotating at the speed of the outer (HP) rotor, but he did not determine the feasibility of such a design.

Recently, Li *et. al.* (ref. 5,6) used more advanced numerical methods (namely the transfer matrix method and the component mode synthesis method) to determine the steady state and transient responses of a dual rotor system incorporating intershaft squeeze film dampers. The oil film in the intershaft damper they studied was also rotating at the speed of the inner (LP) rotor. They also were able to determine that the system became unstable above the engine's critical speed. They suggested that the operating speed of the engine should be below this critical speed. Their results indicated that, below the critical speed, the use of an intershaft squeeze film damper in a rotor system is effective in reducing amplitude response and bearing loading, especially for the bearing loading at the location of the intershaft damper and adjacent rotor bearing supports.

In reference 7, Alderson conducted an experimental investigation on a two spool rig with an intershaft squeeze film damper. The oil film in his damper was also rotating at the speed of the inner (LP) rotor. He also determined that the system was unstable above the first critical speed. He was able to show that this unstable whirl was nonsynchronous with the speed of any of the rotors, and that the instability was driven by destabilizing hydrodynamic forces in the intershaft damper that develop when the system tends to whirl at a speed less than the damper spin speed. To remove the instability, he replaced the intershaft squeeze film damper with a spring cage.

From the above discussion, one may conclude that intershaft squeeze film dampers are desirable in high performance dual rotor turbomachinery, if their inherent instability above the engine's first critical speed could be overcome. In this paper, we study the stability of two Jeffcott rotors with two intershaft squeeze film dampers. It will be shown that the instability of the intershaft squeeze film damper is caused by the rotation of the oil in the previously proposed damper configurations. If the oil is rotating and the rotor is whirling, then the rotating oil will tend to damp the whirling motion below the engine's critical speed. Above the critical speed the rotating oil tends to enhance the forward whirl of the rotor thus causing the instability. A new design (ref. 8,9) to eliminate the oil film rotation in the intershaft squeeze film damper is discussed. It is shown that this design is stable for all speeds.

PREVIOUSLY PROPOSED INTERSHAFT DAMPERS

Figure 1 illustrates the two previously proposed intershaft squeeze film damper configurations. Figure 1 (a) shows the configuration in which the intershaft damper's oil film is rotating with the speed of the inner (LP) rotor. This is achieved by constraining the inner race of the intershaft rolling element bearing to rotate with the speed of the LP rotor by using a squirrel cage (a dog mechanism is sometimes used). The oil film is confined between two rings that are fitted between the inner race of the ball bearing and the LP rotor. This is the configuration (or variations of it) that was experimentally tested in references 2,4 and 7. Figure 1 (b) shows the configuration in which the intershaft damper's oil film is rotating with the speed of the outer (HP) rotor. This is achieved by constraining the outer race of the intershaft rolling element bearing to rotate with the speed of the HP rotor by using a squirrel cage. The oil film is confined between two rings that are fitted between the outer race of the ball bearing and the HP rotor.

Another configuration proposed earlier (ref. 4) consists of two intershaft rolling element bearings and two oil films, one rotating at the speed of the inner rotor and one rotating at the speed of the outer

rotor. This configuration is just the combination of the configurations shown in figure 1. It will be shown later that such a configuration would also be unstable above the engine's fundamental critical speed.

(a)

(b)
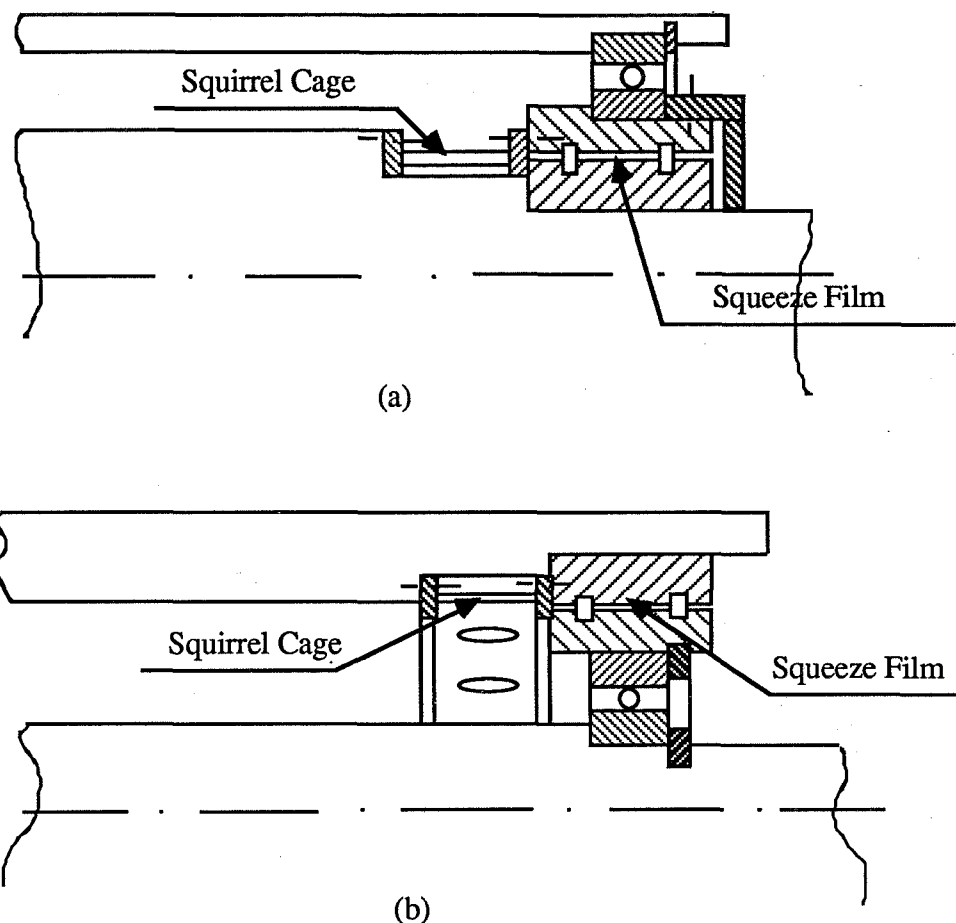
Figure 1 Previous designs

HYDRODYNAMIC FORCES IN INTERSHAFT DAMPERS

Figure 2 shows the nomenclature used in an intershaft squeeze film damper. At any angle θ measured from the whirling (r , t, z) coordinate system, which is centered at the center of the bearing but whirling with the journal (with z perpendicular to the plane of the paper), the film thickness h is given by

$$h = c - e \cos \theta \tag{1}$$

where c is the clearance, and e is the eccentricity of the journal in the bearing.

The forces generated in a squeeze film damper are usually calculated based on Reynolds equation[†]. Although more elaborate analytical models of the forces in squeeze film dampers exist (ref. 11), which include the effects of fluid inertia, they will not be used here since the instability can be completely described based on the more simple model based on Reynolds equation. Also for values of squeeze

---

[†] For a derivation of Reynolds equation see, for instance, reference 10.

Reynolds number significantly less than 10, the effects of fluid inertia can be neglected (ref. 12), but the instability would still exist.
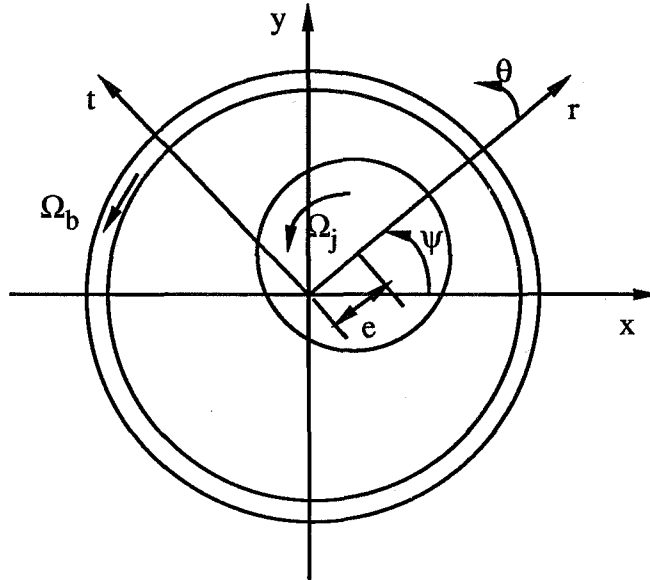
Figure 2 Intershaft Squeeze Film Damper

Reynolds equation is the differential equation that the pressure in the oil film bearing has to satisfy. For an intershaft squeeze film damper, Reynolds equation is

$$\frac{1}{R}\frac{\partial}{\partial \theta}\left(\frac{h^3}{\mu R}\frac{\partial p}{\partial \theta}\right)+\frac{\partial}{\partial z}\left(\frac{h^3}{\mu}\frac{\partial p}{\partial z}\right)=-12\,(\,e\,\dot{\psi}\sin\theta+\dot{e}\cos\theta\,)\,+6\,(\,\Omega_b+\Omega_j\,)\,\frac{\partial h}{\partial \theta} \qquad (2)$$

where R is the radius of the bearing, μ is the viscosity of the oil, p is the pressure, $\dot{e}$ and $e\dot{\psi}$ are the radial and tangential velocities of the journal with respect to the bearing, respectively, and Ω_b and Ω_j are the angular velocities of the bearing and the journal respectively. For the intershaft damper of figure 1 (a), we have $\Omega_b = \Omega_j = \Omega_1$, where Ω_1 is the rotational speed of the inner (LP) rotor, while for the intershaft damper of figure 1 (b), we have $\Omega_b = \Omega_j = \Omega_2$, where Ω_2 is the rotational speed of the outer (HP) rotor. We will study the forces in the damper of figure 1 (a), that is we have $\Omega_b = \Omega_j = \Omega_1$, but the results can be applied to the damper of figure 1 (b) just by replacing Ω_1 with Ω_2.

For short dampers, with length to diameter ratio less than 0.25, the short bearing approximation (ref. 10) is usually used, which implies that the oil flow in the damper is predominantly axial and thus the pressure gradient in the θ-direction is much smaller than the pressure gradient in the z-direction and can be neglected in equation (2). In this case, Reynolds equation can be integrated with respect to z subject to the boundary conditions that the pressure is atmospheric at z = L/2 and at z = - L/2, then the pressure becomes

$$p=\frac{6\,\mu}{h^3}\left(\frac{L^2}{4}-z^2\right)[\,\dot{e}\cos\theta+e\,(\,\dot{\psi}-\Omega_1\,)\sin\theta\,] \qquad (3)$$

66

The forces acting on the journal are obtained by integrating the pressure over both θ and z. Thus the radial and tangential forces are given by

$$F_r = -\int_{\theta_1}^{\theta_2} \int_{-\frac{L}{2}}^{\frac{L}{2}} p \cos\theta \; R \; d\theta \; dz$$

$$F_t = -\int_{\theta_1}^{\theta_2} \int_{-\frac{L}{2}}^{\frac{L}{2}} p \sin\theta \; R \; d\theta \; dz$$

respectively, where θ_1 and θ_2 represent the extent of the film. The forces in the damper depend heavily on cavitation, but since the instability under investigation is not caused by cavitation, and will, in fact, occur for both cavitated and uncavitated dampers, thus, for simplicity, we are going to assume an uncavitated damper and we have a full film and $\theta_1 = 0$ and $\theta_2 = 2\pi$. This would be the case if the damper was highly pressurized. In this case the damper forces become

$$F_r = -\frac{\mu R L^3}{c^3} \frac{\pi(1+2\varepsilon^2)}{(1-\varepsilon^2)^{5/2}} \dot{e} \tag{4}$$

$$F_t = -\frac{\mu R L^3}{c^3} \frac{\pi}{(1-\varepsilon^2)^{3/2}} e(\dot{\psi} - \Omega_1) \tag{5}$$

where $\varepsilon = e/c$, is the eccentricity ratio. The tangential force F_t acts in the direction opposite of the whirl if $\dot{\psi} > \Omega_1$, while if $\dot{\psi} < \Omega_1$ then F_t acts in the direction of the whirl. This is the case in which the oil is rotating at the speed of the LP rotor Ω_1 (fig. 1 (a)). For the intershaft squeeze damper of figure 1 (b) in which the oil is rotating at the speed of the HP rotor Ω_2, the tangential force F_t acts in the direction opposite of the whirl if $\dot{\psi} > \Omega_2$, while if $\dot{\psi} < \Omega_2$ then F_t acts in the direction of the whirl.

It should be noted that the radial force acting on the journal, equation (4), is a damping force that is proportional to the radial velocity of the journal, however, it is a nonlinear damping force because of the dependence on the eccentricity of the journal in the damper. For small oscillations of the journal in the damper, the damping force can be linearized, and the linear damping coefficient C will be

$$C = \frac{\pi \mu R L^3}{c^3} \tag{6}$$

Similarly, it can be shown that, for small oscillations, the linearized damping coefficient for the tangential force is also given by equation (6). Thus, if we consider the plane of the damper in figure 2 to be a complex plane, then the force acting in the damper, for small oscillations, considering equations (4)-(6), is

$$F_d = -C[\dot{Z}_e - i\Omega_1 Z_e] \tag{7}$$

where F_d is the complex linearized damping force acting in the damper, Z_e is the position vector of the journal in the damper in the complex plane, and $i = \sqrt{-1}$.

Consider a rotor system consisting of two Jeffcott rotors of masses m_1 and m_2, as shown in figure 3. The inner rotor, which represents the low pressure (LP) rotor in a two spool gas turbine, is mounted on two identical rolling element bearings (which are assumed to be rigid and massless), and is rotating at Ω_1, and has a stiffness K_1. The outer rotor, which represents the high pressure (HP) rotor, is mounted on two intershaft squeeze film dampers (similar to those in figure 1 (a)), and is rotating at Ω_2, and has a stiffness K_2.
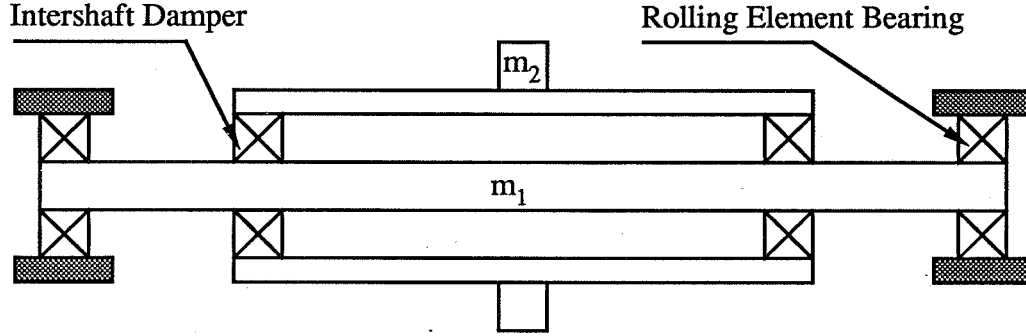
Figure 3 Schematic of the rotor system under investigation

Since the rotor system shown in figure 3 is symmetric, then we can use the planar rotor model introduced by Crandall in reference 13, shown in figure 4, to model this system. The outer massless ring of figure 4 represents the journal of the LP rotor rotating at Ω_1 in the ball bearings. The mass of the LP rotor is represented by the second outer ring which has mass m_1 and is rotating at Ω_1. The flexibility of the LP rotor is represented by the springs of stiffness $K_1/2$ connected between the two outermost rings. The two intershaft squeeze film dampers are represented by the rotating dashpots of linearized coefficients C, and they are rotating between the ring representing the mass of the LP rotor and the outer race of the ball bearing in figure 4 which represents the inner race of the ball bearing of figure 1(a) and is constrained to rotate at Ω_1. The mass of the HP rotor is represented by the disk of mass m_2 in the center of figure 4. The flexibility of the HP rotor is represented by the springs of stiffness $K_2/2$. It should be noted that we did not incorporate in this model the stiffness of the retaining spring, that is we are assuming that the intershaft squeeze film damper is constrained to rotate at the speed of the LP rotor by using a dogging mechanism rather than by a squirrel cage. This will not affect the stability analysis, since the instability is caused by the hydrodynamic forces in the oil film, however, if a squirrel cage is used then it will affect the critical speeds of the rotor system.

Considering figure 4 to be a complex plane, and neglecting gyroscopic effects, then the equations of motion can be obtained directly from figure 4, as

$$m_1 \ddot{Z}_1 + K_1 Z_1 = 2 F_d \tag{8}$$
$$m_2 \ddot{Z}_2 + K_2 Z_2 = K_2 Z_3 \tag{9}$$
$$K_2 (Z_3 - Z_2) = - 2 F_d \tag{10}$$

where F_d is given by equation (7) with

$$Z_e = Z_1 - Z_3 \tag{11}$$

We have used here Z to represent the position vectors in the complex plane, i.e. Z = x + iy, with the subscripts 1 for the LP rotor, 2 for the HP rotor, and 3 for the position of the intershaft rolling element bearing. Equations (8) and (9) are the equations of motion of the LP and HP rotors, respectively, and equation (10) represents the force balance at the intershaft bearing.
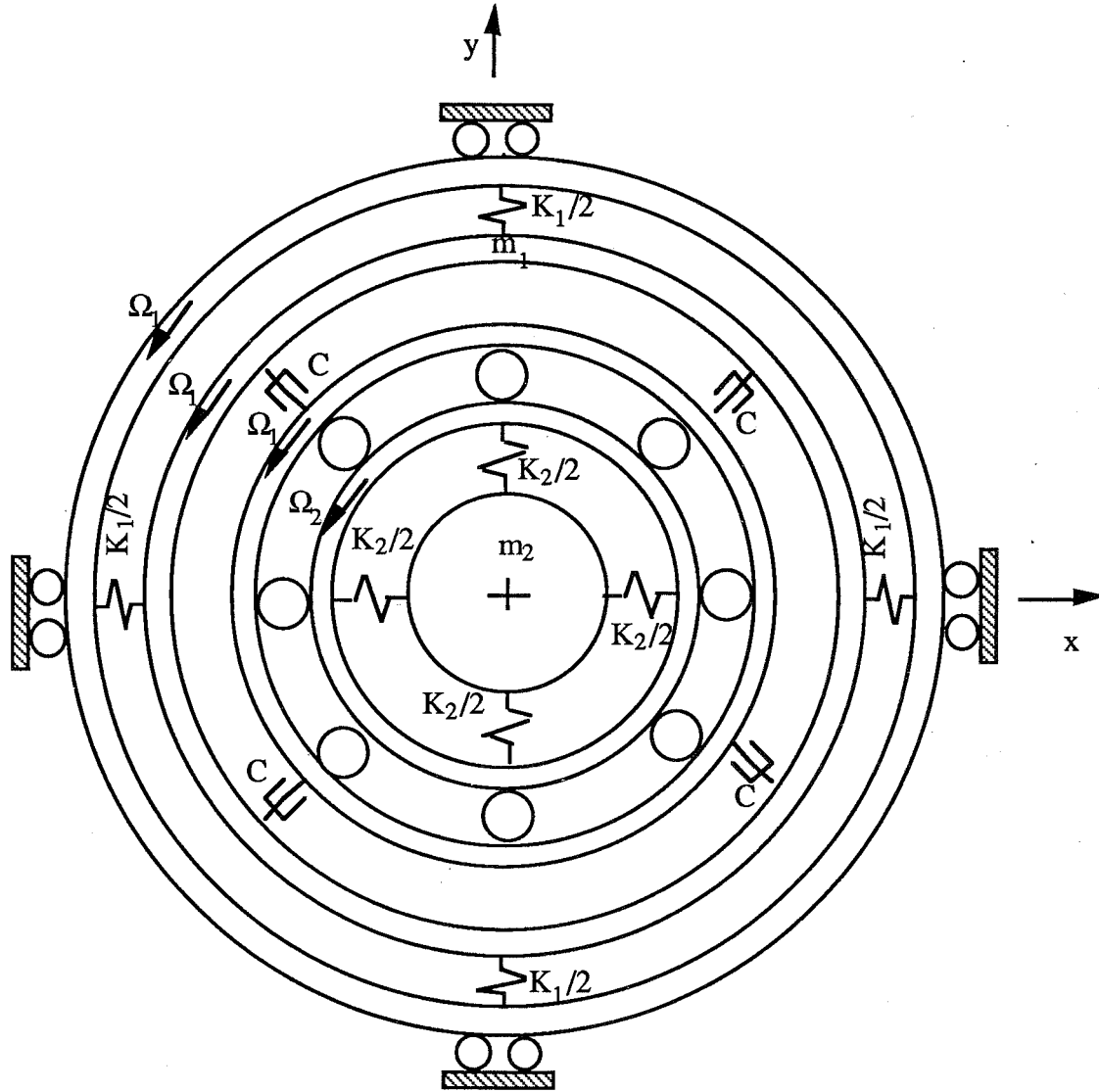
Figure 4 Planar rotor model

We begin by studying the undamped case. If the oil film was rigid, then the system would be undamped, as can be easily visualized in figure 4, if the dashpots become rigid. That would be the case if the damping coefficient became infinite. In this case the system can be thought of as the two-mass-two-spring system of figure 5, as the motions in the x and y directions are uncoupled. Then equations (8) and (9) reduce to

$$\begin{bmatrix} m_1 & 0 \\ 0 & m_2 \end{bmatrix} \begin{Bmatrix} \ddot{x}_1 \\ \ddot{x}_2 \end{Bmatrix} + \begin{bmatrix} K_1 + K_2 & -K_2 \\ -K_2 & K_2 \end{bmatrix} \begin{Bmatrix} x_1 \\ x_2 \end{Bmatrix} = \begin{Bmatrix} 0 \\ 0 \end{Bmatrix} \qquad (12)$$

in the x-direction, with similar equations in the y-direction. The motion in the complex plane has exactly the same natural frequencies for the motion in both the x and y directions. It is useful to think of these natural frequencies as forward and backward whirling motions. Thus this system exhibits two forward whirls and two backward whirls corresponding to the four degrees of freedom the system possesses.
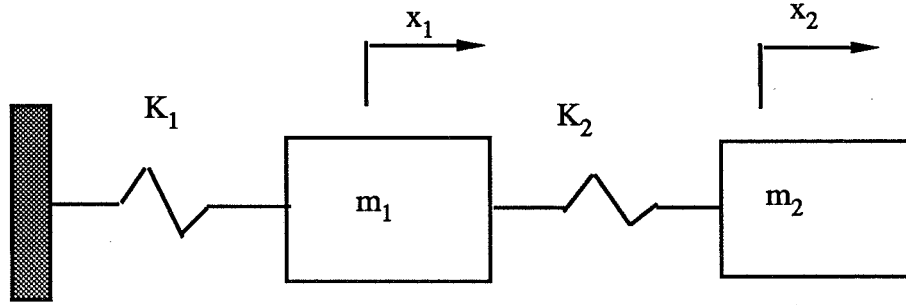
Figure 5 Undamped model of system

The characteristic equation for the system described by equation (12) is

$$\omega_n^4 - [\, \omega_{11}^2 + (\mu + 1)\, \omega_{22}^2 \,]\, \omega_n^2 + \omega_{11}^2\, \omega_{22}^2 = 0 \tag{13}$$

where $\omega_{11}^2 = K_1/m_1$, $\omega_{22}^2 = K_2/m_2$, $\mu = m_2/m_1$, and ω_n is a natural frequency of the system. ω_{11} is the natural frequency of the LP rotor alone, and ω_{22} is the natural frequency of the HP rotor alone. The natural frequencies of the system can be obtained by solving the quadratic of equation (13) and we get

$$\omega_{n2,1}^2 = \frac{1}{2} \{\, [\, \omega_{11}^2 + (\mu + 1)\, \omega_{22}^2 \,] \pm \sqrt{D} \,\} \tag{14}$$

where

$$D = \omega_{11}^4 + 2\,(\mu - 1)\, \omega_{11}^2\, \omega_{22}^2 + (\mu + 1)^2\, \omega_{22}^4 \tag{15}$$
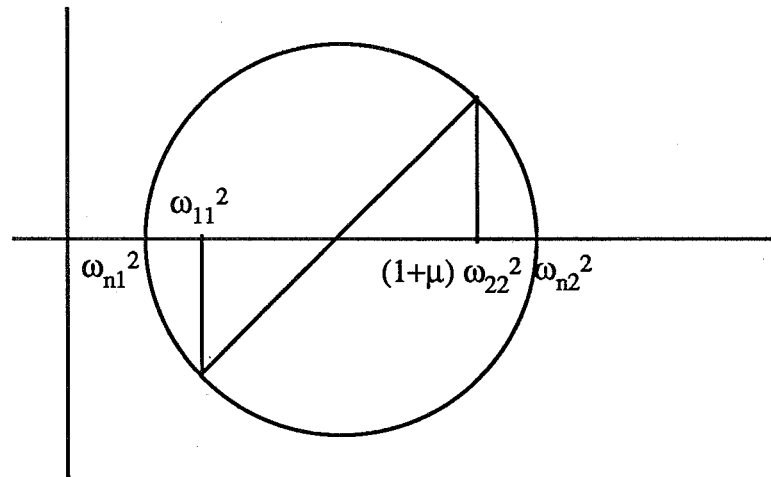
Figure 6 Mohr's circle representation in the ω^2-plane

ω_{n1} is the first natural frequency and ω_{n2} is the second natural frequency of the system. It should be emphasized that there are two forward whirls: one at ω_{n1} and the other at ω_{n2} , and there are two backward whirls one at $-\omega_{n1}$ and the other at $-\omega_{n2}$. It will prove beneficial to know the relative magnitudes of ω_{n1},

ω_{n2} and ω_{11}. To do so, we use the Mohr's circle representation of equations (13) and (14) (ref. 14), which is shown in figure 6, and from which it can be seen that

$$\omega_{n2}{}^2 > \omega_{11}{}^2 > \omega_{n1}{}^2 \qquad (16)$$

To study the stability of the damped system, we assume that Z_1, Z_2 and Z_3 have $e^{i\omega t}$ time behavior, where ω is a complex quantity. If the imaginary part of ω is negative, then the system is unstable. Substituting equations (7), (9), (10) and (11) into equation (8), and after some manipulation, we get

$$\omega^4 - [\, \omega_{11}^2 + (\mu + 1)\, \omega_{22}^2 \,]\, \omega^2 + \omega_{11}^2\, \omega_{22}^2 + \frac{i\,\eta\,\omega_{11}\,\omega^2\,(\omega^2 - \omega_{11}^2)}{(\Omega_1 - \omega)} = 0 \qquad (17)$$

where $\eta = K_2/(2\,C\,\omega_{11})$ is a nondimensional parameter. It should be noted that as $\eta \to 0$, i.e. as $C \to \infty$, equation (17) reduces to equation (13) for the undamped system. This would be the case if the oil film becomes rigid. Solving the above quadratic, we get

$$\omega^2 = \frac{1}{2} \left\{ [\, \omega_{11}^2 + (\mu + 1)\, \omega_{22}^2 \,] \pm \sqrt{D - 4\,\frac{i\,\eta\,\omega_{11}\,\omega^2\,(\omega^2 - \omega_{11}^2)}{(\Omega_1 - \omega)}} \right\} \qquad (18)$$

We can solve either equation (17) or (18) numerically to obtain the characteristic roots for this system. However, we need to find analytically an expression to determine the effect of the intershaft damper on the stability of the system, and also we need an indication of the regions of instability. We can consider the effect of relaxing the rigid damper for the undamped system, and introduce some damping into the undamped system, and study its effects on the stability. This corresponds to studying the system for small values of η. Thus, expanding the square root in equation (18) and neglecting terms of $O(\eta^2)$, equation (18) becomes

$$\omega^2 = \frac{1}{2} \left\{ [\, \omega_{11}^2 + (\mu + 1)\, \omega_{22}^2 \,] \pm \sqrt{D} \left(1 - \frac{i\,2\,\eta\,\omega_{11}\,\omega^2\,(\omega^2 - \omega_{11}^2)}{(\Omega_1 - \omega)\,D} \right) \right\} \qquad (19)$$

The real part of equation (19) represents the square of the undamped natural frequencies $\omega_{n1}{}^2$ and $\omega_{n2}{}^2$. To obtain the damped frequencies ω^2, we have to iterate on equation (19) in the neighborhood of $\omega_{n1}{}^2$ for the first mode, and in the neighborhood of $\omega_{n2}{}^2$ for the second mode. Note that there is a sign change in the imaginary part of ω in equation (19) when we are studying the motion in the neighborhood of $\omega_{n1}{}^2$, from that when we are studying the motion in the neighborhood of $\omega_{n2}{}^2$. Thus we have two equations to iterate on, for the first mode

$$\omega^2 = \omega_{n1}^2 + \frac{i\,\eta\,\omega_{11}\,\omega^2\,(\omega^2 - \omega_{11}^2)}{(\Omega_1 - \omega)\,\sqrt{D}} \qquad (20)$$

and for the second mode

$$\omega^2 = \omega_{n2}^2 - \frac{i\,\eta\,\omega_{11}\,\omega^2\,(\omega^2 - \omega_{11}^2)}{(\Omega_1 - \omega)\,\sqrt{D}}$$ (21)

Iterating on equation (20) in the neighborhood of ω_{n1} we get (neglecting terms of $O(\eta^2)$)

$$\omega = \omega_{n1} - \frac{i\,\eta\,\omega_{11}\,\omega_{n1}\,(\omega_{11}^2 - \omega_{n1}^2)}{2\,(\Omega_1 - \omega_{n1})\,\sqrt{D}}$$ (22)

for the forward whirl in the first mode. Note that, by equation (16), $\omega_{11}^2 > \omega_{n1}^2$, and thus the quantity $(\omega_{11}^2 - \omega_{n1}^2)$ is always positive. Equation (22) shows that the forward whirl in the first mode will be stable as long as Ω_1, the speed of the LP rotor, is less than ω_{n1}, the fundamental natural frequency of the system. If $\Omega_1 > \omega_{n1}$, the imaginary part of ω will be negative and the forward whirl in the first mode will be unstable.

Iterating on equation(20) in the neighborhood of $-\omega_{n1}$, we get (neglecting terms of $O(\eta^2)$)

$$\omega = -\omega_{n1} + \frac{i\,\eta\,\omega_{11}\,\omega_{n1}\,(\omega_{11}^2 - \omega_{n1}^2)}{2\,(\Omega_1 + \omega_{n1})\,\sqrt{D}}$$ (23)

for the backward whirl in the first mode. Equation (23) shows that the backward whirl in the first mode is always stable, irrespective of the speeds of the rotors, since the imaginary part of ω is always positive.

For the forward whirl in the second mode, we iterate on equation (21) in the neighborhood of ω_{n2}. Thus (neglecting terms of $O(\eta^2)$)

$$\omega = \omega_{n2} - \frac{i\,\eta\,\omega_{11}\,\omega_{n2}\,(\omega_{n2}^2 - \omega_{11}^2)}{2\,(\Omega_1 - \omega_{n2})\,\sqrt{D}}$$ (24)

Also, by equation (16), $\omega_{n2}^2 > \omega_{11}^2$, and thus the quantity $(\omega_{n2}^2 - \omega_{11}^2)$ is always positive. Equation (24) shows that the forward whirl in the second mode is stable if the speed of the LP rotor Ω_1, is less than ω_{n2}, the second natural frequency of the system. If $\Omega_1 > \omega_{n2}$ the forward whirl in the second mode will become unstable, as the imaginary part of ω in equation (24) would be negative.

Iterating on equation (21) in the neighborhood of $-\omega_{n2}$, we get (neglecting terms of $O(\eta^2)$)

$$\omega = -\omega_{n2} + \frac{i\,\eta\,\omega_{11}\,\omega_{n2}\,(\omega_{n2}^2 - \omega_{11}^2)}{2\,(\Omega_1 + \omega_{n2})\,\sqrt{D}}$$ (25)

for the backward whirl in the second mode. It can be seen from equation (25) that the imaginary part of ω is always positive, for the backward whirl in the second mode, and thus the backward whirl in the second mode will always be stable, irrespective of the speeds of the rotors.

Thus, we have shown that, for the intershaft squeeze film damper of figure 1(a), the backward whirls are always stable, while the forward whirls become unstable if the speed of rotation of the LP rotor surpasses the natural frequencies of the system. Thus, the intershaft squeeze film damper of figure 1(a)

will become a destabilizing device if the speed of the LP rotor surpasses the fundamental critical speed. For the intershaft squeeze film damper of figure 1(b), as mentioned earlier, all the above stability analysis will be valid, if we replace Ω_1 by Ω_2, the speed of the HP rotor, in all of the equations. Thus, for the intershaft squeeze film damper of figure 1(b), the backward whirls are always stable, while the forward whirls become unstable if the speed of rotation of the HP rotor surpasses the natural frequencies of the system. Also, we conclude that the intershaft squeeze film damper of figure 1(b) will become a destabilizing device if the speed of the HP rotor surpasses the fundamental critical speed.

DESCRIPTION OF THE INSTABILITY

If a tangential force acts in the same direction as the whirl, then it would be adding energy to the whirl, and thus results in the system spiralling outwards with an ever growing whirl amplitude (ref. 15). In the preceding sections, we had shown that the intershaft squeeze film damper of figure 1 (a) produced a tangential force acting on the journal in the same direction as the forward whirl if $\dot{\psi} < \Omega_1$. Thus it is pumping energy into the forward whirl and causing the instability. This energy is obtained from the kinetic energy of the spinning of the LP rotor. The intershaft squeeze film damper of figure 1 (b) produces a tangential force acting on the journal in the same direction as the forward whirl if $\dot{\psi} < \Omega_2$. Thus it is pumping energy into the forward whirl obtained from the kinetic energy of the spinning of the HP rotor, and causing the instability.

On the other hand, if the tangential force is acting in the opposite direction of the whirl, then it would be removing energy from the whirl. This is the damping mechanism of squeeze film dampers in general. For the intershaft squeeze film damper of figure 1 (a) this occurs when $\dot{\psi} > \Omega_1$, while for the intershaft squeeze film damper of figure 1 (b) this occurs when $\dot{\psi} > \Omega_2$. Also, this occurs for the backward whirls, the tangential force is always opposing the whirl.

From the above analysis it can be seen that the threshold of instability of intershaft squeeze film dampers is when the whirl frequency $\dot{\psi}$ is equal to the speed of rotation of the oil (Ω_1 for the intershaft squeeze film damper of figure 1 (a), and Ω_2 for the intershaft squeeze film damper of figure 1 (b)). For free vibration, the whirl frequency $\dot{\psi}$ of the rotor system is its natural whirling frequency. Thus rotor systems incorporating intershaft squeeze film dampers of the configuration shown in figure 1 (a) become unstable if the speed of rotation of the LP rotor Ω_1 is larger than the lowest natural whirling frequency of the system, while for rotor systems incorporating intershaft squeeze film dampers of the configuration shown in figure 1 (b), they become unstable if the speed of rotation of the HP rotor Ω_2 is larger than the lowest natural whirling frequency of the system. It is important to interpret Ω_1 and Ω_2, for the intershaft dampers of figure 1(a) and figure 1(b), respectively, as being the speed of oil rotation in the damper, in the absence of vibration. This oil film rotation is due to the spinning of the journal and the bearing at the speed of either the LP or the HP rotor.

The design proposed by Courage (ref. 4) incorporating two oil films, one rotating at Ω_1 and one rotating at Ω_2 will also be unstable if both Ω_1 and Ω_2 are above the lowest natural whirling frequency (first critical speed) of the rotor system, since the tangential forces in both of the oil films will act to enhance the whirl. If one of the rotors is operating above the critical speed and the other below it, then the stability of the rotor system will depend on the amount of energy being pumped into the whirl by the unstable damper and the amount of energy removed from the whirl by the stable damper.

A pictorial representation of the instability is shown in figure 7. The outer ring in figure 7 represents the bearing while the inner ring represents the journal. If the oil in the gap is rotating at a speed

73

Ω, then as the journal whirls in the bearing at a speed ω, the oil film will produce a drag force on the journal opposite to the whirl if ω is larger than Ω (figure 7 (a)), and thus acts to damp the whirl. While if Ω is larger than ω then a drag force acts on the journal in the direction of the whirl (figure 7 (b)), and thus acts to enhance the whirl. If the oil film is stationary, then the oil film will always produce a drag force opposing the whirl (figure 7 (c)), and thus will always be stable.

(a) $\omega > \Omega$ (b) $\omega < \Omega$ (c) $\Omega = 0$
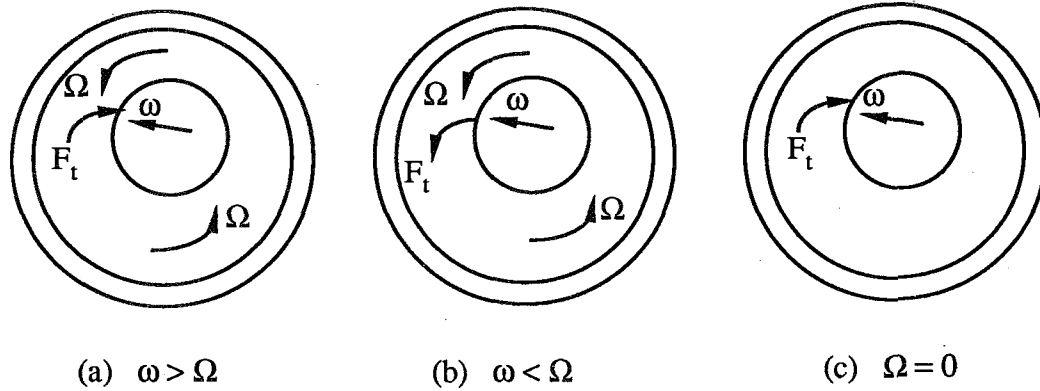
Figure 7 Instability mechanism

STABLE INTERSHAFT DAMPER

If the rotor system is operating above a natural frequency it is said to be operating supercritically. Usually high performance turbomachinery operate supercritically, above several critical speeds, but because of the instability described above, rotating systems incorporating either of the intershaft squeeze film dampers shown in figure 1 cannot operate supercritically.

From the discussion in the preceding section, it can be seen that the reason for the instability is the rotation of the oil film. The oil film is rotating because the journal and the bearing are both rotating, at Ω_1 for the damper of figure 1 (a) and at Ω_2 for the damper of figure 1 (b). It can also be seen that if the oil film was stationary (figure 7 (c)) then the intershaft squeeze film damper would be stable irrespective of the speed of either the LP or the HP rotor. A stationary oil film can only be achieved if both the journal and the bearing are not rotating.

To show that the intershaft squeeze film damper will be stable if both the journal and the bearing are not rotating, let us find the forces acting on the journal. In this case, Ω_j and Ω_b are both zero, and if we substitute in Reynolds equation, equation (2), and solve for the pressure, and then integrate the pressure over θ and z, as we did before, we will find that the tangential force acting on the journal is

$$F_t = -\frac{\mu R L^3}{c^3} \frac{\pi}{(1 - \varepsilon^2)^{3/2}} e \dot{\psi} \tag{26}$$

Thus from equation (26) it can be seen that the tangential force F_t, for an intershaft damper with a stationary oil film, always acts in the opposite direction of the whirl, and thus it is always removing energy from the whirl. Also, if we substitute for $\Omega_1 = 0$ in the stability analysis equations, it can be seen that the intershaft damper with a stationary oil film is always stable.

A new design of intershaft squeeze film dampers (ref. 8,9) to eliminate the instability by incorporating a stationary oil film is shown in figure 8. In this design two intershaft rolling element bearings are used. The outer race of the outer bearing is rotating with the speed of the HP rotor, and the inner race of the inner bearing is rotating with the speed of the LP rotor. The inner race of the outer bearing and the outer race of the inner bearing are both held stationary by two squirrel cages connected to the engine frame. The oil film is confined in an annulus between the nonrotating outer race of the inner bearing and the nonrotating inner race of the outer bearing. Thus neither the rotation of the LP rotor nor the rotation of the HP rotor will reach the oil film, which will act only to damp the whirling vibration of the rotor system. The squirrel cages, which are light springs, aside from keeping the oil film stationary, provide a means for centering the squeeze film damper.
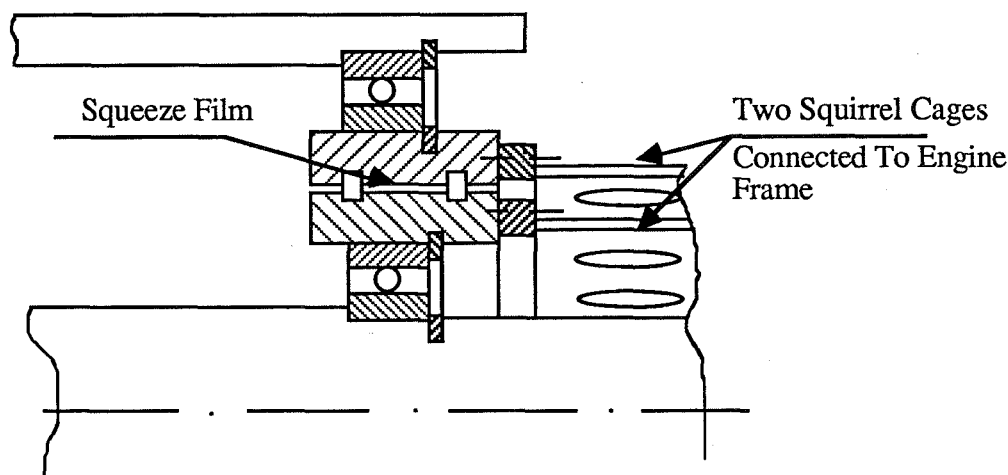
Figure 8 Stable intershaft squeeze film damper

The main advantage of this design is that intershaft squeeze film dampers can be used in rotating machinery that operate supercritically without becoming unstable. The other advantages of using intershaft squeeze film dampers are also retained, namely, the reduction of bearing loading, the reduction of cyclic stresses both in the bearings and in the support structure, and the reduction of the amplitude of vibration (ref. 2,5). Also the use of intershaft bearings results in the decrease of rubbing between the rotors and the reduction of shaft deflections (ref. 1).

The disadvantage of this design of intershaft squeeze film dampers is that the damper must be located close to the support structure. Thus one of the advantages of using intershaft bearings is lost, namely the obstruction of the aerodynamic flow path. Also, because the damper must be located close to the support structure, it may not be always possible for the engine designer to locate the damper at the best possible locations to damp the engine modes effectively. If the damper is located near a node of one or more of the important modes of the engine, then it will provide very little damping to these modes. The use of long squirrel cages may be a remedy for such a situation, but since the squirrel cages act as soft springs, then having unnecessary flexibility at the intershaft bearing location may be detrimental to the overall dynamics of the engine. Thus such a solution should be assessed carefully.

Another disadvantage may be the cost of an additional ball bearing. The stable design of the intershaft squeeze film damper requires two intershaft ball bearings instead of one. Usually engine designers try to minimize the number of bearings in the engine. If the designer had the luxury of adding another ball bearing to the engine, then he may choose to place it in a non-intershaft location, and this may well reduce the bearing loadings. But again this may not always be possible, since this would require that the support structure be close to the rotor in yet another location.

CONCLUSION

A stability analysis of rotors incorporating intershaft squeeze film dampers was presented. A rotor model consisting of two Jeffcott rotors with two intershaft squeeze film dampers was investigated. Examining the system characteristic equation for the conditions at which the roots indicate an ever growing unstable motion, result in the stability conditions. The reason for the instability of the previously proposed intershaft squeeze film dampers above the engine's first critical speed, is shown to be the rotation of the oil film. If the oil film is rotating at a speed above the critical speed of the engine, then it will be adding energy to the whirl from the spinning rotor, thus causing the instability.

A new design of intershaft squeeze film dampers in which the oil film is stationary is described. This design is shown to be stable irrespective of the speeds of rotation of the rotor system. The advantages and disadvantages of such a design are also discussed, and it is pointed out that although it may not be always possible to place the damper, with this design, in the best possible location to damp the engine modes effectively, this is the only stable intershaft squeeze film damper.

REFERENCES

1. Gunter, E. J., Li, D. F., and Barrett, L. E., "Unbalance Response of a Two Spool Gas Turbine Engine with Squeeze Film Bearings", ASME paper 81-GT-219, presented at the Gas Turbine Conference & Products Show, March 9-12, 1981.

2. Hibner, D. H., Kirk, R. G., and Buono, D. F., "Analytical and Experimental Investigation of the Stability of Intershaft Squeeze Film Dampers - Part 1: Demonstration of Instability", *Journal of Engineering for Power*, Trans. ASME, Vol. 99, No. 1, Jan. 1977, pp. 47-52.

3. Hibner, D. H., Bansal, P. N., and Buono, D. F., "Analysis and Experimental Investigation of the Stability of Intershaft Squeeze Film Dampers - Part 2: Control of Instability", *Journal of Mechanical Design*, Trans. ASME, Vol. 100, No. 3, July 1978, pp. 558-562.

4. Courage, J. B., "Experimental Study of an Intershaft Squeeze Film Bearing", Second International Conference on Vibrations in Rotating Machinery, I. Mech. E., 1980, pp. 375-380.

5. Li, Q., Yan, L., and Hamilton, J. F., "Investigation of the Steady-State Response of a Dual-Rotor System With Inter-Shaft Squeeze Film Damper", *Journal of Engineering for Gas Turbine and Power*, Trans. ASME, Vol. 108, No. 4, Oct. 1986, pp. 605-612.

6. Li, Q., and Hamilton, J. F., "Investigation of the Transient Response of a Dual-Rotor System With Intershaft Squeeze Film Damper", *Journal of Engineering for Gas Turbine and Power*, Trans. ASME, Vol. 108, No. 4, Oct. 1986, pp. 613-618.

7. Alderson, R. G., "Instability of an Intershaft Squeeze Film Damper in a Two-Spool Rotor Dynamics Simulator", Rotordynamic Instability Problems in High-Performance Turbomachinery, NASA Conference Publication 2443, 1986, pp. 315-323.

8. El-Shafei, A., "A New Design of Intershaft Squeeze Film Dampers", Proceedings of the Vibration Institute, 1988, pp. 15-23.

9. El-Shafei, A., "Stable Intershaft Squeeze Film Damper", U.S. Patent number 4,781,077, November 1988.

10. Szeri, A., Tribology : Friction, Lubrication, and Wear , Hemisphere Publishing Co., New York, 1980.

11. El-Shafei, A., "Dynamics of Rotors Incorporating Squeeze Film Dampers", Ph.D. Thesis, Department of Mechanical Engineering, Massachusetts Institute of Technology, 1988.

12. El-Shafei, A., "Fluid Inertia Effects in Squeeze Film Dampers", presented at Damping 89, West Palm Beach, FL, February 1989, pp. GAA 1-15.

13. Crandall, S. H., "The Role of Damping in Vibration Theory", *Journal of Sound and Vibration*, Vol. 11, No. 1, 1970, pp. 3-18.

14. Den Hartog, J. P., Mechanical Vibrations, Dover, New York, 1985.

15. Crandall, S. H., "The Physical Nature of Rotor Instability Mechanisms", in Rotor Dynamical Instability, (M. L. Adams, editor), AMD-Vol. 55, ASME, N.Y., 1983.

MEASUREMENTS OF PRESSURE DISTRIBUTIONS AND FORCE COEFFICIENTS IN A SQUEEZE FILM DAMPER – PART I: FULLY OPEN ENDED CONFIGURATION

S.Y. Jung, L.A. San Andres, and J.M. Vance
Department of Mechanical Engineering
Texas A&M University
College Station, Texas 77843-3123, U.S.A.

Experimental measurements of pressure distributions and force coefficients obtained from a squeeze film damper test rig executing a circular centered orbit are presented. The test rig has been designed to study the effect of fluid inertia on the pressure field and dynamic force response on a damper configuration with a relatively large clearance. Past measurements of the squeeze film damper force characteristics have been carried out at squeeze film Reynolds numbers not exceeding a value equal to 10. In the present paper, following contemporary applications, operations at Reynolds numbers up to fifty are tested for CCO's with an orbit radius=0.8 ($Re \leq 10$ at $\epsilon = 0.5$). The results obtained from a fully open ended damper are presented in detail. The effects of fluid inertia, cavitation and the open end geometry on the pressure distributions and force coefficients are discussed.

NOMENCLATURE

C	=SFD radial clearance
C_{dRe}	$=\rho\omega L R^3/C$ damping coefficient conversion factor
C_{iRe}	$=\rho L R^3/C$ inertia coefficient conversion factor
C_f	$=\mu\omega R^3 L/C^2$ force conversion factor
C_p	$=\mu\omega R^2/C^2$ pressure conversion factor
C_{pRe}	$=C_p \cdot Re = \rho\omega^2 R^2$ pressure conversion coefficient
C_{tt}	=dimensionless direct damping coefficients
	$=-f_t/\epsilon$, normalized by $\mu R^3 L/C^3$
D	=damper journal diameter
D_{rr}	=dimensionless direct inertia coefficients
	$=f_r/\epsilon$, normalized by $\mu R^3 L/\omega C^3$
f_r, f_t	=dimensionless radial and tang. film forces normalized by C_f
	$=\int p\cos\theta d\theta$, $\int p\sin\theta d\theta$, respectively
L	=damper journal length

p	=dimensionless pressure normalized by C_p
R	=damper journal radius
Re	=$\omega C^2/\nu$ modified Reynolds number
Z	=axial coordinate
ϵ	=dimensionless orbit radius
θ	=circumferential coordinate
μ	=absolute viscosity
ν	=kinematic viscosity
ρ	=density
ϕ	=$90° + \tan^{-1} f_r/f_t$, phase angle
ω	=frequency of damper journal center motion

INTRODUCTION

Squeeze film dampers have been successfully used to control vibration in turbomachinery. Numerous studies both theoretically and experimentally have been presented for squeeze film dampers. However, due to the fluid film pressure distortion factors such as oil grooves, end seals, cavitation, and fluid inertia, experimental results are often not consistent with predictions.

In the 1970's, many researchers [1-5] measured the hydrodynamic pressure field and damping coefficients from a number of squeeze film damper test rigs and compared them to the conventional solution of Reynolds equation. Correlation between experimental measurements and theoretical predictions was qualitatively reasonable but quantitatively poor in most cases.

In the 1980's, the effect of fluid inertia on the pressure distribution and dynamic force response of squeeze film dampers was shown to be of great importance [6-10]. Experimental measurements [11-15] demonstrated the significant effect of fluid inertia through both the direct measurements of film pressure and forces and the indirect measurements from the dynamic response of rotor systems.

Most measurements of a squeeze film damper have been carried out at squeeze film Reynolds numbers not exceeding 10. However, in contemporary practical applications, the squeeze Reynolds number ranges from 10 to 50. Thus the need exists for experimental measurements to cover the maximum practical range of Reynolds numbers up to Re=50.

The objective of this paper is to present an experimental study on the effect of fluid inertia and cavitation on the pressure distributions and force coefficients. Two types of squeeze film dampers with its journal executing a circular centered orbit are tested: fully open ended and partially sealed configurations. The results obtained from a fully open ended test rig and a partially sealed test rig are presented in part I and II, respectively. The range of Reynolds number tested is between 2 and 50. Measured fluid film pressure profiles and force coefficients are compared with existing theoretical predictions.

EXPERIMENTAL FACILITY AND PROCEDURE

Description of the SFD Test Apparatus

The schematic drawing in Figure 1 shows the structure of the squeeze film damper (SFD) test rig. The damper journal with an outer diameter of 12.7 cm (5 inch) and a length of 2.4 cm (0.94 inch) is mounted with a press fit on the outer race of a ball bearing. An O-ring seal is installed at the left end face of the damper journal and provides a full proof of a no leak seal. The L/D ratio is equal to 0.188 and simulates a short bearing configuration typical of a real engine damper application. The clearance is 0.159 cm (0.0625 inch). The large clearance produces large values of Reynolds number at low speeds so that significant effects of fluid inertia are produced.

The end plate of the journal secures the right end face of the journal. The outer diameter of the end plate is used to measure the orbital motion of the journal during operation. The end plate not only preserves alignment of the housing and journal, but also provides a circumferential end cavity. The width and depth of the end cavity are 0.44 cm (11/64 inch) and 0.40 cm (0.156 inch), respectively. The end cavity is utilized with ancillary hardware to produce several different configurations such as short, long, and finite length bearings using different types of end seals.

The ball bearing supporting the damper journal is mounted on a replaceable eccentric sleeve that lockes to the shaft with a special retainer. The shaft is driven by a constant speed electric motor at 1770 rpm (29.5 Hz). The motor end of the shaft is supported by two more ball bearings (not shown in Figure 1) mounted on stiff supports to minimize lateral movement of the shaft and the damper journal. The shaft is connected to the motor by a flexible coupling to prevent axial loads on the journal.

The bearing housing has numerous holes for oil inlet and outlet, pressure transducers, and proximity probes. Figure 2 shows a sketch of the squeeze film land. At the axial location Z0, two 0.24 cm (3/32 inch) diameter holes located at the circumferential locations 270° (top) and 90° (bottom) serve as the oil inlets to the damper annulus. The two oil inlet holes have check valves to prevent flow reversals from the squeeze film region. Dial pressure gauges are connected to the inlet lines in order to measure the oil supply pressure.

At two different axial locations, Z1=0.56 cm (0.22 inch) and Z2=1.67 cm (0.66 inch), a total of 16 holes are distributed in the circumferential direction for installation of pressure transducers (PT). These holes may be used to directly measure the temperature of the fluid film inside the damper using a dummy pressure transducer with a small hole plugged with a thermocouple wire. The unused holes in the housing are plugged with dummy pressure transducers to prevent lubricant leakage.

At the axial location Z3=3.72 cm (1.46 inch), a single 0.64 cm (1/4 inch)

diameter oil outlet is located at the circumferential location 270° (top) of the housing in order to get a completely submerged arrangement. Oil is never pumped out of the damper oil outlet, but flows naturally. The bearing housing has a hole for proximity probes (PP) at the axial location Z3 and circumferential locations 180° (left).

The Plexiglas cover with a lip seal covers the end of the bearing housing and insures a completely submerged arrangement and sufficient oil in the squeeze film region. The completely submerged arrangement prevents air entrance into the squeeze film region.

Experimental Procedure

Figure 3 shows the instrumentation arrangement for measurement of the fluid film pressure and real time calculation of the film force coefficients at a specified axial location of the SFD test rig.

In the case of a circular centered SFD, since the time variations in circumferential pressure measured at any location on the damper annulus should be identical for any one cycle of the journal, the fluid film pressure profile for a centered orbit motion can be measured with only one pressure transducer. Furthermore, since the orbit motion is centered, only one proximity probe is required to determine the dynamic eccentricity ratio.

Therefore, one proximity probe was installed at the axial location Z3 and the circumferential location 180° on the outside diameter of the end plate. The proximity probe measures the journal displacement, from which the variation of film gap in the squeeze film region can be determined. Two dynamic pressure transducers were installed at two different axial locations Z1 and Z2 and circumferential location 180° to study the axial pressure variation caused by end leakage. The variation of the pressure distribution in both the axial and the circumferential directions are monitored with two dynamic pressure transducers. The piezo-electric pressure transducers used can measure only the dynamic variation of film pressure. Thus, a strain-gage pressure transducer to measure absolute pressure was installed at the axial location Z1 and the circumferential location 330°. Absolute value of pressure obtained from the pressure transducer gives information about the cavitation pressure.

A thermocouple type T was embedded with an epoxy resin into a small hole drilled into a dummy pressure transducer at the axial location Z1 and the circumferential location 210°. The thermocouple is flush with the wall of the bearing housing so that the temperature of the oil film in the squeeze film region is directly measured. The value of temperature was input for calculation of the viscosity of the oil and the corresponding Reynolds number. The increase of the temperature of the oil is mainly due to shear friction of the oil and heat conduction from the ball bearing supporting the damper journal.

The squeeze film Reynolds number $Re = \omega C^2 / \nu$ physically represents the ratio of the fluid inertia force to the viscous force. Observation of the variation

in Reynolds number is very important to study the effects of fluid inertia on the pressure distribution and force coefficients. Since the whirling frequency ω of the journal and the radial clearance C of the SFD test rig are fixed values, the oil viscosity is the only factor that can be varied to obtain a change in the Reynolds number.

Oil viscosity was measured for a range of temperatures prior to experimental tests using a Synchro-Lectric viscometer (LVF model). Oil viscosity formulae were obtained in terms of temperature using a mathematical relation suggested in the ASTM D-341. Three kinds of oils have been used in the experimental tests; SAE30 oil (engine oil), ISO22 oil (turbine oil), and DOW10 oil (silicone oil). The range of temperature measured was between $27° C(80° F)$ and $49° C(120° F)$. The corresponding Reynolds numbers range from Re=2 to Re=7 for SAE30 oil, Re=17 to Re=35 for ISO22 oil, and Re=42 to Re=48 for DOW10 oil.

Oil supply pressures were about 68.75 KPa (10 Psig) which allowed a flow rate equal to 200 ml per min. for SAE30 oil, and about 13.8-20.6 KPa (2-3 Psig) for lower viscosity oils. Higher oil supply pressures can not be applied to the damper because of deformation of the plexiglas cover. Also, higher oil supply pressures produce a notable distortion of the fluid film pressure field, because the two small oil inlets directly supply oil into the squeeze film region (there is no circumferential oil inlet groove). The oil inlet groove is often employed in squeeze film dampers to prevent distortion of the pressure field due to inlet holes. Previous experimental measurements have shown that an oil groove has a large effect on the pressure distortion [11,13]. Since experiments with a circular centered orbit should yield pressure distributions independent of the location of the pressure transducer, it is very important to get rid of potential distortion factors for better comparison between experiment and analysis.

In the experimental measurement reported here, 60 data points per cycle per pressure transducer and proximity probe were taken. Each measurement consisted typically of 3 cycles. The force coefficients are the averaged values obtained from integration of these 3 cycles of the measured pressure profiles.

EXPERIMENTAL RESULTS AND DISCUSSIONS

Experimental tests have been performed on the squeeze film damper (SFD) test rig to measure dynamic pressure distributions and force coefficients with orbit radii equal to 0.5 and 0.8. Table I shows the conversion factors for proper dimensional values of pressure and force coefficients for the three kinds of oils used in the experimental work. These factors are used to get the corresponding dimensional values of the measured dimensionless pressure and force coefficients. To predict the measured pressure distributions and film force coefficients, a modified short bearing solution [16] is used. The analytical model used included the effects of finite length and fluid inertia.

Pressure Distributions

Figures 4 and 5 show comparisons between the measured and predicted pressure profiles for orbit radius equal to 0.5 and 0.8, respectively. The viscous lubrication solution produces antisymmetric pressure profiles with respect to the maximum film thickness ($\omega t^* = \pi$), while the additional pressure due to the fluid inertia is symmetric with respect to $\omega t^* = \pi$ [14]. Referring to the combined pressure profile including the additional inertial pressure, the main effects of fluid inertia are that the positive dynamic peak pressure is smaller than the negative dynamic peak pressure, and the dynamic pressure has a negative value at the minimum film thickness ($\omega t^* = 0$) while it has a positive value at the maximum film thickness ($\omega t^* = \pi$).

The pressure profile with a orbit radius $\epsilon = 0.8$ corresponds to a cavitated film as shown in Figure 5. The absolute levels of pressure measured are close to zero absolute and thus, these indicate vapor cavitation in the lubricant film.

According to conventional lubrication theory, negative dynamic pressure is produced in the diverging section of bearing while positive dynamic pressure is produced in the converging section of bearing. Contrarily, as shown in Figure 5, negative pressure exists in the converging section of the SFD. It has been generally assumed that the positive pressure profile is unaffected by cavitation, but it is presumed here that vapor cavitation influences the positive pressure region.

For reduced oil viscosities, the extent of the vapor cavitation becomes smaller. For $\epsilon = 0.8$, the measurements showed that the cavitation completely disappeared at Re=22.1. Figure 6 shows the measured pressure which corresponded to ISO22 oil.

An important characteristic of the open ended configuration is the large pressure drop in the axial direction due to the substantial flow in the axial direction. In Figures 5 and 6, the amount of pressure drop measured at axial location Z2 is about 40% of the peak positive pressure at axial location Z1. The modified short bearing solution [16] predicts 46% of pressure drop between the two axial locations. The measurements confirm that the modified short bearing model can adequately describe the axial pressure drop in a parabolic form. However, the predicted pressure profile at the axial location Z2 is poor in the negative dynamic pressure region. The peak negative pressure drop measured at the axial location Z2 is about 20% of that at Z1 at large Reynolds numbers (Re≥20). The parabolic variation of the axial pressure predicted from the modified short bearing solution is therefore not valid in the negative pressure region where the Reynolds number is large. Since the film is completely submerged, the negative pressure produced in the diverging section creates reversed flow in the axial direction. Thus, a Bernoulli effect is likely to be significant which violates the boundary condition p=0 at the end of the damper.

Figure 7 shows dynamic pressure waves obtained at Reynolds number equal to 44.2. In these figures the distortion of the antisymmetric shape of the viscous

pressure profile is magnified, and the pressure profile is dominated by the effects of fluid inertia. The negative peak pressure is about three times the positive peak pressure in magnitude. The analytical predictions deteriorate for these large Reynolds numbers.

During the pressure measurements at small Reynolds number with $\epsilon=0.5$ and at large Reynolds number with $\epsilon=.8$, the pressure signals on an oscilloscope were fluctuating, as seen on the Figures 4 and 7. Thus the fluid flows at these large Reynolds numbers may not be laminar and the Bernoulli effects may become more significant at low viscosities. Also there is a noise interference at low levels of pressure. For an orbit radius $\epsilon = 0.5$, it was not possible to measure the pressure distribution at large Reynolds number (Re$\geq$10) because of the large ratio of noise to measured values.

During operation of the SFD test rig no bubbles came out of the squeeze film region, but many minute bubbles simultaneously appeared in the oil a few seconds after stopping the test rig and oil supply pump. It is presumed that the air dissolved in the oil came out of solution when the external oil supply pressure was removed.

Force Coefficients

Experimental fluid film forces and force coefficients are determined by numerical integration of the measured pressure waves around the damper journal surface. For the analytical predictions, a full film assumption (2π film) with orbit radii $\epsilon = 0.5$ and 0.82 are used. Since the pressure profiles for $\epsilon = 0.8$ are cavitated at small Reynolds numbers (Re$\leq$ 10), corresponding predictions are excluded here. The force coefficients are calculated locally and corresponded to a unit axial width of the damper at the specific axial locations.

Figures 8 show the local damping coefficients C_{tt} computed from the measured pressure profiles. Since cavitation is present in the pressure profiles of $\epsilon = 0.8$ and for Reynolds numbers less than 10, the measured damping coefficients must be regarded as equivalent damping coefficients, i.e. equal to $(C_{tt} - D_{tr})$. But at Reynolds numbers larger than 15, the damping coefficients are purely direct coefficients because of no cavitation in the measured pressure profiles.

Generally, the predictions for the local damping coefficients using the modified short bearing solution [16] compare favorably with measurements at the axial location Z1. However, the predicted coefficients are poor at the axial location Z2. The main reason is that the parabolic axial pressure profile obtained from the short bearing theory does not properly predict the axial pressure drop in the negative region when both Reynolds number and orbit radius are large. A level of the dimensional values of damping achieved in the test rig can be easily obtained if the measured damping coefficients Ctt are multiplied by $C_{dRe}/$Re (C_{dRe} is given Table I).

Figures 9 show the local inertia coefficients D_{rr} calculated from the mea-

sured pressure data. For $\epsilon = 0.8$ at Reynolds number below Re=10, the inertia coefficients are to be regarded as an equivalent inertia coefficient, i.e. equal to $(D_{rr} - C_{rt})$ due to the observed cavitation in the measured pressure profiles. Since the region of cavitation increases as the Reynolds number decreases, the equivalent inertia coefficients correspond mainly to the cross coupled damping coefficients at small Reynolds number with $\epsilon=0.8$. The dimensional values of inertia coefficients can be obtained by multiplication of C_{iRe}/Re in Table I.

For a orbit radius $\epsilon = 0.8$ at Reynolds number less than Re=10, the inertia coefficients at both the axial location Z1 and Z2 are negative, showing the cross coupled damping force is dominant. (Cross coupled damping has been described as dynamic stiffness [17,18]). For Reynolds number larger than 15, the inertia coefficients become positive, which means that fluid inertia overcomes the effect of the cross coupled damping and acts as an added mass on the journal. The prediction of the local inertia coefficients are poor at the axial location Z2 near the end of the damper journal as in the case of the damping coefficient prediction. Once again, the parabolic axial pressure profile can not be used in the negative pressure region.

Damping coefficients are seen to be large at small Reynolds number and indicate a dominance of viscous effects. As the Reynolds number increases, the inertia coefficients eventually approach the same level of the damping coefficients as shown in Figures 8 and 9, and show that the fluid inertia forces become dominant

San Andres [9,10] determined fluid film forces and force coefficients based on the assumption that fluid inertia do not affect the velocity profiles or flow rates. The important results were

1) The dimensionless damping coefficient C_{tt} is purely viscous and not affected greatly by fluid inertia.

2) The fluid inertia force increases linearly with Reynolds number so that the dimensionless inertia coefficient D_{rr}/Re has a constant value for small to moderate Reynolds number.

However, since the above assumption is valid for very small Reynolds number (Re$\leq$1), as the fluid inertia forces approach the same order of magnitude as viscous forces for large Reynolds number (Re$\geq$10), the effect of fluid inertia forces on the velocity profile then becomes significant and needs to be considered. When the effect of the fluid inertia forces on the velocity profiles or flow rates is included in the analysis, the dimensionless damping coefficient C_{tt} and inertia coefficient D_{rr}/Re, both become strongly dependent on the Reynolds number [16]. Experimental evidence supporting these results is shown in Figures 8 and 9.

Figure 10 shows the force phase angle calculated from the force coefficients given in Figures 8 and 9. It is important to notice how the point of application of the total fluid film force relative to the position of the maximum film thickness changes as the Reynolds number increases. If the viscous film force is dominant,

the radial film force is very small compared to the tangential film force and the phase angle approaches $\phi = 90°$; while if the inertial film force is dominant, the radial film force is very large (outward) compared to the tangential film force and the phase angle ϕ approaches $\phi = 180°$. Thus, phase angles above 90° indicate a film radial force component due to fluid inertia. Predictions of phase angle obtained from the modified short bearing solution agree well with the measurements.

CONCLUSIONS

Experimental measurements have been performed on an open ended squeeze film damper executing circular centered orbits. Dynamic pressure measurements were obtained for two orbit radii, $\epsilon = 0.5$ and 0.8. Corresponding force coefficients were calculated by numerical integration of the measured pressure profiles From the experimental measurements presented, the following conclusions can be described:

1) The parabolic axial pressure profile obtained from the modified short bearing solution can adequately predict the axial pressure drop in the positive dynamic pressure region, but not in the negative dynamic pressure region. These effects are more pronounced at large Reynolds numbers.

2) Cavitation observed in the submerged damper corresponds to vapor cavitation. The vapor cavitation influences not only the negative pressure field in the diverging region of a damper, but also the positive pressure field in the converging region of the damper.

3) Inertia coefficients D_{rr}/Re (radial film force) become comparable to damping coefficients C_{tt} (tangential film force) as Reynolds number increases. Both the measured inertia and damping coefficients increase with increasing Reynolds numbers.

The experimental results obtained from a partially sealed configuration are presented in Part II.

REFERENCES

[1] Thomsen K. K. and Andersen H., "Experimental Investigation of a Simple Squeeze Film Damper", ASME *J. of Eng. for Industry,* May 1974, pp.427-430

[2] Vance J. M. and Kirton A. J., "Experimental Measurement of the Dynamic Force Response of a Squeeze Film Bearing Damper", ASME *J. of Eng. for Industry* , Nov. 1975, pp. 1282-1290

[3] Tonnesen J.,"Experimental Parametric Study of a Squeeze Film Bearing", ASME *J. of Lubrication Technology*, April 1976, pp. 206-213

[4] Feder E., Bansal P. N., and Blanco A.,"Investigation of Squeeze Film Damper Forces Produced by Circular Centered Orbits", ASME *J. of Eng. for Power*, Vol. 100, Jan. 1978, pp. 15-21

C-2

[5] Miyachi T., Hoshiya S., Sofue Y., Matsuki M., and Torisaki T., "Oil Squeeze Film Dampers for Reducing Vibration of Aircraft Gas Turbine Engines", ASME paper no. 79-GT-133, 1979

[6] Szeri, A. Z., Raimondi, A. A., and Giron-Duarte, A., "Linear Force Coefficients for Squeeze-Film Dampers", *J. of Lubrication Technology* , Vol. 105, July 1983, pp. 326-334.

[7] Tichy, J. A., "The Effect of Fluid Inertia in Squeeze Film Damper Bearings; A Heuristic and Physical Description", ASME paper no. 83-GT-177.

[8] Tichy, J. A., "A Study of the Effect of Fluid Inertia and End Leakage in the Finite Squeeze Film Damper", ASME paper no. 86-Trib-62, 1986

[9] San Andres, L., and Vance, J. M, "Effects of Fluid Inertia and Turbulence on the Force Coefficients for Squeeze Film Dampers", ASME paper no. 85-GT-191, 1985.

[10] San Andres, L., and Vance, J. M., " Effects of Fluid Inertia on Finite Length Squeeze Film Dampers", ASLE Trans. Vol. 30, 3, 1987, pp. 384-393

[11] Tecza J. A., Giordano J. C., Zorzi E. S., and Drake S. K.,"Squeeze Film Damper Technology: Part 2 - Experimental Verification Using a Controlled Orbit Test Rig", ASME paper no. 83-GT-248, 1983

[12] Tichy J. A.,"Measurements of Squeeze Film Bearing Forces to Demonstrate the Effect of Fluid Inertia", ASME paper no. 84-GT-11, 1984

[13] Ramli M. D., Roberts J. B., and Ellis J. "Determination of Squeeze Film Dynamic Coefficients from Experimental Transient Data", ASME paper no. 86-Trib-17, 1986

[14] San Andres L. A. and Vance J. M.,"Experimental Measurement of the Dynamic Pressure Distribution in a Squeeze Film Bearing Damper Executing Circular Centered Orbits", ASLE Trans., Vol. 30, 3, July 1987, pp. 373-383

[15] Burrows C. R., Kucuk N. C., and Sahinkaya M. N., "Estimation of Squeeze Film Bearing Inertia, Damping and Stiffness Coefficients", *ASME Rotating Machinery Dynamics*, Vol. 1, Sep. 1987, pp. 109-114

[16] S. Y. Jung, "Effects of Fluid Inertia and Cavitation on the Force Coefficients of a Squeeze Film Damper", Ph.D. Dissertation, Dept. of Mechanical Eng., Texas A&M University, May 1990

[17] Rabinowitz, M. D., and Hahn, E. J., "Optimal Design of Squeeze Film Supports for Flexible Rotors", *J. of Eng. for Power*, July 1983, pp. 487-494.

[18] Gunter, E. J., Barrett, L. E., and Allaire, P. E., "Design of Nonlinear Squeeze-Film Dampers for Aircraft Engines", *J. of Lubrication Technology*, Jan. 1977, pp. 57-64.

conversion factor	C_{pRe} Kpa (psi)	C_{dRe} N sec/m (lbf sec/in)	C_{iRe} N sec^2/m (lbf sec^2/in)
SAE30	119.75 (17.37)	616.99 (3.523)	3.328 (0.0190)
ISO22	123.06 (17.85)	634.03 (3.620)	3.420 (0.0195)
DOW10	128.98 (18.71)	664.56 (3.795)	3.584 (0.021)

TABLE I. Conversion factors for a SFD test rig at 26.7° C

1. Housing
2. End cavity
3. Journal
4. Eccentric sleeve
5. Sleeve holder
6. End plate
7. Plexiglas cover and Lip seal
8. Housing support
9. Shaft
10. Antirotation ear
11. O-ring

PT: Pressure Transducer
PP: Proximity Probe
PG: Pressure Gauge
CV: Check Valve
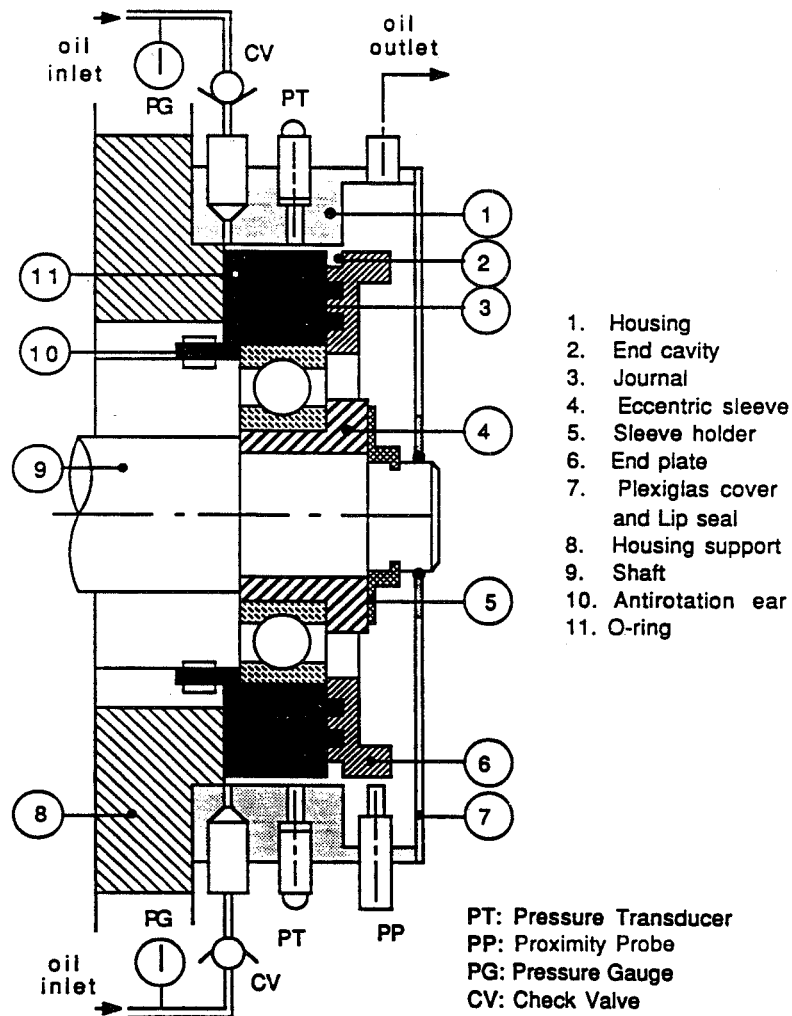
Fig. 1   Schematic drawing of a SFD test rig
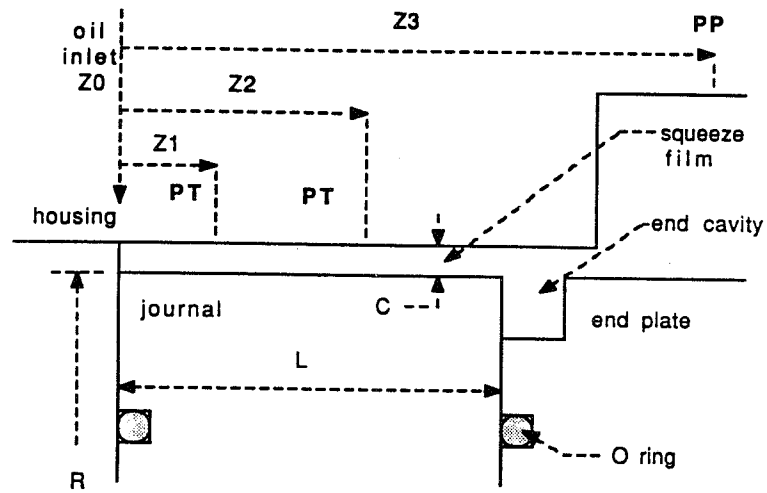
Fig. 2   SFD geometry of an open ended configuration

Z1=0.56 cm (0.2200 inch)   L=2.39   cm (0.94 inch)
Z2=1.67 cm (0.6575 inch)   R=6.35   cm (2.50 inch)
Z3=3.71 cm (1.4600 inch)   C=0.159 cm (0.0625 inch)

L/D=0.188

PT : Pressure Transducer   PP : Proximity Probe
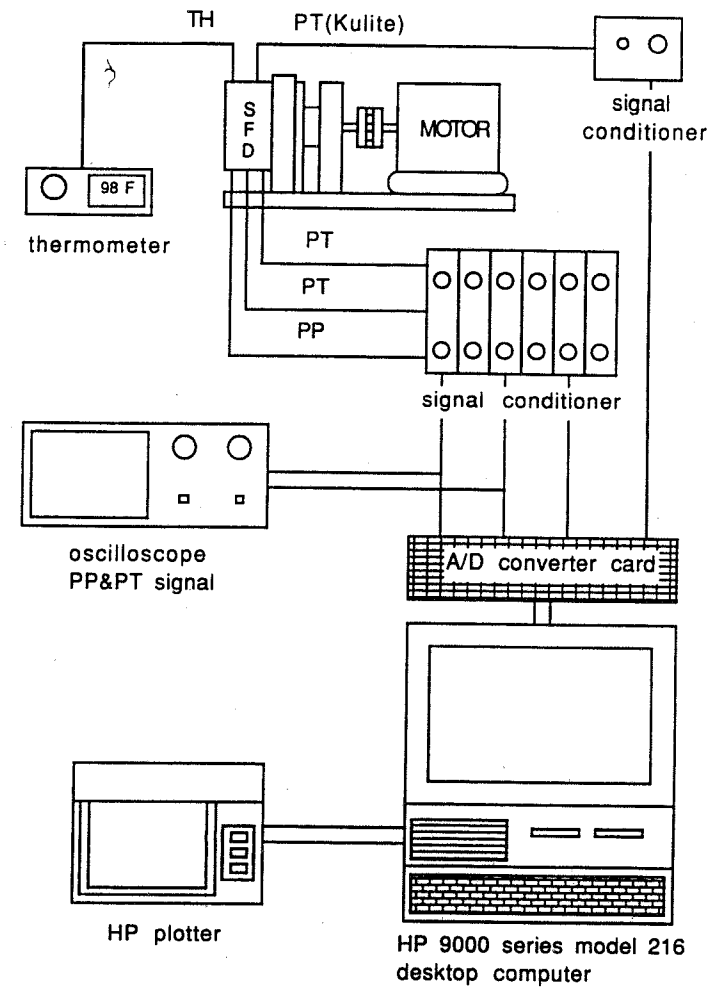
Fig. 3   Schematic diagram of instruments
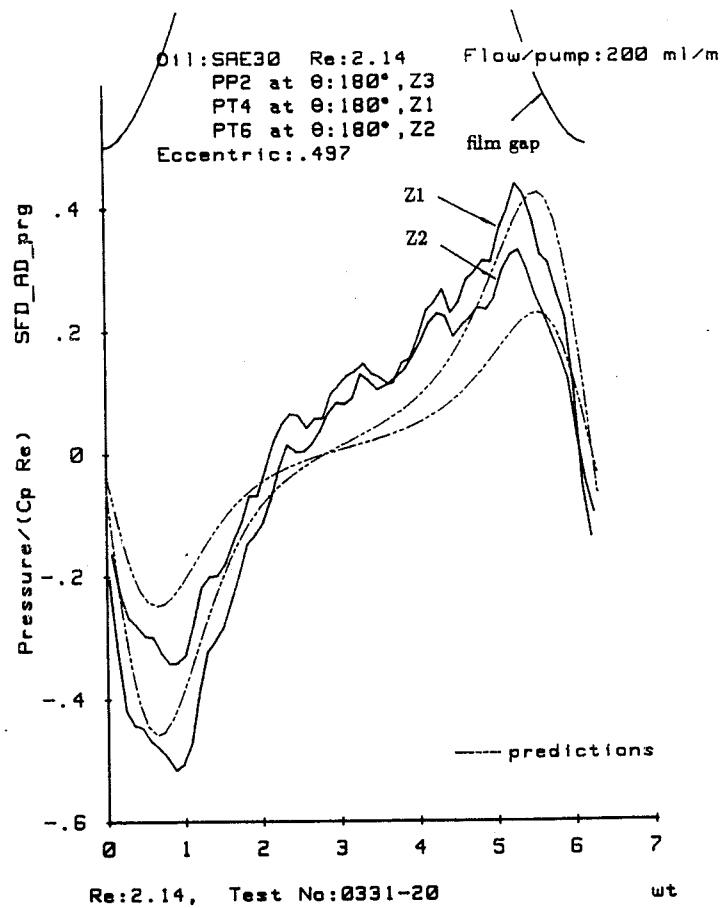
Fig. 4   Dimensionless pressure profiles,

open ended configuration, Re=2.14, $\epsilon = 0.5$
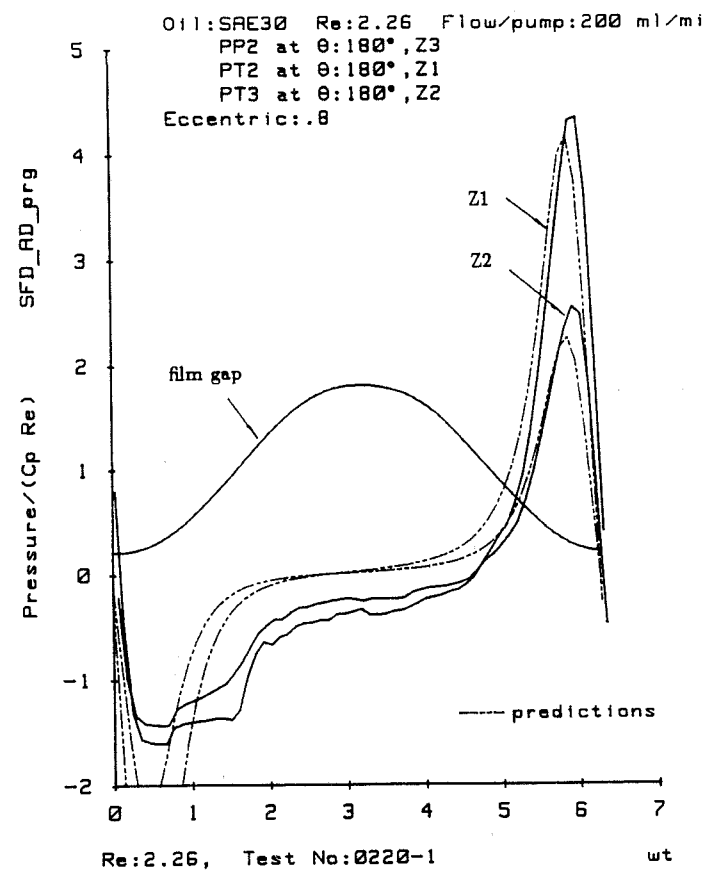
Fig. 5   Dimensionless pressure profiles,

open ended configuration, Re=2.26, $\epsilon = 0.8$
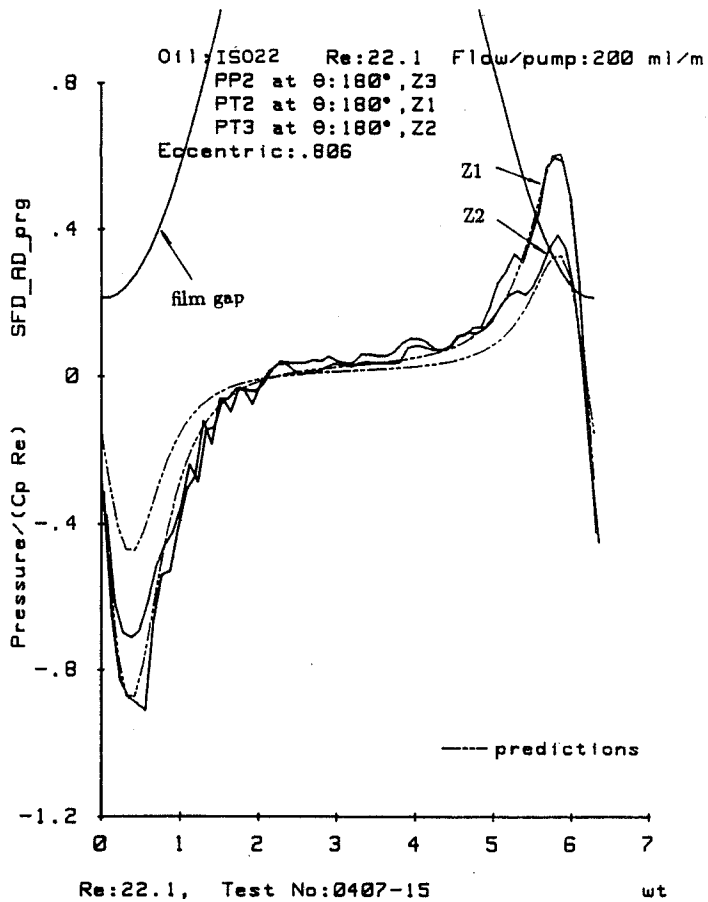
Oil:ISO22   Re:22.1   Flow/pump:200 ml/m
   PP2 at θ:180°,Z3
   PT2 at θ:180°,Z1
   PT3 at θ:180°,Z2
Eccentric:.806

film gap

Z1
Z2

---- predictions

Re:22.1,   Test No:0407-15

Fig. 6   Dimensionless pressure profiles,
         open ended configuration, Re=22.1, $\epsilon = 0.8$

Oil:DOW10   Re:44.2   Flow/Pump:800ml/min
   PP2 at θ:180°,Z3
   PT2 at θ:180°,Z1
   PT3 at θ:180°,Z2
Eccentric:.82

film gap

Z1
Z2

---- predictions

Re:44.2,   Test No:0827-14
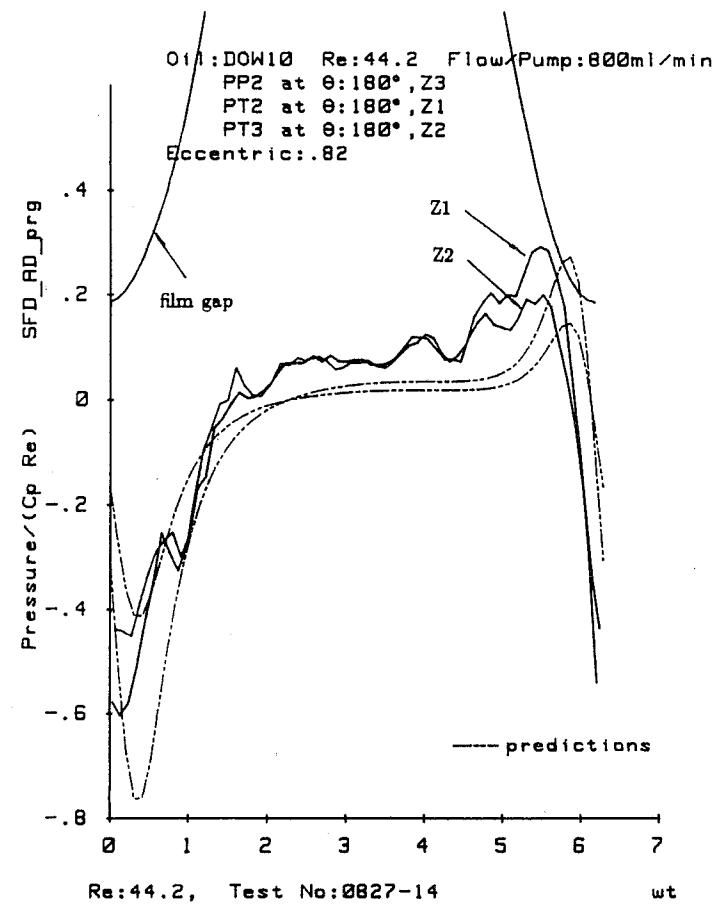
Fig. 7   Dimensionless pressure profiles,
         open ended configuration, Re=44.2, $\epsilon = 0.8$
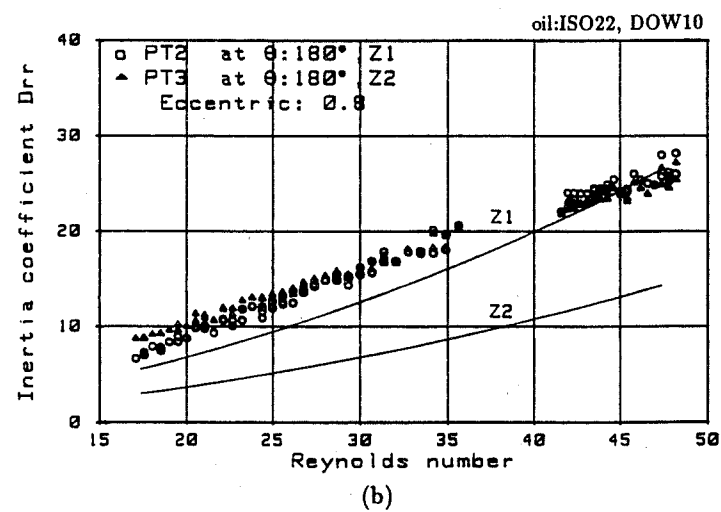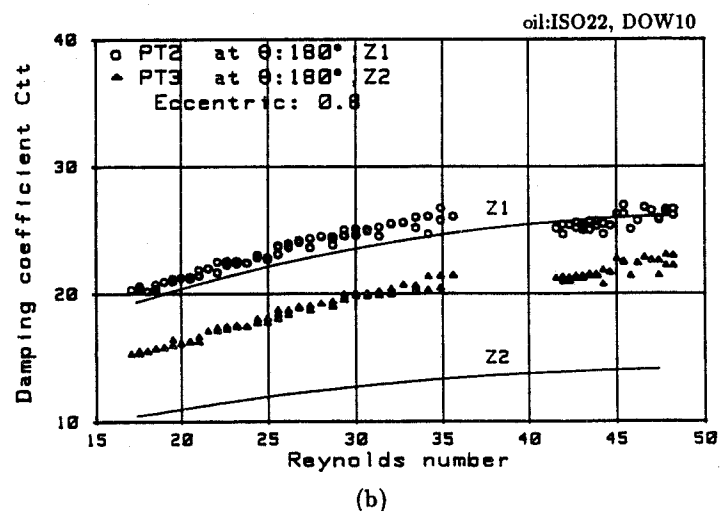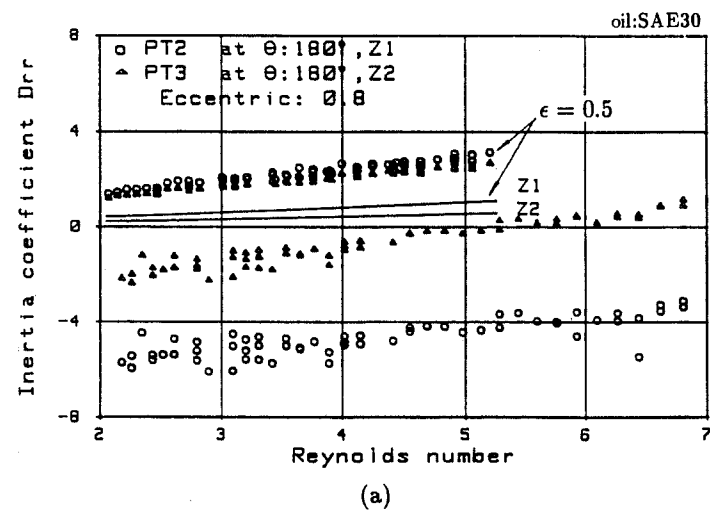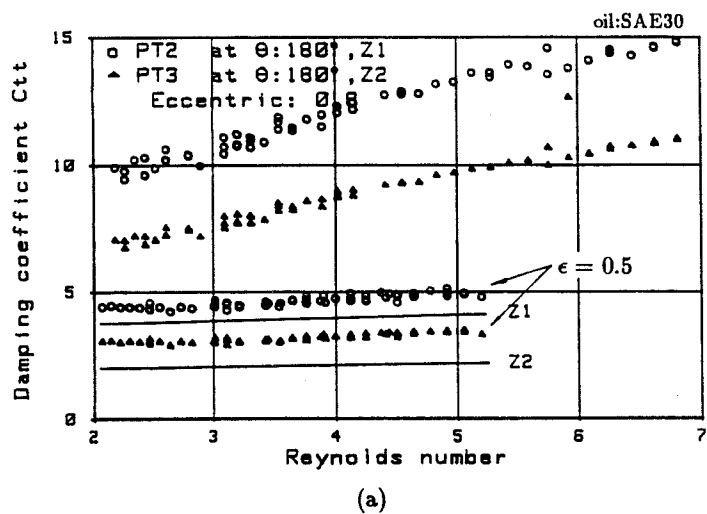
Fig. 8   Dimensionless damping coefficients vs. Reynolds no.

Fig. 9   Dimensionless inertia coefficients vs. Reynolds no.

(a)

(b)
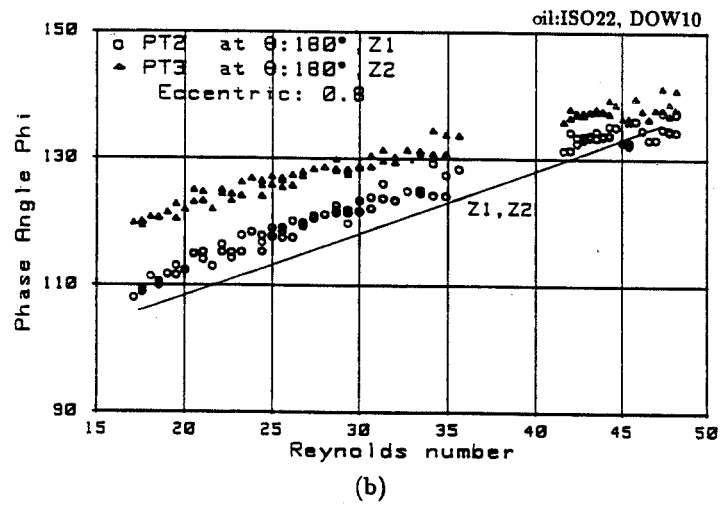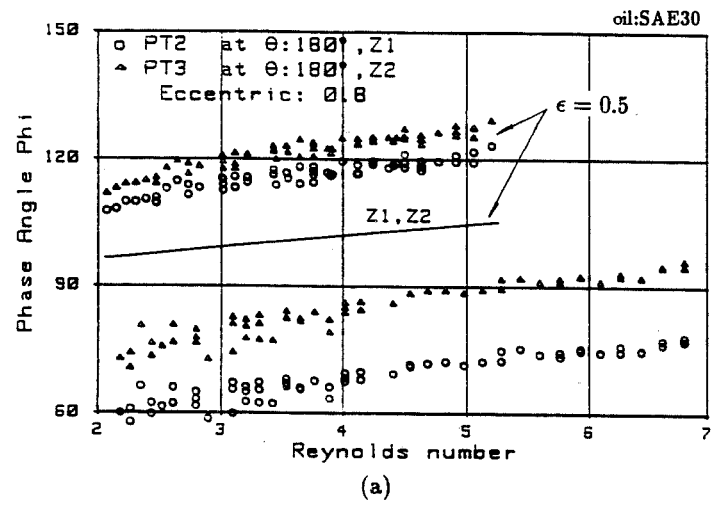
Fig. 10 Phase angle vs. Reynolds number

94

MEASUREMENTS OF PRESSURE DISTRIBUTIONS AND FORCE COEFFICIENTS IN A SQUEEZE FILM DAMPER - PART II: PARTIALLY SEALED CONFIGURATION

S.Y. Jung, L.A. San Andres, and J.M. Vance
Department of Mechanical Engineering
Texas A&M University
College Station, Texas 77843-3123, U.S.A.

In part I, a squeeze film damper (SFD) test rig and measurement procedures were explained, and the experimental results obtained from an open ended damper were presented. In this paper, the experimental results measured from a partially sealed SFD test rig executing a circular centered orbit are presented and discussed. A serrated piston ring is installed at the damper exit. This device involves a new sealing concept which produces high damping values while allowing for oil flow to cool the damper. In the partially sealed damper, large cavitation regions are observed in the pressure fields at orbit radii $\epsilon = 0.5$ and $\epsilon = 0.8$. The cavitated pressure distributions and the corresponding force coefficients are compared with a cavitated bearing solution. The experimental results show the significance of fluid inertia and vapor cavitation in the operation of squeeze film dampers. Squeeze film Reynolds numbers tested reach up to Re=50, spanning the range of contemporary applications.

NOMENCLATURE

C	=SFD radial clearance
C_{dRe}	=$\rho\omega L R^3/C$ damping coefficient conversion factor
C_{iRe}	=$\rho L R^3/C$ inertia coefficient conversion factor
C_f	=$\mu\omega R^3 L/C^2$ force conversion factor
C_p	=$\mu\omega R^2/C^2$ pressure conversion factor
C_{pRe}	=$C_p \cdot Re = \rho\omega^2 R^2$ pressure conversion coefficient
C_{tt}	=dimensionless direct damping coefficients
	=$-f_t/\epsilon$, normalized by $\mu R^3 L/C^3$
D	=damper journal diameter
D_{rr}	=dimensionless direct inertia coefficients
	=f_r/ϵ, normalized by $\mu R^3 L/\omega C^3$
f_r, f_t	=dimensionless radial and tang. film forces normalized by C_f
	=$\int p\cos\theta d\theta$, $\int p\sin\theta d\theta$, respectively.

L	=damper journal length
p	=dimensionless pressure normalized by C_p
R	=damper journal radius
Re	=$\omega C^2/\nu$ modified Reynolds number
Z	=axial coordinate
ϵ	=dimensionless orbit radius
θ	=circumferential coordinate
θ_a	=cavitation termination position
θ_c	=cavitation inception position
μ	=absolute viscosity
ν	=kinematic viscosity
ρ	=density
ϕ	=$90° + \tan^{-1} f_r/f_t$, phase angle
ω	=frequency of damper journal center motion

INTRODUCTION

In Part I, a companion paper, a squeeze film damper (SFD) test apparatus and experimental procedure were detailed, and the experimental results obtained for an open ended configuration were presented and compared with a modified short bearing solution.

In this paper, the experimental results measured from a partially sealed SFD test rig executing a circular centered orbit are presented. The squeeze film damper is sealed with a serrated piston ring to partially prevent side leakage of lubricant so that the damping capability of the damper is increased. The serrated piston ring is described in detail and its function is explained in the next section. The experimental conditions are the same as in the open ended SFD test rig described in Part I.

In the partially sealed damper, a large cavitation region in the pressure field is observed at orbit radii $\epsilon = 0.5$ and $\epsilon = 0.8$. The cavitated pressure distributions and the corresponding force coefficients (both damping and inertia) are compared with a cavitated bearing solution. The squeeze film Reynolds number tested are within the range of contemporary applications.

EXPERIMENTAL TEST RIG AND PROCEDURE

The overall structure of the damper test rig and experimental procedure have been described in detail in Part I and thus, related details are omitted here. Figure 1 shows the axial geometry of the partially sealed SFD configuration. A serrated piston ring (see Figure 2) is placed at the cavity (or piston ring groove) at the end of damper journal. The other experimental conditions, such as oil supply pressure and locations of pressure and temperature transducers, are the same as described in Part I. However, in the partially sealed damper, the

oil temperature increases more rapidly because of the reduced axial flow rates through the damper.

With a uniform conventional piston ring located at the damper end, early experimental measurements showed that no leakage through the end seal occured. Under this condition, measured film pressures and forces reproduced closely the predictions given for the fully sealed SFD model. Therefore, the levels of damping forces obtained were large and quite accurately predicted with the inertial SFD fluid flow model [1].

Since a damper without through flow does not represent conditions found in practice, the piston ring end seal was modified to allow some amount of oil leakage. The idea of enlarging the circumferential groove in which the piston ring is located was discarded after experiments indicated that the piston ring cocks in the groove and distorts the pressure field. A piston ring with a radial split was also found not attractive since the pressures would be distorted due to the localized jet effect at the piston ring opening.

A piston ring with a large number of small axial grooves around the circumference allows a sufficient amount of oil circulation, and does not distort the rotating pressure field. This condition is only insured provided that the lubricant inlet pressures are not too large so as not to induce distorting effects at the inlet holes in the squeeze film.

As shown by a schematic drawing in Figure 2, the serrated piston ring consists of a piston ring of inner and outer diameters equal to 12.23 cm (4.816 inch) and 13.02 cm (5.125 inch), respectively, and with thickness and width equal to 3.97 mm (5/32 inch). 72 semi-circular holes of radius 0.79 mm (1/32 inch) are drilled every 5° on the outer surface of the piston ring. The total area of grooves is 8 times larger than the area of the inlet holes. This number was chosen so that the total pressure loss factor for the holes in the piston ring is similar to the loss factor at the inlet holes.

Preminary experiments were aimed to determine, first, if the rotating pressure wave was distorted by the presence of the piston ring holes, and second, to measure the absolute levels of film pressure generated in the squeeze film region.

The preminary tests showed that the film pressure wave was not distorted and remained stationary with respect to the rotating shaft. Therefore, a single pressure transducer was needed to reproduce the pressure field around the journal surface.

The most important preliminary finding was that film cavitation did occur as the observed dynamic pressure waves showed a uniform region of minimum dynamic pressures. Experimental measurements of absolute pressure showed that the region of film cavitation represented pressures which are close to zero absolute. Thus, it is presumed that the form of cavitation observed in the experimentation corresponded to incipient boiling (vapor cavitation) of the lubricant at low values of absolute pressure.

From the discussion above, it is apparent that the measurements show the film pressure to attain large levels of subatmospheric pressures which remain during a substantial portion of the total time required to describe a complete journal orbit. This comment is made here since current theoretical treatments often consider film cavitation to start at pressure levels very close, but lower than, atmospheric pressure. This form of cavitation relates to the release of air dissolved in the oil or the ingress of external air in the film region, and is likely to occur if the damper is not completely flooded in oil [2].

The partially sealed damper, due to the reduced side leakage, produces a smaller axial pressure drop and larger peak pressures and damping levels when compared to the open end damper. The most important outcome of this is that the pressure field is significantly disturbed due to the large extent of vapor cavitation in the pressure field. In this case, the supply pressure can not be large enough to suppress the cavitation. Because higher supply pressures to suppress the cavitation produce enough flow through the check valves to hold them open and produce distortion of the pressure wave due to backflow through the inlet holes. Consequently the damping level achieved from the partially sealed damper can be greatly reduced or widely varied depending on the extent of vapor cavitation taking place in the pressure profiles. Another important factor is fluid inertia which tends to move the position of cavitation inception toward the minimum film gap and to decrease the peak pressure [3,4].

The following experimental measurements show the effects of vapor cavitation and fluid inertia on the pressure fields and force coefficients.

EXPERIMENTAL RESULTS AND DISCUSSIONS

Pressure profiles

Figures 3 and 4 show the dimensionless dynamic film pressure distribution vs. time at axial locations, Z1 and Z2, for orbit radii $\epsilon = 0.47$ and 0.76, respectively. Reynolds numbers are Re=2.07 and 2.3, respectively. These pressure profiles are significantly affected by vapor cavitation. As described before, the cavitation pressure is close to zero absolute. The damper is completely submerged in oil which prevents the ingress of external air. Thus, it is presumed that the measured cavitation here corresponds to vapor cavitation.

In these figures, the double dotted lines are the pressure profiles predicted at the two axial locations Z1 and Z2 by the cavitation analysis [3,4]. The analysis includes extended cavitation effects on the pressure distribution using the Swift-Stieber conditions [5,6]. In order to compare experimental measurements with the cavitated pressure predictions, the predicted absolute pressure profile has been shifted to the measured dynamic pressure profile, because the measurement with the absolute pressure transducer established the cavitation pressure here as absolute zero. To predict the cavitated pressure field, the position θ_a of cavitation termination is taken from the measured pressure profile and leakage

coefficient values, $CL_l = 0.0$ and $CL_r = 0.18$, are used. The cavitation end points for $\epsilon = 0.47$ and $\epsilon = 0.76$ are about $\theta_a = 30°$ and $\theta_a = 350°$, respectively, as shown in Figures 3 and 4. $\theta_c = 141.3°$ and $\theta_c = 158.7°$ are predicted by the analysis as the corresponding positions of cavitation inception, respectively. The prediction of cavitation inception points and the whole of the pressure field agrees well with the experimental measurement. The above comparisons using the Swift-Stieber conditions show that the cavitation effect is significant on pressure distributions.

Generally, a much larger level of the measured peak pressure is expected from the partially sealed damper when compared to that from the open ended damper (see Part I). But at small Reynolds numbers the peak pressure measured from the partially sealed damper is only slightly larger than that obtained from the open ended damper. The two main reasons for this are 1) a smaller orbit radius of the partially sealed damper and 2) a larger extent of vapor cavitation in the pressure fields. The peak pressure of a SFD or a journal bearing is so sensitive to large orbit radius or eccentricity ratio that a small reduction of orbit radius causes a large reduction of the peak pressure. Furthermore, as shown in the vapor cavitation analysis [3], the peak pressure is greatly reduced as the extent of the vapor cavitation increases.

Figure 5 depicts pressure waves measured at Reynolds number equal to Re=22.1 and an orbit radius $\epsilon = 0.81$. As shown in the previous pressure comparison, the double dotted line is the pressure profile predicted at the axial location Z1 using the cavitation analysis which includes vapor cavitation effects on the pressure field. The position θ_a of cavitation termination is $\theta_a = 130°$ which was taken from the measured pressure profile. But, instead of the seal coefficients $CL_l = 0.0$ and $CL_r = 0.18$, the seal coefficients $CL_l = CL_r = 0.0$ are required, which implies no side leakage from the damper.

The prediction of pressure profiles using the analysis gets degraded as the Reynolds number becomes large, because an assumption that fluid inertia does not affect the velocity profiles is used in the cavitated long bearing analysis [3]. The assumption is valid for Re$\leq$10. Thus, as shown in Figure 5, the prediction is not good at large Reynolds number (note the different seal coefficients required), and also the pressure profiles shown in Figure 6 which were measured using DOW10 oil, can not be compared with any predictions. However, it is very interesting to compare these pressure profiles with those of the open ended damper.

The relevant difference between these configurations are

1) The peak pressures measured from the partially sealed damper are much larger than those from the open ended damper.

2) As orbit radius increases, the extent of cavitation greatly increases. The pressure profiles of the partially sealed damper are more extensively cavitated than those of the open ended damper.

3) The pressure profiles of the partially sealed damper show less fluid inertia

effects than those of the open ended damper. The main effects of fluid inertia on the pressure profile are that the positive peak pressure is smaller than the negative peak pressure, and the pressure has a negative value at the minimum film thickness region ($\omega t = 0$) while it has a positive value at the maximum film thickness region ($\omega t = \pi$). Moreover, as fluid inertia becomes dominant in the film forces, the shape of the pressure profile tends to change from antisymmetric to symmetric with respect to the maximum film thickness. The measured pressure profiles of the partially sealed damper are fairly antisymmetric, while the pressure profiles of the open ended damper are more symmetric with respect to $\omega t = \pi$ at large Reynolds numbers.

Force coefficients

Local damping and inertia coefficients and phase angles for orbit radii equal to $\epsilon = 0.5$ and 0.8 are obtained by integrating the measured pressure field around the journal of the damper. Since the measured pressure wave has been determined to be synchronous with speed, the relation of the pressure/time curve to that of pressure/angle curve around the journal surface is well known. In the numerical calculations, the entire pressure wave has been used to determine film forces and force coefficients. The pressure signals at orbit radius $\epsilon = 0.5$ with large Reynolds numbers were not large enough to measure so that the corresponding force coefficients are presented here.

Figures 7 show the local damping coefficients C_{tt} measured at the axial locations Z1 and Z2. Since the measured pressure fields at small Reynolds number are greatly cavitated, as shown in the previous pressure profiles, these damping coefficients shown in Figure 7(a) represent the equivalent damping coefficients C_{eq} equal to $(C_{tt} - D_{tr})$.

In Figure 7(a), the solid lines are predictions of damping coefficients at the axial location Z1 for $\epsilon = 0.5$ and 0.8. These lines are obtained from a curvefit of damping coefficients predicted from a cavitated bearing solution [3,4], based on the measured cavitated pressure profiles. Considering the effect of vapor cavitation on the entire pressure field, the predictions of damping coefficients are fairly matched with the measurements. Figure 7(b) shows comparison of damping coefficients at large Reynolds numbers where cavitation disappeared. Thus an uncavitated model is used to calculate the damping coefficients with the seal coefficients $CL_l = CL_r = 0.0$. The predicted damping coefficients remain constant for increasing Reynolds numbers.

The level of local damping achieved from the partially sealed damper is about twice that from the open ended damper for the whole range of Reynolds numbers. The actual (dimensional) damping can be determined if the measured dimensionless damping coefficients C_{tt} are multiplied by the damping conversion factor C_{dRe}/Re. (see Table I of Part I)

Figures 8 show the local inertia coefficients D_{rr} at the axial locations Z1 and Z2. For Reynolds numbers below Re=10 in Figure 8(a), the local inertia force

100

coefficients D_{rr} represent the equivalent inertia coefficients $D_{eq} = D_{rr} - C_{rt}$ due to the cavitation taking place in the pressure field (Figures 3 to 5). Once again the solid lines in Figure 8(a) are predictions of inertia coefficients obtained from the cavitated bearing solution [3,4]. The predictions are fairly matched with the measurements. However, the solid line in Figure 8(b) represents a prediction of inertia coefficients calculated from an uncavitated film model with the seal coefficients $CL_l = CL_r = 0.0$.

When compared with the inertia coefficients measured from the open ended damper, the (negative) values of the equivalent inertia coefficients from the partially sealed damper are about twice as much as at small Reynolds number, due mainly to the large cross coupled damping coefficient ("dynamic stiffness") caused by the cavitated pressure field. However, for large Reynolds number, the pure inertia coefficients of the partially sealed damper show the same magnitude as those of the open ended damper, while the pure damping coefficients of the partially sealed damper are about three times as those of the open ended damper. Therefore, the ratio of the fluid inertia force to the fluid viscous force measured from the partially sealed damper is less than that of the open ended damper. That is, the partially sealed damper has been less influenced by fluid inertia than the damper with open ends. This phenomenon was also found in the comparison of pressure distributions measured from the two types of squeeze film dampers.

The force phase angle ϕ determined from the ratio of the radial film force to the tangential film force is shown in Figures 9. The predictions are good as shown in Figure 9(a). Since the pressure profiles at Reynolds numbers less than Re=10 are greatly cavitated, phase angles are below $\phi = 90°$. But as Reynolds number increases, the extent of cavitation is reduced and the fluid inertia force is dominant so that phase angle becomes larger than $\phi = 90°$ as shown in Figure 9(b).

CONCLUSIONS

Experimental tests have been performed on a partially sealed squeeze film dampers to measure fluid film pressure distributions and force coefficients with circular centered orbits with both $\epsilon = 0.5$ and 0.8. The measurements performed completely cover the practical range of Reynolds number which reaches Re=50.

From the experimental measurements described, the following conclusions can be obtained

1) There is a small pressure drop in the axial direction. It is thus apparent that the partially sealed configuration will give substantial levels of damping due to the uniformity of the pressure in the axial direction.

2) However, the present experimental results show that the development of the region of negative dynamic pressure is sharply detained by vapor cavitation. The extent of vapor cavitation greatly reduces both damping and inertia coefficients, and the phase angles are below 90°.

3) The extent of cavitation is larger at low Reynolds numbers (lowest temperature) than at higher Reynolds numbers. This is due to the effect of increasing temperature which diminishes the fluid viscosity and consequently, reduces the level of generated pressures.

4) The partially sealed configuration has been less influenced by fluid inertia than the open ended configuraton. Larger extent of vapor cavitation region has been observed in the partially sealed configuration than in the open ended configuration. The effect of cavitation must be properly included in the analysis if accurate predictions are to be made.

ACKNOWLEDGMENTS

REFERENCES

[1] San Andres, L. A., "Effect of Fluid Inertia on Squeeze Film Damper Force Response", Ph.D. Dissertation, Dept. of Mechanical Eng., Texas A&M University, December 1985

[2] Zeidan, F. Y., "Cavitation Effects on the Performance of Squeeze Film Damper Bearings", Ph.D. Dissertation, Dept. of Mechanical Eng., Texas A&M University, August 1989

[3] Jung, S. Y. and Vance, J. M., "Effects of Vapor Cavitation and Fluid Inertia on the Force Coefficients of a Squeeze Film Damper, Part I- Analysis of a Long Squeeze Film Damper", to be presented at the 1990 annual meeting of STLE in Denver

[4] Jung, S. Y. and Vance, J. M., "Effects of Vapor Cavitation and Fluid Inertia on the Force Coefficients of a Squeeze Film Damper, Part II- Experimental Comparisons", to be presented at the 1990 annual meeting of STLE in Denver

[5] Swift, H. W., "The Stability of Lubricating Films in Journal Bearings", *Proceedings Institute of Civil Engineers*, Vol. 233, London, 1932, pp. 267-288

[6] Stieber, W., "Das Schwimmlager", VDI, Berlin, 1933

Fig. 1 SFD geometry of a partially sealed configuration

oil inlet
Z0
Z3
PP
Z2
Z1
PT
PT
squeeze film
housing
serrated piston ring
journal
C
end plate
L
O ring
R
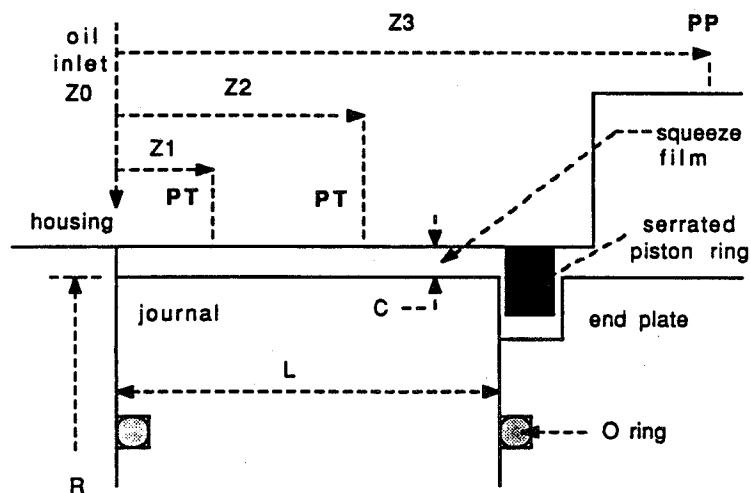
L/D=0.188

Z1=0.56 cm (0.2200 inch)   L=2.39 cm (0.94 inch)
Z2=1.67 cm (0.6575 inch)   R=6.35 cm (2.50 inch)
Z3=3.71 cm (1.4600 inch)   C=0.159 cm (0.0625 inch)

PT : Pressure Transducer   PP : Proximity Probe

Fig. 2 Geometry of a serrated piston ring

A
5° 5°
radius 0.79 mm
a
A
r
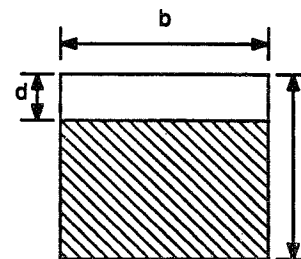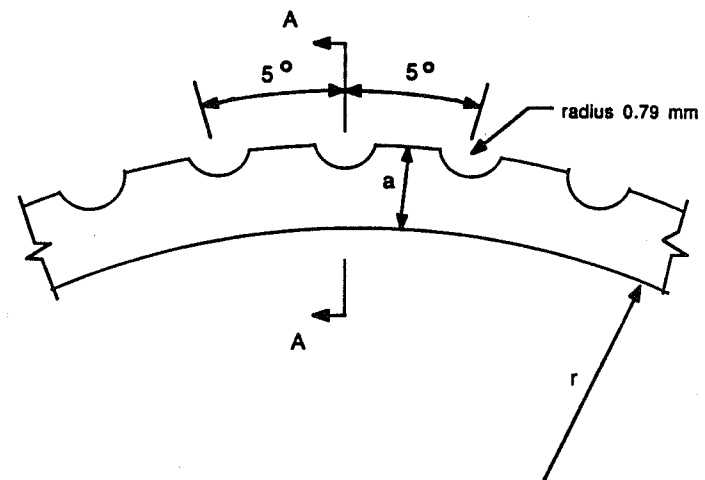
b
d
c
Section A-A

a=3.97 mm (5/32 in)
b=3.97 mm (5/32 in)
c=3.97 mm (5/32 in)
d=0.79 mm (1/32 in)
r=61.2 mm (2.408 in)

(Note : 72 holes of radius 0.79 mm are equally spaced)
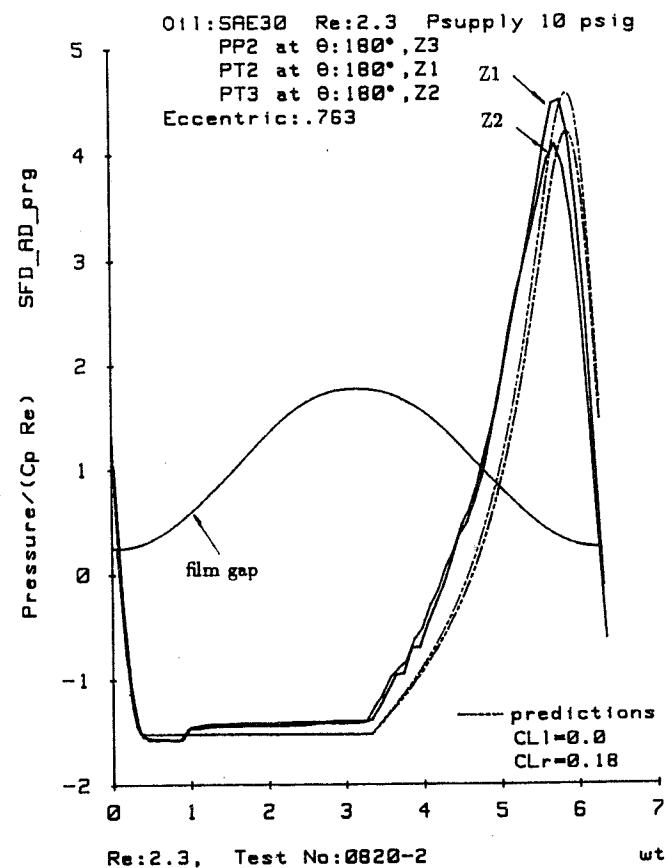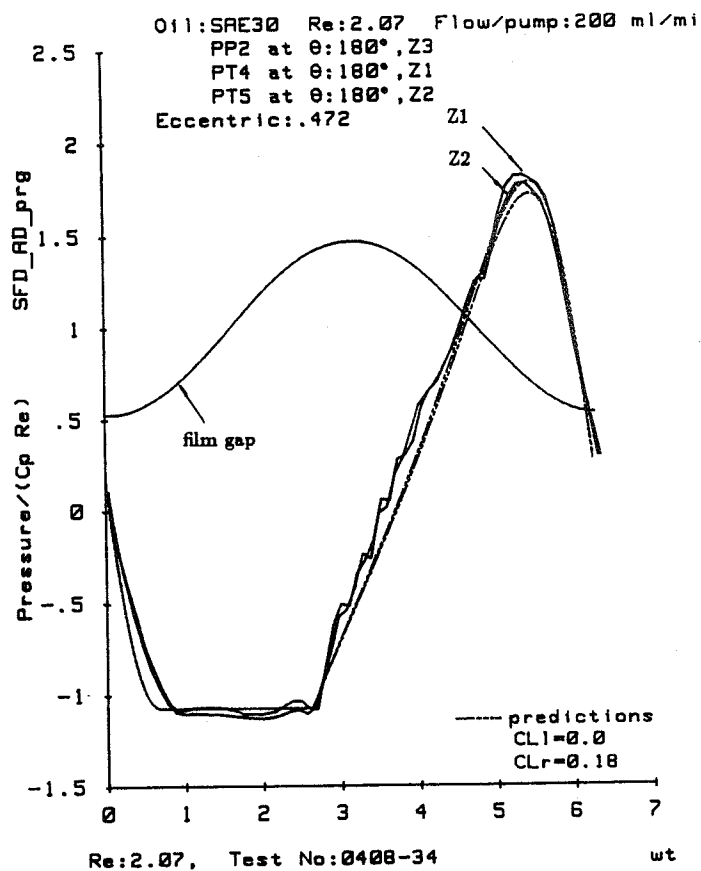
Fig. 3 Dimensionless pressure profiles, partially sealed configuration, Re=2.07,

$\epsilon = 0.47$

Fig. 4 Dimensionless pressure profiles, partially sealed configuration, Re=2.3,

$\epsilon = 0.76$
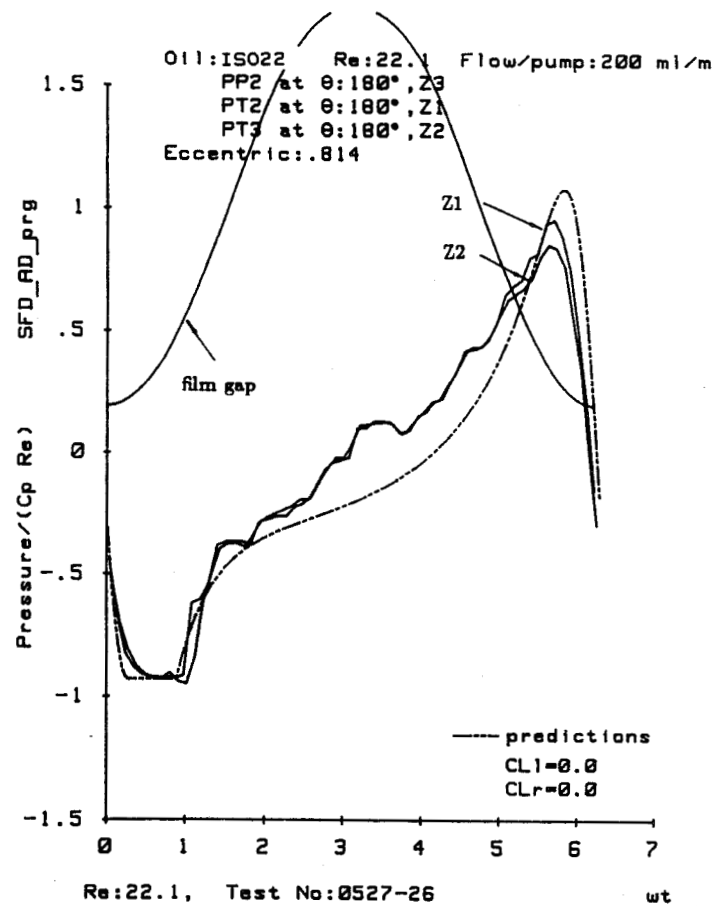
Fig. 5   Dimensionless pressure profiles, partially sealed configuration, Re=22.1,

$\epsilon = 0.81$
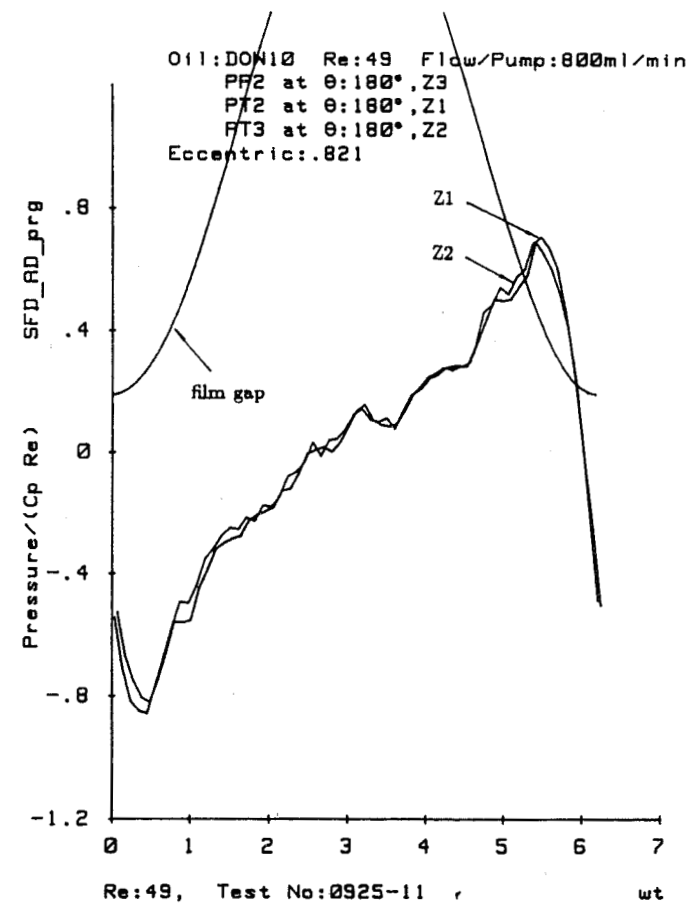
Fig. 6   Dimensionless pressure profiles, partially sealed configuration, Re=49.0,

$\epsilon = 0.82$
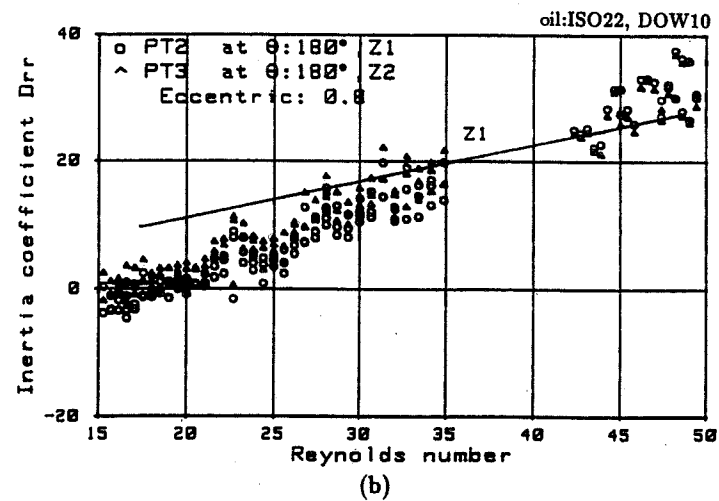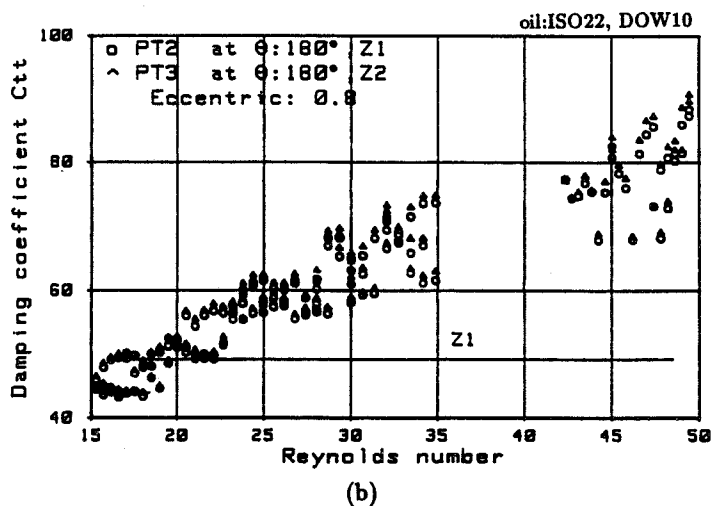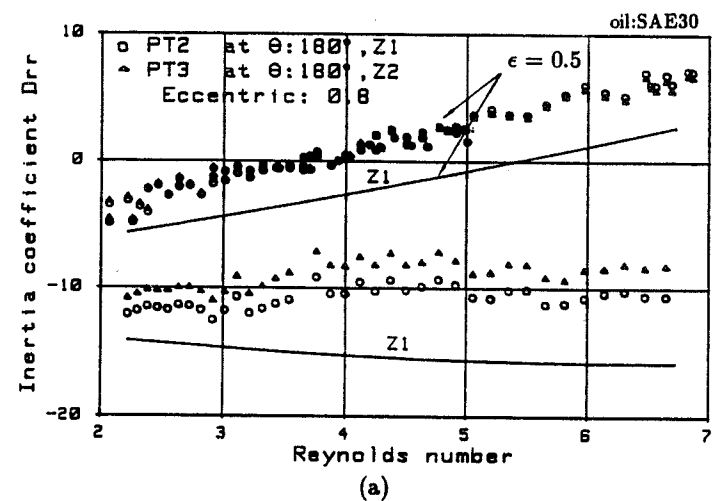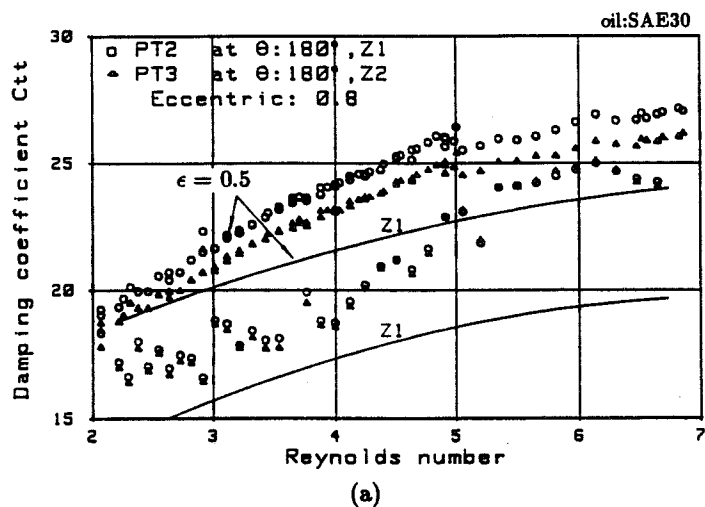
Fig. 7 Dimensionless damping coefficients vs. Reynolds no.

Fig. 8 Dimensionless inertia coefficients vs. Reynolds no.
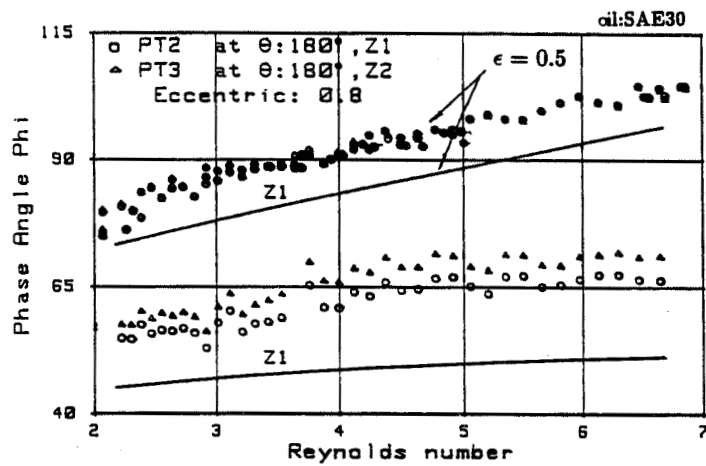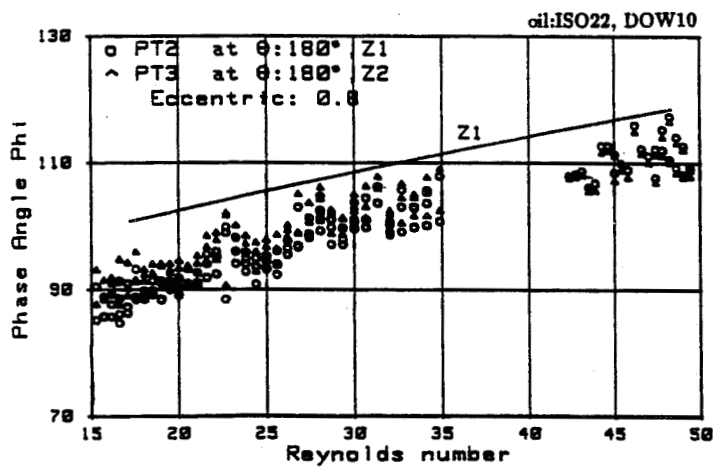
Fig. 9   Phase angle vs. Reynolds number

107

EXPERIMENTAL INVESTIGATIONS OF EXCITING FORCES CAUSED BY FLOW IN LABYRINTH SEALS*

G. Thieleke and H. Stetter
Institut für Thermische Strömungsmaschinen
und Maschinenlaboratorium
University of Stuttgart
Pfaffenwaldring 6
D-7000 Stuttgart 80, Federal Republic of Germany

The interaction of the flow through the labyrinth seals with the shaft of the rotor can have an effect on the stability of turbomachines. Thus, the excited forces, so-called cross forces or non-conservative forces, arise, which act perpendicular to the rotor eccentricity. This effect is caused by an unsymmetrical pressure distribution within the labyrinth cavities.

Experimental investigations are carried out for different types of labyrinth geometries: two staggered labyrinths with teeth on the stator and grooved rotor as well as a full and a convergent stepped labyrinth. These labyrinths can be found on the tip shrouding of bladings in steam or gas turbines. The following parameters are varied in the test-facility: geometry of the labyrinth seals (number of cavities, inlet region), shaft rotation, pressure difference on the seal, entry-swirl and eccentricity of the rotor.

The results are presented for stiffness coefficients of the labyrinth seals, leakage flow and circumferential flow in each cavity which was measured with special probes. Generally, the inlet swirl has the greatest influence on the coefficients of the seals. The experimental results are compared with theoretical results and are in good agreement.

109

1 Nomenclature

A	Area
B	Height of labyrinth seal strip
c	Stiffness–term
c	Circumferential velocity of flow
c_{uo}	Inlet swirl
d	Damping–term
D	Diameter
E_0^*	Flow characteristic
e	Dimensioned eccentricity
F	Force
F_B	Reference force
f	Cross-sectional area of control volume
F_0	Cross-sectional area for centered shaft-position
g_i	Value of parameter of $\overline{K_Q^*}$
H	Local radial clearance
h_d	Hydraulic diameter
j	Complex unity
$k = C_R/(B + C_R)$	Factor of area change
K_Q	Cross force spring-coefficient
K_R	Restoring force spring-coefficient
m	Inertia–term
m, N	Number of cavities
$m_{R;S}, n_{R;S}$	Coefficients for friction factor
$\dot{m}$	Leakage flow
$\dot{m}_i$	Leakage flow per circumferential length
$\dot{M}_0$	Leakage flow for centered shaft-position
p	Pressure
P_0	Pressure before seal
P1	Position of probe
Q	Cross force
R	Restoring force
R	Gas constant
Re	Reynolds number
r, R_R	Shaft radius
$\Delta r, C_R$	Nominal clearance
T	Temperature
t	Time
t, L	Pitch of seal strips
u_w	Rotor peripheral velocity
$u = c/R_R\omega$	Dimensionless circumferential velocity of flow
U	Length on which shear stress acts
z	Number of seal strips
β^*	Flow coefficient
$\epsilon = e/C_R$	Eccentricity ratio, perturbation parameter
μ	Flow coefficient
ν	Kinematic viscosity

ρ Density of fluid
π Pressure ratio (p_a/p_0)
φ Peripheral angle
τ Dimensionless time
σ Shear stress
ω Shaft angular velocity
Ω Shaft precessional velocity

subscripts

0   zeroth-order component
1   first-order component
c cosine
i i-th chamber value
Q cross
R rotor, restoring
r radial-direction
S stator
s sine
u circumferential direction
w shaft
y y-direction
z z-direction
$-$ mean-value
$*$ dimensionless value

Not presented notations are declared in text.

2   Introduction

In order to carry out a thorough stability analysis of turbomachine rotors, it is essential to know all the forces causing oscillations. These forces, acting on the rotating subassembly units of the rotor shaft, can effect the stability behaviour in such a way that the operation is seriously disturbed or even impossible. The major causes for rotor instability are mostly exciting forces resulting from fluid–mechanisms, which are found in journal bearings and in labyrinth seals. The interaction between the flowing medium and the rotor shaft cause a transmission of energy to the flexural oscillation system. That leads to rotor–instability, if damping is not sufficient.

In order to be able to judge the stability qualities in advance, the engineer has to carry out oscillation analyses. For that he needs information about the dynamic characteristics of the seals which are characterized by stiffness, damping and inertia terms. When these properties are known the fluid–mechanisms can be described in a linear equation of motion, i.e., equation (1).

$$\begin{pmatrix} F_y \\ F_z \end{pmatrix} = \begin{pmatrix} c_{yy} & c_{yz} \\ c_{zy} & c_{zz} \end{pmatrix} \begin{pmatrix} y \\ z \end{pmatrix} + \begin{pmatrix} d_{yy} & d_{yz} \\ d_{zy} & d_{zz} \end{pmatrix} \begin{pmatrix} \dot{y} \\ \dot{z} \end{pmatrix} + \begin{pmatrix} m_{yy} & m_{yz} \\ m_{zy} & m_{zz} \end{pmatrix} \begin{pmatrix} \ddot{y} \\ \ddot{z} \end{pmatrix} \qquad (1)$$

These quantities must be known in order to design the dynamics of turbomachines properly.

Experimental results of labyrinth seal forces have been presented by Benckert and Wachter [1], [2]. They investigated several multistage types of different labyrinth seals and found out that for long seals the shaft rotation has a great influence.

Childs and Scharrer [3] surveyed experimentally the dynamic characteristics of long straight through

111

labyrinths. On this test facility, the stiffness behaviour as well as the damping characteristics could be determined, since the rotor carries out an oscillation motion in addition to its rotational motion.

Leong and Brown [4] surveyed long straight through labyrinths with different cavity geometries. The seal strips were attached to the stator. Their results show, that with increasing peripheral velocity of the rotor, the cross–coupled stiffness coefficients decrease and can become even negative.

Rajakumar and Sisto [5] and Serkov [6] investigated the flow forces for short straight through labyrinths. They found out, that the inlet swirl compared to the shaft rotation has a great influence on the cross forces.

In reviewing previous experimental investigations, there is a clear need for testing of short prevalent labyrinth seals, which can be found on the tip shrouding of bladings in steam or gas turbines.

3 Test–Facility

The investigations are carried out on a labyrinth test–facility at the 'Institut für Thermische Strömungs-maschinen und Maschinenlaboratorium' of Stuttgart University. The test–facility was originally set up in [1], [2] and has now been modified to fit the changed requirements. Using this setup the inlet flow is the same as in the shroud ring seals of a real turbine stage (e.g., overlapping of guide– and rotor–bladings, radial streamline variation).

The cutaway (figure 16) shows one of the shroud ring seals with grooved rotor and teeth on the stator to be examined. The flow force in the labyrinth seals is always determined by integration of the measured pressure in axial direction and along the perimeter. In the axial direction each cavity is looked at individually and then all cavities are summed up. The reduction of these results to components gives the cross and the restoring force Q and R. The influence of the following parameters have been surveyed:

- *Inlet state before the first seal tip* π, c_{u0}. It depends on the pressure ratio being at the seal and the inlet swirl of the flow. A nozzle ring in conjunction with a vacuum assembly can produce different swirl components c_{u0}. The measuring of the resulting circumferential component of the labyrinth flow is made with three–hole-cylinder probes specially developed for this purpose (see figure 1). Since the probes are also used in the area of the labyrinth strips and near the rotor surface, the wall effect on the calibration factors, defined in figure 1, must be tested and taken into consideration. The test medium is air which expands to the ambient conditions.

- *Eccentricity of the rotor* ϵ. The eccentricity is varied from negative over the centered position to positive values.

- *Peripheral velocity of rotor* u_w. The rotational rotor speed is increased from $u_w = 0 m/s$ upto over $u_w = 100 m/s$. The influence of the direction of rotor rotation is likewise being tested.

- *Geometry of the seal.* Measurements are made with 15 different labyrinth configurations. They can be subdivided into three different types of labyrinths; grooved, interlocking and stepped labyrinths (figures 18). Besides the number of cavities, the inflow contour of the labyrinth was also varied.

Figure 2 shows a summary of variations of the test parameters.

$$Pm = \frac{P2+P3}{2}$$

$$FMP = \frac{P1-Pm}{P1} = f(Ma)$$

$$CPTOT = \frac{Pt-P1}{P1-Pm} = f(FMP) \Longrightarrow Pt$$

$$CPDYN = \frac{Pt-Ps}{P1-Pm} = f(FMP) \Longrightarrow Ps$$

$$RCF = \frac{Tg-Ts}{Tt-Ts} = f(FMP) \Longrightarrow Ts$$

α...Tuning of angle $\Delta P = P2 - P3 = 0 \Longrightarrow \alpha$

$$\sin\alpha = \frac{Cu}{C} \Longrightarrow Cu$$

$$\cos\alpha = \frac{Cax}{C} \Longrightarrow Cax$$
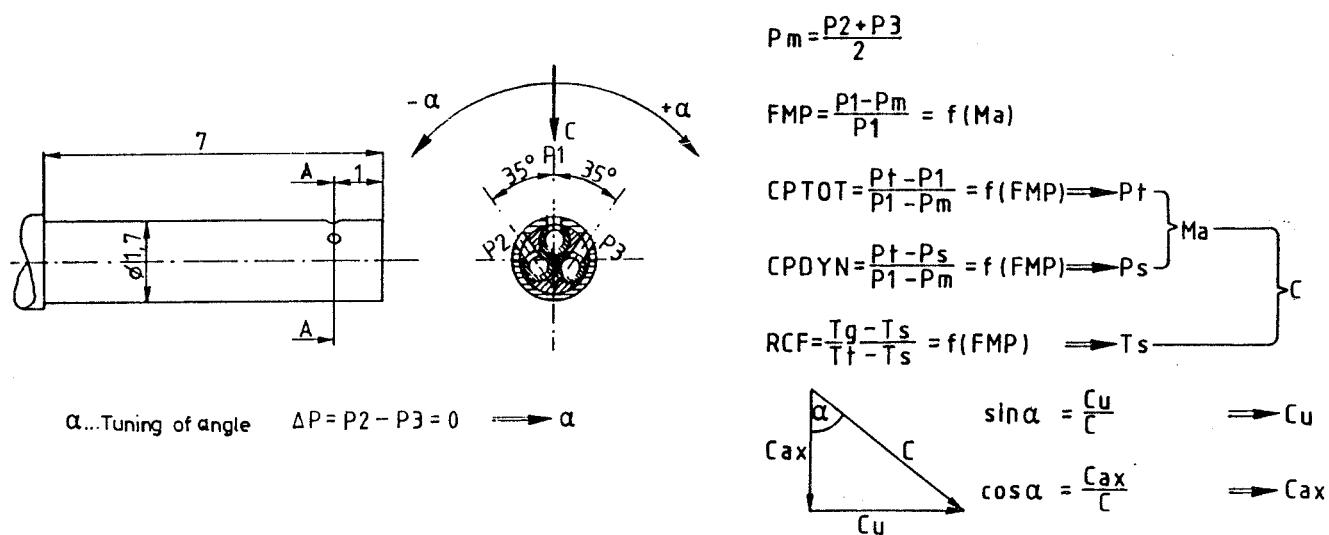
Figure 1: Three–hole-cylinder probe

Variation of Test Parameters

inlet state	pressure ratio	p_a/p_0 [-]	0,5	0,3	0,25
	inlet swirl	c_{u0} [m/s]	0	80	120
				3 steps	
dimensionless rotor eccentricity	$\epsilon = \frac{e}{\Delta r}$	ϵ [-]	+0,7	0	-0,7
				5 steps	
peripheral velocity of rotor		u_w [m/s]	+100	0	-100
				5 steps	

	typ	A1-3	G1	K1-7	M1-4
labyrinth geometry	number of cavites	7	3	4	8
		5		3 (*)	7
		4		2 (**)	5
				1	3

(*)   2 variations of strips
(**) 3 variations of cavities

Figure 2: Variation of test parameters

113

4 Analysis of test data

The results are presented as follows:

- Variation of the flow forces in the individual cavity as dimensionless cross and restoring force in each cavity. The restoring force R_i^* acts against the rotor eccentricity ϵ (centering effect) and the cross force Q_i^* acts perpendicular to ϵ.

- Variation of the forces in the entire labyrinth as dimensionless cross force spring coefficient $\overline{K_Q^*}$ dependent on the test parameters and the flow characteristic E_0^*. The quantity E_0^* is the ratio of the inlet swirl energy and axial pressure drop.

- Leakage characteristic

The definitions for the calculation of the forces and the stiffness coefficients are summarized in figure 17.

5 Experimental Results

For the different labyrinth types of M– and A–configuration, the figures 19, 20 show the pressure distribution and the resulting rotor loads, i.e. cross and restoring force Q_i^* and R_i^*. The pressure distribution $p_i^*(\varphi)$ is related to the static pressure difference. For three eccentricities ($\epsilon = 0$ and $\epsilon \pm 0,66$), the pressure distributions depending on the individual labyrinth cavities and its circumferential angle φ are depicted. The flow conditions π, c_{u0}, u_w are noted in the figures.

For centered position ($\epsilon = 0$), the pressure distributions along the perimeter of the rotor are almost constant in the individual cavities. Thus, the resulting forces Q_i^* and R_i^* are nearly zero. But looking at the pressure drop in the axial direction shows that the pressure drop depends on the geometry of the cavity (transitions of the staggered grooves). Figure 3 shows the resulting flow coefficient μ_i as a function of the cavity number i for the M1 to M4–configuration.

$$\mu_i = \frac{\dot{m}}{A_i}\sqrt{\frac{p_0 v_0}{p_i^2 - p_{i+1}^2}}$$
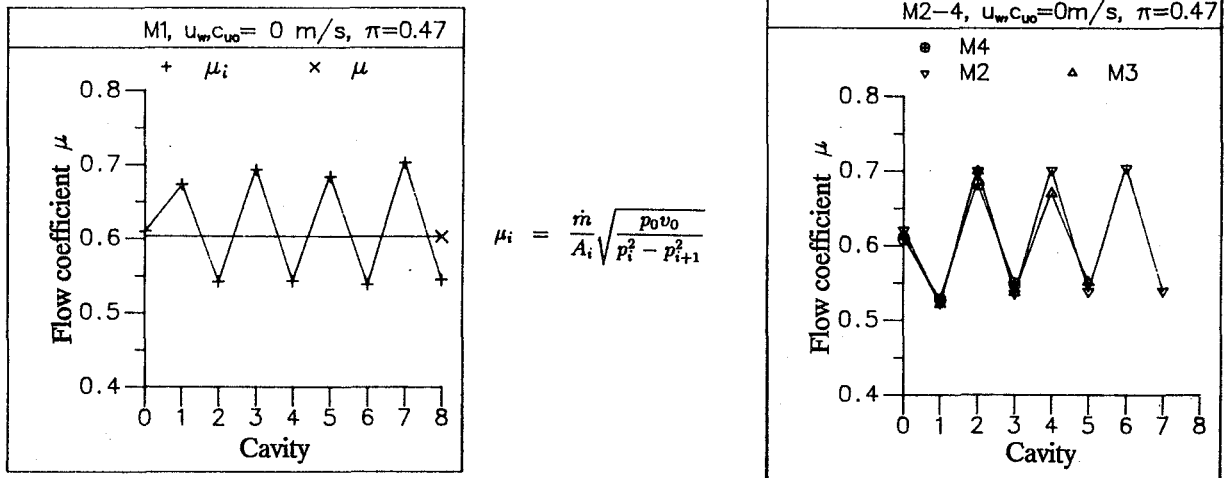
Figure 3: Flow coefficient μ_i of M1–M4–configurations

For positive and negative eccentricity ($\epsilon \pm 0,66$), the variations of pressure in the circumferential direction are almost identical. This correspondence for $\pm\epsilon$, which must come about for a perfect labyrinth geometry and an exactly adjusted rotor, is even more evident for Q_i^* and R_i^*.

The results show, that it is not the first cavity which provides the highest contribution of cross force. In the front part of the labyrinth, the cross force rises to its maximum and drops then continuously. For the M2-configuration the maximum is located in the 2. cavity (see figures 19, 21). This pattern is independent of inlet swirl, eccentricity and pressure rate. It was detected for all M-configurations. But the increase of the cross force in the front part depends on the inflow contour of the labyrinth. Relatively high gradients dQ_i^*/di were measured for the inflow contour with rotor groove and opposite long seal tip (M2 to M4-configuration). In figure 4 this is depicted for the M3 and M4-configuration.
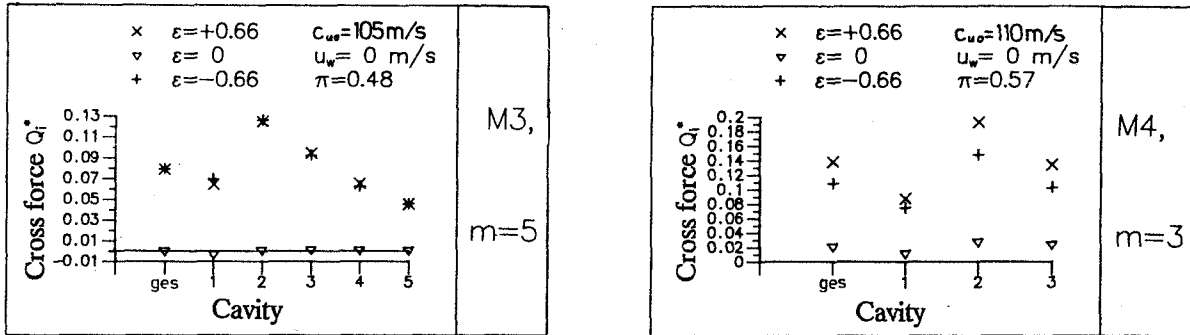
Figure 4: Cross force Q_i^* of M3- and M4-configuration

The increase of the cross force dQ_i^*/di is smaller for a inflow contour with rotor stage and opposite short seal tip (M1-configuration, see figure 5).
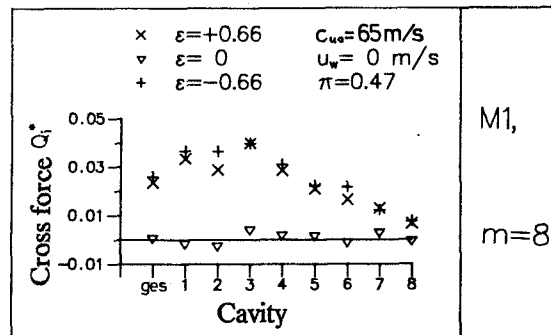
Figure 5: Cross force Q_i^* of M1-configuration

115

Apparently, the changed inflow geometry brings about a different inflow condition at the labyrinth. An extension of the space in front of the first seal tip results in a larger increase of the cross force in the front part of the labyrinth.

Like the experiments, analytical investigations show different cross force characteristics for each cavity when varying the boundary conditions. The boundary conditions are: the pressure distribution and the circumferential velocity distribution of the labyrinth flow along the perimeter in front of the first seal tip, and the flow coefficient μ_0. Furthermore, the boundary conditions at the exit of the labyrinth may also have an influence.

The influence of the inflow geometry on the cross force characteristics could be proved for the A–full-labyrinth as well (see fig. 6).
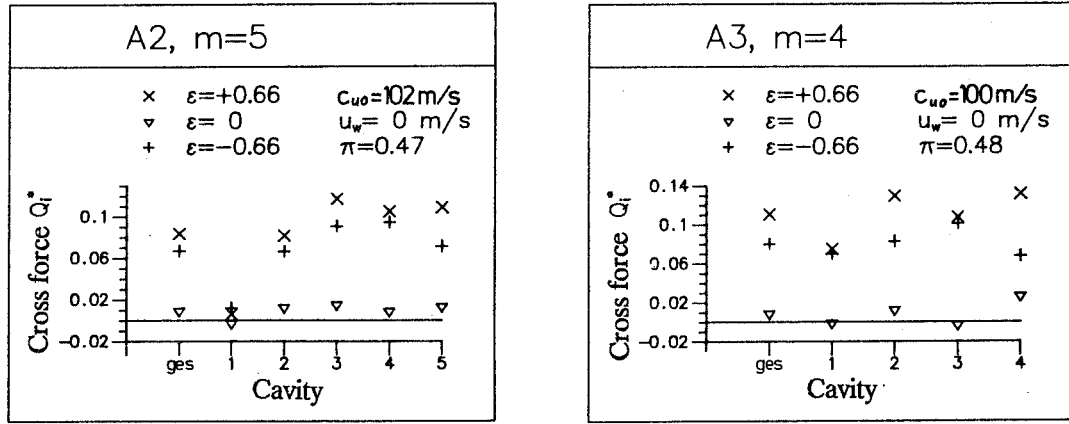
Figure 6: Cross force Q_i^* of A2– and A3–configuration

For the M2–configuration, fig. 21 shows the influence of the inlet swirl c_{u0} and the eccentricity ϵ on the cross force– and restoring force characteristics.

In contrast to Q_i^*, the restoring force is alternating along the cavities. Hence the resultant restoring force $\overline{R_i^*}$, recorded at the cavity number $i = ges$, is almost zero (see fig.7).
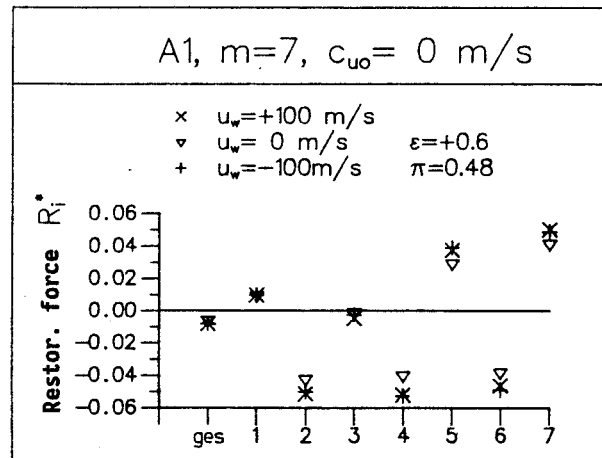
Figure 7: Restoring force R_i^* of A1–configuration

116

This characteristic is even more evident for the A–full–labyrinth. Pressure maxima and –minima respectively dependent on the cavity number occur in the area of the narrowest gap ($\varphi = 180°$). Similar to the Lomakin–effect [7], the losses due to friction and inflow respectively at each seal strip varying along the circumferential direction are responsible for that. That means, besides the dependence on the arrangement of the seal strips, the flow coefficient μ is also a function of the peripheral angle φ.

The alternating run of the restoring force R_i^* is independent from the peripheral velocity of the rotor. This is shown in figure 7 for the A1–configuration with 7 cavities and $c_{u0} = 0 m/s$.

For the M1–(m=8) and M4–configuration (m=3) the figure 8 illustrates Q_i^* versus cavity number i for different u_w and superposed c_{u0}.
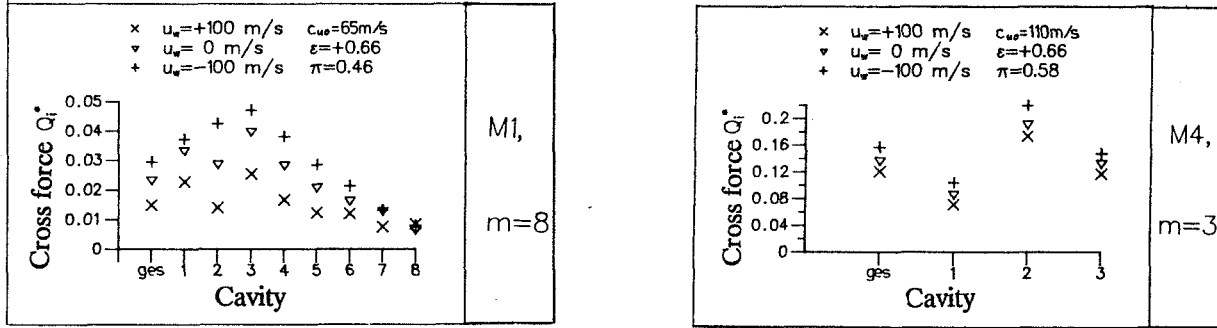
Figure 8: Cross force Q_i^* of M1– and M4–configuration

If the shaft rotates in the opposite direction of the inlet swirl, the value of u_w becomes negative. By definition the inlet swirl is positive in the direction of the peripheral angle φ. Changing the direction of u_w different situations in turbines and compressors can be simulated. Figure 8 shows that the cross force for $u_w = -95m/s$ is higher compared to $u_w = 0m/s$.

This effect can be explained by the ratio of decelerating to accelerating friction areas at rotor and stator. It has an effect on the distribution of the circumferential component of the labyrinth flow along the seal. The variation of c_u along the cavities shows that the amount of cross force doesn't depend on the amount of circumferential velocity of the labyrinth flow, but on the change of the circumferential flow between the cavities. For negative u_w the swirl changes are maximal (see fig. 9) and consequently the cross force as well.

With the help of flow–measuring probes it was ascertained that the circumferential component of the labyrinth flow is nearly not radial–changing within the cavities. Fig. 10 illustrates c_u versus the cavity number i for centered shaft position. Only in the vicinity of the stator surface the c_u–components are not constant. This is because of the effect of the boundary layer. Hence the circumferential velocity of the labyrinth flow in the cavities can be approximated by a mean circumferential velocity.
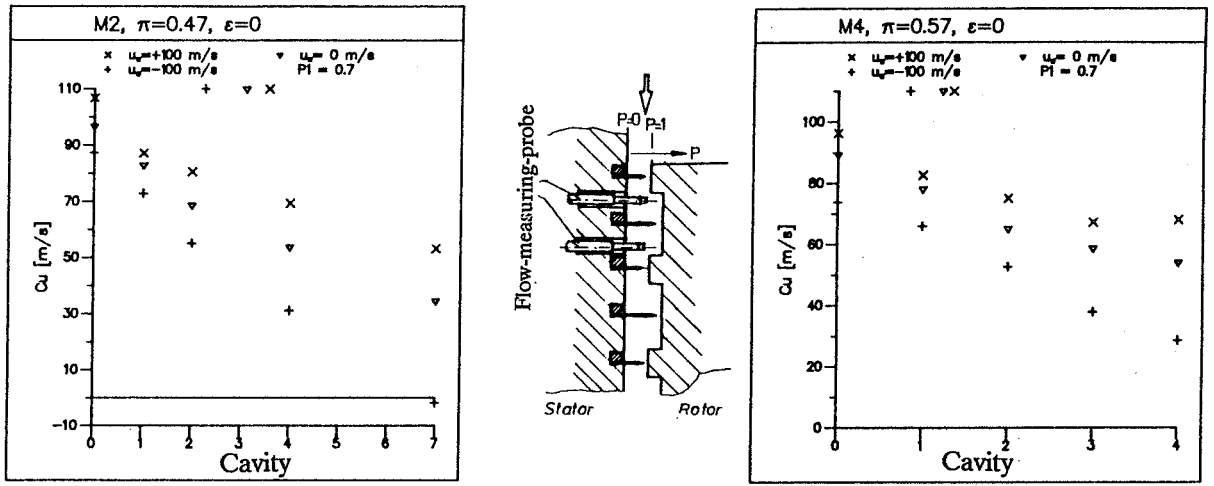
Figure 9: Circumferential velocity c_u with superposed rotor speed
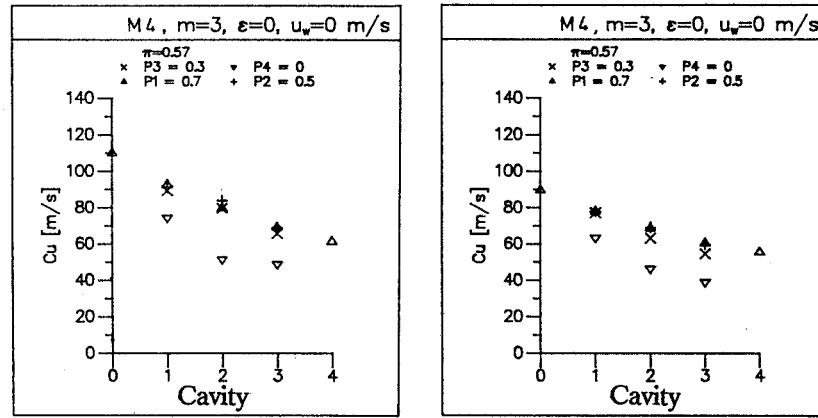
Figure 10: Circumferential velocity c_u of M4–configuration

Even for eccentric rotor position the c_u–components are almost constant in radial direction. Furthermore, fig. 25 shows for the M4–configuration the variation of c_u in the peripheral direction in each cavity. An approximation of c_u in terms

$$c_{u,i} = c_{um,i} + \epsilon \left(c_{u,c,i} \cos \varphi + c_{u,s,i} \sin \varphi \right) \tag{2}$$

confirms the assumptions of equations (9) and (11), see figure 25.

The relationship between the total cross force $\overline{Q^*}$ and the eccentricity ϵ is linear for all configurations as the plots in figure 11 show.

The characteristic field of the spring coefficient $\overline{K_Q^*}$ as a function of π, c_{u0} and u_w is shown in figure 22 and 23. These characteristic fields enable a separate investigation of the varied test parameters and its effects on the spring coefficient. It shows that the inlet swirl has the greatest influence on $\overline{K_Q^*}$.

118
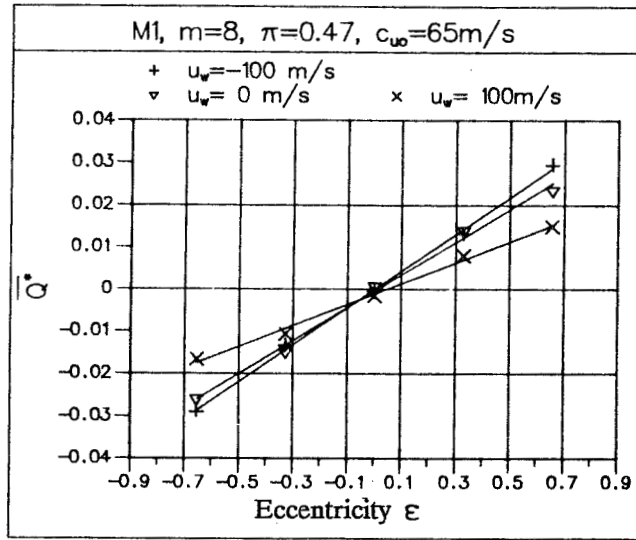
Figure 11: Cross force $\overline{Q^*}$ versus eccentricity ϵ of M1–configuration

Introducing the flow–characteristic E_0^*, the results can be transferred to seals in real machines. Fig. 12 shows for the M–configurations the obtained spring coefficients and the approximated curves. The approximating function is given by the nonlinear equation $\overline{K_Q^*} = g_1 + g_2 E_0^{*g_3}$. The coefficient g_1 corresponds to spring coefficient $\overline{K_Q^*}$ for axial inflow ($E_0^* = 0$).
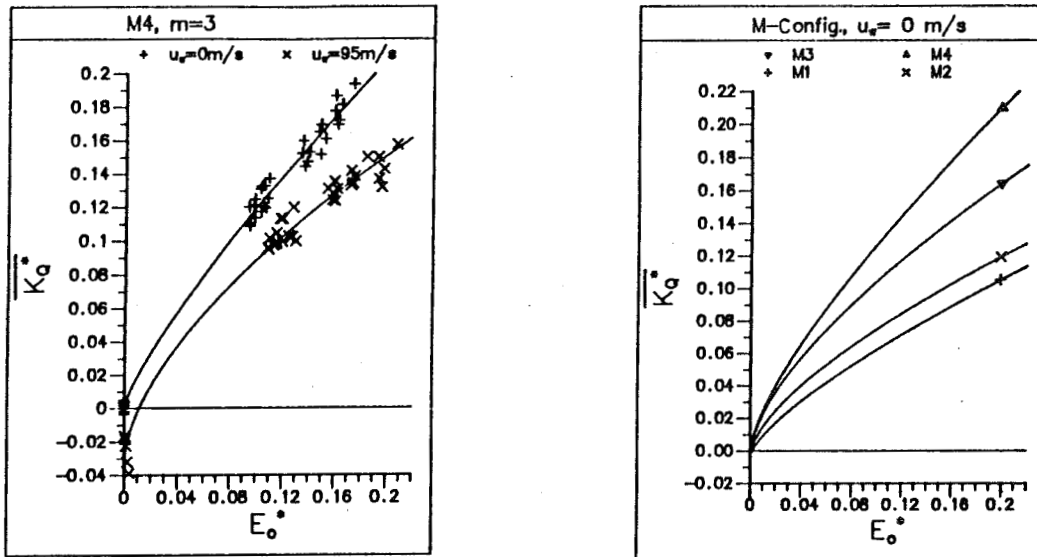
Figure 12: $\overline{K_Q^*}$ versus E_0^* of M–configuration

The comparison of the four M–configurations shows that the parameters $g_{1,2,3}$ depend on the number of cavities (see table 1).

In addition, table 1 shows the flow coefficient β^* for $E_0^* = 0$. The relationship between the leakage flow $\dot{m}$ and the flow coefficient β^* is:

$$\dot{m} = \beta^* \sqrt{\frac{\Delta r}{mt}} A_{res} \sqrt{\frac{p_0^2 - p_a^2}{p_0/\rho_0}}$$

Configurat.	u_w [m/s]	g_1	g_2	g_3	β^*
M1	0	-0,0031	0,3551	0,7336	1,9
M1	47	-0,0092	0,3809	0,7687	1,86
M1	94	-0,0115	0,4174	0,8252	1,79
M2	0	-0,0023	0,3533	0,6591	1,84
M2	47	-0,0081	0,3210	0,6489	1,82
M2	94	-0,018	0,298	0,60	1,76
M3	0	-0,0016	0,4726	0,6485	1,78
M3	47	-0,0139	0,4843	0,6710	1,76
M3	94	-0,0327	0,5091	0,6636	1,72
M4	0	0,0008	0,7586	0,8059	1,68
M4	47	-0,0109	0,5063	0,6472	1,67
M4	94	-0,0326	0,4826	0,6004	1,64
A1	0	0,0030	0,7316	0,8132	1,56
A1	47	0,0004	0,6954	0,7743	1,55
A1	94	0,0062	0,7616	0,8274	1,53
A2	0	0,0020	0,7747	0,8978	1,55
A2	47	0,0010	0,7132	0,8362	1,54
A2	94	-0,0007	0,6859	0,8046	1,52
A3	0	0,0044	1,0057	0,8812	1,45
A3	47	-0,0013	0,7879	0,7544	1,44
A3	94	-0,0058	0,7110	0,6955	1,42

Table 1: Values of the parameters $g_{1,2,3}$ $\overline{K_Q^*}$ and β^* of M– and A–labyrinth

Furthermore, the characteristic fields of the restoring force spring coefficient $\overline{K_R^*}$ as a function of the test parameters are depicted in the fig. 24.

6 Analysis

In order to compare the experimental with the theoretical results an analysis was developed. It bases on Iwatsubo's [8] and Child's [9] basic equations for compressible flow in a labyrinth seal. The continuity and momentum equation will be derived for a single cavity control volume as shown in figure 13.
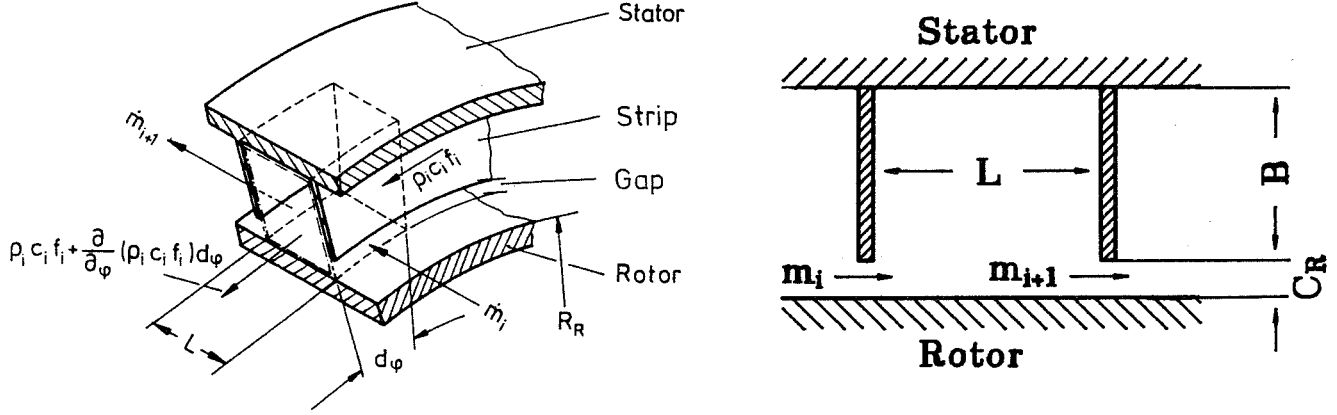
Figure 13: Cavity control volume

The governing equations are

- Continuity equation:

$$\frac{\partial}{\partial t}\left(\rho_i f_i\right) + \frac{1}{R_R}\frac{\partial}{\partial \varphi}\left(\rho_i f_i c_i\right) + \dot{m}_{i+1} - \dot{m}_i = 0 \tag{3}$$

- Momentum equation:

$$\begin{aligned}
\frac{\partial}{\partial t}\left(\rho_i f_i c_i\right) &= -\frac{1}{R_R}\frac{\partial}{\partial \varphi}\left(\rho_i f_i c_i^2\right) - \frac{f_i}{R_R}\frac{\partial p_i}{\partial \varphi} + \dot{m}_i c_{i-1} - \dot{m}_{i+1} c_i \\
&\quad -\sigma_{t,Si} U_{Si} + \sigma_{t,Ri} U_{Ri}
\end{aligned} \tag{4}$$

- Leakage equation:

$$\dot{m}_i = \mu_i H_i \sqrt{\frac{p_i^2 - p_{i+1}^2}{RT}} \tag{5}$$

with leakage mass flow per circumferential length

- Friction equation:

$$\begin{aligned}
\sigma_{t,Si} &= \frac{1}{2}\rho_i c_i^2 \lambda_{Si} = \frac{1}{2}\rho_i c_i^2 n_{Si}\left(\frac{|c_i| h_{di}}{\nu}\right)^{m_{Si}}\text{sign}(c_i) \\
\sigma_{t,Ri} &= \frac{1}{2}\rho_i (R_R\omega - c_i)^2 \lambda_{Ri} \\
&= \frac{1}{2}\rho_i (R_R\omega - c_i)^2 n_{Ri}\left(\frac{|R_R\omega - c_i| h_{di}}{\nu}\right)^{m_{Ri}}\text{sign}(R_R\omega - c_i)
\end{aligned} \tag{6}$$

with h_d as hydraulic diameter.

121

- Ideal gas law:

$$\frac{p_i}{\rho_i} = \mathrm{R}T \tag{7}$$

- Normalization of the variables:

$$u_i = \frac{c_i}{R_R\omega} \qquad \tilde{p}_i = \frac{p_i}{P_0} \qquad \tilde{f}_i = \frac{f_i}{F_0} \qquad \dot{\tilde{m}}_i = \frac{\dot{m}_i}{\dot{M}_0} \qquad \tau = \omega t \tag{8}$$

The solution procedure is similar to the perturbation analysis used by Childs [10]:

- Linearized zeroth and first–order perturbation equations describe the pressure and velocity distributions for the centered (index '0') and eccentered (index '1') shaft position. The following perturbation variables are defined:

$$
\begin{aligned}
u_i &= u_{0,i} + \epsilon u_{1,i} \qquad \tilde{p}_i = p_{0,i} + \epsilon p_{1,i} \qquad \tilde{f}_i = f_{0,i} + \epsilon f_{1,i} \\
H_i &= C_R + \epsilon H_{1,i} \qquad \mu_i = \mu_{0,i} + \epsilon \mu_{1,i}
\end{aligned} \tag{9}
$$

where $\epsilon = e/C_r$ is the eccentricity ratio.

- The zeroth–order solution for the circumferential velocity (zeroth–order momentum equation) is

$$
\begin{aligned}
0 = & \frac{RT\dot{M}_0}{\omega P_0} \left(u_{0,i-1} - u_{0,i}\right) \\
& - \frac{1}{2} R_R p_{0,i} u_{0,i}^2 n_{Si} \left(\frac{|u_{0,i}R_R\omega| h_{di}}{\nu}\right)^{m_{Si}} \mathrm{sign}(\omega u_{0,i}) U_{Si} \\
& + \frac{1}{2} R_R p_{0,i} \left(1 - u_{0,i}\right)^2 n_{Ri} \left(\frac{|\left(1 - u_{0,i}\right) R_R\omega| h_{di}}{\nu}\right)^{m_{Ri}} \mathrm{sign}\left(\omega \left(1 - u_{0,i}\right)\right) U_{Ri}
\end{aligned} \tag{10}
$$

The partial differential equations (first–order solution) will be reduced to linear complex equations by introducing the following assumptions for the perturbation variables:

- Elimination of circumferential angle φ:

$$
\begin{aligned}
p_{1,i} &= p_{1,i,c}\cos\varphi + p_{1,i,s}\sin\varphi \qquad u_{1,i} = u_{1,i,c}\cos\varphi + u_{1,i,s}\sin\varphi \\
h_{1,i} &= \frac{H_{1,i}}{C_R} = -y_i\cos\varphi - z_i\sin\varphi \qquad \mu_{1,i} = \mu_{1,i,c}\cos\varphi + \mu_{1,i,s}\sin\varphi
\end{aligned} \tag{11}
$$

- Complex variables:

$$
\begin{aligned}
\underline{p}_{1,i} &= p_{1,i,c} + j p_{1,i,s} \qquad \underline{u}_{1,i} = u_{1,i,c} + j u_{1,i,s} \\
\underline{h}_{1,i} &= -y_i - j z_i \qquad \underline{\mu}_{1,i} = \mu_{1,i,c} + j \mu_{1,i,s}
\end{aligned} \tag{12}
$$

- Elimination of time t with harmonic seal motion (circular orbit with frequency Ω around the centered position, see fig. 14) :

$$\underline{h}_{1,i} = \hat{\underline{h}}_{1,i} e^{j\Omega t} \tag{13}$$

and corresponding response for the other perturbations variables:

$$
\begin{aligned}
\underline{u}_{1,i} &= \hat{\underline{u}}_{1,i} e^{j\Omega t} = \hat{\underline{u}}_{1,i} e^{j\frac{\Omega}{\omega}\tau} \\
\underline{p}_{1,i} &= \hat{\underline{p}}_{1,i} e^{j\frac{\Omega}{\omega}\tau} \qquad \underline{\mu}_{1,i} = \hat{\underline{\mu}}_{1,i} e^{j\frac{\Omega}{\omega}\tau}
\end{aligned} \tag{14}
$$

yields to the complex continuity and momentum equation:

- Complex continuity equation:

$$\left(j\frac{\Omega}{\omega} - ju_{0,i} + \frac{RT\dot{M}_0}{\omega P_0 F_0}\left(\frac{p_{0,i}}{p_{0,i}^2 - p_{0,i+1}^2} + \frac{p_{0,i}}{p_{0,i-1}^2 - p_{0,i}^2}\right)\right)\hat{\underline{p}}_{1,i}$$

$$-\frac{RT\dot{M}_0}{\omega P_0 F_0}\frac{p_{0,i+1}}{p_{0,i}^2 - p_{0,i+1}^2}\hat{\underline{p}}_{1,i+1} - \frac{RT\dot{M}_0}{\omega P_0 F_0}\frac{p_{0,i-1}}{p_{0,i-1}^2 - p_{0,i}^2}\hat{\underline{p}}_{1,i-1} - jp_{0,i}\hat{\underline{u}}_{1,i}$$

$$= \left(jkp_{0,i}\left(u_{0,i} - \frac{\Omega}{\omega}\right) + \frac{RT\dot{M}_0}{\omega P_0 F_0}\right)\hat{\underline{h}}_{1,i}$$

$$-\frac{RT\dot{M}_0}{\omega P_0 F_0}\hat{\underline{h}}_{1,i+1} + \frac{RT\dot{M}_0}{\omega P_0 F_0}\left(\frac{\hat{\underline{\mu}}_{1,i}}{\mu_{0,i}} - \frac{\hat{\underline{\mu}}_{1,i+1}}{\mu_{0,i+1}}\right) \tag{15}$$

- Complex momentum equation:

$$-\frac{RT\dot{M}_0}{\omega P_0 F_0}\frac{p_{0,i-1}\left(u_{0,i-1} - u_{0,i}\right)}{p_{0,i-1}^2 - p_{0,i}^2}\hat{\underline{p}}_{1,i-1}$$

$$+\left(\frac{RT\dot{M}_0}{\omega P_0 F_0}\frac{p_{0,i}\left(u_{0,i-1} - u_{0,i}\right)}{p_{0,i-1}^2 - p_{0,i}^2} - j\frac{RT}{R_R^2\omega^2}\right.$$

$$\left.-\frac{1}{2}\frac{R_R}{F_0}\left(U_{Ri}n_{Ri}\mathrm{Re}_{Ri}^{m_{Ri}}\left(u_{0,i} - 1\right)^2\mathrm{sign}(\omega(1 - u_{0,i})) - U_{Si}n_{Si}\mathrm{Re}_{Si}^{m_{Si}}u_{0,i}^2\mathrm{sign}(\omega u_{0,i})\right)\right)\hat{\underline{p}}_{1,i}$$

$$-\frac{RT\dot{M}_0}{\omega P_0 F_0}\hat{\underline{u}}_{1,i-1}$$

$$+\left(jp_{0,i}\frac{\Omega}{\omega} - jp_{0,i}u_{0,i} + \frac{RT\dot{M}_0}{\omega P_0 F_0} - \frac{R_R}{F_0}p_{0,i}\left(U_{Ri}n_{Ri}\mathrm{Re}_{Ri}^{m_{Ri}}\left(u_{0,i} - 1\right)\mathrm{sign}(\omega(1 - u_{0,i}))\right.\right.$$

$$\left.\left.-U_{Si}n_{Si}\mathrm{Re}_{Si}^{m_{Si}}u_{0,i}\mathrm{sign}(\omega u_{0,i})\right)\right)\hat{\underline{u}}_{1,i}$$

$$= \left(\frac{RT\dot{M}_0}{\omega P_0 F_0}\left(u_{0,i-1} - u_{0,i}\right)\right)\hat{\underline{h}}_{1,i} + \frac{RT\dot{M}_0}{\omega P_0 F_0}\left(u_{0,i-1} - u_{0,i}\right)\frac{\hat{\underline{\mu}}_{1,i}}{\mu_{0,i}} \tag{16}$$

- With equations (15), (16) a system equation for all cavities is formed and solved by linear equation algorithms. As a result the values of the complex amplitude $\hat{\underline{p}}_{1,i}$ and $\hat{\underline{u}}_{1,i}$ ($\hat{\underline{p}}_{1,i} = \hat{p}_{1,ic} + j\hat{p}_{1,is}$) are found.

- The flow force for the seal (see equation (1)) is found by integrating the first–order pressure perturbation along and around the shaft of the rotor. For the i-th cavity it is

$$F_{y,i}(t) = -P_0 R_R \epsilon \pi \int_0^L \left(\hat{p}_{1,ic}\cos\Omega t - \hat{p}_{1,is}\sin\Omega t\right) dx$$

$$F_{z,i}(t) = -P_0 R_R \epsilon \pi L \left(\hat{p}_{1,i,c}\sin\Omega t + \hat{p}_{1,i,s}\cos\Omega t\right) \tag{17}$$

- Introducing a rotating coordinate–system (see figure 14) the rotating forces are

$$F_{r,i} = -P_0 R_R \epsilon \pi L \hat{p}_{1,i,c} \qquad F_\varphi = -P_0 R_R \epsilon \pi L \sum_{i=1}^N \hat{p}_{1,i,s} \tag{18}$$
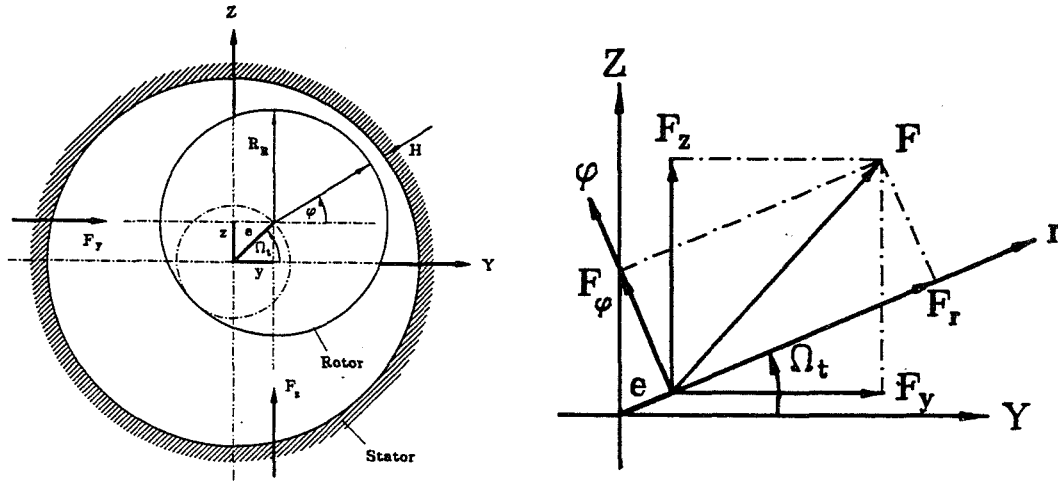
Figure 14: Harmonic seal motion and transformation of the coordinate system

- With the assumed orbit about the centered position the structure of the matrices of equation (1) becomes

$$c_{yy} = c_{zz}, \ c_{yz} = -c_{yz}; \qquad d_{yy} = d_{zz}, \ d_{yz} = -d_{yz}; \quad \ldots \tag{19}$$

- The searched coefficients can be found by a least square fitting for different frequencies of Ω:

$$F_r = \epsilon C_r \left(c_{yy} + d_{yz}\Omega - m_{yy}\Omega^2 \right)$$

$$F_\varphi = -\epsilon C_r \left(c_{yz} - d_{yy}\Omega - m_{yz}\Omega^2 \right) \tag{20}$$

7 Comparison of the Results

Comparisons of theoretical and experimental results of the exciting cross–coupled stiffness coefficient c_{yz} respectively spring coefficients $\overline{K_Q^*}$ are made for the staggered labyrinth, configuration M4. The correlation is as follows:

$$\overline{K_Q^*} = -\frac{c_{yz}C_R}{\Delta p_{st}R_R mL} \tag{21}$$

The results are presented for $\overline{K_Q^*}$ as a function of the flow characteristic E_0^*. The friction parameters (see equation (6)) for the evaluations are set to

$n_{Ri} = 0,079 \qquad m_{Ri} = -0,25 \qquad n_{Si} = 0,15 \qquad m_{Si} = -0,25.$

The other input data like flow coefficient μ_i and boundary conditions are derived from experimental results, see figure 3.

The results are in good agreement with the spring coefficients $\overline{K_Q^*}$ (see figure 15).
Furthermore, an identification algorithm is currently under development. Its aim is to determine the friction factors $n_{R;Si}$ and $m_{R;Si}$ for each cavity based on the zeroth–order solution for the circumferential velocity (see quation (10)) of the staggered labyrinth . The first results (see figure 23) confirm the assumptions of this bulk–flow-theory, equations (9), (11).
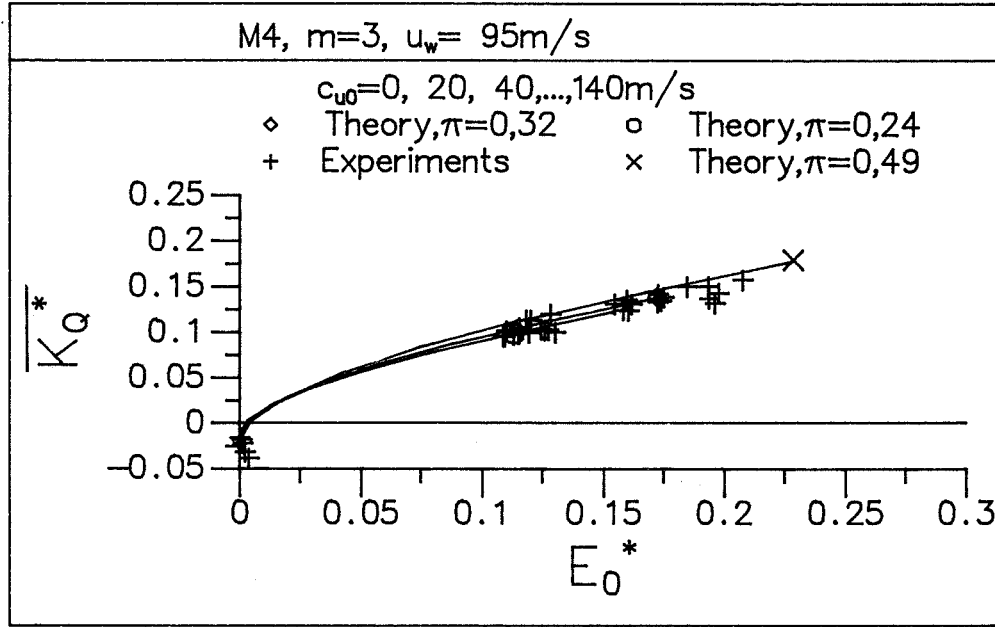
Figure 15: Comparison of theory and experiment

8   Conclusions

Experimental results have been presented for stiffness coefficients and leakage flow of different types of labyrinth geometries, such as grooved, interlocking and convergent stepped labyrinths. The influence of rotor speed, pressure ratio, inlet swirl and labyrinth geometry on the coefficients has been investigated.

The results of this study support the following conclusions:

- The cross force and restoring force are linear to eccentricity. Thus, the force–motion equation (1) is confirmed experimentally.

- The inlet swirl has the greatest influence on the cross–coupled stiffness coefficient $\overline{K_Q^*}$.

- The relationship between $\overline{K_Q^*}$ and the flow characteristic E_0^* depends on the test parameters.

- The cross force in each cavity depends on the change of circumferential velocity from cavity to cavity.

- The restoring force shows an alternating behaviour along the seal. Thus, the total restoring force is nearly zero.

- The results of the presented analysis are in good agreement with the experimental results. The experiments verify the assumptions of the analysis.

References

[1] Benckert,H.: Strömungsbedingte Federkennwerte in Labyrinthdichtungen. Diss. Univ. Stuttgart, 1980

[2] Benckert,H.,Wachter,J.: Flow Induced Spring Coefficients of Labyrinth Seals for Applications in Rotordynamic. NASA Conference Publication 2133, Rotordynamic Instability Problems in High-Performance Turbomachinery 1980

[3] Childs,D.W., Scharrer J.K.: Experimental Rotordynamic Coefficient Results for Teeth-on-Rotor and Teeth-on-Stator Labyrinth Gas Seals. Trans. ASME (Journal of Engineering for Gas Turbines and Power) Vol. 108 (1986) S.599-604

[4] Leong, Y.M.M.S. ,Brown,R.D.:Experimental Investigations of Lateral Forces Induced by Flow Through Model Labyrinth Glands. NASA Conference Publication 2338, Rotordynamic Instability Problems in High-Performance Turbomachinery 1984

[5] Rajakumar,C., Sisto,F.: Experimental Investigations of Rotor Whirl Excitation Forces Induced by Labyrinth Seal Flow. 11th ASME Biennial Conference on Mechanical Vibration and Noise 1987, S.263-272

[6] Serkov,S.A.: Die Bestimmung von aerodynamischen Kräften in Turbinendichtungen zur Erhöhung der Grenzstabilität. Wärme, Vol.92, 1986, No.4-5, S.79-83

[7] Lomakin,A.A.: Calculation of Critical Speed and Securing of the Dynamic Stability of the Rotor of Hydraulic High Pressure Machines with References to Forces Arising in Seal Gaps. Energomashino-strojenie 4, 1958, H. 4, S. 1-5

[8] Iwatsubo,T.,Matooka,N., Kawai,R.: Flow Induced Force of Labyrinth Seal. NASA Conference Publication 2250, Rotordynamic Instability Problems in High-Performance Turbomachinery 1982

[9] Childs,D.W.,Scharrer,J.K.: An Iwatsubo-Based Solution for Labyrinth Seals: Comparison to Experimental Results. Trans. ASME (Journal of Engineering for Gas Turbines and Power) Vol.108 (1986) S.325-331

[10] Childs,D.W., Chang-Ho Kim: Analysis and Testing for Rotordynamic Coefficients of Turbulent Annular Seals with Different, Directionally Homogeneous Surface-Roughness Treatment for Rotor and Stator Elements. NASA Conference Publication 2338, Rotordynamic Instability Problems in High-Performance Turbomachinery 1984
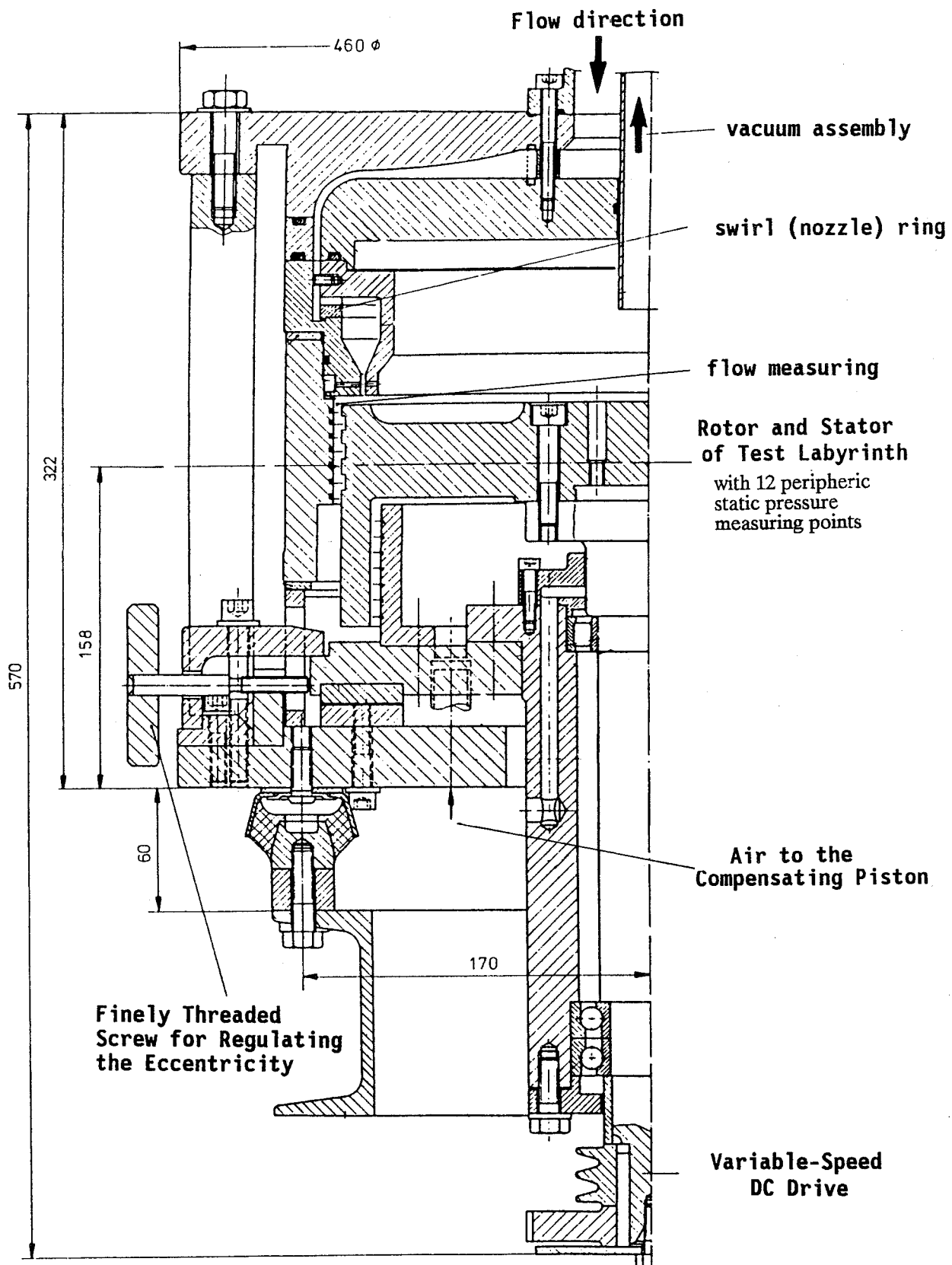
Figure 16: Testing facility of labyrinths
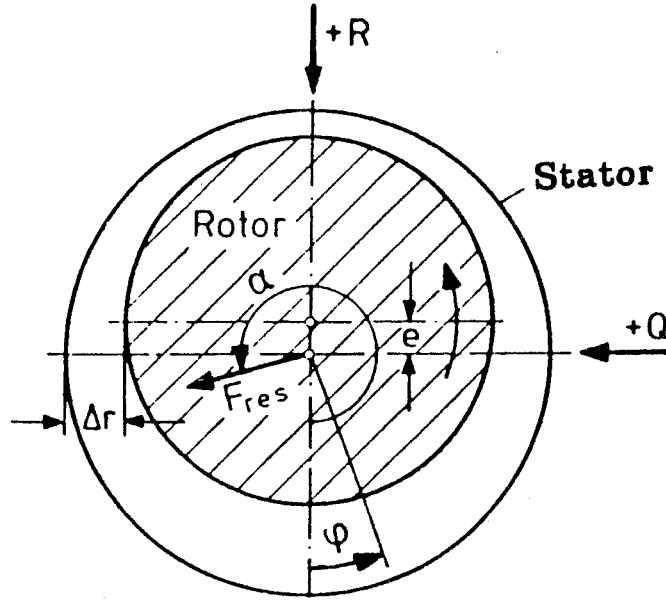
Inlet state	:	(p_0, T_0, c_{u0})		
Static pressure difference	:	Δp_{st}	$=$	$p_0 - p_a$
Relative pressure per cavity $\quad$ i	:	$p_i^*(\varphi)$	$=$	$(p_i(\varphi) - p_a)/\Delta p_{st}$
Flow characteristic	:	E_0^*	$=$	$\frac{1}{2}\rho_0 c_{u0}^2/\Delta p_{st}$
Reference force	:	F_B	$=$	$\Delta p_{st} r m t$

Cross force

$$Q_i^* \quad = \quad \int_0^{2\pi} p_i^*(\varphi)\sin\varphi\, d\varphi$$

$$Q_{ges}^* \quad = \quad \sum_{i=1}^{m} Q_i^*$$

$$\overline{Q^*} \quad = \quad Q_{ges}^*/m$$

Dimensionless spring coefficient :

$$\overline{K_Q^*}(E_0^*) \quad = \quad d\overline{Q^*}/d\frac{e}{\Delta r}$$

Dimensioned spring coefficient :

$$K_Q \quad = \quad \overline{K_Q^*}\, \frac{F_B}{\Delta r}$$

Resulting labyrinth load :

$$Q \quad = \quad \overline{K_Q^*}\, \epsilon\, F_B$$

Restoring force

$$R_i^* \quad = \quad \int_0^{2\pi} p_i^*(\varphi)\cos\varphi\, d\varphi$$

$$R_{ges}^* \quad = \quad \sum_{i=1}^{m} R_i^*$$

$$\overline{R^*} \quad = \quad R_{ges}^*/m$$

(labyrinth mean value)

$$\overline{K_R^*}(E_0^*) \quad = \quad d\overline{R^*}/d\epsilon$$

$$K_Q \quad = \quad \overline{K_Q^*}\, \frac{F_B}{\Delta r}$$
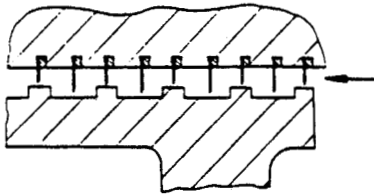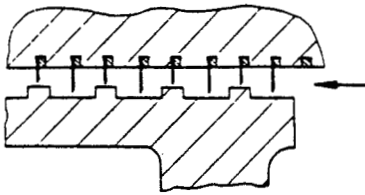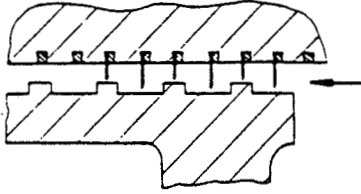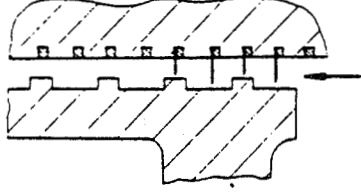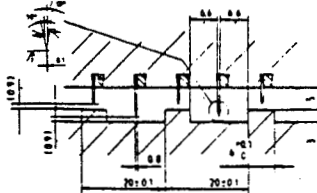
$$R \quad = \quad \overline{K_R^*}\, \epsilon\, F_B$$

Figure 17: Definitions of test data analysis

128

M-Staggered-Labyrinth

Nr.	Typ	
1		Number of cavities m=8 Inlet region: tooth on inflow
2		Number of cavities m=7 Inlet region: groove on inflow
3		m=5
4		$\phi\ D_s$ = 315 mm $\Delta\ r_N$ = 0,91mm $\phi\ D_{RK}$ = 299 mm $\Delta\ r_K$ = 0,91mm $\phi\ D_{RN}$ = 305 mm m = 3

A-Full-Labyrinth
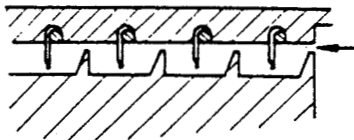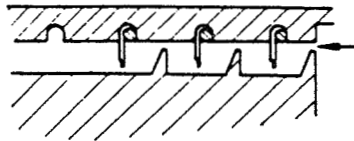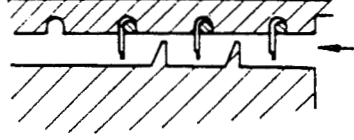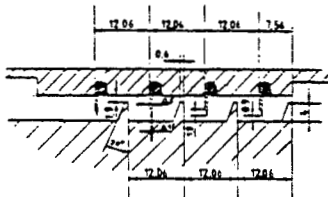
Nr.	Typ	
1		Number of cavities m=7 Inlet region: tooth on inflow
2		Number of cavities m=5 Inlet region: tooth on inflow
3		Number of cavities m=4 Inlet region: groove on inflow
4		$\phi\ D_s$ = 311,77 mm $\phi\ D_{h2}$ = 307,9 mm $\phi\ D_{h1}$ = 301,8 mm $\phi\ D_R$ = 299,88 mm $\Delta\ r_N$ = 1,9 mm $\Delta\ r_K$ = 0,98 mm

Figure 18: M-staggered and A-full-labyrinth
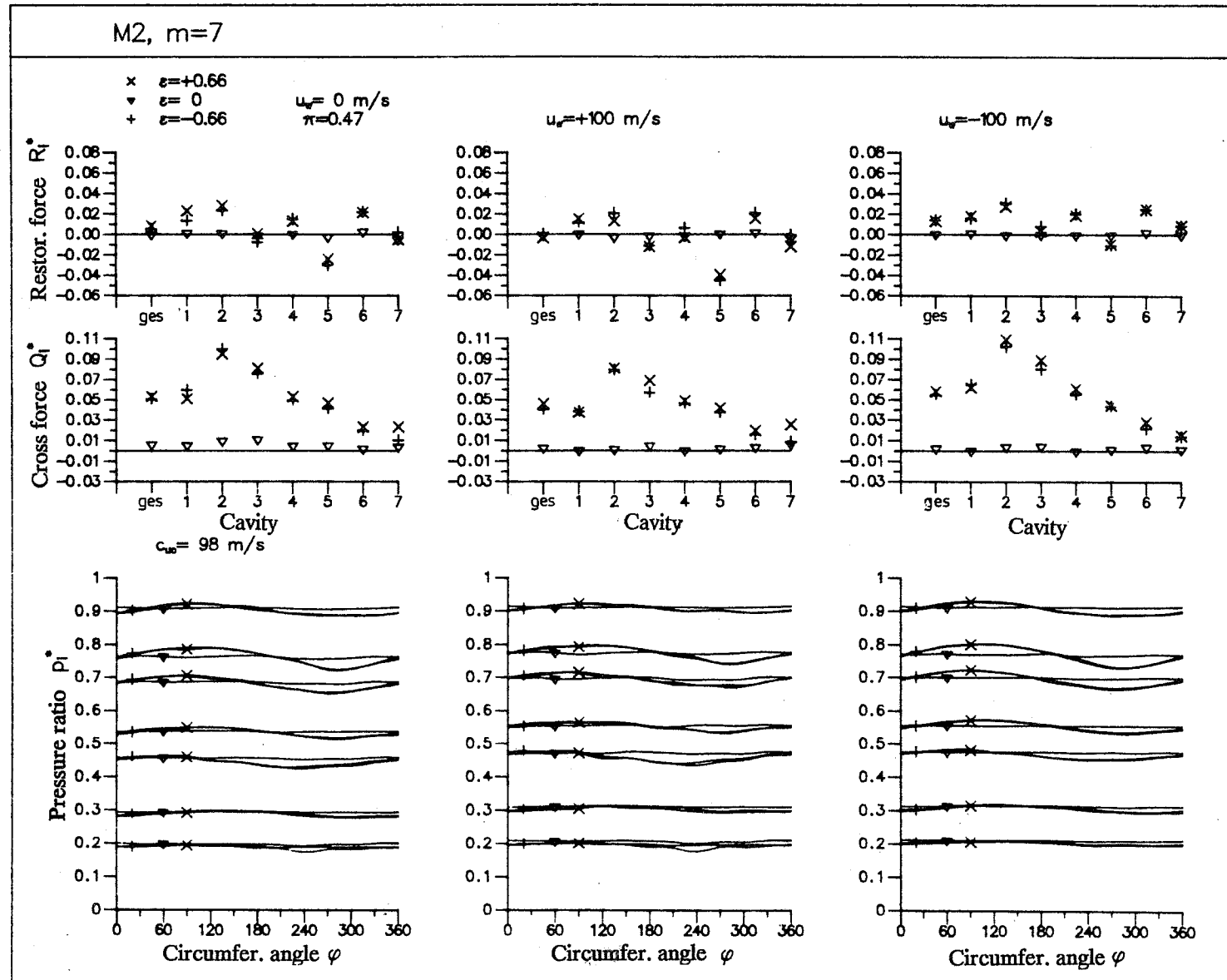
Figure 19: Characteristic of $p_i^*(\varphi)$, Q_i^*, R_i^* of M2

130

Figure 20: Characteristic of $p_i^*(\varphi)$, Q_i^*, R_i^* of A1

131
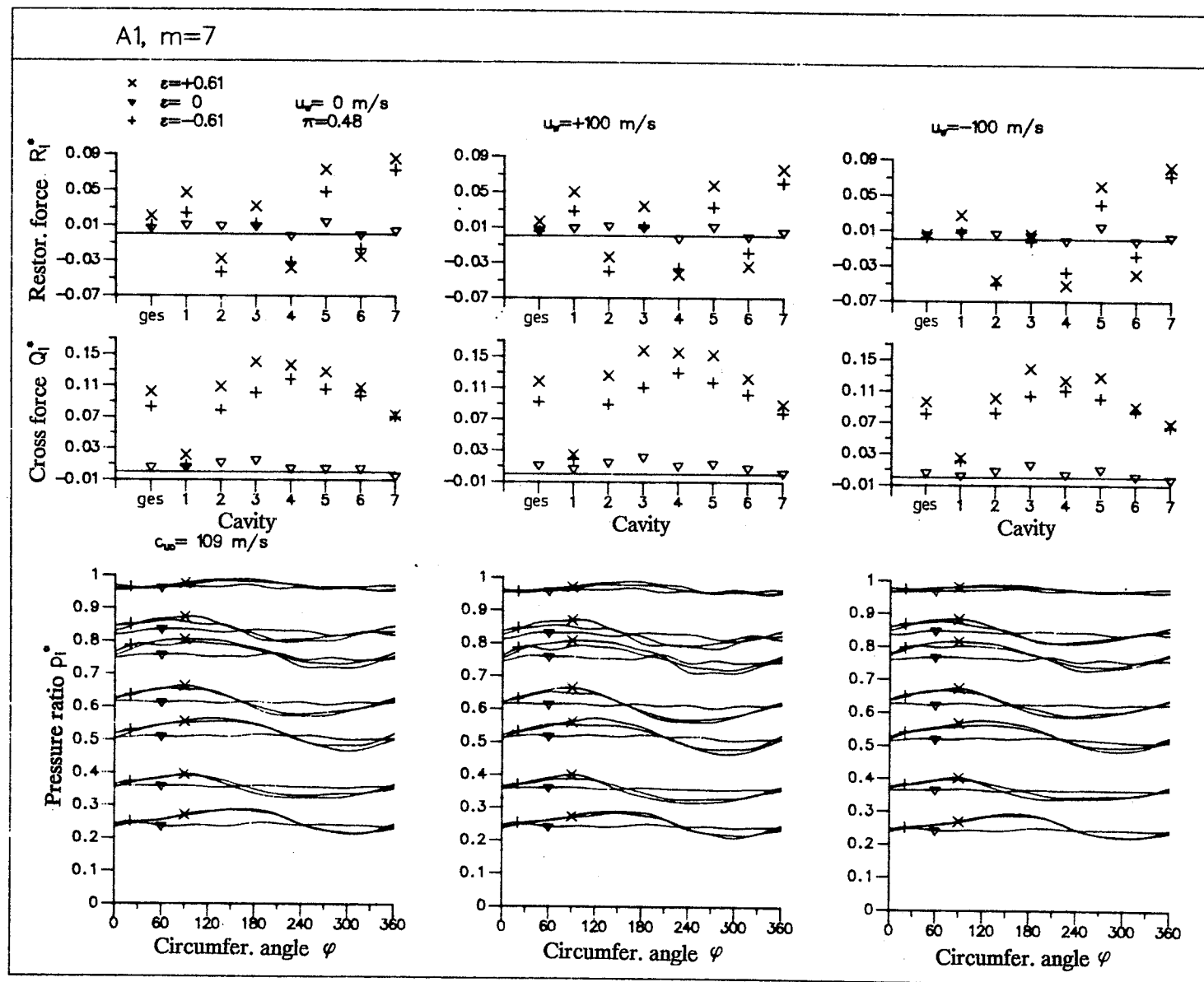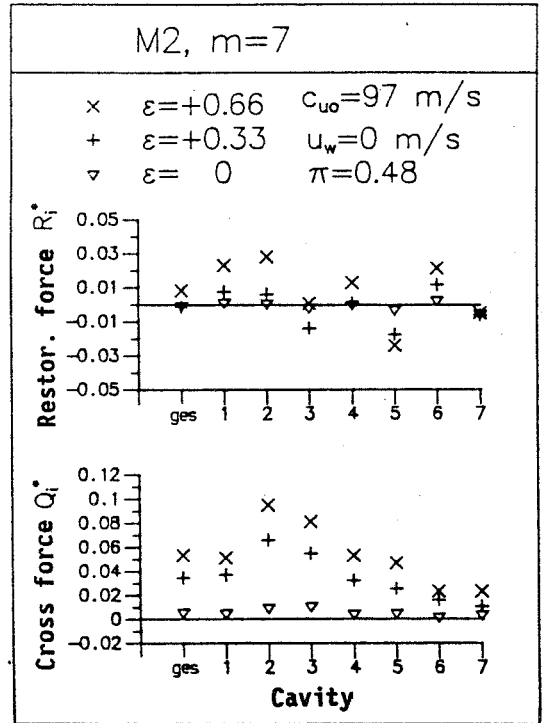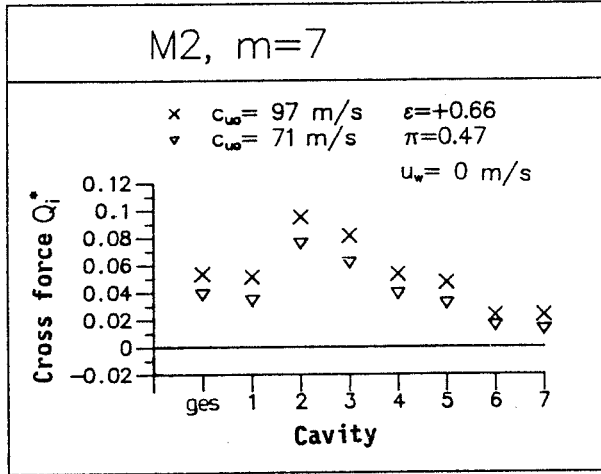
Figure 21: Q_i^* versus c_{u0}, ϵ of M2
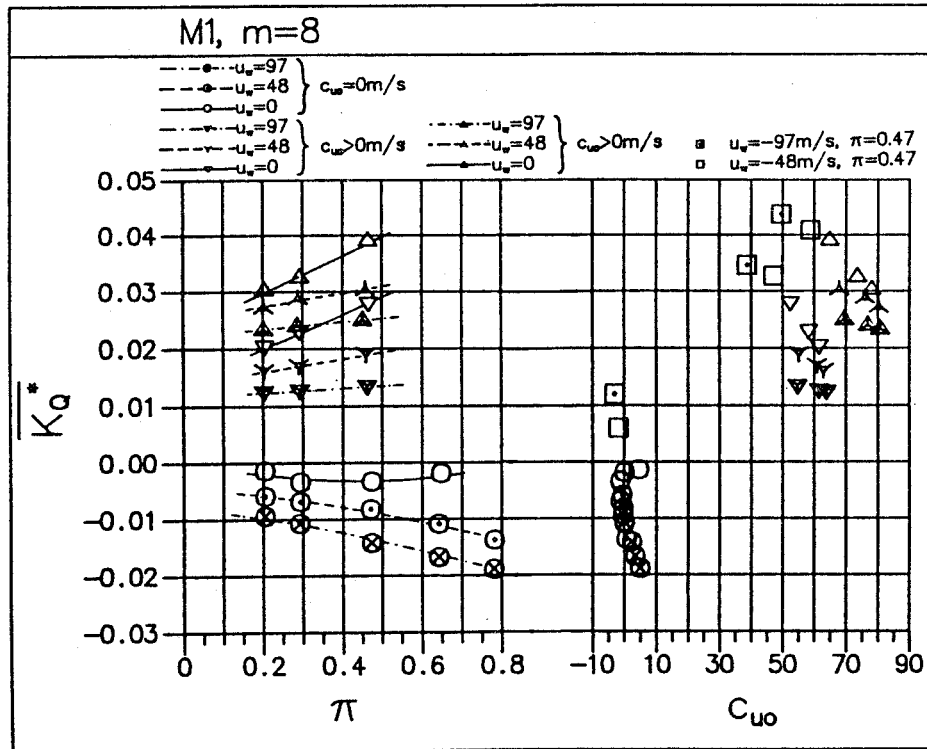
Figure 22: Characteristic field $\overline{K_Q^*}$ of M1
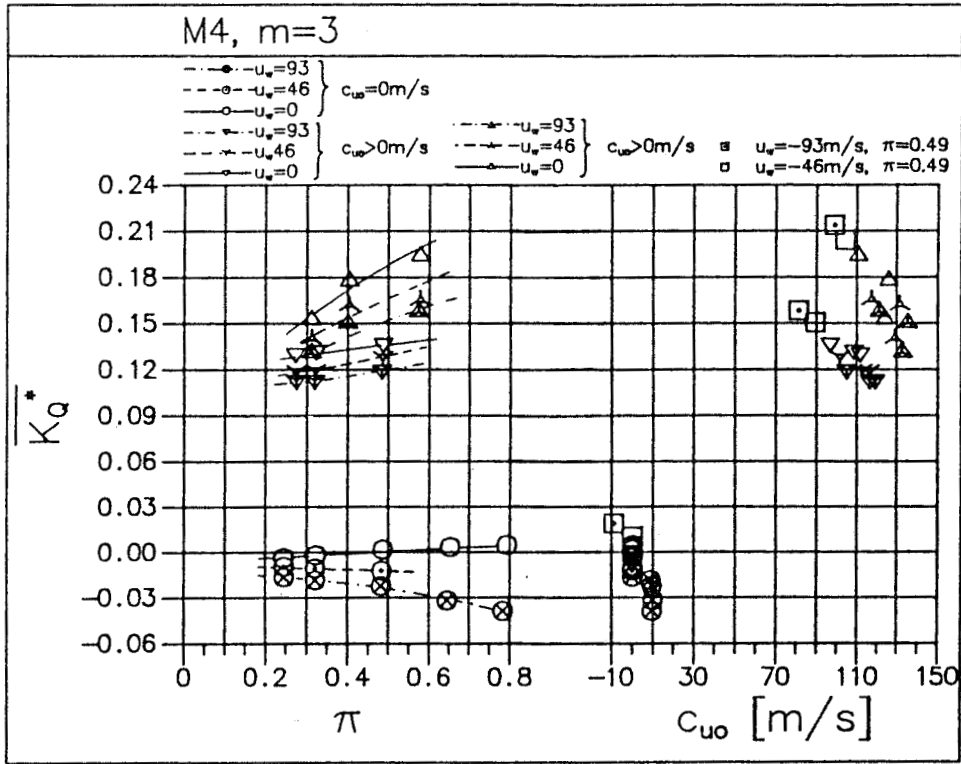
Figure 23: Characteristic field $\overline{K_Q^*}$ of M4
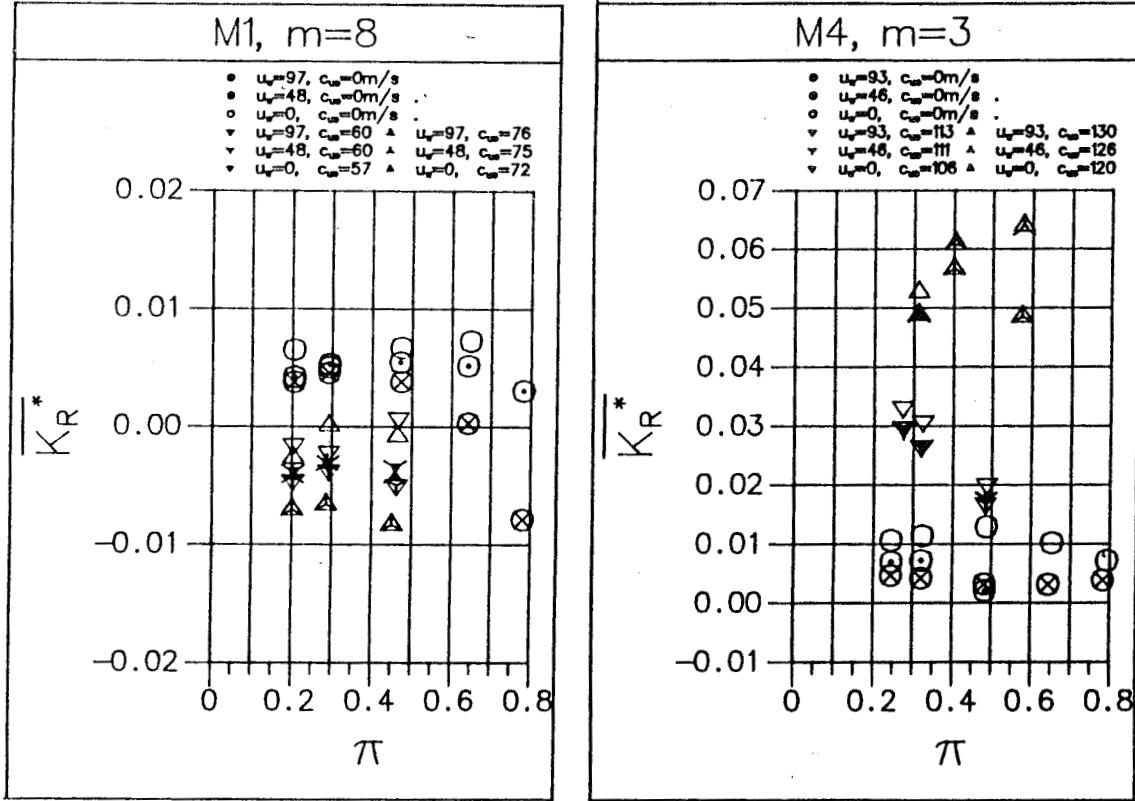
Figure 24: Characteristic field $\overline{K_R^*}$ of M1 and M4
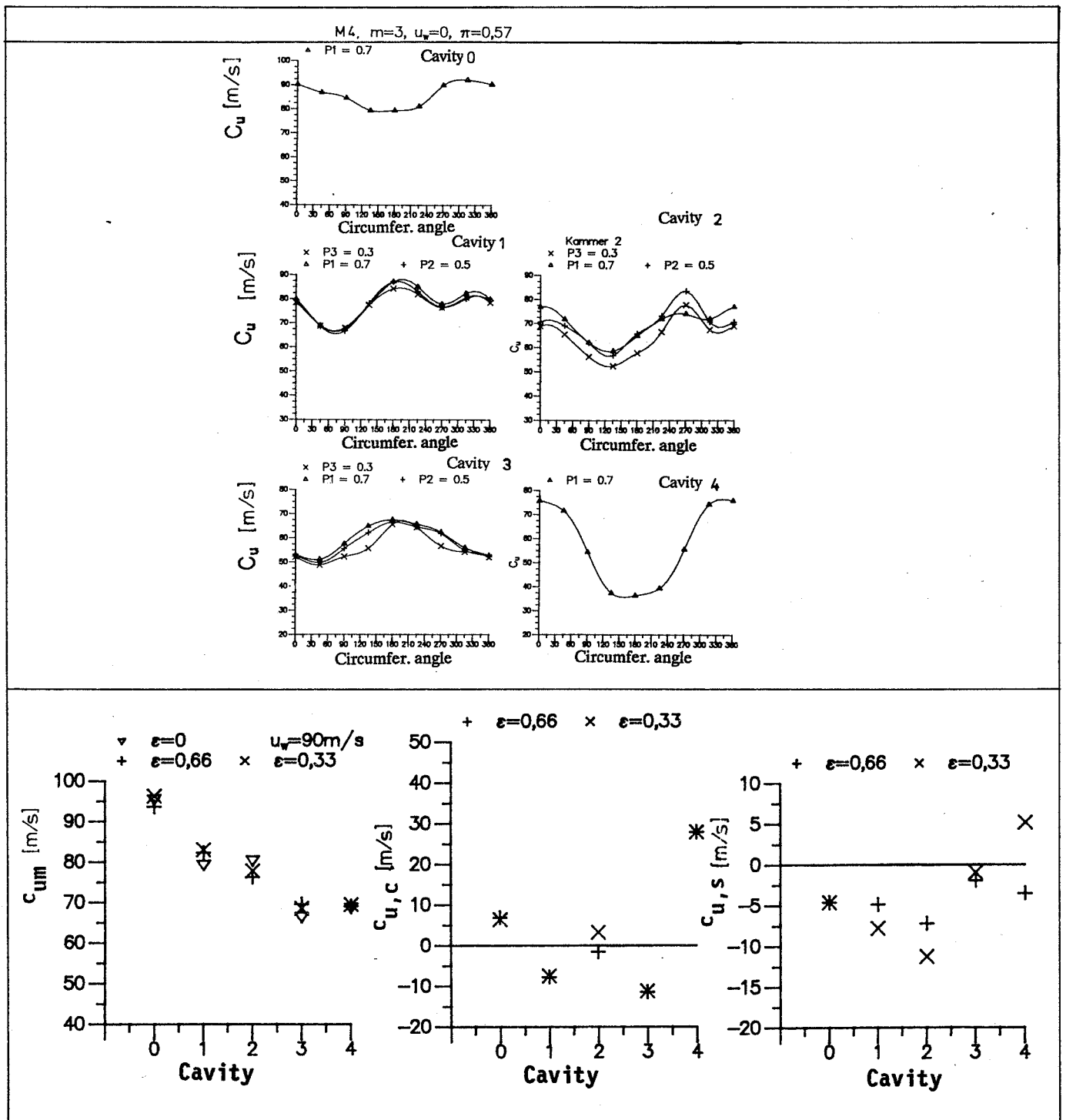
Figure 25: Circumferential velocity c_u versus cavity i and peripheral angle φ of M4

STATIC AND DYNAMIC PRESSURE DISTRIBUTIONS IN A
SHORT LABYRINTH SEAL

K.T. Millsaps and M. Martinez-Sanchez
Massachusetts Institute of Technology
Gas Turbine Laboratory
Cambridge, Massachusetts 02139, U.S.A.

1. Introduction

Although important progress has been made in the last few years on the understanding of labyrinth seal fluid mechanics, and in particular, on the generation of side forces by such seals, there is still a need for quantitative data and theoretical correlation on several points, particularly with respect to dynamic effects. The widely quoted test results of Benckert and Wachter [1] covered adequately a range of flow and geometric parameters, but only for static offsets. Good correlation to linearized theory has been achieved for these data [2], [3]. Several authors have reported measurements of a dynamic nature [4], [5], [6], [7], but their tests lacked control over important parameters, making comparison to theory difficult. Scharrer and Childs [8] presented the first set of dynamic data in which inlet swirl as well as vibratory frequency were adequately controlled, although a single shaking frequency was used. They reported directly measured force data for three 16-tooth rotors with different sealing clearances, and obtained good correlation to theory on the effect of some of the parameters.

No data of this type have been obtained for short (one or two cavity) seals, of interest in aerospace applications, including turbine tip shrouds. There are also no published data (static or dynamic) on labyrinth seals with honeycomb land.

As part of an investigation into turbine blade-tip destabilizing forces, sponsored by NASA Marshall SFC, we have built a seals test rig in which spin rate, circular whirl rate, direction and amplitude of inlet swirl angle, and eccentricity can all be controlled over wide ranges, and measurements can be made at gap Reynolds numbers up to about 2×10^4 (previous data have been limited to well below 10^4). In this paper, we describe this facility and present preliminary data for a one-cavity labyrinth seal with a flat, stator-mounted land.

2. Test Facility

Tests are conducted using air in an open loop with atmospheric discharge. The overall layout is shown in Fig. 1. The test rotor is forced to execute a circular whirl motion while spinning. This is accomplished by mounting the rotor shaft bearings eccentrically on an inner rotating assembly (Fig. 2), which is driven by a belt independently of the in-line rotation drive. The rotating parts are shown in Fig. 3. The test seal is mounted on the left-hand rotor (28 cm diameter), with seal air flow being from left to right. Pressurized air is also introduced behind this rotor to balance the thrust. The pulley sheaf for the whirl drive can be seen at the right-hand end of the rotating housing. Variable amounts of shaft eccentricity can be introduced by appropriate rotation of eccentric inserts placed between the rotating bearing housing and the outer bearing races (Fig. 4).

Pressurized air is fed from an annular plenum through replaceable swirl vane rings into the pre-seal cavity (Fig. 3). Close spacing of the vanes is used to ensure azimuthal uniformity. The convergence in the vane passage imparts high velocity, and hence high azimuthal momentum, to the inlet flow. Flow swirl angles from zero to about 60° can be generated in this way.

135

The main data obtained are pressure time histories at four points (90° spaced) in the gland. These are acquired by flush-mounted, fast response Kulite XCS-190 transducers, which have a 5 psid range. To increase the response sensitivity, the transducers are referenced to an auxiliary pressure-averaging plenum, which is connected by thin tubes to several points on the gland and is filled with a porous material for damping purposes. In this way, only the necessary pressure non-uniformity component is measured.

Rotor displacements are measured to within ±0.1 mil by two orthogonally mounted Bently Nevada CSN-5 proximeters. Other measurements include flow rate, using a Venturi flow meter, and accelerometer data, mainly for health monitoring purposes. The spin and whirl motors are velocity controllable, in both directions, ±6000 RPM for spin and ±3000 RPM for whirl.

The transducer data are digitized at up to 10 kHz by a 12-bit, 32-channel Lecroy A/D converter, and then stored in a computer disc. 256 whirl orbits are acquired and phase-lock averaged in each test, using synchronizing signals derived from two photocell-photodiode pairs in combination with a chopper wheel. This gives 32 averaged samples per whirl orbit from each transducer. Fitting a cosine curve to these data allows calculation of both components of the pressure force acting on the rotor, and rotating in space at the whirl frequency. In principle, any one of the four transducers would suffice for this; the others provide redundancy and cross-checking. A typical trace of raw voltage vs. angular location in the whirl cycle for one of the pressure channels is shown in Fig. 5. Most of the noise is effectively removed by the averaging procedure as shown in Fig. 6.

The approximate range of parameters that can be covered with this facility is shown in Fig. 7 for a seal with 10 mm cavity length, as used in this study. The left-hand boundary is a line of Reynolds number (based on gap and gap flow velocity) equal to 10^4. This is not, however, a hard limit and, as noted, many experimenters have worked below it. For rocket turbopump applications, however, we do wish to operate above this range to avoid complications with the transition regime of the discharge coefficient. The right-hand boundary is a value of order unity for the parameter K, defined as $K = \ell$ tan6°/δ (ℓ = gland length, δ = mean gap). For too small values of K, the exit gap is larger than the jet width from the first gap, and excessive carry-over is expected. Clearly, use of a longer seal will allow correspondingly wider gap sizes, hence higher Reynolds numbers for a given pressure ratio; lengths up to about 1.8 cm can be easily accommodated.

The upper boundary in Fig. 7 corresponds to choked exit flow. Again, this is not a hard limit, but we wish to restrict attention to the subsonic regime of interest for shroud seals in low pressure ratio turbopump turbines.

3. Experimental Results

The range of parameters used in the tests reported here is listed in Table 1. Figures 8 and 9 show the direct and cross-forces calculated from the measured pressure distributions, using the gland length times the seal perimeter as the effective area for integration. The data in Figs. 8 and 9 are for zero rotor spin. The forces are presented vs. whirl speed (positive in the pre-swirl direction) and pre-swirl vane angle. For the direct forces (Fig. 8), positive sign indicates a force in the direction opposite that of the rotor displacement. For the cross-forces (Fig. 9), positive sign indicates a force tending to drive forward whirl, i.e. in the pre-swirl direction. Data are presented for inlet swirl angles of 0°, 15°, and 30°. For zero inlet swirl, the direct force is almost independent of whirl frequency as is predicted by theory. The direct force decreases with inlet swirl.

The cross-force increases with inlet swirl and decreases with whirl speed. Figure 10 shows cross-force vs. whirl RPM with no inlet swirl or shaft rotation for three different inlet pressures (mass

flow rates). The forces increase with flow rate. Figure 11 shows the same cross-force but now normalized by the ratio of flow rate to design flow. Notice that the data are collapsed to a single curve. This also works quite well for the direct forces. The reason for this is that the magnitude of the pressure wave scales with mass flow but the relative phase (the angle between the minimum whirling gap and the maximum pressure) is virtually independent of flow for a given whirl speed. This is the case for zero inlet swirl. However, when inlet swirl exists, the theory suggests that the flow normalized forces should be plotted vs. a reduced whirl speed if they are to effectively collapse. One possible whirl parameter is $\Omega \cdot R_s / V_i$, where Ω is the whirl speed (rads/sec), R_s is the seal radius, and V_i is the inlet swirl velocity.

Once cross-force vs. whirl is available, the cross-stiffness and direct damping coefficients are readily obtained. A least squares linear curve fit is used to obtain the zero-frequency crossing. This is the cross-stiffness K_{xy}. Figure 12 shows K_{xy} vs. inlet swirl angle for several different seal rotation speeds. In general, it is seen that rotation in the direction of pre-swirl tends to reduce the cross-stiffness, while rotation in the direction opposite that of swirl tends to increase the zero-frequency force. The direct damping, C_{xx}, is the slope of the cross-force vs. whirl curve fit line. Figure 13 shows the direct damping vs. inlet swirl angle for several different seal rotation speeds. The damping generally increases with swirl inlet velocity. The spin rate is seen to have a substantial impact on both stiffness and damping coefficient.

4. Discussion

The data were compared to theoretical predictions based on a lumped parameter Kostyuk-Iwatsubo type model [2], [9]. Briefly, the continuity and momentum equations for the single gland labyrinth are first solved for the centered position. These steady state parameters are used in a linear perturbation expansion. When harmonic behavior is assumed, a system of linear algebraic equations in pressure and velocity perturbations are obtained (see Ref. [9] for details). These are solved to yield the pressure amplitude and phase relative to the minimum whirling gap. The actual computations were done in non-dimensional form. The dimensionless parameters which introduce the most uncertainty are the flow coefficients μ_1 and μ_2 for the first and second knife, respectively. In general, μ_2 is greater than μ_1 due to the kinetic energy carry-over. Let the effective flow area divergence be defined by

$$\alpha = \frac{\mu_2 \delta_2^*}{\mu_1 \delta_1^*}$$

(1)

For $\alpha = 1$, theory indicates zero direct force (for zero preswirl, spin, and whirl). It is clear, however, from Fig. 8, that a significant direct force does exist for this case. One possible explanation for this is the large sensitivity of direct forces to small departures of α from unity. In fact, the value of α required to explain the data can be extracted from the theoretical [9] direct force for zero spin, whirl, and swirl:

$$F_d = \pi R_s \ell \frac{\alpha(\alpha-1)}{\left(1+\alpha^2\right)^{3/2}} \frac{P_i^2 - P_e^2}{\sqrt{P_i^2 + \alpha^2 P_e^2}} \frac{r}{\delta^*}$$

(2)

where R_s is the seal radius, ℓ the gland length, P_i and P_e are the inlet and discharge pressures, r is the eccentricity and δ^* the nominal gap. We obtain from Eq. (2) and Fig. 8 the value $\alpha = 1.113$.

137

On the other hand, α has only a very minor effect on the cross-forces according to theory. An equivalent statement is that, as α varies, there are significant effects on the spatial phase angle of the forces, and somewhat less on the force magnitude, while the cross-force component changes little. Thus, our direct data on phase angle can be also used to extract α, and the range is indeed found to be 1.1 to 1.2.

Referring to Figs. 9 and 13, the data for zero inlet swirl and zero spin indicate non-zero damping, C_{xx} (slope of cross-force vs. whirl), although with zero cross-force at zero whirl ($K_{xy} = 0$). The linear theory predicts these features. In particular, the predicted C_{xx} at zero whirl is 17 N sec/m, while the data (Fig. 13) indicate 23 N sec/m.

Figure 14 shows a comparison of the cross-force data to linearized theory for zero spin, 30° inlet swirl. The zero-frequency crossing (K_{xy}) is well predicted, while the data show once again a larger slope (more damping) than theory indicates. The agreement as to K_{xy} is worse for 15° since, as shown in Fig. 9, there is an as yet unexplained non-linearity of cross-force versus swirl. This may be a result of the inlet swirl being significantly different from its design value, a circumstance that needs to be verified.

5. Conclusions

The Labyrinth Seal Test Facility, which has been built to cover a wide range of test conditions not previously obtained, has been completed and is fully operational. Rotordynamic coefficient measurements for a single gland labyrinth seal were made for many different flow rates, whirl speeds, shaft speeds, and inlet swirls. To the authors' knowledge, these are the first such controlled measurements for either a single gland or at a Reynolds number above transition (10^4). There is reasonable agreement between the experimentally obtained data and the simple Kostyuk-Iwatsubo Theory. However, many more comparisons over a wider range of parameters is necessary. The impact of different flow coefficients for the first and second knives on the rotordynamic coefficients has been found. While this effect is dominant for the direct forces, it should also be incorporated into calculations of cross-forces where it has an impact under many conditions.

References

1. Benckert, H. and Wachter, J., "Flow-Induced Coefficients of Labyrinth Seals," NASA CP-2133, May 1980.

2. Lee, O.K., Martinez-Sanchez, M. and Czajkowski, E., "Prediction of Force Coefficients for Labyrinth Seals," NASA CP-2338, 1984, pp. 235-256.

3. Scharrer, J.K. and Childs, D.W., "An Iwatsubo-Based Solution for Labyrinth Seals: A Comparison to Experimental Results," *J. of Gas Turbines and Power*, Vol. 108, April 1986, pp. 325-331.

4. Wright, D.V., "Labyrinth Seal Forces on a Whirling Rotor," *Rotor Dynamic Instability*, Proceedings of the ASME Applied Mech., Bioeng. and Fluids Engineering Conf., Houston, TX, 1983, pp. 19-31.

5. Iwatsubo, T., Matsuoka, N. and Kawai, R., "Flow-Induced Force and Flow Pattern of Labyrinth Seals," NASA CP-2133, 1982, pp. 205-222.

6. Brown, R.D. and Leong, Y.M.M.S., "Experimental Investigation of Lateral Forces Induced by Flow Through Model Labyrinth Glands," NASA CP-2338, 1984, pp. 187-210.

7. Hisa, S., "Steam Excited Vibrations in Rotor-Bearing Systems," *Proc. of the International Conf. on Rotordynamics*, Tokyo, Japan, Sept. 1986, pp. 635-641.

8. Childs, D.W. and Scharrer, J.K., "Theory vs. Experiment for the Rotordynamic Coefficients of Labyrinth Gas Seals: Part II-A, Comparison to Experiment," *ASME Rotating Machinery Dynamics*, Vol. 1, 1987, pp. 427-434.

9. Millsaps, K.T., "Analysis of Aero-Elastic Forces in Labyrinth Seals and the Design of an Experimental Facility to Measure Them," Master's Thesis, Department of Aeronautics and Astronautics, MIT, 1987.

TABLE 1
OPERATING PARAMETERS FOR THIS WORK

Seal Radius	150 mm
Number of Seal Glands	1
Gland Length	10 mm
Dam Height	5 mm
Type of Land	Flat, on stator
Mean Seal Gap	0.813 mm
Seal Eccentricity	0.185 mm
Inlet Total Pressure	1.48 to 1.69 atm
Discharge Pressure	1 atm
Air Temperature	280°K
Inlet Swirl Angle	0°, 15°, 30°
Whirl Speed	-2500 to +2500 RPM
Spinning Rate	-4200 to +4200 RPM
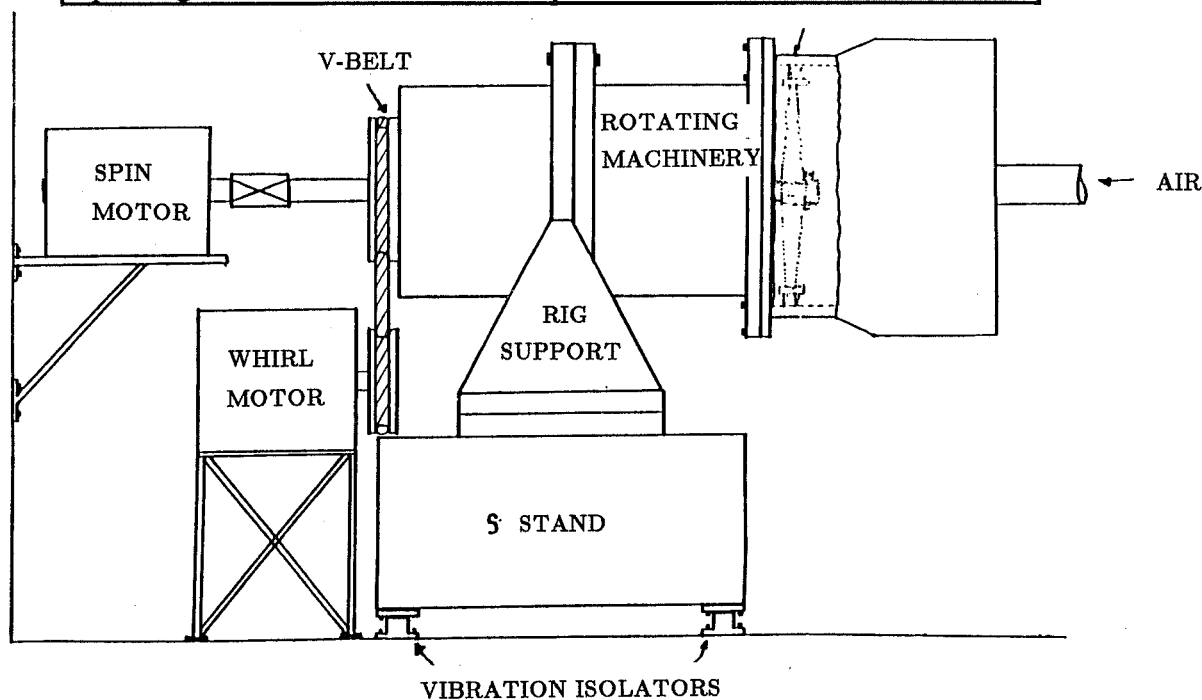
Figure 1. Side view of labyrinth seal test facility.
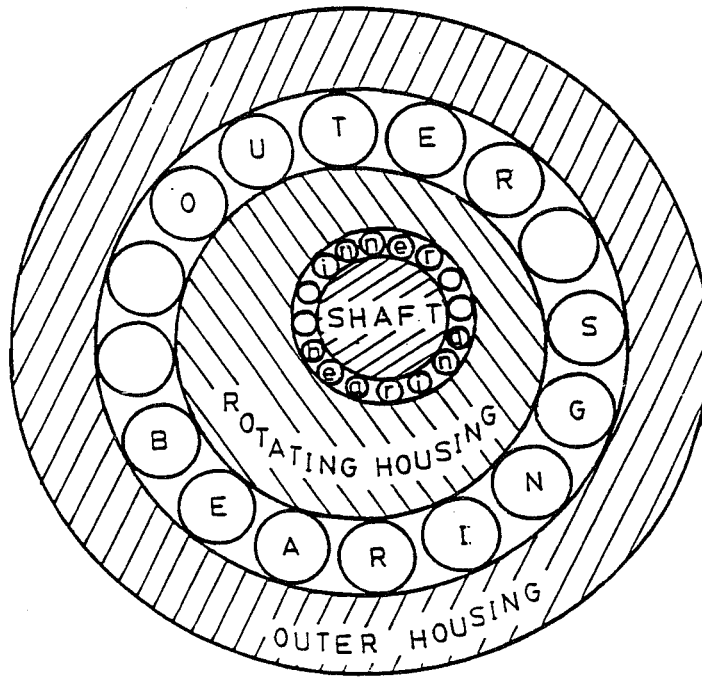
Figure 2. Mechanism for producing spinning/whirling shaft.
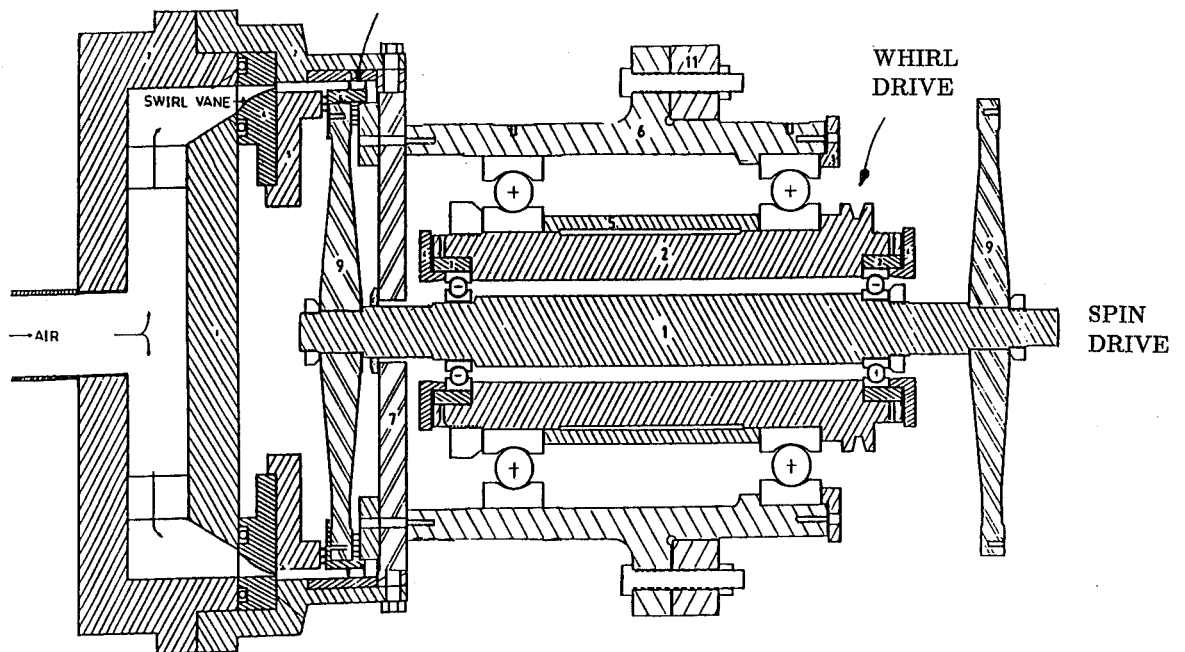
Figure 3. Cross-section of test section along with whirl/spin producing
rotating machinery. The air flow through the apparatus is shown by arrows.
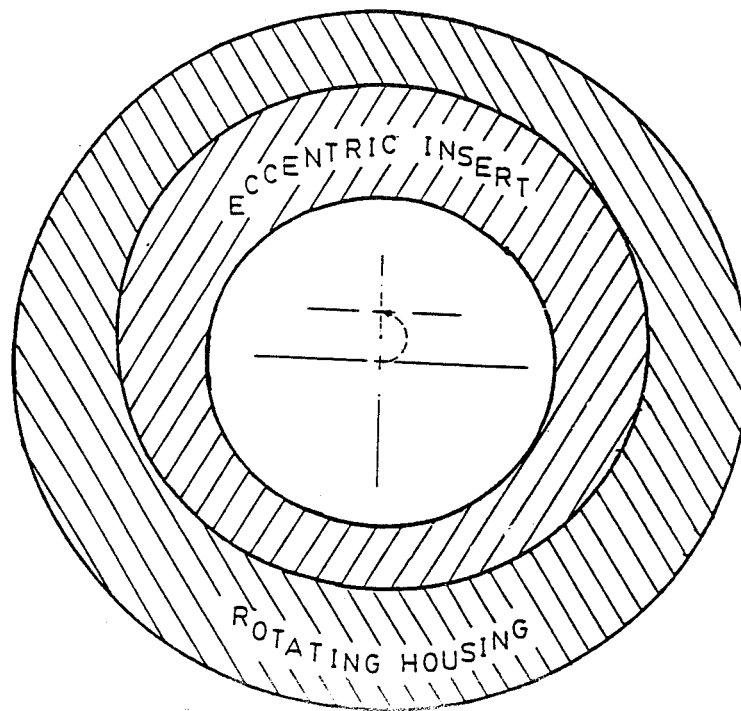
Figure 4. Mechanism for producing variable whirl eccentricity.
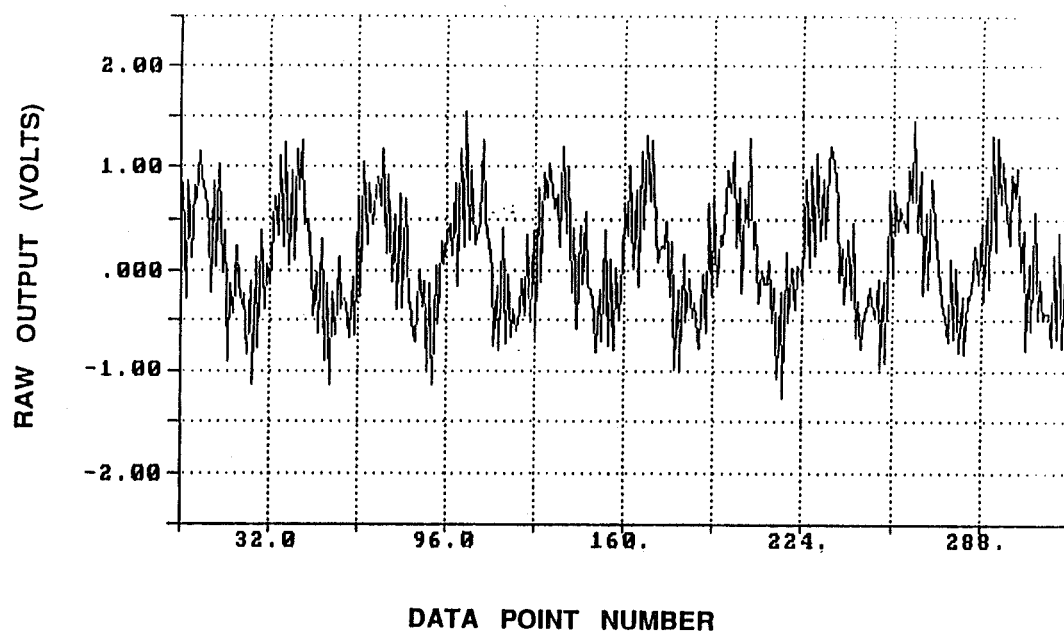
DATA POINT NUMBER

Figure 5. Raw voltage from a Kulite vs. data point number.
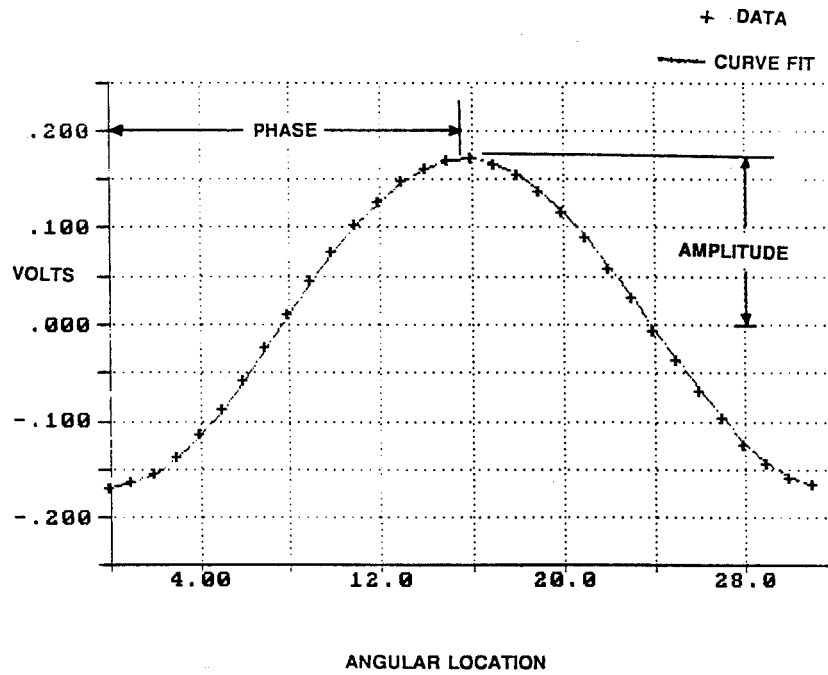
Figure 6. Typical 4 transducer composite phase-locked average pressure data along with least squares curve fit.
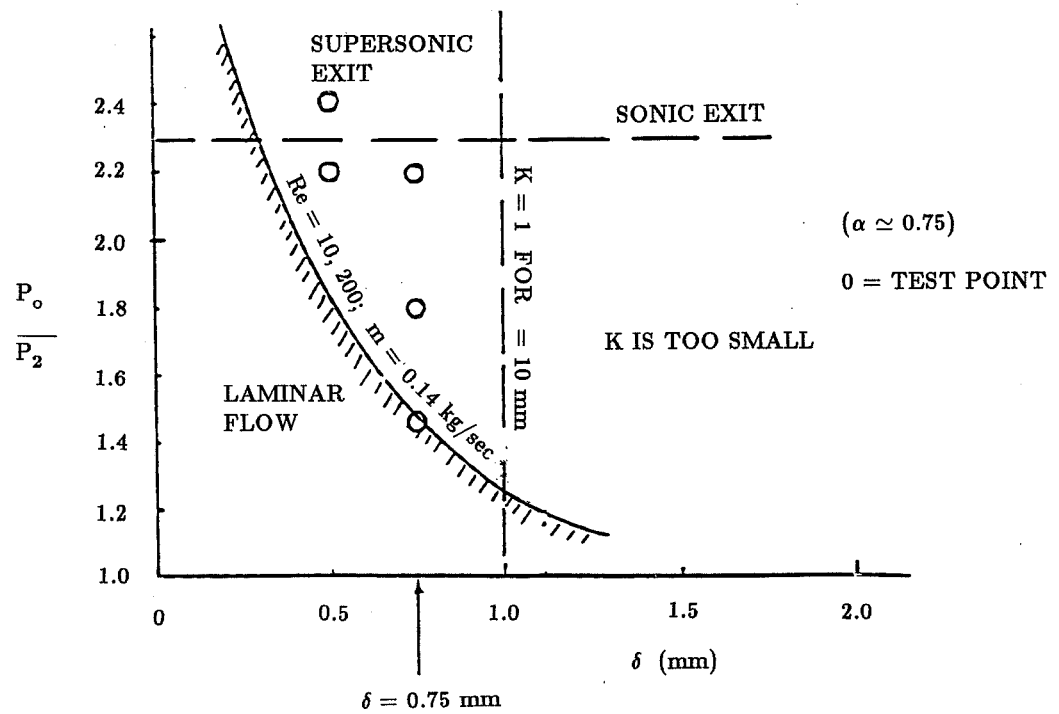
Figure 7. Approximate operational boundaries for test seal with l=10mm.
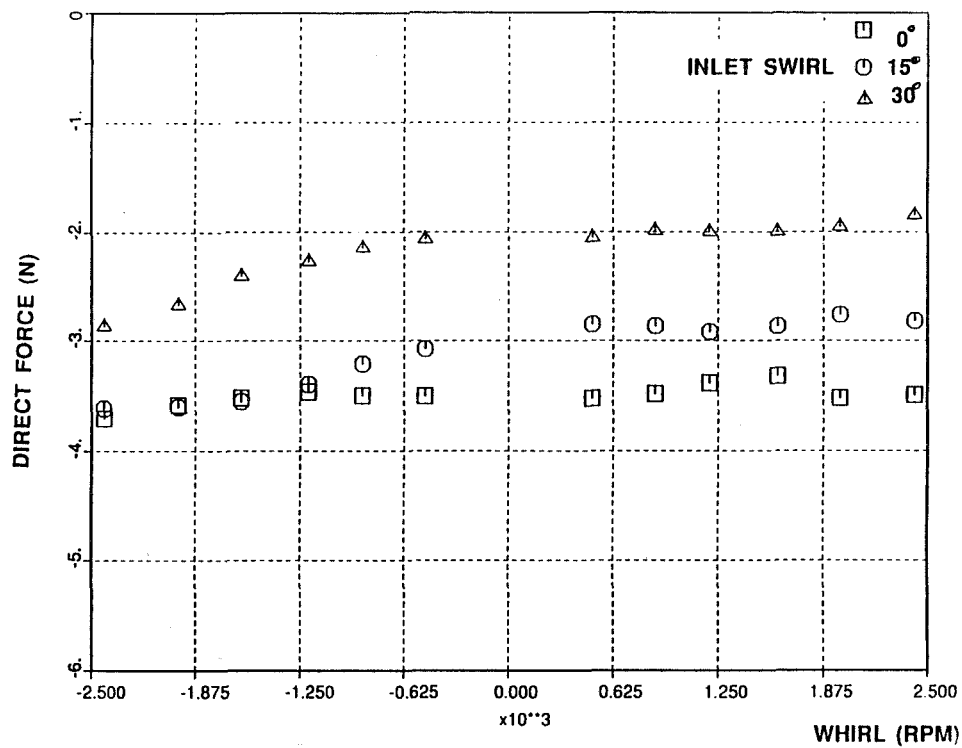
Figure 8.   Direct force vs. whirl RPM for three different values of inlet swirl.
m=0.166 kg/s.
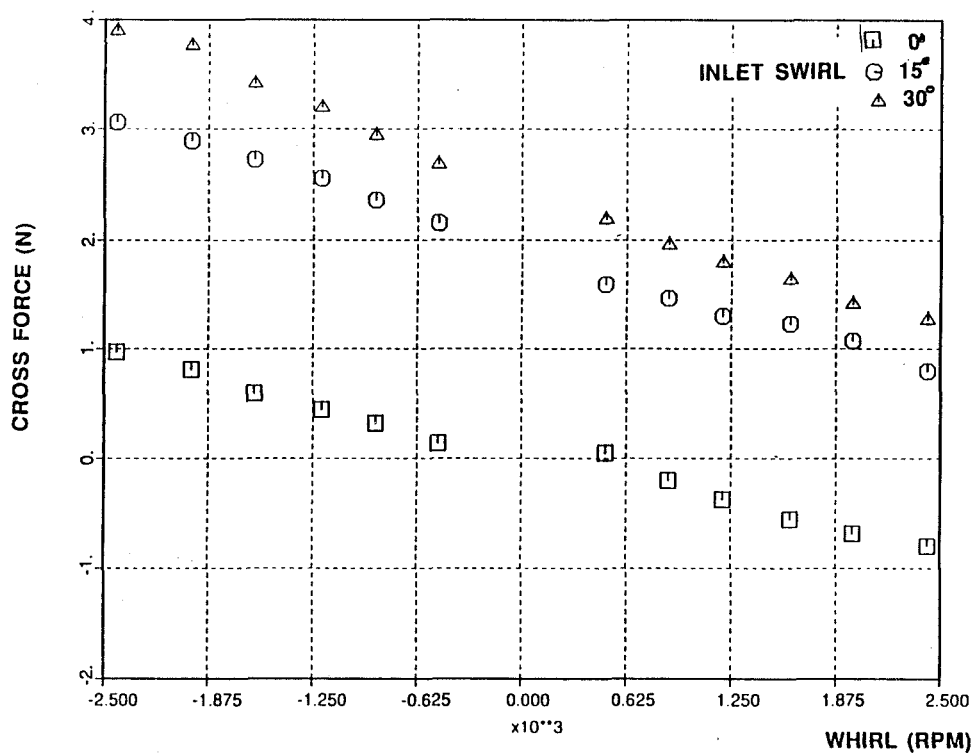
Figure 9.   Cross-force vs. whirl RPM for three different values of inlet swirl.
m=0.166 kg/s.

143
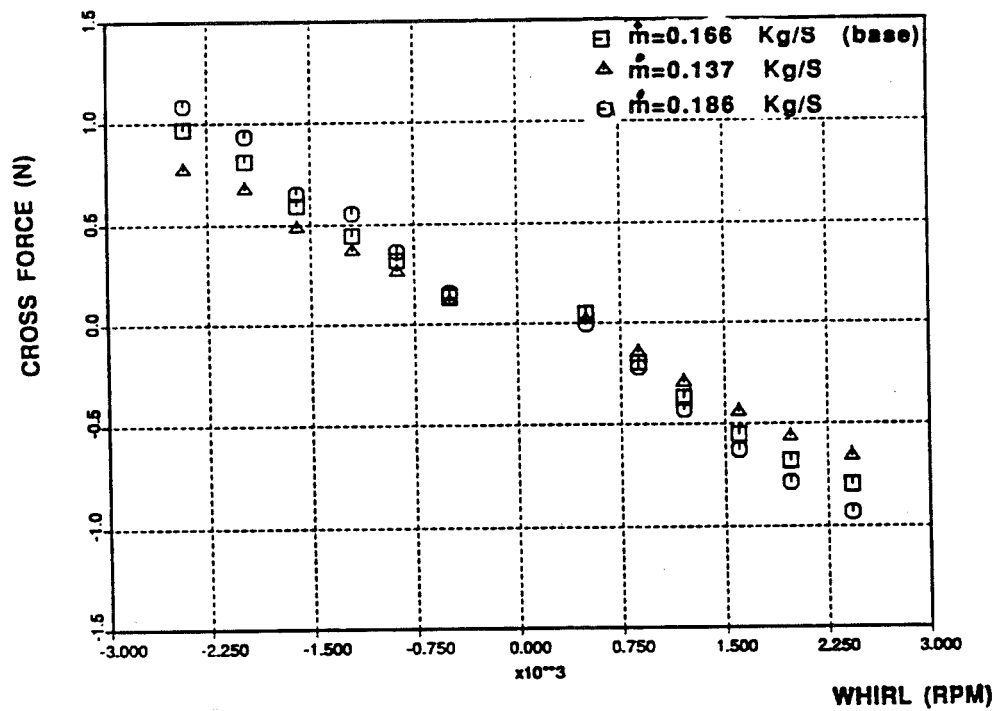
Figure 10. Cross force vs. whirl RPM for three different mass flow rates. All conditions are with no inlet swirl or shaft rotation.
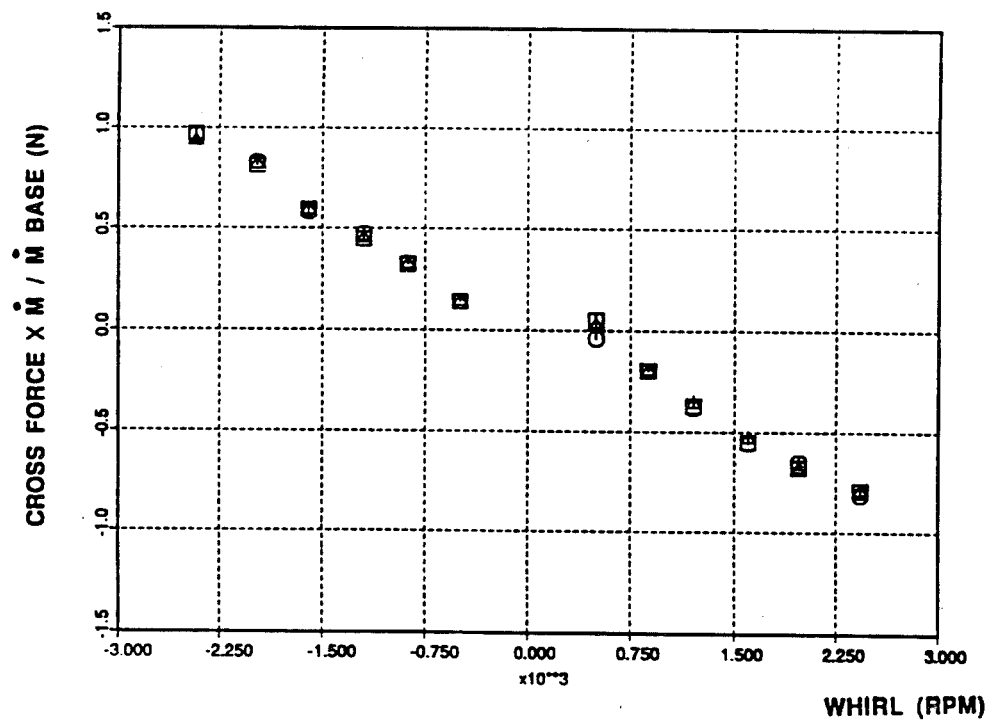
Figure 11. Cross force, normalized by the base mass flow vs whirl RPM. This is the same data as shown above.

144
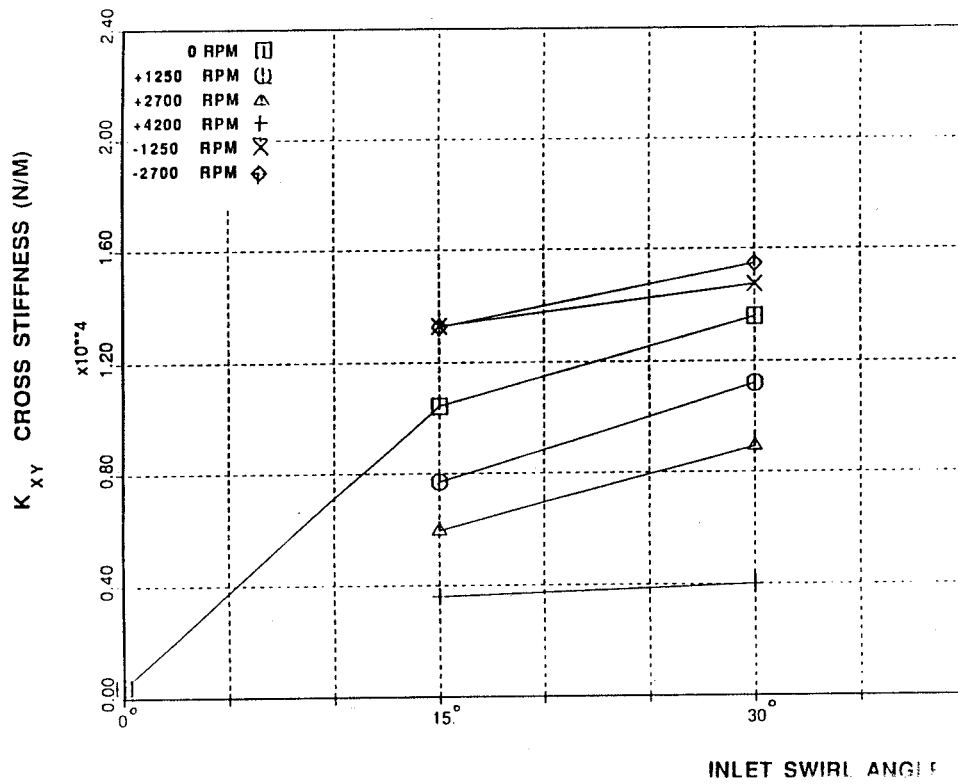
Figure 12. Cross stiffness vs. inlet swirl for six different values of spin.
m=0.166 kg/s.
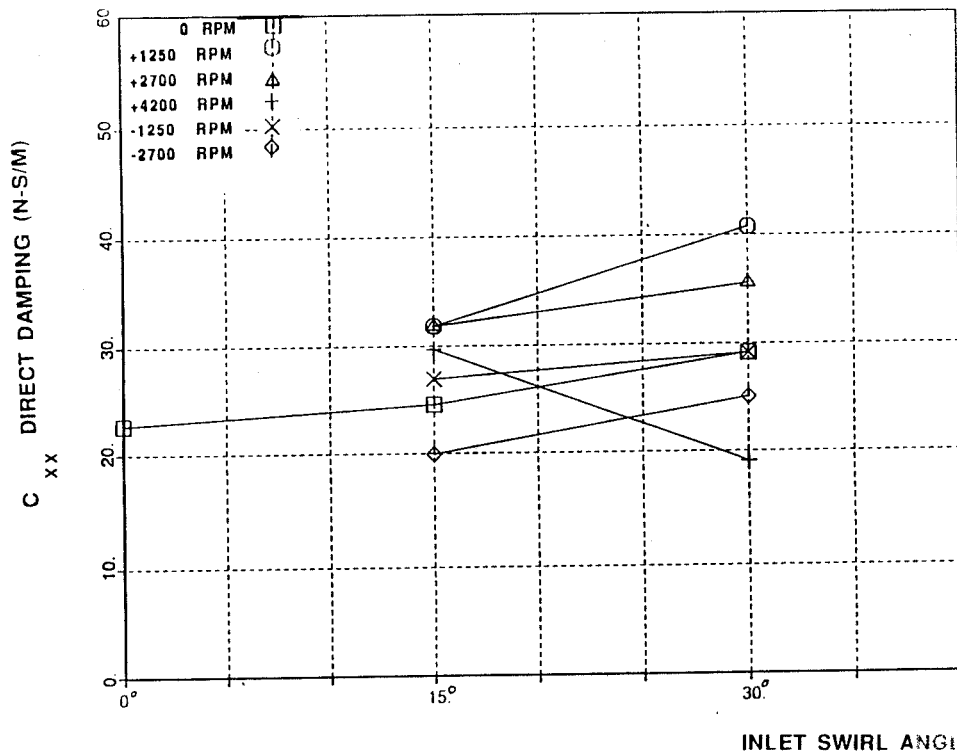
Figure 13. Direct damping vs. inlet swirl for six different values of spin.
m=0.166 kg/s.

145
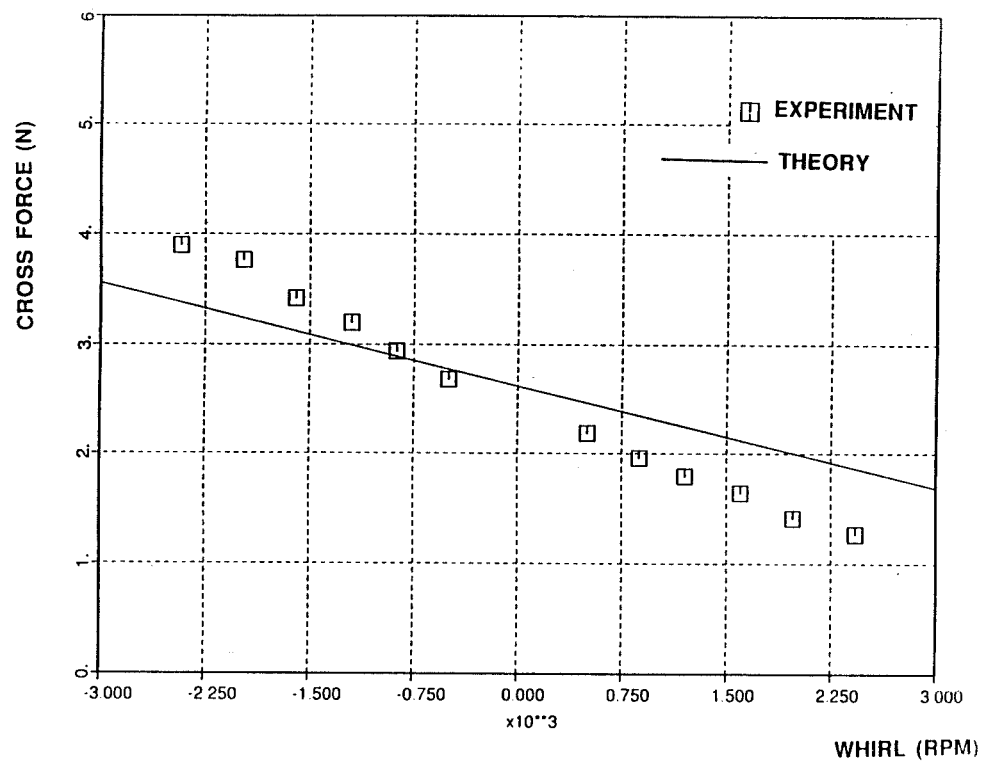
Figure 14. Comparison of experimental data with theory. The inlet swirl for this case is 30 degrees and the mass flow is 0.166 kg/s.

N92-14356

EVALUATION OF ROTORDYNAMIC COEFFICIENTS OF LOOK-THROUGH LABYRINTHS
BY MEANS OF A THREE VOLUME BULK FLOW MODEL

R. Nordmann and P. Weiser
Department of Mechanical Engineering
University of Kaiserslautern
Kaiserslautern, Federal Republic of Germany

To describe the compressible, turbulent flow in a labyrinth seal, a three volume bulk flow model is presented. The conservation equations for mass, momentum and energy are established in every control volume. A perturbation analysis is performed, yielding zeroth order equations for centric rotor position and first order equations describing the flow field for small rotor motions around the seal center. The equations are integrated numerically. From perturbation pressure, the forces on the shaft and the dynamic coefficients are calculated.

NOMENCLATURE

F_1, F_2	Forces on the shaft in x,y direction
u_1, u_2	shaft displacements
K, k	direct and cross-coupled stiffness
D, d	direct and cross-coupled damping
p	pressure
u, v, w	axial, radial and tangential velocity
T	temperature
ρ	density
z, r, φ	axial, radial and tangential coordinate
t	time
L	length of labyrinth chamber
B	depth of labyrinth chamber
R	shaft radius

C_r	nominal clearance
S	seal fin thickness
L_t	total seal length
e	eccentricity ratio, perturbation parameter
r_O	radius of circular shaft orbit
h	seal clearance
ω	rotational frequency of the shaft
Ω	precession frequency of the shaft
p_a	pressure before labyrinth
p_b	pressure behind labyrinth
w_O	swirl
R_g	perfect gas constant
$\varkappa$	specific heat ratio
τ	shear stress
λ	friction factor
Re	Reynolds number
D_H	hydraulic diameter
M	Mach number
k_{rel}	relative surface roughness
ζ_e	entrance loss factor
ζ_I	loss factor at seal fin entrance
μ	laminar viscosity
i	imaginary unit

SUBSCRIPTS

0	zeroth order
1	first order
s	stator
r	rotor
z	axial
φ	circumferential
f	fluid–
cu	chamber, upper wall
cs	chamber, side wall
S	Sine
C	Cosine
e	seal entrance
rel	relative
I, II, III	Indices for the different control volumes

INTRODUCTION

Labyrinth seals, commonly used in turbomachinery to reduce the leakage loss, can have a strong influence on the dynamic behavior of a turbine or a compressor, especially for high performance machines. In some cases, the fluid forces generated in labyrinths caused severe rotor instabilities. Therefore, the design engineer needs information concerning the possible influences that a labyrinth can have on the dynamics of a rotating system.

For mathematical modeling, the seal forces can be described in terms of stiffness and damping parameters, the so-called rotordynamic seal coefficients (see Eq.1).

$$\begin{bmatrix} K & k \\ -k & K \end{bmatrix} \begin{bmatrix} u_1 \\ u_2 \end{bmatrix} + \begin{bmatrix} D & d \\ -d & D \end{bmatrix} \begin{bmatrix} \dot{u}_1 \\ \dot{u}_2 \end{bmatrix} = - \begin{bmatrix} F_1 \\ F_2 \end{bmatrix} \tag{1}$$

These coefficients are input parameters for rotordynamic investigations and have to be determined by fluid mechanics methods. In contrast to WEISER and NORDMANN (1987,1988,1989), where we used Finite-Differencing methods (FDM) to solve the conservation equations in conjunction with a turbulence model, Florjancic developed a more conventional three volume bulk flow method which takes advantage from FDM calculations and reduces the computational effort dramatically. In 1987, KLAUK has already developed a three volume model for the compressible flow in labyrinths, which is extended in WEISER (1989). In this approach, the energy equation and the equation of state for a perfect gas is used in addition to the previously existing model.

MATHEMATICAL MODELING

Many attempts have been made for the calculation of labyrinth coefficients, e.g. see the publications of KOSTYUK(1975), CHILDS(1984) or WYSSMANN(1984). Flow visualization experiments show, that for look-through labyrinths, the flow field can be divided in two characteristic regions: a vortex flow in the seal chamber and a jet flow region beneath the seal strip and the groove.

Therefore, the calculation domain is divided into three control volumes (CV), see Fig.1: one in the seal chamber accounting for the vortex flow and two volumes representing the jet flow beneath chamber and seal fin. Fig.1 also gives an impression of the bulk velocities in the different volumes.
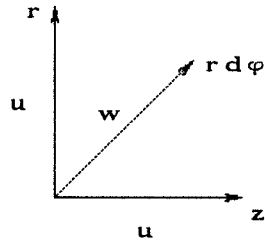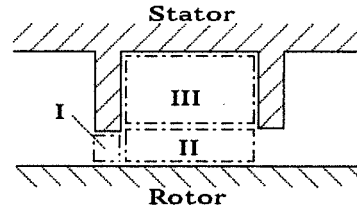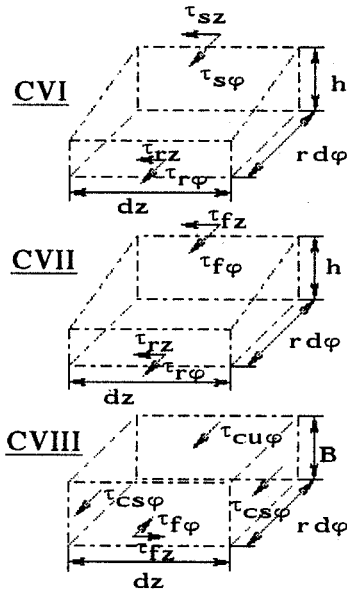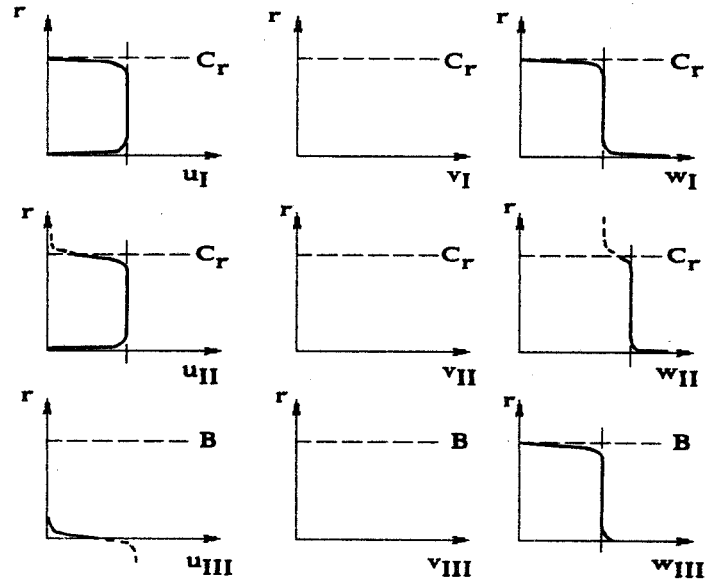
Fig. 1: 3-volume bulk flow model

For mathematical description, we use the momentum, continuity and energy equation in every control volume. Paying attention to the following assumptions:

- compressible medium ($\rho \neq$ const.)
- constant laminar viscosity μ

- modelling of turbulence by wall shear stresses
- no shear stresses within the fluid (exception: jet friction shear stress in the contact region of CV II and CV III)
- no radial shear stresses
- first order radial velocities only in CV II and III

150

we obtain the following set of equations to describe the turbulent, compressible seal flow (equations shown here for teeth-on-stator seal):

CV I:

$$-\frac{\partial p}{\partial z} h - \tau_{sz} - \tau_{rz} = \rho h \left\{ \frac{\partial u}{\partial t} + u \frac{\partial u}{\partial z} + \frac{w}{r} \frac{\partial u}{\partial \varphi} \right\}$$

$$-\frac{1}{r} \frac{\partial p}{\partial \varphi} h - \tau_{s\varphi} - \tau_{r\varphi} = \rho h \left\{ \frac{\partial w}{\partial t} + u \frac{\partial w}{\partial z} + \frac{w}{r} \frac{\partial w}{\partial \varphi} \right\}$$

$$
\begin{aligned}
0 = &\frac{\partial}{\partial t} \left\{ \frac{p}{\varkappa-1} h + \rho h \left(\frac{u^2}{2} + \frac{v^2}{2} + \frac{w^2}{2} \right) \right\} + \\
&\frac{\partial}{\partial z} \left\{ \rho u h \left(\frac{\varkappa}{\varkappa-1} \frac{p}{\rho} + \frac{u^2}{2} + \frac{v^2}{2} + \frac{w^2}{2} \right) \right\} + \\
&\frac{1}{r} \frac{\partial}{\partial \varphi} \left\{ \rho w h \left(\frac{\varkappa}{\varkappa-1} \frac{p}{\rho} + \frac{u^2}{2} + \frac{v^2}{2} + \frac{w^2}{2} \right) \right\} + \\
&\tau_{r\varphi} (w - R \omega)
\end{aligned}
$$

(2)

$$
0 = \frac{\partial}{\partial t} \left(\rho h \right) + \frac{\partial}{\partial z} \left(\rho u h \right) + \frac{1}{r} \frac{\partial}{\partial \varphi} \left(\rho w h \right)
$$

CV II:

$$-\frac{\partial p}{\partial z} h - \tau_{fz} - \tau_{rz} = \rho h \left\{ \frac{\partial u}{\partial t} + u \frac{\partial u}{\partial z} + v \frac{\partial u}{\partial r} + \frac{w}{r} \frac{\partial u}{\partial \varphi} \right\}$$

$$-\frac{1}{r} \frac{\partial p}{\partial \varphi} h - \tau_{f\varphi} - \tau_{r\varphi} = \rho h \left\{ \frac{\partial w}{\partial t} + u \frac{\partial w}{\partial z} + v \frac{\partial w}{\partial r} + \frac{w}{r} \frac{\partial w}{\partial \varphi} \right\}$$

(3)

$$-\frac{\partial p}{\partial r} h = \rho h \left\{ \frac{\partial v}{\partial t} + u \frac{\partial v}{\partial z} + v \frac{\partial v}{\partial r} + \frac{w}{r} \frac{\partial v}{\partial \varphi} \right\}$$

$$
\begin{aligned}
0 = &\frac{\partial}{\partial t} \left\{ \frac{p}{\varkappa-1} h + \rho h \left(\frac{u^2}{2} + \frac{v^2}{2} + \frac{w^2}{2} \right) \right\} + \\
&\frac{\partial}{\partial z} \left\{ \rho u h \left(\frac{\varkappa}{\varkappa-1} \frac{p}{\rho} + \frac{u^2}{2} + \frac{v^2}{2} + \frac{w^2}{2} \right) \right\} + \\
&\frac{1}{r} \frac{\partial}{\partial \varphi} \left\{ \rho w h \left(\frac{\varkappa}{\varkappa-1} \frac{p}{\rho} + \frac{u^2}{2} + \frac{v^2}{2} + \frac{w^2}{2} \right) \right\} + \\
&\frac{\partial}{\partial r} \left\{ \rho v h \left(\frac{\varkappa}{\varkappa-1} \frac{p}{\rho} + \frac{u^2}{2} + \frac{v^2}{2} + \frac{w^2}{2} \right) \right\} + \\
&\tau_{r\varphi} (w - R \omega)
\end{aligned}
$$

151

$$0 = \frac{\partial}{\partial t}\left(\rho\, h\right) + \frac{\partial}{\partial z}\left(\rho\, u\, h\right) +$$
$$\frac{1}{r}\frac{\partial}{\partial \varphi}\left(\rho\, w\, h\right) + \frac{\partial}{\partial r}\left(r\,\rho\, v\, h\right)$$

CV III:

$$-\frac{\partial p}{\partial z}\, B + \tau_{fz} - \tau_{cuz} = 0$$

$$-\frac{1}{r}\frac{\partial p}{\partial \varphi} - \frac{2B}{L}\,\tau_{cs\varphi} - \tau_{cu\varphi} + \tau_{f\varphi} = \rho\, B\left\{\frac{\partial w}{\partial t} + v\frac{\partial w}{\partial r} + \frac{w}{r}\frac{\partial w}{\partial \varphi}\right\} \qquad (4)$$

$$-\frac{\partial p}{\partial r}\, B = \rho\, B\left\{\frac{\partial v}{\partial t} + v\frac{\partial v}{\partial r} + \frac{w}{r}\frac{\partial v}{\partial \varphi}\right\}$$

$$0 = \frac{\partial}{\partial t}\left(\rho\, B\right) + \frac{1}{r}\frac{\partial}{\partial \varphi}\left(\rho\, w\, B\right) + \frac{\partial}{\partial r}\left(r\,\rho\, v\, B\right)$$

As already mentioned, the modeling of flow turbulence is performed using semi-empirical wall shear stress formulations which is the usual way in bulk flow analysis, see for example CHILDS(1984), SCHARRER(1987). The fluid shear stress in the contact region of CV II and CV III is described in the same manner as WYSSMANN(1984) suggested. All shear stress components can be written in a generalized form:

$$\tau_{ij} = \frac{1}{2}\,\rho\,\lambda_i\,V_j\,V_{rel}$$

with

$$\lambda_i = n\left\{1 + \left[C_1 k_{rel} + \frac{C_2}{Re}\right]^m\right\} \qquad (5)$$

and

$$Re = \frac{D_H V_{rel}}{\mu/\rho} \quad .$$

V_{rel} is the relative velocity, V_j the component of the resulting velocity vector which is in the same direction as the shear stress component to be calculated. Index i indicates the appropiate shear stress (s: stator-, r: rotor etc.) and index j gives the direction (z: axial, φ: tangential). With these definitions, we obtain the following relations:

<u>CV</u> <u>I</u>:

Rotor: $V_{rel} = \left((w_I - R\omega)^2 + u_I^2 \right)^{0.5}$ Stator: $V_{rel} = \left(w_I^2 + u_I^2 \right)^{0.5}$

$V_\varphi = w_I - R\omega$ $V_\varphi = w_I$

$V_z = u_I$ $V_z = u_I$

<u>CV</u> <u>II</u>:

Rotor: $V_{rel} = \left((w_{II} - R\omega)^2 + u_{II}^2 \right)^{0.5}$ Stator: $V_{rel} = \left(w_{II}^2 + u_{II}^2 \right)^{0.5}$

$V_\varphi = w_{II} - R\omega$ $V_\varphi = w_{II}$

$V_z = u_{II}$ $V_z = u_{II}$

Jet: $V_{rel} = \left((w_{II} - w_{III})^2 + (u_{II} - u'_{III})^2 \right)^{0.5}$ with $u'_{III} = u_{II}(1 - \beta_v)$

$V_\varphi = w_{II} - w_{III}$

$V_z = u_{II} - u'_{III}$

(6)

<u>CV</u> <u>III</u>:

Jet: $V_{rel} = \left((w_{II} - w_{III})^2 + (u_{II} - u'_{III})^2 \right)^{0.5}$

$V_\varphi = w_{II} - w_{III}$

$V_z = u_{II} - u'_{III}$

Chamber side wall:

$V_{rel} = \left(w_{III}^2 + u''^2_{III} \right)^{0.5}$ with $u''_{III} = u'_{II} \dfrac{B}{L}$

$V_\varphi = w_{III}$

Upper wall in the seal groove:

$V_{rel} = \left(w_{III}^2 + u'^2_{III} \right)^{0.5}$

$V_\varphi = w_{III}$

$V_z = u'_{III}$

The parameters introduced in the shear stress formulations according to MOODY (1944) are

$n = 0.001375$
$m = 0.33333$
$C_1 = 10^4$
$C_2 = 10^6$

For the fluid shear stress, m, C_1 and C_2 are zero; n is set to 3.762 (according to WYSSMANN). To account for the real flow situation in the labyrinth, n is multiplied with the factor β, which depends on geometry and performance data.

BOUNDARY CONDITIONS

For the solution of the differential equations, boundary conditions have to be specified. To calculate the pressure, density and axial velocity at the seal entrance, we use the same relations as NELSON(1985), calculating the entrance values depending on the Mach number:

$$P_e = P_a \left[1 + \frac{(\varkappa - 1)(\zeta_e + 1)}{2} M_e^2 \right]^{\frac{\varkappa}{1-\varkappa}}$$

$$\rho_e = \rho_a \left[1 + \frac{(\varkappa - 1)}{2} M_e^2 \right]\left[1 + \frac{(\varkappa - 1)(\zeta_e + 1)}{2} M_e^2 \right]^{\frac{\varkappa}{1-\varkappa}} \qquad (7)$$

$$T_e = \frac{P_e}{R_g \rho_e} \qquad\qquad M_e = \frac{u_e}{\sqrt{\varkappa R_g T_e}}$$

$$\zeta_e = \sqrt{\frac{5.3}{\lg(Re)}} - 1$$

At the entrance of every seal fin, there occurs a pressure drop due to the acceleration of the fluid. Therefore, the equations 7 are used in a modified form with a constant loss factor ζ_I:

$$P_I = P_{II} \left[1 + \frac{(\varkappa - 1)(\zeta_I + 1)}{2} M_{II}^2 \right]^{\frac{\varkappa}{1-\varkappa}}$$

$$\rho_I = \rho_{II} \left[1 + \frac{(\varkappa - 1)}{2} M_{II}^2 \right] \left[1 + \frac{(\varkappa - 1)(\zeta_I + 1)}{2} M_{II}^2 \right]^{\frac{\varkappa}{1-\varkappa}} \qquad (8)$$

$$T_{II} = \frac{P_{II}}{R_g \, \rho_{II}} \qquad\qquad M_{II} = \frac{u_{II}}{\sqrt{\varkappa \, R_g \, T_{II}}}$$

The model parameters β, β_v and ζ_I are determined with the help of the Finite-Difference programs of NORDMANN and WEISER(1987,1988,1989).

PERTURBATION ANALYSIS

In order to determine the seal forces, we assume that the rotor performs only small motions around the seal center. Then we can describe the dependent variables with a perturbations series, truncated after the linear term:

$$u = u_0 + e\,u_1 \qquad\qquad p = p_0 + e\,p_1 \qquad\qquad h = C_r + e\,h_1$$

$$v = v_0 + e\,v_1 \qquad\qquad T = T_0 + e\,T_1 \qquad\qquad\qquad (9)$$

$$w = w_0 + e\,w_1 \qquad\qquad \rho = \rho_0 + e\,\rho_1$$

As perturbation parameter, we choose the relative eccentricity e, which is the ratio of the shaft eccentricity and the nominal clearance:

$$e = \frac{r_0}{C_r} \qquad\qquad (10)$$

Inserting these expressions into the governing equations, separating terms without e and with e^1 yields two sets of equations: the zeroth order relations describe the flow field for a centric rotor position and the first order terms stand for the flow situation at small eccentric shaft motion.

ELIMINATION OF TEMPORAL AND CIRCUMFERENTIAL DERIVATIVES

While the zeroth order equations depend only on the axial coordinate z, the first order set contains also derivatives with respect to time t, tangential and radial coordinates. Assuming that the shaft moves on a small circular orbit (see Fig. 2), the seal clearance can be written as

$$h = h_0 + e\,h_1 = C_r - X(t)\cos\varphi - Y(t)\sin\varphi \qquad (11)$$
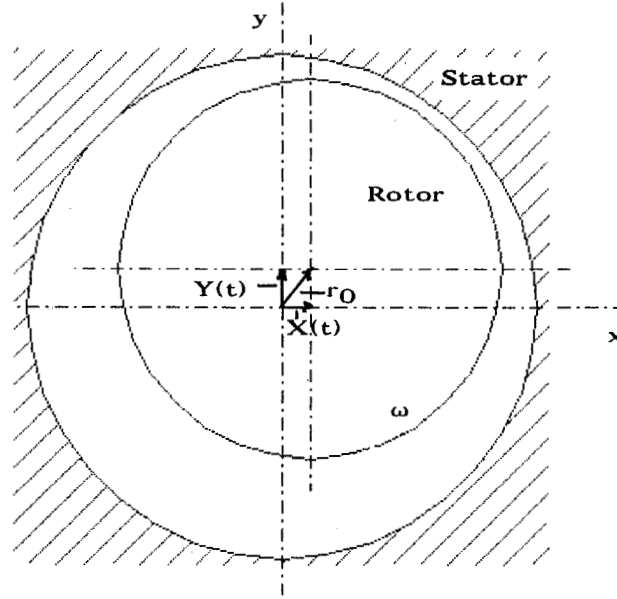
Fig. 2: Circular shaft orbit

For the dependent variables, we prescribe a corresponding solution:

$$u_1 = u_{1_c}\cos\varphi + u_{1_s}\sin\varphi \qquad p_1 = p_{1_c}\cos\varphi + p_{1_s}\sin\varphi$$

$$v_1 = v_{1_c}\cos\varphi + v_{1_s}\sin\varphi \qquad T_1 = T_{1_c}\cos\varphi + T_{1_s}\sin\varphi \qquad (12)$$

$$w_1 = w_{1_c}\cos\varphi + w_{1_s}\sin\varphi \qquad \rho_1 = \rho_{1_c}\cos\varphi + \rho_{1_s}\sin\varphi$$

Now, the circumferential derivatives can be calculated analytically. Separating the equations with respect to sine and cosine terms and introducing complex variables:

$$\overline{u}_1 = u_{1_c} + i\, u_{1_s} \qquad\qquad \overline{p}_1 = p_{1_c} + i\, p_{1_s}$$

$$\overline{v}_1 = v_{1_c} + i\, v_{1_s} \qquad\qquad \overline{T}_1 = T_{1_c} + i\, T_{1_s} \qquad (13)$$

$$\overline{w}_1 = w_{1_c} + i\, w_{1_s} \qquad\qquad \overline{\rho}_1 = \rho_{1_c} + i\, \rho_{1_s}$$

we obtain a now complex system of first order equations.

As already mentioned, we assume a circular shaft orbit, which gives for the time dependence of the clearance

$$\overline{h}_1 = r_0\, e^{i\Omega t} \qquad (14)$$

Again, similar expressions for the variables are established:

$$\overline{u}_1 = \hat{u}_1\, e^{i\Omega t} \qquad \overline{w}_1 = \hat{w}_1\, e^{i\Omega t} \qquad \overline{T}_1 = \hat{T}_1\, e^{i\Omega t}$$

$$\overline{v}_1 = \hat{v}_1\, e^{i\Omega t} \qquad \overline{p}_1 = \hat{p}_1\, e^{i\Omega t} \qquad \overline{\rho}_1 = \hat{\rho}_1\, e^{i\Omega t} \qquad (15)$$

Thereby, the derivatives with respect to time can be expressed analytically. Finally, the radial derivatives in CV II and III are modeled with

$$\frac{\partial \hat{v}_{II}}{\partial r} = \frac{\left(\rho_{III_0}\, \hat{v}_{III_1} - \rho_{II_0}\, \hat{v}_{II_1} \right)}{\rho_{II_0}\, C_r}$$

$$\qquad (16)$$

$$\frac{\partial \hat{v}_{III}}{\partial r} = -\frac{\left(\rho_{III_0}\, \hat{v}_{III_1} - \rho_{II_0}\, \hat{v}_{II_1} \right)}{\rho_{III_0}\, B}$$

After having performed these steps, the first order equations do only depend on z. The solution starts with a numerical integration of zeroth order equations

157

with respect to the boundary conditions. The first order solution using the perturbed boundary conditions yields the pressure distribution in the seal for small rotor motions. The forces are obtained by a pressure integration:

$$F_1 = -\int_0^{L_t} \int_0^{2\pi} p \cos\varphi \, r \, d\varphi \, dz \quad = \quad -r_0 \frac{\pi r}{C_r} \int_0^{L_t} p_{1_c} \, dz$$

$$F_2 = -\int_0^{L_t} \int_0^{2\pi} p \sin\varphi \, r \, d\varphi \, dz \quad = \quad -r_0 \frac{\pi r}{C_r} \int_0^{L_t} p_{1_s} \, dz$$

(17)

Because we have to determine 4 parameters (K, k, D, d), the calculation of first order equations has to be done twice for two different rotor precession frequencies ($\Omega=0$ and $\Omega=\omega$). Then the rotordynamic coefficients can be calculated:

$$K + \Omega d \quad = \quad \frac{\pi r}{C_r} \int_0^{L_t} p_{1_c} \, dz$$

$$-k + \Omega D \quad = \quad \frac{\pi r}{C_r} \int_0^{L_t} p_{1_s} \, dz$$

(18)

COMPARISON TO EXPERIMENTS AND OTHER BULK-FLOW-THEORIES

1. Example

BENCKERT(1980) investigated experimentally a three chamber look-through labyrinth. Due to the design of his test rig, he could only measure stiffnesses. The data of the labyrinth are

R : 150 mm	T_a: 300 K
L : 7.75 mm	working fluid: air
B : 5.5 mm	number of chambers : 3
S : 0.25 mm	
C_r: 0.5 mm	No shaft rotation !
p_a: 1.425 bar	
p_b: 0.953 bar	

158

Fig.3 and 4 show the comparison to the experimental data for different preswirl conditions. While the 3-volume approach predicts a positive direct stiffness according to the measurements, the theory of CHILDS(1984) gives the opposite sign for K. The agreement between experiment and 3-volume model is good, especially showing that the model presented is capable to ensure sufficient accuracy in the calculation of dynamic seal parameters even for short labyrinth seals where the approaches of CHILDS or WYSSMANN have some problems.

Comparison of measurement, bulk theory of CHILDS and 3-volume model

Fig. 3: Direct stiffness K

Comparison of measurement, bulk theory of CHILDS and 3-volume model
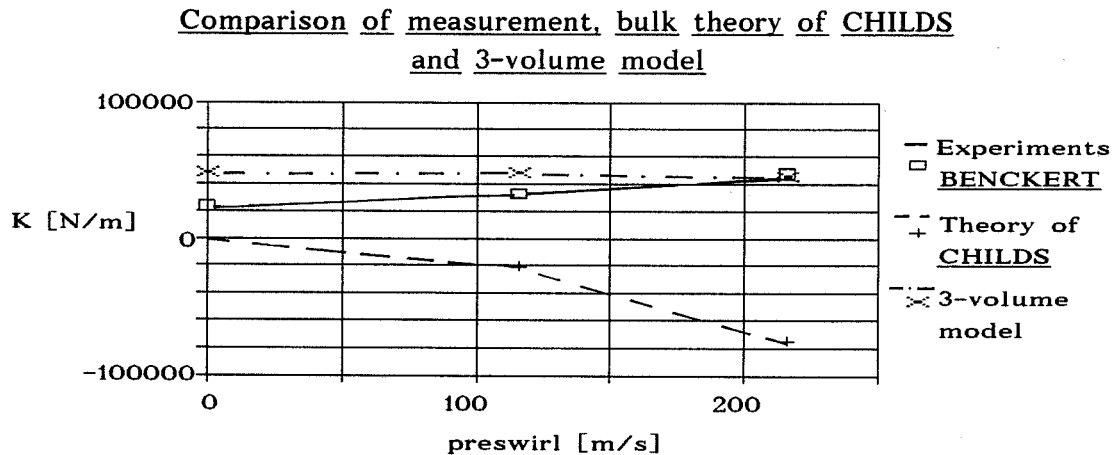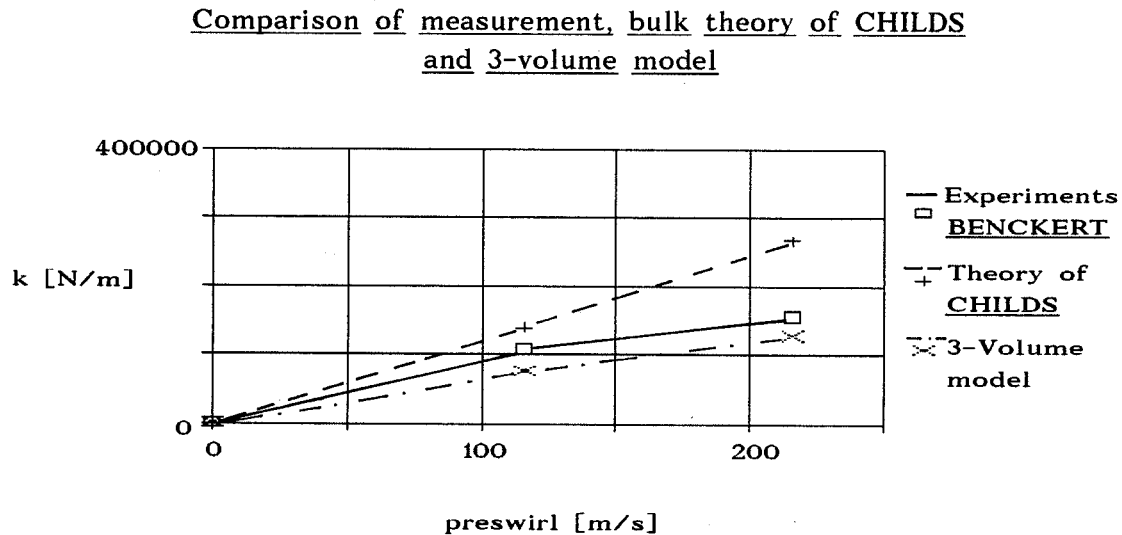
Fig. 4: Cross-coupled stiffness k

2. Example

In a paper published 1986, WYSSMANN shows a comparison of measured data for a 15-chamber look-through labyrinth. The experiments were carried out by CHILDS(1984). WYSSMANN compares the measurements to his 2-volume approach. For a 16-strip seal with fins on stator, the results of the experiments, of WYSS-MANN and the 3-volume model are shown in Fig. 5 - 7.

Comparison of measurement, bulk theory of WYSSMANN and 3-volume model

Fig. 5: Direct stiffness

Comparison of measurements, bulk theory of WYSSMANN and 3-volume model
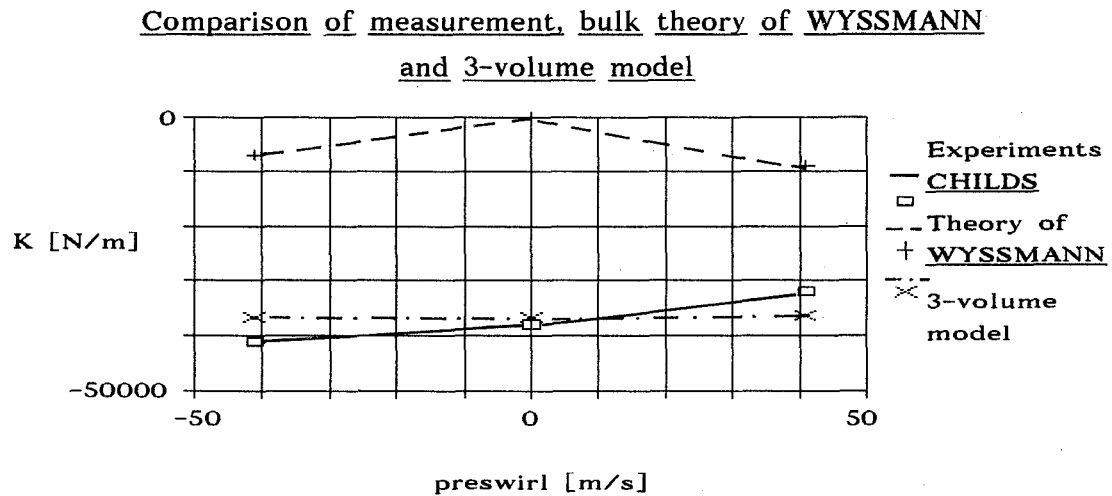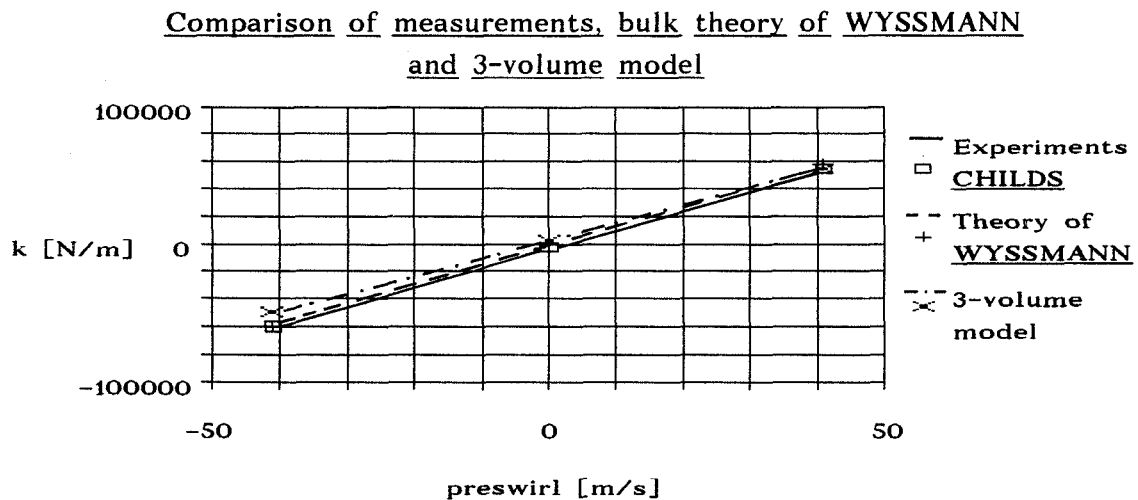
Fig. 6: Cross-coupled stiffness

Comparison of measurement, bulk theory of WYSSMANN and 3-volume model
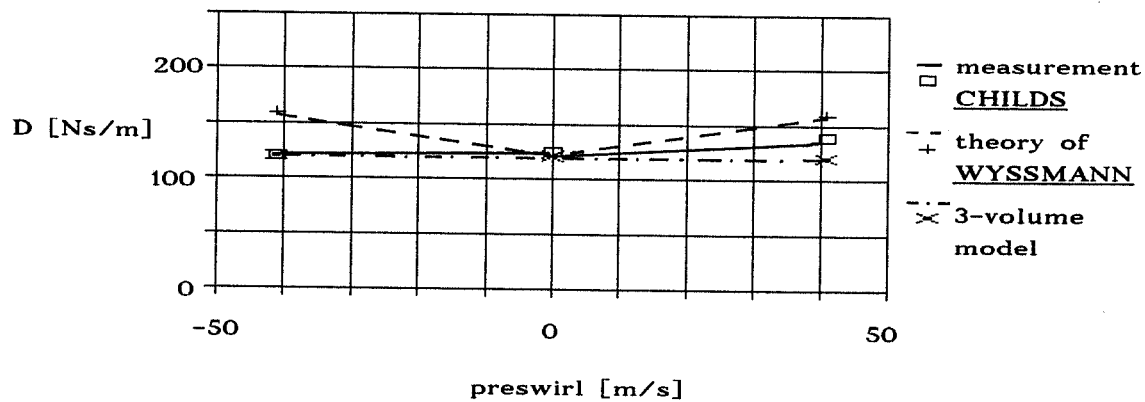
Fig. 7: Direct damping

In contrast to the 2-volume theory, the model presented here predicts the direct stiffness more accurate.

CONCLUSION

A new bulk flow model has been presented for the calculation of the rotor-dynamic seal parameters. The theory uses a three volume approach, and conservation equations for mass, momentum and energy are set up for every control volume. A perturbation analysis yields zeroth and first order equations. The integration of first order pressure perturbation results in the desired dynamic coefficients.

The comparison to experiments shows good agreement; compared to other bulk flow models, the present theory allows a much better calculation of the direct stiffness. This is mostly due to the determination of the model parameters with the help of the FDM programs, as a comparison to an earlier 3-volume model of KLAUK, which was developed in 1987 and did not have the benefit of using FDM results, shows.

REFERENCES

BENCKERT, H.:
"Strömungsbedingte Federkennwerte in Labyrinthdichtungen"
Dissertation TU Stuttgart, 1980

CHILDS, D. W., SCHARRER, J. K.:
"An Iwatsubo Solution for Labyrinth Seals Comparison of
Experimental Results"
NASA 2338, May 1984

CHILDS, D.W.; SCHARRER, J.K.:
"Experimental Rotordynamic Coefficients Results for Teeth-on-Rotor-
and Teeth-on-Stator Labyrinth Gas Seals"
NASA CP 2443, 1986, p.259-276

FLORJANCIC, S.:
"Annular Seals of High Energy Centrifugal Pumps"
Dissertation, Swiss Federal Institute of Zurich, 1990

KLAUK, E.:
"Berechnung der rotordynamischen Koeffizienten von mit kompressiblen
Medien durchströmten Labyrinthdichtungen unter Anwendung von
Mehr-Volumen-Modellen"
Diplomarbeit, University of Kaiserslautern, 1987; AG Machine Dynamics

KOSTYUK, A. G.:
"Circulation Forces over the Shrouding and their Influence on the
Threshold Capacity of Large Turbine Units"
Teploenergetika, 1975, Vol.22,No.3, p. 41-46

MOODY, L. F.:
"Friction Factors for Pipe Flow"
Trans. ASME 66 (November 1944), p. 671-684

NELSON, C. C.:
"Rotordynamic Coefficients for Compressible Flow in Tapered Annular
Seals"
Journal of Tribology, Vol 107, July 1985

NORDMANN, R., DIETZEN, F. J., WEISER, H. P.:
"Calculation of Rotordynamic Coefficients and Leakage for Annular
Gas Seals by Means of Finite-Difference Techniques"
11th Biennial Conference on Mechanical Vibration and Noise,
Boston, 27-30   Sept. 1987

NORDMANN, R., WEISER, H.P.:
"Rotordynamic Coefficients for Labyrinth Seals Calculated by
Means of a Finite-Difference Technique"
NASA, CP 3026, 1988

SCHARRER, J. K.:
"Theory versus Experiment for the Rotordynamic Coefficients
of Labyrinth Gas Seals: Part I - A Two Control Volume Model"
The 11th Biennial Conference on Mechanical Vibrations and Noise,
Boston, 27-30 Sept. 1987

WEISER, H. P., NORDMANN, R.:
"Calculation of Rotordynamic Labyrinth Seal Coefficients by Means
of a Threedimensional Finite-Difference Method"
Accepted for presentation for: 12th Biennial Conference on
Mechanical Vibration and Noise, Montreal, Sept. 1989

WEISER, H. P.:
"Ein Beitrag zur Berechnung der dynamischen Koeffizienten von
Labyrinthdichtungssystemen bei turbulenter Durchströmung mit
kompressiblen Medien"
Ph. D. Thesis, University of Kaiserslautern 1989

WYSSMANN, H. R., PHAM, T. C., JENNY, R. J.:
"Prediction of Stiffness and Damping Coefficients for
Centrifugal Compressor Labyrinth Seals"
ASME Journal of Engineering for Gas Turbines and Power,
Oct. 1984, B. 106, p. 920-926

WYSSMANN, H.R.:
"Theory and Measurement of Labyrinth Gas Seal Coefficients for Rotor
Stability of Turbocompressors"
NASA CP 2443, 1986, p.237-258

163

TEST RESULTS FOR ROTORDYNAMIC COEFFICIENTS OF THE SSME HPOTP TURBINE INTERSTAGE SEAL WITH TWO SWIRL BRAKES*

Dara W. Childs, Erian Baskharone, and Christopher Ramsey
Turbomachinery Laboratory
Mechanical Engineering Department
Texas A&M University
College Station, Texas 77843-3123, U.S.A.

Test results are presented for the HPOTP Turbine Interstage Seal with both the current and an alternate, aerodynamically-designed, swirl brake. Tests were conducted at speeds out to 16,000 *rpm*, supply pressures up to 18.3 *bars*, and the following three inlet-tangential-velocity conditions: (a) no preswirl, (b) intermediate preswirl in the direction of rotation, and (c) high preswirl in the direction of rotation. The back pressure can be controlled independently and was varied to yield the following four pressure ratios: 0.4, 0.45, 0.56, and 0.67.

The central and simplest conclusion to be obtained from the test series is that the alternate swirl brake consistently outperforms the current swirl brake in terms of stability performance. The alternate swirl-brake's whirl-frequency ratio was generally about one half or less than corresponding values for the current design. In many cases, the alternate design yielded negative whirl-frequency-ratio values in comparison to positive values for the current design. The alternate design can be directly substituted into the space currently occupied by the current design. There is no change in leakage performance.

PRECEDING PAGE BLANK NOT FILMED

NOMENCLATURE

A	Rotor shake amplitude (L)
C, c	Direct and cross-coupled damping coefficients (FT/L)
$\overline{C}$	Normalized direct damping coefficient (T)
Cr	Radial clearance; illustrated in figure 1, (L)
D	Rotor diameter (L)
K, k	Direct and cross-coupled stiffness coefficients (F/L)
$\overline{K}, \overline{k}$	Nondimensional direct and cross-coupled stiffness coefficients (dimensionless)
$f = k/C\omega$	Whirl frequency ratio (dimensionless)
L	Axial seal length (L)
P	Seal pressure (bar)
Pra	Pressure ratio = discharge pressure/supply pressure
Rs	Seal radius (L)
V	Seal inlet tangential velocity (L/T)
X, Y	Rotor to stator relative displacement components
$\dot{m}$	Seal mass flow rate (M/T)
$u_{\theta 0} = U_{\theta 0}/Rs\omega$	Nondimensional inlet tangential velocity
$U_{\theta 0}$	Inlet tangential velocity (L/T)
ω	Shaft angular velocity $(1/T)$

Subscripts

b	Sump Value
r	Reservoir value, radial component
t	Tangential component
X, Y	Rectangular coordinate directions

INTRODUCTION

Background and Motivation

One of the early steps in eliminating subsynchronous vibration problems in the Space Shuttle Main Engine(SSME) High Pressure Oxygen Turbopump(HPOTP) involved redesign of the turbine interstage seal. The redesign (Scharrer, 1989) consisted of the following sequential steps: (a) replace the original, stepped, tooth-on-rotor labyrinth with a smooth-rotor/honeycomb-stator design, and (b) introduce a swirlbrake upstream of the honeycomb seal. The initial redesign markedly reduced, but did not eliminate, the subsynchronous whirl; however, the addition of the swirl brake completely eliminated the subsynchronous motion over the full, steady-state, range of the unit.

166

A side view of the current seal with its installed swirlbrake is illustrated in figure 1. A detailed view of this swirl brake is provided in figure 2. A proposed alternative design is illustrated in figure 3. The current design uses radial slots to reduce the tangential velocity of the flow approaching the seal, the alternate design uses a standard aerodynamic design based on the approach velocity vector to smoothly eliminate the tangential velocity component. The alternate design turning vanes have a constant thickness and their entrance sections are not rounded. The second author of this paper developed the basic design of figure 3.
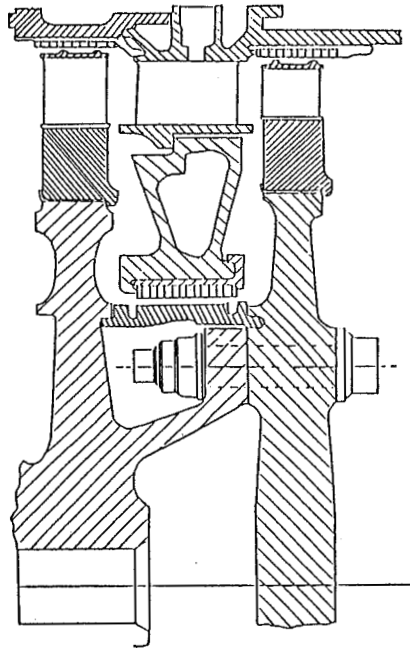
1. HPOTP turbine interstage seal(relative seal dimensions are not to scale).
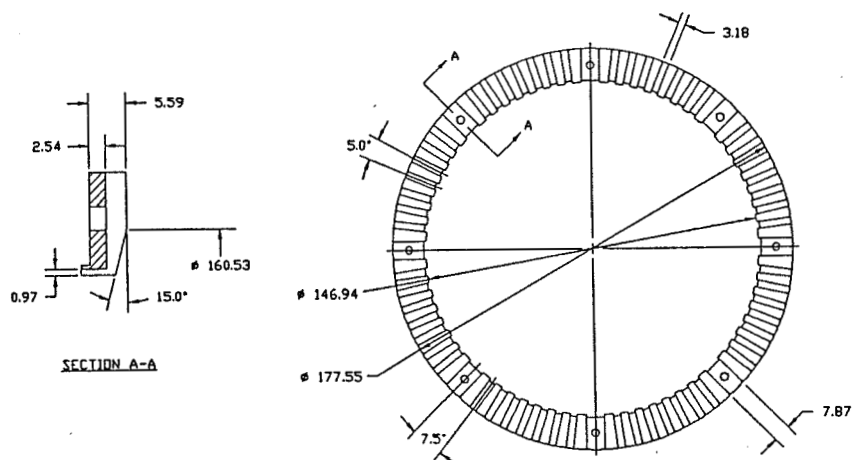
2. Current swirl-brake design.

167

To appreciate the design constraints on these swirl brakes, observe in figure 1 that the leakage flow approaches the seal with a predominantly radial inflow direction with very little axial velocity. The swirl brake reduces the tangential velocity or "swirl" of the leakage flow before it enters the seal to reduce the seal's rotordynamic destabilizing forces. The slots in the swirl brakes are specifically provided for this purpose. The effectiveness of the swirl brake is maximized by minimizing the axial distance between the swirl brake and the adjacent turbine wheel. Unfortunately, the large axial excursions permitted by the HPOTP balance piston at startup and shutdown force the axial spacing to higher than desirable values. The alternate design of figure 3 maintains the same(minimum) axial clearance throughout its radial expanse.

SECTION A-A

NOTES:
① AT POINT ① , VANE FACE TO BE TANGENT TO A RADIAL LINE.
② AT POINT ② TANGENT TO VANE FACE TO BE 31° FROM A RADIAL LINE AS SHOWN
③ BETWEEN POINT ① AND ② VANE FACE SHOULD HAVE A CONSTANT RADIUS
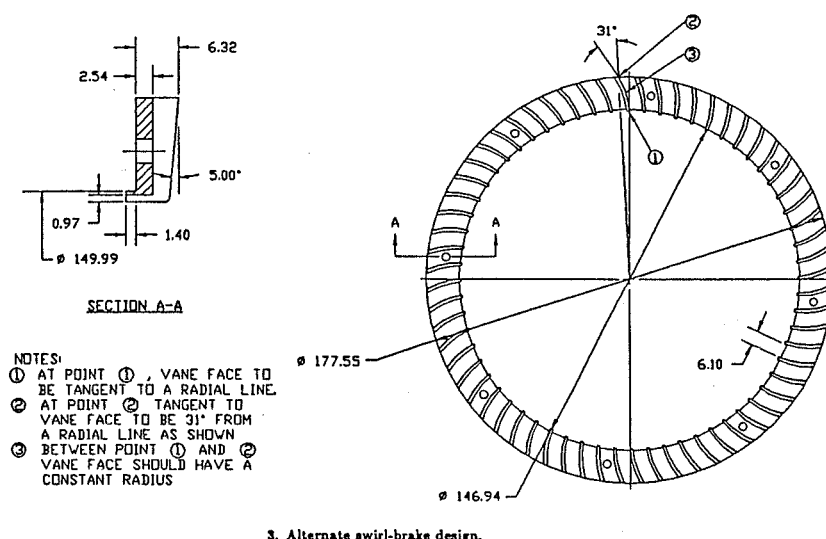
3. Alternate swirl-brake design.

Figure 4 illustrates the basic honeycomb-stator design. As illustrated, the honeycomb uses a $1.40mm$ $(0.055in)$ cell width and $3.81mm$ $(0.150in)$ cell depth. The swirl brakes are attached by screws to this piece. The seal section illustrated in figure 4 was provided by Rocketdyne; the two swirl brakes were manufactured by local machine shops.

For small motion about a centered position, the motion/reaction-force model for an annular seal is

$$-\left\{\begin{matrix} R_X \\ R_Y \end{matrix}\right\} = \begin{bmatrix} K & k \\ -k & K \end{bmatrix} \left\{\begin{matrix} X \\ Y \end{matrix}\right\} + \begin{bmatrix} C & c \\ -c & C \end{bmatrix} \left\{\begin{matrix} \dot{X} \\ \dot{Y} \end{matrix}\right\}$$

(1)

168
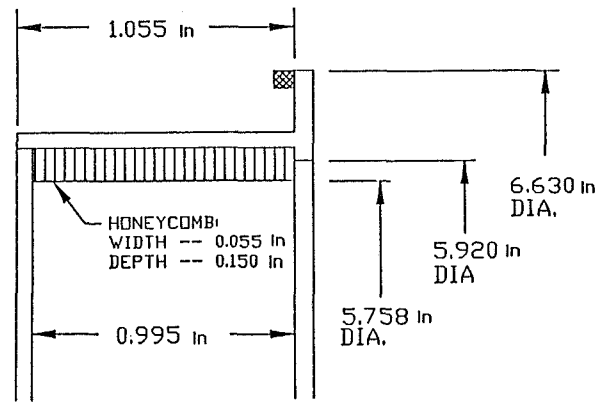
4. Seal stator dimensions.

where X,Y are components of the rotor displacement vector relative to the housing, and R_X, R_Y are components of the reaction vector acting on the rotor. Test results were obtained for the rotordynamic coefficients (K, k, C) and leakage for the HPOTP turbine interstage seal with the current and alternate swirl brakes. In terms of equation(1), swirl brakes are provided to minimize the cross-coupled stiffness coefficient k. The original published results for swirl brakes were by Benchert and Wachter(1980).

Test Apparatus Modifications

The basic configuration of the test apparatus has been discussed in several earlier publications (Childs et al., 1986, Childs and Scharrer, 1988, etc.). However, since these publications, the apparatus and facility have been modified by adding a new compressor with a consequent increase in supply pressure from 7.1 to 18 *bars*. This increase in supply pressure yields an increase in the transient forces which the rig measures. With the original compressor, the full supply pressure had to be dropped to atmosphere across the seal to achieve reasonable force amplitudes. The new compressor introduced the possibility of independently varying the back pressure (and hence pressure ratio and density) of the seal for a range of inlet pressures. Figure 5 illustrates the modifications which permit pressure-ratio control. A labyrinth back-pressure seal has been inserted downstream of the test seal. Two ports have been introduced between the test seal and the back-pressure seal for either injecting or venting air flow.

Figure 5 also illustrates a modification to the inlet flow field of the seal. In the previous apparatus, swirl vanes to prerotate the fluid were positioned immediately upstream of the seal inlet. The guide vane designs of Childs et al.(1986) were used here. The suggestion was made that introducing an axial spacing between the

169
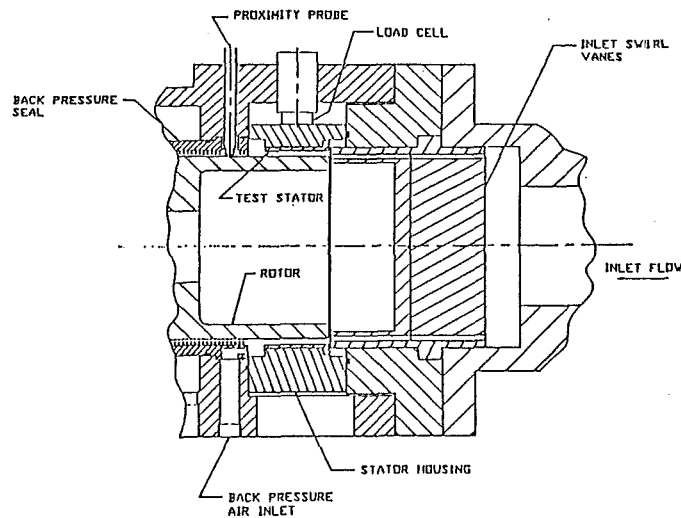
5. Back pressure and inlet modifications.

preswirl vanes and the seal could reduce "jetting" of flow from the vanes into the test seal. While the new arrangement permits direct access for measurement of the inlet velocity direction with a pitot-head probe, the velocity head is too low for accurate measurement.

Figure 6 illustrates the apparatus modification which was developed to simulate the radial approach velocity that occurs in the HPOTP. As illustrated, the preswirled flow approaches the rotor axially, proceeds radially outwards at the end of the rotor, and then radially inwards between the swirl brake and the rotor. With this design, the tangential velocity of the flow leaving the inlet guide vanes is known, but the tangential velocity of the flow actually entering the swirl brakes and the seal itself is not. The inlet preswirl arrangement illustrated in figure 6 is less than ideal, but the constraints involved in fitting the swirl brake designs into an existing apparatus precluded the development of a more representative geometry. Observe in figure 6 the axial-clearance differences for the two swirl brake designs.

ROCKETDYNE SWIRL BRAKE   TAMU SWIRL BRAKE
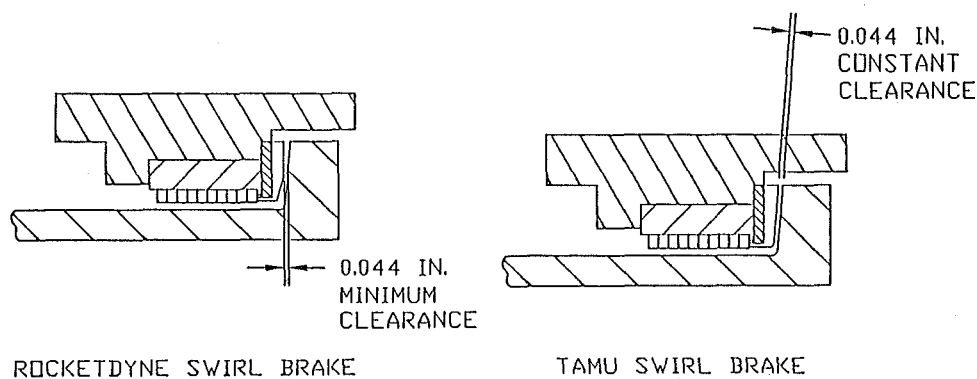
6. HPOTP turbine-interstage-seal test configuration.

170

Test Procedure and Parameter - Identification Changes

In addition to the above-cited changes in hardware, changes have been introduced in the excitation and parameter-identification methods. In prior tests, three different excitation frequencies were used with rotordynamic coefficients calculated at each frequency. Theoretically, the rotordynamic coefficients should be independent of excitation frequency, and the results at different excitation frequencies should be the same. For some seals, generally those with low magnitude rotordynamic coefficients, rotordynamic coefficients showed frequency dependency, while for others the coefficients were, as predicted, independent of frequency.

For the present test cases, a fast swept-sine wave excitation was used with the frequency increasing from 35 to 75 Hz. Bolleter et al.(1985) used this approach earlier for impeller tests. The excitation amplitude is around $.090mm$ with each sweep lasting approximately one second. Swept-sine-wave excitation is repeatedly applied to the rotor with intervening periods of zero-excitation of approximately 2 to 3 seconds. The no-excitation interval is inserted to allow the vibration which has been applied to the rotor to decay and to complete computer calculations. The excitation is initiated based on a phasor hole on the shaft. Hence, within reason, each swept-sine-wave excitation input and response should be identical, and by averaging the time histories of the input and response over many tests, spurious or random excitation should be reduced or eliminated. Ewins(1986) provides a thorough discussion of swept-sine-wave excitation for modal identification in conventional structural-dynamics.

To appreciate the application of swept-sine-wave excitation to the current modal identification problem, consider the following statement of the equations of motion for the seal housing.

$$M_S \left\{ \begin{array}{c} \ddot{X}_S \\ \ddot{Y}_S \end{array} \right\} = \left\{ \begin{array}{c} F_{RX} \\ F_{RY} \end{array} \right\} - \left[\begin{array}{cc} K & k \\ -k & K \end{array} \right] \left\{ \begin{array}{c} X \\ Y \end{array} \right\} - \left[\begin{array}{cc} C & c \\ -c & C \end{array} \right] \left\{ \begin{array}{c} \dot{X} \\ \dot{Y} \end{array} \right\} \qquad (2)$$

F_{RX}, F_{RY} are the measured reaction forces acting on the stator housing. The acceleration components of the housing are denoted by $\ddot{X}_S, \ddot{Y}_S$ and are also measured. The test apparatus only permits motion in the X direction, hence the model becomes

$$\left\{ \begin{array}{c} F_{RX} - M_S \ddot{X}_S \\ F_{RY} - M_S \ddot{Y}_S \end{array} \right\} = \left\{ \begin{array}{c} F_X \\ F_Y \end{array} \right\} = \left\{ \begin{array}{c} K \\ -k \end{array} \right\} X + \left\{ \begin{array}{c} C \\ -c \end{array} \right\} \dot{X} \qquad (3)$$

The displacement $X(t)$ is also measured and can be considered the input to the model. An analog circuit is used to generate $F_{RX} - M_S \ddot{X}_S$ and $F_{RY} - M_S \ddot{Y}_S$ from measured reaction-force and acceleration components. The swept-sine-wave excitation yields time-averaged histories $\tilde{F}_X(t_i), \tilde{F}_Y(t_i), \tilde{X}(t_i)$; $t_i = 1, 2, ...$ over 35 swept-sine-wave excitation inputs. The Fourier transform version of Eq. (3) is

$$\begin{Bmatrix} \hat{F}_X \\ \hat{F}_Y \end{Bmatrix} = \begin{Bmatrix} K + jC\omega \\ -k - jc\omega \end{Bmatrix} \hat{X} = \begin{Bmatrix} Z \\ -z \end{Bmatrix} \hat{X} \qquad (4)$$

where the "hat" denotes Fourier-transformed variables. The variables $\hat{F}_X, \hat{F}_Y, \hat{X}$ are obtained by calculating the FFT of the time-averaged histories $\hat{F}_X(t_i), \hat{F}_Y(t_i), \hat{X}(t_i)$.

The impedance functions of Eq. (4) are defined from the Fourier variables by

$$Z = \hat{F}_X / \hat{X}, \quad z = -\hat{F}_Y / \hat{X},$$

and the rotordynamic coefficients are accordingly defined by

$$K = Re(Z), \quad C = Im(Z)/\omega \qquad (5.a)$$

$$k = Re(z), \quad c = Im(z)/\omega \qquad (5.b)$$

Example plots are shown in figures 7 through 9. Only frequency data from 40 to 70 Hz are used from these transfer functions in calculating rotordynamic coefficients. The average (over frequency) of $Re(\hat{F}_X/\hat{X})$ and $Re(-\hat{F}_Y/\hat{X})$ define K and k. The average slopes of $Im(\hat{F}_X/\hat{X})$ and $Im(-\hat{F}_Y/\hat{X})$ define C and c. Note in figures 7 through 9 that there is a significant deviation about the average and slopes; however, no systematic error is apparent. By a least-squares curve fit, figures 7 through 9 yield the following coefficients.

$$K = 5.46 \times 10^5 N/m, \quad C = 194.0 N sec/m$$

$$k = 2.50 \times 10^4 N/m$$

The standard deviation for these variables is

$$\sigma_K = 4.10 \times 10^3 N/m, \quad \sigma_C = 8.75 N sec/m$$

$$\sigma_k = 5.25 N/m$$

No results are presented for the cross-coupled stiffness coefficient c, because the relative uncertainty of this parameter is too high.

A review of figures 7 through 9 shows that calculation of rotordynamic coefficients at three arbitrary frequencies could yield different and quite misleading results. The swept-sine-wave approach eliminates random errors involved in the calculations and provides a basis for examination of any systematic errors due to changes in excitation frequency.
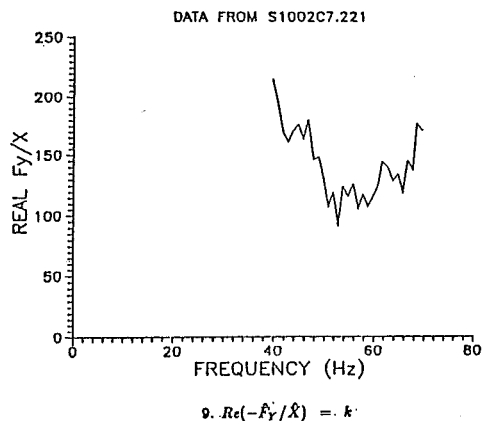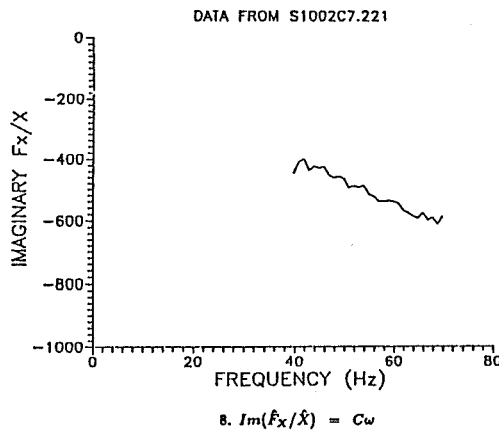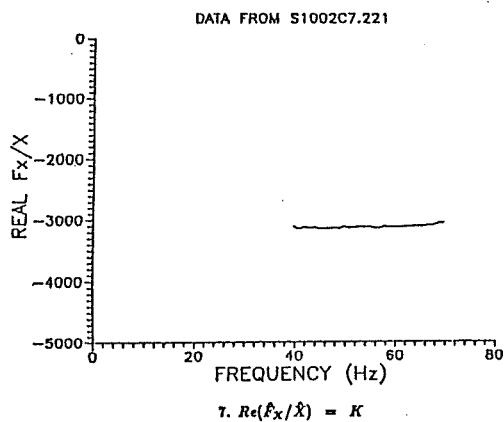
DATA FROM S1002C7.221

7. $Re(\hat{F}_X/\hat{X}) = K$

DATA FROM S1002C7.221

8. $Im(\hat{F}_X/\hat{X}) = C\omega$

DATA FROM S1002C7.221

9. $Re(-\hat{F}_Y/\hat{X}) = k$

EXPERIMENTAL RESULTS

Introduction

The test apparatus and facility used for this study were developed as part of an extended, joint, NASA-USAF funded research program for annular gas seal studies. The test fluid is air. As noted in the proceeding section, the test apparatus provides an excitation about the centered position and has been thoroughly discussed in earlier publications.

Test Variables

When shaking about the centered position, the following four independent variables can be controlled: *supply pressure, pressure ratio, rotor speed,* and *inlet circumferential velocity.* The pressure ratio used here is discharge pressure divided by supply pressure; hence $Pra = 1$ implies no pressure difference, and $Pra \cong 0$ implies an infinite supply pressure. Test points for these independent variables are shown in table 1. Reference to the symbols of table 1 is helpful and necessary to understand the figures which follow.

173

The reservoir pressures, as measured upstream of the flowmeter, are given in table 1. These values differ (slightly) from the actual inlet pressure because of frictional losses and acceleration of the fluid due to inlet guide vanes. Tests are not run at zero pressure difference, since a small pressure difference is necessary to keep the rotor from shifting axially and rubbing the inlet-guide-vane assembly. No zero-rotor-speed tests were run, since rotor rotation is necessary to prevent damage to the thrust bearing during shaking.

Table 1. Definition of symbols used in figures.

Supply Pressures	Pressure Ratios	Rotor Speeds	Inlet Circumferential Velocities

1 - 7.9 bar
2 - 13.1 bar
3 - 18.3 bar
	1 - .50
	2 - .42
	3 - .35
	4 - .30
		1 - 5000 cpm
		2 - 12000 cpm
		3 - 16000 cpm
			0 - Zero tangential
			    velocity
			1 - Intermediate velocity
			    with rotation
			2 - High velocity with
			    rotation

There were three test points for inlet circumferential velocity: one zero pre-rotation and two prerotated in the direction of shaft rotation. The zero-prerotation case is obtained with straightening vanes. The two different magnitudes of positive inlet circumferential velocity correspond to different inlet-guide-vane geometry depths. The calculated inlet tangential velocity tends to decrease with rotor speed, since the rotor grows with increased speed and reduces the leakage. The ratio of inlet circumferential velocity to rotor surface velocity ranges from zero to about 0.8.

Measurement of leakage flowrates showed no differences between the two swirl-brake designs.

Whirl-Frequency Ratio Definition

For a circular orbit of amplitude A and precessional-frequency ω, the resultant radial and tangential forces developed by the seal model of equation (1) are

$$-F_r/A = K + c\omega$$

$$F_t/A = k - C\omega \tag{6}$$

From a stability standpoint, the destabilizing tangential force F_t is of most interest. A positive cross-coupled stiffness k is destabilizing because it "drives" the forward

orbital motion of the rotor. Positive direct damping C and a negative cross-coupled stiffness are stabilizing because they oppose the orbital motion.

A convenient measure of seal stability is the whirl frequency ratio, which is a nondimensionalized ratio of cross-coupled stiffness to direct damping forces with a circular orbit.

$$whirl - frequency\, ratio = f = \frac{k}{C\omega} \qquad (7)$$

Relative Uncertainty

The uncertainty in the dynamic coefficients can be determined using the method described by Holman(1978). The uncertainty in the force, excitation frequency, and displacement measurements are 0.55 N (0.125 lb), 0.065 Hz, and 0.0013 mm (0.05 mils), respectively. Before normalization, the nominal calculated uncertainty in the stiffness coefficients is 6.7 N/mm (38 lb/in) and 0.014 N-s/mm (0.082 lb-s/in) for the damping coefficients. The predicted uncertainties are generally satisfactory in comparison to nominal values for K, k, and C.

The principal source of uncertainty in the *resultant* force measurement is the acceleration measurement for the stator, not the piezo-electric force transducer measurements. The "normal" accelerometers used in the tester have a resolution of 5×10^{-3} g's. Although more sensitive accelerometers are available, they can not generally be used when testing honeycomb seals, because high-frequency accelerometer "spikes" are frequently seen with these seals, presumably because of a Helmholtz-acoustic excitation.

Test Results

Figure 10 illustrates K for the current(Rocketdyne) swirl brake design versus inlet tangential velocity for three supply pressures and four pressure ratios. Generally speaking, K increases with increasing running speed, supply pressure, and pressure ratio. Although not illustrated, comparable results are obtained with the alternate(TAMU) swirl brake design. The increase in K with increasing running speed arises due to a reduction in clearance. When K is nondimensionalized, removing the influence of clearance changes, no speed influence is present.

Figure 11 illustrates k for the current and alternate swirl brake designs. Observe that the alternate swirl-brake design consistently yields much lower values for this coefficient. In some cases, the alternate design actually yields negative values for k versus positive values for the current design. Negative k values would oppose forward whirl of the turbopump.

Figure 12 illustrates C for the current swirl brake. C is observed to decrease slightly with increasing running speed. Although not illustrated, comparable damping results were obtained for the alternate swirl brake design.
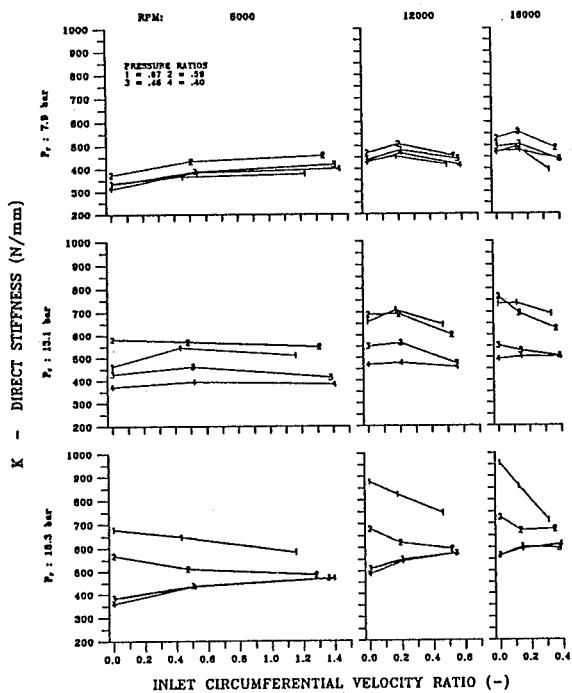
10. Direct stiffness K for the current swirl-brake design.
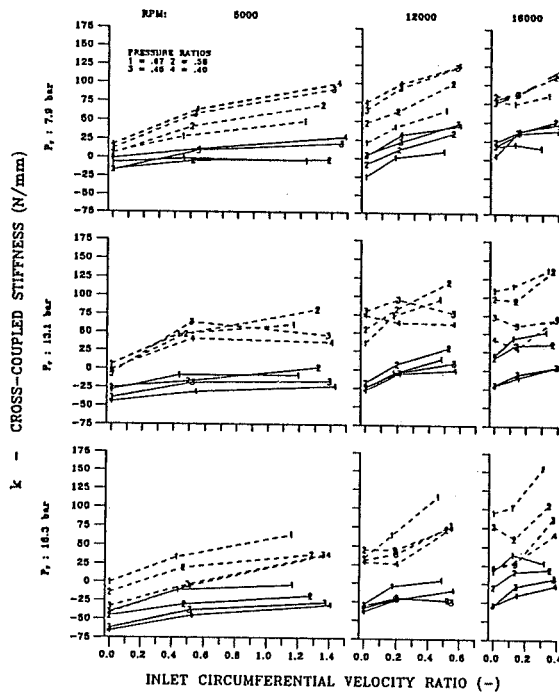
11. Cross-coupled-stiffness k for the current and alternate swirl-brake designs.
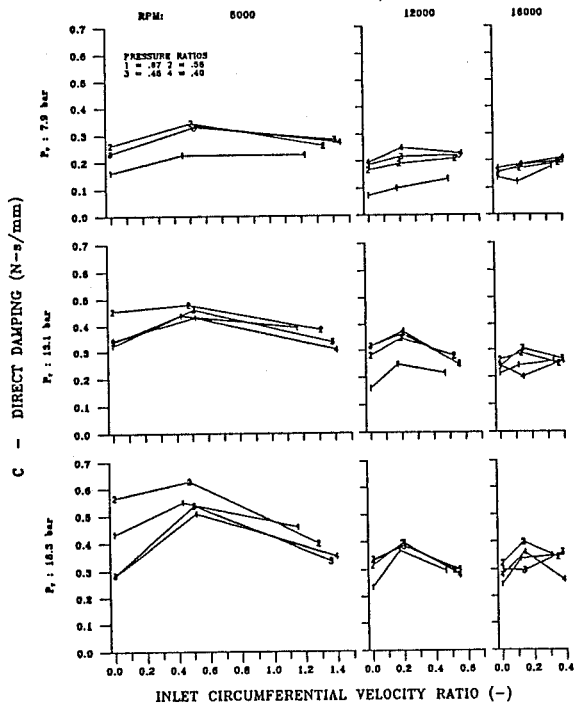
12. Direct damping C for the current swirl-brake design.
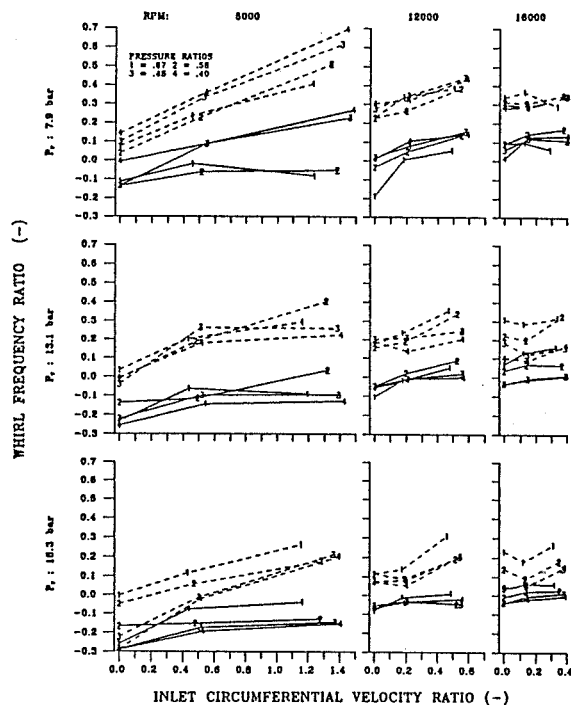
13. Whirl-frequency ratio f for the current and alternate swirl-brake designs.

176

Figure 12 illustrates C for the current swirl brake. C is observed to decrease slightly with increasing running speed. Although not illustrated, comparable damping results were obtained for the alternate swirl brake design.

Figure 13 illustrates the whirl-frequency ratio f for the current and alternate swirl-brake designs demonstrating the improved rotordynamic-stability performance of the alternate design. In all cases, the alternate design yields lower values for f. In many cases, the alternate design yields negative values for f versus positive values for the current design.

As noted in the introduction, the present tests include the pressure ratio as a parameter for the first time. Field experiences have demonstrated that centrifugal compressors using teeth-on-stator labyrinth seals become less stable as the average density is increased, Kirk and Donald(1983). One of the influences of a change in pressure ratio with a fixed supply pressure is a density variation of the fluid within the seal. Specifically, as the pressure ratio is increased, the density increases while ΔP decreases. From figure 13, at the lowest speed and supply pressure, stability is improved by increasing the pressure ratio(and average density) and decreasing ΔP. However, at the highest supply pressure, stability is improved by decreasing the pressure ratio, i.e., decreasing density while increasing ΔP. The high supply-pressure results are consistent with Kirk and Donald's experience with centrifugal compressors.

SUMMARY AND CONCLUSIONS

Test results are presented for the rotordynamic coefficients of the HPOTP turbine interstage seal with the current swirl brake and an alternate design swirl brake. The two swirl-brake designs yield identical leakage performance and comparable results for direct stiffness and damping; however, the alternate design has much better stability performance over all operating conditions.

Test results since Benchert and Wachter(1980) demonstrate that almost any swirl brake will improve rotordynamic stability by reducing the inlet tangential velocity and consequently reducing the cross-coupled stiffness coefficient. However, the stability improvement accruing to an aerodynamic design is clearly demonstrated to be substantial by the present test results. Given the critical nature of these devices for rotordynamic stability of many machines, a thorough aerodynamic design is clearly in order.

177

REFERENCES

Benchert, H., and Wachter, J.(1980), "Flow Induced Spring Coefficients of Labyrinth Seals for Application in Rotordynamics," NASA CP2133, Proceedings of the workshop: Rotordynamic Instability Problems in High Performance Turbomachinery, held at Texas A&M University, 12-14 May 1980, pp. 189-212.

Bolleter, U., Wyss, A., Welte, I., and R. Sturchler, (1985), "Measurement of Hydrodynamic Matrices of Boiler Feed Pump Impellers," *ASME Journal of Vibrations, Stress and Reliability in Design,* Vol. 109, pp. 144-151.

Childs, D. W., and Scharrer, J.(1988), "Theory Versus Experiment for the Rotordynamic Coefficients of Labyrinth Gas Seals: Part II - A Comparison to Experiment," *ASME Journal of Vibration, Acoustics, Stress, and Reliability in Design*, Vol. 110, No. 3, July 1988, pp. 281-287.

Childs, D. W., Nelson, C. E., Nicks, C., Scharrer, J., Elrod, D., and Hale, K.(1986), "Theory Versus Experiment for the Rotordynamic Coefficients of Annular Gas Seals: Part 1-Test Facility and Apparatus",*ASME Transaction Journal of Tribology,* Vol. 108, pp. 426-432.

Ewins, D. J.(1986), "Modal Testing: Theory and Practice," Research Studies Press Ltd.

Kirk, R. G., and Donald, G. N.(1983), "Design Criteria for Improved Stability of Centrifugal Compressors," Rotor Dynamical Instability, ASME presented at *The Applied Mechanics, Bioengineering and Fluids Engineering Conference,* Houston, Texas, 20-22 June 1983.

Holman, J. P.(1978), *Experimental Methods for Engineers,* McGraw Hill, 1978, pp. 45.

Scharrer, J.(1989), discussion of the paper, "Annular Honeycomb Seals: Test Results for Leakage and Rotordynamic Coefficients; Comparisons to Labyrinth and Smooth Configurations," by D. Childs et al., *ASME Journal of Tribology,* pp. 793-301.

SEAL-ROTORDYNAMIC-COEFFICIENT TEST RESULTS FOR A MODEL SSME ATD-HPFTP TURBINE INTERSTAGE SEAL WITH AND WITHOUT A SWIRL BRAKE*

Dara W. Childs and Christopher Ramsey
Turbomachinery Laboratory
Mechanical Engineering Department
Texas A&M University
College Station, Texas 77843-3123, U.S.A.

Test results are presented and compared to theory for a model Space Shuttle Main Engine(SSME) Alternate Turbopump Development(ATD) High-Pressure Fuel Turbopump (HPFTP) with and without swirl brakes. Tests are conducted with supply pressures out to 18.3 *bars* and speeds out to 16,000 *rpm*. Seal back pressure is controlled to provide four pressure ratios at all supply pressures. Three inlet guide vanes are used to provide the following three fluid prerotation cases: (a) no prerotation, (b) moderate prerotation in the direction of rotation, and (c) high prerotation in the direction of rotation. Test results demonstrate the pronounced favorable influence of the swirl brake in reducing the seal destabilizing forces. Without the swirl brake, the cross-coupled stiffness k increases monotonically with increasing inlet tangential velocity. With the swirl brake, k tends to either be constant or decrease with increasing inlet tangential velocity. Direct damping either increases or remains relatively constant when the swirl brake is introduced. Direct stiffness is relatively unchanged. No measurable differences in leakage were detected for the seal with and without the swirl brake.

Comparisons between Scharrer's(1988) theory and measurements for the seal without a swirl brake indicate that the predictions can be used to provide design guidelines only. Specific predictions for rotordynamic coefficients should be treated cautiously, since systematic differences were observed between theory and experiment due to changes in running speed, supply pressure, and pressure ratio.

NOMENCLATURE

C, c	Direct and cross-coupled damping coefficients (FT/L)
K, k	Direct and cross-coupled stiffness coefficients (F/L)
$\overline{K}, \overline{k}$	Nondimensional direct and cross-coupled stiffness coefficients (dimensionless)
$f = k/C\omega$	Whirl frequency ratio (dimensionless)
L	Axial seal length (L)
Pra	Pressure ratio = discharge pressure/supply pressure
Rs	Seal-tip radius (L)
X, Y	Rotor to stator relative displacement components
$u_{\theta 0} = U_{\theta 0}/Rs\omega$	Nondimensional inlet tangential velocity
$U_{\theta 0}$	Inlet tangential velocity (L/T)
ω	Shaft angular velocity $(1/T)$

INTRODUCTION

Background and Motivation

For small motion about a centered position, the motion/reaction-force model for an annular gas seal is

$$-\begin{Bmatrix} F_X \\ F_Y \end{Bmatrix} = \begin{bmatrix} K & k \\ -k & K \end{bmatrix} \begin{Bmatrix} X \\ Y \end{Bmatrix} + \begin{bmatrix} C & c \\ -c & C \end{bmatrix} \begin{Bmatrix} \dot{X} \\ \dot{Y} \end{Bmatrix} \tag{1}$$

where X, Y are components of the rotor displacement vector relative to the housing, and F_X, F_Y are components of the reaction vector acting on the rotor. Further, K, k, C, c, are denoted as the direct stiffness, cross-coupled stiffness, direct damping, and cross-coupled damping coefficients, respectively. If one assumes a circular orbit of the seal at amplitude A and precessional frequency ω, the radial and tangential force coefficients can be stated

$$-F_r/A = K + c\omega \qquad F_\theta/A = k - C\omega \tag{2}$$

Hence, K and c act in the radial direction and would be expected to predominantly influence rotor critical speeds, and k and c act in the tangential direction and would be expected to predominantly influence rotor stability. For a typical gas labyrinth seal, K and c have a negligible influence on rotordynamics; however, k can significantly degrade stability, while C can significantly improve stability. The cross-coupled stiffness coefficient k arises due to fluid rotation within the seal, and Wachter and Benchert(1980) demonstrated that a "swirl brake" consisting of radial ribs upstream of the seal, which reduce the inlet tangential velocity, could substantially reduce or eliminate k.

180

C-3

Pratt and Whitney(P&W) is in the process of developing an Alternate Turbopump Development(ATD) version of the SSME high pressure Turbopumps. The guidelines for their design requires direct interchangeability with the current Rocketdyne turbopumps and emphasizes reliability, reusability, and reduced manufacturing and maintenance costs. The units are nominally similar to the current designs; e.g., the ATD-HPFTP uses a three stage fuel pump driven by a two-stage turbine. However, various details related to rotordynamics are quite different. For example, the ATD-HPFTP has a high pressure drop across the turbine interstage seal; whereas, the current HPFTP does not. Because of the high-pressure drop, the rotordynamic coefficients increase sharply, and rotordynamics analysis of the ATD-HPFTP indicated a strong sensitivity of rotordynamic stability to the turbine interstage seal. Further analysis strongly suggested that a swirl brake be provided to reduce or eliminate the destabilizing forces developed by this seal.

The present test program compares predictions(Scharrer, 1988) and measurements for a model version of the seal, with and without a swirl brake, to establish a degree of confidence in seal calculations for the ATD turbopumps. Results are presented to answer the following questions:

(a) How effective is the swirl brake in improving the stability characteristics of the seal, and

(b) How good is Scharrer's theory in predicting rotordynamic coefficients?

Test Hardware

As noted above, tests were undertaken for a model ATD-HPFTP turbine interstage seal which differs in the following details from the actual seal design:

(a) The radius is smaller. The model seal has a labyrinth tip diameter of about 14.3cm versus the actual dimensions of about 20.2cm. This change was required by constraints of the test apparatus.

(b) The test seal has twelve cavities versus five for the turbopump seal. This change was required to increase the measured force levels in the test apparatus, since the pressure drop across the seal is much lower in the test apparatus than the turbopump.

(c) Test clearances between the labyrinth teeth and the honeycomb stator coincide with cold, nonrotating, conditions but are looser than hot operation conditions for the turbopump.

The model seal is otherwise identical with the ATD design using the same nominal axial clearance between the first labyrinth tooth and the swirl brakes, the same swirl-vane, tooth, and honeycomb-stator geometries.

Figure 1 illustrates the model seal dimensions, and figure 2 illustrates the swirl brake geometry. There are 145 individual vanes with a pitch between vanes of 3.12mm at their base radius of 7.42cm. Each vane is 2.1mm deep. The directions of the air approaching and leaving the swirl vanes in figure 2 are not necessarily representative of the performance of either the model or the turbopump swirl brake. They are provided to illustrate the intended function of the vanes in eliminating the tangential velocity entering the seal.

.254 mm — 7.5° BOTH SIDES
2.0 mm
2.0 mm
.709 mm RAD.
7.36 cm

0.31 MM CLEARANCE
HONEYCOMB INSERT
STATOR INSERT
SWIRL BRAKE ATTACHMENT
SWIRL BRAKE VANE
0.51 mm CLEARANCE
ROTOR
2.5 mm
7.16 cm

1. Model seal dimensions.

3.56 mm
0.51 mm
EXIT VELOCITY
0.51 R. TYP.
2.1 mm
6.10 mm
APPROACH VELOCITY

2. Swirl vane geometry.
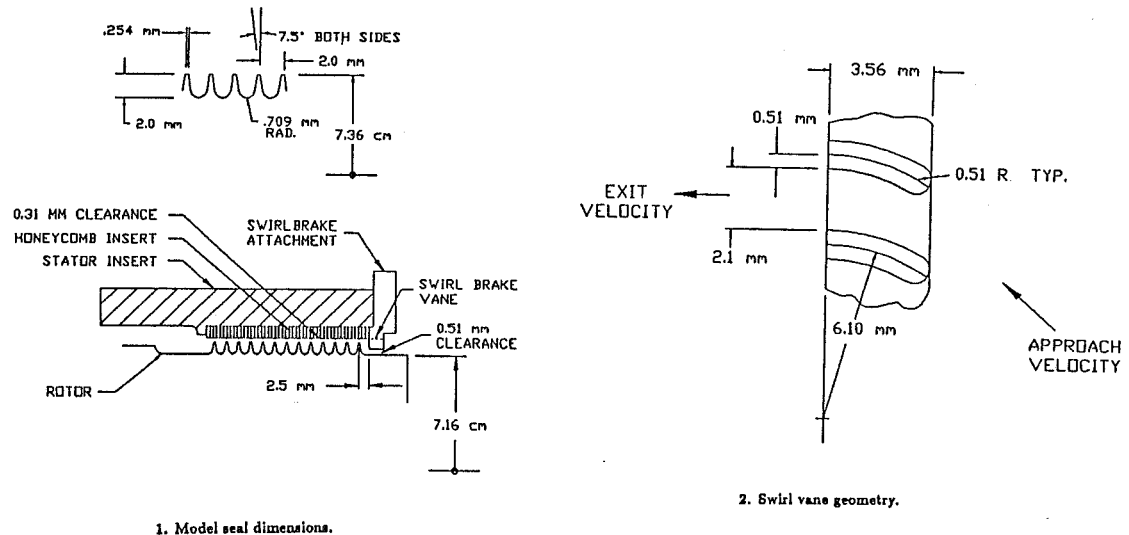
Test Apparatus

The basic configuration of the test apparatus has been discussed in several earlier publications(Childs et al., 1986, Childs and Scharrer, 1988, etc.). Childs et al.(1990) have recently provided a discussion of modifications of the apparatus and facility involving: (a) the addition of a new compressor which increases the available supply pressure from 7.1 to 18 *bars*, (b) modification of the inlet preswirl arrangements, and (c) introduction of a swept-sine-wave excitation approach. With the original compressor, the full supply pressure was discharged across the test seal to obtain seal-amplitude forces which were large enough to measure. With the elevated supply pressure, the back pressure can be varied independently from the supply pressure and still yield measurable force amplitudes. Hence, the pressure ratio across the seal has been introduced as an independent parameter, and shorter seals can now be tested.

The basic apparatus is unchanged. The rotating seal is shaken horizontally by a hydraulic shaker, the reaction force components on the stator, due to relative seal motion, are measured and then corrected to account for stator acceleration, and the relative motion between the seal and stator are measured. From these measurements, the seal rotordynamic coefficients are calculated.

Scharrer's Theory(1988)

Scharrer uses a two-control-volume model to represent the known velocity distribution of a labyrinth seal illustrated in figure 3. The velocity field involves a through-flow leakage region next to the rotor and a vortex flow field in the labyrinth cavity. Scharrer's two-control-volume model has one control volume from the labyrinth tip to the stator and the second control volume in the labyrinth cavity. A free jet is assumed to exist between the two control volumes. The model for the seal involves the following equations:

(a) an empirical leakage equation,

(b) circumferential-momentum equations for both control volumes, and

(c) continuity equations for the two control volumes.

The circumferential momentum equation for flow in the cavity includes the shear stresses at the solid boundary and a jet shear stress between the vortex flow and the through flow. Hirs(1973) turbulence model is used to define the sheer stresses between solid boundaries and the fluid.
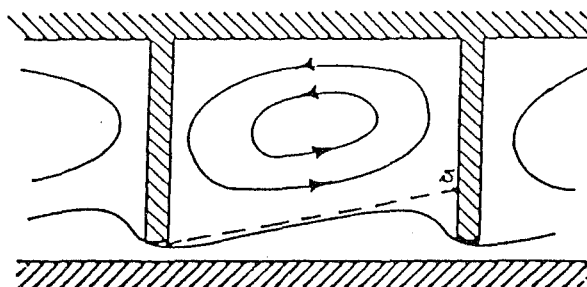
3. Labyrinth-seal flow field.

Comparisons between Scharrer's theory and test results have been presented previously by Childs and Scharrer(1988) for teeth-on-stator(smooth-rotor) and teeth-on-rotor (smooth-stator) seals and by Hawkins and Childs(1988) for teeth-on-rotor seals with honeycomb stators. These results were for 5.08 *cm* long seals with the original 7.1 *bar* supply pressures at three clearances and showed generally reasonable agreement between theory and experiments.

EXPERIMENTAL RESULTS

Introduction

The test apparatus and facility used for this study were developed as part of an extended, joint NASA-USAF funded research program for annular gas seal studies.

The test fluid is air. As noted in the preceding section, the test apparatus provides an excitation about the centered position and has been thoroughly discussed in earlier publications.

Test Variables

When shaking about the centered position, the dynamic-seal apparatus is capable of controlling the following four independent variables: *supply pressure, pressure ratio, rotor speed*, and *inlet circumferential velocity*. The pressure ratio used here is discharge pressure divided by supply pressure; hence $Pra = 1$ implies no pressure difference, and $Pra \cong 0$ implies an infinite supply pressure. Test points for these independent variables are shown in table 1. Reference to the symbols of table 1 is helpful and necessary to understand the figures which follow.

The reservoir pressures, as measured upstream of the flowmeter, are given in table 1. These values differ (slightly) from the actual inlet pressure because of frictional losses and acceleration of the fluid due to inlet guide vanes. Tests are not run at zero pressure difference, since a small pressure difference is necessary to keep the rotor from shifting axially and rubbing the inlet-guide-vane assembly. No zero-rotor-speed tests were run, since rotor rotation is necessary to prevent damage to the thrust bearing during shaking.

Table 1. Definition of symbols used in figures.

Supply Pressures	Pressure Ratios	Rotor Speeds	Inlet Circumferential Velocities
1 - 7.9 bar 2 - 13.1 bar 3 - 18.3 bar	1 - .50 2 - .42 3 - .35 4 - .30	1 - 5000 cpm 2 - 12000 cpm 3 - 16000 cpm	0 - Zero tangential velocity 1 - Intermediate velocity with rotation 2 - High velocity with rotation

There were three test points for inlet circumferential velocity: one zero prerotation and two prerotated in the direction of shaft rotation. The zero-prerotation case is obtained with straightening vanes. The two different magnitudes of positive inlet circumferential velocity correspond to different inlet-guide-vane geometry depths. The calculated inlet tangential velocity tends to decrease with rotor speed, because the rotor grows with increased speed and reduces the leakage. The ratio of inlet circumferential velocity to rotor surface velocity ranges from zero to about 0.8.

Measurement of leakage flowrates showed no differences with and without the swirl brake.

184

Relative Uncertainty

The uncertainty in the dynamic coefficients can be determined using the method described by Holman(1978). The uncertainty in the force, excitation frequency, and displacement measurements are 0.55 N (0.125 lb), 0.065 Hz, and 0.0013 mm (0.05 mils), respectively. Before normalization, the nominal calculated uncertainty in the stiffness coefficients is 6.7 N/mm (38 lb/in) and 0.014 N-s/mm (0.082 lb-s/in) for the damping coefficients. The predicted uncertainties are generally satisfactory in comparison to nominal values for K and k. They are generally unsatisfactory for c and are only satisfactory for C at the highest supply pressure. Hence, data are presented for K and k at all test conditions, for C at the highest supply pressure, and are not presented for c.

The principal source of uncertainty in the *resultant* force measurement is the acceleration measurement for the stator, not the piezo-electric force transducer measurements. The accelerometers used for these tests have a resolution of 5×10^{-3} g's. Although more sensitive accelerometers are available, they can not generally be used when testing honeycomb seals, because high-frequency accelerometer "spikes" are frequently seen with these seals, presumably because of a Helmholtz-acoustic excitation of the honeycomb cavities.

Test Results

Figure 4 illustrates experimental and theoretical values for K versus $u_{\theta 0}$ for three speeds, three supply pressures, and four pressure ratios. The experimental results presented are for no swirl brake; however, very similar results were obtained with the swirl brake. Solid lines denote test results; dashed lines denote theoretical predictions. The theory does an adequate job of predicting K at low speeds; however, as the speed increases, K is progressively under predicted. The test results are much more sensitive to changes in the pressure ratio than the theory. Moreover, the theory predicts that K increases as Pra decreases, while tests show an opposite trend. The changes in K due to changes in speed are primarily due to changes in clearances. Nondimensionalization, which eliminates the influence of clearance, eliminates the apparent speed dependency.

Figure 5 illustrates k versus $u_{\theta 0}$ for the seal with and without swirl brakes. For the seal without the swirl brake, $u_{\theta 0}$ is the actual(calculated) normalized tangential velocity entering the seal. With the swirl brake, $u_{\theta 0}$ is the normalized tangential velocity entering the swirl brake. Obviously, the swirl brake sharply reduces k. At low speeds, k's rate of increase with increasing $u_{\theta 0}$ is decreased. At higher speeds, k actually decreases as $u_{\theta 0}$ increases.

Figure 6 compares theory versus experiment for k for the seal without the swirlbrake. The theory does an adequate job at low speeds and low pressures but does poorly as the supply pressure and speed increase. Generally speaking,
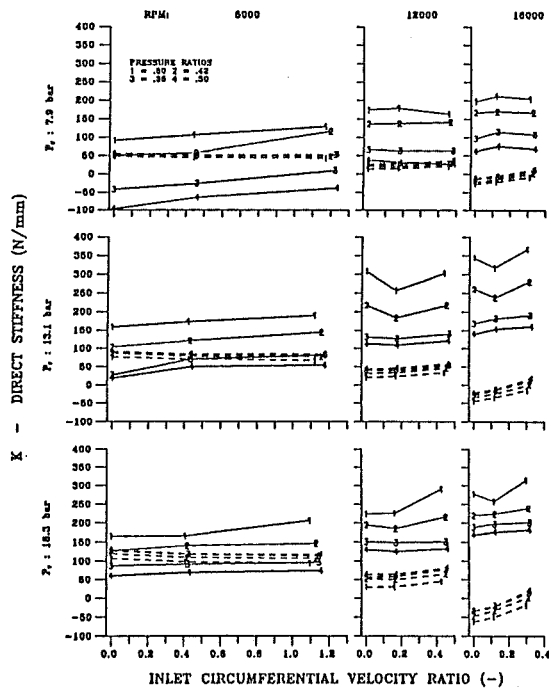
4. K versus $u_{\theta 0}$ for the seal without the swirl brake, for three speeds, three supply pressures, and four pressure ratios. Solid lines denote test data; dashed lines denote theory.
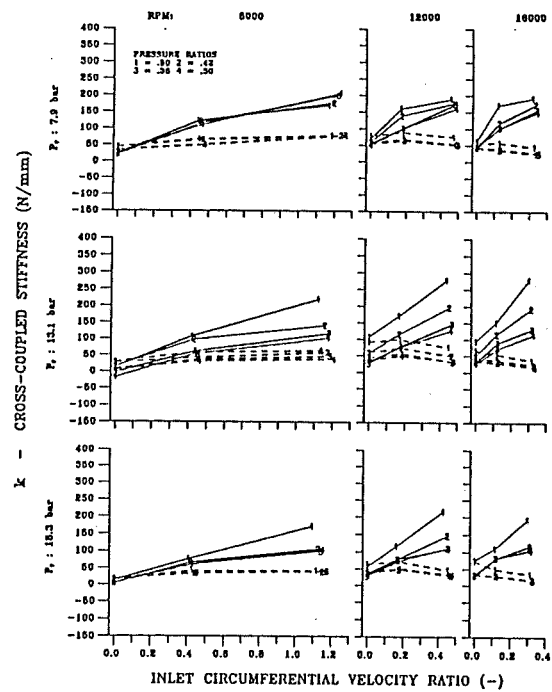
5. k versus $u_{\theta 0}$ for the seal with and without swirl brakes for three speeds, three supply pressures, and four pressure ratios. Dashed lines denote the seal with a swirl brake, solid lines without.
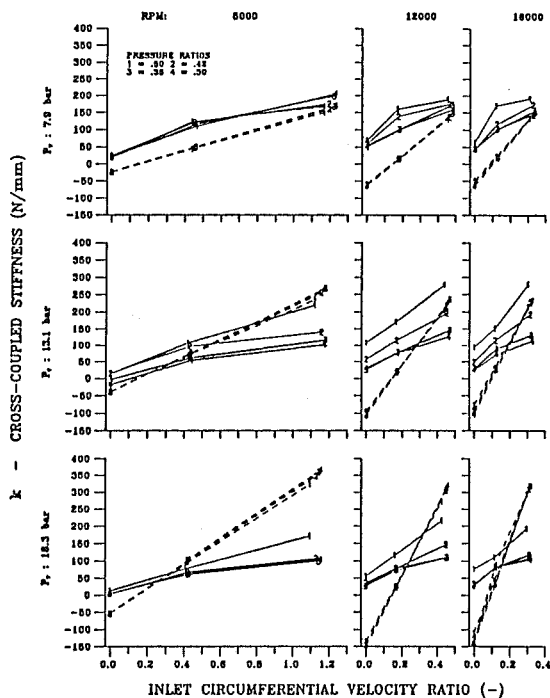
6. k versus $u_{\theta 0}$ for the seal without a swirl brake. Dashed lines represent the theory; solid lines represent test results.
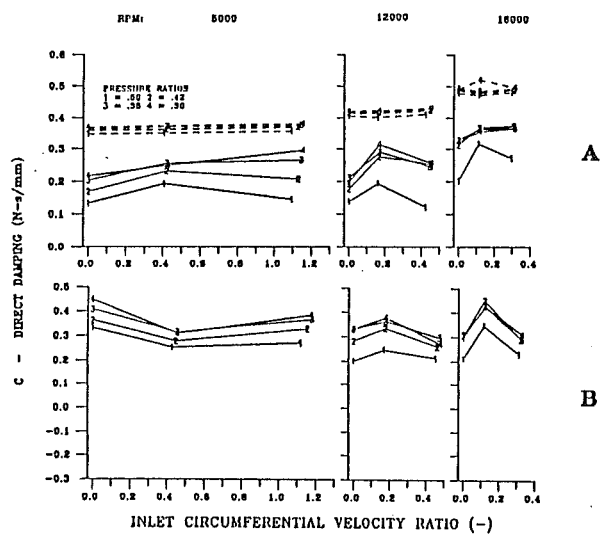
7. Theory versus experimental results for C; $P_r = 18.3 bars$:
   (A) Theory versus experiment for the seal without a swirl brake,
   (B) Experimental results with a swirl brake.

186

for low $u_{\theta 0}$, k is underpredicted, and measured k values increase more slowly than theoretical predictions as $u_{\theta 0}$ is increased. Measured results are much more sensitive to changes in the pressure ratio than predictions.

Figure 7 illustrates C versus $u_{\theta 0}$. The A frame of this figure provides theory versus experiment comparisons for the seal without the swirl brake. The B frame provides experimental results for the seal with the swirl brake. C is seen to be comparatively insensitive to changes in $u_{\theta 0}$. In A, the theory is seen to substantially overpredict C. Also, measured values of C are more sensitive to changes in Pra than theoretical predictions. Comparing the experimental results in A and B illustrates that the swirl brake increases C substantially at low speeds but has only a minimal influence at higher speeds. As noted earlier, test results are only presented for C at the highest supply pressure because of problems with excessive uncertainties at lower supply pressures.

A convenient overall measure of seal stability is the whirl-frequency ratio which is a nondimensionalized ratio of the destabilizing tangential force due to k and the stabilizing forces due to C. From equation(2), the definition is

$$f = k/C\omega$$

where ω is the shaft speed. Figure 8 illustrates f versus $u_{\theta 0}$. Theory versus experimental results are presented for the seal with no swirl brake. Measured results are much more sensitive to changes in the pressure ratio than predictions. Typically, f is underpredicted at low values for $u_{\theta 0}$, and measured values for f increase more slowly with increasing $u_{\theta 0}$ than predicted. For the results available, correlation between theory and experiment improve as running speed increases.

Figure 9 compares f versus $u_{\theta 0}$ results with and without the swirl brake. Obviously, the swirl brake sharply reduces f and sharply increases stability of the seal. The scaling used in this figure suggests that the swirl brake is becoming less effective as speed increases; however, figure 10 shows that the swirl brake is exceptionally effective at the highest speed. With the swirl brake, f decreases with increasing $u_{\theta 0}$ and is much lower.
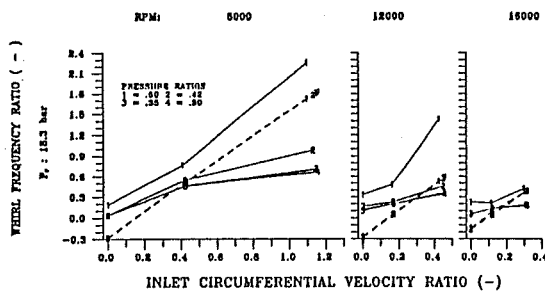
8. Theory and experimental results for f versus $u_{\theta 0}$, no swirl brake; $P_r = 18.3 bars.$
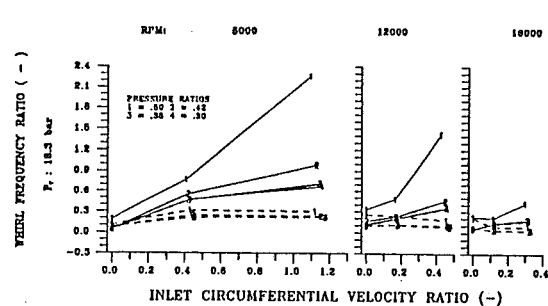
9. f versus $u_{\theta 0}$ with and without a swirl brake; $P_r = 18.3 bars.$
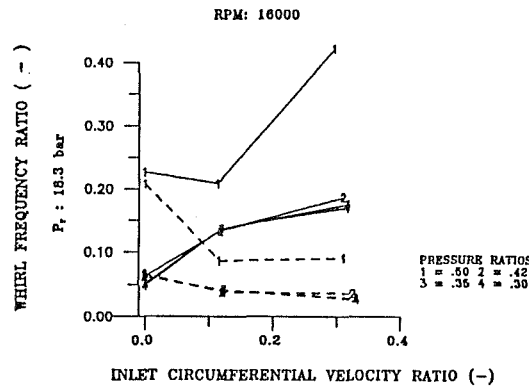
10. f versus $u_{\theta 0}$ with and without a swirl brake; $\omega = 16,000 rpm$; $P_r = 18.3 bars$.

Discussion

The outstanding effectiveness of the swirl brake in reducing destabilizing forces developed by the seal largely speaks for itself. The present results echo those of a companion paper, Childs et al.(1990), in emphasizing the advantages accruing to an aerodynamically designed swirl brake.

As noted earlier, Scharrer's(1988) theory uses Hirs(1973) results to model the wall shear stresses on the fluid. Hirs' model defines the stress on the fluid at a wall in terms of the friction-factor definition

$$\lambda = nR^m$$

where the Reynolds number R is defined in terms of the average bulk-flow velocity relative to the wall. The empirical parameters n, m characterize wall roughness. The present theoretical predictions used

$$nr = 0.079, \qquad mr = -0.25 \tag{3}$$

for the smooth rotor, and

$$ns = 0.047, \qquad ms = -0.1275 \tag{4}$$

for the honeycomb stator surfaces. The results of equation (3) were developed by Yamada(1962) from measurements of flow between rotating cylinders. The results of equation(4) are from Ha(1989) and are based on flat-plate test results for the honeycomb cell dimensions used in this study. When friction factors based on the coefficients of equation(4) are plotted on a Moody diagram, the equivalent relative roughness parameter is about 0.03. When the friction factor was increased(arbitrarily) by about a factor of twenty, much better agreement between theory and measurements were obtained. The authors have no explanation for this

188

result and do not endorse this sort of arbitrary manipulation of the model; however, the results suggest that higher energy dissipation is present in the seal than accounted for by Scharrer's(1988) model. Since the empirical model used for leakage predictions does not account for a deliberately roughened stator, no comparisons are presented between theory and experiment for leakage.

SUMMARY AND CONCLUSIONS

Swirl-Brake Effectiveness

The aerodynamically-designed swirl brake proposed for the ATD-HPFTP turbine interstage seal is remarkably effective. It reduces k markedly and actually yields a reduction in k with increasing values for $u_{\theta 0}$.

Theory versus Experiment

A summary review of theory versus experiment for the rotordynamic coefficients and the whirl frequency ratio follows:

K: The theory does a good job at low speeds; however, as the speed increases, K is substantially underpredicted. As the speed is increased, increasing supply pressure magnifies this difference between theory and experiment. Measured values of K are more sensitive to changes in Pra than predicted. Also, in contrast to predictions, measured K values increase with increasing Pra.

k: The theory does a good job at low speeds and low supply pressures. Increases in either the speed or supply pressure degrades agreement between theory and prediction. Typically, k is underpredicted for zero $u_{\theta 0}$ and increases more slowly than predicted. Also, k is much more sensitive to changes in Pra than predicted.

C: The theory underpredicts C, but the correlation improves(slightly) as speed is increased. Measured results are more sensitive to changes in Pra than predicted.

$f = k/C\omega$: The theory does a reasonable job, and the comparison between theory and experiment improves as speed is increased. Measured f values are higher than predicted at low values of $u_{\theta 0}$. A reasonable prediction of f results from compensating errors in predicting C(too high) and k(too low) for higher values of $u_{\theta 0}$.

Conclusions

The results presented here support the following general conclusions:

(a) The proposed swirl brake design is remarkably effective.

(b) Scharrer's(1988) theory can provide some basic guidance for the analysis of tooth-on-rotor/honeycomb stator annular seals; however, discrepancies between theory and measurements can be pronounced. An improved theoretical model for this type of seal is clearly needed.

REFERENCES

Benchert, H., and Wachter, J.(1980), "Flow Induced Spring Coefficients of Labyrinth Seals for Application in Rotordynamics," NASA CP2133, Proceedings of the workshop: Rotordynamic Instability Problems in High Performance Turbomachinery, held at Texas A&M University, 12-14 May 1980, pp. 189-212.

Childs, D. W., Baskharone, E. A., and Ramsey, C.(1990), "Test Results for Rotordynamic Coefficients of the SSME HPOTP Turbine Interstage Seal With Two Swirl Brakes," submitted for review *ASME Journal of Tribology*, Feb. 1990.

Childs, D. W., and Scharrer, J.(1988), "Theory Versus Experiment for the Rotordynamic Coefficients of Labyrinth Gas Seals: Part II - A Comparison to Experiment," *ASME Journal of Vibration, Acoustics, Stress, and Reliability in Design*, Vol. 110, No. 3, July 1988, pp. 281-287.

Childs, D. W., Nelson, C. E., Nicks, C., Scharrer, J., Elrod, D., and Hale, K.(1986), "Theory Versus Experiment for the Rotordynamic Coefficients of Annular Gas Seals: Part 1-Test Facility and Apparatus," *ASME Transaction Journal of Tribology*, Vol. 108, pp. 426-432.

Ha, T. W.(1989), "Friction Factor Data for Flat-Plate Tests of Smooth and Honeycomb Surfaces," TL-SEAL-1-89, Turbomachinery Laboratory Report, Texas A&M University, May 1989.

Hawkins, L., Childs, D., and Hale, K.(1988), "Experimental Results for Labyrinth Gas Seals With Honeycomb Stators: Comparisons to Smooth Stator Seals and Theoretical Predictions," *ASME Journal of Tribology*, Vol. 111, No. 1, pp. 161-168, Jan. 1989.

Hirs, G. G.(1973), "A Bulk-Flow Theory for Turbulence in Lubricant Films," *ASME Journal of Lubrication Technology*, April 1973, pp. 137-146.

Holman, J. P.(1978), *Experimental Methods for Engineers*, McGraw Hill, 1978, pp. 45.

Scharrer, J.(1988), "Theory Versus Experiment for the Rotordynamic Coefficients of Labyrinth Gas Seals: Part I - A Two Control Volume Model," *ASME Journal of Vibration, Acoustics, Stress, and Reliability in Design*, Vol. 110, No. 3, July 1988, pp. 270-280.

Yamada, Y.(1962), "Resistance of Flow Through an Annulus with an Inner Rotating Cylinder," *Bull. JSME*, Vol.5, No. 18, 1962, pp. 302-310.

SUPPRESSION OF SUBSYNCHRONOUS VIBRATION IN THE SSME HPFTP

David G. Becht, Larry A. Hawkins, Joseph K. Scharrer,
and Brian T. Murphy
Rockwell International
Canoga Park, California 91304, U.S.A.

SSME HPFTP hot-fire dynamic data evaluation and rotordynamic analysis both confirm that two of the most significant turbopump attributes in determining susceptibility to subsynchronous vibration are impeller interstage seal configuration and rotor sideload resulting from turbine turnaround duct configuration and hot gas manifold. Recent hot-fire testing has provided promising indications that the incorporation of roughened "damping" seals at the impeller interstages may further increase the stability margin of this machine. A summary of the analysis which led to the conclusion that roughened seals would enhance the stability margin is presented herein, along with a correlation of the analysis with recent test data.

NOMENCLATURE

DN	Bearing Bore Diameter (mm) times shaft speed (rpm)
FMOF	First Manned Orbital Flight
FPL	Full Power Level
FWR	Forward Wear Ring
Grms	Accelerations (G's) root mean square
HPFTP	High Pressure Fuel Turbopump
HGM	Hot Gas Manifold
LOSI	Linear Onset Speed of Instability
RWR	Rear Wear Ring
SSME	Space Shuttle Main Engine
TAD	Turnaround Duct

INTRODUCTION

Since SSME testing began in mid-1975, it became apparent that two of the key design features which determined the high pressure fuel turbopump's susceptibility to subsynchronous vibration were the interstage seal configuration and the turbine turnaround duct configuration (affecting aerodynamic sideload). The purpose of this paper is to present the evolution of the design and supporting rotordynamic analyses of the turbopump, which ultimately led to increased stability margin and the elimination of subsynchronous vibration from the SSME HPFTP.

TURBOPUMP DESCRIPTION

A cross section of the SSME HPFTP rotor is shown in figure 1. Its rotating assembly weight of only 578 N (130 lbs), combined with a maximum rating of 57.4 MW (77,000 hp), makes it one of the highest power-to-weight ratio machines ever built. Table 1

shows some of the more significant operating parameters associated with the Full Power Level (FPL) rating.

The turbopump consists of three identical pump stages driven on a common built-up shaft by a two stage turbine. The shaft is supported radially by two pairs of preloaded duplex bearings. All four bearings have 45 mm bores, and operate at a DN in excess of 1.6 million. The outer race of each bearing can slide axially in its housing to accommodate shaft growth/contraction and small amounts of axial travel brought on by changes in thrust balance. Transient thrust imbalances experienced during start-up and shut-down are reacted by an additional mechanical bearing at the pump end of the shaft. During mainstage operation (>12,000 cpm), the shaft lifts off this bearing as a balance piston, integral with the third stage pump impeller, becomes active.

The turbopump has a pair of high-pressure interstage seals located between the 1st and 2nd stage pump impellers and the 2nd and 3rd stage pump impellers. The influence of these interstage seals, along with the aerodynamic sideload generated by the turbine discharge gases flowing through the turnaround duct and hot gas manifold, on the rotordynamics of the turbopump is appreciable, as will be developed later.

DISCUSSION OF SUBSYNCHRONOUS VIBRATION

Two primary mechanisms are postulated as potential causes of turbopump subsynchronous vibration of the type experienced on this machine: 1) forced vibration response due to interaction of the rotor with a support nonlinearity such as bearing deadband, and 2) self-excited rotor whirl at the first rotor mode frequency.

The first mechanism, called deadband interaction, refers to the behavior of a rotor passing through the bearing deadband clearance of at least one of its bearings. If a rotor's orbit passes through the bearing deadband, it will experience reduced effective stiffness compared to an orbit which does not pass through the deadband. This reduced stiffness may potentially lower the rotor vibration mode frequencies. If the rotor is operated at a speed that is just less than twice the natural frequency of a rotor mode, deadband interaction can lower the frequency of that mode to one half of the operating speed. The synchronous forcing function (unbalance) may then excite the second harmonic of this mode, causing all harmonics and the fundamental to respond. The result is a forced vibration response of the rotor mode at 50% of the synchronous frequency. This phenomenon is well documented in papers by Ehrich, Bently, and Childs (references 1-3). In the SSME HPFTP operating at FPL, the synchronous speed is 1.8 to 1.9 times the predicted first rotor mode frequency. Thus, subsynchronous vibration at 50% of the synchronous frequency can result if conditions are correct for deadband interaction.

The second mechanism, referred to as limit cycle whirl, can occur with any machine that possesses whirl drivers capable of causing one of the rotor modes to become unstable. If a rotor mode becomes linearly unstable, its orbit will grow until some nonlinearity in the system limits further growth. Such nonlinearities may be 1) the nonlinear load-deflection characteristic of ball bearings or other rotor support elements, and 2) light rubbing at various seal locations.

The potential whirl drivers in the HPFTP include cross-coupled stiffness of the pump impellers or impeller interstage seals, turbine aerodynamic forces, and internal rotor friction. Current estimates for the interstage seal coefficients, bearing stiffnesses, and other rotor support parameters result in a rotor that has a linear

stability threshold speed greater than 50,000 cpm. However the nonlinear stability threshold could be less than the linear value due to interaction of the rotor with system nonlinearities such as bearing deadband. Since the linear first mode is nominally 52% to 55% of synchronous, limit cycle whirling of the first mode could produce 47% to 52% subsynchronous vibration response.

ROTORDYNAMIC ANALYSIS AND TEST RESULTS

Rotordynamic Model The linear elastic model of the rotating assembly (shown in figure 2) is comprised of cylindrical and tapered finite element beam elements. Complete descriptions of the model and the solution technique are presented by Murphy et al. (ref. 4).

All of the key elements in the model are defined throughout the turbopump operating speed range using appropriate computer codes. Ball bearing load-deflection curves are obtained using an industry standard quasi-static rolling element bearing program by Jones (ref. 5). The bearing stiffness is then combined in series with a bearing support stiffness before input to the rotordynamic model. The relatively small rotordynamic coefficients for the impeller wear ring seals were estimated using results from the short seal analysis of Childs (ref. 6), since no theory currently exists to adequately predict rotordynamic coefficients for incompressible flow labyrinth seals. The turbine interstage seal coefficients were calculated using the analysis by Scharrer (ref. 7). Both turbine stages are unshrouded, and the load split between them is 50/50, so experience dictates that the aerodynamic cross-coupling be based on an efficiency factor of $\beta=1.5$ (ref. 8). Interstage seal coefficients for the roughened seal configuration are calculated with a bulk flow model for arbitrary clearance functions (ref. 9). Table 2 lists all these coefficients for the FPL rating.

Nonlinear Analysis As outlined previously, the proposed scenarios by which subsynchronous vibration is generated in the HPFTP all involve interaction of the rotor with nonlinearities in its support elements. Therefore meaningful predictions of subsynchronous response can only be performed using a nonlinear rotordynamic model, specifically performing a transient simulation. In this nonlinear simulation model, the equations of motion are integrated numerically with time to yield steady state responses. Due to the on/off nature of some of the nonlinearities, all results reported herein employed first order integration schemes with a time step of about 12 microseconds.

In the so called deadband interaction scenario, where subsynchronous vibration would nominally be at 50% of pump speed, the nonlinear model can easily be made to exhibit this phenomenon by adjusting the eccentricities, bearing deadband, and unbalance distribution (all well within expected tolerance bands). For cases where the vibration is at other than 50%, it has been hypothesized that it is a limit cycle whirl of the first rotor mode. This type of motion has also been simulated with the nonlinear rotordynamic model. To achieve this, however, it was found necessary to lower the logarithmic decrement of the first mode by altering the bearing and interstage seal coefficients. Changes to the coefficients on the order of 5% to 10%, in addition to reducing the static sideloads by 25%, were necessary to bring on the limit cycle whirl. These changes reduced the log dec by about half, while still maintaining a linear onset speed of instability (LOSI) greater than 50,000 cpm.

Numerous studies of HPFTP subsynchronous vibration behavior have been conducted employing both the deadband interaction and the limit cycle whirl models. The

standard approach is to adjust mass and seal eccentricities to match measured synchronous and subsynchronous housing acceleration levels for a given test of a particular unit. This model is then used as a basis for investigating the sensitivity of the HPFTP to various parameter changes. One of the more comprehensive studies was done by matching the model to a particular Phase II unit which displayed 4.0 Grms of synchronous vibration and 1.5 Grms of 50% subsynchronous vibration at 109% power level. Figure 3 shows typical results employing the deadband interaction mechanism to induce the subsynchronous vibration, and in this case shows how variations in turbine sideload affects the amplitude of the synchronous and subsynchronous vibration components.

Influence of Interstage Seal Design For the original three stepped labyrinth seal design incorporated prior to the whirl problem, the LOSI was predicted to be about 20,000 cpm (ref. 10). With the incorporation of the stepped smooth seals, the predicted LOSI was increased to about 40,000 cpm. Additional stiffness in the ball bearing support structures was also an important contributor to this increase. Subsequent engine testing confirmed these predictions, as it was possible to operate up to full power level. However, the HPFTP henceforth experienced moderate levels of subsynchronous vibration, and an increase in stability margin was considered desirable. An example of housing accelerometer data typical of this configuration turbopump is shown in figure 4. In this particular test, the subsynchronous vibration frequency was at approximately 53% of synchronous, and comparable to synchronous in amplitude during certain portions of the test. Several tests with this configuration turbopump also showed subsynchronous vibration amplitudes greater than synchronous.

Rotordynamic analyses performed subsequent to the 1976 whirl investigation indicated that the stability margin of the pump could be further enhanced by changing the configuration of the impeller interstage seals from the 3-stepped smooth to a straight smooth design. This would effectively increase the stiffness and damping coefficients generated by the seals, and the LOSI was predicted to be greater than 50,000 cpm. Many model parameters are not valid beyond 50,000 cpm, so the actual value is not relevant. Engine test results, given in table 3, confirmed that the amplitude of subsynchronous vibration decreased significantly with the incorporation of the straight smooth interstage seal configuration. The percentage of turbopumps which displayed detectable levels was also somewhat lower, as indicated in table 3.

The goal of eliminating subsynchronous vibration completely led to consideration of other interstage seal configurations, specifically the straight rough design. Rotordynamic analyses performed as early as 1983 predicted that the stability margin of the HPFTP could be further enhanced by changing the impeller interstage seal configuration from the straight smooth to a straight rough design, which was predicted to provide increased damping by the seals for just a slight decrease in stiffness.

Since LOSI could not be used as an indicator of relative stability, a logarithmic decrement criteria was established at this point. A comparison of first mode log dec's at FPL shows the straight smooth configuration at 0.14, while the straight rough configuration has a log dec of 0.22. Therefore enhanced stability margin would be expected for turbopumps incorporating the roughened interstage seal design.

Influence of Turn Around Duct Design At approximately the same time as the change from a 3-stepped to a straight smooth seal, a change was proposed for the turbine turnaround duct design which was intended to improve turbine efficiency and reduce the turbine temperatures. This new design came to be known as the FPL turnaround

duct configuration, and was incorporated into the development configuration of the HPFTP in 1981, soon after the straight smooth interstage seals. A block change was subsequently made to the pump design, incorporating these and other rotordynamically less significant modifications, the resulting configuration henceforth referred to as Phase I.

It was eventually determined that the analytical tools available at that time did not adequately predict the turbine aerodynamic effects, and the FPL turnaround duct actually had higher resistance and greater transverse pressure differential across the turbine than the FMOF configuration. This had the effect of increasing the aerodynamic sideload acting on the rotor to about 1.33 times that of the FMOF duct. As illustrated in figure 3, this increase in sideload was predicted to suppress subsynchronous vibrations. This prediction was verified by test, with almost no occurrences of subsynchronous vibration ever experienced on the Phase I HPFTP.

After considerable ground testing and flights with the Phase I HPFTP, it became apparent that the reduced turbine efficiency and higher tempuratures generated by the FPL turnaround duct were detrimental to the life of the turbine blades, and the turnaround duct configuration had to be returned to the FMOF design, except with thicker sheet metal walls (called FMOF II). Again, this modification along with several other rotordynamically less significant changes were instituted in a block change in 1985, with the resulting configuration referred to as Phase II.

<u>Influence of Hot Gas Manifold Design</u> Since modifications to the turbine turnaround duct had failed to be effective in reducing the resistance to turbine hot gas flow, a different approach was subsequently adopted. With the advent of improved aerodynamic analysis techniques, such as CFD analysis, it was determined that one significant contributor to turbine flow resistance was the relatively inefficient 3-duct hot gas manifold used to channel the turbine discharge flow from the turbopump to the main injector. A design alternative was proposed, which predicted that two recontoured ducts could transfer the hot gas more efficiently than the current 3-duct arrangement, thus reducing turbine back pressure and turbulence in the hot gas flow. A further consequence of this modification was predicted to be lower transverse pressure across the turbine and correspondingly lower rotor aerodynamic sideload. As predicted in figure 3, the reduced sideload (about 0.56 x FMOF sideload) would be expected to increase the amplitude and frequency of occurrence of subsynchronous vibration in a Phase II HPFTP used in conjunction with a 2-duct hot gas manifold.

Coincidently, the first 2-duct hot gas manifold powerhead and the first HPFTP to incorporate straight rough interstage seals were completed and ready for development testing at approximately the same time, May 1989. To minimize the risk of testing a new powerhead design with an unproven HPFTP design, the 2-duct hot gas manifold engine was first tested with a Phase II pump that had significant test time on other engines and had not experienced subsynchronous vibration. However, with its first test on the 2-duct HGM engine, it exhibited subsynchronous vibration at rated power level, as illustrated in figure 5, which Phase II pumps rarely ever did. Based on other performance data, it was verified that the turbine had achieved the predicted reduction in turbulence and transverse pressure differential. Consequently, the appearance of subsynchronous vibration in this Phase II pump confirmed the predicted reduction in stability margin resulting from the lower rotor sideload.

The next test on the 2-duct HGM engine was conducted with the first roughened interstage seal turbopump, and it did not experience subsynchronous vibration at any power level, as shown in figure 6. Since that time, the straight rough interstage seals have been tested in 3 different turbopumps, a total of 23 tests and over 12,000

seconds on several different engines, including both the 2-duct and 3-duct HGM, and encompassing all power levels up to and including FPL. None of the tests to date have shown any indication of subsynchronous vibration on this configuration HPFTP. Turbopumps which incorporate this change are currently being prepared for certification as part of the sustained flight configuration.

CONCLUSION

In general, the stability trends observed throughout the HPFTP test history have been simulated quite accurately by the current rotordynamic model. Two points continue to be reinforced through all the numerous parametric studies performed with this model. First, the stability ratio of the interstage seal configuration, evolving from stepped labyrinth to stepped smooth to straight smooth and eventually to straight rough, always had a significant influence on the machine's susceptibility to subsynchronous vibration and its associated amplitude. Second, the same conclusion can be made regarding the influences of aerodynamic sideload, as its contributing components evolved from FMOF I TAD to FPL TAD to FMOF II TAD to 2-duct HGM. Finally, it appears that a long standing goal of increasing the stability margin sufficiently to totally suppress subsynchronous vibration in this machine may be realized through the incorporation of straight rough impeller interstage seals.

REFERENCES

1. Ehrich, F. F., "Subharmonic Vibrations of Rotors in Bearing Clearance", ASME Paper 66-MD-1, Design Engineering Conference and Show, Chicago, Ill., May 1966.

2. Bently, D., "Forced Subrotative Speed Dynamic Action of Rotating Machinery", ASME Paper 74-PET-16, Petroleum Mechanical Engineering Conference, Dallas, Texas, Sept 1979.

3. Childs, D. W., "Fractional-Frequency Rotor Motion Due to Nonsymmetric Clearance Effects", ASME Paper 81-GT-145, International Gas Turbine Conference and Products Show, Houston, Texas, March 1981.

4. Murphy, B.T., Scharrer, J.K., and Hawkins, L.A., "The SSME HPFTP Wavy Interstage Seal: Part II-Rotordynamic Analysis", ASME Publication DE-Vol. 18-2, Machinery Dynamics - Applications and Vibration Control Problems, 1989, pp. 95-100.

5. Jones, A. B., "A General Theory for Elasically Constrained Ball and Radial Roller Bearings Under Arbitrary Load and Speed Conditions", ASME Journal of Basic Engineering, Vol. 82, 1960, p. 309.

6. Childs, D. W., "Dynamic Analysis of Turbulent Annular Seals Based on Hir's Lubrication Equation", ASME Journal of Lubrication Technology, Vol. 105, No. 3, 1983, pp. 437-445.

7. Scharrer, J.K., "Theory Versus Experiment for the Rotordynamic Coefficients of Labyrinth Gas Seals: Part I-A Two Control Volume Model," ASME Transactions Journal of Vibrations, Acoustics, Stress, and Reliability in Design, Vol. 110, No. 3, July 1988, pp. 270-280.

8. Alford, J.S., "Protecting Turbomachinery From Self-Excited Rotor Whirl", ASME Journal of Engineering for Power, 1965, pp. 333-344.

9. Scharrer, J.K. and Nunez, D.J., "The SSME HPFTP Wavy Interstage Seal: Part I-Seal Analysis", Publication DE-Vol. 18-2, Machinery Dynamics - Applications and Vibration Control Problems, 1989, pp. 101-108.

10. Childs, D. W., "The Space Shuttle Main Engine High Pressure Fuel Turbopump Rotordynamic Instability Problem", ASME Journal of Engineering for Power, Vol. 100, 1978, pp. 48-57.

Table 1. FPL Operating Parameters for SSME HPFTP

Rotating Speed	36,600 cpm	36,600 rpm
Pump Flow Rate	67,000 lpm	17,000 gpm
Pump Inlet Pressure	23.5 Bar	341 psi
Pump Discharge Pressure	482 Bar	6,990 psi
Turbine Inlet Tempurature	994 K	1,790 R
Turbine Inlet Pressure	338 Bar	4,900 psi
Power	57.4 MW	77,000 hp

Table 2. Rotordynamic Coefficients for Rotor Support Elements

	K_{xx} (lbs/in)	K_{xy} (lbs/in)	C_{xx} (lb-sec/in)
Ball Bearing (w/ Support)	370,000		
1st Stage Imp FWR+RWR	45,000	5,000	2.7
2nd Stage Imp FWR+RWR	29,000	4,600	2.5
3rd Stage Imp FWR	7,700	1,500	0.0
Turbine Interstage Seal	3,300	2,800	1.5
Alford's (each turb stage)		18,700	
1-2 Pump Interstage Seal	460,000	253,000	106
2-3 Pump Interstage Seal	460,000	253,000	106

Table 3. Occurrence of Subsynchronous Vibration with the Three Stepped and Straight Smooth Seals

Seal Type	# Units Tested	# Units w/ Subsync	%	Avg Subsync Amplitude	Avg Sync Amplitude
Three Step	63	13	21%	5.1 Grms	5.9 Grms
Str Smooth	70	12	17%	1.2 Grms	4.9 Grms
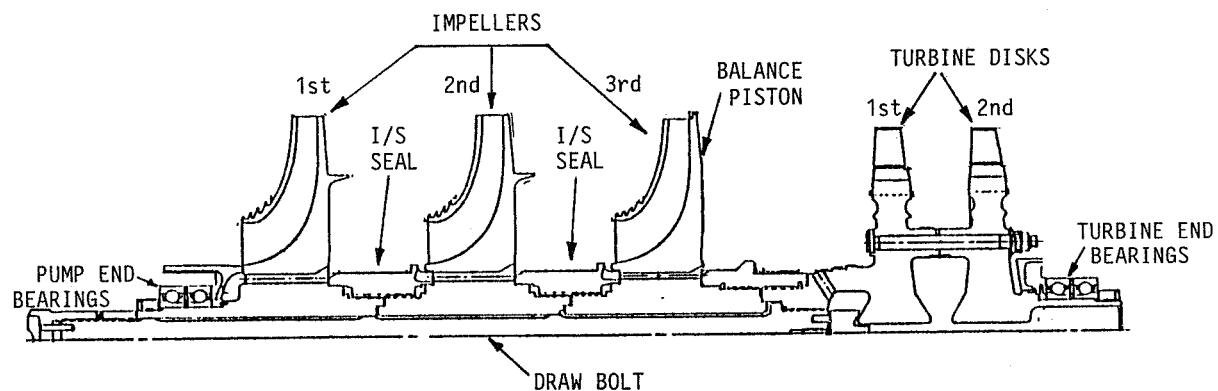
FIGURE 1. HALF CROSS SECTION OF HIGH-PRESSURE FUEL TURBOPUMP
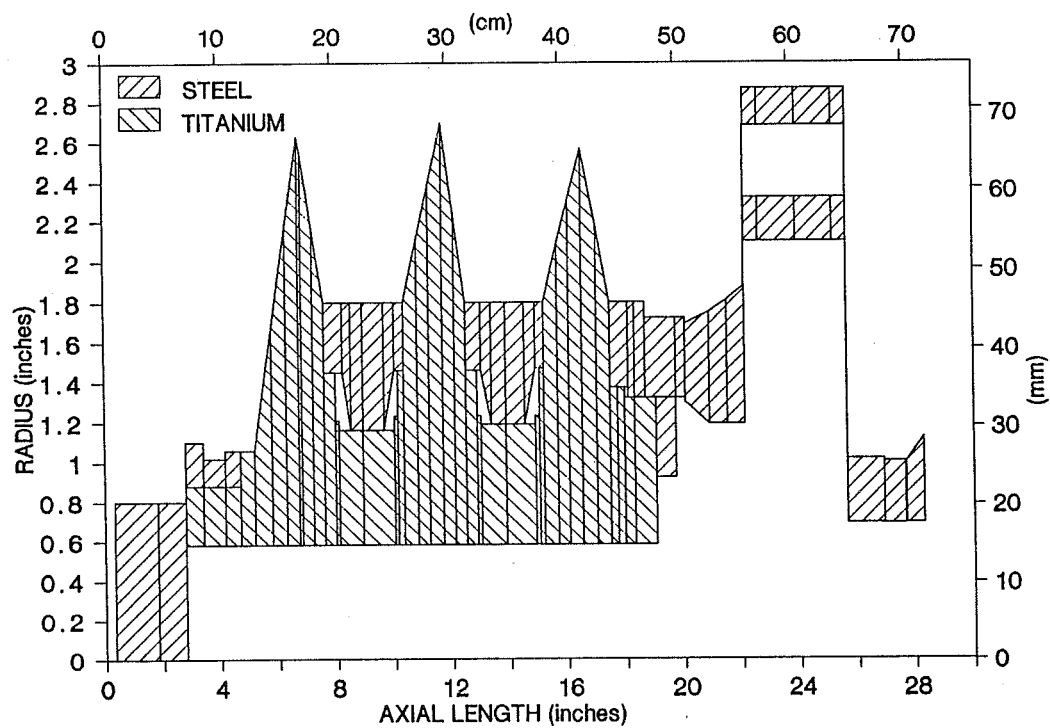
FIGURE 2. SSME HPFTP ROTORDYNAMIC SHAFT ELASTIC MODEL.

TURBINE SIDELOAD VARIATION
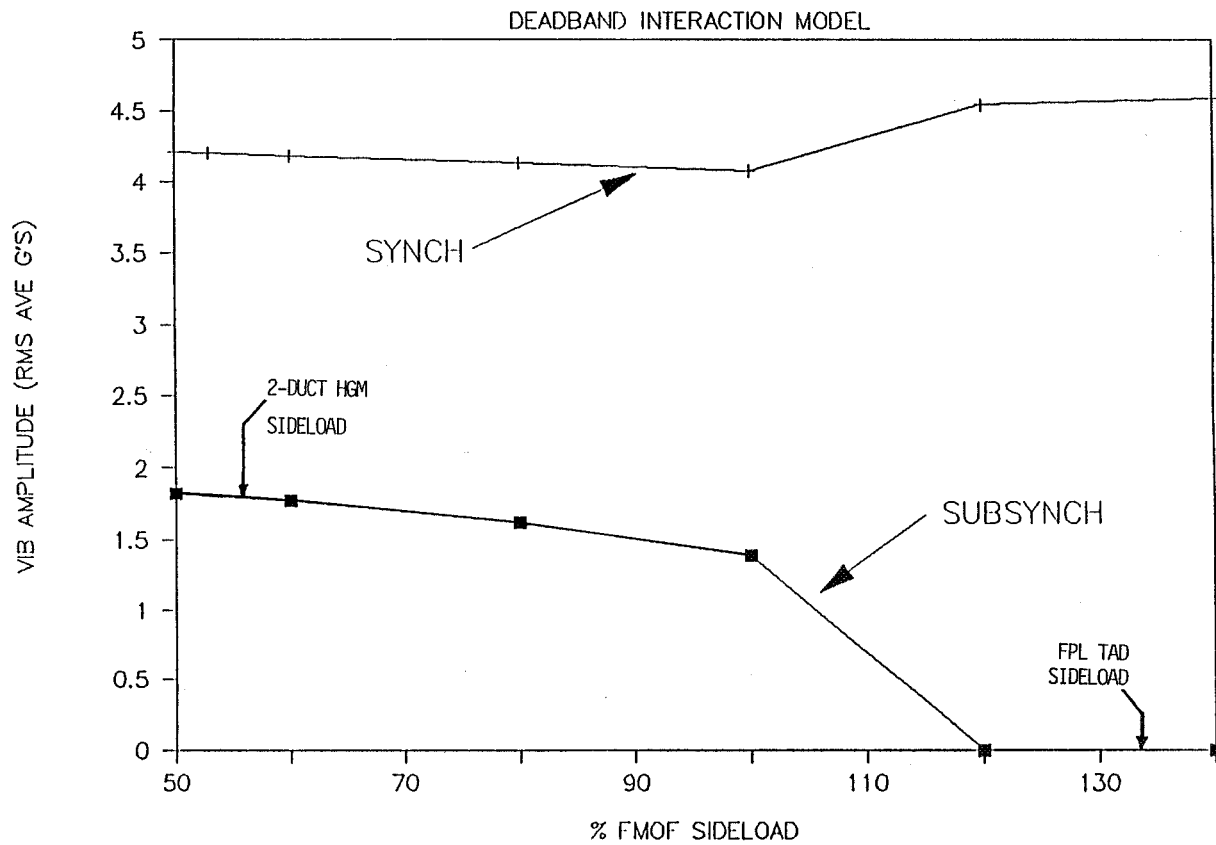
FIGURE 3. TURBINE SIDELOAD INFLUENCE ON VIBRATION AMPLITUDE

SYNCHRONOUS

SUBSYNCHRONOUS

VOLTS/LINE=.08951/4.

FREQUENCY, HERTZ

TIME BASE EXP.=.5

RMS POWER SPECTRAL DENSITY
750-077-0112 SSME PMPS TR 2   100% RPL
HPFP RAD 180 CH-2

BANDWIDTH=4. HERTZ
COMPOSITE RMS=13.47 G'S

FILTER 1. KILOHERTZ L/P

TIME 14:24:134.0-14:24:137.0

G'S
PER HZ

SUBSYNCHRONOUS

SYNCHRONOUS

FREQUENCY, HERTZ

CHANNEL BIAS CAL RANGE=746.   CAL VOLTS=1.043
TIME BASE EXPANSION=1.   ATTENUATOR SETTING=53   FRAME COUNT=11

FIGURE 4.   TURBOPUMP VIBRATION SPECTRA WITH
3-STEPPED I/S SEALS, FMOF TAD

200

SSME -- POWER SPECTRAL DENSITY -- TEST 901-599
FASCOS HPFP 0 -- S+ 6.0 - 9.2 -- POWER LEVEL PROFILE 100. %RPL
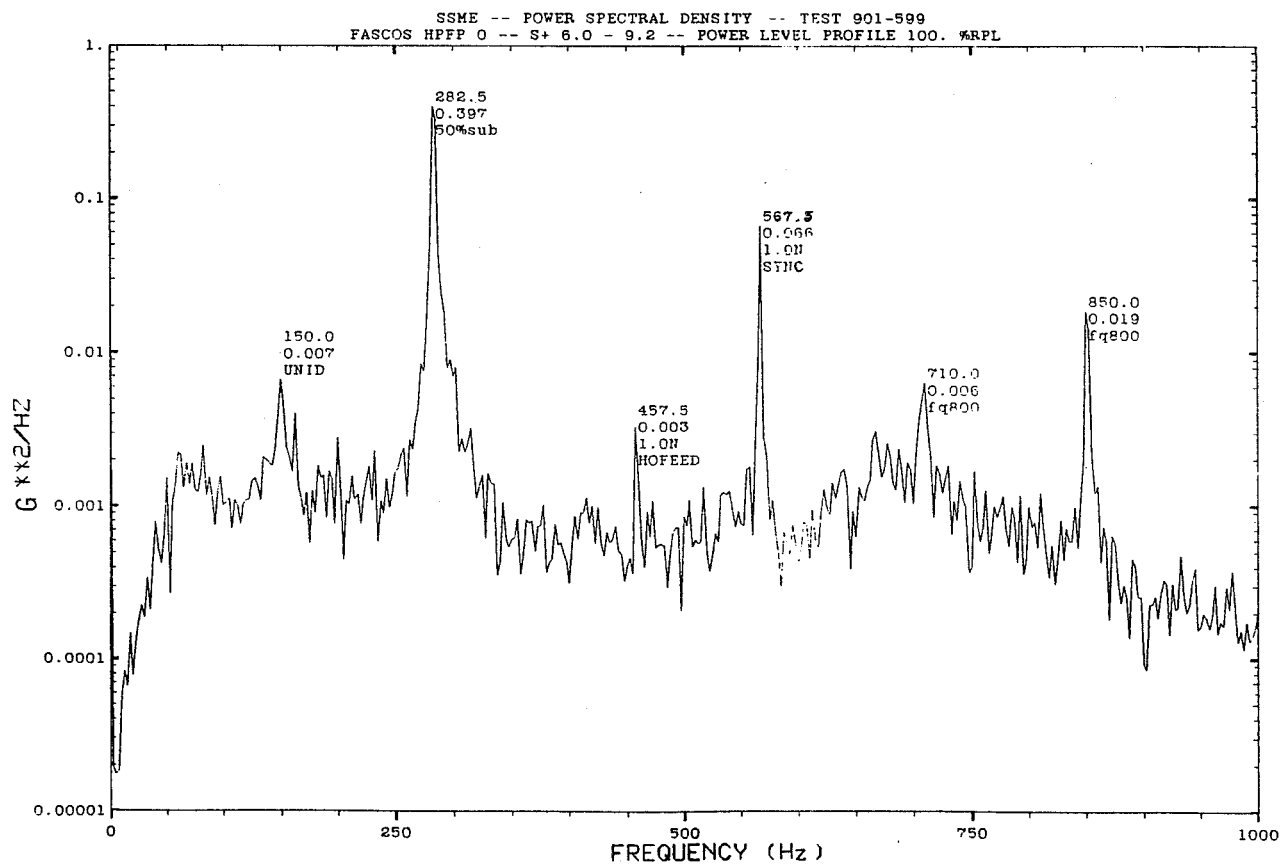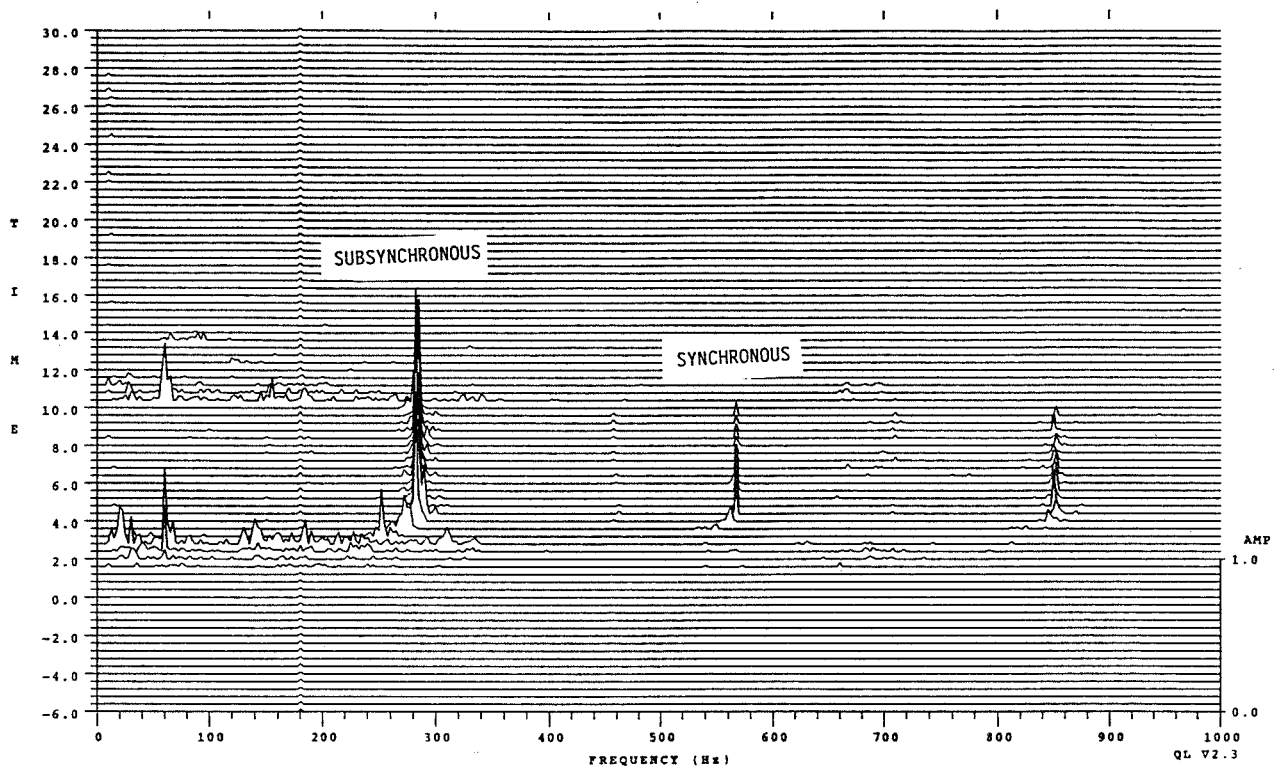
FIGURE 5.   TURBOPUMP VIBRATION SPECTRA WITH
STR-SMOOTH I/S SEALS, 2-DUCT HGM

201
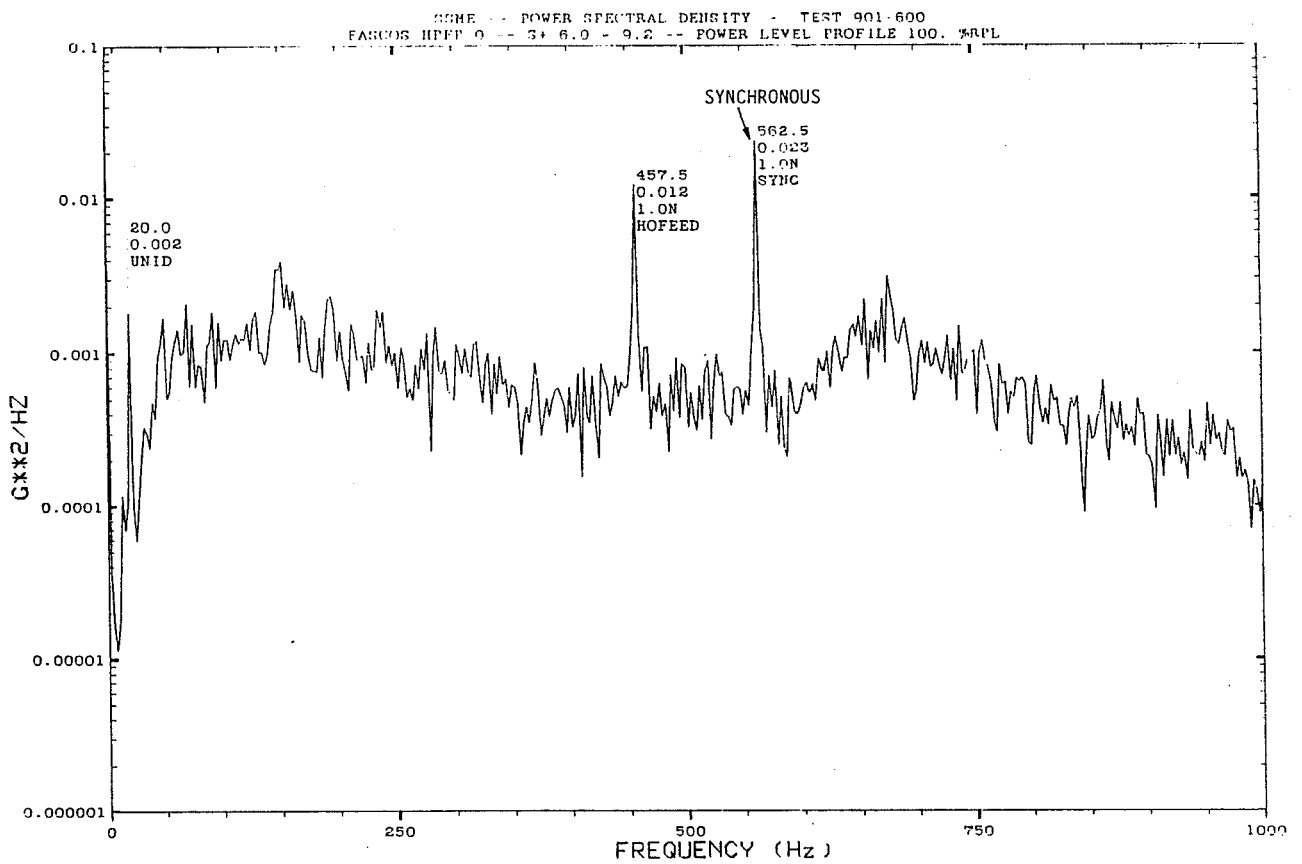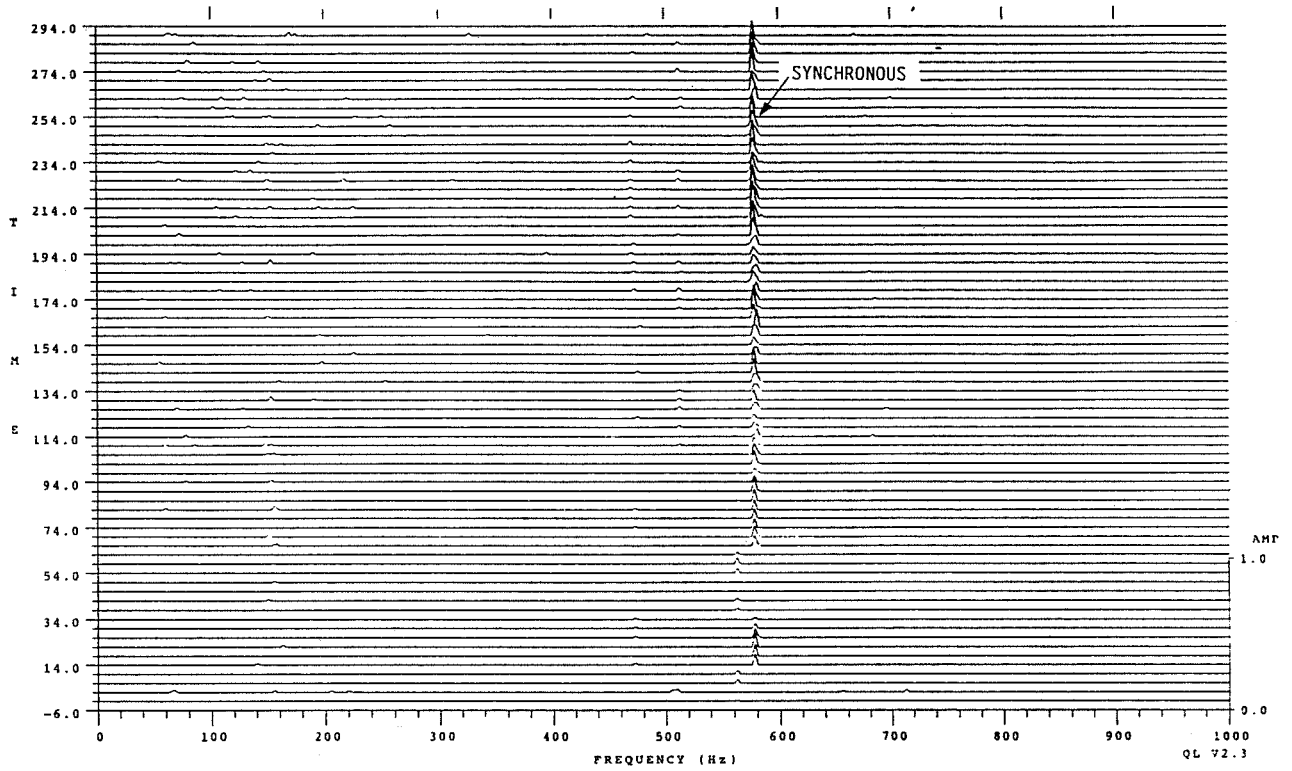
FIGURE 6.   TURBOPUMP VIBRATION SPECTRA WITH
STR-ROUGH I/S SEALS, 2-DUCT HGM

DETERMINATION OF ROTORDYNAMIC COEFFICIENTS FOR LABYRINTH SEALS AND APPLICATION TO ROTORDYNAMIC DESIGN CALCULATIONS

P. Weiser and R. Nordmann
Department of Mechanical Engineering
University of Kaiserslautern
Kaiserslautern, Federal Republic of Germany

In today's rotordynamic calculations, the input parameters for a Finite Element Analysis (FEA) determine very much the reliability of Eigenvalue and Eigenmode predictions. While modelling of an elastic structure by means of beam elements etc. is relatively straightforward to perform and the input data for journal bearings are usually known exactly enough, the determination of stiffness and damping for labyrinth seals is still the subject of many investigations. Therefore, the rotordynamic influence of labyrinths is often not included in FEA for rotating machinery because of a lack of computer programs to calculate these parameters. This circumstance can give rise to severe vibration problems especially for high performance turbines or compressors, resulting in remarkable economic losses.
The forces generated in labyrinths can be described for small motions around the seal center with the linearized force-motion relationship of eq. 1:

$$\begin{bmatrix} K & k \\ -k & K \end{bmatrix} \begin{bmatrix} u_1 \\ u_2 \end{bmatrix} + \begin{bmatrix} D & d \\ -d & D \end{bmatrix} \begin{bmatrix} \dot{u}_1 \\ \dot{u}_2 \end{bmatrix} = - \begin{bmatrix} F_1 \\ F_2 \end{bmatrix} \tag{1}$$

where K, k are the direct and cross-coupled stiffness and D, d are the direct and cross-coupled damping. These elements are the so-called dynamic labyrinth coefficients.
Several years ago, we started with the development of computer codes for the determination of rotordynamic seal coefficients. The following sections will introduce our different approaches to evaluate the dynamic fluid forces generated by turbulent, compressible labyrinth seal flow.

203

NOMENCLATURE

K, k	Direct and cross-coupled stiffness	G	Labyrinth leakage
D, d	Direct and cross-coupled damping	r_a	Radius from seal center to stator
u_1, u_2	Rotor displacements		
$\dot{u}_1$, $\dot{u}_2$	Rotor velocities	r_i	Radius from seal center to end of seal fin
F_1, F_2	Labyrinth fluid forces		
Φ	General variable	x,y	cart. coordinates
Γ_Φ	Diffusion coefficient	$\overline{x},\overline{y}$	rot. coordinate system
S_Φ	Source term	w_i	preswirl
r, φ, z	Cylinder coordinates	τ	shear stress
η	Transformation coordinate	u,v,w	axial, radial and circumferential velocities
e	Perturbation parameter		
r_0	Rotor eccentricity		
Ω	Rotor precession frequency		
ω	Shaft rotational frequency		
h	Local seal clearance		
C_r	Nominal clearance		

Indices

0	Zeroth order	a	before labyrinth
1	First order	b	behind labyrinth

COMPUTATIONAL FLUID DYNAMICS METHODS (CFD)

The compressible, turbulent, time dependent and threedimensional flow in a labyrinth seal can be described by the Navier-Stokes equations in conjunction with a turbulence model. Additionally, equations for mass and energy conservation and an equation of state are required. These equations can be solved with the aid of a finite difference procedure. To determine the desired coefficients, two methods have been developed:

- 2-dimensional procedure based on a perturbation analysis
- 3-dimensional theory using a moving frame of reference rotating with the shaft.

PERTURBATION ANALYSIS

To describe the labyrinth seal flow, we use the time-averaged conservation equations for momentum, mass and energy and the equation of state for a perfect gas. The correlation terms of the turbulent fluctuation quantities are modeled via the k-ε turbulence model of LAUNDER and SPALDING /1/. All these equations can be arranged in the following generalized form:

$$\frac{\partial}{\partial t}(\rho \Phi) + \frac{\partial}{\partial z}(\rho u \Phi) + \frac{1}{r}\frac{\partial}{\partial r}(r\rho v \Phi) + \frac{1}{r}\frac{\partial}{\partial \varphi}(\rho w \Phi)$$

$$- \frac{\partial}{\partial z}\left(\Gamma_\Phi \frac{\partial \Phi}{\partial z}\right) - \frac{1}{r}\frac{\partial}{\partial r}\left(r\Gamma_\Phi \frac{\partial \Phi}{\partial r}\right) - \frac{1}{r}\frac{\partial}{\partial \varphi}\left(\frac{1}{r}\Gamma_\Phi \frac{\partial \Phi}{\partial \varphi}\right) = S_\Phi$$

(2)

where Φ stands for any of the dependent variables(e.g. velocities, pressure, temperature, density), Γ_Φ is the diffusion coefficient and S_Φ the source term. To calculate the dynamic coefficients, several assumptions are introduced:

1. small rotor motions around the seal center on a circular orbit
2. coordinate transformation
3. perturbation series expansion for the dependent variables
4. solutions for the dependent variables corresponding to the temporal and circumferential variation of the seal clearance function

Assumption 1 assures that we can use eq. 1 to calculate the dynamic coefficients.
When supposing that the shaft rotates on a circular orbit, one can imagine that the local seal clearance h varies in time for every location φ=const. To avoid the use of time dependent calculation grids, we transform the governing equations to another coordinate system by introducing a new radial coordinate η whereby the eccentrically moving shaft is converted to a shaft rotating in the center of the seal (see Fig. 1).
The third assumption, together with assumption 1, implies that the perturbation series

$$\Phi = e^0 \Phi_0 + e^1 \Phi_1 + e^2 \Phi_2 + \dots + e^n \Phi_n \qquad n = 1 \dots \infty \qquad (3)$$

for the dependent variables can be truncated after the linear term.
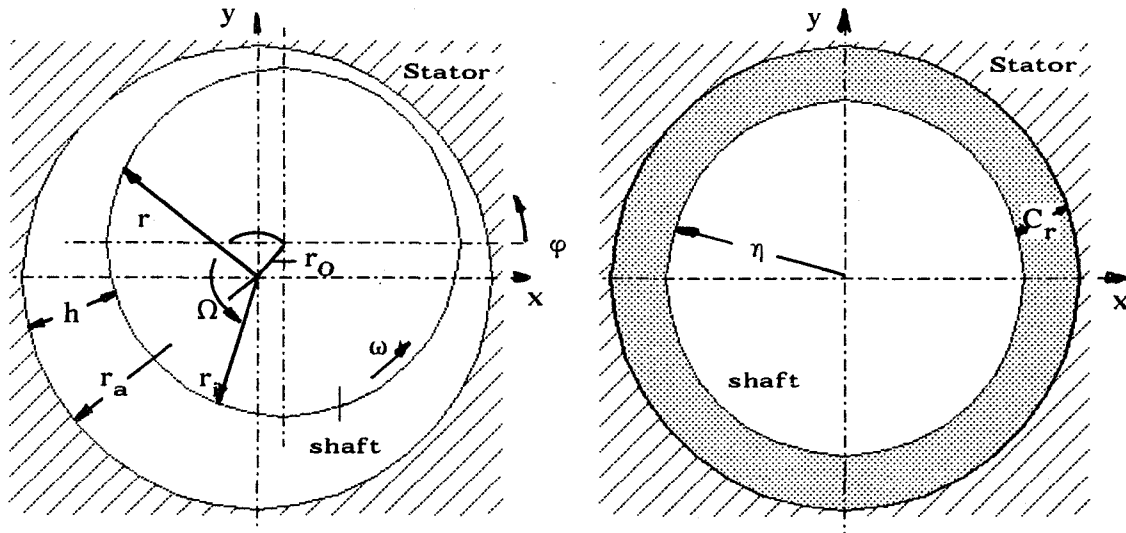
Fig. 1: Coordinate transformation

Inserting these equations for every dependent variable into the basic conservation relations yields two sets of equations. The zeroth order set describes the flow in the centric labyrinth while the first order equations are governing the flow field for small eccentric shaft motions. The last assumption allows the elimination of the temporal and circumferential derivatives in the first order equations analytically.

The seal clearance function for a circular shaft precession orbit around the seal center can be stated as

$$h = h_0 + e\,h_1 = C_r - X(t)\cos\varphi - Y(t)\sin\varphi \qquad (4)$$

Corresponding to this function, we assume that the dependent variables vary in the same way concerning the circumferential direction.

Thereby, the circumferential derivatives can be calculated analytically. After separating the equations into sine and cosine terms and rearranging them by introducing complex variables, solutions for the first order variables corresponding to the temporal change of seal clearance due to a circular shaft orbit are prescribed, allowing the elimination of the derivatives with respect to time. Finally, we obtain two sets of differential equations which have to be solved subquently in order to determine the desired coefficients.

THREEDIMENSIONAL METHOD

In contrast to the perturbation analysis, where we have made many assumptions to reduce the computational effort, the threedimensional procedure shows much greater generality in avoiding these restrictions. Again, the time-averaged conservation equations are solved

in conjunction with the already mentioned k-ε model.

To determine the dynamic coefficients we assume that the shaft moves on a circular orbit with precession frequency Ω around the seal center. Since this would normally result in a time dependent problem we introduce a rotating coordinate system which is fixed at the shaft center (Fig. 2). In this moving frame of reference, the flow is stationary. Due to the rotating coordinate system, centrifugal and coriolis forces occur in the equations for radial and circumferential momentum.
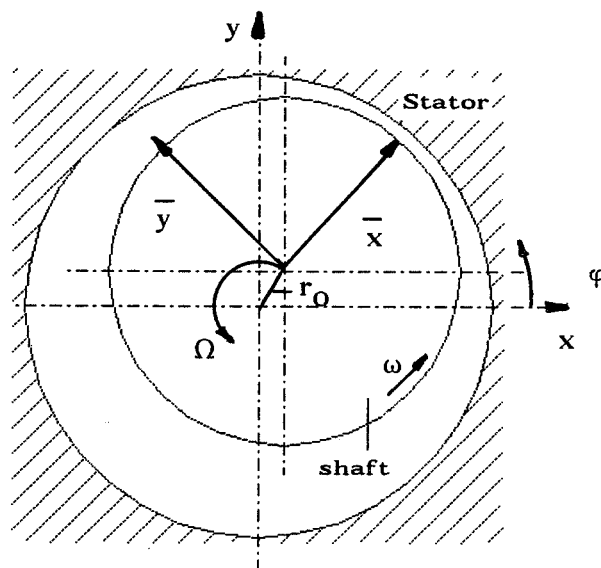
Fig. 2: Rotating coordinate system

SOLUTION PROCEDURE FOR THE CFD-METHODS

Because of the complexity of the derived equations, no analytic solution can be obtained. Therefore, there is a need for a numerical algorithm to solve the equations with the aid of a computer. We made our decision for the Finite Difference Method (FDM), which is well established in fluid dynamics.

The FDM procedure starts with the discretization of the calculation domain, which must be performed in a different manner for the two methods: While we can use a twodimensional Finite Difference grid for the perturbation analysis (Fig. 3), the threedimensional approach requires additional grids in the circumferential direction (Fig. 4).
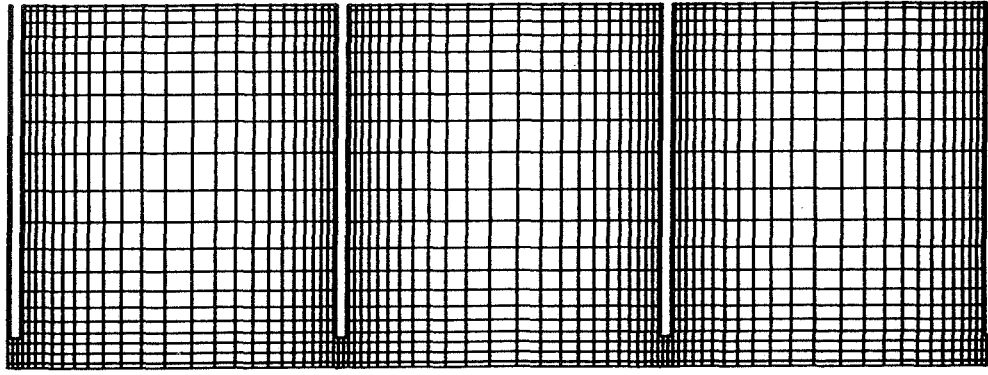
Fig. 3: Grid for perturbation method
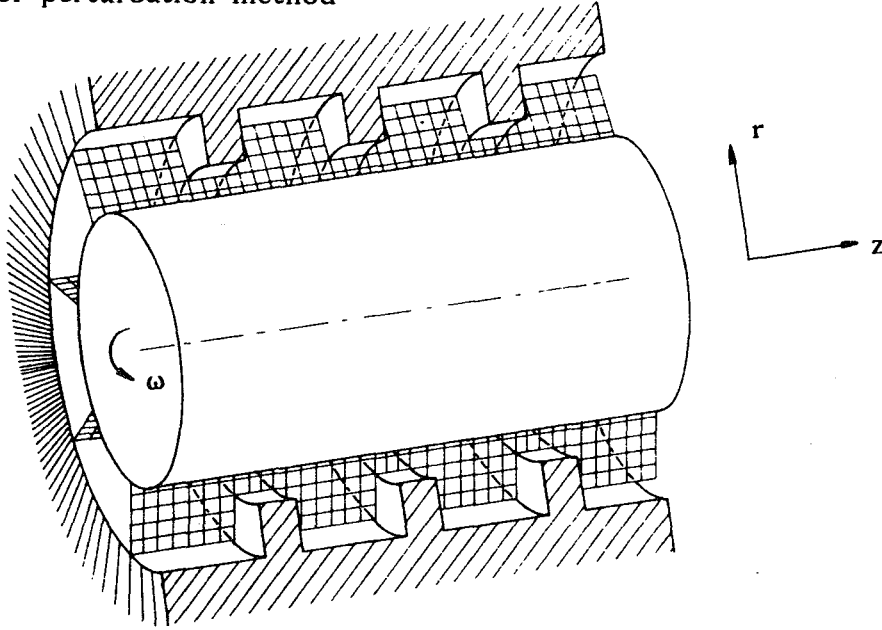
Fig. 4: 3D Finite Difference grid

In the next step, the generalized equation (2) is integrated over a control volume linking every node point with his neighbours in space. The resulting algebraic equations are then solved for the zeroth and first order equations (perturbation analysis) or the 3D equations respectively.

Finally, the dynamic forces are calculated from the pressure distribution on the rotor surface for two precession frequencies $\Omega=0$ and $\Omega=\omega$, resulting in two sets of forces. Then the dynamic coefficients are determined from eq. 1, where the prescribed circular shaft orbit is introduced:

$$- F_1 = r_0 \left(K + \Omega d \right)$$

$$- F_2 = r_0 \left(- k + \Omega D \right)$$

(5)

For more detailed information concerning the perturbation analysis or the 3D algorithm, readers are referred to WEISER and NORDMANN /2,3/.

SIMPLIFIED METHODS

While the CFD algorithms require a lot of computer storage and cpu time, the simplified methods described in this chapter show a reduced effort to determine the rotordynamic labyrinth coefficients.

THREE VOLUME BULK FLOW MODEL

Following the conventional approach (see for example IWATSUBO /4/ or CHILDS /5/), a three volume bulk flow model has been developed based on the conservation equations for mass, momentum and energy working with velocities, pressure, density and temperature, which are averaged over the control volume height.

Flow visualization experiments show, that for look-through labyrinths, the flow field can be divided in two characteristic regions: a vortex flow in the seal chamber and a jet flow region beneath the seal strip and the groove. Therefore we use three control volumes (CV) to describe the flow situation in the labyrinth (Fig. 5).

To account for the flow turbulence, wall shear stresses and a fluid shear stress in the contact region of CV II and CV III are introduced. Following SCHARRER /6/, a vortex velocity in the chamber is assumed. The constants appearing in the shear stress formulations are determined with the aid of the CFD programs for centric shaft position.

Again, a perturbation analysis in connection with the implementation of solutions for the temporal and circumferential variation of the dependent variables is performed, resulting in the already known two sets of differential equations, which now depend only on the axial coordinate z. After their numerical solution, the forces and the dynamic seal coefficients are calculated by a pressure integration over the shaft surface.

More information concerning the bulk flow model can be found in NORDMANN and WEISER /7,8/.
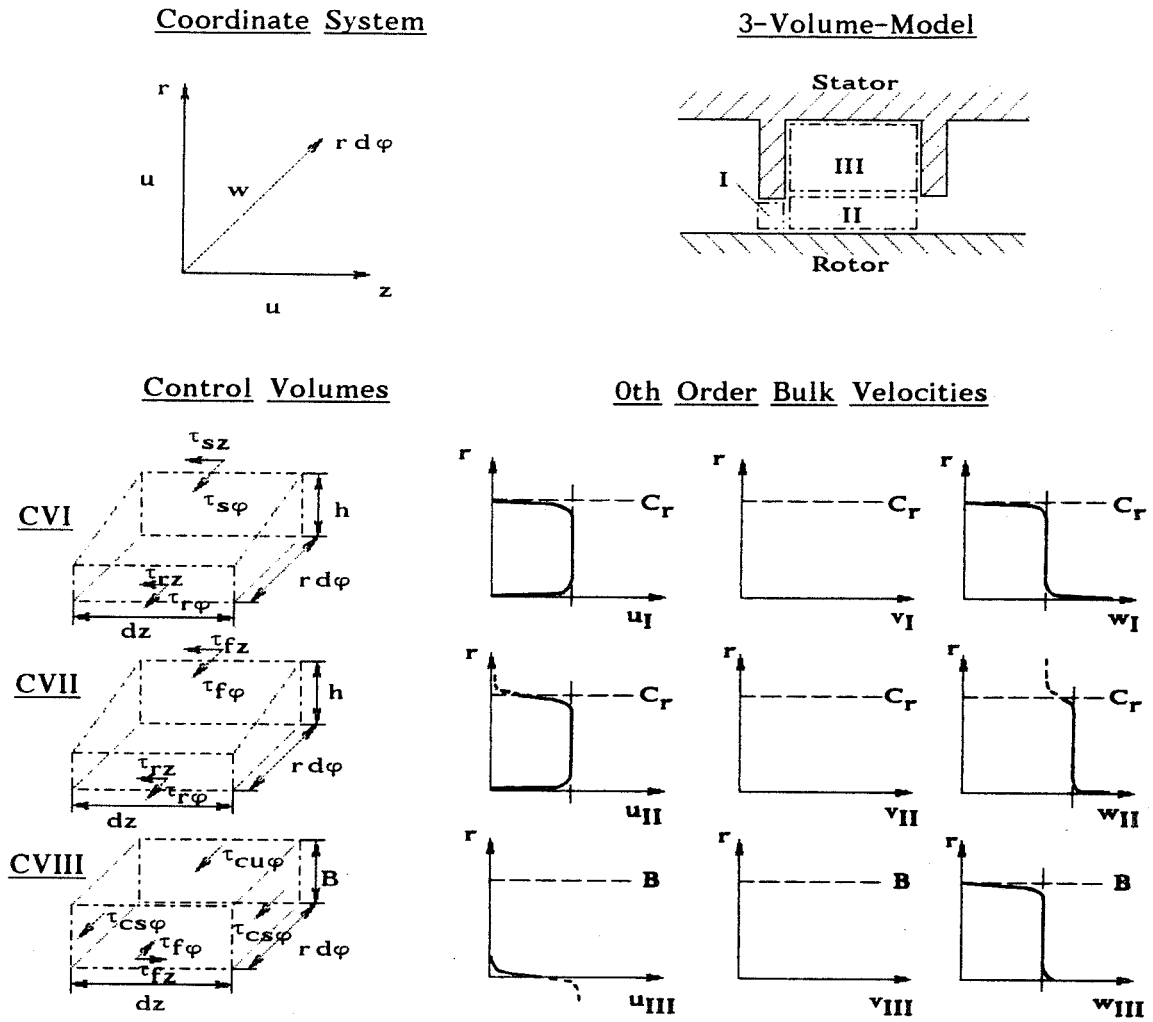
Fig. 5: Three volume bulk flow model

CORRELATION EQUATIONS FOR THE DYNAMIC COEFFICIENTS

Already in the design stage of a turbine or a compressor, the estimation of labyrinth coefficients is important for inclusion of these effects into rotordynamic calculations. Therefore, we developed approximation formulas for the desired stiffnesses and dampings to provide a tool for the design engineer, which can give some information about the rotordynamic seal influence to be expected. These correlations are based on extensive FD calculations for a model labyrinth, where performance data and geometry were varied in a wide range of practical interest.

First, the influence parameters which will be included in the correlation to perform must be defined (shown in Fig. 6).
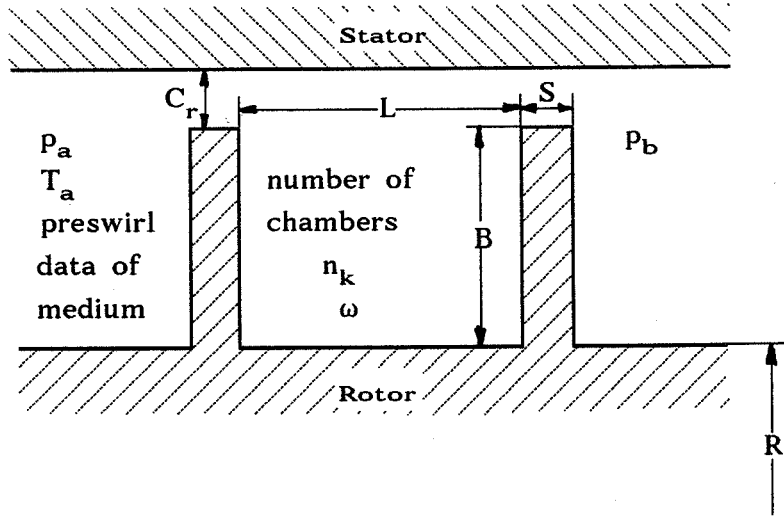
Fig. 6: Influence parameters for the correlation of dynamic coefficients

For the approximation equations, several definitions are used:

$$G = \alpha\, k_{\ddot{u}}\, D_m\, C_r\, \pi\, G_{kr}\, q \qquad G_{kr} = \sqrt{9.80665 \times \left(\frac{2}{\varkappa+1}\right)^{\frac{\varkappa+1}{\varkappa-1}}} \;\sqrt{p_a\, \rho_a}$$

$$D_m = \frac{1}{2}\, \frac{2\,R + C_r + B\,m}{2} \qquad m = \begin{array}{l} 0 : \lbrace\ \text{Strips on stator} \\ 1 : \lbrace\ \text{Strips on rotor} \end{array}$$

$$q = \begin{cases} n_k \lessgtr 7: & \sqrt{\dfrac{1}{n_k}\dfrac{1-\varepsilon_z^2}{1-\varepsilon_{kr}} - \varepsilon_{kr}\dfrac{(1-\varepsilon_z^2)}{n_k^2(1-\varepsilon_{kr})^2}} \\[4mm] n_k \gtrless 7: & \sqrt{\dfrac{1}{n_k}\dfrac{1-\varepsilon_z^2}{1-\varepsilon_{kr}}} \end{cases}$$

(6)

$$\alpha = \frac{\sqrt{14.44 - (C_r/S - 4)^2} - 26.656}{-33.32} \quad \text{for } 0.2 \le C_r/S < 4 \quad \text{and}$$

$$\alpha = 0.675 \qquad\qquad\qquad \text{for } C_r/S \ge 4$$

$$k_{\ddot{u}} = \sqrt{\frac{n_k}{n_k(1-j_{\ddot{u}})} + j_{\ddot{u}}} \qquad j_{\ddot{u}} = 1 - \left(1 + 16.6\frac{C_r}{L}\right)^{-2}$$

$$\varepsilon_z = \frac{p_b}{p_a} \qquad \varepsilon_{kr} = 0.528 \text{ (air)}$$

DESCRIPTION OF DIRECT STIFFNESS

The approximation for the direct stiffness consists of three parts:
- stiffness for axial flow situation (K_0)
- stiffness induced by shaft rotation (K_ω)
- stiffness induced by preswirl velocity (K_{w_i})

From FD calculations, we found that the influence of preswirl changes sign for labyrinths with more than 5 strips and that K becomes negative for multi-chamber seals. This is included in the following formulas:

$$K = K_0 + K_\omega + K_{w_i} \qquad \text{for } n_k \leqslant 5$$

$$K = K_0 + K_\omega - K_{w_i} \qquad \text{for } n_k > 5 \tag{7}$$

with

$$K_0 = C_1^* \, f_g \, f_{n_k} \, f_P \, f_\tau$$

$$f_g = R \frac{L_5^2}{h_m^2}$$

$$\lambda = \left(2(p_a - p_b) - \frac{G_5^2}{\rho_m A_s^2} \right) \frac{2 h_m \rho_m A_{sp}^2}{G_5^2 L_5}$$

$$f_p = (p_a - p_b)(1 + \zeta)$$

$$\psi = \left(\frac{\lambda L_5}{2 h_m} + \zeta + 1 \right)$$

$$A_{sp} = 2 \pi R C_r$$

$$h_m = 0.5 (B + C_r)$$

$$f_n = \begin{array}{l} (100 - 10 n_k) ; n_k > 10 \\ (10 n_k - n_k^2) ; n_k < 10 \end{array}$$

$$K_\omega = C_2^* \frac{p_a}{p_b} w_m$$

$$\rho_m = 0.5 (p_a + p_b) / (R_g T_a)$$

$$L_5 = 4 L + 5 S$$

$$f_\tau = \frac{\lambda}{\psi^2}$$

$$K_{w_i} = C_3^* \frac{p_a}{p_b} \left(\frac{w_i}{D_m} \right)^2$$

G_5 : Leakage for 5 strip Labyrinth

CROSS-COUPLED STIFFNESS

The cross-coupled stiffness is directly related to the leakage loss of the labyrinth. Also, the influence of geometry, shaft rotation and preswirl are included:

$$t_g = C_4^* \left(\frac{R}{C_r} \right)^2 \frac{L}{B}$$

$$t_{w,\omega} = \frac{2}{D_m} \left(w_i \left(n_k - \sqrt{2} \right) - w_m \left(n_k - 2.5 \right) D_m C_5^* \right) \tag{8}$$

$$k = G t_g t_{w,\omega}$$

The average circumferential velocity w_m is determined using the 1/7-power law.

DIRECT DAMPING

To describe the direct damping D, some of the previously defined functions are used. The influence of shaft rotation, preswirl and geometry are found to be smaller than for the stiffnesses:

$$D = D_0 + D_\omega + | D_{w_i} |$$

$$D_0 = C_6^* f_g f_p f_\tau$$

$$D_\omega = C_7^* \frac{p_a}{p_b} w_m \tag{9}$$

$$D_{w_i} = C_8^* \frac{p_a}{p_b} \frac{w_i}{D_m}$$

The correlation coefficients were determined from the FD calculation results for the data variations of the chosen model labyrinth:

$$C_1^* = 3.141 \ 10^{-2} \quad C_2^* = 16.0 \ Kg/(m \ s) \quad C_3^* = 2.80 \ 10^{-2} \ Kg$$

$$C_4^* = \begin{cases} 4.2 \ 10^{-3} & (\text{strips on rotor}) \\ 3.5 \ 10^{-3} & (\text{strips on stator}) \end{cases} \quad C_5^* = 1.50 \ m^{-1} \quad C_6^* = 1.571 \ 10^{-3} \ s$$

$$C_7^* = 0.18 \ N s^2/m^2 \quad C_8^* = 1.60 \ 10^{-2} \ N s^2/m$$

COMPARISON OF THE DIFFERENT APPROACHES WITH MEASUREMENTS

1. Example: A three chamber look-through labyrinth

To compare the two FDM, the bulk flow model and the correlation equations to measurements, we have chosen a look-through labyrinth which was experimentally investigated by BENCKERT /9/ (seal data given in /2/).

213
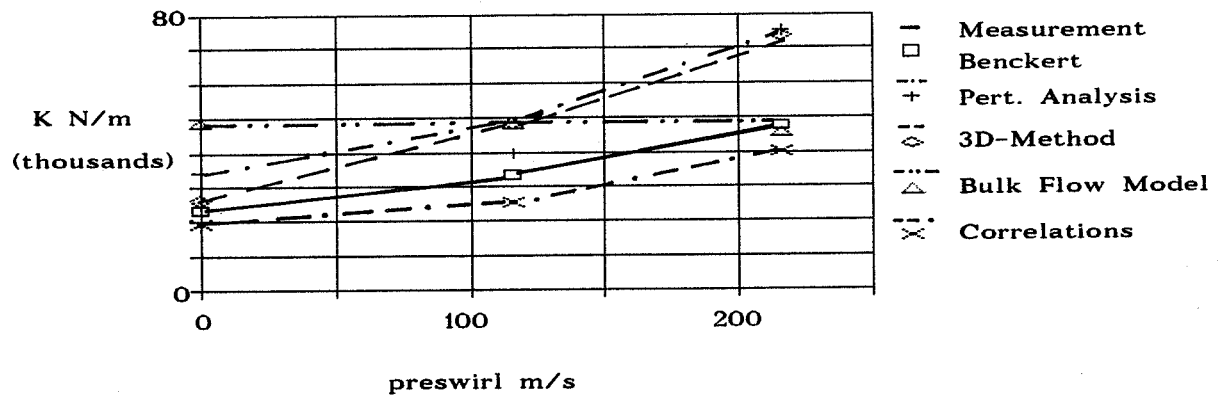
Fig. 7 : Direct Stiffness
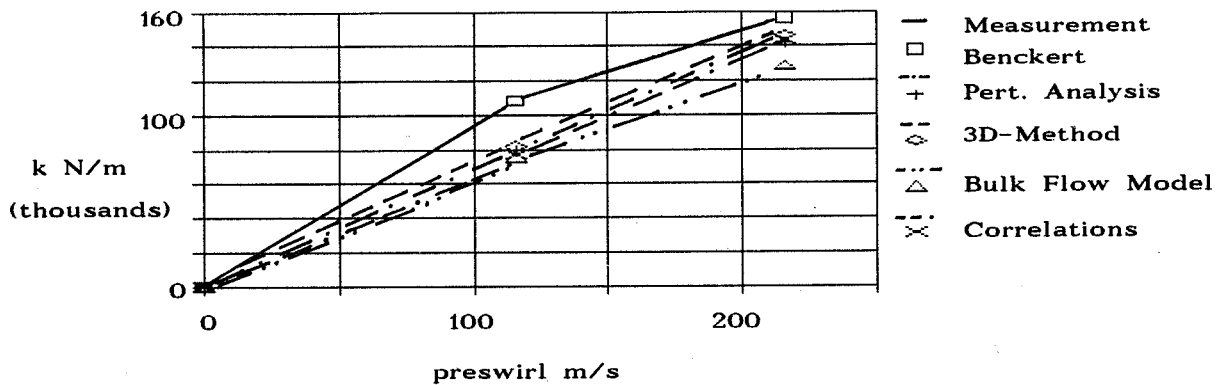
Fig. 8 : Cross-coupled Stiffness

2. Example: A multi-chamber look-through labyrinth seal

SCHMIED /10/ published experimental results obtained by CHILDS for a 12 strip stator labyrinth (seal data given in /10/). The comparisons in Fig. 9 - 11 show the results of perturbation analysis, bulk flow model and correlation for the stiffnesses and the direct damping.
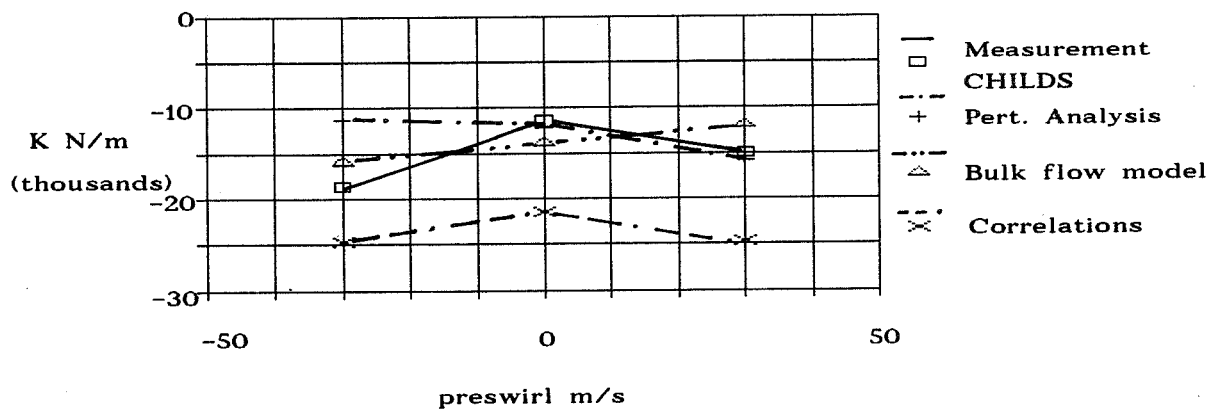
Fig. 9 : Direct Stiffness
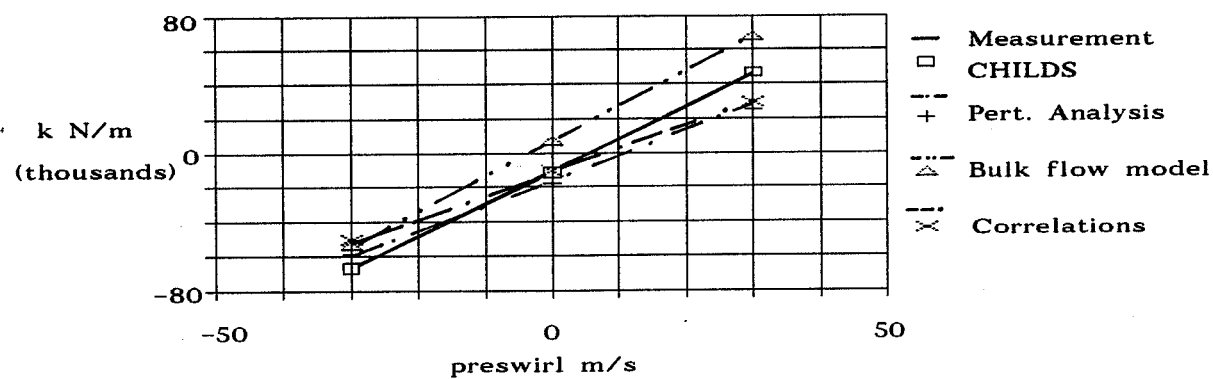
Fig. 10: Cross-coupled stiffness
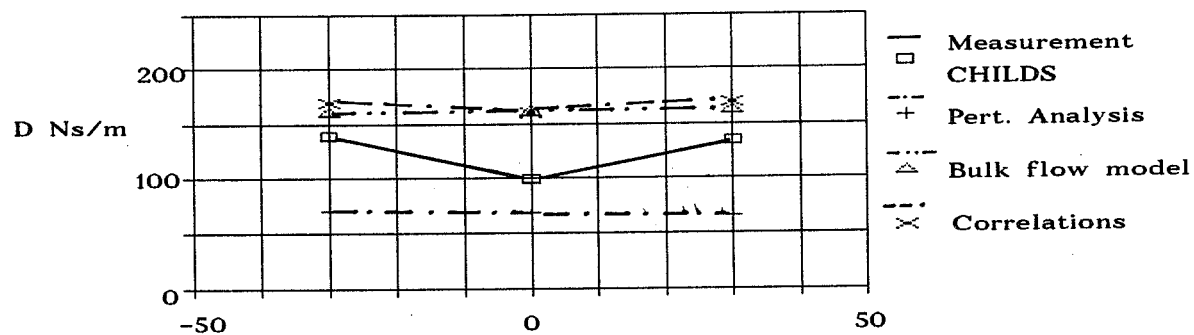
Fig. 11: Direct damping

215

APPLICATION OF SEAL DYNAMICS CALCULATION TO ROTORDYNAMIC DESIGN AND VIBRATION INVESTIGATIONS

In 1988, SCHMIED /10/ published rotordynamic calculations for a high performance injection compressor, where he included the most important fluid interaction influences coming from journal bearings, oil ring seals and labyrinths. Fig. 12 shows a sketch of the compressor rotor discretization and gives the basic data. The labyrinth data are given in /10/. SCHMIED uses the program MADYN to perform the eigenvalue calculations. In this chapter, a comparison is made to SCHMIEDs results for the first forward bending mode with straight through shroud and hub labyrinths, the comb-grooved balance piston and ideally floating oil ring seals.

Fig. 12: Investigated rotor
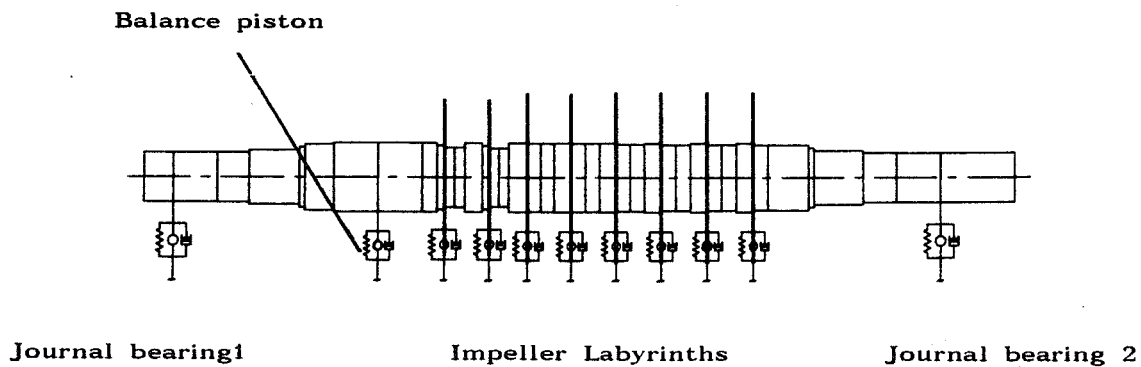
Basic compressor data:

Suction pressure:	198 bar	Mass flow:	47.5 kg/s	Op. speed:	13400 rpm
Discharge pressure:	700 bar	Rotor mass:	265 kg		
Mol. weight of gas:	20.05	Bearing dist.:	1565 mm		

COMPARISON TO SCHMIED'S RESULTS FOR THE SIXTH STAGE SHROUD LABYRINTH

SCHMIED uses the labyrinth seal model of WYSSMANN /11/ to determine the rotordynamic coefficients. For the sixth stage shroud labyrinth, his calculations show negative direct stiffness values. As can be recognized in Fig. 13 to 15, the results of our investigations with the perturbation analysis, the bulk flow model and the correlation equations yield positive direct stiffness as expected. The agreement of cross-coupled stiffness and direct damping to the values obtained with WYSSMANNs theory is good. Especially, the different procedures presented in this paper are in relatively good agreement with each other for all rotordynamic parameters. This statement holds also true for all other labyrinth seals of the investigated compressor.
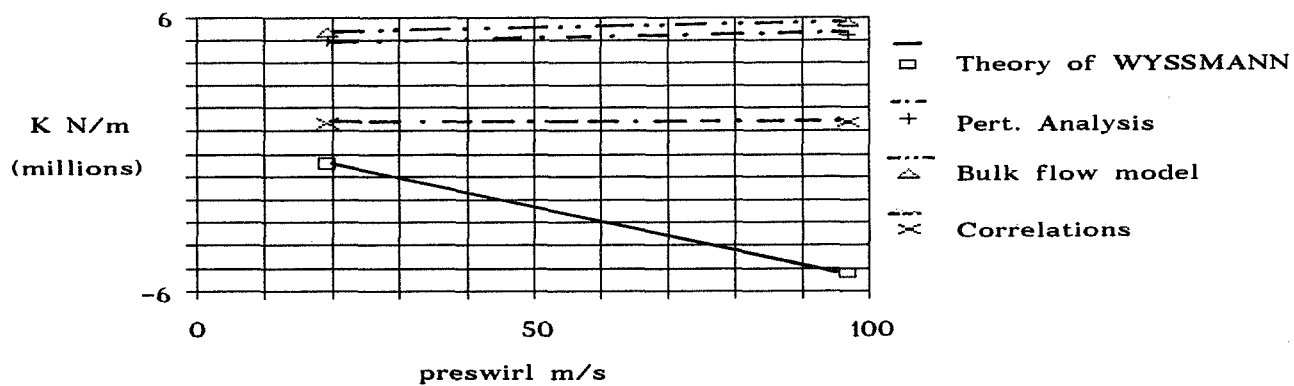
Fig. 13: Direct Stiffness
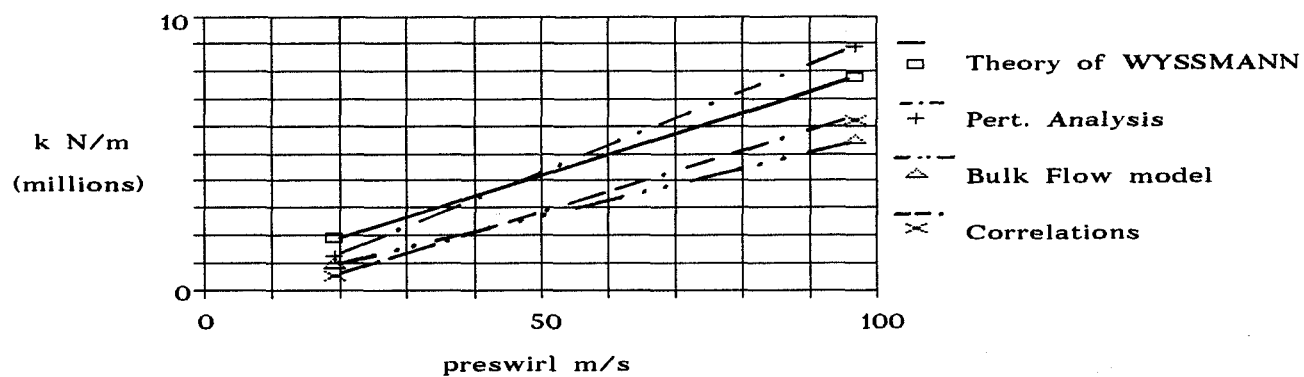
Fig. 14: Cross-coupled Stiffness
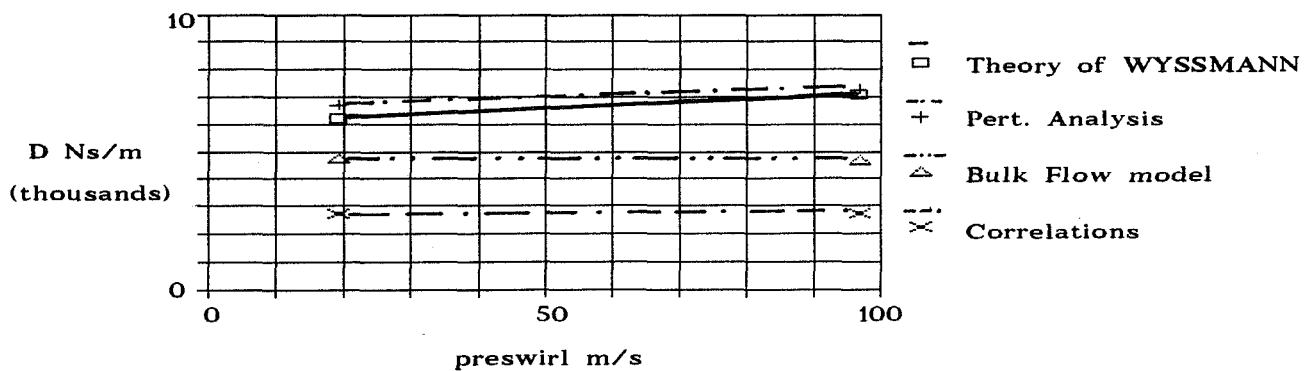
Fig. 15: Direct Damping

217

SCHMIED investigated three cases of rotordynamic interest:
- "ideal": rotor running in journal bearings, no labyrinth influence
- "with swirl brakes": labyrinth influence included for low preswirl conditions
- "without swirl brakes": labyrinth influence included for high preswirl conditions

For these cases, we have calculated the eigenfrequencies and modal dampings of the rotor system using the Finite-Element program of DIEWALD /12/ . In Fig. 16 and 17, comparisons are presented for the first forward bending mode. For the "ideal" system, the calculations show nearly the same results. Because of the labyrinth coefficients obtained with the FD perturbation analysis for the hub and shroud labyrinths and the bulk flow model for the balance piston, the first eigenfrequency is higher than in SCHMIEDs calculations. This is mainly due to the positive direct stiffnesses for the impeller labyrinths. Also the modal damping shows great differences.
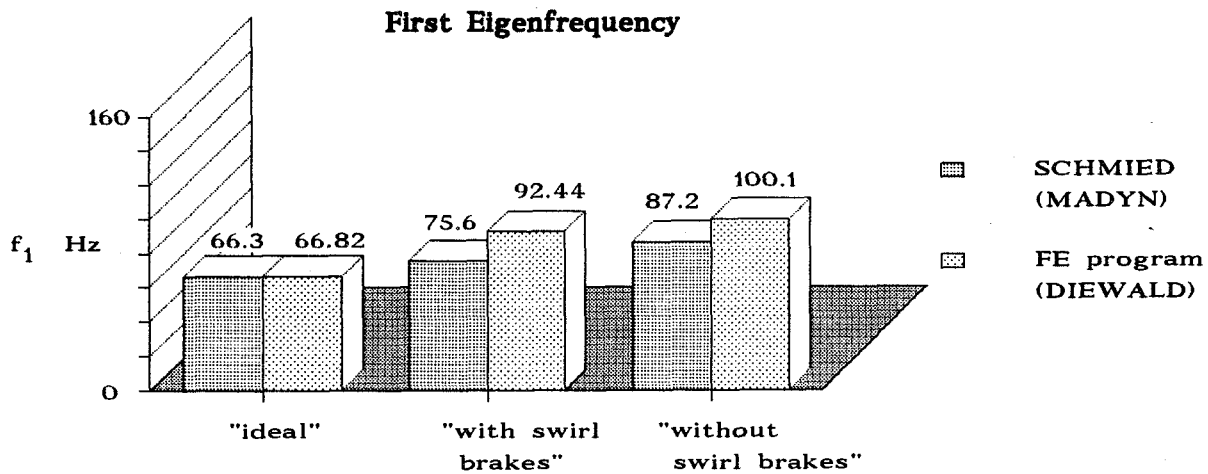
Fig. 16: Comparison of first eigenfrequency
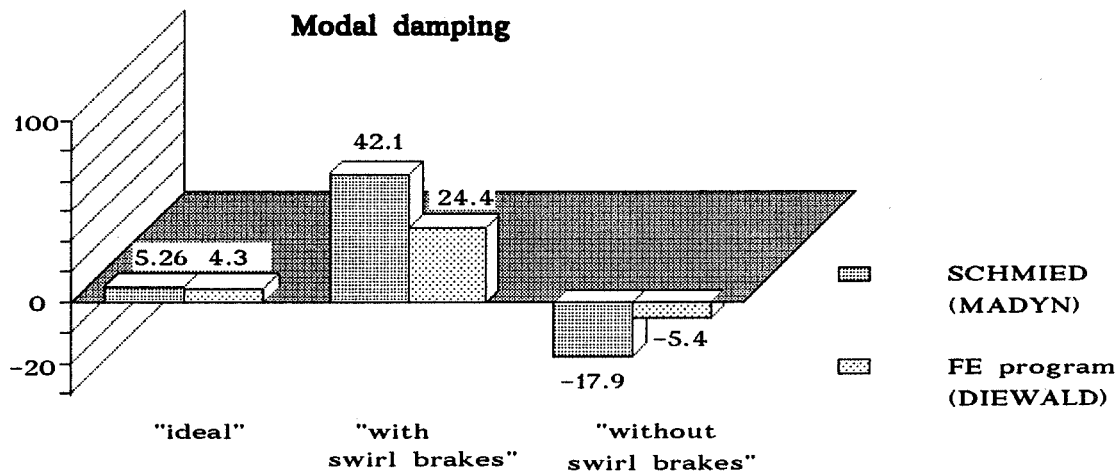
Fig. 17: Modal damping of first forward bending mode

CONCLUSION

Four calculation methods have been described allowing calculation of the dynamic labyrinth coefficients. Comparisons to experiments show good agreement for all methods and all investigated cases.

The practical example of rotordynamic calculations for a high-performance compressor has shown that the determination of labyrinth coefficients must be performed as exactly as possible in order to predict the eigenfrequencies and modal dampings correctly. Also, it has been proved that the methods presented in this paper are superior for this task to the existing theories.

LITERATURE

/1/   LAUNDER, B. E., SPALDING, D. B.:
      "The Numerical Computation of Turbulent Flows"
      Computer Methods in Applied Mechanics and Engineering 3,
      (1974), S. 269 - 289

/2/   NORDMANN, R., WEISER, H.P.:
      "Rotordynamic Coefficients for Labyrinth Seals Calculated by
      Means of a Finite-Difference Technique"
      NASA CP 3026, 1988

/3/   WEISER, H. P., NORDMANN, R.:
"Calculation of Rotordynamic Labyrinth Seal Coefficients by Means
of a Threedimensional Finite-Difference Method"
Biennial Conference on Mechanical Vibration and Noise, Montreal 1989

/4/   IWATSUBO, T.; TAKAHARA, K.; KAWAI, R.:
"A New Model of Labyrinth Seal for Prediction of the Dynamic Force"
NASA CP 2338, 1984

/5/   CHILDS, D. W., SCHARRER, J. K.:
"An Iwatsubo-Based Solution for Labyrinth Seals - Comparison with
Experimental Results"
NASA CP 2338, 1984

/6/   SCHARRER, J. K.:
"Theory versus Experiment for the Rotordynamic Coefficients
of Labyrinth Gas Seals: Part I - A Two Control Volume Model"
The 11th Biennial Conference on Mechanical Vibrations and Noise,
Boston, 27-30 Sept. 1987

/7/   NORDMANN, R.; WEISER, H.P.:
"A Three Volume Bulk Flow Model for the Calculation of Rotordynamic
Coefficients of Look-Through Labyrinths"
Third International Symposium on Transport Phenomena and Design of
Rotating Machinery, Honolulu, USA, 1990

/8/   NORDMANN, R.; WEISER, H.P.:
"Evaluation of Rotordynamic Coefficients of Look-Through Labyrinths
by Means of a Three Volume Bulk Flow Model"
The Sixth Workshop on Rotordynamic Instability Problems in High Per-
formance Turbomachinery, College Station Texas, USA, 1990

/9/   BENCKERT, H.:
"Strömungsbedingte Federkennwerte in Labyrinthdichtungen"
Dissertation TU Stuttgart, 1980

/10/   SCHMIED, J.:
"Rotordynamic Stability Problems and Solutions in High Pressure
Turbocompressors"
NASA CP 3026, 1988

/11/   WYSSMANN, H. R., PHAM, T. C., JENNY, R. J.:
"Prediction of Stiffness and Damping Coefficients for
Centrifugal Compressor Labyrinth Seals"
ASME Journal of Engineering for Gas Turbines and Power,
Okt. 1984, B. 106, S. 920 - 926

/12   DIEWALD, W., NORDMANN, R.:
"Dynamic Analysis of Centrifugal Pump Rotors with Fluid-Mechanical
Interactions"
11th Biennial Conference on Mechanical Vibration and Noise,
Boston, 27-30 Sept. 1987

EXPERIMENT OF STATIC AND DYNAMIC CHARACTERISTICS OF SPIRAL GROOVED SEALS

T. Iwatsubo, B.C. Sheng, and M. Ono
The Faculty of Engineering
Kobe University
Kobe, Japan

The leakages and the dynamic characteristics of six types of spiral grooved seals are experimentally investigated. The effect of the helix angle of the seal is investigated mainly under the conditions of the same nominal clearances, land and groove lengths, and groove depths. The dynamic characteristics are measured for various parameters such as preswirl velocity, pressure difference between inlet and outlet of the seal, whirling amplitude, whirling speed, and rotating speed of the rotor. The results are also compared with those of parallel grooved seals obtained previously. The results show that the leakage increases with the increase of the helix angle, but as the rotating speed increases, the leakages of the larger helix angle seals quickly drop. The leakage of the SS/SGR seal (smooth-stator/spiral-grooved-rotor seal) drops faster than that of the SGS/SR seal (spiral-grooved stator/smooth-rotor seal). It is found that a circumferential flow can be produced by the flow along the helix angle direction, and this circumferential flow acts as a negative swirl. For the present helix angle range, there is an optimum helix angle with which the seal has a comparatively positive effect on the rotor stability. Compared with the SGS/SR seals, the SS/SGR seal has a worse effect on the rotor stability.

1. INTRODUCTION

Spiral grooved seals used in turbopumps have the advantage of less leakage due to their pumping effect, and have a smaller possible contact area with the rotor in comparison to smooth seals. However, knowledge about their dynamic characteristics is very limited. In a theoretical study, Iwatsubo et al. (ref. 1) modeled the flows in the spiral grooved seals by considering the pumping effect due to the spiral grooves, and analyzed the static and dynamic characteristics of SS/SGR seals by a short-seal solution. In an experimental study, Kanki et al. (ref. 2) measured the static and dynamic characteristics of two SGS/SR seals with different lengths. Recently, Childs et al. (ref. 3) experimentally investigated six SGS/SR seals with different helix angles (15° ~ 70°). In practice, the small helix angle seals are usually used in conventional pumps. So the investigation of the small helix angle seals is necessary and important. Sometimes, the SS/SGR seals are also adopted in pumps due to their excellent pumping effect. But unfortunately, their dynamic characteristics have not been experimentally investigated yet.

In this experiment, the static and dynamic characteristics of the five SGS/SR seals and one SS/SGR seal are measured under the condition of asynchronous whirling motion. These seals have comparatively small helix angles (0.83° ~ 15.1°). The effects of the preswirl velocity, pressure difference between inlet and outlet of the seal, whirling amplitude, whirling speed, and rotor rotating speed on the static and dynamic characteristics of the seals are investigated. The results are also compared with those of the parallel grooved seal.

2. NOMENCLATURE

B	: Groove depths
C	: Radial clearance of seal
C_{xx}, C_{xy}	: Damping coefficients
e	: Whirling amplitude of rotor
F_x, F_y, F_r, F_θ	: Seal forces for x, y, r, and θ directions
K_{xx}, K_{xy}	: Stiffness coefficients
L	: Seal length
L_l, L_g	: Land and groove widths
M_{xx}	: Inertia coefficients
N	: Number of lands or grooves
ΔP	: Pressure difference between inlet and outlet of seal
R, D	: Rotor radius and diameter
r, θ	: Radial and tangential coordinates
t	: Time
V_t	: Preswirl velocity
V_{ts}	: Preswirl velocity at zero rotating speed
x, y	: Fixed coordinates
α	: Helix angle
Ω	: Whirling speed of rotor
ω	: Rotating speed of rotor

3. TEST APPARATUS AND MEASUREMENT

The test apparatus has been illustrated in reference 4 in detail. So the apparatus is only outlined here. The assembly and layout of the test facility are shown in Fig. 1 and Fig. 2, respectively. The working fluid, that is water, is injected into the apparatus through three pairs of preswirl passages to yield different swirl velocities as shown in the cross section B of Fig. 1. The water passes through the clearance between the seal and rotor, then it flows through the outlets.

The preswirl velocity is adjusted by the six valves in order to obtain arbitrary values.

The bearing part which consists of two ball bearings is used to yield the rotating and whirling motions of the rotor. An inside sleeve and an outside sleeve which have 0.05 mm eccentricity to each other are attached between the two bearings, as shown in the cross section A. By rotating the two eccentric sleeves relatively, an arbitrary whirling amplitude can be adjusted in the range of 0 mm ~ 0.1 mm. The sleeves of both sides are synchronously driven by a motor through timing belts to obtain a whirling motion. The whirling speeds and their directions are controlled by an electric inverter. The rotating

speed and the direction of the rotor can also be changed by the other motor controlled by an electric inverter.

The geometries of the spiral grooved seals are shown in Fig. 3. There are five spiral-grooved-stator/smooth-rotor seals and one smooth-stator/spiral-grooved-rotor seal to be tested as shown in Table 1. These seals have the same nominal clearances, land and groove lengths, and groove depths, but they have different helix angles.

The measuring system consists of the measurements of rotating and whirling speeds of the rotor, pressure, preswirl velocity, leakage, fluid force, and displacement of the rotor. The fluid forces acting on the stator are measured by load cells as shown in the cross section C. The signals from the measuring instrument are recorded by a data recorder and analyzed by a computer.

The experimental conditions are shown in Table 2.

4. FLUID FORCE MODEL OF SEAL

For a small centered whirling motion of the rotor, the fluid reaction force in the seal can be represented as a linear function of the displacement, velocity and acceleration of the rotor, as follows:

$$-\left\{ \begin{array}{c} F_x \\ F_y \end{array} \right\} = \left[\begin{array}{cc} M_{xx} & 0 \\ 0 & M_{xx} \end{array} \right] \left\{ \begin{array}{c} \ddot{x} \\ \ddot{y} \end{array} \right\} + \left[\begin{array}{cc} C_{xx} & C_{xy} \\ -C_{xy} & C_{xx} \end{array} \right] \left\{ \begin{array}{c} \ddot{x} \\ \ddot{y} \end{array} \right\} + \left[\begin{array}{cc} K_{xx} & K_{xy} \\ -K_{xy} & K_{xx} \end{array} \right] \left\{ \begin{array}{c} x \\ y \end{array} \right\} \quad (1)$$

In the test, the whirling motion the rotor is given by

$$x = e \cos \Omega t, \qquad y - e \sin \Omega t \quad (2)$$

Substituting Eq. (2) into Eq. (1) and transferring the fixed coordinate system to a radial and tangential coordinate system, the following expressions are obtained.

$$-F_r/e = -\Omega^2 M_{xx} + \Omega C_{xy} + K_{xx}$$

$$-F_\theta/e = \Omega C_{xx} - K_{xy} \quad (3)$$

To determine the dynamic coefficients of $M_{xx}, C_{xx}, C_{xy}, K_{xx}$ and K_{xy}, for a given rotating speed, F_r/e and F_θ/e are measured for the different forward and backward whirling speeds, then F_r/e is approximated by a quadratic function, and F_θ/e by a linear function of Ω. According to Eq. (3), inertia coefficient M_{xx}, damping coefficients C_{xx}, C_{xy}, and stiffness coefficients K_{xx}, K_{xy} are represented by the curvature, the slopes and the intercepts (at $\Omega = 0$) of the curves of F_r/e and F_θ/e, respectively.

5. TEST RESULTS AND DISCUSSION

5.1 Leakage

The seal leakages versus the pressure difference are shown in Fig. 4. As the helix increases, the leakages show a tendency to increase. The leakages

225

versus the rotating speed are shown in Fig. 5. The leakages of spiral seals drop monotonically with the increase of the rotating speed. It can be seen that the larger the helix angle is, the faster the leakage drops. The leakage of the SS/SGR seal (seal 7) is larger than that of the SGS/SR seal (seal 3), but with the increase of the rotating speed it quickly drops. Namely, the SS/SGR seal has the stronger pumping effect.

5.2 Fluid Force Coefficients
(a) Effect of rotating speed

The fluid force coefficients F_r/e and F_θ/e of parallel grooved seal 1, spiral grooved seal 3, and seals 5 and 7 are illustrated in Fig. 6. These results show that the radial force coefficients of seal 1, seal 3 and seal 7 almost do not vary with the rotating speed, but the radial force coefficient of seal 5 decreases with the increase of the rotating speed. In these seals, the tangential force coefficients tend to increase as the rotating speed increases. The tangential force coefficient of seal 7 increases at the fastest rate, and its sign varies from negative to positive, which means it has a negative effect on the rotor stability.

(b) Effect of preswirl velocity

Figure 7 shows the effect of preswirl velocities on the force coefficients of a parallel grooved seal (seal 1). From this figure, the effect of preswirl velocities on F_r/e can not be recognized, but the effect of preswirl velocities on F_θ/e is very distinct. The positive preswirl velocity causes F_θ/e to vary towards positive values, so that the unstable area is enlarged. The effect of the negative preswirl velocity on F_θ/e is exactly the opposite that of the positive preswirl velocity. The effect of preswirl velocities on the force coefficients of the spiral grooved seals is similar to that of the parallel grooved seal. To compare the effect of preswirl velocities on these seals, the upper limits of the unstable area, that is the intersections between the approximated lines of F_θ/e and axis of Ω/ω, are shown in Fig. 8. They are measured for different positive preswirl velocities. According to these results, as the helix angle α increases from 0° to 3.32°, the values of the upper limits decrease, but as the helix angle increases more than 3.32°, these values begin to increase. Seal 3 ($\alpha = 3.32°$) has the minimum value which means the best effect on the rotor stability.

(c) Effect of pressure difference

The force coefficients are also measured for several pressure differences between the inlet and outlet of the seal. The results show that for different seals, the force coefficients only change their values, they do not change their qualitative characteristics. This tendency is similar to that of the parallel grooved seal. One of these results is shown in Fig. 9.

(d) Effect of whirling amplitude

Figure 10 shows the effect of whirling amplitude on the fluid force F_r and F_θ of seal 4. The results show that the absolute values of the fluid forces linearly increase with the increase of whirling amplitude. This means that under the present experimental conditions the relation between the fluid forces and the displacement can be correctly expressed by the approximated Eq. (1).

(e) Effect of helix angle

     To compare the effects of the helix angles, the force coefficients of five
seals measured under the same conditions are shown in Fig. 11. These force
coefficients show the same qualitative tendencies. However, they show some
quantitative differences. Though the preswirl velocity is not given ($V_{ts} = 0$),
the tangential force coefficients of the spiral grooved seals show a result
similar to that of the parallel grooved seal under a negative preswirl velocity
(refer to Fig. 7). Namely, the unstable areas shift to the negative side of
Ω/ω. Furthermore, the sequence of these values is the same as that of Fig. 8
in which seal 3 also has the minimum value. This phenomenon may be explained
by the opposite circumferential flow caused by the helix angle. It is obvious
that the fluid in the seal clearance will flow along the grooves, and the vel-
ocity of the flow can be divided into the circumferential and axial components.
The circumferential velocity is just opposite to the rotating velocity of the
rotor, because in order to obtain the pumping effect the rotor always rotates
in the direction opposite to the helix direction. This circumferential flow,
in fact, acts as a negative swirl. Both the parallel grooved seal and the ver-
tical grooved seal ($\alpha = 90°$) do not produce this circumferential flow; there-
fore, at least one optimum helix angle with which the seal gets the maximum
negative swirl ought to exist for a constant operating condition. For the
present experimental condition, seal 3 ($\alpha = 3.32°$) is the optimum seal.
     According to this discussion, a positive swirl also ought to be produced
by the SS/SGR seal. Indeed, this phenomenon can be confirmed by the results
shown in Fig. 12. This figure shows the force coefficients of the SGS/SR
seal 3 and the SS/SGR seal 7. The results of the tangential force coefficients
show that the SS/SGR seal is worse than the SGS/SR seal from the point of view
of the rotor stability.

5.3 Stiffness, Damping, and Inertia Coefficients

     The stiffness coefficients, damping coefficients and inertia coefficients
of seal 1 – 5 are shown in Fig. 13. The inertia coefficients M_{xx} of the seals
have the same tendencies, and they almost do not vary as the rotating speed.
The direct damping coefficients C_{xx} are always positive and much larger than
the cross-coupled damping coefficients C_{xy}. The parallel grooved seal has a
relatively large C_{xx}, and the spiral grooved seal 5 has a relatively small C_{xx}.
The cross-coupled damping coefficients C_{xy} are almost negative, which implies
that there is a negative effect on the rotor stability according to Eq. (3).
Seal 3 has a relatively small value of C_{xy}. The direct stiffness coefficients
K_{xx} show the positive values, while the cross-coupled stiffness coefficients
K_{xy} show values that are almost negative. So in general, these stiffness coef-
ficients contribute to the stability of the rotor system. With the increase
of the rotating speed, the direct stiffness coefficients K_{xx} of the larger
helix angle seals tend to increase. Attention should be paid to the variation
of K_{xy}. As the helix angle α increases from 0° to 3.32°, the values of K_{xy}
decrease, but as the helix angle continues to increase, these values begin to
increase. Seal 3 ($\alpha = 3.32°$) has the minimum value.
     Childs et al. (ref. 3) investigated the static and dynamic characteristics
of six SGS/SR seals with the comparatively large helix angles ($\alpha = 15° \sim 70°$).
It should be pointed out that their dynamic coefficients are different from
those of the present experiment. In the first place, their dynamic coeffi-
cients are obtained from a fixed axial Reynolds number over a range of rotating

speeds; while the present ones are obtained from a fixed rotating speed (equivalent to a fixed circumferential Reynolds number) over a range of rotating ratios (Ω/ω). Next, their dynamic coefficients are measured under the condition of synchronous rotor motion; while the present ones are measured under the condition of asynchronous rotor motion. For these reasons, the two results can not be compared directly. However, the two results have a similar effect on the stiffness coefficients for the helix angles. According to the results of Childs et al., the direct stiffness coefficient K_{ef} (equivalent to $-K_{xx}$, here) decreases at first, then increases as the helix angle α increases from 15° to 70°. The seal with the 30° helix angle has the minimum value of K_{ef}, which means it has a comparatively positive effect on the rotor stability.

The stiffness coefficients, damping coefficients and inertia coefficients of SGS/SR seal 3 and SS/SGR seal 7 are shown in Fig. 14. Seal 7 has relatively large values of C_{xx} and C_{xy}, which means the better damping effects in comparison with seal 3. For K_{xx} and K_{xy}, seal 7 also has the larger values. The increase of K_{xx} gives a positive effect to the rotor stability, but the increase of K_{xy} gives a negative effect to the rotor stability. In particular, when the rotating speed increases, K_{xy} of seal 7 tends to increase rapidly. According to K_{xy}, the SS/SGR seal is worse than the SGS/SR seal in rotor stability.

6. CONCLUSIONS

The static and dynamic characteristics of spiral grooved seals have been investigated and compared with those of a parallel grooved seal. The results of the spiral grooved seals and the parallel grooved seal show similar characteristics for the pressure difference and the whirling amplitude; however, the spiral grooved seals also show some specific characteristics, as follows:

(1) With the increase of the helix angle, the leakage increases, but as the rotating speed increases, the leakages of the larger helix angle seals quickly drop. The SS/SGR seal has a stronger pumping effect than that of the SGS/SR seal.

(2) For the SGS/SR seals, a circumferential flow can be produced by the flow along the helix angle direction, and this circumferential flow acts as a negative swirl. For this experimental helix angle range, an optimum helix angle exists with which the seal produces the maximum negative swirl. On the contrary, the SS/SGR seal produces a positive swirl velocity.

(3) The SS/SGR seal is worse than the SGS/SR seal in rotor stability.

REFERENCES

(1) Iwatsubo, T., Yang, B.C., and Ibaraki, R., "Theoretical Approach to Obtaining Dynamic Characteristics of Noncontacting Spiral-Grooved Seals," NASA CP-2443, 1986, pp. 155-187.

(2) Kanki, H., and Kwakami, T., "Experimental Study on the Static and Dynamic Characteristics of Screw Grooved Seals," ASME Design Tech. Conf. Pub. DE-Vol. 2, 1987, pp. 263-272.

(3) Childs, D.W., Nolan, S.A., and Kilgore, J.J., "Test Results for Turbulent Annular Seals, Using Smooth Rotors and Helically Grooved Stators," ASME Journal of Tribology (89-Trib-11) 1989.

(4) Iwatsubo, T., Sheng, B.C., and Matsumoto, T., "An Experimental Study on the Static and Dynamic Characteristics of Pump Annular Seals," NASA CP-3026, 1988, pp. 229-252.

Table 1 Seal dimensions

Seal	N	$\alpha(°)$	D(mm)	L/D	C(mm)	L_l(mm)	L_g(mm)	B(mm)
1 (GS/SR)	-	0	70.35	0.5	0.175	1.6	1.6	1.2
2 (SGS/SR)	1	0.83	70.35	0.5	0.175	1.6	1.6	1.2
3 (SGS/SR)	4	3.32	70.35	0.5	0.175	1.6	1.6	1.2
4 (SGS/SR)	8	6.65	70.35	0.5	0.175	1.6	1.6	1.2
5 (SGS/SR)	12	10.0	70.35	0.5	0.175	1.6	1.6	1.2
6 (SGS/SR)	18	15.1	70.35	0.5	0.175	1.6	1.6	1.2
7 (SS/SGR)	4	3.32	70.35	0.5	0.175	1.6	1.6	1.2

where GS/SR means grooved-stator / smooth-rotor.
SGS/SR means spiral-grooved-stator / smooth-rotor.
SS/SGR means smooth-stator / spiral-grooved-rotor.

Table 2 Experimental conditions

Pressure difference	ΔP(kPa)	294, 588, 784, 882
Rotating speed	ω (rpm)	$500 \sim 4500$
Whirling speed	Ω (rpm)	$\pm 600 \sim \pm 2400$
Whirling amplitude	e (μm)	$20 \sim 60$
Preswirl velocity	$V_t/\omega R$	$-2.59 \sim 2.75$
Temperature of water	T(°C)	19

Fig. 1 Test apparatus assembly

Fig. 2 Test facility layout

(a) Smooth-stator/spiral-grooved-rotor seal (SS/SGR seal)

(b) Spiral grooved-stator/smooth-rotor seal (SGS/SR seal)
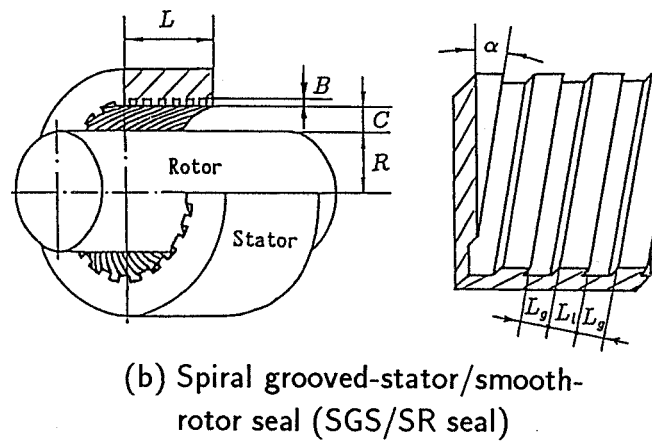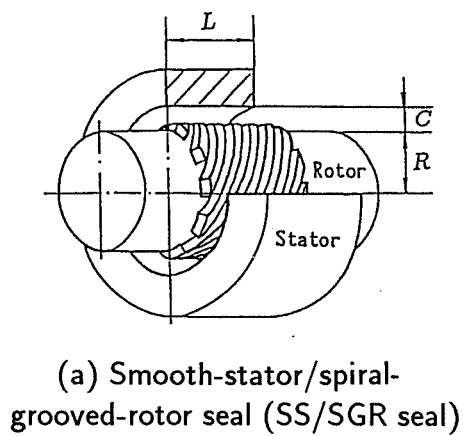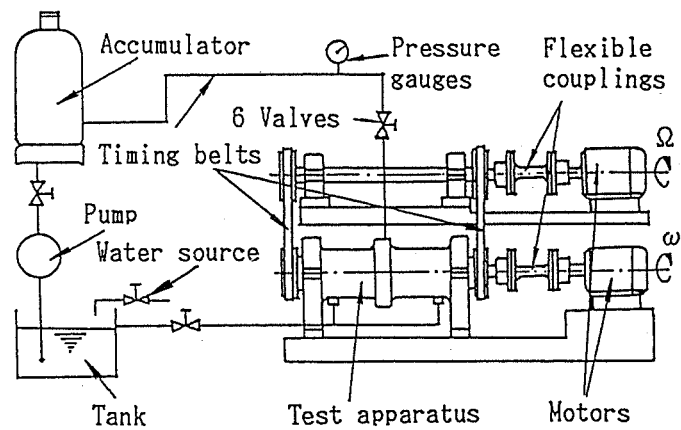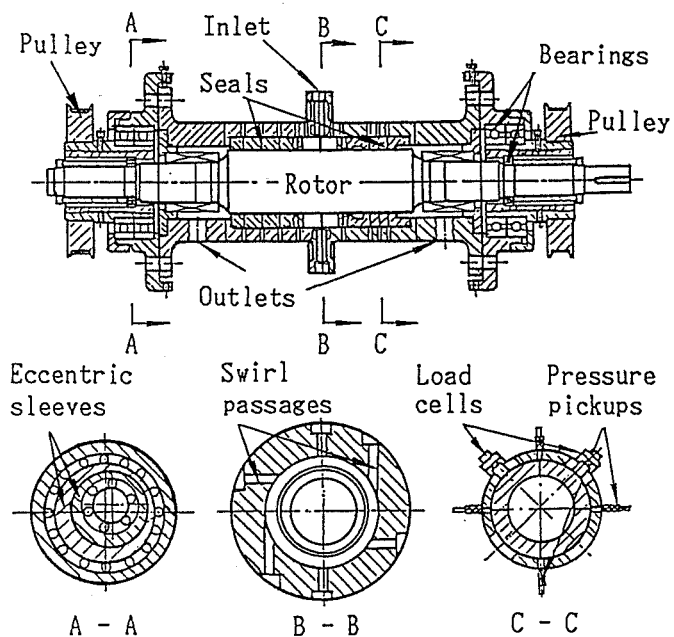
Fig. 3 Spiral grooved seals
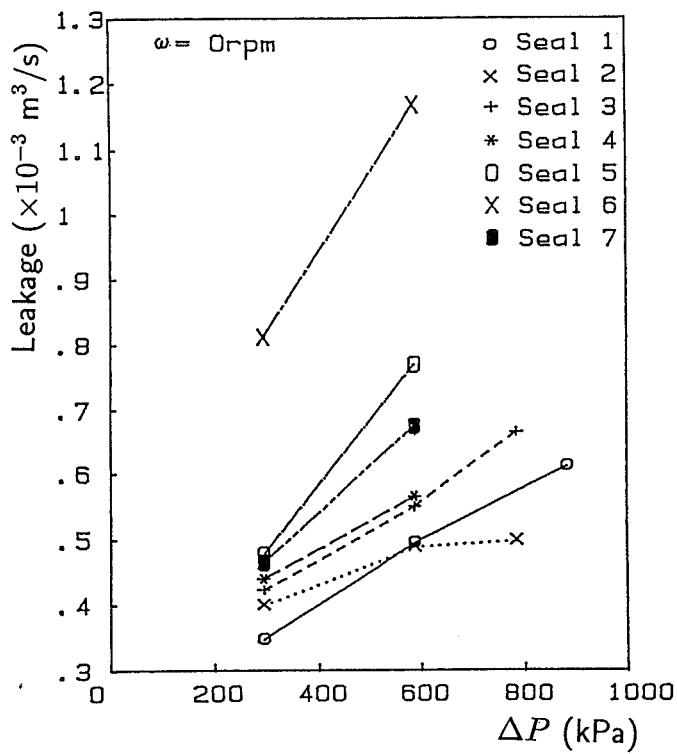
Fig. 4 Leakage versus ΔP
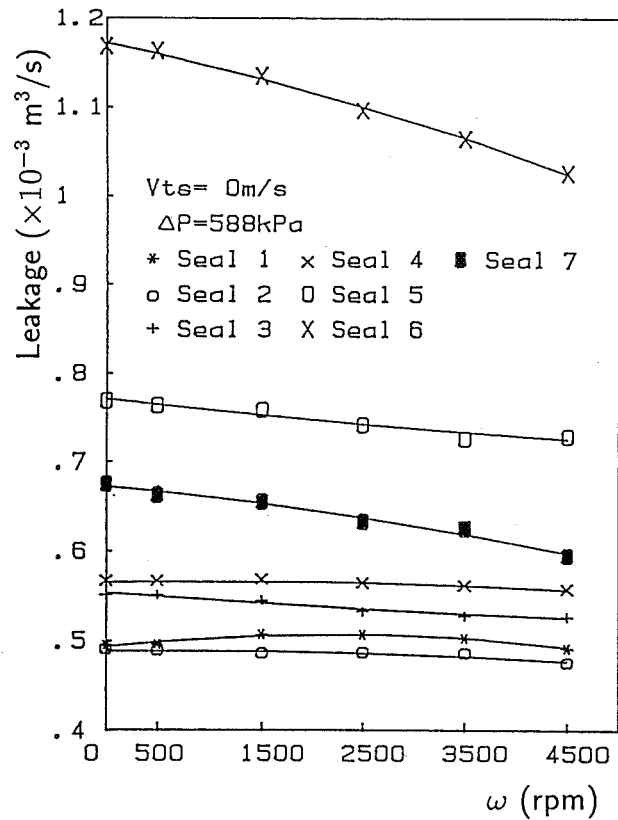
Fig. 5 Leakage versus rotating speed
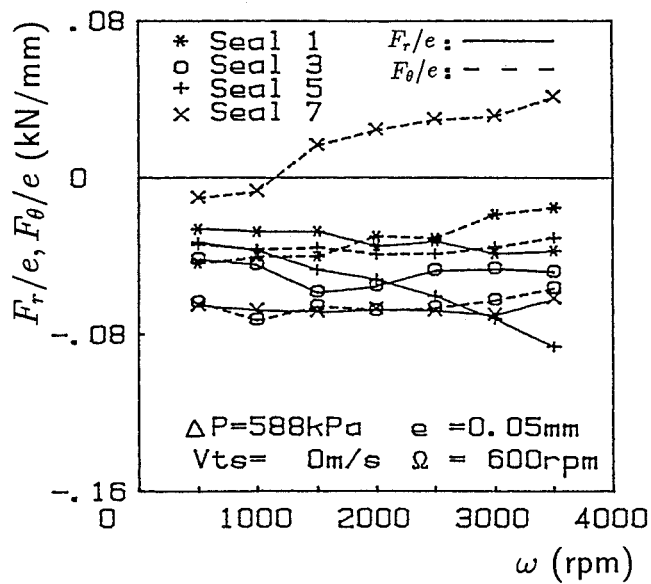
Fig. 6 Effect of rotating speed
on F_r/e and F_θ/e
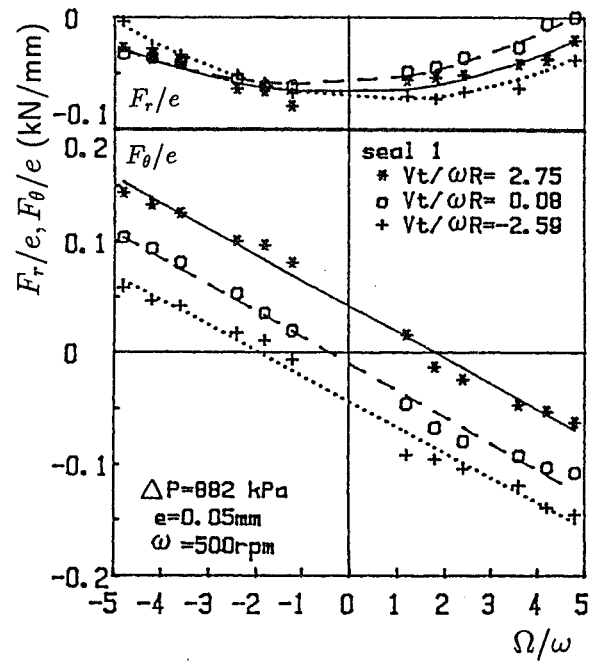
Fig. 7 Effect of preswirl velocity on F_r/e
and F_θ/e for parallel grooved seal

231
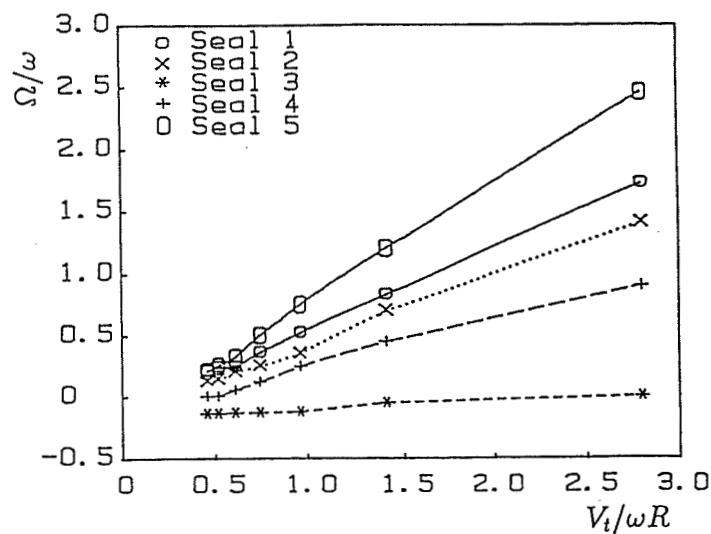
Fig. 8 Upper limit of unstable area for positive preswirl velocity
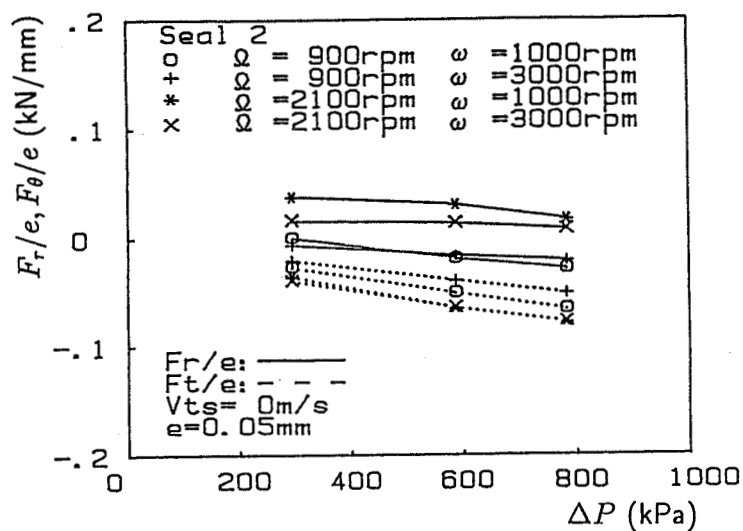
Fig. 9 Effect of pressure difference on F_r/e and F_θ/e
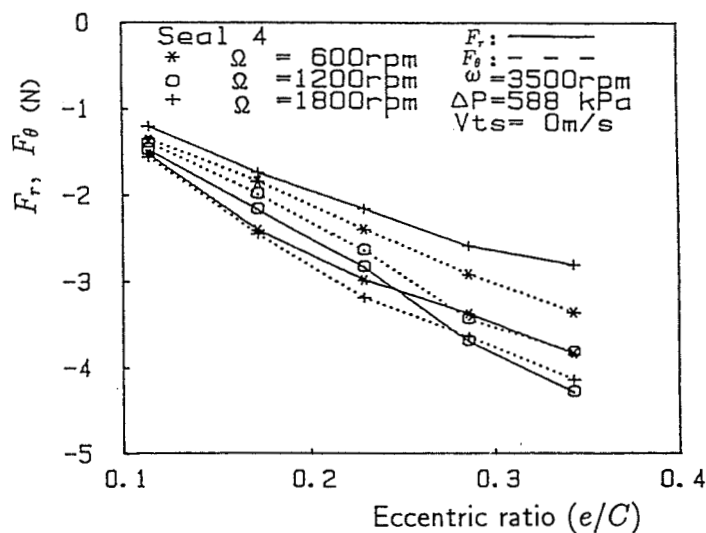
Fig. 10 F_r and F_θ versus eccentric ratio
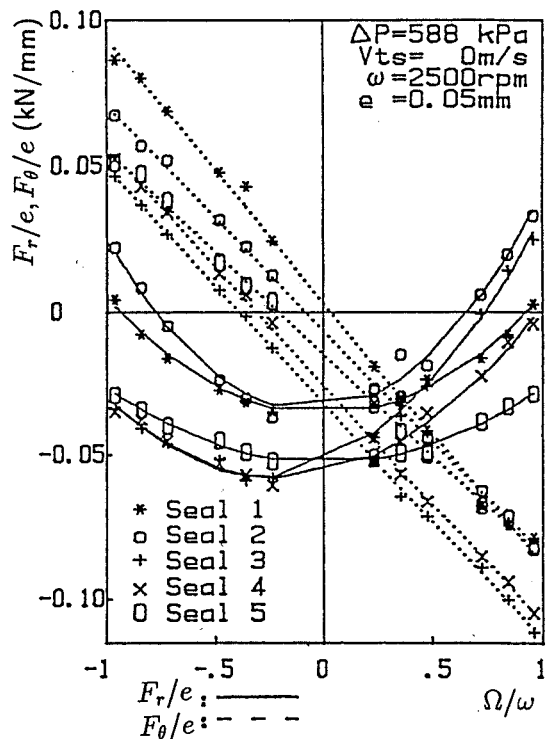
Fig. 11 Effect of helix angle on F_r/e and F_θ/e
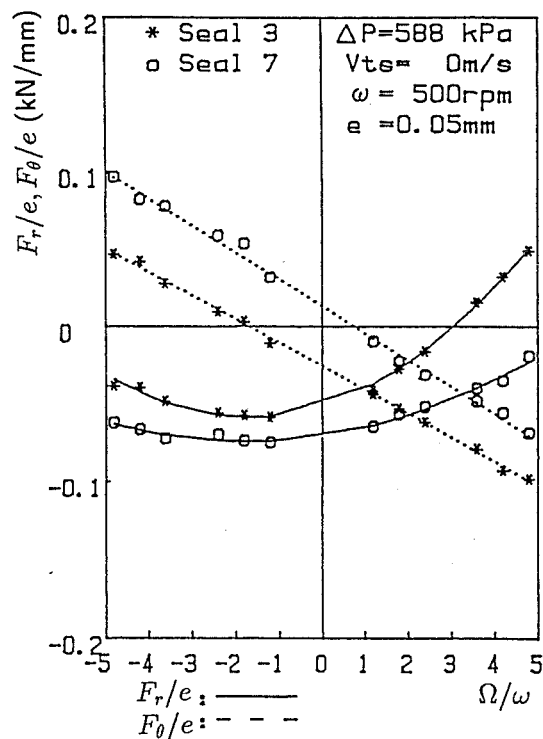
Fig. 12 Comparison of force coefficients for seal 3 and seal 7
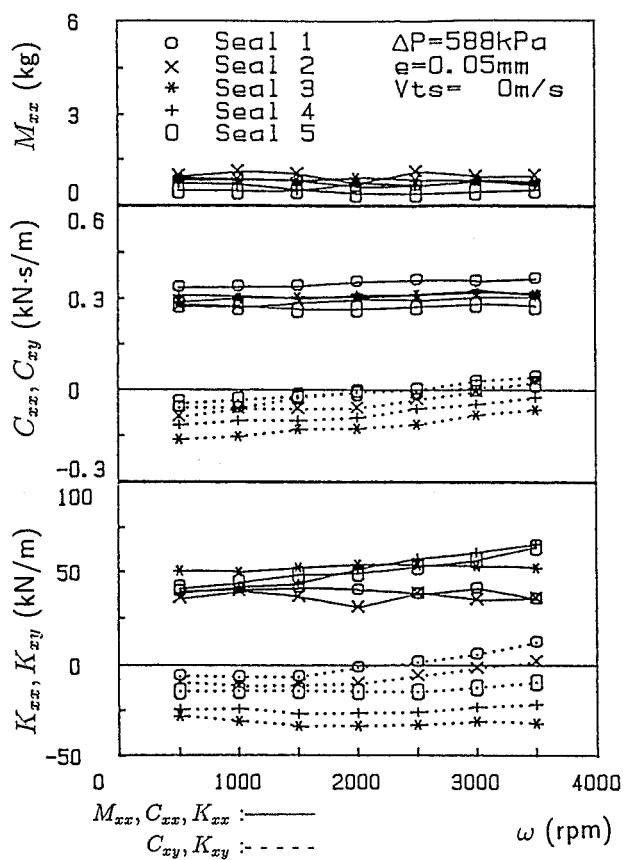
Fig. 13 Dynamic coefficients for rotating speed
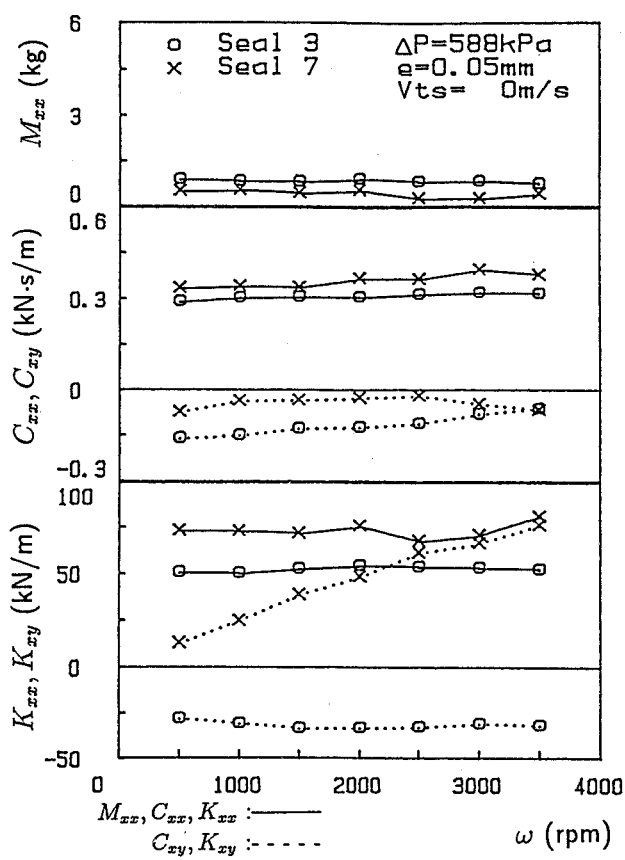
Fig. 14 Comparison of dynamic coefficients of seal 3 and seal 7

ANNULAR SEALS OF HIGH ENERGY CENTRIFUGAL PUMPS: PRESENTATION OF FULL SCALE MEASUREMENT*

S. Florjancic and R. Stürchler
Sulzer Brothers, Limited
Winterthur, Switzerland

T. McCloskey
Electric Power Research Institute
Palo Alto, California, U.S.A.

Prediction of rotordynamic behaviour for high energy concentration centrifugal pumps is a challenging task which still imposes considerable difficulties. While the mechanical modelling of the rotor is solved most satisfactorily by FE techniques, accurate boundary conditions for arbitrary operating conditions are known for journal bearings only. Little information is available on the reactive forces of annular seals, such as neck ring and interstage seals and balance pistons, and on the impeller interaction forces.

The present work is focused to establish reliable boundary conditions at annular seals. For this purpose a full scale test machine was set up and smooth and serrated seal configurations measured. Dimensionless coefficients are presented and compared with a state of the art theory.

1. INTRODUCTION

Machine speed, head per stage, and power concentration of multi-stage centrifugal pumps have increased steadily during the last few decades. The increasing power concentration has often contributed to reliability problems, and often rotordynamic phenomena appear to be the main cause (ref. 1). Dynamic interaction forces between rotor and casing will always be present, and may even lead to destruction of the machine. Thus rotordynamic considerations become very important for high energy pumps; reliability of rotating equipment depends strongly on optimized rotordynamic behaviour.

With readily available computer codes (ref. 2), the rotor system can be modelled very well and optimization is possible in the design stage, provided the boundary conditions are known accurately enough. Costly changes after field tests, or more likely after break downs, will be less than optimum and can be avoided.

PRECEDING PAGE BLANK NOT FILMED

Besides well known rotor casing interaction within journal bearings (refs. 3, 4, 5) and reaction forces at the impeller itself (refs. 6, 7), boundary conditions for annular seals are of main interest. Due to the pressure differential and the rotation at the neck ring and interstage seals and balance pistons, considerable reaction forces arise during rotor vibration. The boundary conditions at these elements are generally described by a mathematical model, consisting of a stiffness, a damping and a mass matrix, i.e., the rotordynamic coefficients of the seal.

A review of literature reveals that some information about total reaction forces of annular seals is available, but no published full scale measured data on individual coefficients exist. Contemporary theories (refs. 8, 9) were found to be able to predict available measured results for plain surface seals to some extent, but detailed investigations on serrated or grooved surface patterns are missing.

To validate the theory according to Childs and Nordmann, a full scale test rig for neck ring seals was established and operated at typical Reynolds numbers of boiler feed pumps. Skew symmetric stiffness, damping and mass matrices were measured. Rotordynamic coefficients and hydraulic friction factors of a plain and a serrated seal are presented. New ("as built") and worn conditions for the example of a serrated seal are demonstrated.

Comparison of theoretical results (ref. 9) with measured data is shown and indicates a not very satisfying accuracy. Predictions for rotordynamic coefficients are demonstrated to be generally high for stiffnesses, much too low for cross coupled stiffnesses and about twice as large as the measurement errors for direct damping. The other coefficients are negligible, as found from measurement as well as from theory.

2. TEST EQUIPMENT

2.1 Test Machine

The test apparatus uses the housing, support and excitation device from the test rig used previously for impeller interaction measurements as described in (ref. 6). Figure 1 indicates the general arrangement of the test machine. The test rig is dynamically de-coupled from the ground by the heavy base plate. In the drive end view the hydraulic shaker attached to the swinging frame is on the right side of the test machine. This frame contains the rotor bearings and is supported in a pivot on the left side of the test rig. This arrangement provides that any movement of the hydraulic shaker makes the rotor support move around the pivot. As the radius is very large and the vibration amplitudes induced by the shaker are several magnitudes smaller, a linear vertical movement of the rotor relative to the main housing is attained. Tie rods take up the axial thrust of the otherwise axially free rotor support, and hence radial alignment is maintained for any axial forces.

Figure 2 is a general cross section of the test rig. The inlet is marked with an arrow. From the large annulus around the bearing section, the fluid passes the guide vanes and is led radially inwards to the entrance of the seal. It is now forced through the narrow annular gap formed by the seal insert and the rotor. Behind the seal, the fluid is gathered in a large space and leaves the test machine through the exit.

Figure 3 indicates that the design allows easy exchange of stator inserts in order to measure different surface geometries, while the rotor surface remains unchanged. Four temperature compensated proximity probes of the eddy current type are provided to measure effective rotor movement in the radial direction, and four axial probes were installed to monitor rotor tilting. The rotor is attached directly to a calibrated piece of shaft, which is instrumented with strain gauges to measure the reaction forces at the rotor. The rotating disk, the counter part of the seal insert, is hollow. Hence mechanical mass is reduced and measurement errors of inertial forces are minimized. The back side of the rotor is sealed by a radial flow hydrostatic seal, which does not influence lateral forces measurement. 48 guide blades can be turned in any position, $-75°$ to $+75°$ from the radial direction, by means of a connecting chain, controlled from the outside by four axes. The seal insert against the rotor was modelled in a FE analysis to prove that no misalignment of the seal under pressure and temperature occurs.

A detailed cross section of the seal alone can be seen in figure 4. Two sets of static and total pressures are measured immediately in front of the seal entrance at opposite circumferential locations. The tangential velocity of the water entering the seal can be calculated, using measured flow and the continuity equation. The tangential velocity of the water jet leaving the seal can not be measured. Thus, only static pressure is measured here to calculate the total pressure differential.

Static and dynamic properties of the test machine were calculated and optimized. The FE analysis and measurement of the machine showed a critical first mode above 150 Hz in air and, because of the stiffening effect of the annular seal, above 170 Hz in water.

A tilting of the rotor leads to measurement errors. According to theories of Childs (ref. 10) and Fenwick (ref. 11), the displacement tilt divided by the maximum mean displacement may not be larger than some 3% in order to avoid errors larger than 10% for the stiffness measurement:

$$\frac{\overline{F}_x}{Y} = K_{xx} \cdot \left[1 + RK \cdot \frac{\overline{X}_{in} - \overline{X}_{out}}{Y} \right] \qquad \frac{\overline{F}_y}{Y} = K_{yy} \cdot \left[1 + RK \cdot \frac{\overline{Y}_{in} - \overline{Y}_{out}}{Y} \right] \qquad (1)$$

with $RK = f(L_{seal}/h_o)$ being the theoretical correction factor. For the present test rig it is estimated that $RK \approx 3 \div 3.5$.

To estimate tilting errors, an FE calculation has been done, which indicated a strong general dependency of the displacement tilt on the frequency. Maximum calculated displacement tilt in the vertical (Y-) direction is about 9% for smooth and 4.5% for serrated seals. Calculated tilt in the horizontal direction is less than 1%, as the displacement X is very small. Rotor tilting hence had to be monitored by means of axially placed proximity probes. Measurement indicated generally much smaller tilts, and therefore errors in the stiffness were acceptable.

237

2.2 Test Loop

A key plan of the closed circuit test loop is shown in figure 5. The loop is designed for a maximum temperature of 160 °C and use of demineralized water. Pressure is generated externally, in a Sulzer standard pump, with operating conditions at a best efficiency point of 740 m head at 56 1/s flow. Entrance pressure and flow of the test machine are controlled by valves in the main and the bypass branch. Maximum allowable pressure downstream of the test machine is restricted by the turbine flow meter to 20 bar, enough to prevent vaporization at 160 °C. Combined main and bypass quantities pass partially through the main heat exchanger, depending on the duty point, and are led back to the main pump. System pressure is maintained by a plunger pump, which supplies cooling water for the mechanical seal and the bearings out of a reservoir.

2.3 Instrumentation and Data Acquisition

Dynamic Measurement (ref. 6)

The linear relationship between forces and displacement, of equation (2), is assumed. For rotational symmetry, matrices become skew symmetric and the relation can be written as

$$-\begin{bmatrix} F_x \\ F_y \end{bmatrix} \equiv \begin{bmatrix} K & k_c \\ -k_c & K \end{bmatrix} \cdot \begin{bmatrix} X \\ Y \end{bmatrix} + \begin{bmatrix} C & c_c \\ -c_c & C \end{bmatrix} \cdot \begin{bmatrix} \dot{X} \\ \dot{Y} \end{bmatrix} + \begin{bmatrix} M+M_m & m_c \\ -m_c & M+M_m \end{bmatrix} \cdot \begin{bmatrix} \ddot{X} \\ \ddot{Y} \end{bmatrix} - \begin{bmatrix} F_{xo} \\ F_{yo} \end{bmatrix} \qquad (2)$$

where M_m stands for the mechanical mass of the rotor acting on the calibrated piece of shaft, and F_{xo} and F_{yo} indicate any forces not coherent with the vibration motion. F_{xo} and F_{yo} are only caused by noise of the machine and are small. Synchronous time averaging eliminates the noncoherent forces. As harmonic motion applied, complex notation can be used:

$$X = Re \cdot \left[\overline{X} \cdot e^{j\Omega t} \right] \qquad\qquad F_x = Re \cdot \left[\overline{F}_x \cdot e^{j\Omega t} \right]$$

$$\qquad\qquad\qquad\qquad\qquad\qquad\qquad\qquad\qquad\qquad\qquad (3)$$

$$Y = Re \cdot \left[\overline{Y} \cdot e^{j\Omega t} \right] \qquad\qquad F_y = Re \cdot \left[\overline{F}_y \cdot e^{j\Omega t} \right]$$

Introducing equations (3) into (2) yields the impedance functions D and E:

$$-\begin{bmatrix} \overline{F}_x \\ \overline{F}_y \end{bmatrix} = \begin{bmatrix} \overline{D} & \overline{E} \\ -\overline{E} & \overline{D} \end{bmatrix} \cdot \begin{bmatrix} \overline{X} \\ \overline{Y} \end{bmatrix} \qquad (4)$$

which corresponds to

$$\overline{D} = K + j \cdot \Omega \cdot C - \Omega^2 \cdot (M + M_m)$$

$$\overline{E} = k_c + j \cdot \Omega \cdot c_c - \Omega^2 \cdot m_c$$

(5)

Because of the rotational symmetry and the harmonic motion, alternatively the imaginary parts can also be introduced into equation (2), resulting in a 90° rotation of the system. As linear equations are used, both cases can be superimposed. Of importance is the fact that no assumptions about the orbit path are needed to get these equations. Thus any linear movement is appropriate. However, as only displacement in the vertical direction occurs, rotational symmetry must be assumed, and only six individual coefficients can be extracted.

In the frequency domain, the impedance functions D and E consist of a constant term and a term depending on the square of the excitation frequency in the real part. The imaginary part is represented by a linear term in frequency, only. Obviously there is no a priori knowledge that those functions represent the actual physical behaviour of the annular seal, as any polynomial in the exciting frequency of an arbitrary degree could fit the results. Anyhow, for practical reasons the number of coefficients should be as small as possible.

Equations (5) demonstrate the physical meaning of D and E. In figure 6, the reaction forces created by individual stiffness, damping, and mass terms and their direction relative to the displacement and velocity vector are shown.

At any given operating point, measurement of complex forces F_x and F_y and displacements X and Y with several rapid sweeps of excitation frequency determine the impedance functions D and E. Curve fitting the results to the equations (5), yields the stiffness, damping and mass coefficients that are being sought.

Displacement and force signal processing:

Figure 7 shows the signal flow at the test machine. The rotating piece of shaft is equipped with six strain gauges for measurement of six degrees of freedom. The careful static and dynamic loading of this device resulted in a full 6x6 calibration matrix. Signal wires are led through the shaft, the coupling and the gear box into the rotating amplifier. Hence stable bridge supply is provided for, and signals can be amplified to pass the slip ring assembly without loss of information.

Radial displacement is measured in both the horizontal and vertical direction by two temperature compensating eddy current probes. To check the displacement tilt, four axially placed probes measure the tilting angles α and β of the rotor around the x- and y-axis.

The data acquisition system is triggered to the rotational frequency. Sampling starts at a zero degree rotor position, and one data block is filled with 1024 points after 32 revolutions taking 32 samples per revolution. The excitation signal is generated digitally from a data block of 1024 points and is made synchronous to the data sampling by triggering.

239

Data processing of force and displacement signals is shown in figure 8. After the analog-digital conversion, all signals are averaged. As the excitation signal is phase locked to the rotor position, averaging of 1000 data blocks removes all forces and displacements not coherent to the excitation signal. Forces and moments are then calculated, applying the calibration matrix, and are converted to the stationary reference. No run out compensation is needed for displacement measurements because of the averaging procedure. From α and β, the radial displacement taper can be calculated with the help of some geometrical data.

Signals subsequently undergo a Fourier transform to yield the complex radial displacement and forces in the stationary horizontal and vertical direction. The relative displacement tilt is used to estimate the possible error caused by tilting. Equation (4) finally indicates that the relation between forces and displacements, and impedance functions D and E can be calculated.

To minimize the time of measurement at one operating point, the excitation frequency Ω is varied in a rapid sweep from zero up to about 140% of the running frequency. Some measurements at constant Ω proved that coefficients do not depend on the rapid sweep. Curve fitting of E and D uses only the excitation range from 10% to 120% of the running frequency for accuracy reasons. The running frequency is excluded, to avoid the measurement of geometric tolerance effects. Reliable measurement of one set of stiffness, damping and mass coefficients is thus ensured and needs less than 10 minutes.

Instrumentation for operating conditions:

To compare individual results, operating and boundary conditions must be known. Figure 9 indicates the signal flow for operating conditions. Fluid temperatures in front and behind the seal are measured by two thermoelectric couples. Electric signals are led to a line recorder for a visual check and through the signal conditioning to the data acquisition system.

The pressure of individual locations is led hydraulically to strain gauge type transducers located outside of the machine. This implies that only quasi-static pressure can be measured. Transducers signals are led through signal conditioning to the data acquisition system.

The turbine flow meter yields a flow proportional frequency. This frequency, as well as the measured rotating frequency of the shaft, is not transmitted directly to the data acquisition system. Impulse sampling and averaging takes too much space and time on the computer. Hence, those two results are the only ones to be entered manually.

Signal processing for operating conditions:

Figure 10 shows the processing of the measured operating conditions. Direct readings are treated in the same way as the displacement and force data. The two manually entered frequencies are not subject to sampling and averaging and are multiplied by their calibration factors. Including information about the geometry, all essential operating conditions, including fluid properties, can be derived:

240

- Rotor speed
- Mean temperature (fluid properties)
- Mean static pressure immediately in front and behind the seal
- Mean pressure drop
- Kinetic pressure (pitot tube used allows for relative flow angles up to at least +/- 25°)
- Mean total velocity in front of seal (kinetic pressure)
- Mean meridional velocity in front of and within seal (continuity)
- Mean circumferential velocity in front of seal
- Friction coefficient (static pressure distribution within seal)

With this information, measured rotordynamic coefficients can be presented in nondimensional diagrams, using the circumferential Re-number as the abscissa and the axial to circumferential Re-number ratio as the parameter. Hydraulic behaviour can be presented correspondingly.

Calibration:

All measurement devices, static as well as dynamic, were calibrated carefully, to ensure reliable results.

The Eigenfrequencies of the system were checked in water. Accordingly, impedance functions match measured data most precisely up to about 100 Hz, and a first resonance appears at some 150 Hz. Maximum excitation frequency required during tests is only about 80 Hz, and no resonance effects take place.

For appropriate measurement, it must be ensured that the rotor vibrates with an approximately constant amplitude over the whole excitation frequency range. Therefore, the chirp signal has to be surveyed and adapted, if necessary. Confirmation took place visually in the time or frequency domain during measurement.

A typical example at 2000 rpm is shown in figure 11. The rapid sweep signal is nicely reproduced in the vertical direction, amplitudes being in the range of a strongly vibrating pump; and the response is quite small in the horizontal direction. The frequency spectrum shows the excitation to span the range from 3 to about 40 Hz with fairly constant resulting displacement. Note that the running frequency is removed and that the signal-to-noise ratio is very good. Figure 12 shows the vertical and horizontal forces. The frequency spectrum of the vertical displacement and force shows a moderately even distribution. If the decrease of displacement with increasing frequency were larger, a linearly or quadratically increasing chirp input would have to be used.

3. MEASURING RANGE AND NONDIMENSIONAL PRESENTATION

3.1 Boundary conditions of test loop and test rig:

There is a physical limitation of the measuring range by the test machine. The following operational limits are encountered:

241

Maximum at	20	160	[°C]	Restriction by
speed	4000	4000	[rpm]	Electric drive
inlet pressure	75	70	[bar]	Inlet flange
outlet pressure	2	8	[bar]	Avoid vaporization
pressure differ.	55	55	[bar]	Hydrostatic seal

Below 500 rpm data sampling becomes erratic, and a pressure differential below approximately 2 bar yields forces which are too small to be measured reliably. The minimum temperature is close to the temperature of the environment.

3.2 Measuring range:

Boundary conditions for a centrifugal pump in terms of rotor speed and pressure are approximated by the following equations:

$$\frac{p_1}{p_2} = \left[\frac{n_1 \cdot (D_1)}{n_2 \cdot (D_2)} \right]^2 \tag{6}$$

The axial velocity v through the annular seal is about proportional to the square root of the pressure differential as can be derived from equation (7):

$$dp = rho \cdot \frac{v^2}{2} \cdot \left[\frac{Lambda \cdot L_{seal}}{2 \cdot h_o} + Ze_i + Ze_o \right] \tag{7}$$

Hence v is directly proportional to the running speed. Writing the ratio of axial to circumferential Reynolds number in a seal yields

$$\frac{Re_a}{Re_c} = \frac{v}{\omega \cdot R} \tag{8}$$

As the geometrical dimensions of the seal are directly correlated to the outer diameter D_2 of the impeller, which determines mainly the generated pressure at a certain speed, the scale of the pump can not change the ratio of equation (8). Thus the ratio of the axial to the circumferential Reynolds number must lie in a narrow range:

$$\frac{Re_a}{Re_c} = 0.45 \div 0.95 \tag{9}$$

The range given here is applicable for specific speeds according to boiler feed pumps. For very high specific speed impellers the ratio may become lower.

With this insight, the measuring range can be defined as shown typically in figure 13. Axial and circumferential Reynolds numbers were selected as three fixed ratios, 0.3, 0.6 and 0.9. Six speeds resulting in Re_c's from 20'000 to 280'000 are chosen. Re_a reaches from 6'000 to about 220'000, depending on each Re_c. The large Reynolds number range was attained by varying temperatures from 20 to 160 °C. A summary of operating conditions is shown in figure 14.

Inlet swirl:

With the adjustable guide vanes used, any attainable inlet swirl remains lower than in a pump. Water exiting an impeller has a high circumferential velocity component. This velocity increases as the medium flows radially inwards, reaching a U_{tho} of about 0.7 ÷ 0.8 at the entrance of the seal. Using guide vanes, a maximum of about U_{tho} = 0.15 can be reached, if the whole Re_a range is to be measured at constant U_{tho}.

For direct comparison of coefficients at individual Re-ratios, the inlet swirl has to be approximately equal for all ratios measured. To get detailed information about the influence of inlet swirl on rotordynamic coefficients, a variation from negative to maximum positive pre-rotations was measured at four selected operating points, where the highest inlet swirls can be attained. Results confirm that this procedure provides sufficient information for the extrapolation of coefficients to more realistic inlet swirls.

3.3 Test program and specifications:

The three seal configurations to be discussed are shown in figure 15. The nominal mean diametric seal clearance varies generally from about 0.15 to 0.3% of the seal diameter, depending on the absolute size and the application of the pump, and is doubled for the "worn condition." The seal diameter of 350 mm corresponds approximately to an impeller diameter $D_2 \approx 500$ mm.

Results of a smooth seal and a serrated seal with nominal and twice nominal clearance are presented. Yet, there is still a huge variety of other interesting configurations. All geometries, including some further variants, have been measured under EPRI (Electric Power Research Institute Inc., Palo Alto CA, USA) contract RP 1884-10.

3.4 Nondimensional presentation:

The general definition must include the pressure differential, the radius, the seal clearance, the length and, partially, the angular rotor speed to produce literally nondimensional coefficients. Whether the coefficients depend linearly or by any exponent on those parameters can not be concluded explicitly. Hence, the following definitions are used:

$$F_r^* = \frac{F_r/e \cdot h_o}{L_{seal} \cdot R \cdot dp} \qquad F_t^* = \frac{F_t/e \cdot h_o}{L_{seal} \cdot R \cdot dp}$$

$$K^* = \frac{K \cdot h_o}{L_{seal} \cdot R \cdot dp} \qquad k_c^* = \frac{k_c \cdot h_o}{L_{seal} \cdot R \cdot dp}$$

$$C^* = \frac{C \cdot h_o \cdot \omega}{L_{seal} \cdot R \cdot dp} \qquad c_c^* = \frac{c_c \cdot h_o \cdot \omega}{L_{seal} \cdot R \cdot dp} \tag{10}$$

$$M^* = \frac{M \cdot h_o \cdot \omega^2}{L_{seal} \cdot R \cdot dp} \qquad m_c^* = \frac{m_c \cdot h_o \cdot \omega^2}{L_{seal} \cdot R \cdot dp}$$

Experience with measured data exhibited that normalized rotordynamic coefficients become almost constant against both Re_a and Re_c at constant Re_a to Re_c ratios. This allows a huge amount of information to be condensed by plotting the mean values as bar charts at individual Re-ratios.

Radial and tangential forces can be deduced from equations (2). For a circular vibration orbit with radius e, the displacement, velocity and acceleration vectors become

$$\begin{bmatrix} X \\ Y \end{bmatrix} = \begin{bmatrix} e \cdot \cos(\Omega \cdot t) \\ e \cdot \sin(\Omega \cdot t) \end{bmatrix} \qquad \begin{bmatrix} \dot{X} \\ \dot{Y} \end{bmatrix} = \begin{bmatrix} -e \cdot \Omega \cdot \sin(\Omega \cdot t) \\ e \cdot \Omega \cdot \cos(\Omega \cdot t) \end{bmatrix} \qquad \begin{bmatrix} \ddot{X} \\ \ddot{Y} \end{bmatrix} = \begin{bmatrix} -e \cdot \Omega^2 \cdot \cos(\Omega \cdot t) \\ -e \cdot \Omega^2 \cdot \sin(\Omega \cdot t) \end{bmatrix} \tag{11}$$

Because of the circular symmetry, no phase angle is needed. The simplest case to calculate radial and tangential forces is at t = 0, where $\sin(\Omega \cdot t) = 0$ and the eccentricity is on the x-axis. Hence, F_x becomes F_r and F_y becomes F_t, and the matrix equation (12) can be rewritten as

$$- F_r = K \cdot e + c_c \cdot e \cdot \Omega - M \cdot e \cdot \Omega^2$$
$$\tag{12}$$
$$- F = - k_c \cdot e + C \cdot e \cdot \Omega + m_c \cdot e \cdot \Omega^2$$

Introducing the normalization of equations (10) into equations (12), the following dimensionless presentation is found:

$$- F_r^* = K^* + c_c^* \cdot \left[\frac{\Omega}{\omega} \right] - M^* \cdot \left[\frac{\Omega}{\omega} \right]^2$$
$$\tag{13}$$
$$- F_t^* = - k_c^* + C^* \cdot \left[\frac{\Omega}{\omega} \right] + m_c^* \cdot \left[\frac{\Omega}{\omega} \right]^2$$

Radial and tangential forces are only plotted at one selected ratio of excitation to running frequency, 0.8, as typical ratios for instabilities at high

energy pumps range from about 0.7 to 0.9 (ref. 1). The same scheme as for coefficients is used.

4. MEASURED DATA

4.1 Error Estimation:

High radial stiffness of the measuring shaft, which is attained with a short and compact shape, is required in order to avoid critical speeds. This implies that the measuring system was very susceptible to nonsymmetrical stress distributions. Based on experience, the maximum uncertainty of the dynamic forces is estimated to be ±5%. The uncertainties of the displacement measurement are measured to be within ±2%. The signal conditioning and processing are further sources of deviations. Therefore the accuracy of the measured impedance functions is estimated to be within ±10% (worst case).

The accuracy of the extracted coefficients depends further on the scatter of the measured values and on the deviation of the actual impedance function from the underlying mathematical model. Some of the uncertainties mentioned are absolute values, and thus, the relative measurement errors are quite small for large absolute loads and become large for values close to zero!

Standard deviations of measured data indicate clearly that the direct stiffness and damping coefficients, being the largest values, are matched very well. The cross coupled stiffness is still fairly accurate, results are better with larger inlet swirls and hence, larger absolute coupled stiffnesses. The direct mass at low Reynolds number ratios exhibits satisfactory relative standard deviations. Cross coupled damping and mass terms as well as direct mass terms at higher Re-ratio values can not be considered reliable at all.

For the nondimensional presentation, the errors of the operating conditions need to be known. The mean static pressure measurement was found to vary within ±5%. The accuracy of the pressure transducers lies within 2% (including static drifts), and the flow meter gives results with less than 1% error. The rotor speed is assumed to be erratic by some 2%. The fluid properties are estimated to be within 2% of their true values and geometrical data is judged to be within 5% of the actual dimensions under load and temperature. Those errors add up statistically to possible deviations from operating conditions of approximately 8%. Additionally, for the cross-coupled stiffness, the error of the circumferential inlet velocity, which is about 5%, must be included, as k_c^* varies about linearly with U_{tho}. This results in slightly larger deviations of 9% for the coupled stiffness.

Together with the estimated maximum load measurement error of ±10% and individual deviations from impedance functions, this leads to the following worst case uncertainties of nondimensional rotordynamic coefficients:

K^*: ≈ ± 13 % k_c^*: ≈ ± 16 %
C^*: ≈ ± 13 % c_c^*: ≈ ± 41 %
M^*: ≈ ± 14 % (min.) m_c^*: ≈ ± 115 %
M^*: ≈ ± 21 % (mean Re-ratio)
M^*: ≈ ± 56 % (max.)

Hence, only stiffness coefficients, the direct damping and the direct mass term at smallest Re-ratios are reliable results, but coefficients with large possible errors are of no interest, as their actions on the rotor are negligible.

4.2 Discussion of Test Results:

In order to discuss the test results, bar diagrams have been established. The total average of all points at all Re-ratios reflects whether the test result depends on the individual Re-ratios or not.

Rotordynamic coefficients: (Figures 16 through 19)

OOS:
The smooth, N8 surface roughness seal is shown in figure 16. The direct stiffness exhibits scatter well within the limits of measurement errors, and the nondimensional stiffness of this test series is constant for all Reynolds numbers and for any Re-ratio.

The cross coupled stiffness indicates a dependency on the Re-ratio, but not on the Re-level. Extracted cross coupled stiffnesses were all within the band width of estimated measurement error, even in spite of some inlet swirl variations. For a constant inlet swirl, the cross coupled stiffness decreases with increasing Re-ratios. At higher Re-ratios, the time needed to pass through the seal clearance becomes relatively shorter and, as a consequence, the fluid can not be accelerated in the circumferential direction to the same extent as with lower Re-ratios. However, for this test series the inlet swirl used for individual Re-ratios increased with the Re-ratio, and both effects compensate to some degree.

The direct damping depends on the Re-ratio, too. Yet, at individual Re-ratios, coefficients remain constant over the total Re-range measured, and scatter lies well within the estimated relative error. Cross coupled damping seems to exist at the lowest Re_a/Re_c only. As it is very small, scatter is considerable, and at higher Re-ratios, c_{xy}^* is essentially zero.

The direct mass term exists at lowest Re-ratios, but the relative scatter is considerable and larger than estimated errors. A distinct decrease can be found for increasing Re-ratios. Averaged cross coupled mass coefficients are not reliable at all, as they are practically nonexistent for short seals.

At the chosen whirl frequency ratio of 0.8 (vibration to running frequency), the re-composed radial and tangential forces exhibit constant averaged values at individual Re-ratios, including little relative scatter. The centering radial forces do not depend on the Re-ratios and the tangential forces are braking, though to a lesser extent for higher Re-ratios. The gradient of tangential forces would be smaller or inverted if the attainable inlet swirl, and hence the cross coupled stiffness, were at realistic values of a pump neck ring seal. The cross coupled stiffness can be linearly extrapolated with the inlet swirl, including a parallel offset towards positive inlet swirls, see figure 19. The definition of this straight line as well as numeric values of slopes and offsets for individual configurations and Re-ratios can be found in table 3 of the appendix. Extrapolation to an $U_{tho} = 0.75$ results in all tangential forces becoming driving and diminishing in absolute magnitude with increasing Re-ratios, see overview of extrapolated F_t^*

in table 2. The fact that all extrapolated F_t^* include much larger errors, i.e., approximately ±30%, than estimated for measured values must be stressed.

04S:
Figure 17 presents average values for the N8 surface roughness, serrated seal. Comparison with the smooth seal indicates no drop of the total averaged dimensionless stiffness for the serrated seal. However, for the serrated seal, K_{xx}^* is not entirely constant with Re-ratios and individual differences of the average stiffnesses up to some 10%.

The cross coupled stiffness is reduced considerably in comparison to the values for the smooth seal, but direct damping terms are a little higher than the values of the smooth seal. At the present moderate inlet swirl, the combination of the more advantageous damping and coupled stiffness coefficients from the serrated seal leads to a moderate gain in braking forces around 20%. The extrapolation shown in figures 2 and 3 indicates clearly the driving tendencies at realistic inlet swirls for both smooth and serrated seals. However, the serrated seal is extensively less destabilizing at low Re-ratios; though this advantage diminishes towards high Re-ratios.

04D-M:
Average values of the double clearance, "worn" serrated seal are presented in figure 18. In this configuration the serration depth is reduced from the "new" condition in order to simulate wear, which occurs on both rotor and stator.

The direct stiffness is not quite inversely proportional to the seal clearance, as the definition of nondimensional coefficients would suggest, resulting in higher dimensionless values for the worn condition. A similar slight decrease of nondimensional direct stiffness with increasing Re-ratios as with the single clearance seal is found.

The cross coupled stiffness is approximately inversely proportional to the seal clearance. The averages of the single and double clearance seals are not exactly equal, but scatter of the double clearance seal is notably large at the lowest force levels, and the average of the single clearance seal fits well enough into this band of standard deviations. However, the drop of cross coupled stiffness with increasing Re-ratios is slightly larger for the double clearance seal.

Nondimensional direct damping at low Re-ratios does not confirm the definition equation (10) with respect to seal clearance. As damping of the double clearance seal drops more extensively with Re-ratios, the nondimensional damping values from test series 04D and 04S match better at higher Re-ratios.

The nondimensional mass is approximately twice as large as for the single clearance seal, i.e., the mass becomes more significant for the resulting radial force. Where the nondimensional, direct stiffness is almost 50% higher for the double clearance seal, the associated radial force is only little more than 35% higher. However, the acting dimensional radial force is only about half as large for the 04D series seal, as F_r^* is divided by the double clearance and multiplied by a smaller pressure differential than for the single clearance seal.

The nondimensional tangential force becomes distinctively higher for the double clearance at the lowest Re-ratios because of the high direct damping. At medium and high Re-ratios, there is no gain in the nondimensional tangential force. Values

extrapolated to higher inlet swirls are shown in table 2. Driving dimensionless tangential forces are smaller for the "worn" seal than for the "new" seal. However, the advantage of the "worn" seal being less destabilizing than the "new" seal diminishes with increasing inlet swirl and increasing Re-ratio.

Note that F_t^* of the "worn" seal is approximately one order of magnitude smaller than its two components and that the cross coupled stiffness is very uncertain because of large extrapolation. This implies the possibility of a large relative error of F_t^*.

Well designed swirl breaks cut the inlet swirl to approximately $U_{tho} = 0.4$, and hence, both seal conditions become stabilizing. However, the stabilizing effect of the worn seal will be smaller than the one of the new seal, as the lower pressure drop and the double clearance will result in an approximately 60% smaller dimensional force (see equations (10)).

Flow Resistance: (Figure 20)

Some average values, mainly at low Re-ratio, may not be representative for the friction behaviour, indicated by the large standard deviations. This is not measurement scatter, but the change of the friction factor with Reynolds numbers' which is larger for Lambda values than for rotordynamic coefficients. However, to get a general overview, and in order to compare individual configurations, these charts are very useful.

The bar charts provided are only comparable to each other if measured Re-ranges are approximately equal or if the standard variation indicates constant Lambda values. Re-ranges are the same for the nominal clearance seals, and slightly higher for the double clearance seal. However, the double clearance seal provides quite constant Lambda values at a moderately higher Reynolds number (a factor of 2) in contrast to the Re-range of $Re_{max}/Re_{min} \approx 13$.

A high surface roughness of N8 yields quite large friction factors, the equivalent relative roughness is found to be around 0.02 from the comparison of the smooth seal with the Moody diagram. Indeed, comparison with another measurement at Sulzer Brothers, as published in (ref. 12) and (ref. 13), proves the growth of friction factors from N6 to N8 surfaces to be considerable.

The decrease of Lambda values is largest with increasing Re_a's at lowest Re-ratios and becomes quite small at higher Re-ratios. Furthermore, inlet swirl does not affect the friction factor. Increased leakage flow with swirl breaks hence results exclusively from the lower pressure drop within the impeller side room, caused by the lowering of the rotational velocity, which results in a higher pressure differential across the seal.

Comparison of the serrated seal with the smooth seal shows that there is some gain in friction factors at low Reynolds number, and a definitive increase of Lambda values is attained at higher Re-numbers. For high Re-numbers, the increase is considerable around 30%. From a hydraulic point of view, a high surface roughness is desirable, even with serrated seals. Additionally, the serration geometry might be further optimized, in order to result in higher friction. However, further gain in friction must be compared to the changes in rotordynamic behaviour.

Wear of the serrated seal, as it is simulated with test series 04D indicates, that friction factors rise marginally when the clearance is opened to twice its original value and the serration depth is reduced. Realize that, even for a slightly increased Lambda value, the leakage flow does increase quite drastically with larger seal clearances and hence, Reynolds numbers become larger.

5. CONCLUSIONS

Rotordynamic and hydraulic annular pump seal coefficients of three typical neck ring configurations have been measured at an accuracy for relevant coefficients within less than ±20%. A smooth seal and a serrated seal in new and worn conditions, have been successfully investigated. The effect of surface roughnesses on friction factors for a smooth seal have been discussed. Operating conditions of full size boiler feed pumps were attained. Restrictions were encountered only in the inlet swirl. Normalization and type of presentation for rotordynamic coefficients have proven to be adequate, resulting in constant values over the Reynolds range measured.

The investigation revealed that, from the skew symmetric 2x2 stiffness, damping, and mass matrices used in the present model for interaction forces, the cross coupled damping and the cross coupled mass terms are totally irrelevant. Considerable direct mass terms occur only at very low ratios of axial to circumferential Reynolds numbers. Even the largest mass coefficients change the radial interaction force of an annular seal only by some 10%. Hence, the size of direct mass terms is merely of secondary importance.

In tables 1 through 4, a rough overview of nondimensional interaction forces, including extrapolation of tangential forces, and averaged friction factors of the three configurations is given. However, normalization for rotordynamic and hydraulic coefficients overestimates the influence of the seal clearance. Double clearance values generally tend to be higher than the related single clearance values.

Damping Action:

The driving tangential force is influenced strongest by individual seal configurations at lowest Reynolds number ratios (table 2). All neck ring seals measured resulted in definitively destabilizing tangential forces at realistic inlet swirls (0.7 ÷ 0.8). The serrated seal (04S) exhibits clearly less destabilizing tendencies than the smooth seal (00S). The advantage becomes smaller with increasing Re-ratios, as the influence of the seal surfaces on the circumferential fluid velocity becomes smaller with the shorter passage time. Double clearance seals can reduce the nondimensional driving tangential force, if properly designed (04D). However, with the use of swirl breaks at neck rings or at interstage bushings, where the inlet swirl is zero, only single clearance seals can provide damping action.

Tangential forces can not be compared directly with the earlier measurements as cited in (ref. 12) and (ref. 13), as only a synchronous excitation was available there. The Re-range in those papers is much smaller and no individual coefficients could be measured. Additionally, the inlet swirl available there was quite different from the present ones. However, taking these uncertainties into account,

damping action as presented in (ref. 13), figure 19, compares fairly well to present results measured at medium Re-ratio and lowest Reynolds numbers.

Stiffening Action:

For individual seal designs, the relative changes of radial forces, i.e., primarily of direct stiffness coefficients, are generally lower than for tangential forces, see table 1. It is remarkable that the stiffening effect is not much lowered for the serrated seal. The increase of dimensionless radial forces of the double clearance seal proves that the clearance in the normalization equations is overestimated. Yet, dimensional stiffening effects of worn seals under normal operating conditions in a pump will definitively be lowered, though to more than only half the magnitude of single clearance seals.

Results of radial forces for the serrated seal compare even better than for tangential forces with measurements as presented in (refs. 12, 13). As the direct stiffness is predominant in the radial force and as it does not depend on inlet swirl, individual excitation frequencies and inlet swirls do not affect the comparison.

Flow Resistance:

Averaged Lambda values as are presented in table 4, need to be interpreted very carefully. Generally, friction factors of smooth surfaces do vary considerably in the Re-range measured for these tests (20'000 ÷ 260'000). However, for the present large relative roughnesses (appr. 0.02, according to Moody's diagram), Lambda coefficients become almost constant at moderate Reynolds numbers. Hence, average values are comparable.

The increase of surface roughness from N6 to the actual N8, results in a distinct rise in flow resistance, as has been found by comparison with results from earlier measurement. The measured serrated seal (04S) exhibits very favourable flow resistance when compared to the smooth seal. It shows considerable gain in friction at low Re-numbers, and the greatest improvement is encountered at the largest Re-numbers. Simulated wear reveals slightly higher friction factors, in spite of higher Re-numbers. However, better hydraulic performance could certainly be attained, for example, by a very deep serration and a high ratio of serration to land width. This advantage might be quickly reduced, as the remaining land portions tend to be worn off sooner than wider land portions. Additionally, such a hydraulically optimized serration pattern deteriorates rotordynamic behaviour because of the large serration depth ("Antilomakin" seal).

Final Discussion:

The comparison of rotordynamic and hydraulic coefficients of smooth versus serrated seals clarified that configurations with advantages in one respect may have disadvantages in other respects. However, the presented serrated seal with a surface roughness of N8 is quite favourable in respect to damping capabilities (tangential forces) and exhibits an appealing stiffening effect. Moreover, it displays a fairly high flow resistance.

Obviously, the choice of an appropriate seal configuration depends on the application of the pump, i.e., on whether hydraulic or rotordynamic behaviour is more essential (ref. 14). In any case, rotordynamic behaviour in a boiler feed pump

must be thoroughly considered, when using stepped or deeply serrated anti-stiffness seals in order to gain increased efficiencies.

Unquestionably, not all possible, not even all promising seal configurations have been measured and presented here. One serrated seal has been chosen to be measured in detail, i.e., in new and worn conditions, and has been compared to a plain smooth seal. However, results of the serrated seal measurements are quite attractive, and the serration configuration might be optimized by further investigations.

6. TABLES: SUMMARY OF ROTORDYNAMIC AND HYDRAULIC BEHAVIOUR

Table 1. - SUMMARY OF F_r^*
[frequency ratio 0.8]

Test series:	Fr*:			Re-ratio:		
	a	b	c	a	b	c
00S-V	−0.45	−0.46	−0.44	0.32	0.63	0.94
04S-V	−0.45	−0.43	−0.40	0.32	0.63	0.92
04D-V	−0.63	−0.57	−0.59	0.31	0.62	0.93

Table 2. - SUMMARY OF EXTRAPOLATED F_t^*
[U_{tho} = 0.75   frequency ratio 0.8]
($Ft^* < 0$: braking, $Ft^* > 0$: driving)

Test series:	Ft*:			Re-ratio:		
	a	b	c	a	b	c
00S-V	+0.31	+0.15	+0.10	0.32	0.63	0.94
04S-V	+0.12	+0.12	+0.10	0.32	0.63	0.92
04D-V	+0.04	+0.05	+0.09	0.31	0.62	0.93

Table 3. - EXTRAPOLATION FOR k_c^*, F_t^* AND CRITICAL FREQUENCY RATIO
Note: all values concerning k_c^* are <u>extrapolated</u>!

$$k_c^* = (U_{tho} - x_o) \cdot m$$

$$F_t^* = k_c^* - \Omega/\omega \cdot C^*$$

Critical frequency ratio for $F_t^* = 0$ (change from braking to driving):

$$(\Omega/\omega)_c = (U_{tho} - x_o) \cdot m / C^* = a \cdot U_{tho} - b$$

Test Series:	Re-ratio: [Re_a/Re_c]	x_o [U_{tho}]	m [k_c^*/U_{tho}]	C^* [-]	a [-]	b [-]	$(\Omega/\omega)_c$ $U_{tho}=.75$
00S-V	0.32*⟩	0.0	1.04	0.59	1.76	0.00	1.32
	0.63	0.025	0.59	0.35	1.69	0.04	1.23
	0.94	0.05	0.38	0.21	1.81	0.09	1.26
04S-V	0.32*⟩	0.06	0.87	0.60	1.45	0.085	1.00
	0.63	0.075	0.61	0.36	1.69	0.125	1.14
	0.92	0.09	0.44	0.24	1.83	0.165	1.21
04D-V	0.32*⟩	0.07	1.04	0.84	1.24	0.085	0.85
	0.61	0.095	0.57	0.40	1.42	0.135	0.93
	0.92	0.12	0.48	0.27	1.78	0.215	1.12

*⟩ roughly estimated (from individual measurement points)

Table 4. - SUMMARY OF LAMBDA (GENERAL OVERVIEW)

Test series:	LAMB-EFF			Re-ratio:		
	a	b	c	a	b	c
00S-V	0.066	0.055	0.057	0.32	0.63	0.94
04S-V	0.071	0.069	0.074	0.32	0.63	0.92
04D-V [1⟩]	0.076	0.071	0.073	0.31	0.62	0.93

The following restrictions have to be observed, when comparing above averaged friction factors:

[1⟩] Higher Re-range at double clearance seals:
no large effect, as Lambda values of serrated double
clearance seals do not vary extensively when doubling
Re-numbers

7. LIST OF SYMBOLS

Roman:

b	[m]	seal groove width
C	[Ns/m]	symmetric direct damping coefficient
c	[m/s]	total velocity
c_c	[Ns/m]	skew-symmetric cross-coupled damping coefficient
D_s	[m]	seal diameter (general)
D_2	[m]	outer diameter of impeller
D_h	[m]	hydraulic diameter
dp	[N/m²]	total pressure differential across seal
$\overline{D}$	[N/m]	impedance function, definition in equation (4) and (5)
$\overline{E}$	[N/m]	impedance function, definition in equation (4) and (5)
e	[m]	eccentricity
F_r	[N]	force in radial direction
F_t	[N]	force in tangential direction
F_x	[N]	force in x-direction
$\overline{F_x}$	[N]	complex force in x-direction
F_y	[N]	force in y-direction
$\overline{F_y}$	[N]	complex force in y-direction
h_o	[m]	mean seal gap width
K	[N/m]	symmetric direct stiffness coefficient
k_c	[N/m]	skew-symmetric cross-coupled stiffness coefficient
k_s	[m]	equivalent surface roughness
Lambda	[-]	Friction coefficient, see equation (7)
L_{seal}	[m]	seal length
M	[kg]	symmetric direct mass coefficient
m_c	[kg]	skew-symmetric cross coupled mass coefficient
n	[rpm]	rotor speed
nue	[m²/s]	kinematic viscosity
p	[N/m²]	pressure
p_i	[N/m²]	pressure at inlet of seal
p_o	[N/m²]	pressure at outlet of seal
p(0)	[N/m²]	pressure at z = 0, within seal
p(L)	[N/m²]	pressure at z = L_{seal}, within seal
R	[m]	seal radius R = $D_s/2$

Re	[-]	total Reynolds number, $Re = c \cdot 2 \cdot h_o / nue$
Re_a	[-]	axial Reynolds number, $Re_a = v \cdot 2 \cdot h_o / nue$
Re_c	[-]	circumferential Reynolds number, $Re_c = R \cdot \omega \cdot 2 \cdot h_o / nue$

rho	[kg/m³]	density

t	[s]	time

u	[m/s]	tangential velocity
U_{tho}	[-]	dimensionless tangential velocity, $U_{tho} = u/(R \cdot \omega)$

v	[m/s]	axial velocity

X	[m]	measured horizontal displacement
$\overline{X}$	[m]	complex measured horizontal displacement

Y	[m]	measured vertical displacement
$\overline{Y}$	[m]	complex measured vertical displacement

z	[m]	general axial co-ordinate

Ze_i	[-]	pressure loss coefficient at inlet of seal
Ze_o	[-]	pressure loss coefficient at outlet of seal

Greek:

ε	[-]	relative eccentricity e/h₀

Ω	[rad/s]	angular frequency of excitation
ω	[rad/s]	angular frequency of rotor

Superscripts:

*		dimensionless value

Subscripts:

i	inlet
o	outlet
R	Rotor
S	Stator

254

8. REFERENCES

1. Pace, S.E., Florjancic, S. and Bolleter, U.: Rotordynamic Developments for High Speed Multistage Pumps. Proceedings, 3rd International Pump Symposium, Houston Texas, May 1986.

2. MADYN, Ing. Büro Klement, Alkmaarstr. 37, 6100 Darmstadt 13, W. Germany or TURBO, University of Kaiserslautern, Pfaffenbergstrasse, 6750 Kaiserslautern, W.Germany and others.

3. Orcutt, F.K.: The Steady State and Dynamic Characteristics of a Full Circular Bearing and a Partial Arc Bearing in the Laminar and Turbulent Flow Regimes. Journal of Lubricating Technology, April 1967.

4. Glienicke, J.: Experimentelle Ermittlung der statischen und dynamischen Eigenschaften von Gleitlagern für schnellaufende Wellen. Forschungsberichte VDI-Z Reihe 1, 22, 1970.

5. Lund, J.E. and Thompson, K.K.: A Calculation Method and Data for the Dynamic Coefficients of Oil-lubricated Journal Bearings: Topics in Fluid Film Bearing and Rotor Bearing System Design and Optimisation. ASME, p. 1, 1978.

6. Bolleter, U. and Wyss, A.: Measurement of Hydrodynamic Interaction Matrices of Boiler Feed Pump Impellers. ASME 85-DET-148, 1985.

7. Bolleter, U., Leibundgut, E. and Stürchler, R.: Hydraulic Interaction and Excitation Forces of High Head Pump Impellers. Proceedings of the 3rd Joint ASCE/ASME Mechanics Conference: Pumping Machinery Symposium, San Diego, July 1989.

8. Childs, D.W.: Finite Length Solution for Rotordynamic Coefficients of Turbulent Annular Seals. ASME Transaction Journal of Lubrication Technology, pp. 437-444, Vol. 105, July 1983.

9. Nordmann, R., Dietzen, F.J., Janson, W., Frei, A., Florjancic, S.: Rotordynamic Coefficients and Leakage Flow of Parallel Grooved Seals and Smooth Seals. Fourth Workshop on Rotordynamic Instability Problems in High-Performance Turbomachinery, Texas A&M University, June 1986.

10. Childs, D.W.: Rotordynamic Moment Coefficients for Finite Length Turbulent Seals. IFTOM Conference on Rotordynamic Problems in Power Plants, Rome, Italy, 28.9-1.10 1982.

11. Fenwick, J., DiJulio, R., Ek, M.C., Ehrgott, R., Green, H. and Shaolian, S.: Linear Force and Moment Equations for an Annular Smooth Shaft Seal Perturbed Both Angularly and Laterally. Proceedings of 2nd Workshop of Rotor Instability at Texas A&M University, NASA Contract NAS8-27980.

12. Florjancic, S. and Frei, A.: Bedeutung der Spaltströmung für die Rotordynamik. Proceedings of the 16. Konstruktions-Symposium der DECHEMA, Frankfurt, June 87.

13. Florjancic, S. and Frei, A.: Dichtspaltströmung in Pumpen: Bedeutung für die Rotordynamik und theoretische Betrachtungen. Proceedings of the Pumpentagung Karlsruhe, Oct. 88.

14. Florjancic, D. and Florjancic, S.: Hydraulic and Rotordynamic Influence on the Choice of Different Pump Types. Proceedings of the Conference on Hydraulic Machinery 88, Ljubljana, Sept. 88.
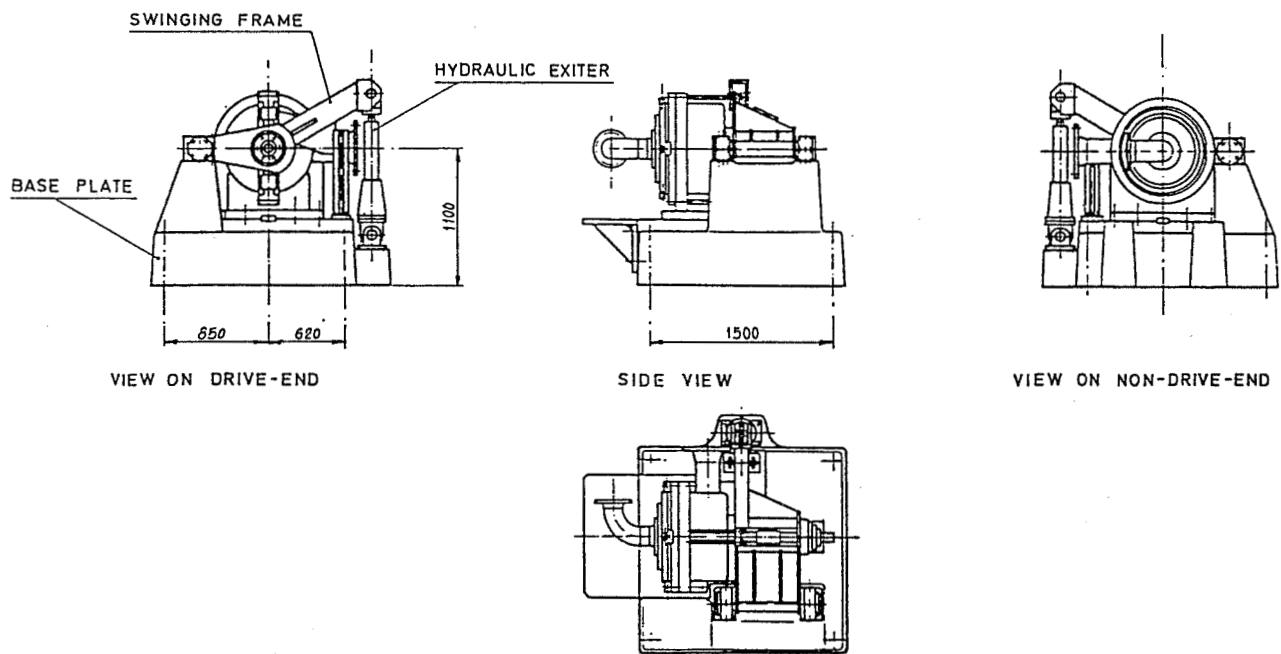
Figure 1. – Arrangement of test machine.
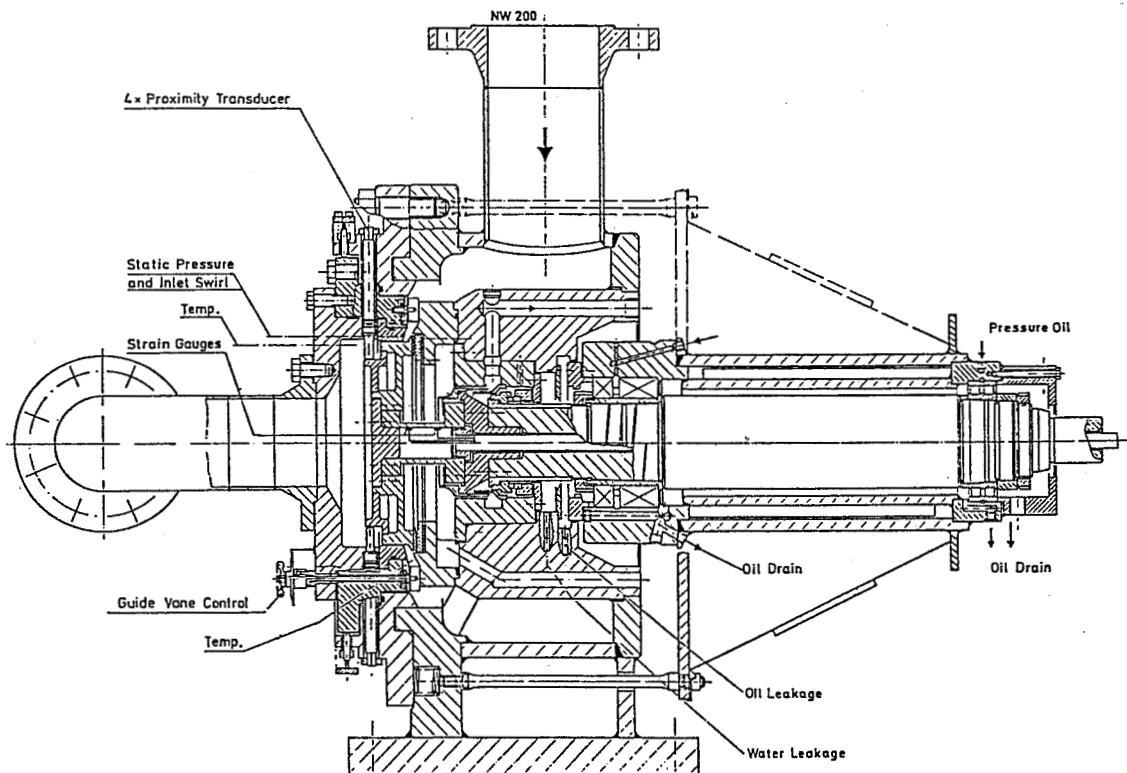
Figure 2. – Cross section of test machine.

256
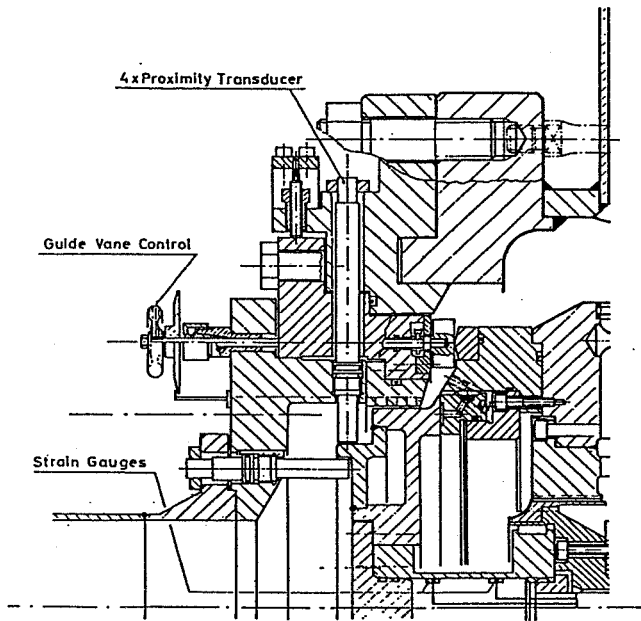
Figure 3. – Rotor, seal and guide vanes, hydrostatic balancing seal.

Straight seal:
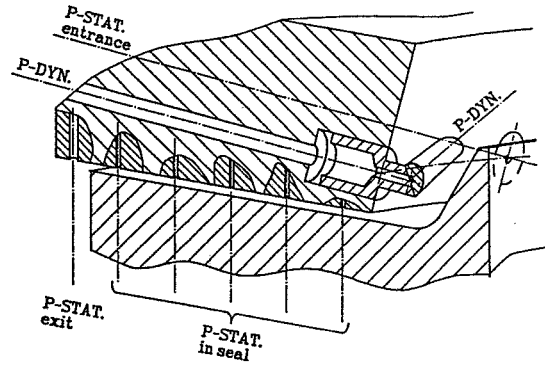
Figure 4. – Detailed cross-section at seal.
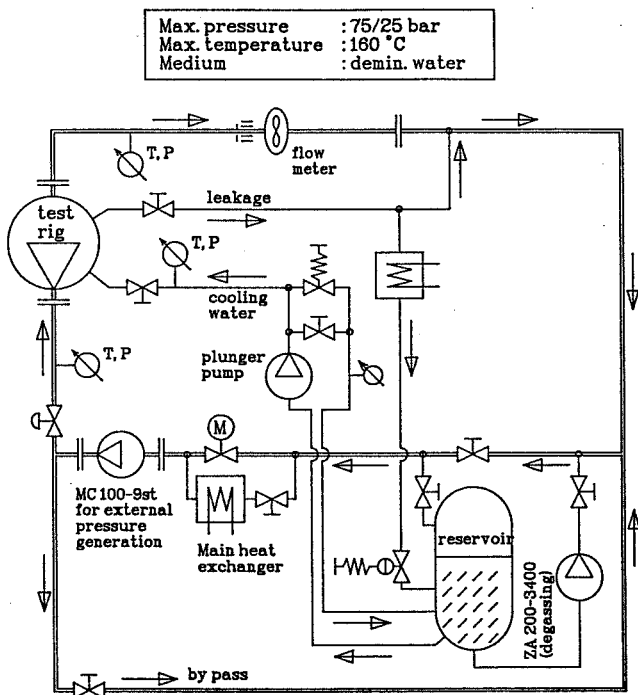
Figure 5. – Test loop.

General case:

a) forward elliptical orbit at arbitary position

b) backward elliptical orbit at arbitary postion

Special case:

c) forward circular orbit at special position $\Omega * t = 0$

d) backward circular orbit at special position $\Omega * t = 0$
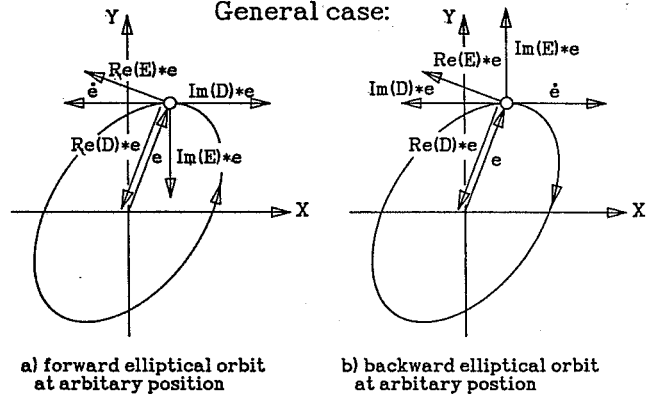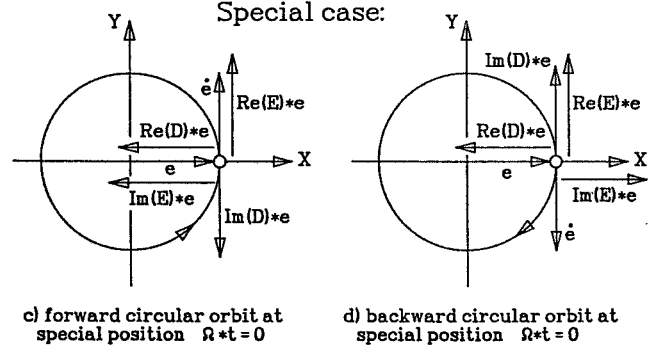
Figure 6. – Physical explanation of impedance functions.

257
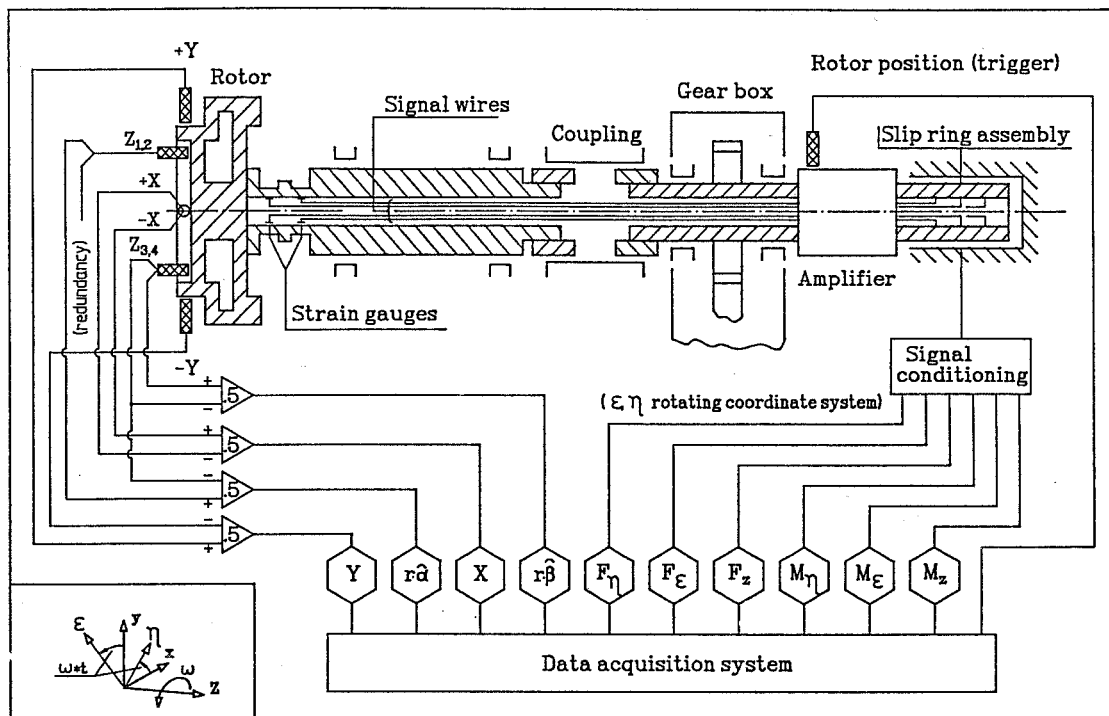
Figure 7. – Signal flow diagram.
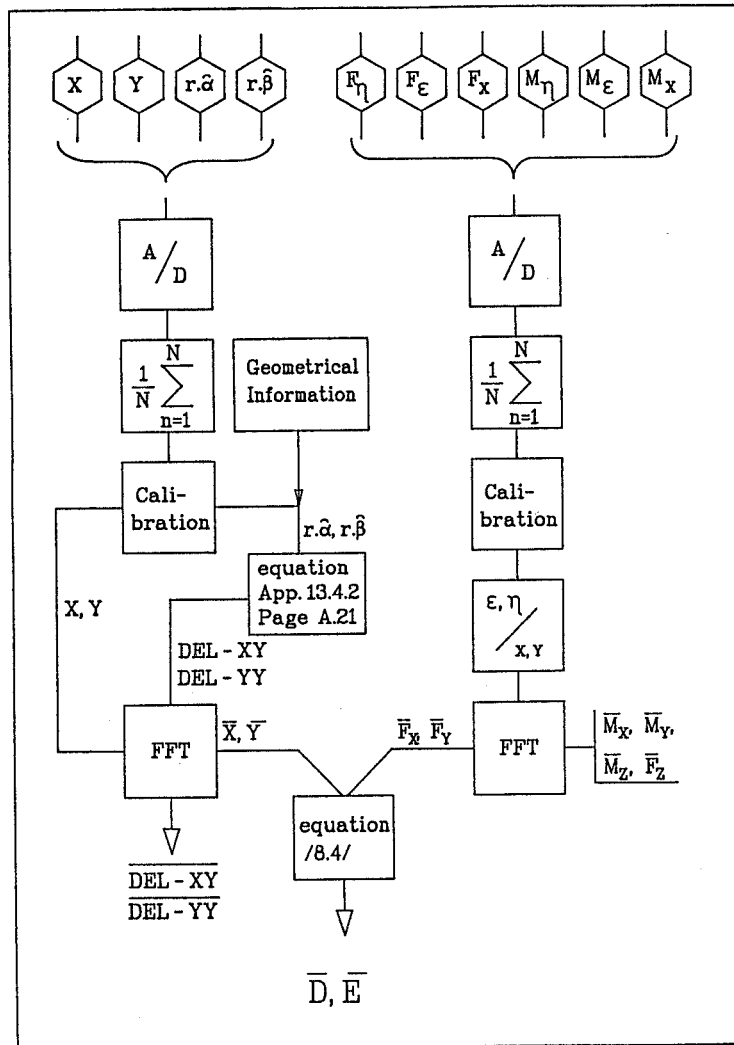
Figure 8. – Signal processing
(impedance functions).
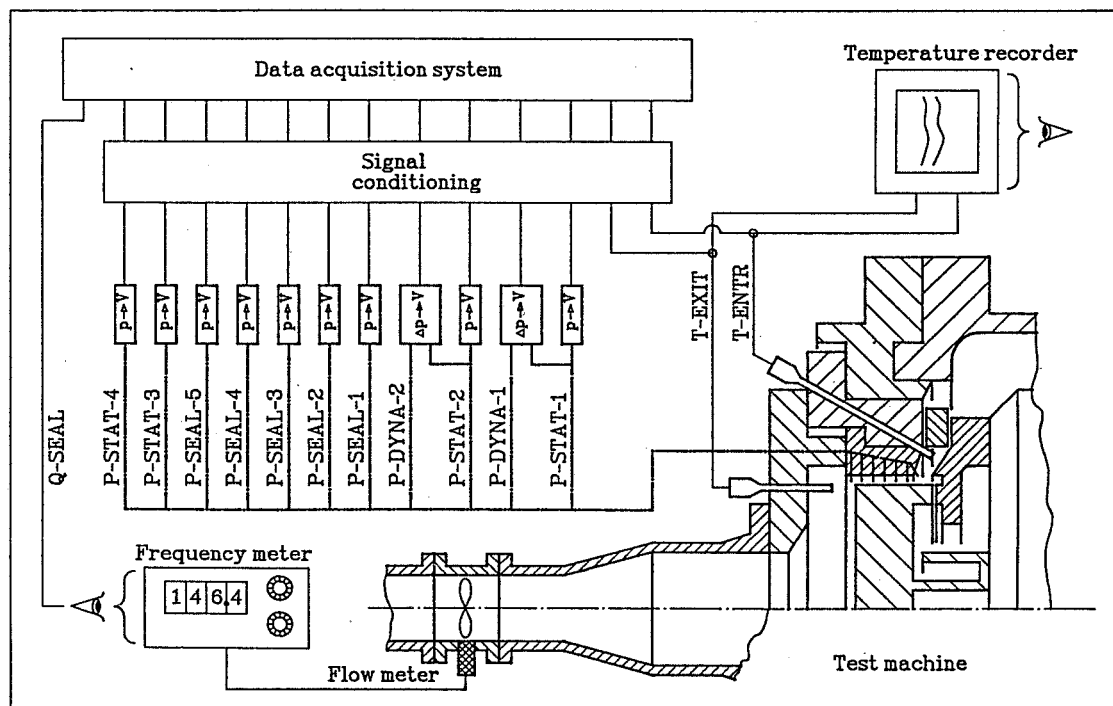
Figure 9. – Measurement of operating conditions.

Seal   Within seal   Seal
exit   (no excitation) entrance

Q-SEAL
N-ROTOR

T-EXIT
T-ENTR
P-STAT-4
P-STAT-3
P-SEAL-5
P-SEAL-4
P-SEAL-3
P-SEAL-2
P-SEAL-1
P-DYNA-2
P-STAT-2
P-DYNA-1
P-STAT-1

Cali-
bration

$\dfrac{A}{D}$

$\dfrac{1}{N}\displaystyle\sum_{n=1}^{N}$

Geometry &
definition
acc. app. 13.4.1

Cali-
bration

Equations
according to
appendix 13.4.2

Re_a, Re_c

P-ENTR, $\triangle$P-ENTR
P-EXIT, $\triangle$P-EXIT
U-ENTR, $\triangle$U-ENTR
LAMBDA, ZETA (δP/δL)
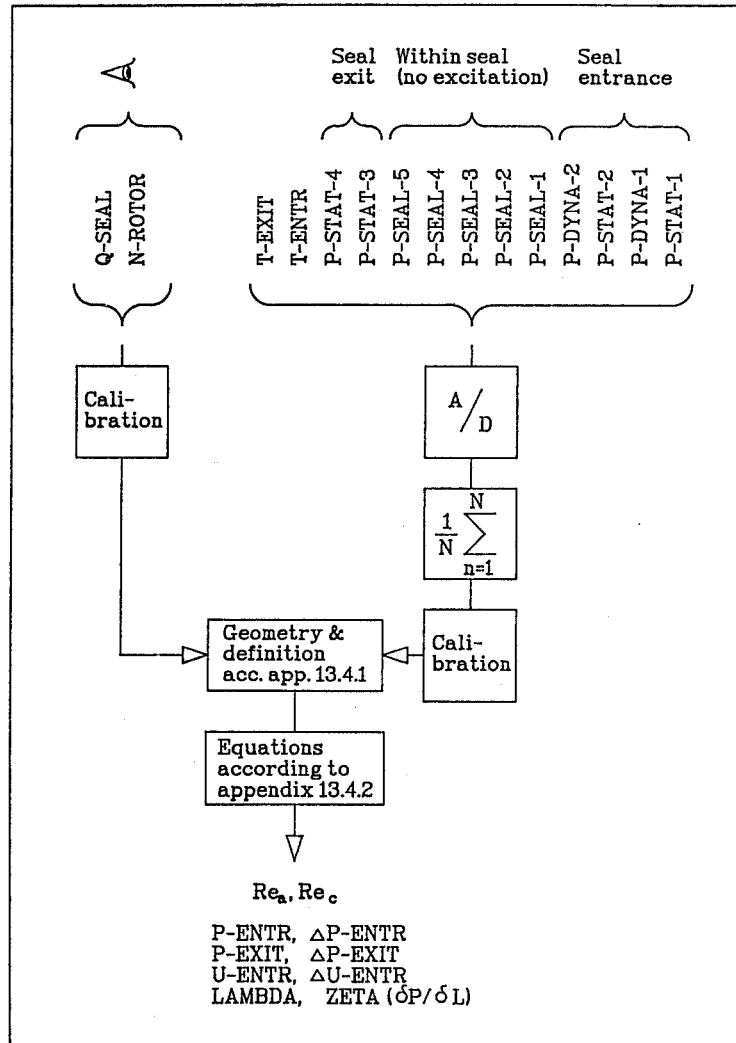
Figure 10. – Signal processing
(operating conditions).
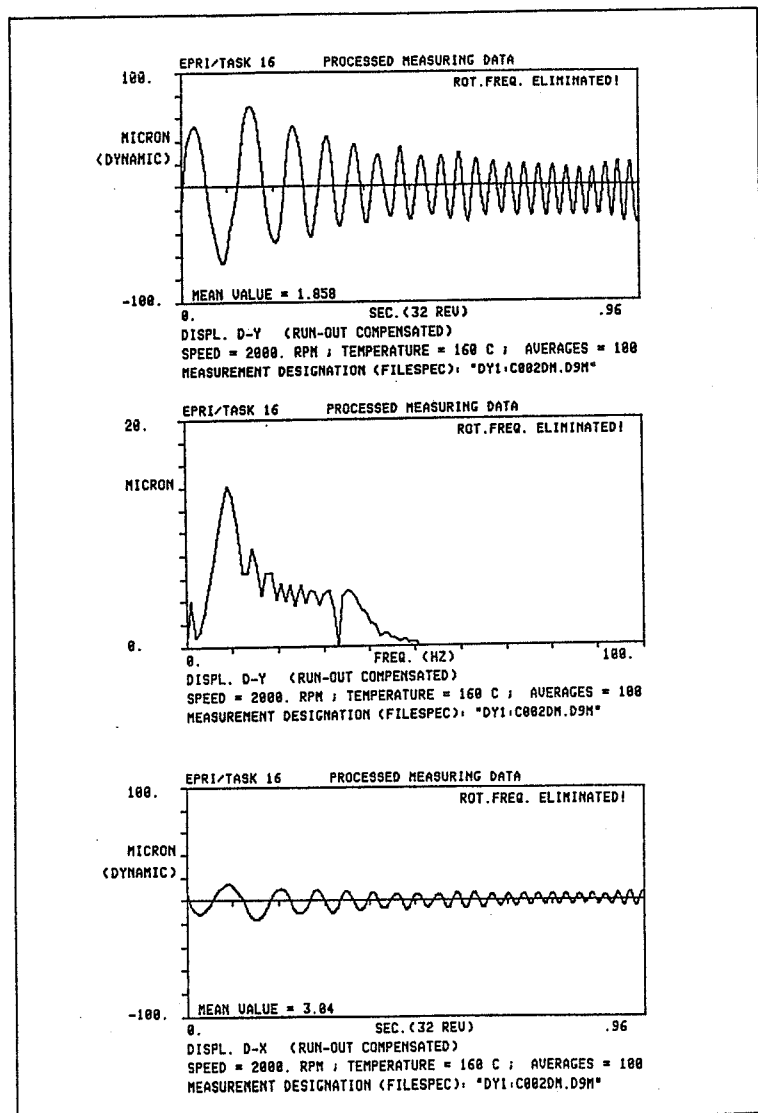
Figure 11. – Resulting displacement,
serrated seal.
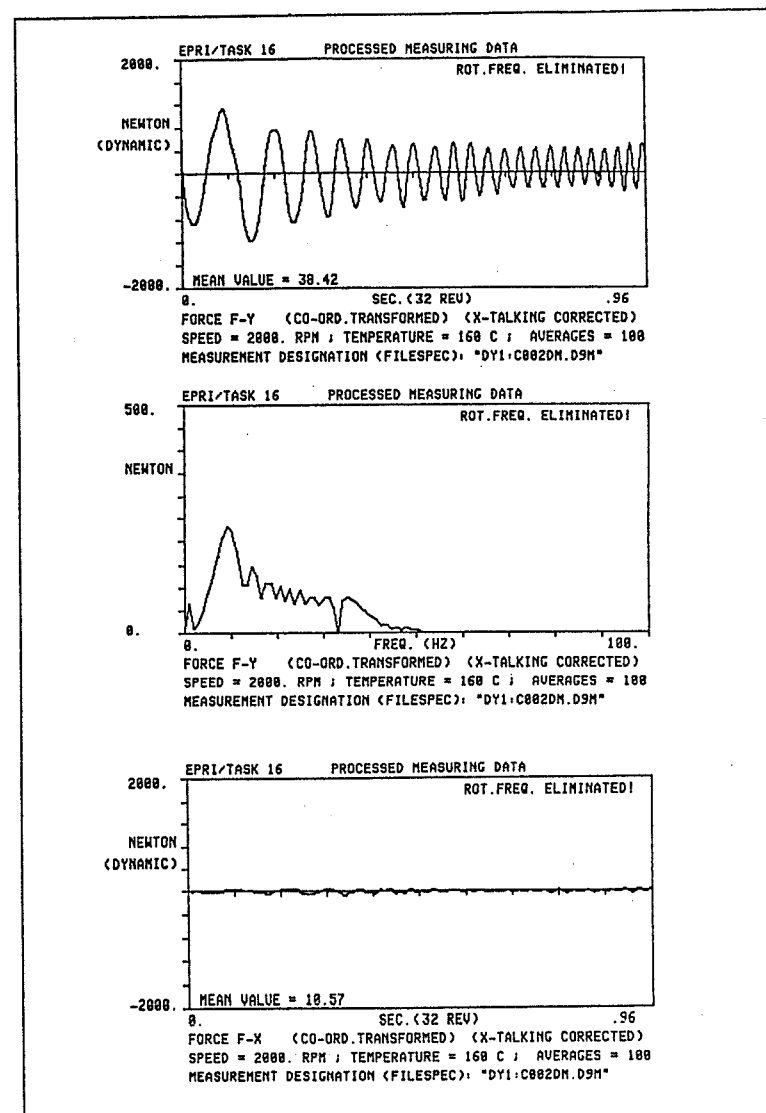
Figure 12. – Resulting forces,
serrated seal.
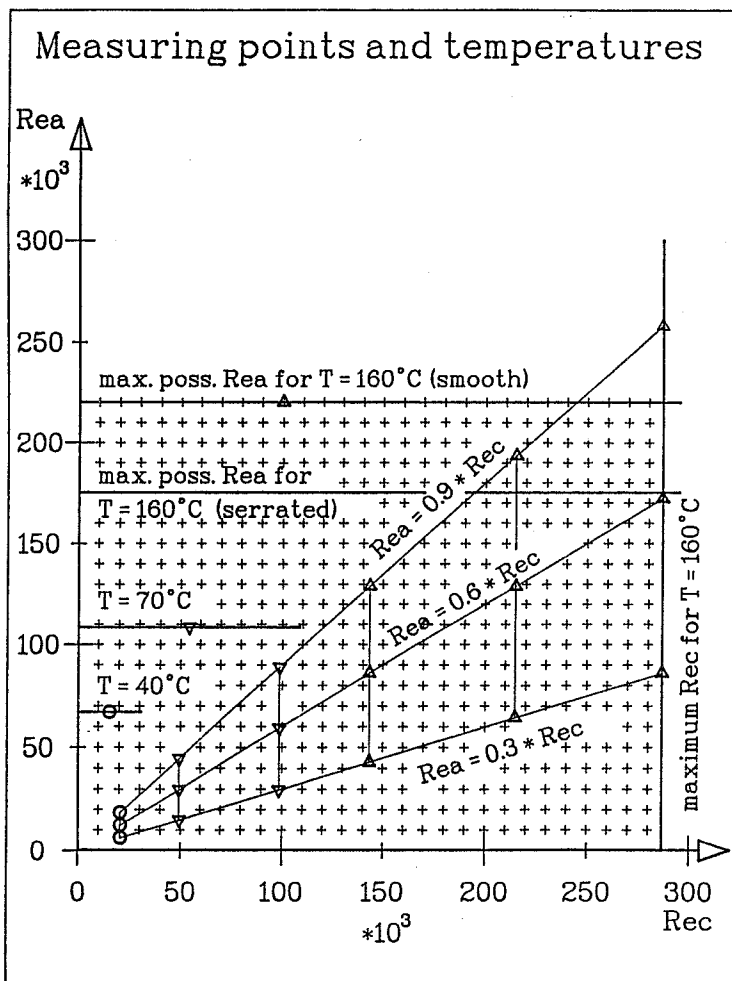
Figure 13. – Measuring range Re_c – Re_a.

Seal diameter:	350	mm	13.78	in
stepped:	350/325	mm	13.8/12.8	in
Radial clearance:	0.37	mm	0.015	in
double:	0.74	mm	0.03	in
Seal length:	40	mm	1.57	in
Water temperature:	20/70/80/160	°C	68/158/176/320	°F
Max. pump speed:	4000	rpm		
Max. pressure difference:	appr. 60	bar	870	p.s.i.
Max. circumf. Re-number:	275'000	[-]		
Max. axial Re-number:	175'000	(rough)		
	225'000	(smooth)		

TYPICAL VALUES FOR BFP'S:

Re_a/Re_c = 0.4 to 0.9   (measured 0,3 ; 0,6 & 0,9)

Re_c = 200'000 to 260'000

Re_a = 100'000 to 150'000

Figure 14. – Test parameters.

Geo-metry	Seal type	Surface	Gap width	Inlet swirl	Tempe-rature	Sketch
00S	straight	plain N8/N8	2.11‰	0.25 + Variation at 4 Points	40/70/160	
04S	straight	serrated N8/N8	2.11‰	0.15 + Variation at 4 Points	40/70/160	
04D	straight	serrated N8/N8	4.23‰	0.15 + Variation at 4 Points	40/70/160	

Definition of surface roughness acc. ISO 1302-1926

VSM 10231	Maximum allowable Surface roughness [1E-6 m]
N9	6,3
N8	3,2
N7	1,6
N6	0,8

Definition of near surface roughness value Ra
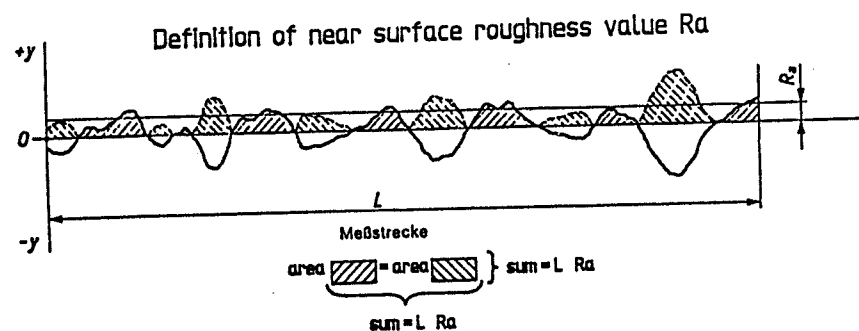
Figure 15. - Seal configurations.

Smooth Seal

EPRI TASK 16, C200SM

K^* [−] ka^* [−] C^* [−] M^* [−] Fr^* [−] Ft^* [−]
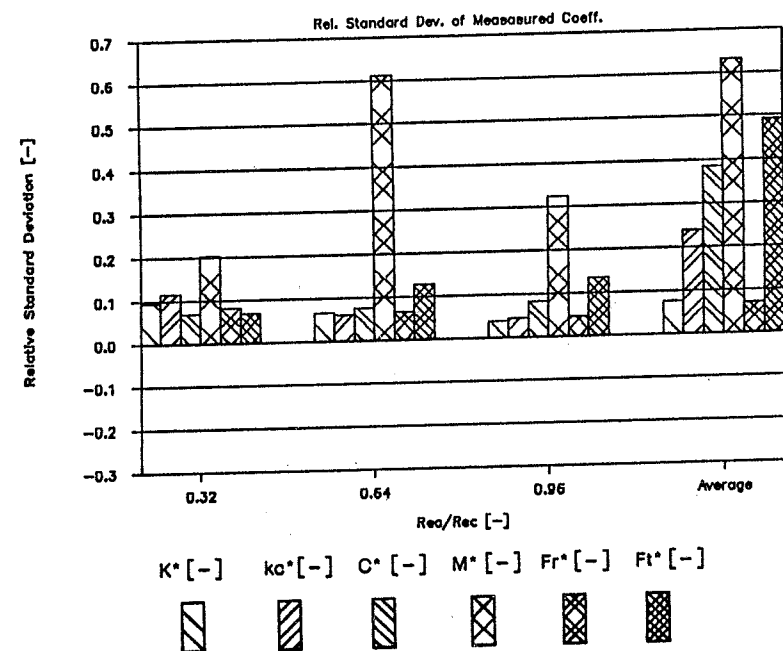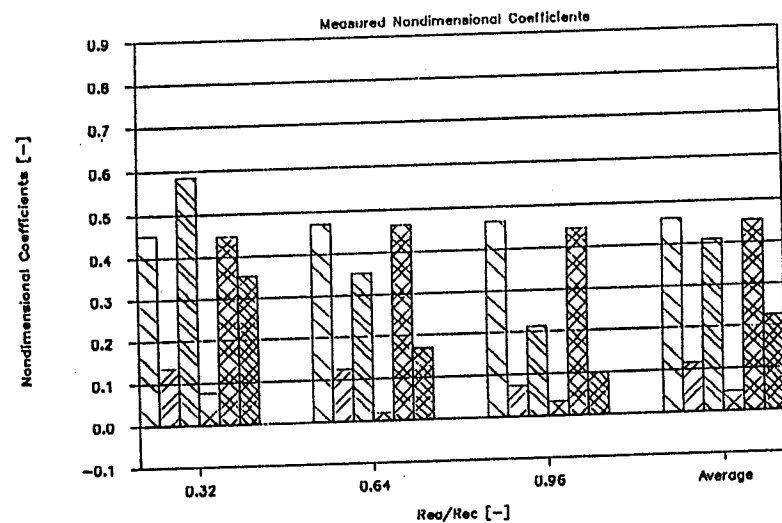
Figure 16. - Test 00S-M, averaged coefficients, f(Re-ratio).

New Serrated Seal

EPRI TASK 16, C204SM

Measured Nondimensional Coefficents

Nondimensional Coefficients [−]

Reo/Rec [−]

0.32   0.65   0.96   Average

Rel. Standard Dev. of Measured Coeff.

Relative Standard Deviation [−]

0.94   1.31   1.71

−2.19

0.32   0.65   0.96   Average

Reo/Rec [−]
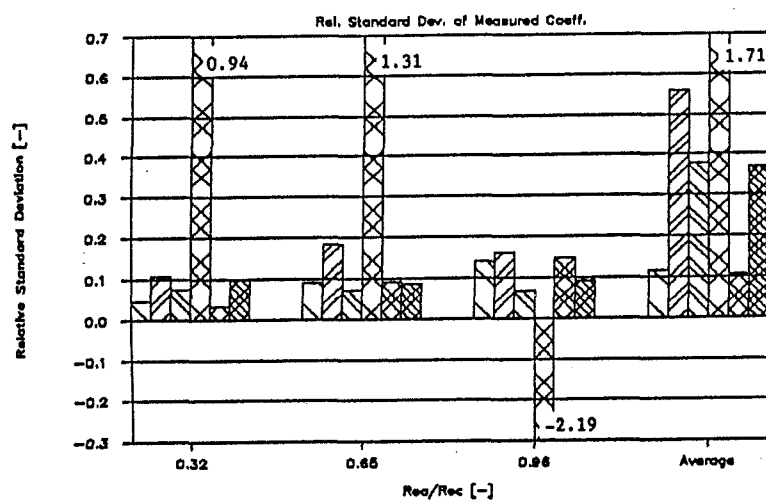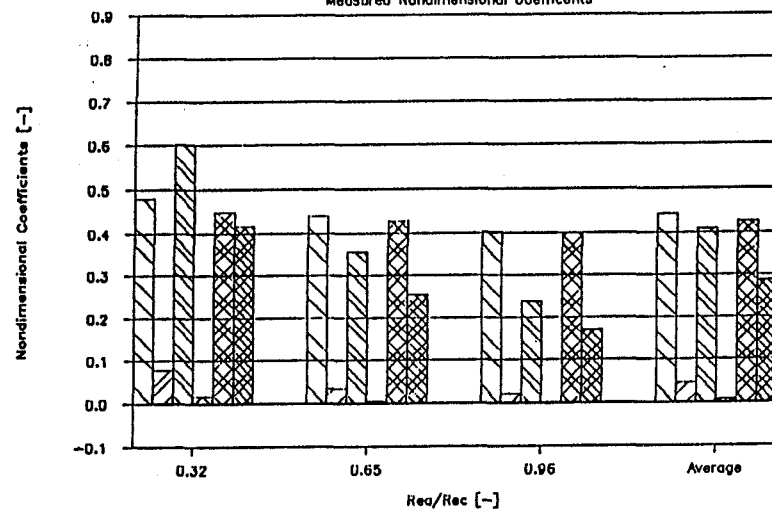
K* [−]   ko* [−]   C* [−]   M* [−]   Fr* [−]   Ft* [−]

Figure 17. − Test 04S−M, averaged coefficients, f(Re−ratio).

Worn Serrated Seal

EPRI TASK 16, C004DM

Rel. Standard Dev. of Measured Coeff.

Relative Standard Deviation [−]

0.32   0.64   0.96   Average

Reo/Rec [−]

Measured Nondimensional Coefficients

Nondimensional Coefficients [−]

0.32   0.64   0.96   Average

Reo/Rec [−]
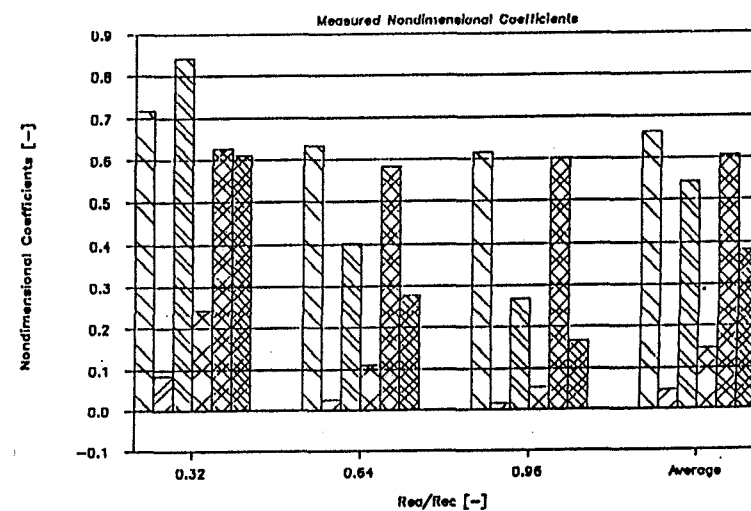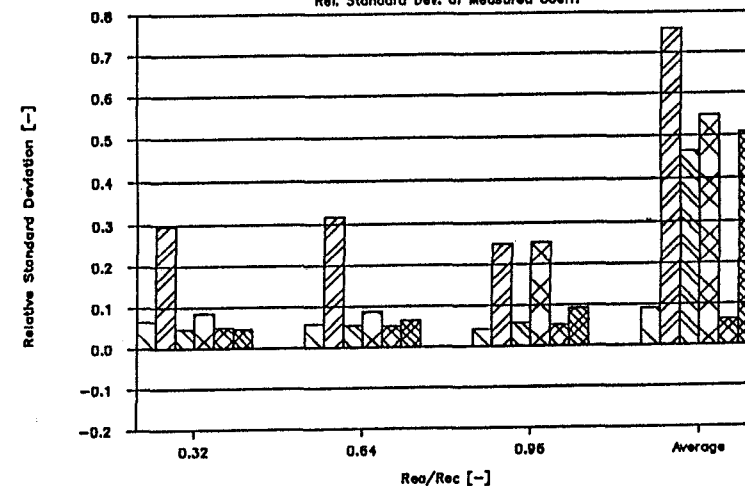
K* [−]   ko* [−]   C* [−]   M* [−]   Fr* [−]   Ft* [−]

Figure 18. − Test 04D−M, averaged coefficients, f(Re−ratio).
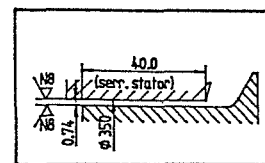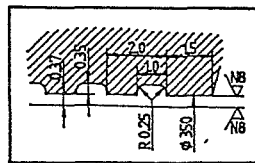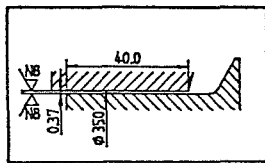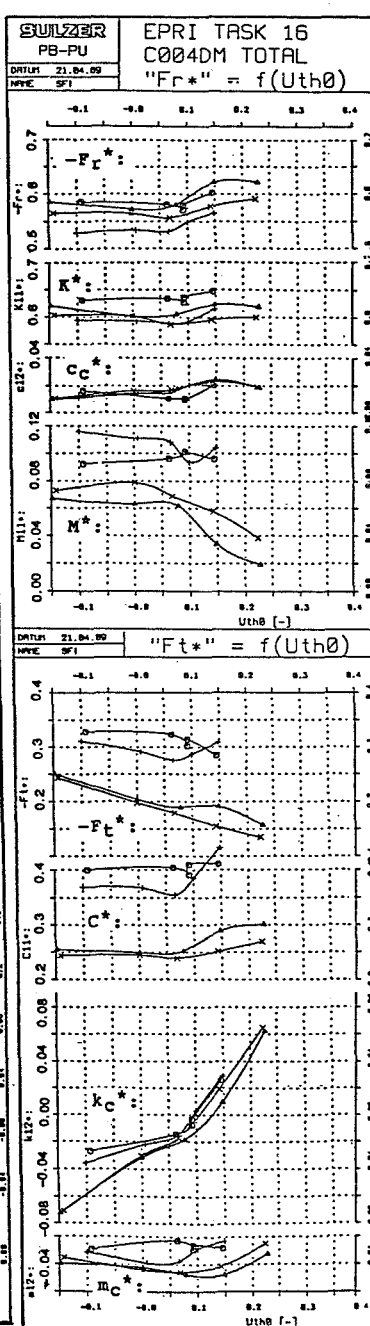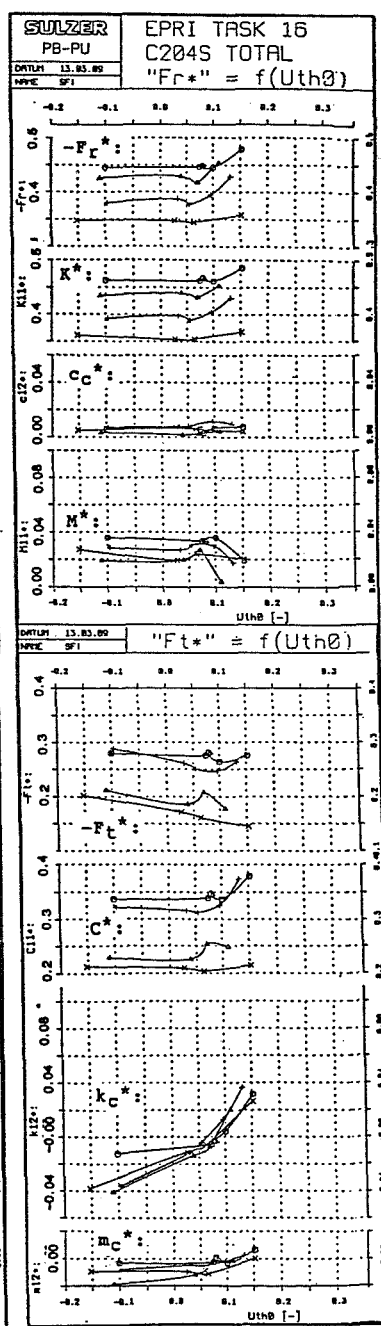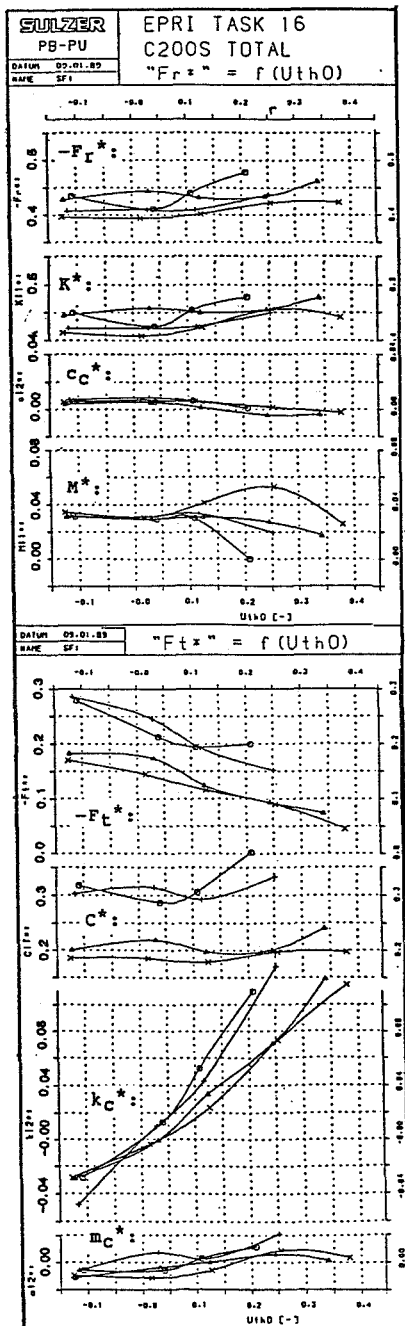
Figure 19. – All tests, coefficients = f(U_{tho}).

266
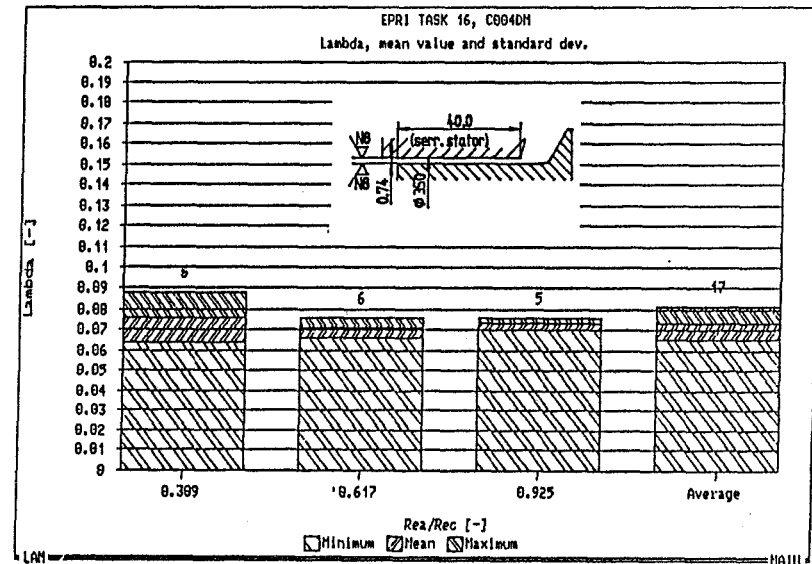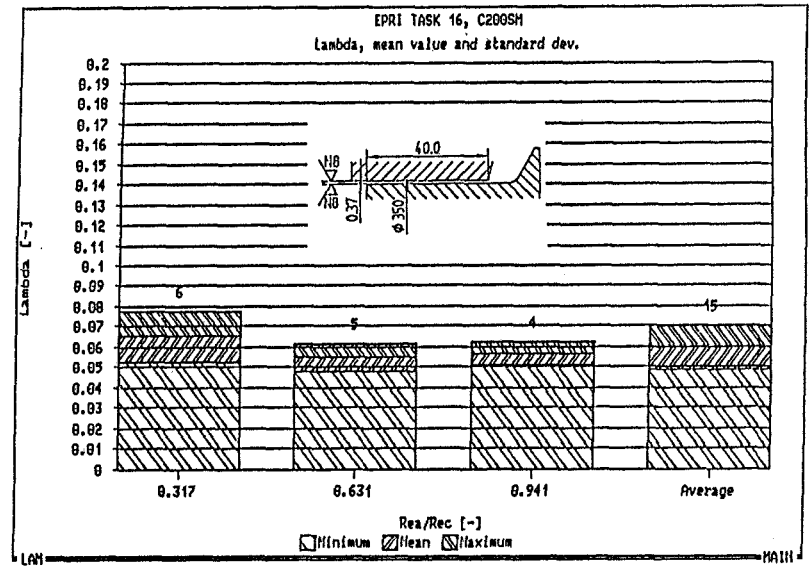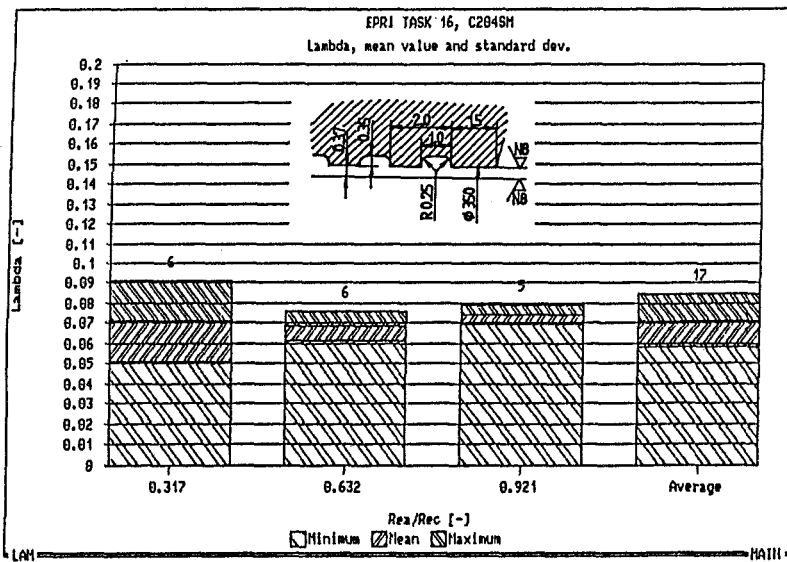
Figure 20. - Lambda bar charts for all tests.

HYDRAULIC ACTUATOR SYSTEM FOR ROTOR CONTROL

Heinz Ulbrich* and Josef Althaus
Institute B of Mechanics
Technical University of Munich
P.O. Box 202420
D-8000 Munich 2, Federal Republic of Germany

In the last ten years several different types of actuators have been developed and fabricated for active control of rotors. This paper deals with a special hydraulic actuator system capable of generating high forces to rotating shafts via conventional bearings. The actively controlled hydraulic force actuator features an electrohydraulic servo valve which can produce amplitudes and forces at high frequencies necessary for influencing rotor vibrations. The mathematical description will be given in detail. The experimental results attained verify the theoretical model. Simulations already indicate the usefulness of this compact device for application to a real rotor system.

1 Introduction

Rotating machinery can be found in many fields of the industrial world; many could be improved with regard to speed of rotors/shafts, weight, noise, longevity and last but not least, safety, by applying active vibration control. The key to success for active measures in the improvement of the dynamics of rotating machinery lies in the availability of suitable actuators which have to satisfy the following requirements: the actuator must be capable of amplitudes in the range of the vibration amplitudes to be influenced on the one hand, and possess an appropriate frequency characteristic on the other hand. In the literature many papers deal with magnetic actuators, e.g. [3,4,5]. Magnetic actuators require a relatively large amount of space compared to the attainable forces. This deficiency may be avoided by the use of hydraulically controlled chambers.

The main topic of this paper is the introduction of a newly developed hydraulic actuator which is able to apply forces to rotating shafts via the bearings. For producing forces (pressure variations) servo valves are used. The regulating distance is caused by elastic deformations of membranes (no cylinder piston arrangements).

All influences which could be of practical relevance (oil compressibility, dynamic effects of the servo valve and the fluid itself) are taken into account in the mathematical description of the system. Applying the theory of plates, the strain in the membranes can be calculated. A limitation of the actuator system is given by the permitted strain which may not be exceeded in any area. Because of the actuator dynamics an appropriate enlargement of the equations of motion for the entire system is necessary. The equations of the actuator dynamics show that the chamber system already applies damping effects to the rotor system without any control input. With the aid of a well adapted controller the damping of the entire system can be essentially improved. This is

*Presently at Technical University of Braunschweig, Braunschweig, Federal Republic of Germany.

PRECEDING PAGE BLANK NOT FILMED

demonstrated by simulations. The input parameters, especially with regard to the actuator system, have been determined by experiment.

For verifying the results achieved by computer simulations two different experimental test facilities have been constructed (see Fig. 4 and Fig. 5). One test rig contains the active chamber system. It allows the evaluation of its characteristic frequency. The experimental results which are attained verify the theoretical model. The second test facility consists of an elastic rotor structure and two different types of magnetic actuators. In further investigations the two test facilities will be combined in order to test the dynamic behavior of the elastic rotor controlled by the active chamber system.

Nomenclature

A	system matrix
A^*	membrane area
b	coefficient of the actuator input
B	control matrix
c, d	bearing coefficients
C_K	lag coefficient of the control force
c_L	membrane stiffness
d_L	passive damping coefficient of the actuator
E	identity matrix
h	force vector
K_{pq}	leakage coefficient
K_v	loop gain of the servo valve
K^*	constant of the oil compressibility and the membrane buckling
M, P, Q	system matrices of the second order system
F^*	control force to the bearing housing
$\mathcal{F}_L$	transfer function describing the fluid dynamics and the stiffness
$\mathcal{F}_P$	transfer function of the chamber pressure
$\mathcal{F}_V$	transfer function considering the servo valve dynamics, the oil compressibility, and the membrane buckling
$\mathcal{F}_{valve}$	transfer function describing the servo valve dynamics
$\mathcal{F}_x$	transfer function of the regulating distance
J_L	Jacobian matrix of translation of the bearing
ΔP	pressure drop in the valve
ΔP_S	supply pressure difference
ΔP_V	chamber pressure difference
q	vector of generalized coordinates
Q	oil flow through the loaded servo valve
Q_V	oil flow through the unloaded servo valve
s	Laplace-operator
t	time
u	control vector

270

U_V	control voltage to the servo valve
U_N	nominal voltage of the servo valve
z	state vector
x, y	acting directions
x_L, y_L	regulating distance (bearing deflection)
ω_V	natural frequency of the servo valve
Ω	rotor frequency
ξ_V	servo valve damping coefficient

2 Description of the Actuator Device

The device of this compact system is shown in Fig. 1 by a schematic. It consists of two components: a commercially-available servo valve, which is able to transform electrical signals into flow- and pressure variations of the hydraulic fluid, and an elastic chamber system, which transduces the pressure variations into displacements and into forces acting on the outer bearing housing (in Fig. 1 only one control direction is displayed).

The servo valve is supplied by the system pressure **P**, which is to be kept constant, and the return pressure **R** ≈ 0. If the spool of the valve is in the neutral position (Fig. 1) the pressure in the chambers is half of the system pressure. After a shift of the spool by an input voltage $U_V \neq 0$, a pressure difference appears between the two output orifices. Because of the elasticity of the membranes this enables a shifting of the rotor in the radial direction. The chamber system itself consists of four cylindrical chambers which are equally spaced in a circle around the bearing housing. Each chamber is sealed on the top and bottom by an elastic membrane. In order to decouple forces into both acting directions, the bearing housing is supported against the membrane system by linear roller guides. The influence of friction is thereby reduced as well. Alternative support solutions are given by design variations. To eliminate the linear roller guides the bearing can be mounted via elastic rods to the outer housing. The two opposing chambers are both controlled by one servo valve (one valve per force direction).

This compact actuator system is capable of generating very large forces and can thereby influence even large turbines weighing several tons. Actuator pistons as an alternative to the deformable chambers have the drawback that they possess relatively large moving masses. In addition, sealing problems and friction forces on the contact surfaces would occur. All these influences have negative impacts on the frequency characteristic. An appropriate design of the membranes enables the desired amplitudes of motion without exceeding the stress limits of the material.

3 Theory

With the aid of the theory of plates the calculation of the stress in the membranes caused by a given load can be performed, e.g. [8]. Experiments have shown that the real stresses are always lower than the calculated stresses. This is caused by the elastic fixing of the membrane in the real

271

system compared to the theoretically stiff fixing. For calculating the stresses the load must be known. Therefore it is necessary to describe the dynamics of this active machine element.

3.1 Chamber System Dynamics

3.1.1 Servo Valve

The dynamics of the servo valves are given by the manufacturer (MOOG, see [2]) as a PT$_2$-element. The valve flow Q_V for the unloaded valve can be given as a function of the input voltage U_V in the *Laplace-domain* (with s as a complex variable)

$$Q_V = K_v \mathcal{F}_{valve} \cdot U_V \quad , \quad \mathcal{F}_{valve} = \frac{1}{1 + \frac{2\xi_v}{\omega_v}s + \frac{1}{\omega_v^2}s^2} \tag{1}$$

where K_v is the loop gain of the valve, which depends on the supply pressure $\Delta P_S = \boldsymbol{P} - \boldsymbol{R}$ (see Fig. 1) and the geometry of the valve itself, ω_v is the natural frequency of the valve, and ξ_v is the damping ratio of the valve. In the case where the valve is loaded, the fluid flow depends on the output pressure ΔP_V (load differential pressure). For this reason the equation for the fluid flow passing a pressure-regulating valve (here between the spool of the valve, inlet- and outlet orifice, see Fig. 1) is applied. In general the fluid flow Q is proportional to the square root of the differential pressure ΔP [1],

$$Q \sim \sqrt{\Delta P} \quad . \tag{2}$$

Applying the relation that the sum of the pressure drops in the valve ΔP and the load pressure ΔP_V is equal to the drop of the supply pressure ΔP_S,

$$\Delta P + \Delta P_V = \Delta P_S \quad , \tag{3}$$

and considering eq. 2 and the fluid flow properties in the valve we obtain

$$Q = Q_V \cdot \sqrt{1 - \frac{\Delta P_V}{\Delta P_S}} \quad . \tag{4}$$

After a linearization in the neighborhood of $\Delta P_V = 0$, eq. 4 becomes

$$Q = Q_V - K_{pq} \cdot \Delta P_V \quad , \quad K_{pq} \text{ leakage coefficient} \quad . \tag{5}$$

The linearization applied in eq. 5 is valid for $\Delta P_V \leq \frac{1}{2}\Delta P_S$ where K_{pq} is theoretically a function of Q_V. For low input voltage $U_V \leq \frac{1}{10}U_N$ (U_N = nominal voltage) this dependance can be neglected. Fig. 2 shows the course of the fluid flow Q as a function of Q_V and the differential pressure of the valve ΔP_V as given by the manufacturer. The slope of these curves at the operating point ($\Delta P_V = 0$) is given by K_{pq} appearing in eq. 5. In contrast to the nonlinear eq. 4 in practice one can establish that even at $U_V = 0$ (which results in $Q_V = 0$, eq. 1) the fluid flow is non-zero for $\Delta P_V \neq 0$. This is caused by leakage where the spool is in the neutral position. The linear eq. 5 takes this into account. Fig. 2 shows this behavior of the valve by the line through the origin with a slope which is non-zero. For derivation of the equation of motion and the transfer characteristic of the entire system (see later), the linear relation by eq. 5 is used. The nonlinearity of the relation between the fluid flow Q and the pressure drop ΔP_V can be taken into account by K_{pq} as a function of Q_V.

272

3.1.2 Influence of Fluid Flow, Membrane Stiffness and Oil Compressibility

The application of the continuity equation results in an additional relation for the fluid flow Q,

$$Q = A^* \cdot \dot{x}_L + K^* \cdot \Delta \dot{P}_V \quad . \tag{6}$$

A^* is the characteristic membrane area, and K^* represents the oil compressibility and the deformation of the membrane into a direction that doesn't lead to a movement of the bearing (membrane buckling), see Fig. 3. K^* is dependent on the oil volume V_L, the bulk modulus of the fluid β_K, and the membrane geometry characterized by K_M,

$$K^* = \frac{V_L}{4\beta_K} + K_M \quad . \tag{7}$$

Simulations have shown that the fluid losses caused by oil inertia, friction and losses at the inlet and outlet orifices are negligible. So the pressure difference at the outlet orifices of the valve is approximately equal to the chamber pressure difference, constant ΔP_V.

3.1.3 Recapitulation of Equations

The equilibrium of forces applied with respect to the membranes (entire arrangement of two membranes acting in one direction) leads to

$$F^* = A^* \cdot \Delta P_V - c_L \cdot x_L \quad , \tag{8}$$

where c_L is the entire membrane stiffness in the force direction and F^* the control force to the bearing housing, see Fig. 3. Including this equation we obtain F^* as a function of the control voltage U_V and the membrane deflection, respectively; the bearing displacement x_L in the direction of the force

$$F^* = \mathcal{F}_V \cdot U_V - \mathcal{F}_L \cdot x_L \quad . \tag{9}$$

$\mathcal{F}_V$ is the transfer function describing the dependence on the control voltage

$$\mathcal{F}_V = \mathcal{F}_{valve} \cdot \frac{\frac{A^* K_v}{K_{pq}}}{1 + C_K \cdot s} \quad , \tag{10}$$

and $\mathcal{F}_L$ is the transfer function considering the influences of the fluid dynamics and the stiffness of the arrangement

$$\mathcal{F}_L = \frac{\frac{A^{*2}}{K_{pq}} s}{1 + C_K \cdot s} + c_L \quad . \tag{11}$$

The constant C_K is represented by the leakage coefficient K_{pq} and by the oil compressibility and membrane buckling K^* eq. 7,

$$C_K = \frac{K^*}{K_{pq}} \quad . \tag{12}$$

273

3.1.4 Representation in Time Domain

For including the actuator system into the complete system, the representation of eq. 9 in the time-domain is more convenient. With the equations above we get a set of differential equations which describe the control force F^* as a function of the input voltage U_V and bearing displacement x_L,

$$F^* = A^* \Delta P_V - c_L x_L \quad ,$$

$$K^* \Delta \dot{P}_V + K_{pq} \Delta P_V + A^* \dot{x}_L = Q_V \tag{13}$$

$$\frac{1}{\omega_v^2} \ddot{Q}_V + \frac{2\xi_v}{\omega_v} \dot{Q}_V + Q_V = K_v U_V \quad .$$

The coefficient c_L describes the additional stiffness effects with regard to the entire system (see later).

3.1.5 Simplification and Interpretation of Equations

For designing control concepts and to explain the fundamental operation, the equations will be simplified. In order to obtain a simple relationship between the control voltage U_V, the regulating distance x_L, and the control force F^*, the PT$_2$-behavior of the servo valve will be approximated by a linear relationship ($\mathcal{F}_{valve} = 1$). This is valid at frequencies under the cut–off frequency of the valve. This simplification leads to the following form

$$C_K \dot{F}^* + F^* = b \cdot U_V - c_L \cdot x_L - d_L \cdot \dot{x}_L \tag{14}$$

where $b = \frac{A^* K_v}{K_{pq}}$ and $d_L = \frac{A^{*2}}{K_{pq}} + C_K c_L$.

The constant C_K representing the oil compressibility and the membrane buckling in the equation above has an important influence. If C_K is negligible the actuator works as a passive spring and damper unit characterized by the coefficients c_L and d_L. Additionally a control force F_C acts that is proportional to the input voltage U_V (see Fig. 9). In the other case, if the frequency $\omega_K = \frac{1}{C_K}$ is below the frequency range of application, the actuator possesses an integral behavior. As a result the feedback of velocities and accelerations leads to stiffness and damping effects. In this case or if ω_K is inside the range of application (PT$_1$ behavior), a proportional behavior (see Fig. 9) can be achieved by an internal phase shifting controller (e.g. feedback of pressure ΔP_V) or an additional passive throttle between the two output orifices.

By an appropriate design of the membrane (constants c_L, A^*, K_M), of the oil volume V_L, of the supply pressure ΔP_S, and by the choice of the suitable valve size (constant K_v and K_{pq}), the actuator can be tuned in an optimal way. In the case of a sudden pressure drop ($\Delta P_S \rightarrow 0$) the rotor bearing is always sufficiently supported by an adequate membrane stiffness c_L.

3.1.6 Transfer Characteristic of Actuator

In the following the transfer characteristic of the complete actuator system is investigated applying a sinusoidal input voltage U_V to the valve. The purpose of this is to get a comparison to

274

the experiments which are described in chapter 3.1.6 and 5. The resulting outputs are the regulating distance x_L and the pressure difference ΔP_V between the opposing chambers. Introducing a mass which simulates the mass of the rotor, including the support system, the control force appearing in eq. 9 has to be equal to

$$F^* = \overset{\cdot\cdot}{m}\ x_L \cdot s^2 \quad . \tag{15}$$

The transfer functions for the regulating distance $\mathcal{F}_x$ and the chamber pressure $\mathcal{F}_P$ can be expressed

$$\mathcal{F}_x \;\; = \;\; \frac{x_L}{U_V} = \frac{b \cdot \mathcal{F}_{valve}}{C_K m \cdot s^3 + m \cdot s^2 + d_L \cdot s + c_L} \quad , \tag{16}$$

$$\mathcal{F}_P \;\; = \;\; \frac{\Delta P_V}{U_V} = \frac{m \cdot s^2 + c_L}{A^*} \cdot \mathcal{F}_x \quad . \tag{17}$$

The coefficients b and d_L are given in eq. 14.

4 Test Facilities

Fig. 4 shows the test rig which was designed to investigate the chamber system experimentally. The investigation is conducted only in the vertical direction. The facility mainly consists of the housing 1 where the four oil chambers 2 are integrated. The distance rod 3 performs the function of the bearing housing and assures that the opposing chambers both move the same absolute distance. For investigating the influence of masses additional masses can be mounted on the distance rod 3. The influence of friction caused by the linear roller guides (see Fig. 1) can be studied by loading the chambers for the horizontal direction with an appropriate pressure in order to press the linear roller guides via distance sleeves 4 on the distance rod. The entire arrangement is mounted on the foundation including the servo valve 5. Servo valve and chambers are connected via pipes 6. Between actuator and hydraulic control unit (not shown in Fig. 4) are the connections to the first stage pressure unit, main control pressure unit (pressure **P** shown in Fig. 1), return pressure unit (indicated by pressure **R** in Fig. 1), and an additional pressure supply for the linear guiding bearings.

To enable a broad range of experimental investigations, variations of the supply pressure ΔP_S, membrane thickness h, contact pressure for the guiding bearings, additional masses m (see eq. 15) and of course the control voltage U_V (function generator) can be conducted.

The measurement equipment installed allows one to gather the following information: regulating distance with the aid of an inductive displacement sensor 7, and oil pressure in the chambers by piezo electric pressure sensors 8. Additional information is given by acceleration pick ups (not shown) mounted on the distance rod and by strain gauges to determine the strain of the membranes.

A special hydraulic unit was designed to assure that the supply pressure is constant. This is required because the fluid flow changes with frequencies up to 200 Hz and higher. These requirements can be met with the aid of a controllable radial piston pump and an appropriate reservoir.

The test rig shown in Fig. 5 is used to investigate different control concepts. It consists of an elastic rotor structure 9, a magnetic bearing 10 for simulating different excitation forces, the bearing unit 11, and actuator system which is presently realized by electromagnetic actuators 12. A further description of the test rig and the test results attained by this facility are given e.g. in [3].

C-4

The active chamber system will be integrated in the test facility Fig. 5 after conclusion of the experiments with the test rig Fig. 4. For this purpose the chambers for the horizontal direction have to be activated by a second servo valve, and the distance rod has to be replaced by the bearing unit. Finally the electromagnetic actuators 12 are substituted by the active chamber system.

5   Transfer Characteristic

In the following the transfer functions $\mathcal{F}_x$ and $\mathcal{F}_P$, eq. 16 and 17, for the regulating distance x_L and the chamber pressure ΔP_V will be investigated. The goal is to compare theoretical and experimental behavior of the actuator and to determine the system parameters. These are the membrane stiffness c_L, the leakage coefficient K_{pq}, the loop gain of the servo valve K_v and the coefficient K^* which describes the oil compressibility and the membrane buckling. The simulation is based on the data shown in Fig. 6 which are equivalent to the data of the test facility. The results can be seen in Fig. 7.

5.1   Theoretical Results

In the plot of the amplitude of the regulating distance in Fig. 7, one can recognize a PT_1 behavior up to a frequency of about 170 Hz. Its cut–off frequency is very low (about 2.2 Hz) and is given by $\frac{c_L}{d_L}$, see eq. 14. Beyond this frequency an extremum occurs in the amplitude at approximately 300 Hz. It corresponds to a pole in the transfer function of x_L and ΔP_V. This extremum results from a function $\alpha(s)$ which can be obtained by the denominator of eq. 16. This function has the value $\alpha(s) = 0$ at the frequency of $\omega_\alpha = 2\pi \cdot 287\ Hz$ ($s = i\omega$),

$$\alpha(s) = m \cdot s^2 + \frac{m}{C_K} \cdot s + \frac{d_L}{C_K} \quad = \quad 0 \tag{18}$$

$$\Longrightarrow \quad \omega_\alpha \quad = \quad \sqrt{\frac{d_L}{C_K m} - \frac{1}{4C_K^2}} \approx \sqrt{\frac{A^{*2}}{K^* m}} \quad . \tag{19}$$

Eq. 19 shows that this frequency is mainly dependent on the membrane area A^*, on the mass m (simulating the rotor mass including the bearing unit) and on the oil compressibility and membrane buckling K^*. The servo valve has no influence.   The expression $\frac{A^{*2}}{K^*}$ can be interpreted as a spring coefficient of the oil support and the membrane buckling. This natural frequency causes a phase shift of 180°. The rest of the curve is characterized by a drop in the amplitude due to the PT_2-behavior of the servo valve, see chapter 3.1.5.   In the plot of the chamber pressure a further zero point can be seen at 110 Hz. It corresponds to the natural frequency of the one-DOF-oscillator, function $\beta(s)$ from eq. 17

$$\beta(s) = m \cdot s^2 + c_L \quad = \quad 0 \tag{20}$$

$$\Longrightarrow \quad \omega_\beta \quad = \quad \sqrt{\frac{c_L}{m}} \quad . \tag{21}$$

This characteristic frequency has no effect on the regulating distance and on the controllability of the rotor system.

5.2 Comparison of Theory and Experiment

Fig. 8 shows the measurements of the regulating distance x_L and chamber pressure ΔP_V. The results are obtained by noise excitation for the input voltage U_V.

A comparison with the results attained by theory shows good agreement. The characteristic frequencies at 110 Hz and 293 Hz are due to the effects described above (functions $\alpha(s)$ and $\beta(s)$, eq. 19 and 21). This shows that all important influences on the transfer characteristic are included in the transfer functions eq. 16 and 17. The step shaped curve at lower frequencies is only caused by the discrete evaluation of the output signals by the measurement electronics.

Measurements of the transfer characteristic of the servo valve (described by a PT_2-system) showed a better amplitude behavior at frequencies beyond the cut–off frequency than predicted by the PT_2-behavior.

The experiments have shown that the simplified equations for describing the performance of the active chamber system, eq. 14, are valid up to the cut–off frequency of the servo valve (here about 200 Hz), see chapter 3.1.5. For a higher frequency range it is necessary to use a servo valve with a higher cut–off frequency and to minimize the oil compressibility and the membrane buckling by minimizing the oil volume and by an appropriate design of the membrane.

6 Example of Application of the Actuator

6.1 Formulation of the Complete System

In designing a controller, a complete mathematical formulation of the system is assumed. A very efficient method of describing the rotor system to be controlled is modeling it as a hybrid multibody system (see [6]). This leads to the second order differential equation

$$M\ddot{q}(t) + P\dot{q}(t) + Qq(t) = \sum_i h_i(q, \dot{q}, \ddot{q}, \Omega, t) \qquad (22)$$

with the vector $q \in \mathbb{R}^f$ of the generalized minimal coordinates (f is the number of degrees of freedom), $M \in \mathbb{R}^{f,f}$ is the mass matrix, $P \in \mathbb{R}^{f,f}$ is the matrix of velocity–proportional forces, $Q \in \mathbb{R}^{f,f}$ is the matrix taking into account the displacement–proportional forces, $h_i \in \mathbb{R}^f$ is the vector of the i-th external force (e.g. control force), Ω is the rotor frequency and t indicates the time.

The control forces acting indirectly (via the rigid bearing unit) on the rotor can be expressed by

$$h_B = J_L^T \cdot \begin{bmatrix} F_x^* \\ F_y^* \end{bmatrix} \quad , \qquad (23)$$

where $J_L \in \mathbb{R}^{2,f}$ is the Jacobian matrix of translation belonging to the subsystem bearing unit and F_x^* and F_y^* the control forces given by differential eq. 13 acting in the x- and y-directions. The radial movement of the bearing described by x_L and y_L (perpendicular to x_L) can be formulated with the

aid of the Jacobian-matrix as

$$\begin{bmatrix} x_L \\ y_L \end{bmatrix} = J_L \cdot q \quad . \tag{24}$$

Introducing an enlarged state space vector

$$z = \begin{bmatrix} q^T, Q_{Vx}, Q_{Vy}, \dot{q}^T, \dot{Q}_{Vx}, \dot{Q}_{Vy}, \Delta P_{Vx}, \Delta P_{Vy} \end{bmatrix}^T \quad , \quad z \in \mathrm{IR}^{2f+6} \quad , \tag{25}$$

with Q_{Vx}, Q_{Vy} as the valve flow serving the x- and y-directions, respectively (eq. 1), and ΔP_{Vx}, ΔP_{Vy} as the valve output pressure supplying the x- and y-directions, respectively, we obtain the state equation

$$\dot{z} = Az + Bu \quad , \tag{26}$$

where A represents the system matrix, B the control matrix and

$$u = [U_{Vx}, U_{Vy}]^T \tag{27}$$

the control vector consisting of the control voltages U_{Vx} proper for x- and U_{Vy} proper for the y-direction.

The matrices used in eq. 26 can be expressed as follows

$$A = \begin{bmatrix} 0 & 0 & E_f & 0 & 0 \\ 0 & 0 & 0 & E_2 & 0 \\ -M^{-1}\overline{Q} & 0 & -M^{-1}P & 0 & M^{-1}J_L^T A^* \\ 0 & -\omega_v^2 E_2 & 0 & -2\xi_v\omega_v E_2 & 0 \\ 0 & \frac{1}{K^*}E_2 & -\frac{A^*}{K^*}J_L & 0 & -\frac{K_{pq}}{K^*}E_2 \end{bmatrix} \quad , \tag{28}$$

$$B = \begin{bmatrix} 0 \\ 0 \\ 0 \\ K_v\omega_v^2 E_2 \\ 0 \end{bmatrix} \quad , \tag{29}$$

where the submatrix $\overline{Q}$ is

$$\overline{Q} = Q + J_L^T J_L \cdot c_L \quad . \tag{30}$$

c_L is the membrane stiffness appearing in eq. 13 and M, P, Q are the system matrices from eq. 22. The matrix $E_j \in \mathrm{IR}^{j,j}$ represents the identity matrix.

6.2 Amplitude Characteristic of the Rotor

A simple rotor running in journal bearings is used. The rotor is supported by the active chamber system on its left side (Fig. 9). In the modeling of the rotor system, mass-, stiffness-, and gyroscopic effects and additional damping by the journal bearings are considered. As admissible shape functions only two mode shapes are taken into account. In most cases higher modes of real rotor systems are damped very well because of bearings or material damping.

In Fig. 10 are plotted frequency response functions versus rotor frequency. The exciting force is caused by an unbalance of the rotor. In Fig. 10a the scaled amplitudes $\frac{A}{A_o}$ at the runner position are displayed without active forces (solid line) and with active forces (dotted line). Fig. 10b shows the scaled nutation angles $\frac{\varphi}{\varphi_o}$ (slope of the elastic line) at the same location. The displacement amplitude shows a significant peak at the first natural frequency (bending vibration) and at the second natural frequency (nutation, indicated by the nutation angle). The feedback is realized by displacement, velocity, and pressure signals taken only at the actuator location. The controller was designed as a "constant controller" for the rotor frequency 100 Hz. Using this very simple controller, the results already demonstrate that a considerable reduction of the resonance amplitudes can be achieved.

7   Conclusion Remarks

The key to attaining the desired influence on the dynamics of rotor systems lies in the availability of suitable actuators. The development of the active chamber systems introduced in this paper will be an essential step towards industrial applications. This actuator works as a spring (membrane stiffness) and damper (hydraulic effects in the servo valve), and in addition to these passive forces a control force is acting proportional to the input voltage at the servo valve. One of the main goals of the paper is to confirm the theoretical model of this new actuator concept by experiment. The theoretical and experimental results achieved by these investigations show a very good conformity. Further experimental investigations of the actuator system included in the rotor system will demonstrate the usefulness of applying this active machine element for active vibration control of rotors. The use of a more sophisticated controller (additional measurement information, adaptive controller realized by special electronic equipment, hybrid controller) will show a wide range of possible applications for such an actuator device.

References

[1] ANDERSON, W.R.: Controlling Electrohydraulic Systems. Marcel Dekker, Inc. New York and Basel, 1988.

[2] THAYER, W.J.: Transfer Functions for Moog Servo Valves. Technical bulletin 103, Moog Inc. Controls Devision, East Aurora, N.Y. 14052, 1965.

[3] FÜRST, S.; ULBRICH, H.: An Active Support System for Rotors with Oil- Film Bearing. 4th International Conference on Vibration in Rotation Machinery of the Institution of Mechanical Engineers, Edinburgh, Scotland. Paper C 261/88, 1988, pp. 61–68.

[4] INNERHOFER, G; HAMMER, J.: Low-Cost Magnetic Bearing Reaction Wheel. Proc. of the IFAC Symp., Oxford, England, 1980.

[5] LIARD,G.: Aktive Magnetlager – ein Schlüssel zu höheren Spindeldrehzahlen. Kugellager-Zeitschrift 56, 213, 1982, pp. 8 - 13.

[6] ULBRICH, H.: Dynamik und Regelung von Rotorsystemen. Fortschr.-Ber. VDI-Z, Reihe 11, NR. 86, 1986.

[7] ULBRICH, H; ALTHAUS, J.: Actuator Design for Rotor Control. Twelfth biennial ASME Conference on Mechanical Vibration and Noise , Montreal, Canada, Sept. 17-20, 1989.

[8] TIMOSHENKO, S.; WOINOWSKY-KRIEGER, S.: Theorie of Plates and Shells. New York, Toronto, London, McGraw-Hill Book Company, 1959.
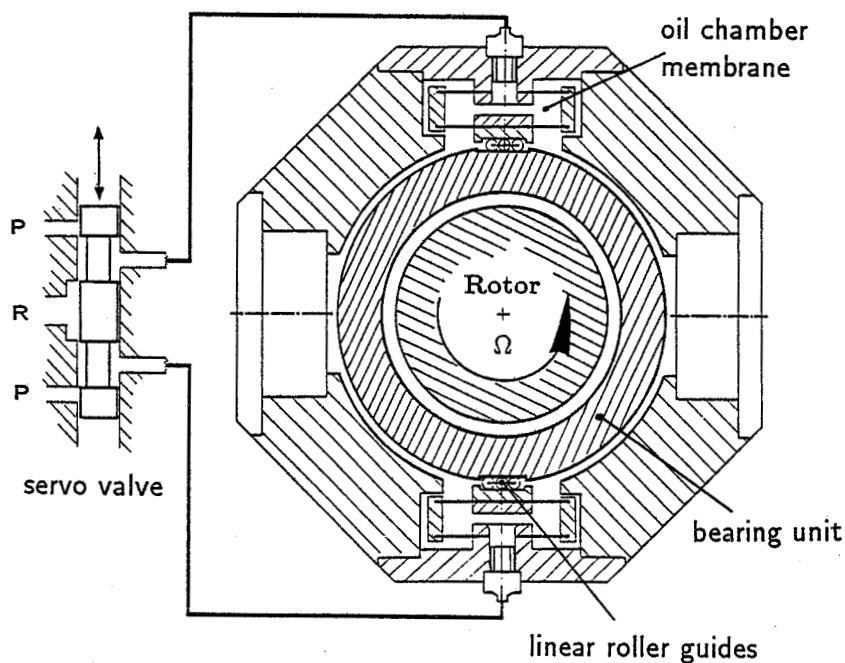
Figure 1: Active chamber system with servo valve
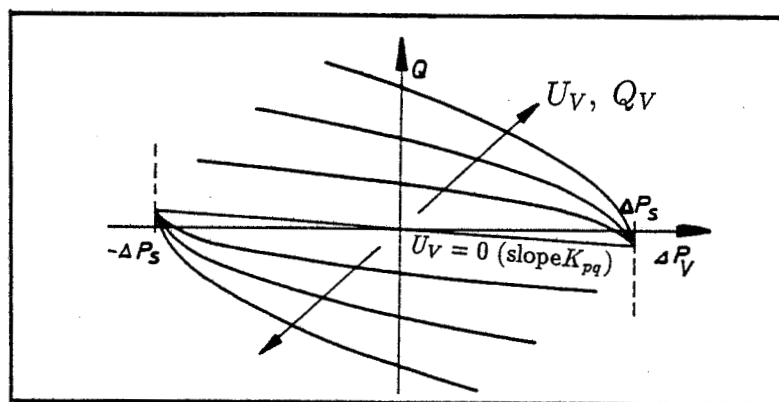
Figure 2: Fluid flow through the valve under load
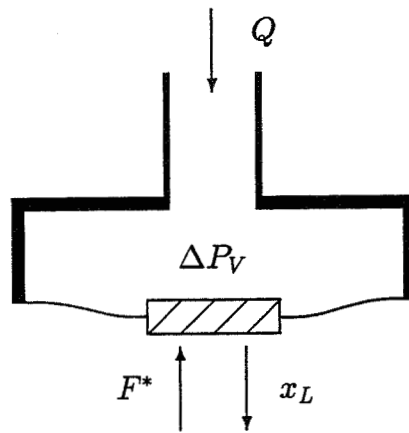
Figure 3: Model of the chamber and elastic membrane
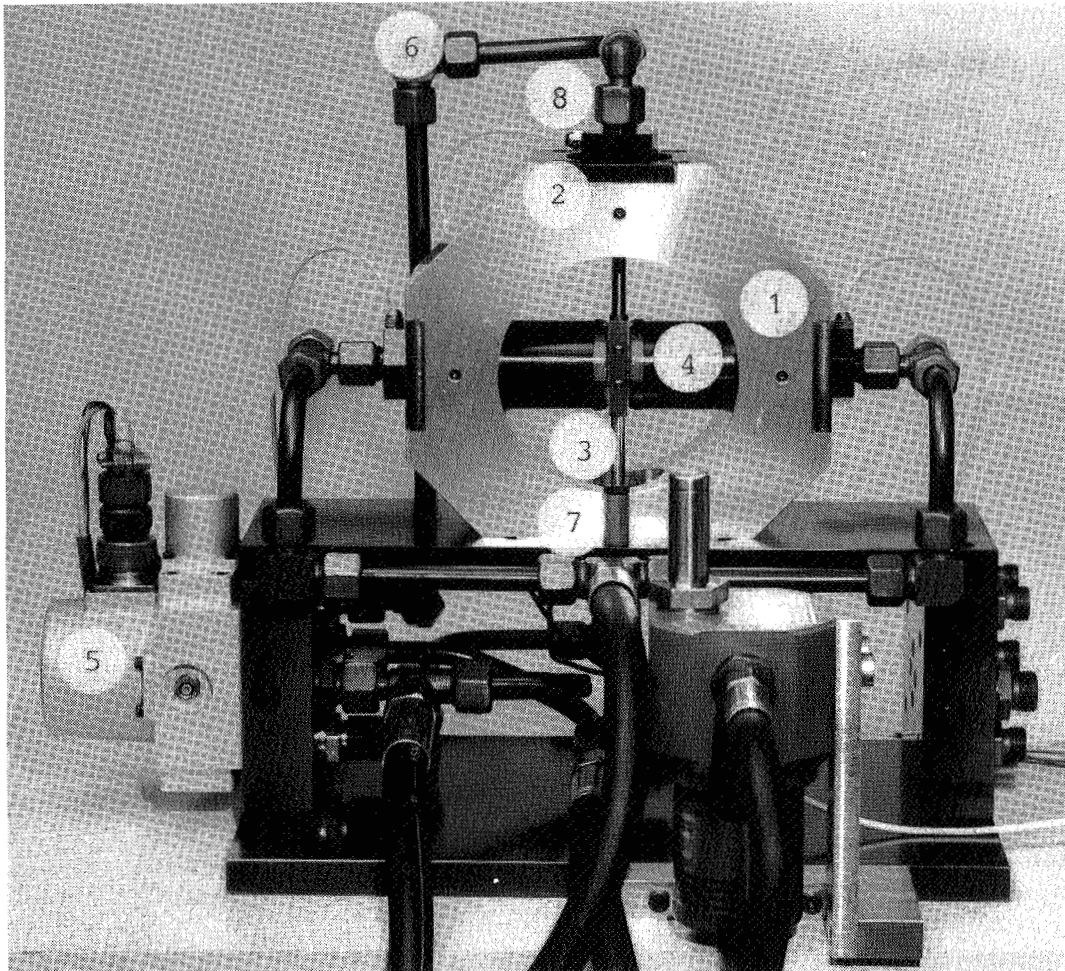
Figure 4: Test rig for active chamber system

281
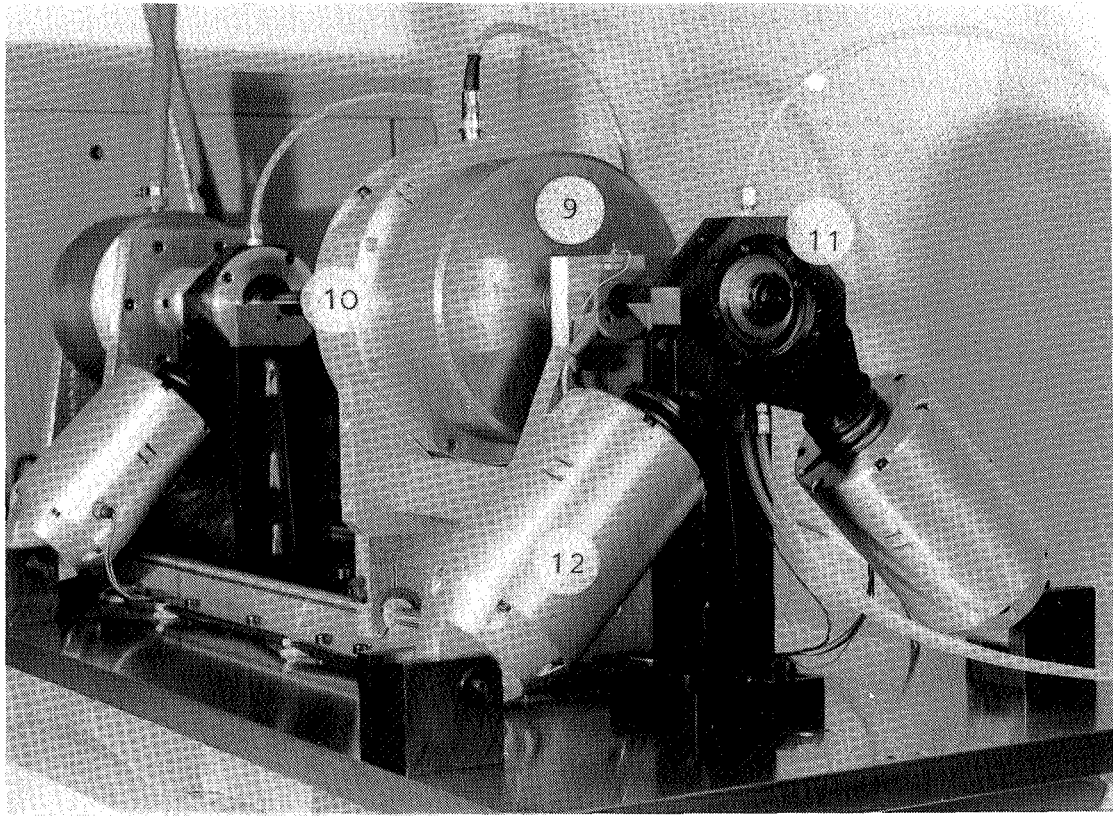
Figure 5: Test rig for rotor control

ξ_v	=	0.55	damping ratio of the servo valve
ω_v	=	1950.00 rad/s	natural frequency of the servo valve
K_{pq}	=	$4.23 \cdot 10^{-12}$ m^5/Ns	leakage coefficient
K_v	=	$1.96 \cdot 10^{-5}$ m^3/Vs	loop gain of the servo valve
A^*	=	$6.54 \cdot 10^{-4}$ m^2	characteristic membrane area
K^*	=	$4.25 \cdot 10^{-14}$ m^5/N	compressibility and membrane buckling
c_L	=	$1.63 \cdot 10^6$ N/m	membrane stiffness
m	=	3.41 kg	mass
U_{V0}	=	1 V	amplitude of the input voltage

Figure 6: Data for the transfer characteristic of the actuator
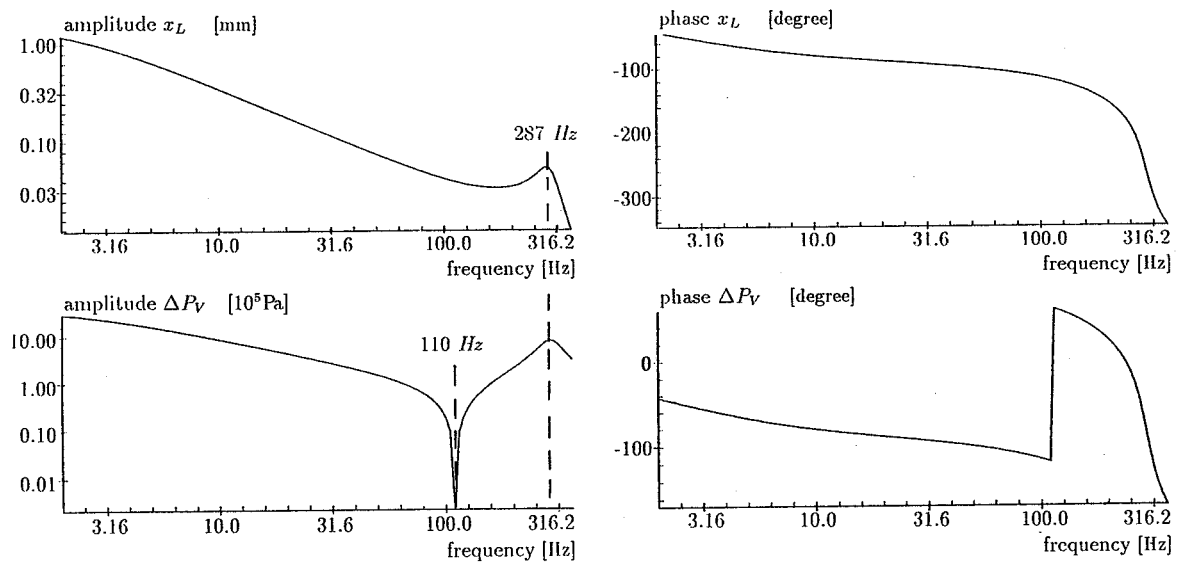
Figure 7: Simulated transfer charateristic
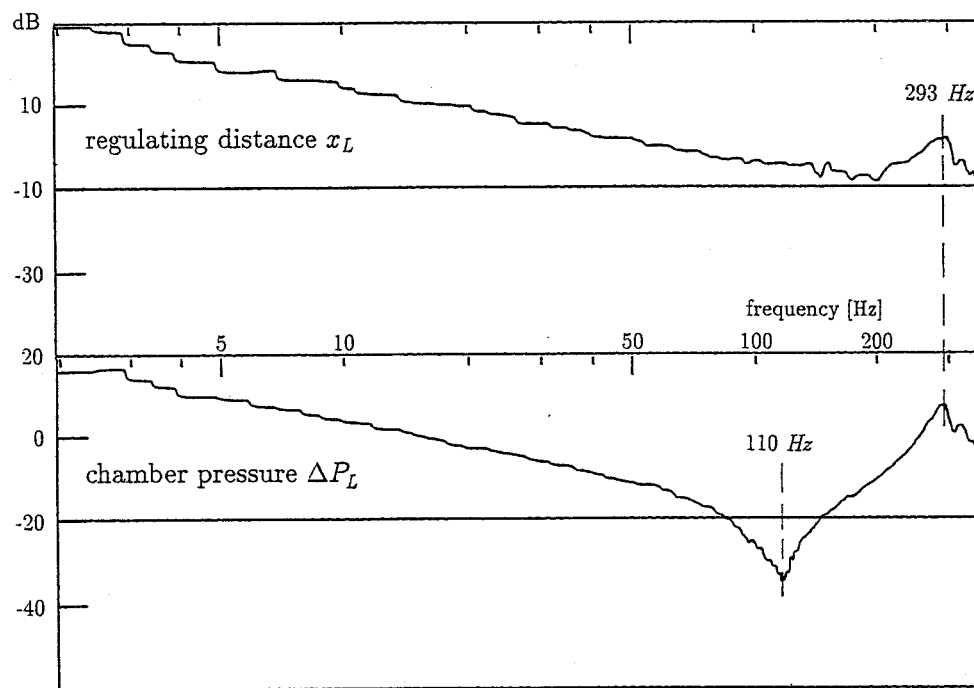
Figure 8: Measurement of the amplitude characteristic

283
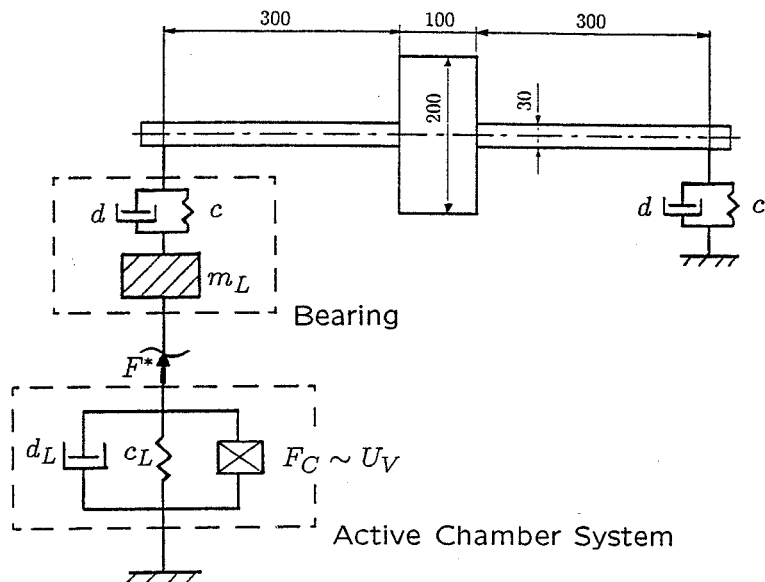
Figure 9: Geometry and mechanical model of the investigated active rotor system

——— without control
– – – with control
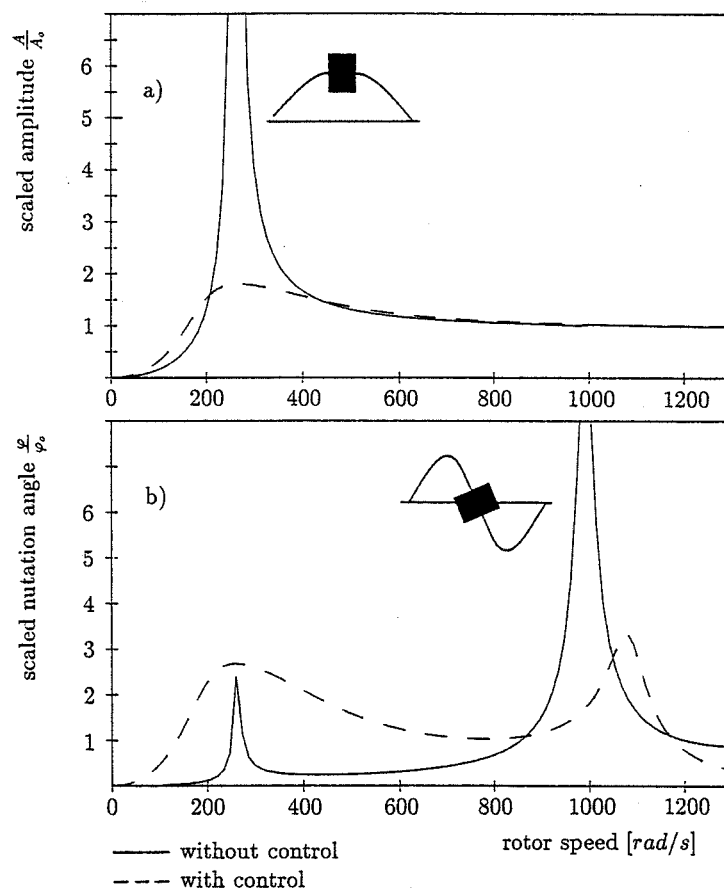
Figure 10: Response of the unbalanced rotor running through the critical speeds
a) runner displacement
b) nutation angle

A SIMPLIFIED METHOD FOR PREDICTING THE STABILITY OF AERODYNAMICALLY EXCITED TURBOMACHINERY

Albert F. Storace
General Electric Aircraft Engines
Cincinnati, Ohio, U.S.A.

A method is presented for the quick and accurate prediction of the stability of aerodynamically excited turbomachinery using real eigenvalue/eigenvector data obtained from a rotordynamics model. An expression is presented which uses the modal data and the transmitted torque to provide a numerical value of the relative stability of the system. This approach provides a powerful design tool to quickly ascertain the effects of squeeze-film damper bearings, bearing location, and support changes on system stability.

INTRODUCTION

The purpose of this paper is to present a method that is easily and economically applied to turbomachines to predict the effects of shaft flexibility, squeeze-film bearing supports, and static structure configuration on the rotor-bearing/static structure system stability relating to rotor aerodynamic cross coupled stiffness (Alford) forces. The method is general in that systems with general rotor support arrangements and multiple spools can be handled. A major advantage of the method is that it allows machine designers to quickly determine the effects on stability of bearing changes, shaft modifications, and bearing support designs to determine appropriate system designs. This paper presents an expression and analysis methodology for predicting system stability that includes the effects of destabilizing forces, rotor/stator dynamic displacements, internal and external damping, and gyroscopic moments. The expression and methodology presented provides an analysis approach that is simplified but at the same time includes all of the modeling detail needed to perform a valid assessment of system stability.

The method provides a timely and cost effective means to initially screen designs without incurring the high computer costs and large amounts of data reduction time required using complex eigenvalue rotor dynamic analysis programs in a repetitive mode. Specifically, the method uses the results of an undamped lateral critical speed analysis and generalized forces derived from the physical destabilizing forces to develop modal equations of motion for a self-excited system. The solution of these equations is then used to develop a modal dimensionless stability criterion. This criterion requires that the energy absorbed by the system exceed the energy imparted to the rotor by unbalanced torque forces if instability is to be prevented.

The method is intended to supplement the more general analysis techniques which are used for final confirmation of the stability predictions.

SYMBOLS

F_X, F_{XR}, F_Y, F_{YR} Aerodynamic forces acting on the rotor N (LBf)

F_{XS}, F_{YS} Aerodynamic forces acting on the stator N (LBf)

X, Y, X_R, Y_R Rotor displacements cm (IN.)

X_S, Y_S Stator displacements cm (IN.)

K_{XY}, K_{YX} Cross-coupling spring rates N/cm (LBf/IN.)

T Compressor or turbine stage torque N-cm (LBf-LB)

β "Alford" coefficient (dim.)

D_P Stage pitch diameter cm (IN.)

H Blade height cm (IN.)

P_X, P_Y Generalized coordinate pair cm (IN.)

ϕ_{XR}, ϕ_{YR}, ϕ_{XS}, ϕ_{YS} Modal displacements (dim.)

G_X, G_Y Generalized forces N (LBf)

m Generalized mass Kg (LBf-SEC^2/IN.)

C Generalized damping coefficient N-SEC/cm (LBf-SEC/IN.)

k Generalized stiffness coefficient N/cm (LBf/IN.)

$\{\phi\}$ Mode shape vector (dim.)

$[K]$ Physical stiffness matrix N/cm (LBf/IN.)

ω Undamped natural frequency (RAD/SEC)

Q Modal Q-factor (dim.)

N Number of rotor stages (dim.)

RPM   Design point speed (REV/MIN)

nb   Number of field damping components (casing, frames, rotors)

na   Number of lumped damping components (mounts, bearings, dampers)

Qa   Component Q-factor for lumped damping components (dim.)

Qb   Component Q-factor for field damping components (dim.)

$\dot{\phi}_b$ Spin speeds for field damping components ($\dot{\phi}_b$ is zero for static components) (RAD/SEC)

N_1 Low pressure rotor speed (REV/MIN)

N_2 High pressure rotor speed (REV/MIN)

MSC   Modal Stability Criterion (dim.)

BACKGROUND

A major destabilizing mechanism acting on turbomachinery stages is the Alford aerodynamic cross-coupling stiffness force (ref. 1). In a fixed frame global coordinate system, this force can be modeled by the following equation.

$$\begin{Bmatrix} F_X \\ F_Y \end{Bmatrix} = \begin{bmatrix} 0 & -K_{XY} \\ K_{YX} & 0 \end{bmatrix} \cdot \begin{Bmatrix} X \\ Y \end{Bmatrix} \qquad (1)$$

where $K_{XY} = K_{YX} = (T \beta / D_p H)$ N/cm, T is the stage torque, D_p is the pitch diameter of the stage, H is the blade height, and β is the change in thermodynamic efficiency per unit change in blade tip clearance, expressed as a fraction of blade height. The physical rationale for these forces is based on an increase of blade efficiency with decreasing tip clearance. Referring to Figure 1, the displacement of the disc centerline resulting from whirl decreases the blade tip clearance in the direction of the displacement. The efficiency of those blades with reduced clearance is improved resulting in a greater than average torque delivered by those blades with reduced clearances. Conversely, on the side of the disc with increased clearances, a less than average torque is imparted to the rotor by those blades. The integrated effect of the circumferential variation of blade torque results in a net torque in the direction of whirl associated with the vector force described in equation 1. As discussed in references 1 and 2, the cross coupled stiffness can be responsible for self-excited rotor instability at high power levels that is characterized by subsynchronous rotor whirl in the direction of rotation. This subsynchronous whirl is generally associated with the first rotor dominated mode and the stability analysis method to be presented in this paper addresses a mode by mode evaluation approach to ascertain the potential for system instability.

Equation 1 expresses the physical forces acting on the rotor. It can be extended to include the forces acting on the case (stator) as follows.

$$\begin{Bmatrix} F_{XR} \\ F_{YR} \\ F_{XS} \\ F_{YS} \end{Bmatrix} = \begin{bmatrix} 0 & -K_{XY} & 0 & K_{XY} \\ K_{YX} & 0 & -K_{YX} & 0 \\ 0 & K_{XY} & 0 & -K_{XY} \\ -K_{YX} & 0 & K_{YX} & 0 \end{bmatrix} \cdot \begin{Bmatrix} X_R \\ Y_R \\ X_S \\ Y_S \end{Bmatrix} \tag{2}$$

These forces will be used in conjunction with the gyroscopically stiffened modes obtained from a real eigenvalue/eigenvector analysis to develop a stability criterion. For a given mode obtained from the real mode set, define P_X and P_Y as the modal coordinate pair describing the generalized response in the vertical and horizontal planes of the system. More will be said later in this paper about the incorporation of gyroscopic effects in the modal data.

The rotor and stator modal displacements at a given stage can then be used to define the physical destabilizing forces acting on the rotor and stator as follows:

$$\begin{aligned}
F_{XR} &= -K_{XY}(Y_R - Y_S) = -K_{XY}P_Y(\phi_{YR} - \phi_{YS}) \\
F_{YR} &= K_{YX}(X_R - X_S) = K_{YX}P_X(\phi_{XR} - \phi_{XS}) \\
F_{XS} &= K_{XY}(Y_R - Y_S) = -F_{XR} \\
F_{YS} &= -K_{YX}(X_R - X_S) = -F_{YR}
\end{aligned} \tag{3}$$

The total generalized forces acting in the X and Y directions can be written

$$\begin{aligned}
G_X &= -K_{XY}P_Y(\phi_{YR}-\phi_{YS})\,\phi_{XR} + K_{XY}P_Y(\phi_{YR} - \phi_{YS})\,\phi_{XS} = \\
&= -K_{XY}P_Y(\phi_{YR} - \phi_{YS})(\phi_{XR} - \phi_{XS})
\end{aligned} \tag{4}$$

$$\begin{aligned}
G_Y &= K_{YX}P_X(\phi_{XR} - \phi_{XS})\,\phi_{YR} - K_{YX}P_X(\phi_{XR} - \phi_{XS})\,\phi_{YS} = \\
&= K_{YX}P_X(\phi_{XR} - \phi_{XS})(\phi_{YR} - \phi_{YS})
\end{aligned}$$

If circular whirl is assumed,

$$\begin{aligned}
\phi_R &= \phi_{XR} = \phi_{YR} \\
\phi_S &= \phi_{XS} = \phi_{YS}
\end{aligned} \tag{5}$$

Then the generalized forces are

$$\begin{aligned}
G_X &= -K_{XY}P_Y(\phi_R - \phi_S)^2 \\
G_Y &= K_{YX}P_X(\phi_R - \phi_S)^2
\end{aligned} \tag{6}$$

The equations of motion for the modal coordinate pair are

$$\begin{aligned}
m\ddot{P}_X + C\dot{P}_X + k\,P_X &= G_X \\
m\ddot{P}_Y + C\dot{P}_Y + k\,P_Y &= G_Y
\end{aligned} \tag{7}$$

Combining these equations and eliminating P_Y,

$$\frac{d^4 P_X}{dt^4} + \frac{2C}{m} \frac{d^3 P_X}{dt^3} + \left(\frac{2k}{m} + \frac{c^2}{m^2}\right)\frac{d^2 P_X}{dt^2} + \frac{2Ck}{m^2} \frac{dP_X}{dt}$$

$$+ \left(\frac{k^2}{m^2} + \frac{K^2_{XY}(\phi_R - \phi_S)^4}{m^2}\right) P_X = 0 \tag{8}$$

For a solution, assume $P_X = p_x e^{st}$ and upon substitution, the following characteristic equation is obtained.

$$s^4 + A_3 s^3 + A_2 s^2 + A_1 s + A_0 = 0 \tag{9}$$

The complex eigenvalues of this equation define the stability boundaries of the system. Specifically, a root with a positive real part indicates an unstable system. Per the Routh stability analysis, an inspection of the coefficients of the characteristic equation determines whether the motion is stable or unstable

For a stable system,

$$A_1 \, A_2 \, A_3 > A_1^2 + A_3^2 \, A_0 \tag{10}$$

Evaluating the terms,

$$A_1 A_2 A_3 = \frac{2Ck}{m^2}\left(\frac{2k}{m} + \frac{c^2}{m^2}\right)\frac{2C}{m}$$

$$= \frac{4C^2 k}{m^3}\left(\frac{2k}{m} + \frac{c^2}{m^2}\right)$$

$$A_1^2 + A_3^2 A_0 = \frac{4C^2 k^2}{m^4} + \frac{4C^2}{m^2}\left(\frac{k^2}{m^2} + \frac{K^2_{XY}(\phi_R - \phi_S)^4}{m^2}\right)$$

Then

$$\frac{c^2}{m} > \frac{K^2_{XY}(\phi_R - \phi_S)^4}{k}$$

Equation 10 can be written as

$$C > \frac{K_{XY}}{\omega}(\phi_R - \phi_S)^2$$

$$\text{or} \quad k > K_{XY}(\phi_R - \phi_S)^2 \, Q \tag{11}$$

where $\omega = \sqrt{k/m}$ = undamped natural frequency,

289

and $Q = k/C\omega = $ modal Q-factor.

Expressing the relative modal displacement on a per stage basis

and the cross-coupling stiffness in terms of the rotor speed and the HP per stage at the design point leads to the following equation.

For stability,

$$\frac{2PE}{\dfrac{713,361}{RPM} Q \sum\limits_{i=1}^{N} \dfrac{\beta_i HP_i}{D_{P_i} H_i} (\phi_{Ri} - \phi_{Si})^2} > 1.0 \quad (12)$$

where $PE = 1/2 \{\phi\}^T [K]\{\phi\} = 1/2\ k = $ modal potential energy and $N = $ the number of rotor stages. Equation 12 represents an energy balance expressed in terms of the pertinent modal parameters for a system mode of vibration and the physical destabilizing forces. If English units are used, then the constant 713,361 RPM-cm-N/HP becomes 63,025 RPM-IN-LB/HP. The accurate calculation of the modal or generalized Q-factor is key to the use of equation 12 for evaluating system stability. It must reflect the effects of both external and internal damping and the modal participation of the various engine components.

The modal Q-factor is given by equation A10 in the Appendix. Substituting this equation into equation 12 yields the following modal stability criterion (MSC). For stability,

$$\frac{2 \sum\limits_{a=1}^{na} \dfrac{PE_a}{Q_a} + \sum\limits_{b=1}^{nb} \left(1 - \dfrac{\dot{\phi}_b}{\omega}\right) \dfrac{PE_b}{Q_b}}{\dfrac{713,361}{RPM} \sum\limits_{i=1}^{N} \dfrac{\beta_i HP_i}{D_{P_i} H_i} (\phi_{Ri} - \phi_{Si})^2} > 1.0 \quad (13)$$

Note that squeeze-film damper elements contribute lumped damping and are included in the summation a=1, 2, 3, ..., na. As an approximation, they are modeled as soft springs in the system vibration analysis and a conservative component Q-factor of 3.0 can be used, although a more exact value can be calculated.

GYROSCOPIC EFFECTS AND ROTOR INTERNAL DAMPING

Figure 2 shows an example of a typical engine system vibration model used to generate modal data for the MSC. This model represents a single plane of a demonstrator engine and is an assemblage of substructure (span) and spring-type elements. It can be built very rapidly and is easily altered and interactively run to generate modal data for MSC evaluation of a wide range of alternative system designs. The span element type, represented by solid lines in Figure 2, includes both flexibility and mass properties and models casings, rotors, and

frames. The spring-type elements model bearings, mounts, and dampers. Gyroscopic moments are incorporated through spin and whirl frequency dependent terms in the mass matrices of the substructures. Note that while the modal data is obtained from an analysis which models a single plane of the engine, it does reflect whirling motion of the rotors. Consider the consequence of cross-axis gyroscopic coupling: (1) lateral motions of the rotor are not planar-the rotor center motion describes a circular orbit, if rotational symmetry prevails; (2) each free vibration mode of the equivalent non-rotating shaft of the planar model is split into two modes which are distinguishable by the sense of whirl motion (relative to the shaft spin). These are forward and backward whirling modes, and since the Alford instability mechanism drives forward whirling modes, the planar model is constrained to provide forward whirling modes for the reference rotor. Figure 3 shows the Campbell diagram (map of natural frequencies vs spin speeds), for the model of Figure 2, referenced to high pressure rotor spin speeds. The frequency lines represent system modes involving forward whirl of the high pressure rotor and backward whirl of the low pressure rotor. The latter are a consequence of counterrotating rotors, and decreasing natural frequency (due to gyro softening) with increasing high pressure rotor speed reflects dominant low pressure rotor participation. Figure 4 shows examples of mode shapes for two high pressure rotor subsynchronous modes at the 13,226 RPM N_2/-11,340 RPM N_1 design point for the Campbell diagram of Figure 3. The 3131 cycle/min (CPM) mode is a fan shaft bending mode and the 8303 CPM mode is a core rotor bending mode, with the core rotor out-of-phase with the core case. For these two modes, the spin speed to whirl frequency ratios $\dot{\phi}_b/\omega$ for the high and low pressure rotors are equal to (4.22, -3.62) and (1.59, -1.36), respectively. The MSC evaluations are based on a mode by mode evaluation at the design point (design speeds and reference rotor torque). The MSC values are calculated for each forward whirl high pressure rotor mode and the minimum value is the basis for the rotor system stability prediction. Since the destabilizing effects of the aerodynamic cross-coupling forces are generally much more significant for the high pressure rotor than for the low pressure rotor, the former is considered as the reference rotor. Hence, the index i in equation 13 ranges over the stages for the high pressure rotor; both power absorption (compressor stages), and power generation (turbine stages) are included in the summation. It will be noted that single mode evaluation is acceptable because the cross-axis stiffness associated with the Alford forces is relatively small and, therefore, little loss in accuracy results from the use of the original mode shapes in the stability calculations.

The incorporation of the modal Q-factor in the MSC results in the implicit inclusion of rotor hysteresis or rotary damping which can be destabilizing if the rotor is undergoing subsynchronous vibration. The spin speed to whirl frequency ratios obtained from the system vibration analysis provide the data needed to correctly incorporate the effects of rotor internal damping in the generalized or modal damping for the mode. Hence, the modal Q-factor provides the effective system damping needed to correctly define the energy absorbed by the turbomachine at resonance.

EXAMPLE STABILITY CALCULATION AND ROTOR WHIRL EXPERIENCE

To demonstrate the calculation method, the MSC values are calculated for each

natural frequency involving high pressure rotor forward whirl at the design point

for the engine model of Figure 2. These natural frequencies are calculated up to the HP rotor synchronous frequency and correspond to the intersection of the Campbell diagram frequency lines and a vertical line passing through the reference rotor design speed (Figure 3). They occur at 1118, 1554, 1665, 3131, 4034, 5966, 6654, 8303, 10632, and 12580 CPM.

For example, for the 8303 CPM high pressure rotor bending mode, the numerator of equation 13 is equal to 122,708. In general, $1 < \beta < 2$. Setting β equal to 2.0 for each stage, the term

$$\sum_{i=1}^{N} \frac{\beta_i HP_i}{DP_i H_i} (\phi_{Ri} - \phi_{Si})^2$$

of equation 13 is equal to 1569 HP/cm^2.

As previously mentioned, the summation i=1, 2, ..., N encompasses both the compressor and turbine stages of the high pressure rotor. Then at the N_2 = 13,226 RPM design speed of the high pressure rotor:

$$\text{The MSC is equal to } \frac{123,067 \text{ N/cm}}{\frac{713,361}{13226}(1569) \text{ N/cm}} = 1.45$$

Table 1 provides the MSC and modal Q-factor for the design point modes. This table shows that the minimum value for the MSC occurs for the 8303 CPM mode and that the system is predicted to be stable.

The modal stability criteria has shown good correlation with experience for various General Electric Aircraft engines.

CONCLUSIONS

The MSC provides a convenient and quick means to perform a rotor stability analysis using modal data readily available from planar system vibration models. It includes all of the significant parameters (gyroscopic moments, damping, rotor/stator relative displacements), and modeling detail needed to perform a valid assessment of rotor stability related to Alford forces. The assumption of circular whirl means that the stabilizing effects of non-axisymmetric rotor and/or engine support stiffness are not included, and this may result in built-in conservatism, depending on the characteristics of the engine system modes.

REFERENCES

1. J. S. Alford, "Protecting Turbomachinery from Self-Excited Rotor Whirl," ASME Trans. Journal of Engineering for Power, Series A, pp. 333-344, Oct. 1965.

2. Childs, D. W.,"The Space Shuttle Main Engine High-Pressure Fuel Turbopump Rotordynamic Instability Problem", ASME Trans. Engineering for Power, Vol. 100, No. 1, January 1978.

3. Gunter, E. J., "Dynamic Stability of Rotor-Bearing Systems," NASA SP-113, U.S. Government Printing Office, Washington,   D. C., 1966.

4. Ehrich, F. F., "Shaft Whirl Induced by Rotor Internal Damping," Journal of Applied Mechanics, June 1964, pp. 279-282.

TABLE I - MODAL STABILITY AND Q-FACTOR VALUES CALCULATED AT THE
DESIGN POINT* FOR THE ENGINE MODEL OF FIGURE 2

NATURAL FREQUENCY (CPM)	MODAL-Q	MSC
1118	12.5	1657
1544	12.4	2643
1665	15.1	1112
3131	20.7	12
4034	16.1	58.9
5966	21.4	246
6654	15.3	7.5
8303	19.3	1.45
10632	16.5	53.7
12580	18.5	6.0

* N_1 = 11340 RPM/N_2 = 13226 RPM
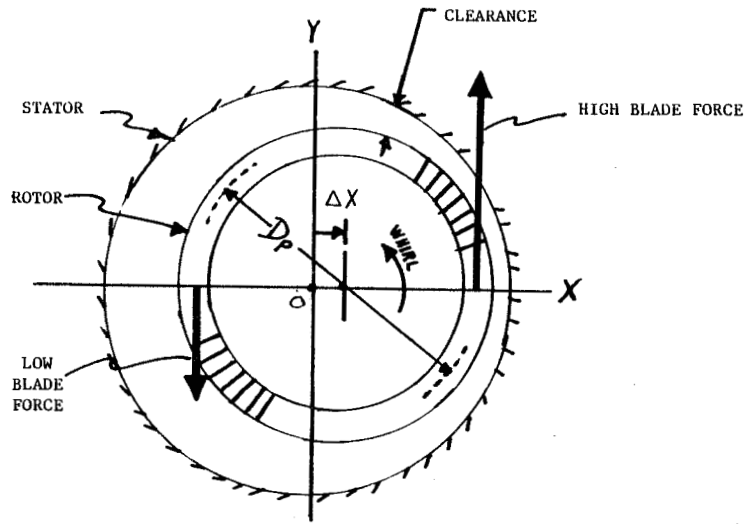
FIGURE 1 - ALFORD INSTABILITY MECHANISM
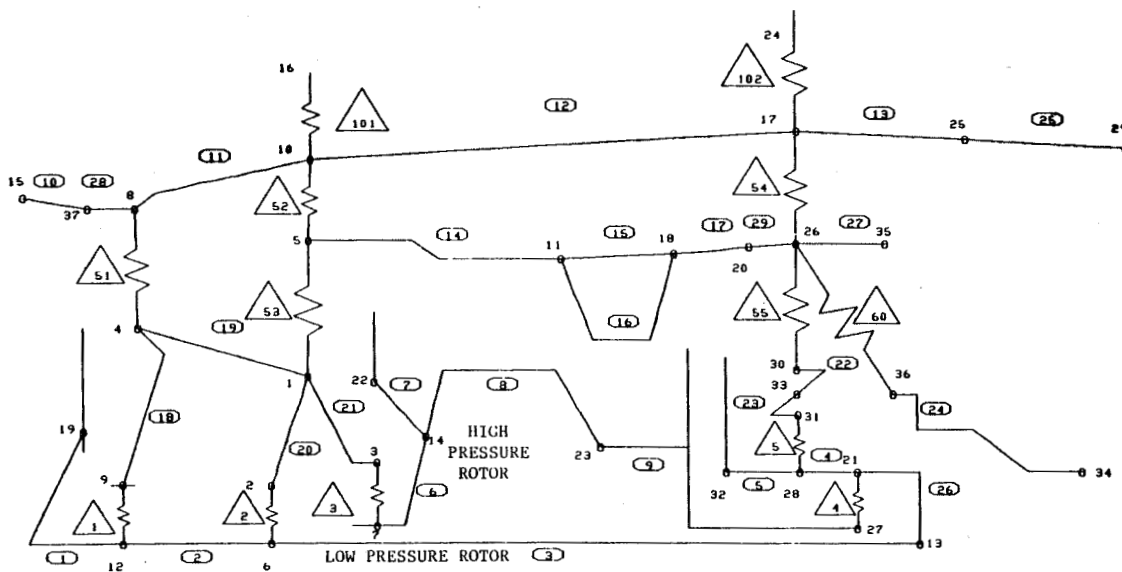
FIGURE 2 - SYSTEM VIBRATION MODEL OF A DEMONSTRATOR ENGINE

FREQ. (KCPM)

14
13
12
11
10
9
8
7
6
5
4
3
2
1

1/REV
HP ROTOR

● HP ROTOR SYNCHRONOUS
  MODES AT INTERSECTIONS
  OF 1/REV LINE AND MODES
  LINES

● SOFTENING DUE TO BACKWARD
  WHIRL OF COUNTERROTATING
  LP ROTOR

1 2 3 4 5 6 7 8 9 10 11 12 13 14

N_2 (KRPM)

DES. POINT
N_2 = +13,226 RPM
N_1 = -11,340 RPM
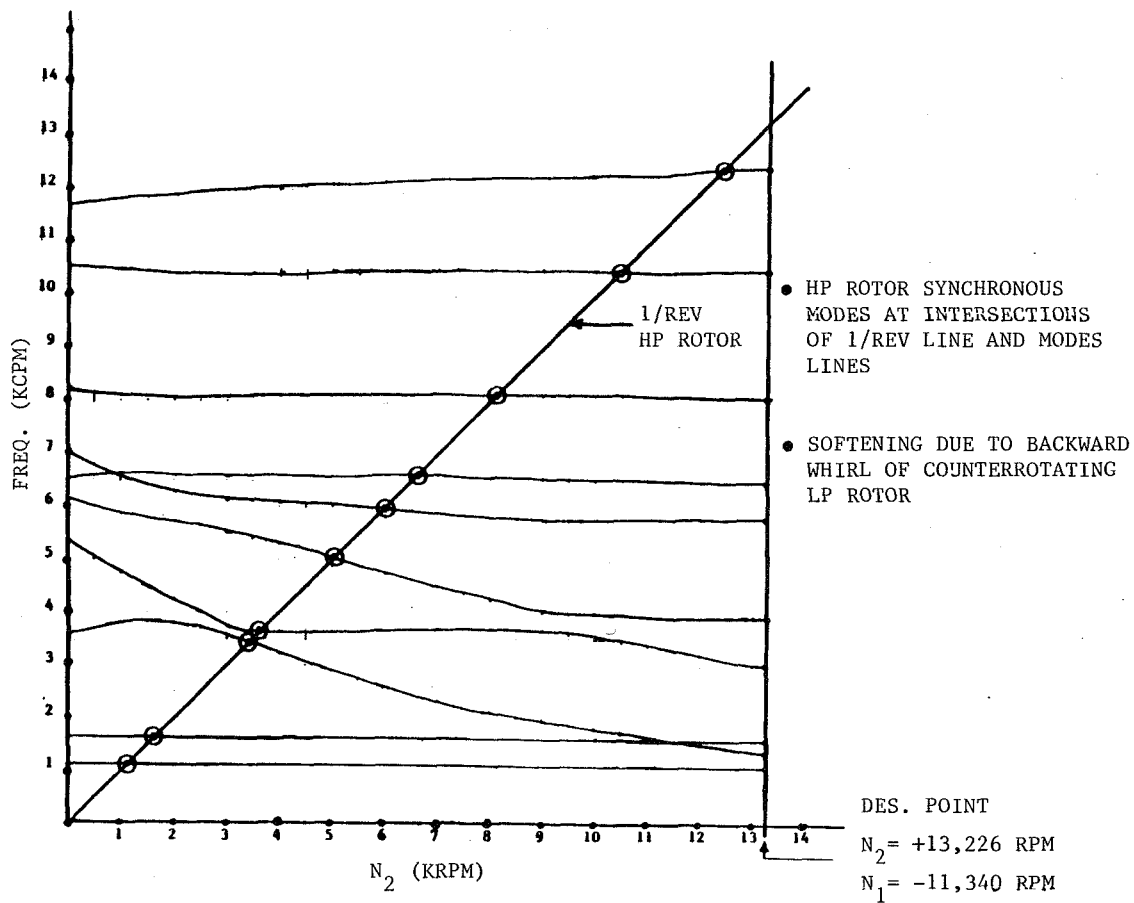
FIGURE 3 - CAMPBELL DIAGRAM
          FORWARD WHIRL MODES FOR HP ROTOR
          BACKWARD WHIRL MODES FOR LP ROTOR

295

HP ROTOR FORWARD WHIRLING MODE AT
THE DESIGN POINT

N1=-11340, N2=13226   RPM=3131.3
                             TOTAL ENERGY 128744
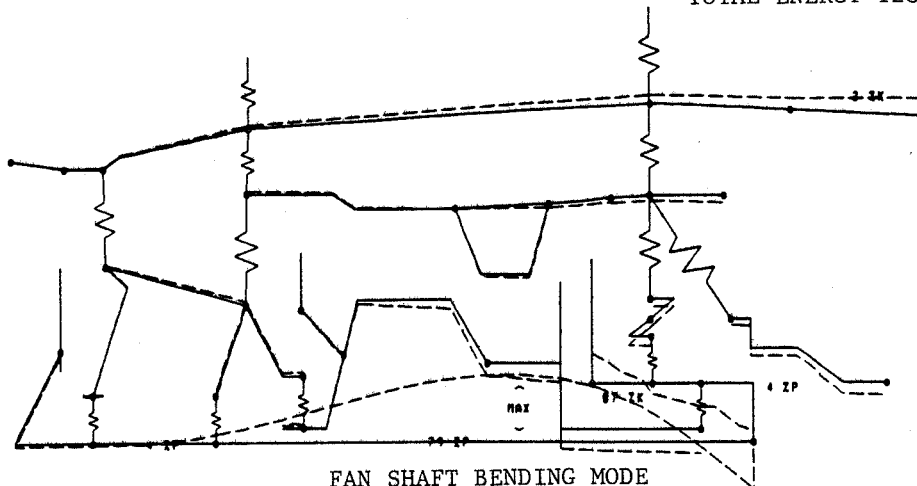
FAN SHAFT BENDING MODE

$$R_{LP} = \frac{-11340}{3131} = -3.62$$

$$R_{HP} = \frac{13226}{3131} = +4.22$$

HP ROTOR FORWARD WHIRLING MODE
AT THE DESIGN POINT

N1=-11340, N2=13226   RPM=8302.6
                             TOTAL ENERGY 679347
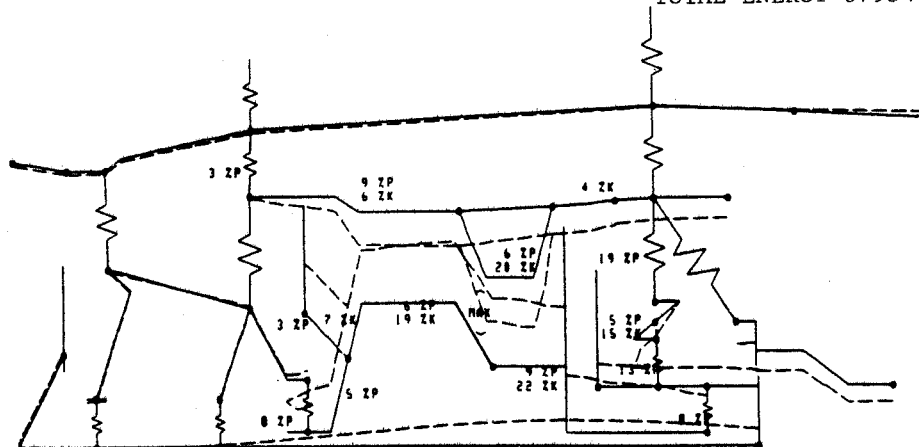
CORE BENDING MODE

$$R_{LP} = \frac{-11340}{8303} = -1.36$$

$$R_{HP} = \frac{13226}{8303} = +1.59$$

FIGURE 4 - EXAMPLES OF HIGH PRESSURE ROTOR SUBSYNCHRONOUS MODES

APPENDIX

DEVELOPMENT OF MODAL Q-FACTOR EQUATION

The equation for the modal Q-factor is developed by summing the damping contributions of the engine components (field damping for casings, frames, and rotor component structures, and lumped damping for mounts, bearings, and squeeze-film dampers).

The Q-factor for the i-th component is defined as

$$Q_i = \frac{2 \pi PE_i'}{E_{Di}} \qquad (A1)$$

where PE_i' is the physical strain energy in the component and E_{Di} is the energy dissipated.

Consider the work done on the system at resonance by an excitation force P at point j expressed in terms of modal data for the system.

$$W_{IN} = \pi P_j \phi_j \, (SF) \qquad (A2)$$

where ϕ_j is the modal displacement at point j and SF is a scale factor relating the modal displacement to the physical displacement.

From equation A1, the energy dissipated by the engine components

is

$$W_D = 2 \pi (SF)^2 \sum_{i=1}^{n} \frac{PE_i}{Q_i} \qquad (A3)$$

where n is the number of components and PE_i is the modal strain energy in the i-th component.

Equating the work done on the system to the energy dissipated leads to a solution for the modal scale factor SF.

$$SF = \frac{\pi P_j \phi_j}{2\pi \sum_{i=2}^{n} \frac{PE_i}{Q_i}} = \frac{P_j \phi_j}{2 \sum_{i=1}^{n} \frac{PE_i}{Q_i}} \qquad (A4)$$

where ϕ_j is the modal displacement at point j.

In reality, the modal scale factor is the modal participation at resonance, or

$$SF = \frac{\tilde{f}}{k} Q \qquad (A5)$$

where $\tilde{f} = P_j \phi_j$ = the generalized force and k is the generalized stiffness.

Hence,

$$Q = (SF)\frac{k}{\tilde{f}} = \frac{P_j \phi_j}{2\sum\limits_{i=1}^{n}\dfrac{PE_i}{Q_i}} \cdot \frac{2PE}{\tilde{f}} = \frac{PE}{\sum\limits_{i=1}^{n}\dfrac{PE_i}{Q_i}} \qquad (A6)$$

Equation A6 provides the modal Q-factor for the system reflecting the damping contributions of the static structures and the rotor component structures. However, in the latter case, the rotors are treated as stationary component structures since the effects of spin and whirl have not been included. Hence, the internal or hysteretic damping associated with a spinning and whirling rotor has been neglected. This damping mechanism is characterized by an internal friction force caused by the rate of change of strain within the rotor. This internal friction force can be represented with the viscous damping model derived in references 3 and 4 as

$$F_t = -C_t \mathcal{S}(\omega - \dot{\phi}) \qquad (A7)$$

where C_t is the viscous damping coefficient for a stationary rotor, $\dot{\phi}$ is the spin speed, ω is the whirl frequency, and $\mathcal{S}$ is the whirl displacement.

Equation A7 represents the follower force (tangential force which leads the whirl displacement $\mathcal{S}$ by 90°) F_t in a rotating coordinate system fixed to the rotor. An equivalent damping coefficient is derived as follows.

$$F_t = -C_{EQ}\omega \mathcal{S} = -C_t \mathcal{S}(\omega - \dot{\phi}) = -C_t \omega \mathcal{S}(1 - \dot{\phi}/\omega) \qquad (A8)$$

Hence, $C_{EQ} = C_t(1 - \dot{\phi}/\omega)$

If Q_R is the component Q-factor for a stationary rotor corresponding to C_t, then an equivalent field Q-factor Q_{EQ} for a whirling and spinning rotor of stiffness k_R can be defined as follows.

$$C_{EQ} = \frac{1}{Q_{EQ}}\frac{k_R}{\omega} = \frac{1}{Q_R}\frac{k_R}{\omega}(1 - \dot{\phi}/\omega)$$

$$\qquad (A9)$$

or

$$Q_{EQ} = \frac{Q_R}{(1 - \dot{\phi}/\omega)}$$

Notice that the equivalent Q-factor Q_{EQ} for the rotor is negative when the rotor speed $\dot{\phi}$ is greater than the whirling speed ω. Physically this means that the damping force F_t acts in the direction of whirling for subsynchronous vibration and is thus destabilizing.

Incorporating the expression for the rotor Q-factor into equation A6 yields the following equation for the modal Q-factor which includes the effects of spinning and whirling rotors.

$$Q = \frac{PE}{\displaystyle\sum_{a=1}^{na} \frac{PE_a}{Q_a} + \sum_{b=1}^{nb} (1-\dot{\phi}_b/\omega) \frac{PE_b}{Q_b}} \qquad \text{(A10)}$$

PE $\quad=\quad$ total system modal potential energy

na $\quad=\quad$ number of lumped damping components (mounts, bearings, dampers)

PE_a $\quad=\quad$ modal strain energy for lumped damping components

Q_a $\quad=\quad$ component Q-factors for lumped damping components

nb $\quad=\quad$ number of field damping components (casings, frames, rotors)

$\dot{\phi}_b$ $\quad=\quad$ spin speeds for field damping components ($\dot{\phi}_b$ is zero for static components)

PE_b $\quad=\quad$ modal strain energy for field damping components

Q_b $\quad=\quad$ component Q-factors for field damping components

ELECTROMECHANICAL SIMULATION OF ACTIVELY CONTROLLED ROTORDYNAMIC SYSTEMS WITH PIEZOELECTRIC ACTUATORS*

Reng Rong Lin and A.B. Palazzolo
Department of Mechanical Engineering
Texas A&M University
College Station, Texas 77843-3123, U.S.A.

A.F. Kascak
Propulsion Directorate
U.S. Army Aviation Systems Command
Lewis Research Center
Cleveland, Ohio 44135, U.S.A.

G. Montague
Sverdrup Technology, Inc.
Lewis Research Center Group
Brook Park, Ohio 44142, U.S.A.

This research developed theories and conducted tests for incorporating piezoelectric pushers as actuator devices for active vibration control. It started from a simple model with the assumption of ideal pusher characteristics and progressed to electro-mechanical models with non-ideal pushers. Effects on system stability due to the non-ideal characteristics of piezoelectric pushers and other elements in the control loop were investigated.

NOMENCLATURE

ADFT	Active damping feedback theory
ADSFT	Active damping and stiffness feedback theory
ASFT	Active stiffness feedback theory
AVC	: Active vibration control
$[C]$	: Damping matrix
C_i^A	: Feedback positive active damping
$[C_D]$	: Proportional damping matrix
C_{D_i}	: Capacitors used in differentiator
C_i	: Capacitors used in 2nd order non-inverting LPF
C_s	: Damping coef. of the piezoelectric stack
e_1	: Eccentricity
$\{F_D(t)\}$	: External forces (disturbance)
F_{ix}	: Imbalance forces in x due to mass imbalance
F_{iy}	: Imbalance forces in y due to mass imbalance
F_{P_i}	: Force produced by the ith pusher
$F_j(S)$	: J^{th} input of the transfer function
$G_{ij}(S)$	: Transfer function between the ith output : the jth input
K	: Feedback gain in amplifier
$[K]$	: Stiffness matrix
$[K^D]$	: Stiffness matrix including the pusher stiffness
$[K^{DD}]$	: Pusher stiffness matrix

$[K_F]$	: Feedback stiffness matrix
K_p	: Preload spring inside the pusher
K_{PA}	: Stiffness of pusher A
K_{PB}	: Stiffness of pusher B
K_{RA}	: Absorber stiffness at pusher A
K_{RB}	: Absorber stiffness at pusher B
K_s	: Stiffness of the stack of piezoelectric discs
LPF	: Low pass filter
M	: Number of actuators
[M]	: Mass matrix
$[M_P]$	: Lumped mass matrix of piezoelectric pushers
N	: Number of degrees of freedom
R_{D_i}	: Resistors used in differentiator
R_i	: Resistors used in 2nd order non-inverting LPF
R_F	: Feedback resistor used in amplifier
R_I	: resistor used in amplifier
T.F.	: Transfer function
V_p	: Probe voltage
Z_i^*	: Pusher tip displacement
$\{\alpha\}$	: Prescribed displacement of the pushers
β_i	: scalar factors used in transfer function match
ζ_i	: i^{th} modal damping
$[\Omega_i]$	: i^{th} natural frequency

INTRODUCTION

There are two major strategies in rotordynamic vibration control: passive control and active control. Passive control is achieved by changing system parameters via passive damping components or devices. Some of these devices are Lanchester dampers, impact dampers, and squeeze-film dampers. Active control uses a servo-controller-actuator system to produce control forces which act directly upon the rotor in response to measured vibrations. Active vibration control has become an area of intense research in rotorbearing system dynamics. Research has been focused on developing effective active vibration control algorithms for machine tools, large space structures, and in robots. Significant efforts are being made to apply active vibration control (AVC) devices to rotating machinery in the petrochemical, aerospace and power utility industries. The advantages of active control over passive, i.e., absorbers and dampers, is the versatility of active control in adjusting to a myriad of load conditions and machinery configurations. This is clearly illustrated when one considers the very narrow bandwidth that a tuned spring mass absorber is effective in. Other advantages of AVC include compact size, light weight, and no lubrication systems needed in the control components, and the satisfactory operation in high or low temperature.

LITERATURE REVIEW

Electromagnetic shakers and magnetic bearings have been used for actuators in the majority of the active vibration control research mentioned in the literature. Magnetic bearings act directly onto the rotor without contact while electromagnetic actuators apply forces onto the rotor indirectly through the bearings. Schweitzer (1985) examined the stability and observability

of rotorbearing systems with active vibration control, and presented an analysis which related force and stiffness to electrical and geometrical properties of electromagnetic bearings.

Nikolajsen (1979) examined the application of magnetic dampers to a 3.2 meter simulated marine propulsion system. Gondhalekar and Holmes (1984) suggested that electromagnetic bearings be employed to shift critical speeds by altering the suspension stiffness. Weise (1985) discussed proportional, integral, derivative (PID) control of rotor vibrations and illustrated how magnetic bearings could be used to balance a rotor by forcing it to spin about its inertial axis. Humphris et al (1986) compared predicted and measured stiffness and damping coefficients for a magnetic journal bearing.

Several papers describe active vibration control utilizing other types of actuators such as pneumatic, hydraulic, electrohydraulic, and eddy current force generators. Ulbrich and Althaus (1989) discussed the advantages and disadvantages of different types of actutors, and examined controlled hydraulical chambers as force actuators. This compact system could develop very large forces and thereby influence even large turbines weighing several tons, however, the difficulty of hydraulic control lies in high frequency (over 100 Hz) response. This was essentially limited by the servo valve implemented and fluid losses. Feng (1986) developed an active vibration control scheme with actuator forces resulting from varying bearing oil pressure. Heinzmann (1980) employed loud speaker coils linked to the shaft via ball bearings to control vibrations.

Crawley and de L..ıs (1983, 1985) used piezoceramics, bonded on the surface of cantilever beams, as actuators either to excite vibrations or to suppress the vibrations by introducing damping to the system. Furthermore, they developed a theoretical background for predicting the amplitude of the vibration induced by piezoceramics. Stjernstrom (1987) bonded piezoceramics on cantilever beams as actuators and sensors to induce the 1st and 2nd vibration modes.

Matsubara et al (1989) employed piezoelectric dampers to suppress chatter vibration during a boring process. These piezoelectric dampers were driven so as to generate damping forces corresponding to the vibration velocity of the boring bar. Tzou (1987) demonstrated the control of bending vibration in non-rotating beams by using layered piezoelectric materials.

This paper considers the effects on the system stability due to the non-ideal characteristics of piezoelectric pushers and other control devices used in the control loop. The piezoelectric actuators are represented by equivalent, linear electric circuit with elements selected so as to match the frequency response function of the circuit to that of the actuator. The differential equations for the circuits are assembled into the structural matrices to form an electro-mechanical model of the system. This model may than be employed to predict instability onset feedback gains, total system stability and total system forced response.

ANALYSIS - GENERAL

The matrix differential equations of motion for a rotor bearing system can be derived by using Newton's 2nd law or by Lagrange's method. Eq.(1) shows the matrix differential equation;

$$[M]_{(N\times N)}\{\ddot{Z}\}_{(N\times 1)} + [C]_{(N\times N)}\{\dot{Z}\}_{(N\times 1)} + [K]_{(N\times N)}\{Z\}_{(N\times 1)} = \{F(t)\}_{(N\times 1)} \qquad (1)$$

where [M], [C], and [K] matrices are the rotor bearing system mass, damping, and stiffness, respectively, N is the number of degrees of freedom, and $\{F\}$ represents the external forces exerted on the system.

Figure 1 (Palazzolo, 1981) shows a general rotor model with translatory and rotational dofs in the XZ and YZ planes. The model is discretized into lumped inertia stations which are connected by massless beam segments. The equilibrium equation of a disk is derived through the consideration of external forces present due to adjacent beam segments and the bearing stiffness forces.

The free vibration equilibrium equations for the entire rotor system are assembled by requiring internal equilibrium and displacement compatibility. Palazzolo (1981) shows how the [M], [K], and [C] matrices are formed for a generic rotorbearing system from basic geometric and material properties.

ANALYSIS - EQUIVALENT CIRCUITS

In previous references (Palazzolo, 1989) the free tip response of a piezoelectric pusher is assumed to be approximately equal to the internal prescribed displacement which is assumed to vary linearly with input voltage. These assumptions are valid only at frequencies well below the resonant frequency of the pusher. The phase lag of the piezoelectric pusher increases with frequency and may cause negative active damping to occur if the phase lag is greater than 90^0. Phase lag is also introduced by the pusher drivers and other electronic components in the control loop.

A linear time-invariant system with input $f(t)$ and with output $r(t)$ can be characterized by its impulse response $g(t)$, which is the response when subjected to an unit impulse input $\delta(t)$. Once the impulse response of the linear system is known, the output of the system $r(t)$, with any input $f(t)$, may be found from the transfer function of the system.

The transfer function of a linear time-invariant system is defined as the Laplace transform of the impulse response with zero initial conditions (Kuo, 1987). In general, if a linear system has p inputs and q outputs, the transfer function between the ith output and the jth input is defined as

$$G_{ij}(S) = \frac{R_i(S)}{F_j(S)} \tag{2}$$

where $F_k(S) = 0$, $k = 1, 2, \ldots, p$, $k \neq j$.

Equivalent electrical circuits are constructed to reproduce the measured transfer (frequency response) functions of the piezoelectric actuators and their amplifier drivers. These linear circuits may then be assembled with the structural system equations.

An electro-mechanical representation of an AVC system, consisting of a soft-mounted pusher, isolation pad, probe, and control devices, is shown in Figure 2. In this figure the buckout circuit removes DC bias from the eddy current displacement sensor, the low pass filter (L.P.F.) is utilized to reduce high frequency noise and improve stability. The figure also shows how the piezoelectric actuator and its amplifier driver are both represented by equivalent 2nd order non-inverting low pass filters. With this model, the non-ideal characteristics of the overall system due to phase lag and frequency dependency can be included.

The differential equation for the differentiator in Figure 2 is

$$-\dot{V}_{in} = R_{D1}C_{D2}\ddot{V}_{out} + \left(\frac{R_{D1}}{R_{D2}} + \frac{C_{D2}}{C_{D1}}\right)\dot{V}_{out} + \frac{1}{R_{D2}C_{D1}}V_{out} \tag{3}$$

304

The corresponding transfer function is then

$$T.F. = \frac{V_{out}(S)}{V_{in}(S)} = \frac{-R_{D2}C_{D1}S}{\left[R_{D1}R_{D2}C_{D1}C_{D2}S^2 + \left(R_{D1}C_{D1} + R_{D2}C_{D2}\right)S + 1\right]} \tag{4}$$

If the variable 'S' in Eq.(4) is replaced by the variable 'jw', then Eq.(4) represents the frequency response function of the differentiator in the frequency domain.

The differential equation for the 2nd order non-inverting low pass filter is

$$V_1 = \frac{R_1 R_2 C_1 C_2}{K}\ddot{V}_2 + \left(-R_1 C_1 + \frac{R_1 C_2}{K} + \frac{R_1 C_1}{K} + \frac{R_2 C_2}{K}\right)\dot{V}_2 + \frac{1}{K}V_2 \tag{5}$$

The corresponding transfer function is then

$$T.F. = \frac{V_2(S)}{V_1(S)} = \frac{\frac{K}{(R_1 R_2 C_1 C_2)}}{S^2 + \left[\frac{1}{C_1}\left(\frac{1}{R_1} + \frac{1}{R_2}\right) + \frac{1}{R_2 C_2}(1 - K)\right]S + \frac{1}{R_1 R_2 C_1 C_2}} \tag{6}$$

Again, if the variable 'S' is replaced by the variable 'jw' in the above equation, Eq.(6) represents the frequency response function in the frequency domain and is shown below.

$$T.F. = \frac{V_2(jw)}{V_1(jw)} = \frac{K}{(1 - R_1 R_2 C_1 C_2 \omega^2) + jw[C_2(R_1 + R_2) + (1 - k)R_1 C_1]} \tag{7}$$

The electrically undamped natural frequency, ω_n, of this circuit is defined by

$$\omega_n^2 = \frac{1}{R_1 R_2 C_1 C_2} \tag{8}$$

and the phase lag angle is

$$\phi = tan^{-1}\frac{\omega[C_2(R_1 + R_2) + (1 - k)R_1 C_1]}{1 - \left(\frac{\omega}{\omega_n}\right)} \tag{9}$$

The following steps summarize a simple procedure to identify the resistances and capacitances of an equivalent 2nd order non-inverting low pass filter.
a)   Make a frequency response plot of the physical system.
b)   Locate the cut-off frequency, ω_n, from this plot.
c)   Assume $R_1 = R_2$ and $C_1 = C_2$.

d) Select C_1 arbitrarily and then calculate R_1 by

$$R_1 = \frac{1}{\omega_n C_1}$$

e) Use $K = 3$ for an undamped electrical system and $K < 3$ for damped electrical system.
f) Construct the electrical circuit using the calculated R and C values.
g) Adjust the damping factor in the equivalent electrical circuit by varying the K value to match the peak magnitude at the cut-off frequency location.
h) Multiply this realized frequency response function by a proper scale factor which represents the magnitude ratio between the known and the realized frequency response functions at $\omega = 0$.

Figure 3 shows the schematic diagram for measuring the frequency response function of a pusher. The pusher is screwed inside a vertical steel cylinder and excited by a signal generator through the pusher driver. The displacement of the free tip of pusher, output for the transfer function, is measured by an eddy current probe. The exciting signal is the input for the transfer function. Both input and output are connected to a spectrum analyzer and the results of the transfer function are sent to a printer.

Figure 4 shows the transfer function of a typical pusher while Figure 5 shows the corresponding transfer function of the equivalent 2nd order non-inverting low pass filter circuit with identified R and C values. This simulation shows a very good correlation between the two transfer functions when the frequency is below 4000 Hz. Note that a jet aircraft engine, depending on the size, normally operates at speeds from 5000 rpm (83.3 Hz) up to 25000 rpm (416.6 Hz). Furthermore, electro-mechanical instability frequencies have always occurred less than 4000 Hz, in our testing.

ANALYSIS - ELECTRO-MECHANICAL SYSTEM MODELING UTILIZING OPPOSING SOFT-MOUNTED ACTUATORS

The stability of the active vibration control system is affected by both the characteristics of the mechanical system (e.g. rotor) and those of the electrical devices (e.g. actuators) used in the control feedback loop. The characteristics, i.e. phase lag, of the electrical devices are incorporated in the mechanical system model by including their transfer function behavior represented by equivalent electrical circuits. Theory for the electro-mechanical model and comparisons between predicted and measured unbalance response and stability are presented.

Electro-Mechanical Model Theory

Let two opposing, soft-mounted pushers be installed at the jth bearing of the rotor system (see Figure 6) where m_b, c_j, and k_j are the mass, damping, and stiffness of the jth bearing, and k_{PA} and k_{PB} are the stiffnesses of pushers A and B and the dashed blocks represent the following components:

Block A: Inverting differentiator
Block B: 4th order non-inverting low pass filter to simulate the Ithaco filter
Block C: 2nd order non-inverting low pass filter to simulate pusher driver B
Block D: 2nd order non-inverting low pass filter to simulate pusher B
Block E: 2nd order non-inverting low pass filter to simulate pusher driver A

Block F: 2nd order non-inverting low pass filter to simulate pusher A

Combining the mechanical and electrical differential equations for the model in Figure 6 yields

$$
\begin{pmatrix}
m_b & 0 & 0 & 0 & 0 & 0 & 0 & 0 & 0 & 0 \\
0 & m_{PA} & 0 & 0 & 0 & 0 & 0 & 0 & 0 & 0 \\
0 & 0 & m_{PB} & 0 & 0 & 0 & 0 & 0 & 0 & 0 \\
0 & 0 & 0 & R_{D1}C_{D2} & 0 & 0 & 0 & 0 & 0 & 0 \\
0 & 0 & 0 & 0 & 1 & 0 & 0 & 0 & 0 & 0 \\
0 & 0 & 0 & 0 & 0 & 1 & 0 & 0 & 0 & 0 \\
0 & 0 & 0 & 0 & 0 & 0 & 1 & 0 & 0 & 0 \\
0 & 0 & 0 & 0 & 0 & 0 & 0 & 1 & 0 & 0 \\
0 & 0 & 0 & 0 & 0 & 0 & 0 & 0 & 1 & 0 \\
0 & 0 & 0 & 0 & 0 & 0 & 0 & 0 & 0 & 1
\end{pmatrix}
\begin{pmatrix}
\ddot{x} \\ \ddot{x}_A \\ \ddot{x}_B \\ \ddot{V}_1 \\ \ddot{V}_2 \\ \ddot{V}_3 \\ \ddot{V}_4 \\ \ddot{V}_5 \\ \ddot{V}_6 \\ \ddot{V}_7
\end{pmatrix}
+
$$

$$
\begin{pmatrix}
c_j & 0 & 0 & 0 & 0 & 0 & 0 & 0 & 0 & 0 \\
0 & C_{RA} & 0 & 0 & 0 & 0 & 0 & 0 & 0 & 0 \\
0 & 0 & C_{RB} & 0 & 0 & 0 & 0 & 0 & 0 & 0 \\
\zeta_1 & 0 & 0 & \left(\frac{R_{D1}}{R_{D2}} + \frac{C_{D2}}{C_{D1}}\right) & 0 & 0 & 0 & 0 & 0 & 0 \\
0 & 0 & 0 & 0 & A_1 & 0 & 0 & 0 & 0 & 0 \\
0 & 0 & 0 & 0 & 0 & A_2 & 0 & 0 & 0 & 0 \\
0 & 0 & 0 & 0 & 0 & 0 & A_3 & 0 & 0 & 0 \\
0 & 0 & 0 & 0 & 0 & 0 & 0 & A_4 & 0 & 0 \\
0 & 0 & 0 & 0 & 0 & 0 & 0 & 0 & A_5 & 0 \\
0 & 0 & 0 & 0 & 0 & 0 & 0 & 0 & 0 & A_6
\end{pmatrix}
\begin{pmatrix}
\dot{x} \\ \dot{x}_A \\ \dot{x}_B \\ \dot{V}_1 \\ \dot{V}_2 \\ \dot{V}_3 \\ \dot{V}_4 \\ \dot{V}_5 \\ \dot{V}_6 \\ \dot{V}_7
\end{pmatrix}
+
$$

$$
\begin{pmatrix}
k_{11} & k_{12} & k_{13} & 0 & 0 & 0 & 0 & k_{18} & 0 & k_{110} \\
k_{21} & k_{22} & 0 & 0 & 0 & 0 & 0 & 0 & 0 & k_{210} \\
k_{31} & 0 & k_{33} & 0 & 0 & 0 & 0 & k_{38} & 0 & 0 \\
0 & 0 & 0 & k_{44} & 0 & 0 & 0 & 0 & 0 & 0 \\
0 & 0 & 0 & k_{45} & k_{55} & 0 & 0 & 0 & 0 & 0 \\
0 & 0 & 0 & 0 & k_{65} & k_{66} & 0 & 0 & 0 & 0 \\
k_{71} & 0 & 0 & 0 & 0 & k_{76} & k_{77} & 0 & 0 & 0 \\
0 & 0 & 0 & 0 & 0 & 0 & k_{87} & k_{88} & 0 & 0 \\
k_{91} & 0 & 0 & 0 & 0 & k_{96} & 0 & 0 & k_{99} & 0 \\
0 & 0 & 0 & 0 & 0 & 0 & 0 & 0 & k_{109} & k_{1010}
\end{pmatrix}
\begin{pmatrix}
x \\ x_A \\ x_B \\ V_1 \\ V_2 \\ V_3 \\ V_4 \\ V_5 \\ V_6 \\ V_7
\end{pmatrix}
=
\begin{pmatrix}
F(t) \\ 0 \\ 0 \\ 0 \\ 0 \\ 0 \\ 0 \\ 0 \\ 0 \\ 0
\end{pmatrix}
$$

(10)

where

$k_{11} = k_j + k_{PA} + k_{PB}$ ． $k_{12} = -k_{PA}$ ． $k_{13} = -k_{PB}$

$k_{18} = k_{PB}\beta_7$ ． $k_{110} = -k_{PA}\beta_8$

$k_{21} = -k_{PA}$ ． $k_{22} = k_{RA} + k_{PA}$ ． $k_{210} = k_{PA}\beta_8$

$k_{31} = -k_{PB}$ ． $k_{33} = k_{RB} + k_{PB}$ ． $k_{38} = -k_{PB}\beta_7$

$k_{44} = \dfrac{1}{C_{D1}R_{D2}}$

$k_{54} = -\omega_1^2 K_1 \beta_2$ ． $k_{55} = \omega_1^2$

$k_{65} = -\omega_2^2 K_2$ ． $k_{66} = \omega_2^2$

$$k_{71} = \omega_3^2 K_3 \beta_1 \zeta_1 \qquad k_{76} = \omega_3^2 K_3 \beta_3 \beta_4 \qquad k_{77} = \omega_3^2$$
$$k_{87} = -\omega_4^2 K_4 \beta_5 \qquad k_{88} = \omega_4^2$$
$$k_{91} = -\omega_5^2 K_5 \beta_1 \zeta_1 \qquad k_{96} = -\omega_5^2 K_5 \beta_3 \beta_4 \qquad k_{99} = \omega_5^2$$
$$k_{109} = -\omega_6^2 K_6 \beta_6 \qquad k_{1010} = \omega_6^2$$

$$(11)$$

and where K_i is the internal zero frequency gain of the individual filter and is defined as

$$K_i = \frac{R_{I_i} + R_{F_i}}{R_{I_i}}, \qquad i = 1, 2 \tag{12}$$

and

$$\omega_i^2 = \frac{1}{R_{2i-1} R_{2i} C_{2i-1} C_{2i}}, \qquad i = 1, 2 \tag{13}$$

$$A_i = \left[\frac{1}{C_{2i-1}} \left(\frac{1}{R_{2i-1}} + \frac{1}{R_{2i}} \right) + \frac{1 - K_i}{R_{2i} C_{2i}} \right], \qquad i = 1, 2 \tag{14}$$

$$\alpha_A = \beta_8 V_7 \tag{15}$$

$$\alpha_B = \beta_7 V_5 \tag{16}$$

$$V_p = \zeta_1 x \tag{17}$$

Finally β_5 and $\hat{\beta}_7$ are the scale factors used to match the amplitudes of the transfer functions of the pusher driver B and pusher B, respectively.

The "electromechanical" element matrices in Eq.(10) are next assembled into the structural finite element model of the rotor bearing system described by Eq.(1). The total system model can then be employed for free or forced vibration response simulation.

TEST RESULT CORRELATION

Figure 7 shows a diagram of the actively controlled rotor bearing system at NASA Lewis. Each bearing has a control circuit as shown in this figure. Unbalance response was obtained by measuring the influence coefficients for an imbalance attached on the outboard disk. Figure 8 shows the measured influence coefficient at the outboard bearing for the controlled and uncontrolled cases. Figure 9 shows that the predicted influence coefficient as obtained from the electromechanical simulation model is in good agreement with the test results. The simulation model employed a proportional damping assumption for the uncontrolled (tare) system.

The Y_O velocity feedback gain was increased in Figure 7 until the system became unstable at zero rpm. The unstable mode shape was measured and appears in Figure 10. Figure 11 shows that the corresponding unstable mode predicted by the electromechanical simulation model is very similar in form and frequency. The instability onset-feedback gain was very sensitive to the amount of passive (uncontrolled) damping of the unstable mode. The measured passive damping ratios for this mode ranged between 0.0011 and 0.011. The measured instability onset feedback gain (β_4) was 5. The predicted value was 7 with a unstable mode passive damping of 0.0011. The utility of the simulation program as a design or trouble shooting tool for actively controlled

systems is demonstrated in Figure 12 which shows how stability can be controlled by changing resistance in the low pass filter.

Figure 13 shows the effectiveness of the control system in controlling two modes utilizing both active damping and stiffness.

SUMMARY

The authors have developed a new means for simulating the electromechanical response of rotorbearing system utilizing a piezoelectric actuator type active vibration control. The simulation results show good agreement with those measured on a two bearing turbine-driven test rig at NASA Lewis.

REFERENCES

[1] Crawley, E.F. and de Luis, J., 1983, "Experimental Verification of Piezoelectric Actuators for Use in Precision Space Structures," AIAA Paper 83-0878.

[2] Crawley, E.F. and de Luis, J., 1985, "Use of Piezoceramics as Distributed Actuators in Large Space Structures," Proceedings of the 26th Structures, Structural Dynamics, and Materials Conference, Part 2, AIAA-ASME-ASCE, Orlando, Florida, April, pp. 126-133.

[3] Feng, G. Xin, N., 1986, "Automatic Control of the Vibration of the Flexible Rotor with Microcomputer," Int. Conf. on Rotordynamics, IFTOMM and JSME, Tokyo, Sept. pp.14-17.

[4] Gondholekar, V., and Holmes, R., 1984, "Design of Electromagnetic Bearing for Vibration Control of Flexible Transmission Shaft," Rotor Dynamic Instability Problem in High Performance Turbomachinery, Texas A&M Univ., May.

[5] Heinzmann, J.D., Flack, R., Lewis, D., 1980, "The Implementation of Automatic Vibration Control in High Speed Rotating Test Facility," Univ. of Virginia Report UVA/464761/MAE80/160.

[6] Hermann, E., 1988, Personal communications, Hartford Insurance, Houston, Texas

[7] Humphris, R., et al., 1986, "Effect of Control Algorithms on Magnetic Journal Bearing Properties," J. Eng. Gas Turbines and Power, ASME, Oct., Vol. 108, pp. 624-632.

[8] Matsubara, T., Yamamoto, H., Mizumoto, H., 1989, "Chatter Suppression by Using Piezoelectric Active Dampers," Rotatory Machinery Dynamics, DE-Vol. 18-1, 12th Biennial Conference on Mechanical Vibration and Noise, Montreal, Quebec, Canada, September, pp. 79-83.

[9] Nikolajsen, J., Holmes, R. and Gondholekar, V., 1979, "Investigation of an Electromagnetic Damper for Vibration Control of a Transmission Shaft," Proc. Instn. Mech. Engr., Vol, 193, pp. 331-336.

[10] Palazzolo, A.B., 1981, "Vibrations of Locally Modified Mechanical and Structural Systems," University of Virginia Dissertation, Mechanical Engineering, January.

[11] Palazzolo, A.B., Lin, R.R., Kascak, A.F., Montague, J., Alexander, R.M., 1989, "Test and Theory for Piezoelectric Actuator - Active Vibration Control of Rotating Machinery,"

ASME Conf., Montreal, Canada, September, Submitted to the ASME Journal of Vibration, Acoustics, Stress, and Reliability in Design for publication.

[12] Palazzolo, A.B., Lin, R.R., Kascak, A.F., Montague, J., Alexander,R.M., 1989, "Piezoelectric Pushers for Active Vibration Control of Rotating Machinery," ASME Journal of Vibration, Acoustics, Stress, and Reliability in Design, Vol. 111, July, pp.298-305.

[13] Schweitzer, G., 1985, "Magnetic Bearings for Vibration Control," Bently Nevada Instability Seminar, Minden Nevada.

[14] Stjernstrom, Scott C., 1987, "Active Vibration Control Using Piezoceramic Transducers," Texas A&M University Thesis, Mechanical Engineering Department, December.

[15] Tzou, H.S., 1987, "Active Vibration Control of Flexible Structures Via Converse Piezoelectricity," Presented at the 20th Midwestern Mechanics Conference, 8/31-9/2, 1987, Developments in Mechanics, pp.1201-1206, Vol. 14-c.

[16] Weise, D., 1985, "Active Magnetic Bearings Provide Closed Loop Servo Control for Enhanced Dynamic Response," Proc. 27th IEEE Machine Tool Conf., October.
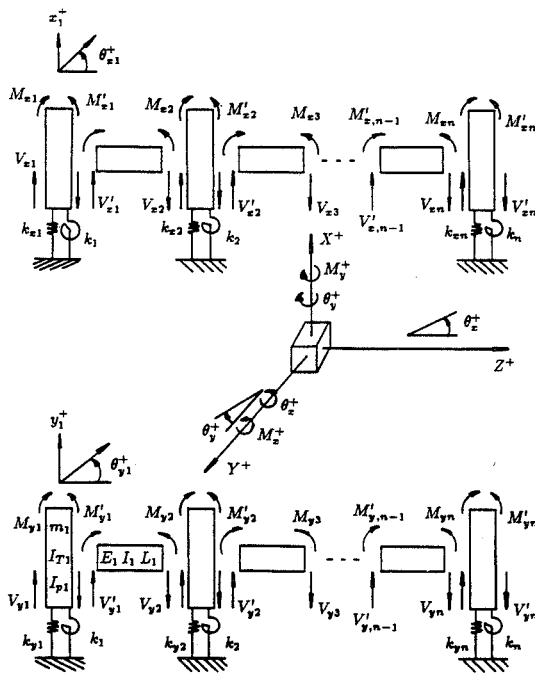
Figure 1 General n-disc rotor bearing system.
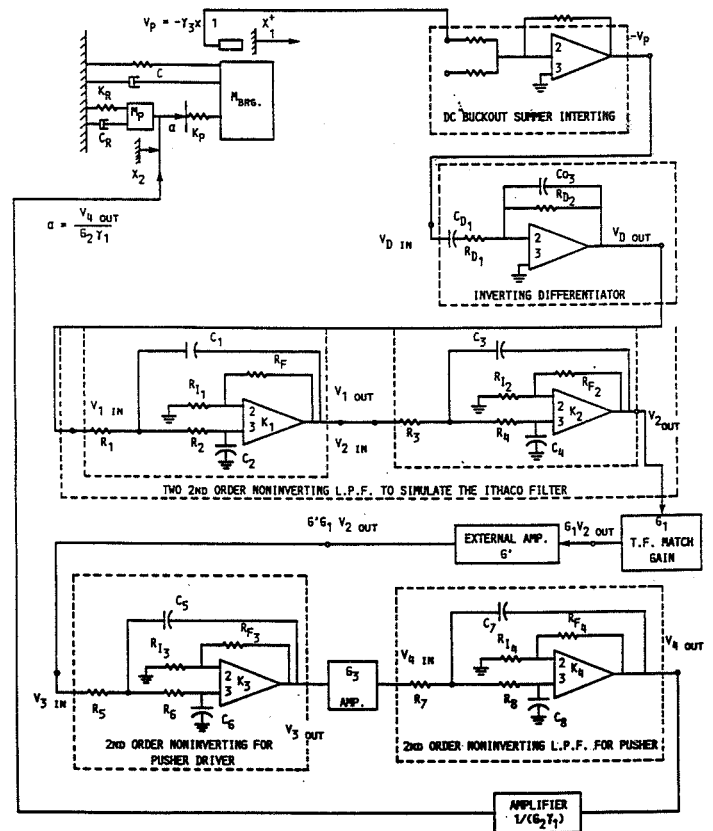
Figure 2 Soft-mounted single pusher with absorber.

310
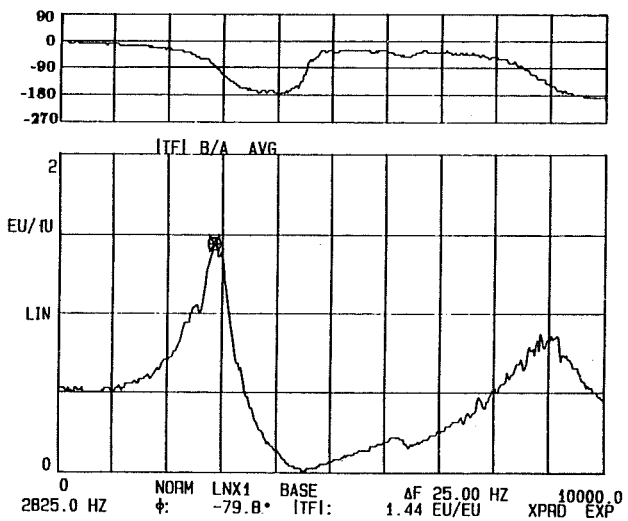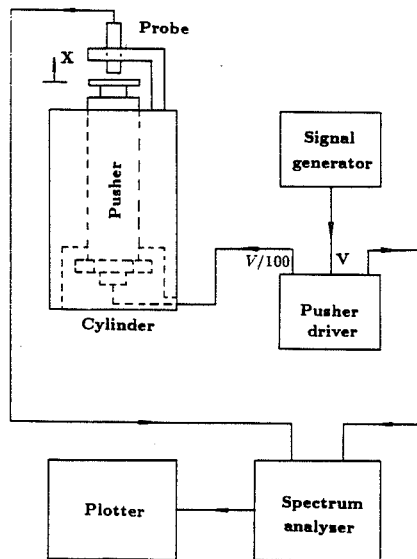
Figure 4   Transfer function plot of a typical pusher.

'Figure 3   Schematic diagram for measuring the pusher frequency response function.
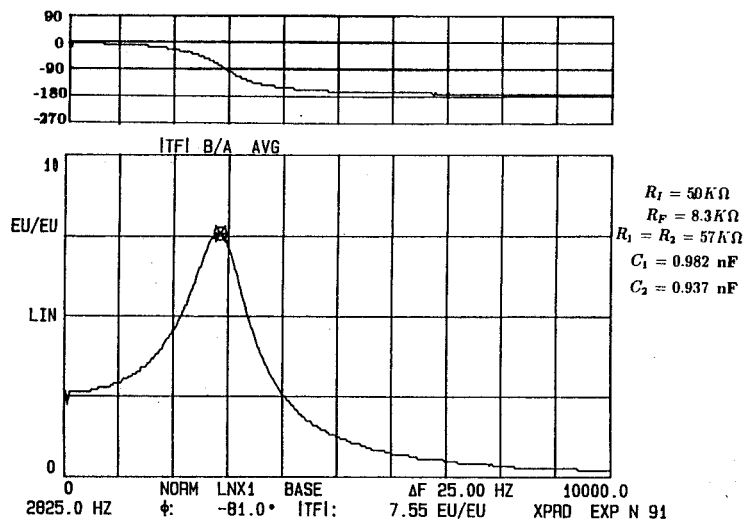
Figure 5   Transfer function plot of realized electrical circuit of pusher A.

311
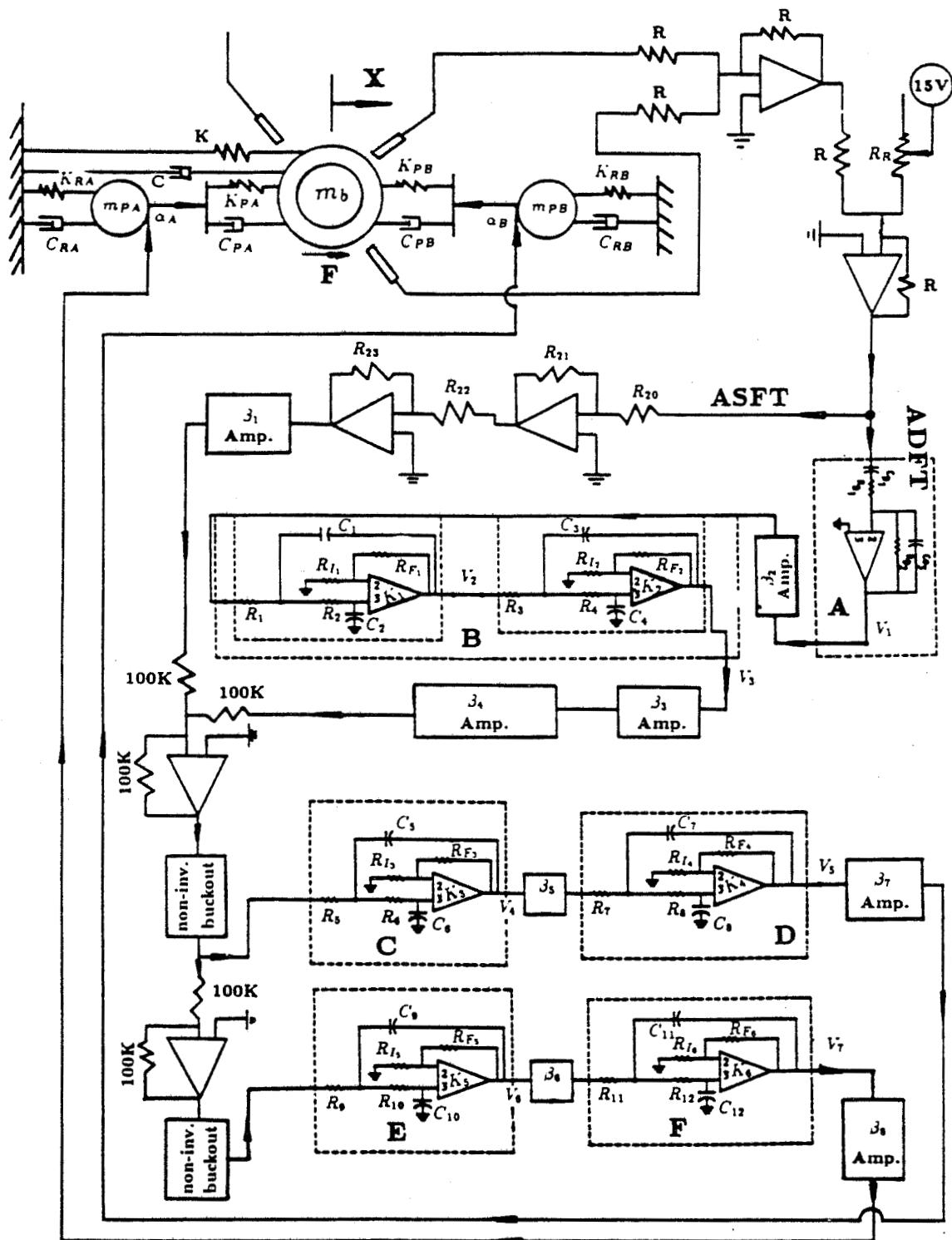
Figure 6 Electro-mechanical model with two opposing soft-mounted pushers.
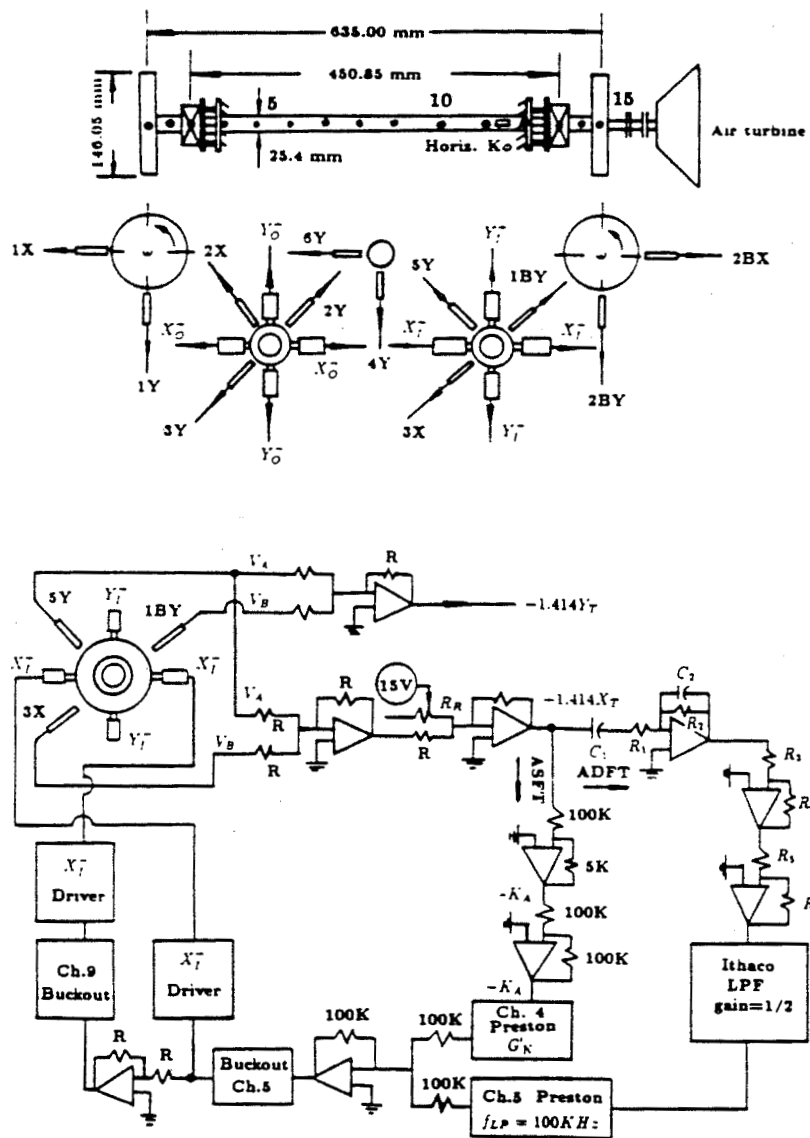
Figure 7 Schematic diagram of sensors, actuators,
and control circuit of NASA test rig.

313

TRIAL WEIGHT: 0.184 GRAM AT 130 DEGREE, R=2 IN
GC: XI=XO=2, YO=YI=6.3, GK=0
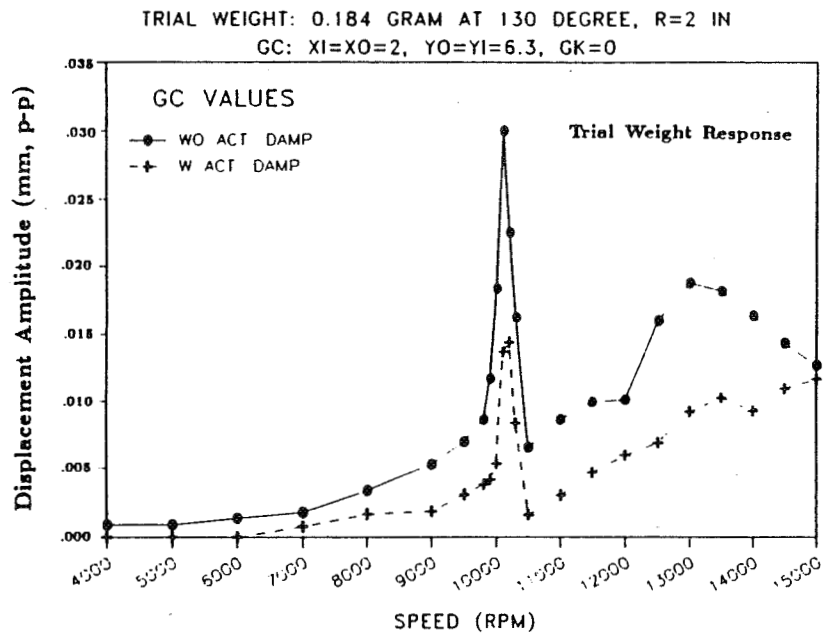
Figure 8 Measured unbalance responses at YO^+_{BRG} with and without ADFT.

UNBAL 0.013 OZ—IN AT DISC(O), SKBRG=1751965 N/M
PROPORT. DAMP (.007,.012, .05) GYRO INCLUDED (0062)
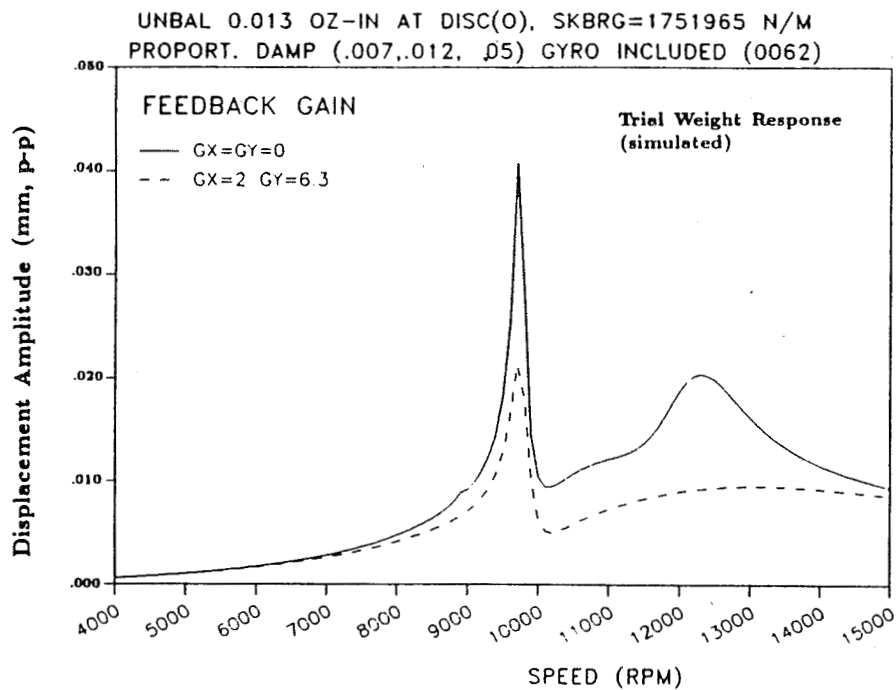
Figure 9 Simulated unbalance responses at YO^+_{BRG} with and without ADFT, with 3-mode proportional damping method.

314
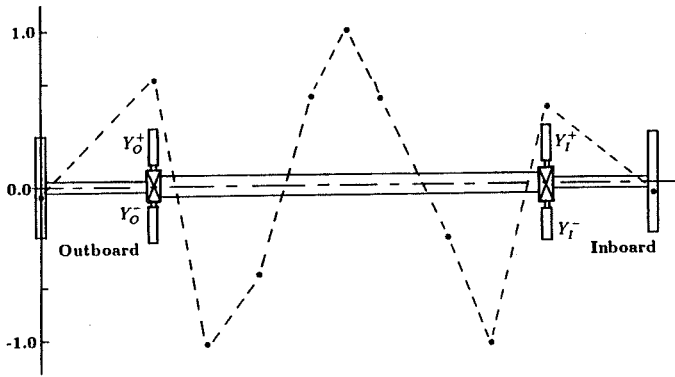
Figure 10 **Measured mode shape of unstable mode at a frequency of 2100 Hz.**
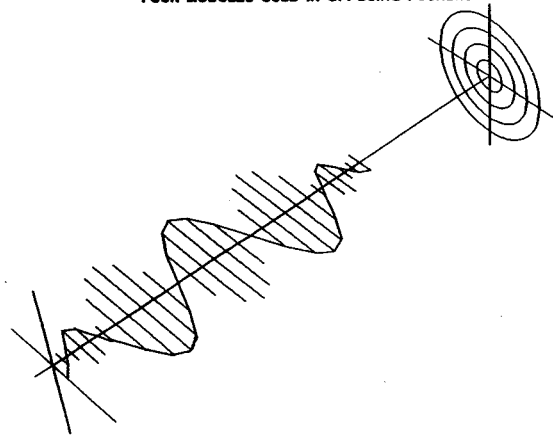
Figure 11 **Predicted mode shape of unstable mode at 2400 Hz.**

ROOT LOCUS PLOT OF UNSTABLE MODE

ELECTRO—MECH (CLOSED LOOP) SKBRG=1751965 N/M W/O GYRO (0062)
PROPORT. DAMP (.007,.12,.05,.0011) (975.67,1106.66,1273.81,14744.51)

4TH ONILPF CUTOFF FREQ.

—●—	500 HZ	$R=0.947\times10^6\,\Omega$	$C=.336\times10^{-9}\,F$
—+—	2000 HZ	$R=0.267\times10^6\,\Omega$	
-★-	3000 HZ	$R=0.158\times10^6\,\Omega$	
—⊙--	6000 HZ	$R=0.789\times10^5\,\Omega$	
—⊙—	10000 HZ	$R=0.474\times10^5\,\Omega$	

R and C indicate resistor R_1, R_2, R_3, R_4 and capacitor C_1, C_2, C_3, C_4 in Figure 7.1
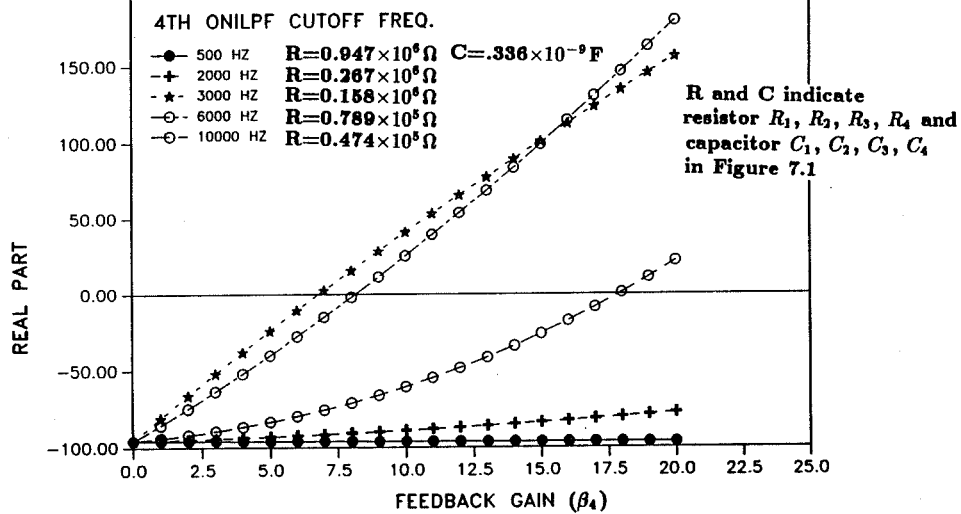
Figure 12 **Effects of cutoff frequency of 4NILPF on the system instability onset gain.**

315
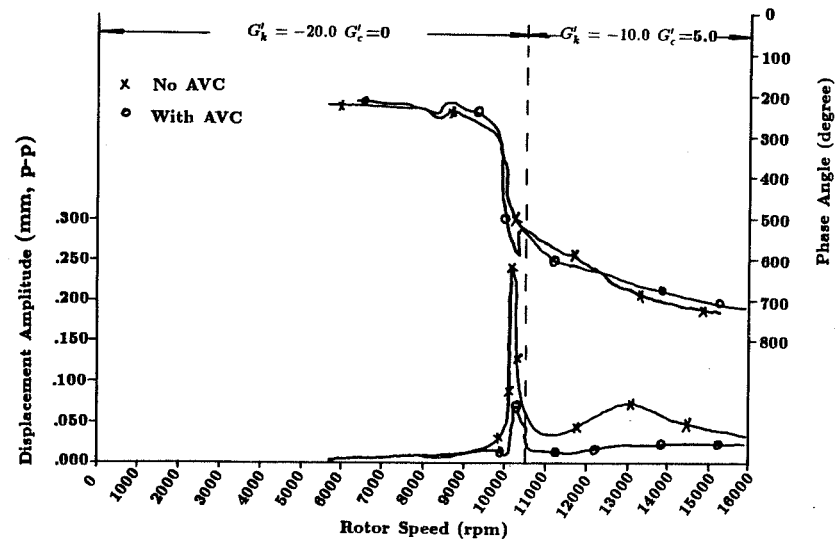
Figure 13   Midspan vibration with and without active damping and stiffness.

DYNAMIC CHARACTERISTICS AND STABILITY ANALYSIS OF SPACE SHUTTLE MAIN ENGINE OXYGEN PUMP

Edgar J. Gunter and Lyle Branagan
Department of Mechanical and Aerospace Engineering
University of Virginia
Charlottesville, Virginia 22903, U.S.A.

This paper deals with the dynamic characteristics of the Space Shuttle high pressure oxygen pump. Experimental data is presented to show the vibration spectrum and response under actual engine operation and also in spin pit testing for balancing. The oxygen pump appears to be operating near a second critical speed and is sensitive to self excited aerodynamic cross coupling forces in the turbine and pump. An analysis is presented to show the improvement in pump stability by the application of turbulent flow seals, preburner seals, and pump shaft cross sectional modifications.

INTRODUCTION

This paper deals with the dynamic characteristics and stability analysis of the oxygen pump employed in the NASA Space Shuttle Main Engine System. Both the hydrogen and oxygen pumps for the SSME are supported on rolling element bearings. These bearings have little inherent damping. As a result of low bearing damping, self excited whirl motion was observed on the hydrogen pump in early tests. Investigations conducted on stability at the University of Virginia and also by D. Childs at Texas A&M, indicated that turbulent flow seals could substantially increase the stability characteristics of the hydrogen pumps. The theory of turbulent flow seals as originally developed by Black, and expanded upon by Allaire and Childs, was applied to the oxygen pump preburner end. A substantial improvement in rotor stability of the oxygen pump could be achieved by stiffening the cross section of the preburner shaft section.

PUMP DESCRIPTION

The oxygen pump consists of a double suction main impeller driven by two stages of overhung turbine. The oxygen pump weighs 77 lbs. and is designed to operate at 29,000 RPM (FPL). The design power of the oxygen pump is approximately 31,000 horsepower.

Figure 1 represents a schematic cross-section of the SSME rocket engine. The oxygen pump, labeled HPOTP, for high pressure oxygen turbopump, appears on one side of the figure. On the opposite side of the figure is the high pressure fuel turbopump, which supplies liquid hydrogen to the rocket nozzle. The liquid oxygen and hydrogen, supplied to the nozzles, are fed in to the combustion chamber of the rocket engine. There are three rocket engines on each shuttle craft. The high pressure oxygen turbopump is designed to supply LOX (liquid oxygen) at 1,153 lbs. per second to the engine.

The supply pressure to the main pump is 4,974 psi and the supply pressure to the small preburner pump is 8,070 psi.
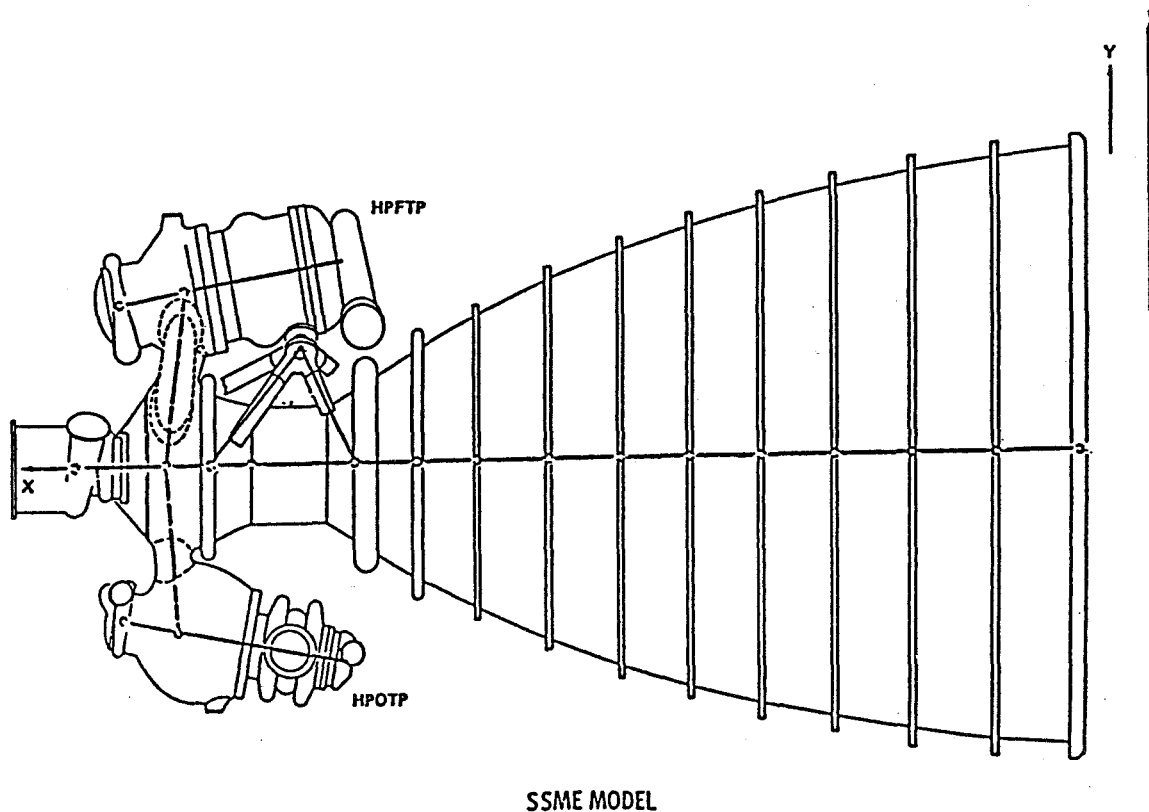
FIGURE 1   SPACE SHUTTLE MAIN ENGINE (SSME) MODEL

Figure 2 represents the cross-section of the HPOTP rotor. The rotor is supported at the pump-end (left) by two 45 mm ball bearings and at the turbine-end (right) by two 55 mm ball bearings. At the right, is shown the two-stage, hot-gas turbine, which drives the oxygen pump. The main pump is represented by the central impeller and is of a dual flow configuration. The impeller wheels act as a balance piston for this design. In a conventional turbopump, a mechanical axial thrust bearing, absent in both the oxygen and hydrogen pumps, takes up the axial load. Overhung from the pump bearing and attached to the main shaft is the preburner impeller. The preburner impeller is used to provide oxygen for the combustion which powers the turbine stages. The oxygen rotor is designed such that it must be assembled. The main impeller slides onto the turbine section and is held in place with a lock nut. The preburner impeller is assembled after the preburner bearings have been positioned.

318
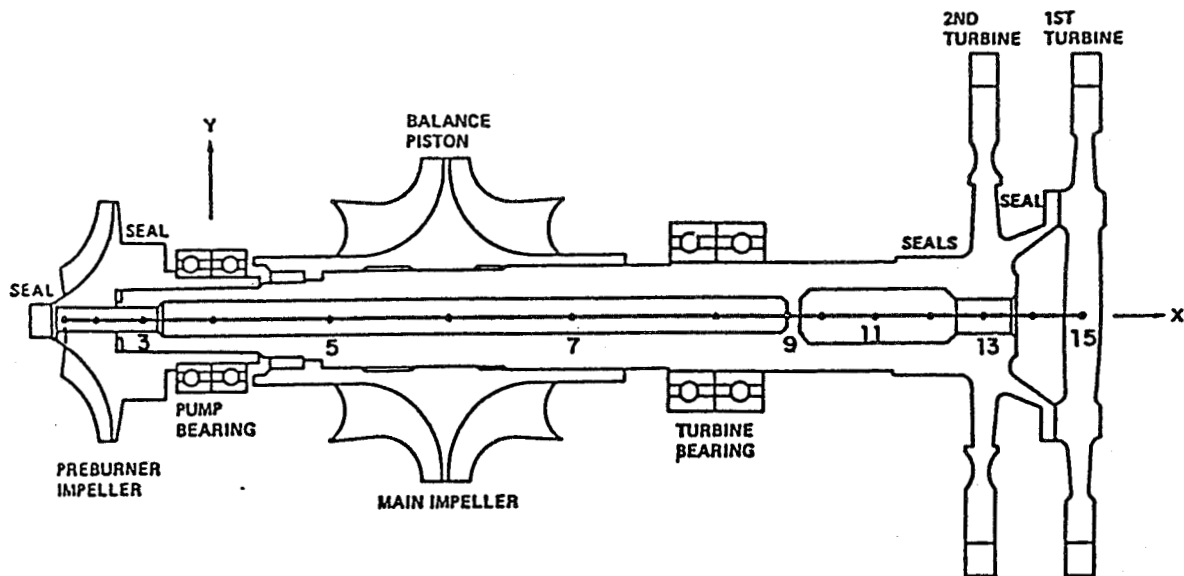
HPOTP ROTOR MODEL

FIGURE 2   HIGH PRESSURE OXYGEN TURBOPUMP (HPOTP) ROTOR MODEL

Figure 3 represents the HPOTP case model. The HPOTP case model shows the location of the impellers, turbine, bearings, and various seals in the pump.
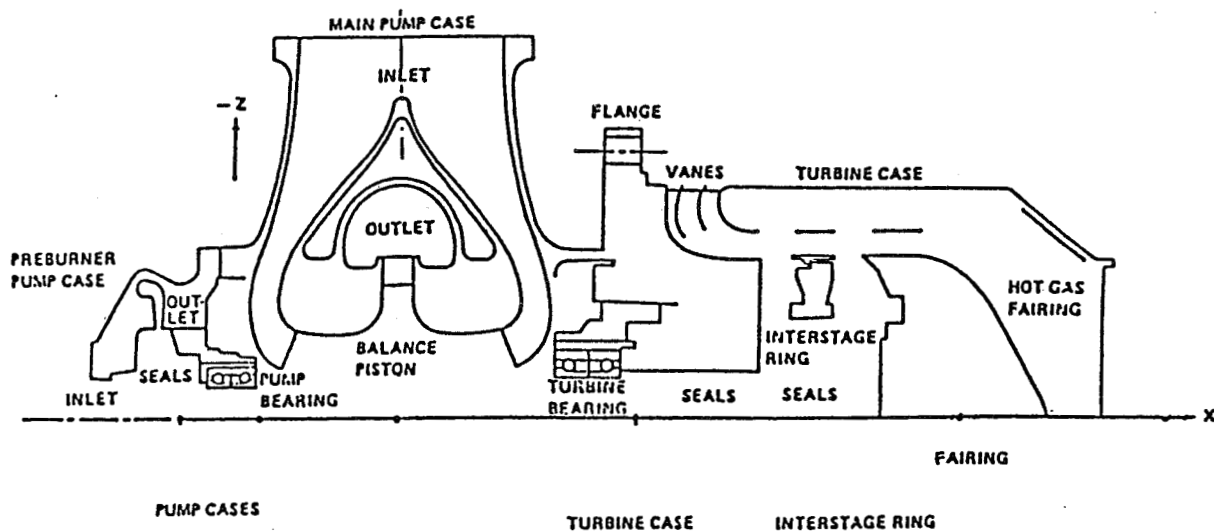
HPOTP CASE MODEL

MODEL "A" (Original NASA Model)

FIGURE 3   HIGH PRESSURE OXYGEN TURBOPUMP (HPOTP) CASE MODEL

319

The oxygen pump was designed to operate from 22,000 RPM (MPL - minimum power level) to 29,000 RPM (FPL - full power level) and is to be free of critical speeds in this vicinity. The design time of operation of the oxygen pump during FPL is approximately 730 seconds.

REVIEW OF EXPERIMENTAL DATA

Figure 4 represents the experimental data obtained during NASA test run 902-065. This figure shows the synchronous motion of a radial accelerometer as a function of oxygen pump shaft speed for both runup and rundown. On runup, two major resonant peaks are clearly seen: approximately, 22,000 RPM and 27,000 RPM. Upon rundown a very predominant peak at 26,000 RPM is observed. According to the original design specifications, there should not be any critical speeds in the operating speed range.
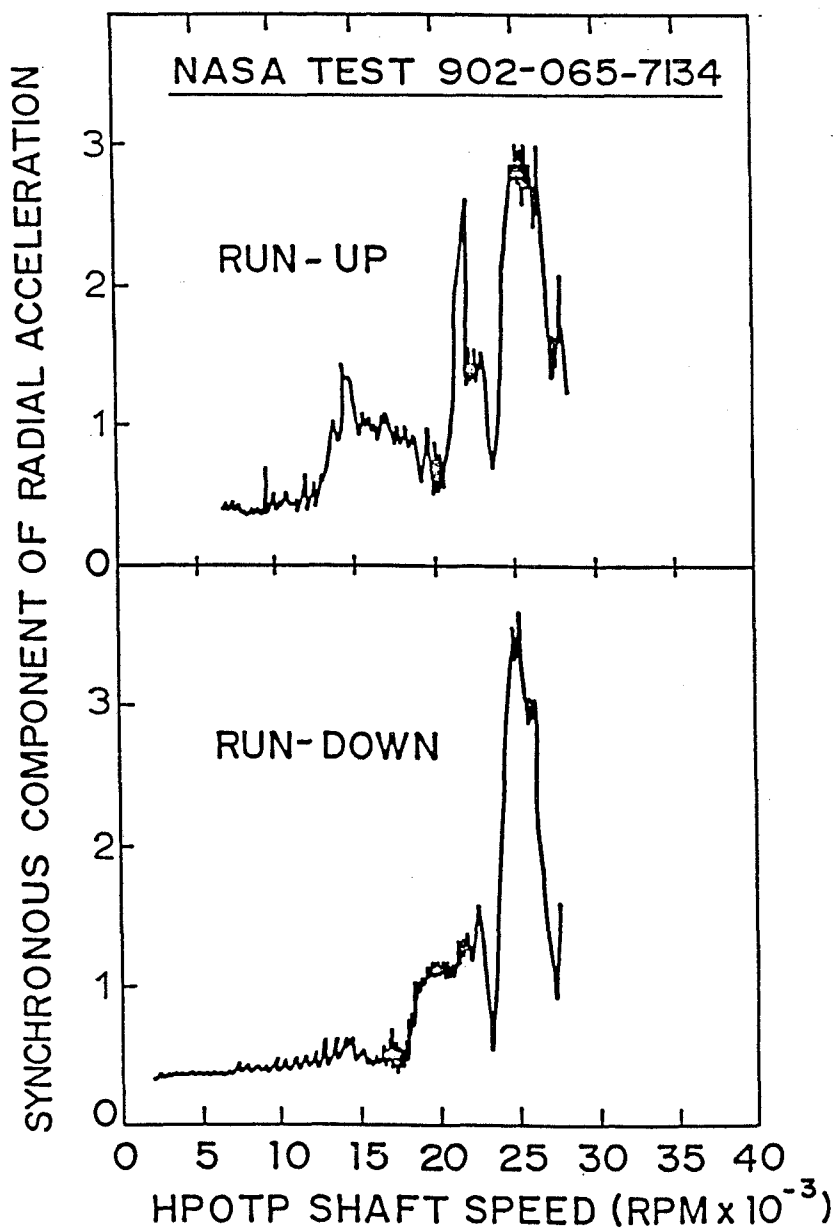
FIGURE 4   HPOT RADIAL 45° ACCELEROMETER

320

Figure 5 represents the same NASA test run (902 - 065), but in this case, the synchronous motion of the oxygen pump casing accelerometer was tracked as a function of hydrogen shaft speed. Since the hydrogen pump operates at a slightly higher speed, the hydrogen pump acts as a vibration exciter, and the synchronous tracking filter (synchronous with the hydrogen pump speed) produces an indication of which resonant frequencies are within this operating speed range.
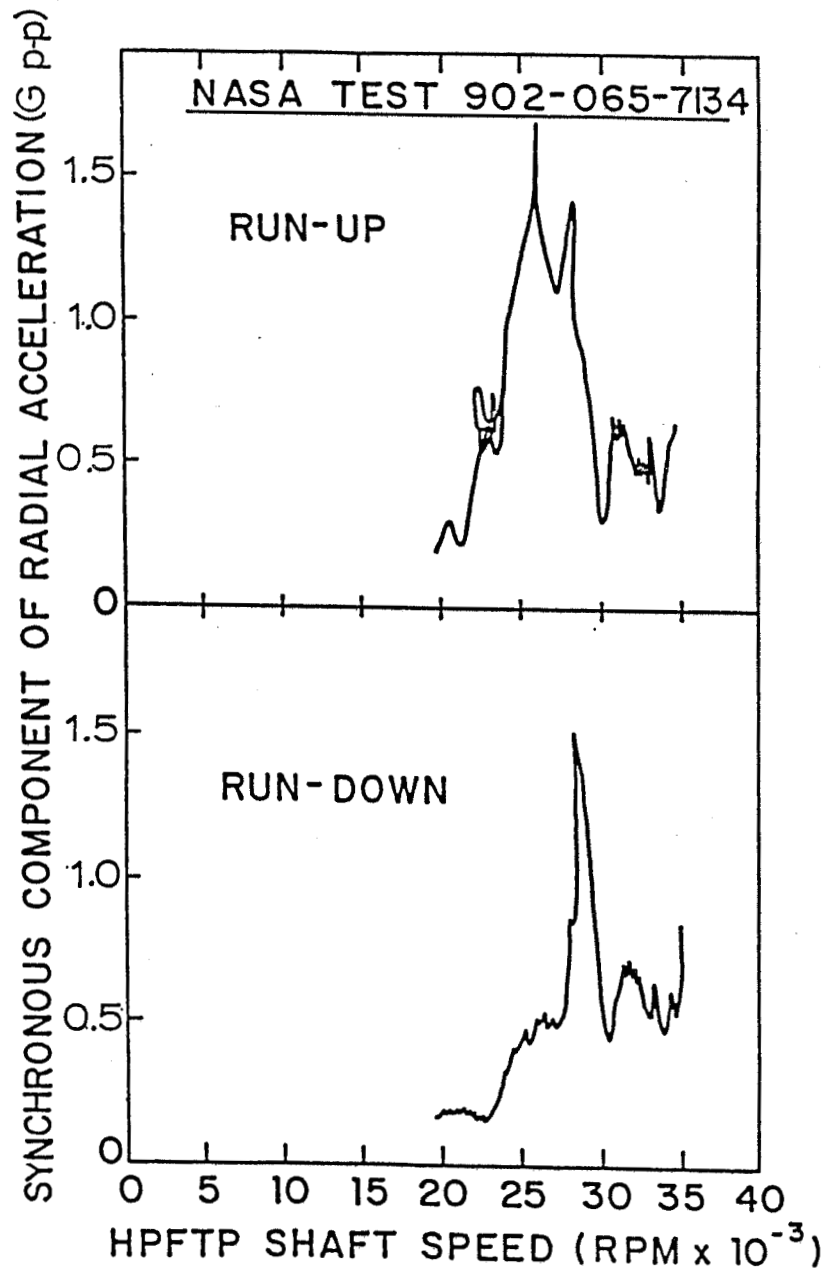
FIGURE 5 HPOT RADIAL 45° ACCELEROMETER

321

From the curve on runup, it is seen that there is a resonant frequency at approximately 25,000 RPM. This information corresponds with the vibration data obtained on runup and rundown as a function of hydrogen or oxygen pump speed. Also observed is a resonant frequency at approximately 28,000 RPM. Upon rundown, this is the predominant frequency observed. From this data, it therefore appears that there are three distinct resonant frequencies in the operating speed range. These resonant frequencies are approximately 22,000 RPM, 26,000 RPM, and 28,000 RPM. The 540 degree phase shift indicates the passage through these three resonant frequencies (Figure 6).
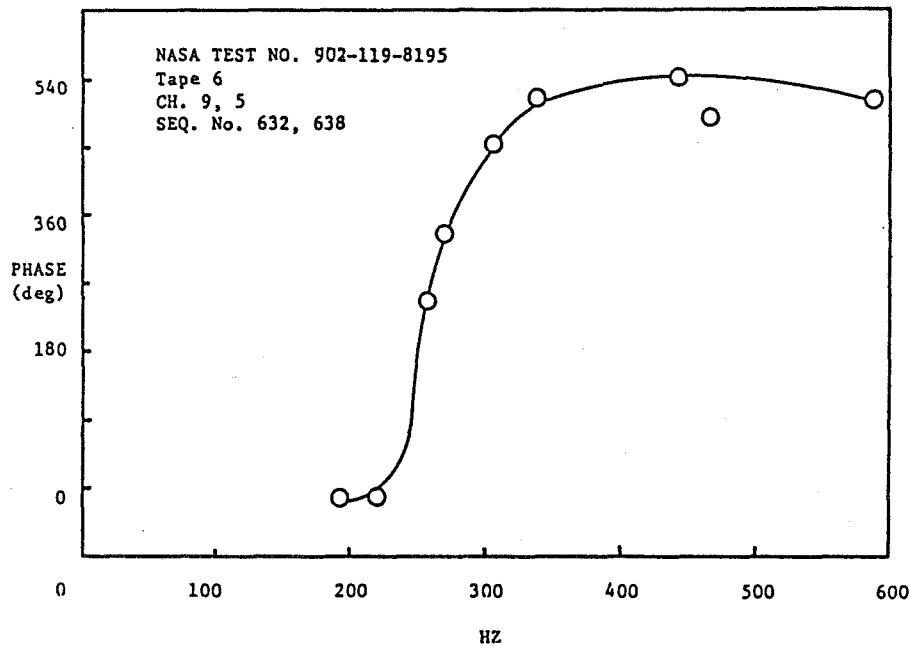
FIGURE 6 PHASE ANGLE BETWEEN HPOT RADIAL 135° AND PBP RADIAL 135° ACCELEROMETERS

Figure 7 represents the frequency spectrum obtained on NASA run 902-119 for the preburner axial 90° accelerometer for speeds ranging from 60% RPL to 100% RPL. In this figure, one is able to discern a low level oxygen pump motion which may be associated with the whirl of the oxygen pump at the first critical speed. This dotted line is designated "O_2 whirl." The frequency spectrum also shows the amplitude due to oxygen pump speed and to hydrogen pump speed. The frequency spectrum shows that there is an oxygen pump resonant frequency at approximately 378 Hz and at 466 Hz (which corresponds to 100% RPL). The amplitude increase indicates a possible resonant speed. The hydrogen pump speed is also clearly seen on this figure with peaks at 468 Hz, and at 587 Hz (the operating speed of the hydrogen pump). It appears that the hydrogen pump may also be operating on a resonant frequency. The fact that the hydrogen pump speed peaks at 468 Hz also indicates a possible oxygen pump resonant frequency at the hydrogen pump operating speed.

322
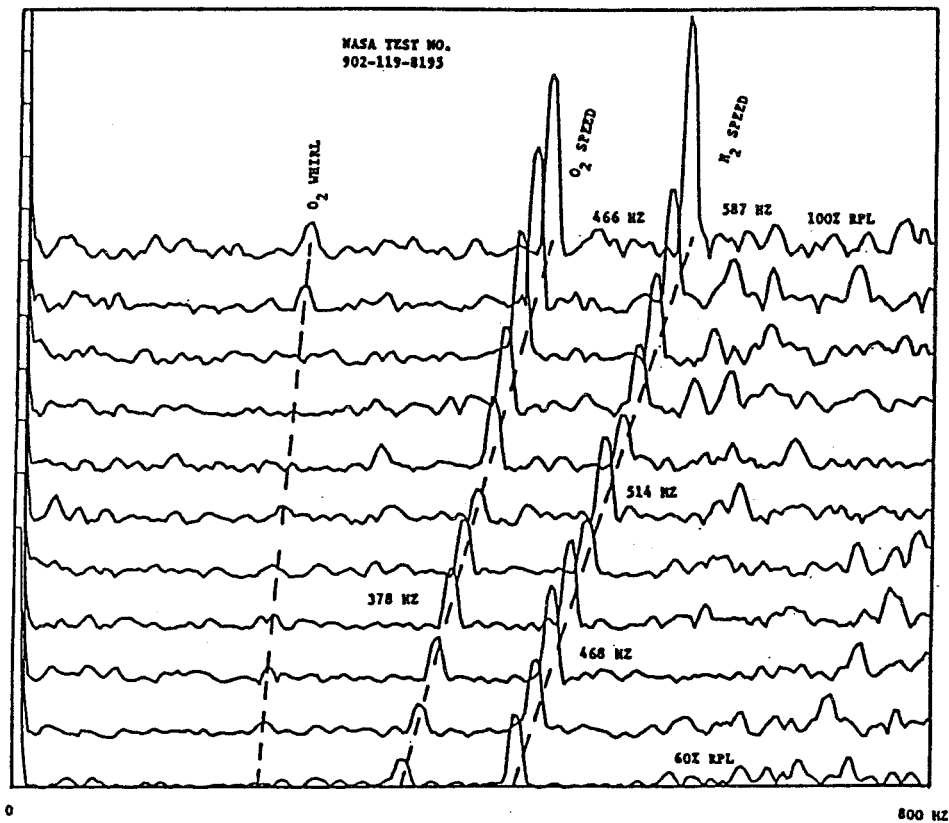
FIGURE 7   PBP AXIAL 90° ACCELEROMETER CASCADE DIAGRAM

Figure 8 represents the synchronous radial acceleration of the oxygen rotor as a function of oxygen pump shaft speed (NASA test 910-136). During runup, two resonances were observed at 22,000 and 25,500 RPM. The resonance at 25,500 RPM appears to dominate. This speed corresponds to operation at 90% rated power level. Upon reaching rated power level, the speed was reduced and the rotor was operated at 90% RPL. Due to continued operation at this speed, the rotor amplitude increased until failure occurred. The upper figure represents the phase angle change while passing through the 25,000 RPM speed range. The 180 degree phase shift shown corresponds to passage through a resonant frequency.

Run 902-193 was a later run of the S.S.M.E. in which the system was operated to 109% of the rated power level. Several spectrums of this run are shown to illustrate the response frequencies encountered with the oxygen and hydrogen pumps.

Figure 9 represents the peak hold spectrum from 0 to 500 Hz encountered with the HPOP 45 degree radial accelerometer. This figure shows that a frequency of 232 Hz at a level of 4 Grms was encountered during acceleration from 0 to 100% RPL. The value of 232 Hz could correspond to the oxygen pump first critical speed. This frequency, in general, was not very pronounced during deceleration.

Figure 10 represents the peak channel hold accelerometer spectrum of the HPOP 45° radial accelerometer during deceleration from 109% to 90 RPL. Not that there is a pronounced resonant frequency at 463 Hz. The magnitude of the peak amplitude is 10 Grms.

323
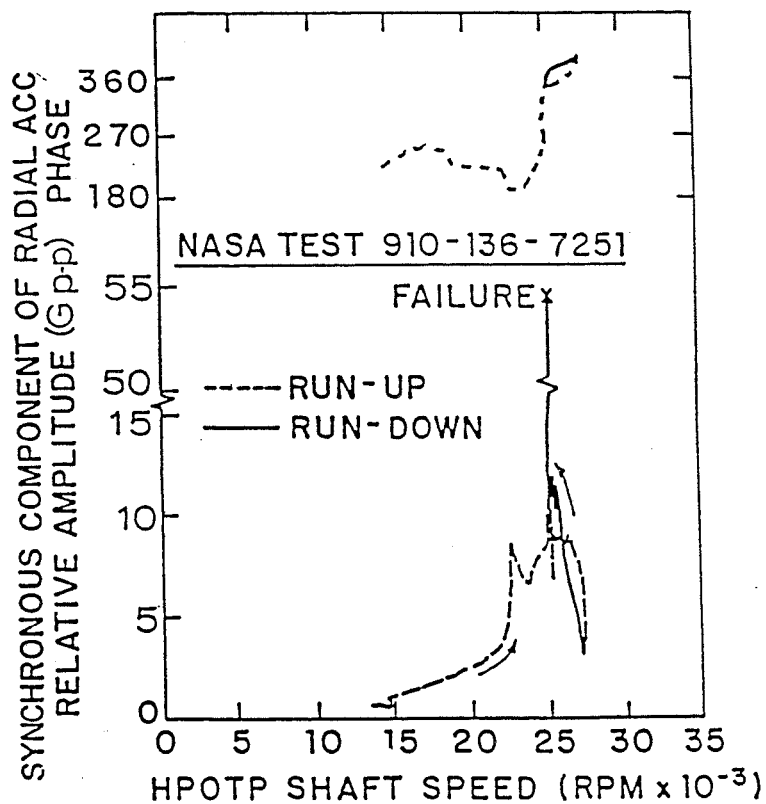
FIGURE 8 SYNCHRONOUS ACCELERATION FOR HPOP RADIAL
ACCELEROMETER DURING FAILURE RUN
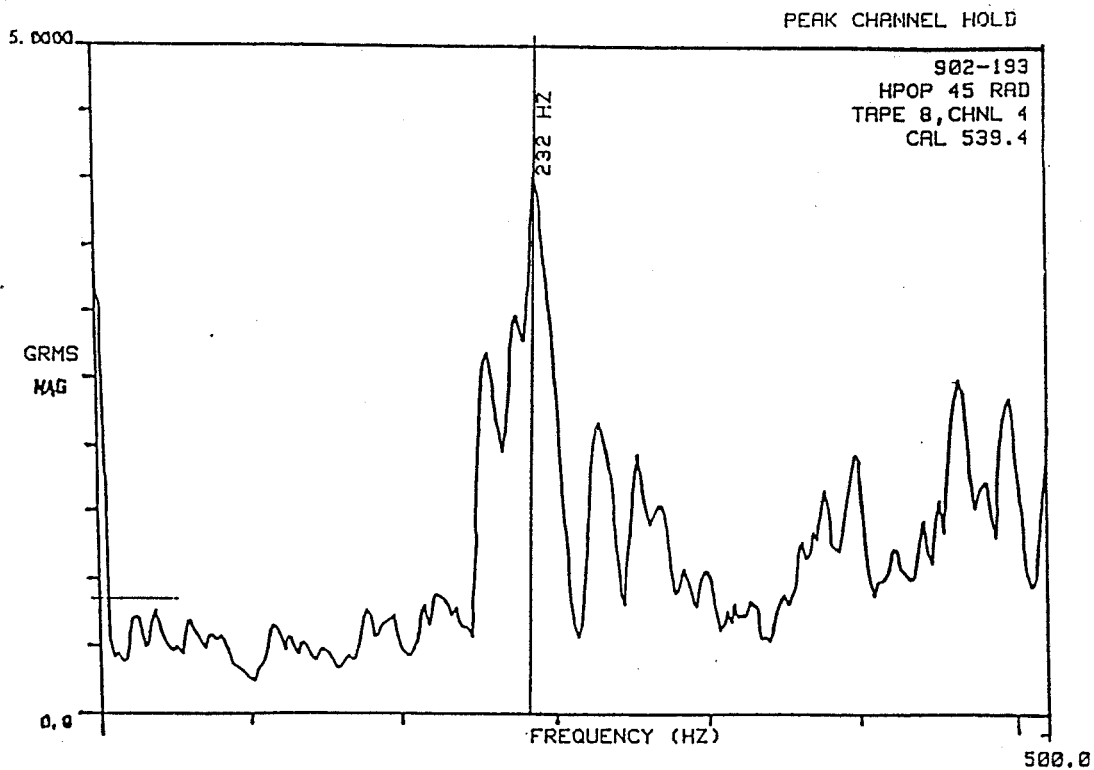
FIGURE 9 HPOP - ENGINE ACCELERATION (0-100% RPL)

324

```
                                                         902-193
                                                      HPOP  45  RAD
                                                     TAPE 8,CHNL 4
                                                        CAL  539.4
```
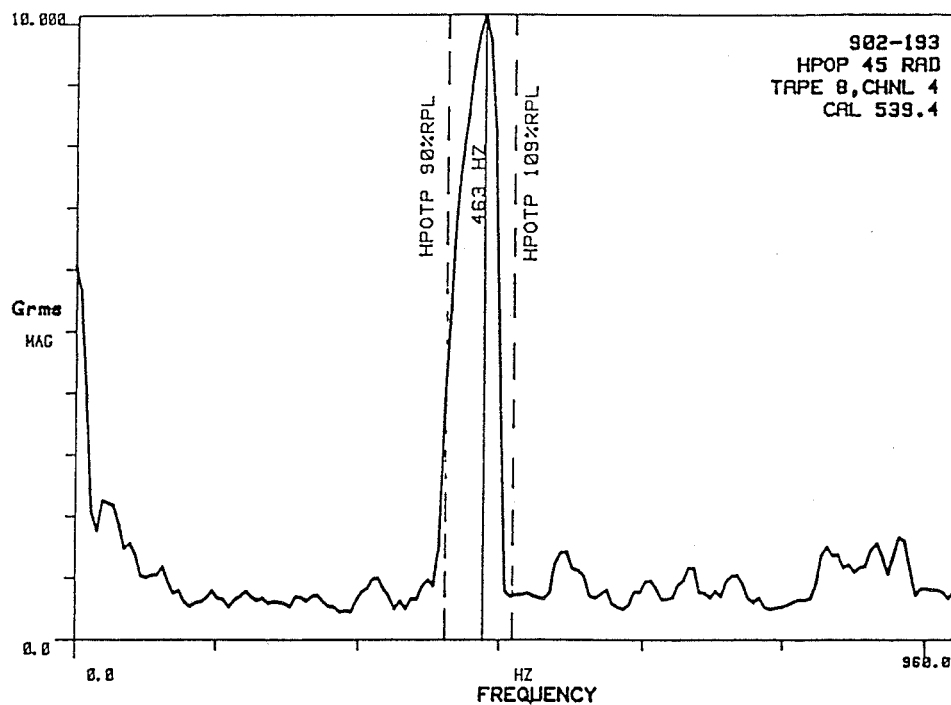
FIGURE 10 HPOP - ENGINE DECELERATION (109-90% RPL)

Examination of the various other accelerometers on the oxygen pump showed a similar characteristic. For example, Figure 11 represents the peak channel hold spectrum for the HPOT 90° accelerometer during the entire coast down from 109% to 0% RPL. Note that this accelerometer shows a peak resonant frequency at 453 Hz.


```
                                                         902-193
                                                      HPOT  90  RAD
                                                     TAPE 8,CHNL 8
                                                        CAL  437.4
```
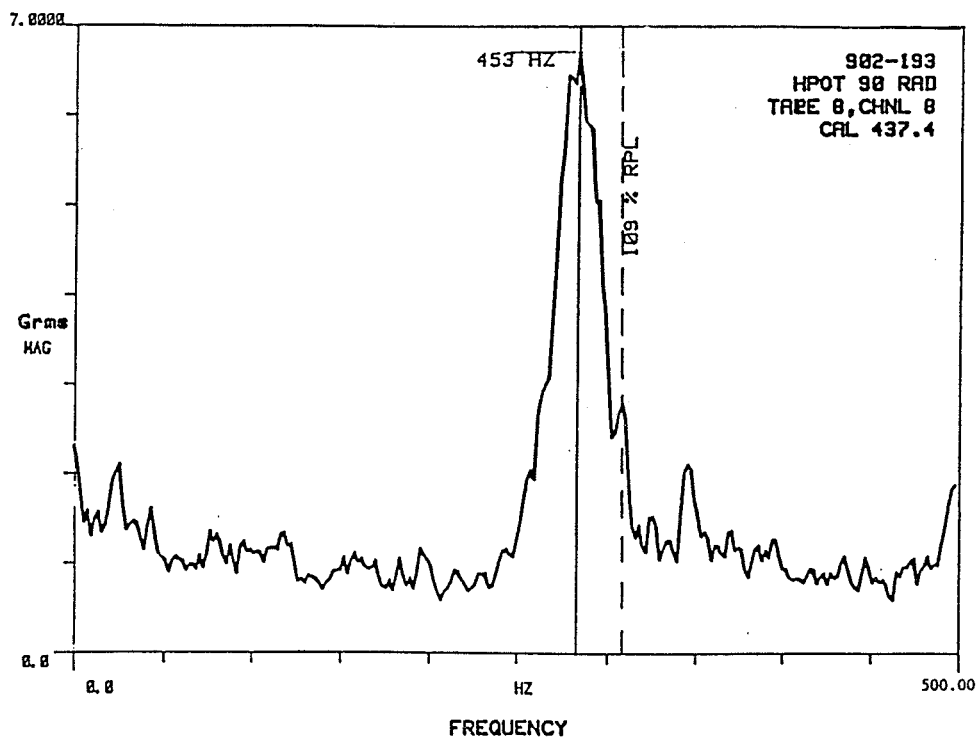
FIGURE 11 HPOT - ENGINE COASTDOWN (109-0% RPL)

325

The data of Run 902-193 indicates that the oxygen pump has a major resonant frequency between 450 and 470 Hz. This response frequency could represent the second critical speed of the oxygen pump. This mode may be particularly sensitive to excitation, because a nozzle bending mode is also predicted in this range.

SCOPE OF INVESTIGATION

One of the major considerations for the stability analysis of the high pressure oxygen pump is the influence of cross-coupling generated by the turbine stages, the main impeller, and the seals. The major seal locations are at the preburner impeller, at the turbine bearing and between turbine stages. The main areas where aerodynamic cross-coupling may be generated are the main impeller and turbine stations.

The critical speeds and stability characteristics for the oxygen pump are highly dependent upon the values of bearing stiffness and damping assumed for the various bearing and seal location. The values for ball bearing stiffness used are modified from experimental data. The values for seal stiffness and damping used were taken from Childs' report. Additional seal and shaft modification were also considered in order to evaluate their influence on stability.

In the experimental analysis of the Space Shuttle Main Engine System, it has been observed that the hydrogen shaft speed is recorded on the oxygen pump accelerometers. The transfer of motion, from one system to another, is due in part to the flexibility and dynamic characteristics of the engine nozzle and hot gas manifold. In this analysis, however, the flexibility of the hydrogen pump, nozzle, and oxygen pump casings are not included.

It is therefore the objective of this investigation to identify the critical speeds and stability characteristics of the oxygen pump only as a function of bearing and seal characteristics. The investigation concentrates on the effects of the bearing characteristics on the critical speeds to determine if an oxygen pump second critical speed could exist in the 460 Hz vicinity and if the pump should exhibit indications of instability.

CRITICAL SPEED ANALYSIS OF THE OXYGEN PUMP

Background

In the original design of the oxygen pump, it was assumed that there would be no critical speed in the operating speed range between MPL (minimum power level) and FPL (full power level). The only critical speed that the pump would incur, would be the first critical speed at approximately 16,000 RPM. Figure 12 represents the original oxygen pump critical speed map, assuming no seals and a rigid casing. Three critical speeds are shown in this field map. Superimposed on the critical speed map are the effective bearing stiffnesses, originally assumed to be present in the oxygen pump for two different ranges of bearing clearance: 1.37 mils and 2.63 mils. The first critical speed was estimated to be 14,000 RPM and the second critical speed was estimated to be 38,000 RPM. A value of 38,000 RPM would place the oxygen pump second critical speed well above the maximum operating speed of the oxygen pump.

One of the earliest indications that the actual stiffnesses may not be as high as previously predicted was obtained from experimental information generated while attempting to balance the pump. Figure 13 represents the oxygen pump rotor unbalance response (4.76 gm-in unbalance located at the preburner location) while being balanced in the spin pit facility. To more clearly indicate the resonant frequency present in the system, the data was conditioned by subtracting the low speed runout for Run

13 of the No. 2 Bently Probe. As can be seen from the amplitude-versus-speed curves experimentally obtained, there is a first critical speed at 10,000 RPM and a second critical speed at 25,600 RPM. The second critical speed obtained in the experimental spin test facility corresponds closely with the incident run of NASA test 910-136.
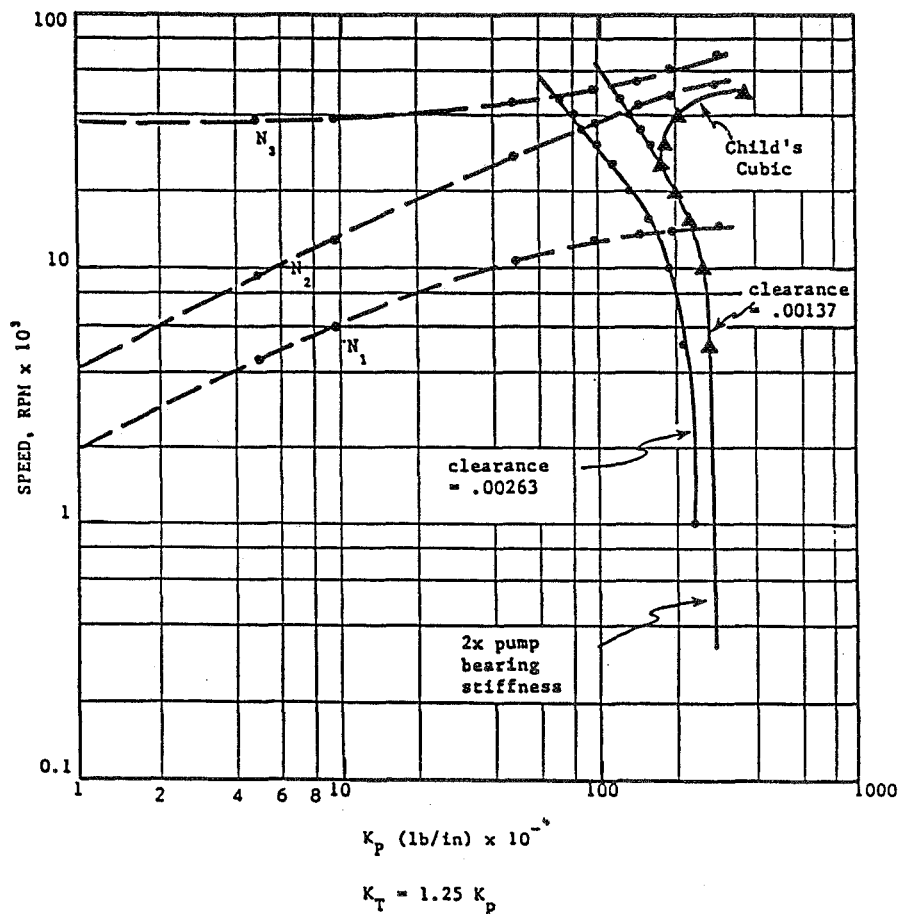
FIGURE 12 ORIGINAL OXYGEN PUMP CRITICAL SPEED MAP - NO SEALS AND
RIGID CASING

In the balance test run on the oxygen pump, it was observed that unbalance at the preburner location had very little effect on the turbine end location and also little response at the first critical speed. An unbalance at the turbine end had a large response at 10,000 RPM, but a little response at the second critical speed of 25,600 RPM. Thus, the experimental spin pit data indicates that the second mode is predominantly a preburner and main impeller mode with little motion at the turbine end. Therefore, if this second mode were excited in the oxygen pump at rated speeds, one would expect to see large amplitudes of motion at the main impeller and preburner locations. Close examination of the failed oxygen pump from run 910-136 indicated possible contacting at either the preburner or main impeller; the turbine end was relatively undamaged. Figure 13 also indicates that after passage through the second critical speed the amplitude, a minimum of 28,000 RPM, begins to increase rapidly again, indicating the onset of a third critical speed.

327
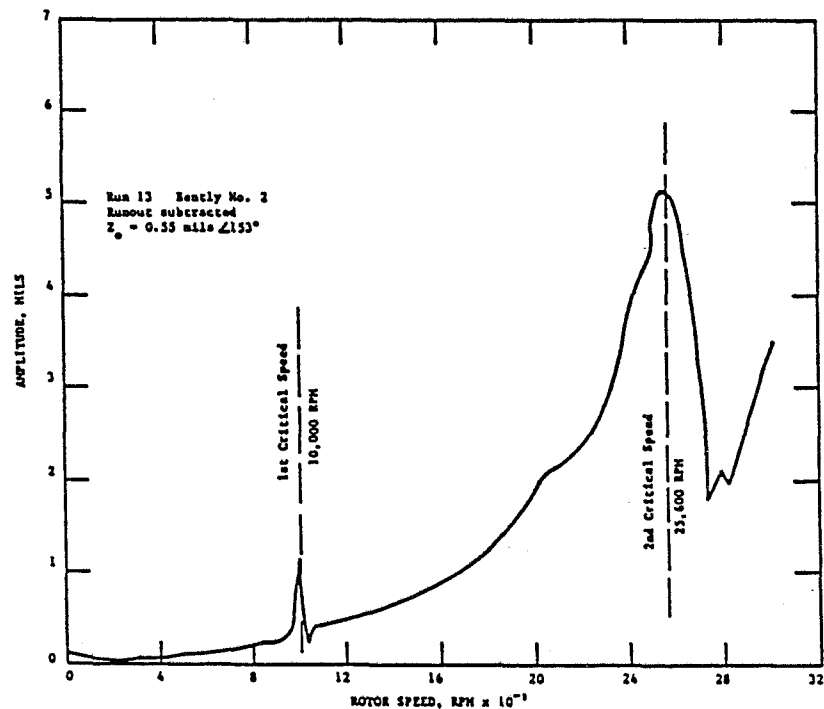
FIGURE 13 OXYGEN PUMP ROTOR UNBALANCE RESPONSE WITH 4.76 GM-IN
AT PREBURNER LOCATION - RUNOUT SUBTRACTED

In order to obtain critical speeds of 10,000 and 25,600 RPM, the original critical speed map indicates that the combined stiffness of the preburner bearings is only 400,000 lb/in, and the combined stiffness of the turbine bearings is only 500,000 lb/in, rather than 1,200,000 lb/in, as originally predicted for the turbine bearings.

Data obtained from the balance spin pit facility on low speed phase and amplitude runout was not repeatable with small unbalance at the preburner end. Such data may indicate that the shaft joints of the preburner and main impeller shift around with unbalance when driven to the second critical speed. This may account for the difficulty encountered in attempting multiplane balancing of the oxygen pump over the two critical speeds.

Computer Models

Critical speeds and mode shapes have been calculated by Rocketdyne, NASA, and the University of Virginia. A lumped mass-elastic section model of the rotor derived from computer analysis was provided to the University by NASA. This model consists of 15 shaft sections with areas, lengths, and inertia properties; shaft diameters were derived from the inertia terms. A second model (UVA) was created using a scale drawing of the pump cross-section. Diameters, taken from the drawing, were combined with the weights, lengths, and inertia terms of the NASA model. Figure 14 shows the three cross sections superimposed on one another. Although the actual rotor has hollow cross sections, both computer models use a solid shaft approximation.

328

CROSS-SECTIONS

ACTUAL ———
COMPUTER MODELS:
NASA ·····
UVA ———
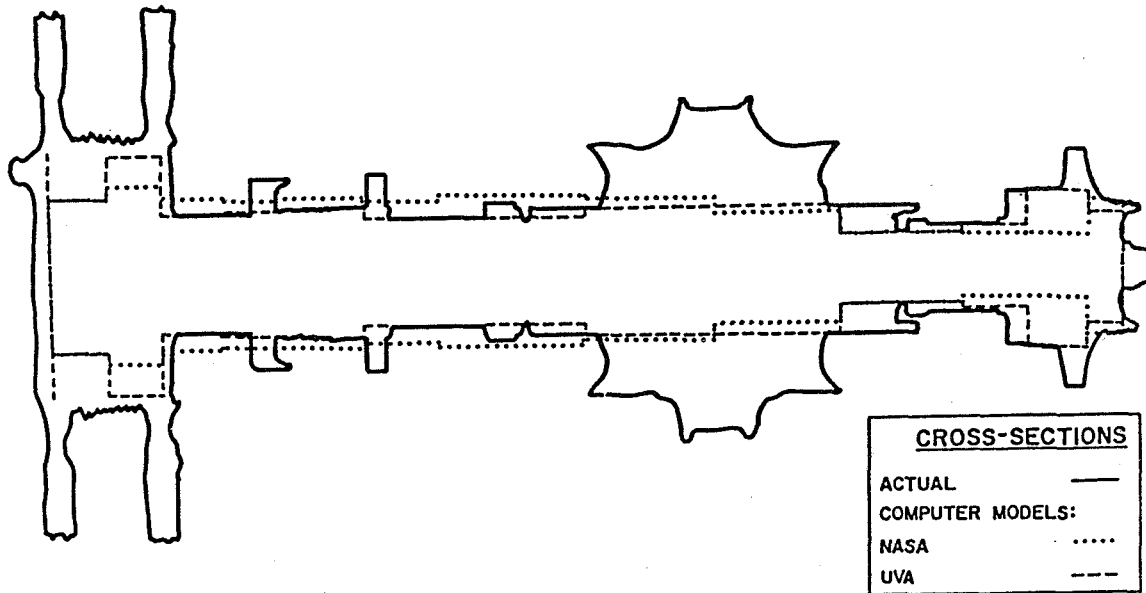
FIGURE 14

There is considerable difference between NASA model and the UVA model at the preburner bearing at the turbine locations. For example, the NASA model assumes a thinner section at the preburner bearing than is assumed by the UVA model. This would accentuate the bending problems of the oxygen pump at the second critical speed. Also, the NASA model assumes a thicker section at the turbine shaft location (station 10) than actually exists (See Table 1). Although one may use experimental data on which to base a computer model, it is not justified to assume a cross section which is thicker than the actual model. Therefore, additional modifications of the NASA model could be done to improve its accuracy.

TABLE 1   COMPARISON OF COMPUTER MODELS FOR OXYGEN PUMP
ROTOR

	ROTOR MODEL: NASA				ROTOR MODEL: UVA		
	SECTION DATA				SECTION DATA		
STATION NUMBER	LENGTH (IN)	OUTSIDE DIAMETER (IN)	WEIGHT (LB)	STATION NUMBER	LENGTH (IN)	OUTSIDE DIAMETER (IN)	WEIGHT (LB)
1	0.772	2.800	0.669	1	0.772	2.3	0.669
2	1.070	1.340	2.377	2	1.070	3.2	2.378
3	1.558	1.347	3.042	3	1.558	1.7	3.043
4	2.583	1.518	1.290	4	2.583	1.5	1.290
5	2.640	2.270	7.757	5	2.640	2.6	7.757
6	2.640	2.975	13.392	6	2.640	2.6	13.392
7	3.170	3.105	8.607	7	3.170	2.2	8.606
8	1.560	2.931	3.404	8	1.560	2.2	3.403
9	0.800	3.102	4.197	9	0.800	2.7	4.197
10	1.120	3.102	0.101	10	1.120	2.6	0.101
11	1.200	3.050	2.473	11	1.200	2.5	2.473
12	1.170	3.102	1.877	12	1.170	2.4	1.877
13	1.115	3.742	12.514	13	1.115	5.0	12.514
14	1.117	3.090	3.415	14	1.117	3.1	3.416
15	0.0	3.090	13.825	15	0.0	5.0	13.825

Critical Speed Analysis

Although there are considerable differences between the UVA and the NASA models, their predictions for the occurrence of the second critical speed are almost identical. Figure 15 represents the oxygen pump first and second forward critical speeds assuming an operating speed of 27,000 RPM. Using the revised combined preburner bearing stiffness of 476,000 lb/in from turbine bearing (Ref. Childs), the first critical speed predicted by the UVA model is 11,000 RPM and the first critical speed predicted by the NASA model is 13,000 RPM. Both models predict the second critical speed at approximately 27,000 RPM.

OXYGEN PUMP
UNDAMPED FORWARD CRITICAL
SPEED MAP
N = 27,000 RPM
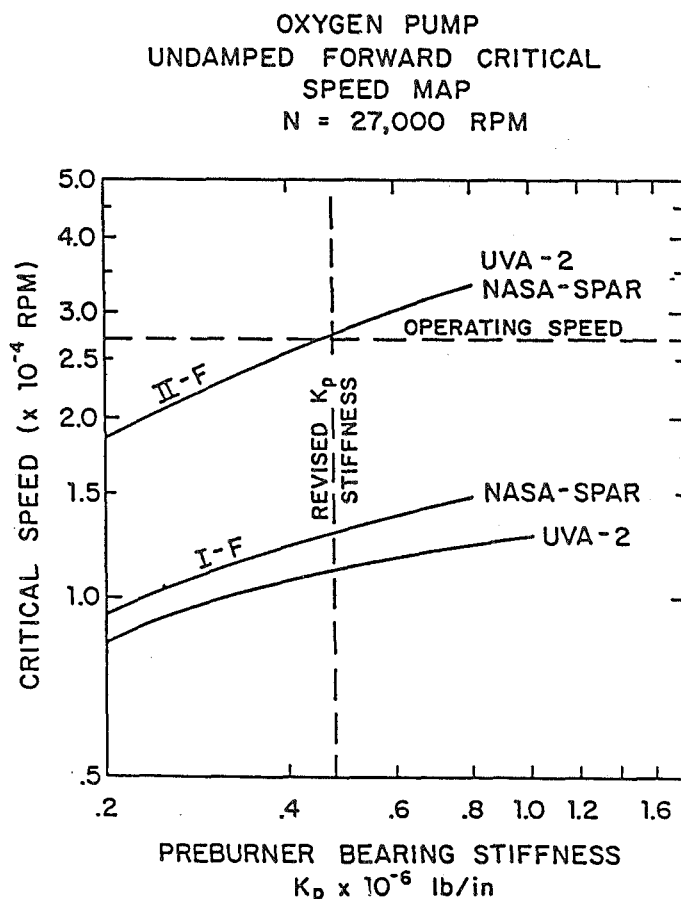
FIGURE 15

As an additional check on the critical speed calculations, a computer program to calculate the forward and backward critical speeds (CRITSPD) was developed by Dr. Gunter. In this particular case, undamped seals as well as bearings were considered. Assuming that the oxygen pump is operating at 27,000 RPM, the forward critical speeds were predicted to be 13,000 RPM, 26,858 RPM and 37,569 RPM.

Another reason for developing the new critical speed program was to calculate the strain energy distribution between the shaft and bearings. Table 2 represents the oxygen pump critical speed and percent of total strain energy in the shaft and the bearings. For example, the table shows that in the first mode 25% of the total strain energy is in rotor bending and 75% is in the bearings. It is of

330

interest to note that the preburner bearing only carries 3% of the strain energy for the first mode; the majority of the energy from shaft bending occurs near the turbine bearing location. One could assume therefore that the preburner bearing stiffness has little influence on the location of the first critical speed. The preburner and the turbine ends of the shaft have little strain energy. Therefore, the first critical speed is predominantly affected by the main turbine bearing and interstage turbine seal.

TABLE 2   CRITICAL SPEED SUMMARY

Critical Speed Analysis of SSME Oxygen Pump
at 27,000 RPM with Derated Bearings

Forward Whirl Analysis

NO. MODE	CRITICAL SPEED (RPM)	SHAFT	BEARING
		(% of total strain energy)	
1	13,000	25	75
2	26,858	19	81
3	37,569	52	48

STATION NO.	FIRST CRITICAL SPEED SHAFT	FIRST CRITICAL SPEED BEARING	SECOND CRITICAL SPEED SHAFT	SECOND CRITICAL SPEED BEARING	THIRD CRITICAL SPEED SHAFT	THIRD CRITICAL SPEED BEARING
	(% of strain energy)		(% of strain energy)		(% of strain energy)	
1	0		0		0	
2	0	0	0	2	0	13
3	0		0		0	
4	0	3	0	50	5	28
5	1		7		31	
6	1		5		5	
7	3		5		5	
8	13	34	3	29	5	7
9	6		0		1	
10	1		0		0	
11	0		0		0	
12	0	9	0	0	0	0
13	0		0		0	
14	0	29	0	0	0	0
15	0		0		0	

[Note: seal strain energy is included under BEARING]

At the second critical speed, predicted to be 26,858 RPM, 81% of the strain energy is in the bearings and 19% is in the shaft. Half of the system strain energy is in the preburner bearing and only 29% is in the main turbine bearing. It is important to note that there is little strain energy connected with either the preburner or the turbine shaft locations. The major strain energy of the shaft is associated with sections 4 through 7, which are the preburner bearing and main impeller locations. From the strain energy distribution of the second mode, it is apparent why the NASA model and the UVA model match in predicting of the second critical speed; this is because the second critical speed is being controlled predominantly by the preburner bearing stiffness. The thickness of the turbine end location has negligible effect on the second critical speed.

A third critical speed of 37,569 RPM is predicted. In this mode, the strain energy is divided equally between the shaft and the bearings. However, at this third mode, the major part of the bearing strain energy is carried at the preburner seal and at the preburner bearing. The fact that over 30% of the total strain energy occurs in only one shaft section, station 5, indicates a considerable amount of local bending.

The experimental data in Figure 7 indicates that the hydrogen pump amplitude appears to increase with speed. If the hydrogen pump has a high level of amplitude at 37,000 RPM, it may excite the oxygen pump third critical speed. It is apparent that this frequency can be increased only by stiffening up the shaft section at this location. The occurrence of the critical speed of the oxygen pump at 37,000 RPM may explain why the experimental data in the experimental test rig (Figure 13) shows amplitude beginning to increase rapidly above 28,000 RPM; the oxygen pump may have been approaching its third critical speed, essentially an overhung preburner mode.

Figure 16 represents the oxygen pump forward and backward critical speeds for various operating rotor speeds, assuming the derated bearing stiffness characteristics. Due to the gyroscopics of the overhung disk, main impeller and preburner ends; forward and backward critical speeds appear. For example, at 27,000 RPM, the difference between first forward and backward critical speeds is 4,000 RPM. The second backward critical speed is approximately 24,325 RPM and the second forward is 26,879 RPM, a difference of 2,500 RPM. The difference between forward and backward critical speeds increase with operating speed. These values of forward and backward critical speeds were calculated using the program ROTSTB, and they correspond closely with the predicted forward and backward values obtained from the CRTSPD program.

FIGURE 16

332
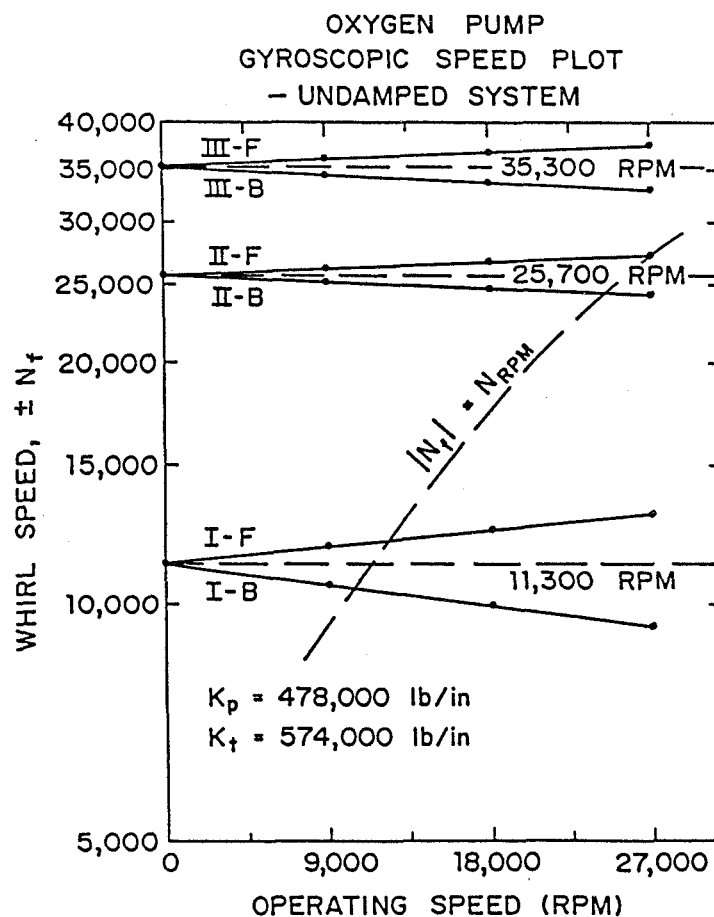
Normally, the occurrence of backward critical speeds in a turborotor is of little concern, since unbalance in a turborotor will excite only the critical speeds of forward synchronous precession. In the case of the SSME configuration, however, in which the oxygen pump is cantilevered off the main nozzle, excitation from the hydrogen pump and nozzle may be transmitted to the oxygen casing by the hot gas manifold. Under these circumstances, a planar excitation could conceivably excite a backward as well as a forward mode. Observation of the experimental data, Figures 4 and 5, shows weak modes at approximately 22,000 and 33,000 RPM. It may be possible that these modes are backward excitations of the oxygen pump.

Figure 17 represents first forward undamped critical speed for the oxygen pump operating at 27,000 RPM. Reduced bearing stiffnesses of 400,000 lb/in for the preburner bearing and 600,000 lb/in for the turbine bearing were assumed. Using the ROTSTB stability program, the first forward critical speed was predicted to be 10,661 RPM. This value correlates well with the critical speeds predicted by Rocketdyne, but is somewhat lower than the value calculated using CRTSPD which includes the effect of seals. It also corresponds well with the critical speeds observed in the spin pit, in which seals were not present. As can be seen from the first mode shape, the maximum amplitude occurs at the overhung turbine and rapidly diminishes as one approaches the preburner end. At a distance of 12 inches from the preburner end, the amplitude is a node point. The small preburner motion is out of phase with the motion of the turbine end.

UNDAMPED 1st FORWARD CRITICAL SPEED OF
OXYGEN PUMP AT 27,000 RPM

N_{1f} = 10,661 RPM

K_p = 400,000 LB/IN

K_t = 600,000 LB/IN

FIGURE 17

333
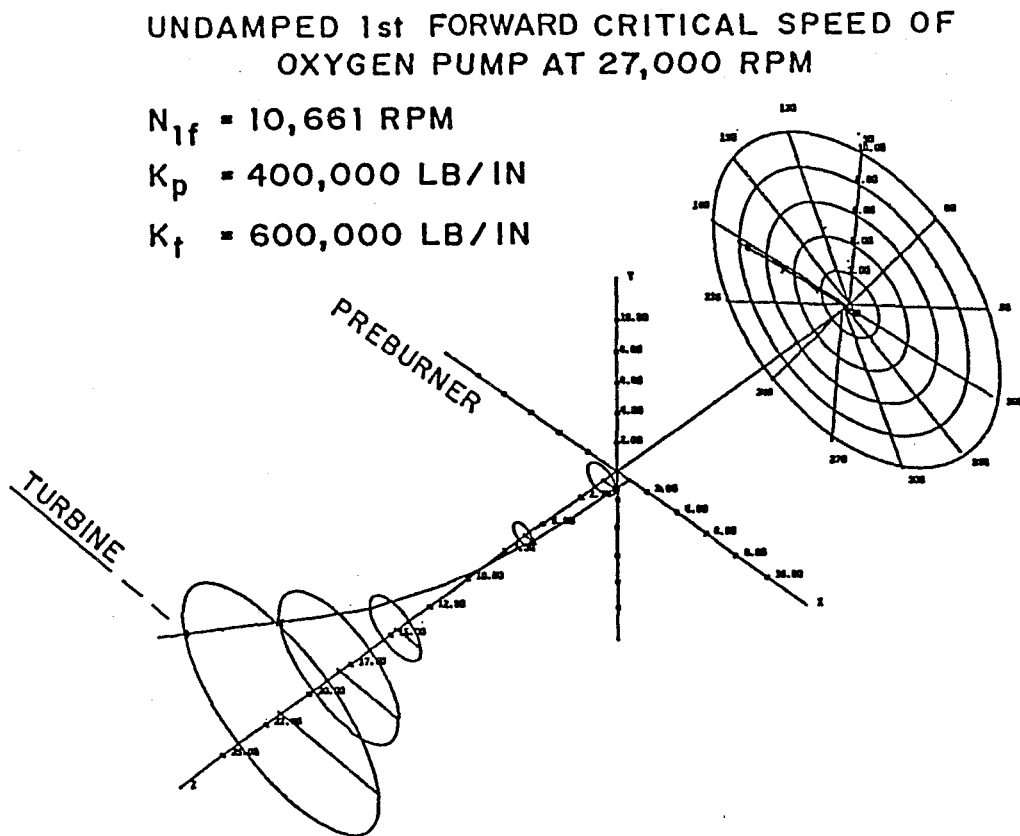
The mode shape, as depicted in Figure 18 for the second forward critical speed without seals, shows that the second critical speed occurs at 25,350 RPM. Examination of the 3-dimensional mode shape, reveals that the turbine motion is a node point and that the maximum amplitude occurs at the main and preburner impellers. It is readily apparent that any attempts to improve the rotor response at 27,000 RPM by trim balancing the turbine stages will have little beneficial effect; balancing must be done at the preburner or main impeller location.

In the undamped critical speed plots, depicted by Figures 17 and 18, the mode shapes were made nondimensional. In an actual rotor, the response of the rotor at a particular speed will be a function of the unbalance distribution and the damping in the system. These figures imply that the rotor cannot be successfully balanced through both critical speeds by single plane balancing of the turbine stage. If the second critical speed cannot be successfully balanced at the preburner impeller due to spline slippage, then the oxygen pump should be redesigned.

UNDAMPED 2nd FORWARD CRITICAL SPEED OF
OXYGEN PUMP AT 27,000 RPM

N_{2f} = 25,350 RPM

K_p = 400,000 LB/IN

K_t = 600,000 LB/IN
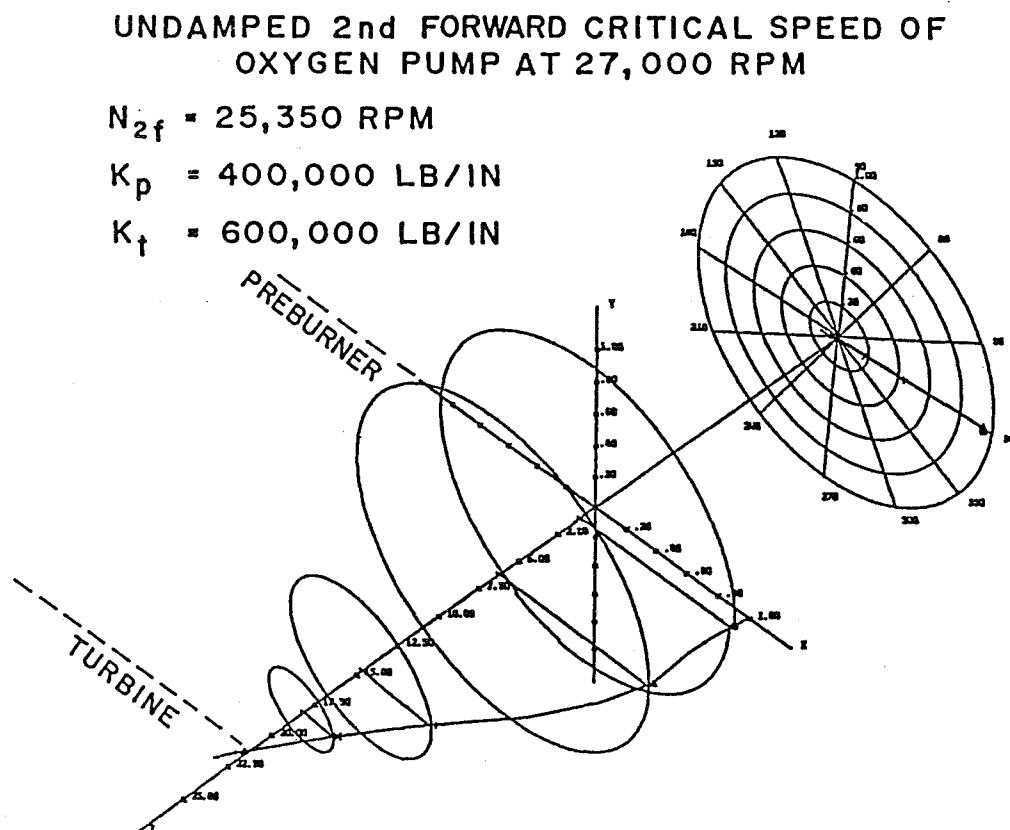
FIGURE 18

STABILITY ANALYSIS: DAMPED MODES

In considering the stability of the oxygen pump rotor, the effects of seal aerodynamic cross-coupling, as well as bearing and seal damping, were investigated. Stiffness and damping characteristics for each of the six seals were taken from a report by D. Childs and were lumped together at three seal locations: preburner seals, turbine seals, and turbine interstage seals. The bearings were modeled using

the derated stiffnesses and minimal damping. The overall stiffness and damping matrix used in the initial stability analysis is presented in Table 3. Aerodynamic effects were later added by means of cross-coupling terms acting at the midpoint of the main impeller. The UVA rotor model was used for the stability analysis because of its better agreement with the experimental critical speed data. The NASA model, with its stiffer turbine section would tend to exaggerate the stability of the first bending mode, an overhung turbine mode.

TABLE 3   STIFFNESS AND DAMPING MATRIX CHILD'S VALUES

(DAMPING AND CROSS-COUPLING)

STATION NUMBER	STIFFNESS				
	K_{xx} (LB/IN)	K_{yx} (LB/IN)	K_{xy} (LB/IN)	K_{yy} (LB/IN)	
2	30,000	-17,000	17,000	30,000	PREBURNER SEAL
4	476,000	0	0	476,000	PREBURNER BEARING
8	574,000	0	0	574,000	TURBINE BEARING
12	21,210	- 4,560	4,560	21,210	TURBINE SEAL
14	38,630	-26,000	26,000	38,360	INTERSTAGE (TURBINE) SEAL

DAMPING

	C_{xx} (LB-SEC/IN)	C_{yx} (LB-SEC/IN)	C_{xy} (LB-SEC/IN)	C_{yy} (LB-SEC/IN)
2	10.5	0.	0.	10.5
4	2.0	0.	0.	2.0
8	2.0	0.	0.	2.0
12	2.8	0.	0.	2.8
14	14.0	0.	0.	14.0

Undamped conditions used a nominal 5.0 lb-sec/in at each station.

Stability calculations, using the rotor stability program ROTSTB, indicate that both bending modes encountered in the operation of the oxygen pump are unstable. Figure 19 displays the sources of this instability. Cross-coupling forces generated by the interstage and turbine tip seals (26,000 lb/in) are forty percent in excess of the theoretical cross-coupling required to destabilize the first mode. While a cross-coupling of 10,450 lb/in acting on the main impeller is sufficient for instability of the second mode,initial calculations indicate that aerodynamic forces could generate aerodynamic cross coupling of the order of 30,000 to 40,000 lb/in. The analysis further indicates that the two modes are independent and that modification must consider both modes.

335

STABILITY THRESHOLD PLOTS

STABILITY THRESHOLD
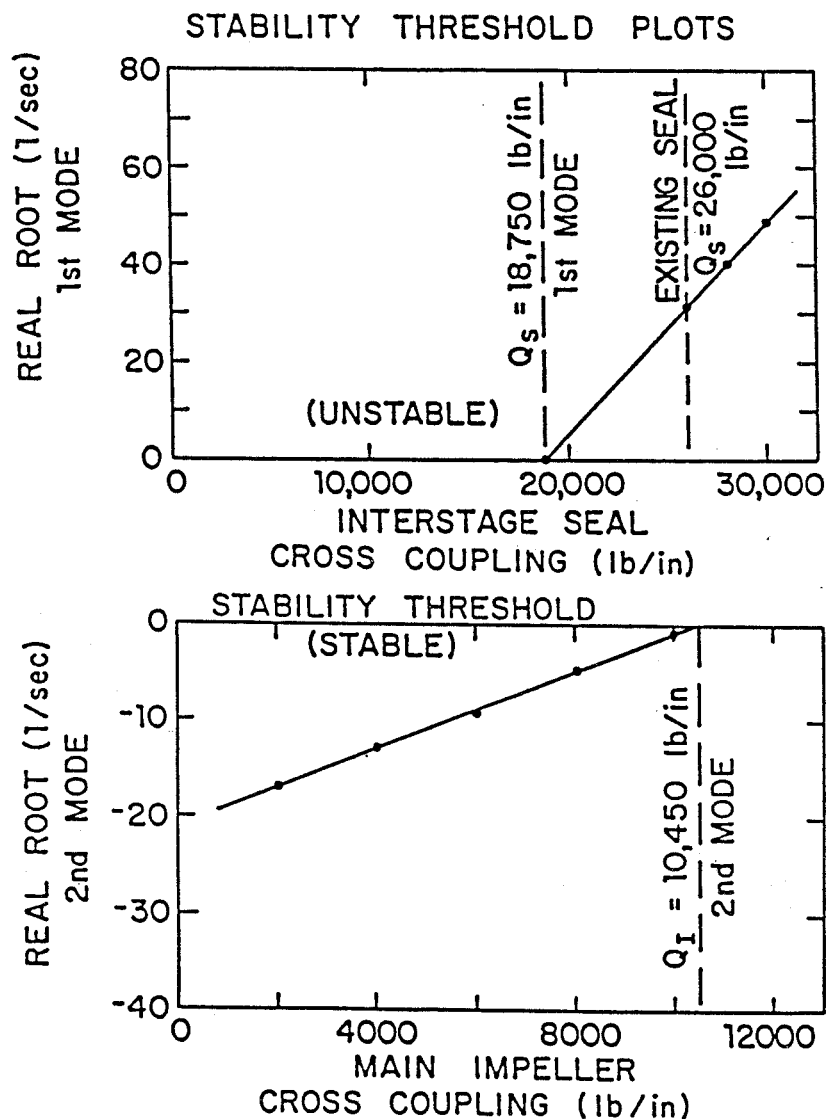
FIGURE 19

The stability analysis in this report assumes a smooth seal acting at the turbine interstage location. D. Childs also presented the stiffness and damping characteristics for the labyrinth seal originally included in the oxygen pump design. Stability calculations with the UVA model, derated bearings, and full seals, substituting the labyrinth interstage seal for the smooth seal, indicate that the rotor is unstable. The configuration with the labyrinth seal, however, is closer to the threshold of stability than with the smooth seal. Further, the first critical frequency is lowered slightly, although there is little effect on the second or third critical frequencies. This indicates that the original labyrinth seal design should be more stable than the smooth configuration.

The most promising modification to improve stability appears to be combining a stiffer turbine bearing with a softer pump bearing and with additional damping at the preburner seals. Varied independently, none of these factors have an appreciable influence on the stability of this system. Varying the damping coefficients and the turbine bearing stiffness at the same time seems to produce the most marked improvement. These results are shown in Figure 20. With the pump bearing stiffness damping exponent of the first mode; however, the effect is asymptotic. A modification of the shaft geometry seems required.

336

1st MODE OXYGEN PUMP
STABILITY FOR VARIOUS VALUES
OF PREBURNER SEAL DAMPING C_p
vs. TURBINE BEARING STIFFNESS K_t
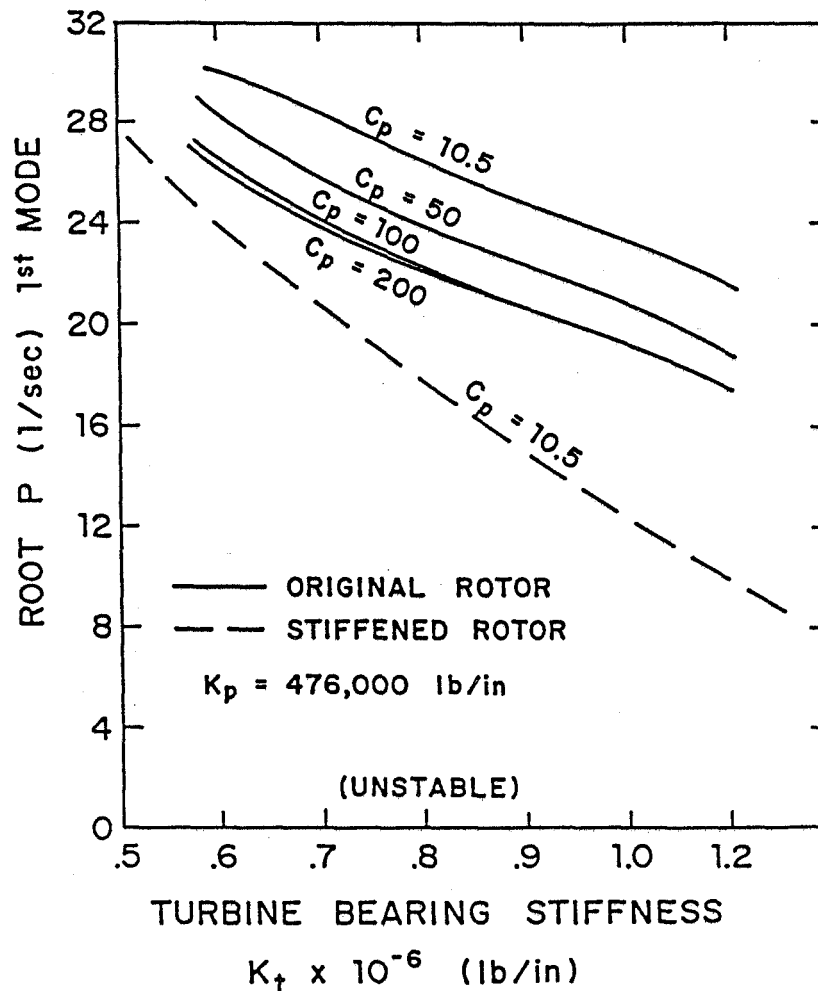
FIGURE 20

A third rotor model was created with a minimum shaft diameter of 2.6 inches at the bearings. The properties of this model, called "stiffened rotor," are presented in Table 4. Figure 21 presents the three rotor cross-sections used in this paper (with a compressed horizontal scale). The NASA model has thick turbine end sections and thin preburner end sections. The UVA model, which gave better agreement with the experimental critical speed data, has thin sections around the bearing locations. Finally, the stiffened rotor shows a nearly uniform cross-section from the preburner to the turbine stages. The dashed line, on Figure 21, portrays the stabilizing influence of this thicker cross section. While the stiffer rotor is an improvement, modification of the seals and bearings is also indicated.

TABLE 4 ROTOR MODEL: STIFFENED ROTOR

Section Data

STATION NUMBER	LENGTH (IN)	OUTSIDE DIAMETER (IN)	WEIGHT (LB)
1	0.772	2.3	0.669
2	1.070	3.2	2.378
3	1.558	2.6	3.043
4	2.583	2.6	1.291
5	2.640	2.6	7.757
6	2.640	2.6	13.392
7	3.170	2.6	8.607
8	1.560	2.6	3.403
9	0.800	2.7	4.197
10	1.120	2.6	0.101
11	1.200	2.6	2.473
12	1.170	2.6	1.877
13	1.115	5.0	12.514
14	1.117	3.1	3.416
15	0.0	5.0	13.825

ROTOR CROSS-SECTION MODELS
FOR OXYGEN PUMP

NASA-SPAR

UVA2

STIFFENED ROTOR

ADDED SHAFT DIAMETER
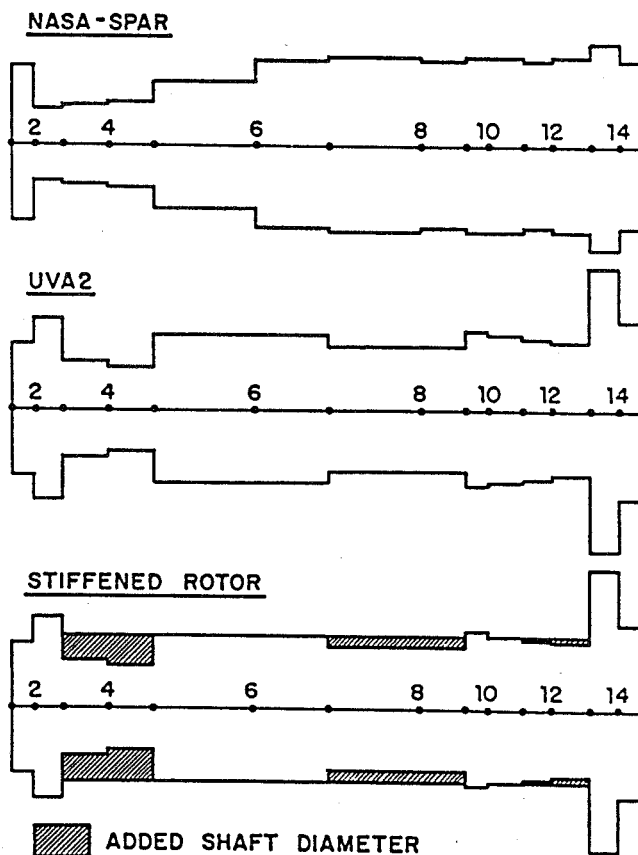
NOTE: HORIZONTAL SCALE IS ONE HALF
VERTICAL SCALE.

FIGURE 21

338

The increase in rotor cross-section at the bearing locations implies bearing redesign. Figure 22 shows that with a significantly stiffer turbine bearing (1,200,000 lb/in) the stability of the first mode can be obtained with a wide choice of pump bearing stiffness and preburner seal damping coefficients.

The second mode presents two difficulties for the operation of the oxygen pump. Its critical frequency lies in the operating range of the pump, at approximately 100% RPL and it is unstable due to the aerodynamic forces on the main impeller. To observe the variation in the second forward critical speed as a function of the various parameters thus far considered, Figure 23 was prepared. This figure corresponds with Figure 22 and shows that a preburner bearing stiffness between 200,000 and 400,000 lb/in, along with the stiffened rotor, would be unacceptable for use in the oxygen pump operating speed range. Operation at a lower stiffness value would require a softer turbine bearing.

OXYGEN PUMP
STIFFENED ROTOR
STABILITY THRESHOLD
FOR VARIOUS LEVELS OF K_p AND C_p

FIGURE 22

339
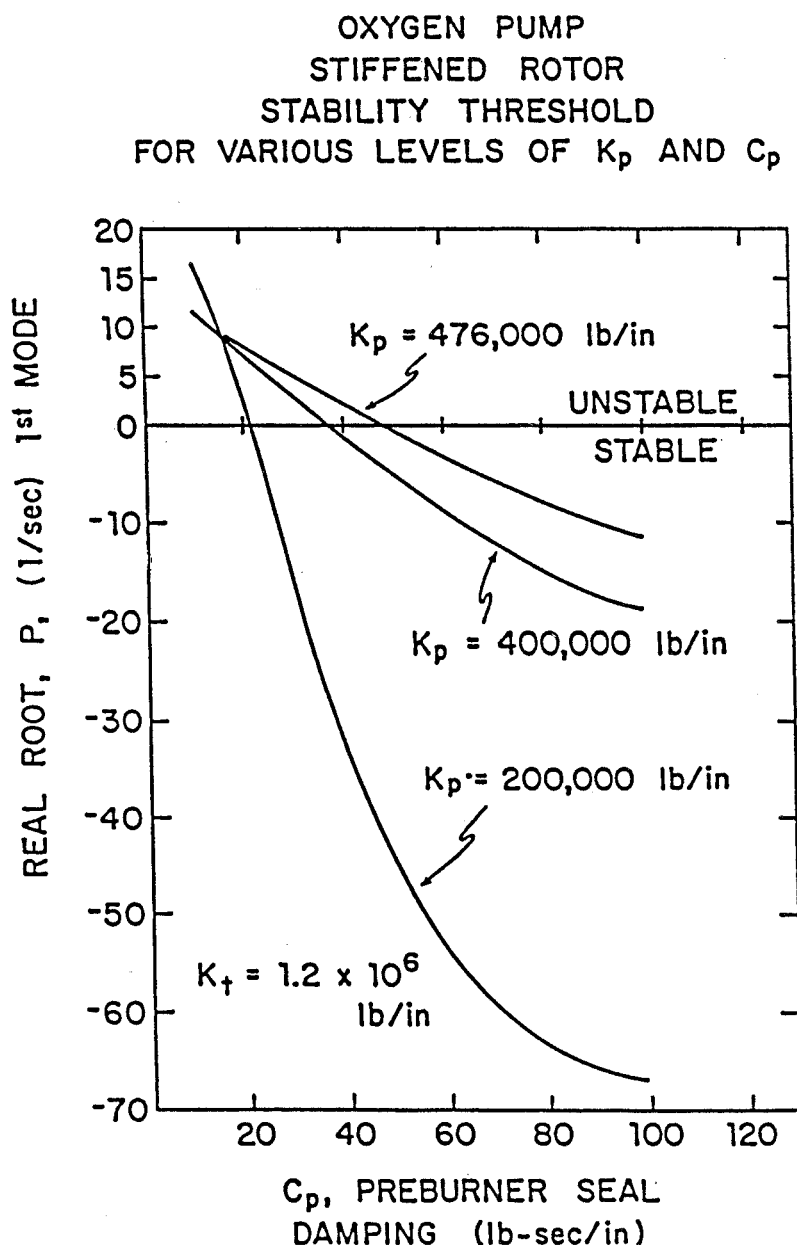
OXYGEN PUMP
STIFFENED ROTOR
SECOND CRITICAL SPEED
FOR VARIOUS LEVELS OF K_p & C_p
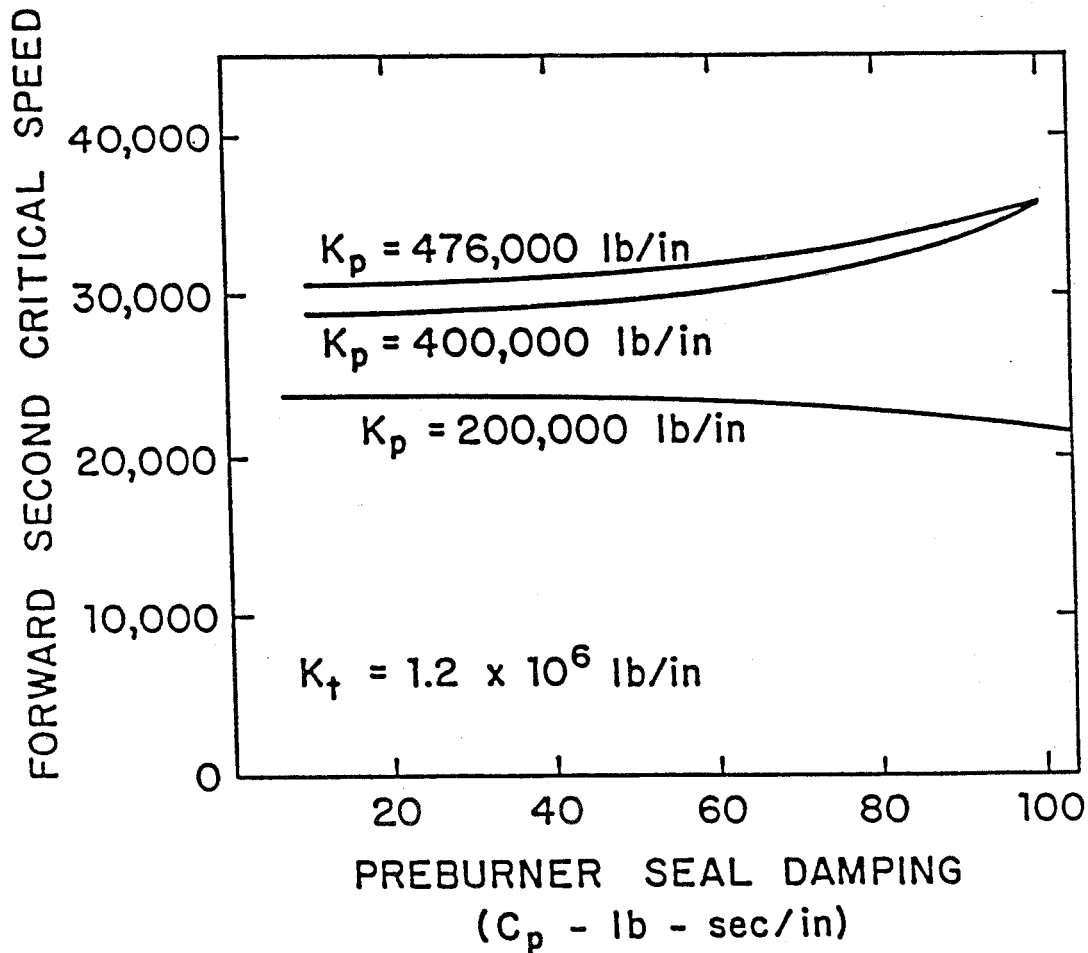
FIGURE 23

Analysis of the stiffened rotor was also performed in a manner similar to that presented in Figure 20. In Figure 24, the stability of the second mode is plotted as a function of the turbine bearing stiffness and of the preburner seal damping. The stability of the first mode is also indicated by the use of solid and dashed lines. A pump bearing stiffness of 200,000 lb/in was selected and the use of a stiffer pump bearing, as discussed previously, would require the inclusion of some additional damping, as indicated by Figure 22. The damping exponent indicates that the use of a stiffened rotor alone will stabilize the second mode. Thus, the selection of bearings and seals for the new rotor cross-section should be based on obtaining a stable first mode and an acceptable second critical speed.

340

DAMPED SECOND MODE
FOR VARIOUS LEVELS OF PREBURNER DAMPING
— STIFFENED ROTOR —
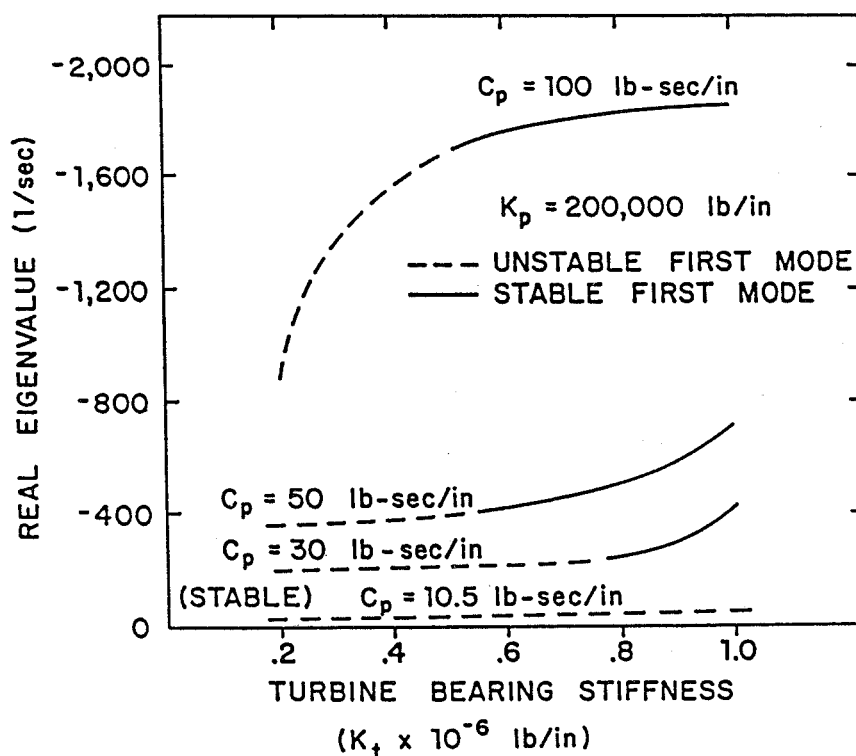
FIGURE 24

CONCLUSIONS

The experimental data available from the test operations of the liquid oxygen pump for the SSME repeatedly show the presence of resonant frequencies within the operating range of the pump. Critical speed analysis indicates that the presence of the second critical frequency is due to the pump and turbine bearings having stiffness values approximately 50% of the original specifications.

In modeling the pump rotor for computer analysis, discrepancies were found between the cross-sections of the NASA model (as derived from the inertia values) and the actual rotor cross-sections. The NASA model has a stiffer turbine section than is warranted. An alternate model (UVA) was developed from the actual rotor cross-section in order to provide a more suitable foundation for the stability analysis. Correlation between experimental balance data and the two rotor models supports the use of the UVA configuration. Little difference exist between the models when considering the second mode; both models predict the second critical speed to be within the operating range of the pump.

The oxygen pump rotor shows two bending modes of interest. The first occurs at 13,000 RPM and is primarily an overhung turbine mode. Due to interstage seal cross-coupling, this mode is linearly unstable. The second mode occurs at 27,000 RPM and is a main impeller-preburner mode. This mode is predicted to be unstable as a result of aerodynamic forces acting on the main impeller, for values in excess of 10,500 lb/in. Thus, both the first and second modes exhibit instability in the linearized system.

The instability of the first two modes, as well as the presence of the second critical frequency within the operating range, indicates modifications of the original oxygen pump rotor may be necessary. Simple adjustment of the bearings and seals will not provide sufficient support and damping

to insure stability: a stiffer shaft is required, primarily at the preburner pump bearing location.

The stability analysis supports the following conclusions:

1) The application of damping at the preburner seal location (by means of a full seal) will slightly improve the stability of the first mode, for damping values as high as 200 lb-sec/in, with the original rotor design.

2) Stiffening the rotor through the pump bearing section increases the effectiveness of the damping acting at the preburner seal location.

3) A large increase in the first mode damping is achieved with the stiffened rotor by reducing pump bearing stiffness from 476,000 to 200,000 lb/in.

4) Reduction of turbine bearing stiffness causes a loss in damping for the first mode, indicating that turbine bearing dead bands should be minimized.

5) For a stiffened rotor and turbine bearing stiffness of 1.2E6 lb/in, a reduced pump bearing stiffness will drop the second critical speed to 24,000 RPM. For preburner seal damping of 40 lb-sec/in, the second mode will be well damped and much less sensitive to rotor unbalance.

6) The stability of the second mode of the stiffened rotor is unaffected by aerodynamic cross-coupling at the main impeller, for values up to 40,000 lb/in. Figure 24, however, shows that the first mode may be unstable if the turbine bearing stiffness falls below 500,000 lb/in.

The stiffened shaft will stabilize the second mode. The addition of stiffer turbine bearings and a full preburner seal should then stabilize the first mode, as well as attenuate the second mode so that it will be insensitive to unbalance.

The following recommendations are made:

1) The original oxygen pump is unsatisfactory from a dynamics standpoint.

2) Modification and suitable redesign of a stiffened oxygen pump rotor and casing is desirable.

3) A full seal should be incorporated at the preburner seal location to increase damping for both the first and second modes.

4) The turbine bearing stiffness should be maintained as high as possible.

5) The use of dead bands in the turbine bearing should be minimized or avoided.

REFERENCES

1. Alford, J. S., 1965, "Protecting Turbomachinery from Self-Excited Whirl," ASME Journal of Engineering for Power, pp. 333-334.

2. Allaire, P. E., Gunter, E.J., Lee, C. P., and Barrett, L. E., "Final Report -- The Dynamic Analysis of the Space Shuttle Main Engine-High Pressure Fuel Turbopump, Part II, Load Capacity and Hybrid Coefficients for Turbulent Interstage Seals, Report No. UVA/528140/ME76/103 (September 1976).

3. Allaire, P. E., Lee, C. P., and Gunter, E. J., "Dynamic Analysis of SSME Plain and Plain Stepped Turbulent Seals," Report No. UVA/528140/MAE78/110, September 1978.

4. Black, H. F., 1969, "Effects of Hydraulic Forces in Annular Pressure Seals on the Vibrations of Centrifugal Pump Rotors," Journal of Mechanical Engineering Science, 11(2), pp. 206-213.

5. Childs, D. W., "Finite-Length Solutions for Rotor-dynamic Coefficients of Turbulent Annular Seals," Journal of Lubrication Technology, Vol. 105, pp. 437-444.

6. Childs, D. W. and Williams, J. P., 1989, "Influence of Impeller Shroud Forces on Turbopump Rotor Dynamics," ASME DE-VOL, 18-1, Rotating Machinery Dynamics, pp. 41-49.

7. Childs, D. W., 1978, "The Space Shuttle Main Engine Pressure Turbopump Rotor Dynamic Instability Problem," ASME Journal of Engineering for Power, Vol. 100, Jan., pp. 48-57.

8. Ek, M. C., 1980, "Solving Subsynchronous Whirl in High-Pressure Hydrogen Turbomachinery of the SSME." J. Spacecraft, Vol 17, No. 3, pp. 208-218.

9. Flack, R. D., Gunter, E. J., and Heinzman, J. D., "Experimental Data Analysis of the Space Shuttle Main Engine -- High Pressure Fuel and Oxidizer Turbopump," Report No. UVA/528140/MAE78/106, June 1978.

10. Gunter, E.J., 1966, "Dynamic Stability of Rotor-bearing Systems," NASA CP-113, Washington.

11. Gunter, E. J., and Flack, R. D., "Experimental Measurements of the Space Shuttle Main Engine Fuel and Oxygen Turbopump Vibration Characteristics," Proceedings of the 27th International Instrumentation Symposium, Indianapolis, Indiana, Instrumentation in the Aerospace Industry - Advances in Test Measurement, Vol. 18, Part 2, pp. 393-397 (April 1981).

12. Gunter, E. J., Barrett, L. E., Palazzolo, A. B., and Allaire, P. E., "Final Report -- Dynamic Analysis of the Space Shuttle Main Engine - High Pressure Fuel Turbopump, Part III, Linearized Stability Analysis," Report No. UVA/528140/ME76/104 (September 1976).

13. Gunter, E. J., Choy, K. C., Allaire, P. E., and Barrett, L. E., "Final Report - - The Dynamic Analysis of the Space Shuttle Main Engine - High Pressure Fuel Turbopump, Part IV, Unbalance Response Analysis," Report No. UVA/528140ME76/105 (September 1976).

14. Heinzman, J. D. and Gunter, E. J., "Experimental Data Analysis of Subsynchronous Excitation of the Space Shuttle Main Engine High Pressure Oxidizer Turbopump," Report No. UVA/528140/MAE78/112, September 1978.

15. Li, D. F. and Gunter, E. J., "Linear Stability Analysis of Dual Rotor Systems -- A Manual for Use with the Computer Program STAB2V2," Report No. UVA/464761/MAE79/154, September 1978.

16. Li, D. F. and Gunter, E. J., "Space Shuttle Main Engine High Pressure Oxidizer Turbopump Critical Speed and Unbalance Response Analysis," Report No. UVA/528140/MAE78/116, October 1978.

ROTOR-TO-STATOR PARTIAL RUBBING AND ITS EFFECTS ON ROTOR DYNAMIC RESPONSE*

Agnes Muszynska, Wesley D. Franklin,
and Robert D. Hayashida
Bentley Rotor Dynamics Research Corporation
Minden, Nevada 89423, U.S.A.

This paper presents results from experimental and analytical studies on rotor–to–stationary element partial rubbings at several locations and their effects on rotor dynamic responses. The mathematical model of a rubbing rotor is given. The computer program provides numerical results which agree with experimentally obtained rotor responses.

INTRODUCTION

Rotor–to–stationary element rubbing is a serious malfunction in rotating machines. It may lead to a catastrophic failure of the machine. The rub phenomena have been recognized for a long time; literature on this subject is, however, relatively scarce and incoherent [1]. This is probably due to the fact that rotor–to–stationary element rub–related phenomena are very complex, involving several physical mechanisms, thus they represent a wide spectrum of rotating machinery dynamic problems. These problems are illustrated in Figures 1 to 4 [2].

Partial rub phenomena occurring at several radial and axial locations of the rotor are discussed in this paper. The results calculated using a mathematical model show good agreement with the experimental data.

MATHEMATICAL MODEL

Using the modal concept, a laterally symmetric (isotropic) rotor bearing/seal system is mathematically modeled for its first three lateral modes. In addition to the three modal mass lateral displacements necessary for the model, the displacements of four other axial locations at which rub can occur are included in the model. Since rub usually occurs at seal locations, the flow–related forces are introduced at these locations in addition to the system stiffness modifications, normal and friction forces, and impact losses generated by the rub. The schematic model is presented in Figure 5. The system is composed of the rotor's modal masses (M_1,M_2,M_3), stiffnesses $(K_1,...,K_7)$, and dampings (D_1,D_2,D_3), bearing/seal's stiffnesses $(K_{B1},...,K_{B4})$, radial dampings $(D_1,...,D_4)$, and fluid average circumferential velocity ratios $(\lambda_1,...,\lambda_4)$, and the rub parameters such as radial clearances $(C_1,...,C_4)$, coefficients of friction $(\mu_1,...,\mu_4)$, restitution coefficients $(\kappa_1,...,\kappa_4)$, and stator stiffnesses $(K_{r1},...,K_{r4})$. The modal parameters may be obtained from numerical analysis (using transfer matrix or finite element methods followed by reduction to three modes), and/or identified experimentally using perturbation techniques. The force equilibrium equations for the system are as follows:

345

$$M_i\ddot{z}_i + D_{si}\dot{z}_i + K_{2i-1}(z_i-\tilde{z}_i) + K_{2i}(z_i-\tilde{z}_{i+1}) = F_{ui}e^{j(\Omega t+\varepsilon_i)} + F_{pi}e^{j\gamma}, \tag{1}$$

$$D_\nu\dot{\tilde{z}}_\nu/\kappa_\nu + \tilde{z}_\nu(K_{B\nu}-jD_\nu\lambda_\nu\Omega) + K_{2\nu-2}\left[\tilde{z}_\nu-z_{\nu-1}\right] + K_{2\nu-1}\left[\tilde{z}_\nu-z_\nu\right] +$$

$$+ f_\nu\left[K_{r\nu}(|\tilde{z}_\nu|-C_\nu)(1+j\mu_\nu)\right]e^{j\delta_\nu} = 0, \tag{2}$$

$$z_i = x_i + jy_i, \quad \tilde{z}_\nu = \tilde{x}_\nu + j\tilde{y}_\nu, \quad i=1,2,3, \quad \nu=1,2,3,4, \quad K_0=0, \quad z_4=0,$$

where Ω is rotative speed, $F_{ui}e^{j(\Omega t+\varepsilon_i)}$ is the mass unbalance force, $F_{pi}e^{j\gamma_i}$ the static radial preload force, f_ν the contact factor, and δ_ν the rub angular location (Fig. 6). When the contact occurs, $(|\tilde{z}_\nu| \geq C_\nu)$ then $f_\nu=1$ and $\kappa_\nu =$ defined restitution parameter value, otherwise $f_\nu=0$ and $\kappa_\nu=1$. The rub forces are modeled in Eq. (2) by the terms $f_\nu\left[K_{r\nu}(|\tilde{z}_\nu|-C_\nu)(1+j\mu_\nu)\right]e^{j\delta_\nu}$ and
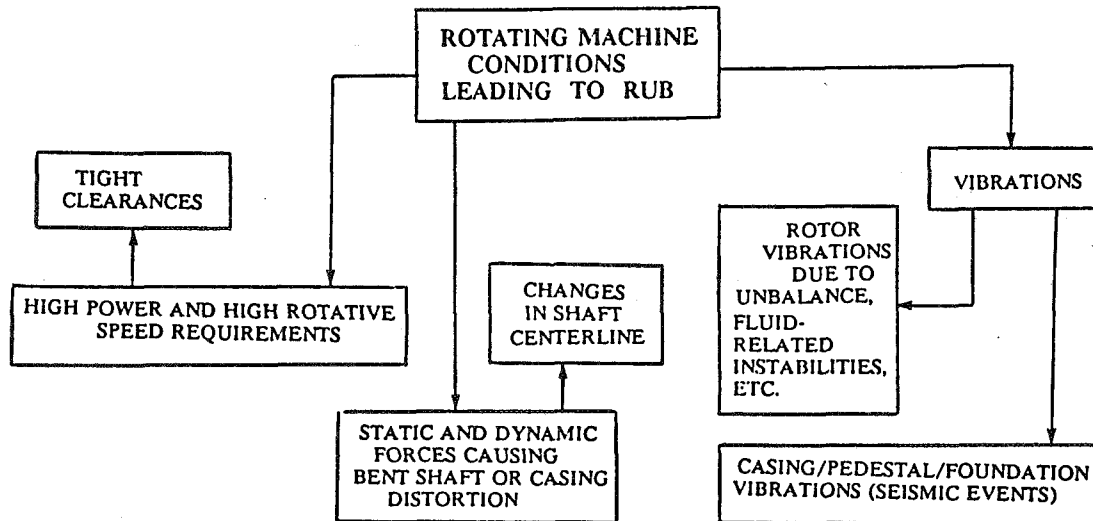
Figure 1. — Rotating machine conditions leading to rotor–to–stationary element rubbing.
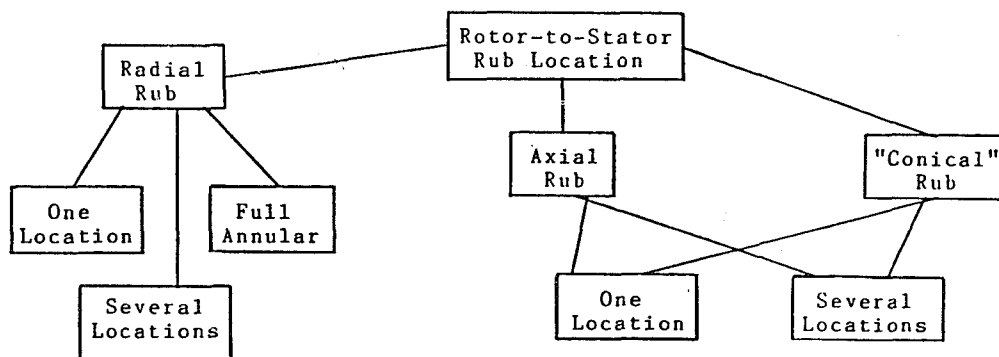
Figure 2. — Rotor–to–stationary element rub location.

346

$D_\nu \tilde{z}_\nu / \kappa_\nu$. The coefficients f_ν describe the timing of "contact" ($f_\nu=1$ for $|\tilde{z}_\nu| \geq C_\nu$) versus "no contact" ($f_\nu=0$ for $|\tilde{z}_\nu| < C_\nu$). The functions $K_{r\nu}(|\tilde{z}_\nu| - C_\nu)$ describe the radially applied additional stiffness force due to contact with the stationary part. They also describe the rotor/stator normal forces. The functions $K_{r\nu}(|\tilde{z}_\nu| - C_\nu)j\mu_\nu$ model the tangentially oriented friction forces. The coefficients κ_ν describe an additional energy loss due to local material
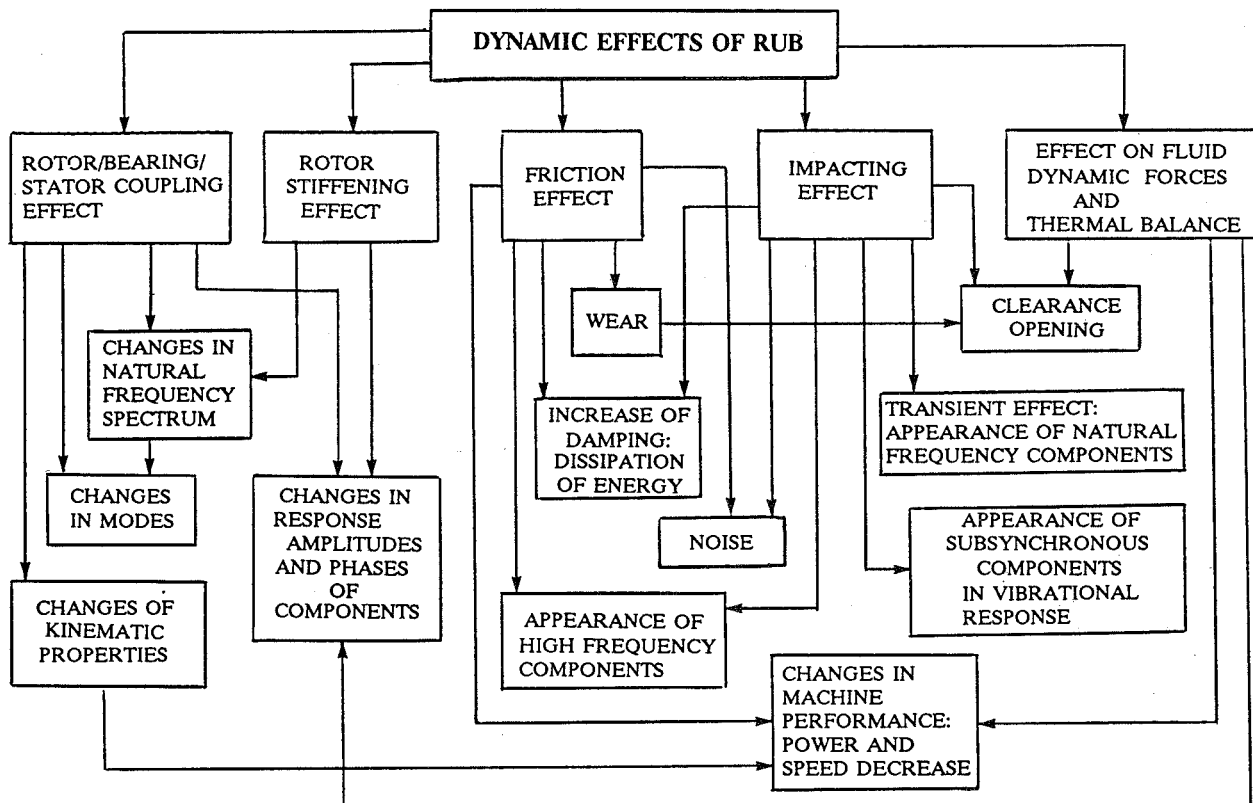
Figure 3. — Dynamic effects of rotor—to—stationary element rubbing.
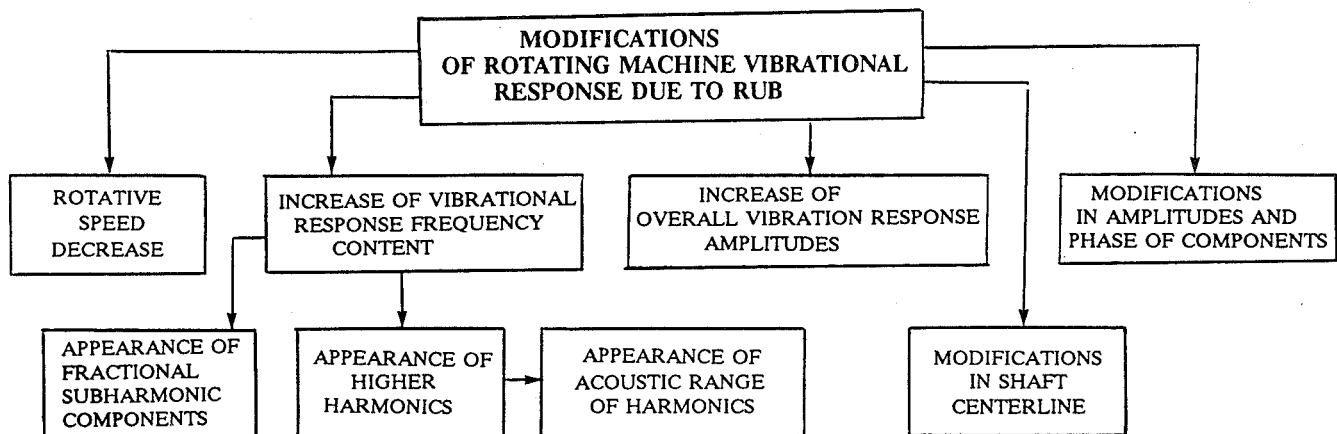
Figure 4. - Modifications of rotating machine vibrational response due to rotor-to-stationary element rubbing.

347

deformation during the impacting condition. The definition of κ_ν, as explained below, differs, however, from the classical restitution coefficient definition.

Before the rotor–to–stator contact occurs, for example, at the first seal, i.e., for $|\tilde{z}_1| - C_1 < 0$ there is $f_1 = 0$ and $\kappa_1 = 1$, thus, from Eq. (2) for $\nu=1$:

$$D_1(\dot{\tilde{z}}_{1(-)} - j\lambda_1\Omega\tilde{z}_1) + (K_{B1} + K_1)\tilde{z}_1 - K_1 z_1 = 0 , \tag{3}$$

where the velocity subscript $(-)$ indicates the "before collision" situation. Following the classical impact theory, during collision only velocities are instantaneously affected. Displacements remain the same. Just after collision, i.e., for $|\tilde{z}_1| - C_1 \geq 0$ there is $f_1 = 1$ and $\kappa_1 < 1$, thus
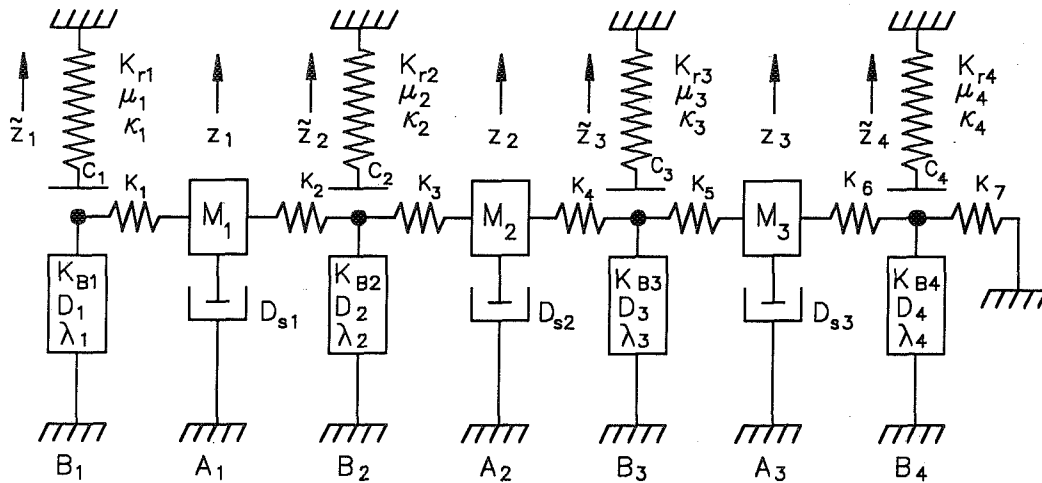
Figure 5. — Rotor system model.
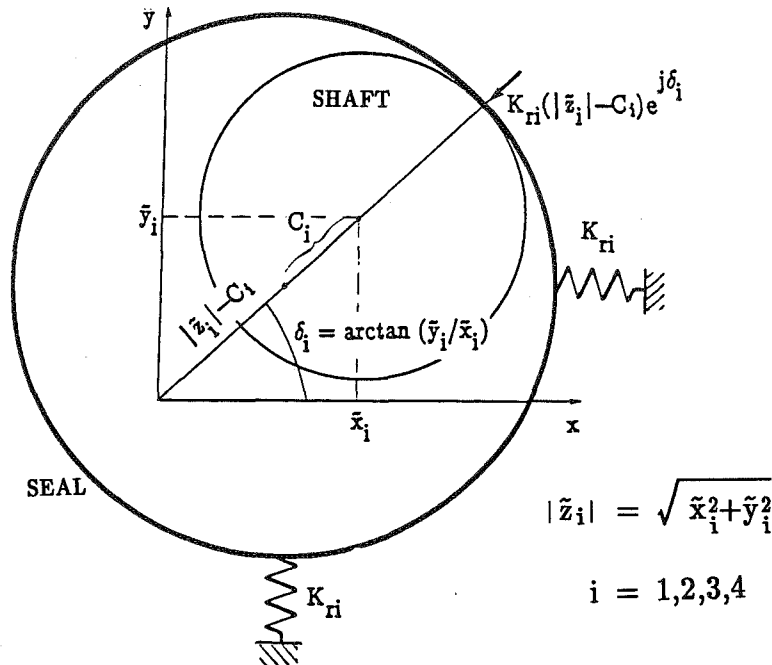
Figure 6. — Rubbing rotor inside a seal.

348

$$D_1(\dot{\tilde{z}}_{1(+)}/\kappa_1 - j\lambda_1\Omega\tilde{z}_1) + (K_{B1}+K_1)\tilde{z}_1 - K_1 z_1 + K_{r1}(|\tilde{z}_1|-C_1)(1+j\mu_1)e^{j\delta_1} = 0 , \qquad (4)$$

where the velocity subscript $_{(+)}$ indicates the "after collision" situation. Taking into account Eqs. (3) and (4) the coefficient of restitution κ_1 is defined as follows:

$$\kappa_1 = \frac{\dot{\tilde{z}}_{1(+)}}{\dot{\tilde{z}}_{1(-)} - K_{r1}(|\tilde{z}_1| - C_1)(1 + j\mu_1)e^{j\delta_1}/D_1} \qquad (5)$$

Note the differences in this definition, as compared to the classical straight impact theory.

In Eq. (5) both velocities $\dot{\tilde{z}}_{1(-)}$ and $\dot{\tilde{z}}_{1(+)}$ have the same sign. There is no justification to assume that in the rotor lateral planar motion the impact against a compliant stator causes velocities to reverse immediately. The second difference is the addition of the stator stiffness—related normal and tangential forces, modifying the "after collision" velocity. When the stator stiffness is low the after collision motion continues in the same direction until, due to an increase of displacement $\tilde{z}_1$, a balance occurs, and $\dot{\tilde{z}}_{1(+)} = 0$. At this moment the motion is reversed. The similar impact situations take place at all possible rub locations $\nu=1,2,3,4$.

ROTOR–TO–STATOR RUB COMPUTER SIMULATION PROGRAM

The computer program was written to help explore the effects of rotor–to–stator rub on rotor vibrational responses.

The computer program is composed of two major subprograms: (1) the linear rotor/bearing/seal system synchronous response with no rub, and (2) the timebase response of the nonlinear system with rub at a selected constant rotative speed. The first of the subprograms allows the user to calculate the static displacement and synchronous ($1\times$) response of the system versus rotative speed, producing transient type data which may be displayed in Bodé or polar plot format. This allows for easy identification of the system three—mode modal characteristics and resonances, indicating at which rotative speeds the largest vibration amplitudes occur. This information is used to determine rotative speed ranges which should be investigated more closely by taking into account the rub effects in the timebase response. The second portion of the program allows a more detailed analysis of the shaft vibrational response caused by external and rub—related exciting forces at the desired rotative speeds, by calculating (using numerical integration) the shaft centerline motion versus time. In addition to the linear parameters of the shaft and support structure, the timebase response subprogram uses the nonlinear properties of the rotating system imposed by outside support structures with limited clearances.

The overall program sequence is shown using the flow chart in Figure 7. The program computes data buffers for both the linear and nonlinear responses at each of the three mass stations, A_i, and each of the four bearing/seal locations, B_ν (Fig. 5), plus buffers indicating positions and time periods of rotor—to—stator contacts. The parameters necessary to allow computation of the synchronous response include the following: the system modal mass at each mass station, the stiffness for each shaft section, the external damping at each mass location, the rotational unbalance force vector, the radial constant preload force and its associated angle, and the fluid radial damping, fluid average circumferential velocity ratio, fluid radial stiffness, and radial clearance at each of the bearing/seal locations.

After the system parameters have been entered and verified, the program begins the execution of the synchronous response calculations. If the synchronous vibration response is not

required, the program skips the calculation and proceeds to the nonlinear calculations described below. Otherwise, the program prompts for the rotative speed range and increment between calculations over which the synchronous calculations are to be performed. Once this data has been entered, the program proceeds to calculate the synchronous response of the rotor at axial locations $A_1,...,A_3$ (disk locations) and $B_1,...,B_4$ (bearing/seal locations). The program solves the linear portion of the equation set (for $\kappa_\nu=1$ and $f_\nu=0$) by assuming solutions of the following form:

1.0	MAIN PROGRAM ENTRY POINT

1.1	RESERVE MEMORY FOR DATA STORAGE

1.2	INITIALIZE WORK STATION

1.3	INPUT LINEAR PARAMETERS

ROTOR MASS
SHAFT STIFFNESS
SHAFT DAMPING
UNBALANCE AMPLITUDE
UNBALANCE PHASE
RADIAL FORCE AMPLITUDE
RADIAL FORCE PHASE
FLUID DAMPING
FLUID AVERAGE VELOCITY RATIO
FLUID RADIAL STIFFNESS
SEAL CLEARANCE

1.4	PROMPT FOR SYNCHRONOUS RESPONSE CALCULATION

N

Y

1.5	CALCULATE SYNCHRONOUS RESPONSE

1.6	DISPLAY SYNCHRONOUS RESPONSE RESULTS

A1   B1   B01   RUB1
A2   B2   B02   RUB2
A3   B3   B03   RUB3
A01 B4   B04   RUB4
A02
A03

1.7	PROMPT FOR NONLINEAR RESPONSE CALCULATION

N

Y

1.8	INPUT NONLINEAR PARAMETERS

INITIAL DISPLACEMENTS
INITIAL VELOCITIES
STATOR STIFFNESSES
FRICTION COEFFICIENTS
RESTITUTION COEFFICIENTS
CONTROL PARAMETERS

1.9	CALCULATE NONLINEAR TIMEBASE RESPONSE

1.10	DISPLAY NONLINEAR TIMEBASE RESPONSE RESULTS

NA1 NB1 CONTACT 1
NA2 NB2 CONTACT 2
NA3 NB3 CONTACT 3
     NB4 CONTACT 4

1.11	PROMPT TO EXTEND NONLINEAR CALCULATIONS

Y

N

1.12	PROMPT TO EXIT PROGRAM

N

Y

1.13	RELEASE WORK STATION

1.14	MAIN PROGRAM EXIT POINT

Figure 7. — Flow chart of main program sequence.

350

$$z_i = A_i e^{j(\Omega t + \alpha_i)} \quad \text{and} \quad \tilde{z}_\nu = B_\nu e^{j(\Omega t + \beta_\nu)}$$

for the unbalance force response, and

$$z_i = A_{oi} e^{j\alpha_{oi}} \quad \text{and} \quad \tilde{z}_\nu = B_{o\nu} e^{j\beta_{o\nu}}$$

for the static radial preload force response. These solutions are then substituted into the original equations (1) and (2), which are eventually solved to get the amplitudes and phases of the response at each location. The maximum amplitude and its angle is calculated for each bearing/seal location by combining the unbalance and preload responses for that location. These values are then compared with the specified radial clearance at the location to determine whether rubs would have occurred. This information is placed in the "RUB" data buffers, which may be displayed in the same manner as the vibration responses. The linear system response data, and potential rub information may be plotted using a Bodé format or listed in tabular format either on the computer screen or a graphics printer.

If the nonlinear calculations are not required, they may be skipped, and the program proceeds to the exit. If they are to be performed, the additional parameters necessary to complete the calculations must be entered. These include the initial displacements and velocities at each location (initial conditions), the stator stiffness, the coefficient of friction at the rotor and stator surfaces, and the impact restitution coefficient at each of the potential rub locations, plus the program control variables, namely operating speed, number of revolutions to compute, and the number of computational steps per revolution.

If the linear calculations by the first portion of the program were performed, the initial displacements and velocities are calculated from the synchronous responses; therefore, any values entered during the data input process will not be used by the program. The initial conditions in the parameter table are also not used when the nonlinear calculations are being extended. The process of extending the nonlinear calculations is discussed later; for now it is sufficient to realize that the initial conditions for the current calculation are obtained from the previous calculation, and their input into the parameter table is not required.

Instead of assuming a solution form and substituting it into the original equations as was done to get the linear solution, the numerical integration algorithm requires that each equation be solved for its highest order derivative. The Runge–Kutta algorithm then uses the values calculated for the highest order derivatives, along with the current state of the system, (shaft positions and velocities) to predict the state of the system at some point in the future. This process continues until the motion for the specified period has been calculated. The accuracy and numerical stability of the algorithm is very sensitive to the step size between computed points. Large step sizes provide increased computational speed at the cost of reduced accuracy and stability, since both accuracy and stability depend on the product of the step size and the value of the highest order derivative. This program uses a variable step size, based on the percentage change between the value for the new point and the current point, to optimize both the computational speed and accuracy. Figure 8 illustrates this process by showing the steps for a possible computation sequence between two data sample times. Since any change from the value of zero will produce percentage changes greater than allowed, the program also has an amplitude threshold which overrides the change requirements between points if the new value is less than the threshold. The threshold and percent change parameters should be picked carefully as they significantly affect both the computational speed and accuracy.

Once the computations are performed and data buffers have been completed, the nonlinear motion may be displayed using an orbit/timebase format or numerically listed.

```
               ---------TIME--------------------->
            T(S)                              T(S+1)      ...           T(S+2)

            CV----------------------------------NV,U
            CV--------------NV,U
            CV------NV,A
                    CV-----NV,A
                            CV-------------------NV,U
                            CV-------NV,A
                                    CV---------NV,A,DS
                                        CV----------...--------NV,A,DS
                                                              CV-----

    T(---) = DATA SAMPLE/STORE TIMES    U  = UNACCEPTABLE AMPLITUDE CHANGE
    CV       = CURRENT VALUE            A  = ACCEPTABLE AMPLITUDE CHANGE
    NV       = NEW VALUE                DS = DATA STORED
```

Figure 8. — Computational sequence for variable step size Runge—Kutta numerical algorithm.

The program allows the nonlinear calculations to be extended. The extension can be used to continue the computational period until a steady—state solution is obtained by using the values at the last computed point as the initial conditions for another computational period. This process can be continued until the steady—state solution has been obtained. The computational results are discussed later in this paper.

ROTOR—TO—STATOR RUB EXPERIMENTAL RIG

A series of tests involving partial rotor—to—stator rub were performed on a two lateral—mode rotor rig. The rotor/stator contact was carefully documented and correlated with the rotor vibrational responses.

The rotor rig (Figs. 9 and 10) consists of a horizontal isotropic two—disk rotor supported at each end by a relatively rigid bronze sleeve—type bearing (Oilite). A 0.5 horsepower ac motor drives the rotor through a flexible coupling. When observed from the motor end of the shaft (inboard end), rotation is in the counterclockwise direction. Horizontal brass screws are mounted adjacent to each of the two rotor disks, both at angle 270°. The rub screws, when used in conjunction with the rotor, allow engaging the rotor in the partial rotor—to—stator rub conditions. Of particular interest in this experiment is the influence of multiple axial locations of partial rub on rotor dynamic response, i.e., rub occurring simultaneously at more than one plane along the machine train.

The XY displacement probes providing the shaft radial displacement data are mounted next to each rotor mass. A Keyphasor® probe mounted vertically at the inboard end provides the once—per—turn reference signal from which all phase angles are measured in the direction against rotation. The shaft observing vertical and horizontal probes are installed at 0 and 270 degrees respectively.

Located at the rotor midspan is a shaft preloading fixture. The fixture consists of a small ball bearing mounted on the shaft and radially supported by four orthogonal springs. Each spring of stiffness 16 lb/in is attached to the stationary fixture frame.

An extremely "light" rub may not be apparent through vibration signals. Shaft vibration data is, therefore, correlated with a rub contact timing signal in a timebase format. This timing signal accurately identifies a rotor—to—stator contact condition. A 1—volt—dc potential is placed

352

A – ELECTRIC MOTOR
B – FLEXIBLE COUPLING
C – INBOARD BRONZE BEARING
D – ELECTRICAL CONTACT DEVICE
E – INBOARD X Y DISPLACEMENT PROBE MOUNT
F – INBOARD MASS
G – INBOARD HORIZONTAL RUB SCREW

H – X Y PRELOAD FIXTURE
I – OUTBOARD HORIZONTAL RUB SCREW
J – OUTBOARD MASS
K – OUTBOARD X Y DISPLACEMENT PROBE MOUNT
L – OUTBOARD BRONZE BEARING
M – ROTOR SHAFT
N – ROTOR BASE
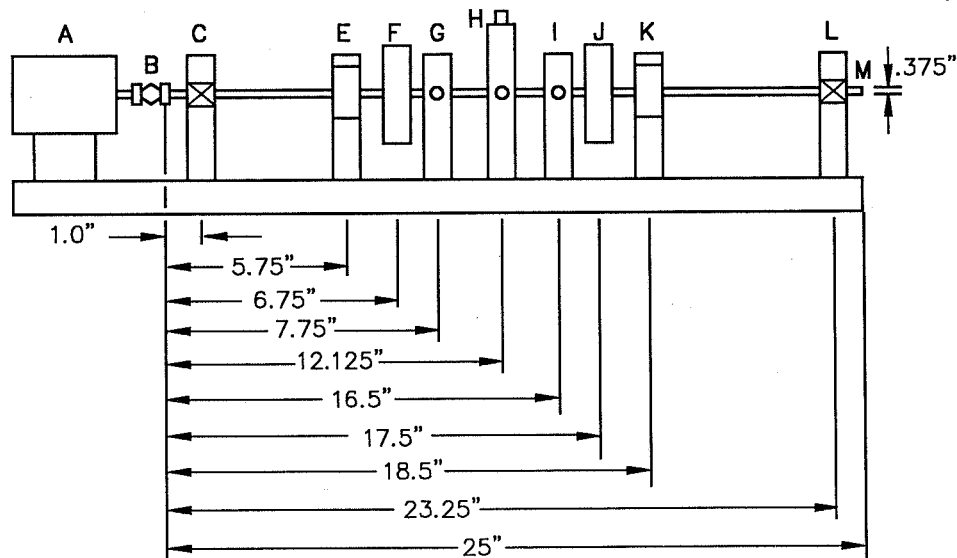
Figure 9. – Experimental rig.

1. MOTOR SPEED CONTROL
2. TRACKING FILTER
3. SPECTRUM ANALYZER
4. COMPUTER
5. 108 DAI
6. X Y PRELOAD FIXTURE
7. BRONZE BEARINGS
8. X Y EDDY CURRENT
   DISPLACEMENT PROBES

9. INBOARD HORIZONTAL RUB SCREW
10. OUTBOARD HORIZONTAL RUB SCREW
11. FLEXIBLE COUPLING
12. ROTOR BASE
13. 3 INCH DIAMETER DISCS
14. ROTOR SHAFT
15. KEYPHASOR PROBE
16. dc DUAL POWER SUPPLY
17. ELECTRIC MOTOR
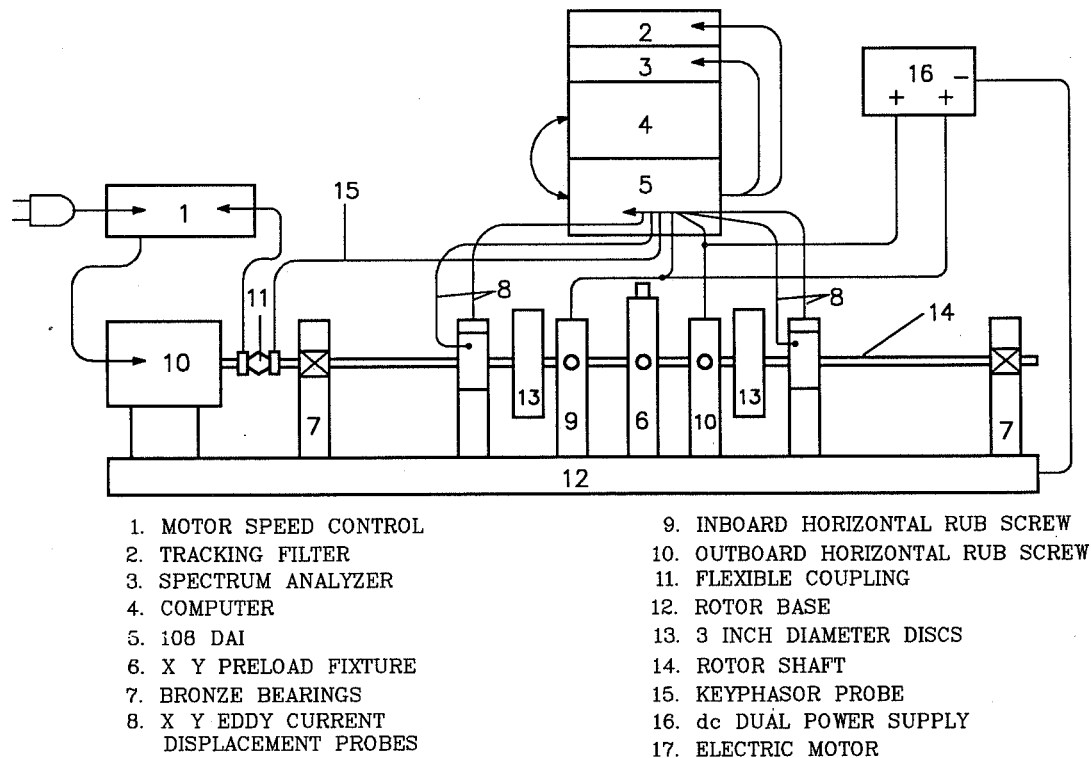
Figure 10. – Experimental Data acquisition system.

across the rotor and an electrically isolated rub screw. The mechanical/electrical contact between the rotor shaft and each rub screw provides a circuit yielding continuity position/timing data correlated to both the Keyphasor and vibration signals.

The vibration information from the proximity probes is presented in shaft orbit and timebase formats, and eventually processed through filters and an FFT analyzer to determine the frequency components contributing to the overall waveform. The information on lateral vibration from different axial locations of the shaft can then be correlated to provide rotor deflection shape.
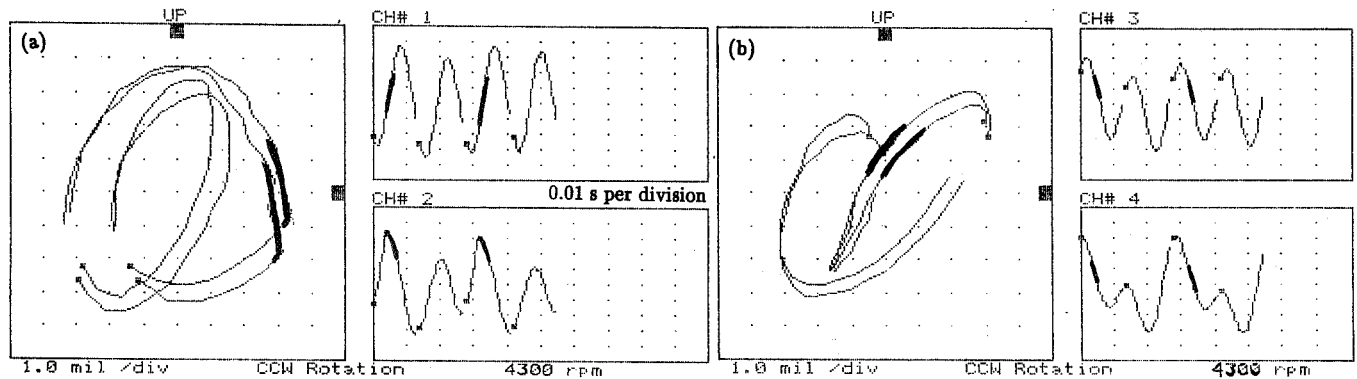
Figure 11. - Rubbing rotor inboard (a) and outboard (b) responses at a constant rotative speed 4300 rpm. Rubbing timing is marked using thick lines.
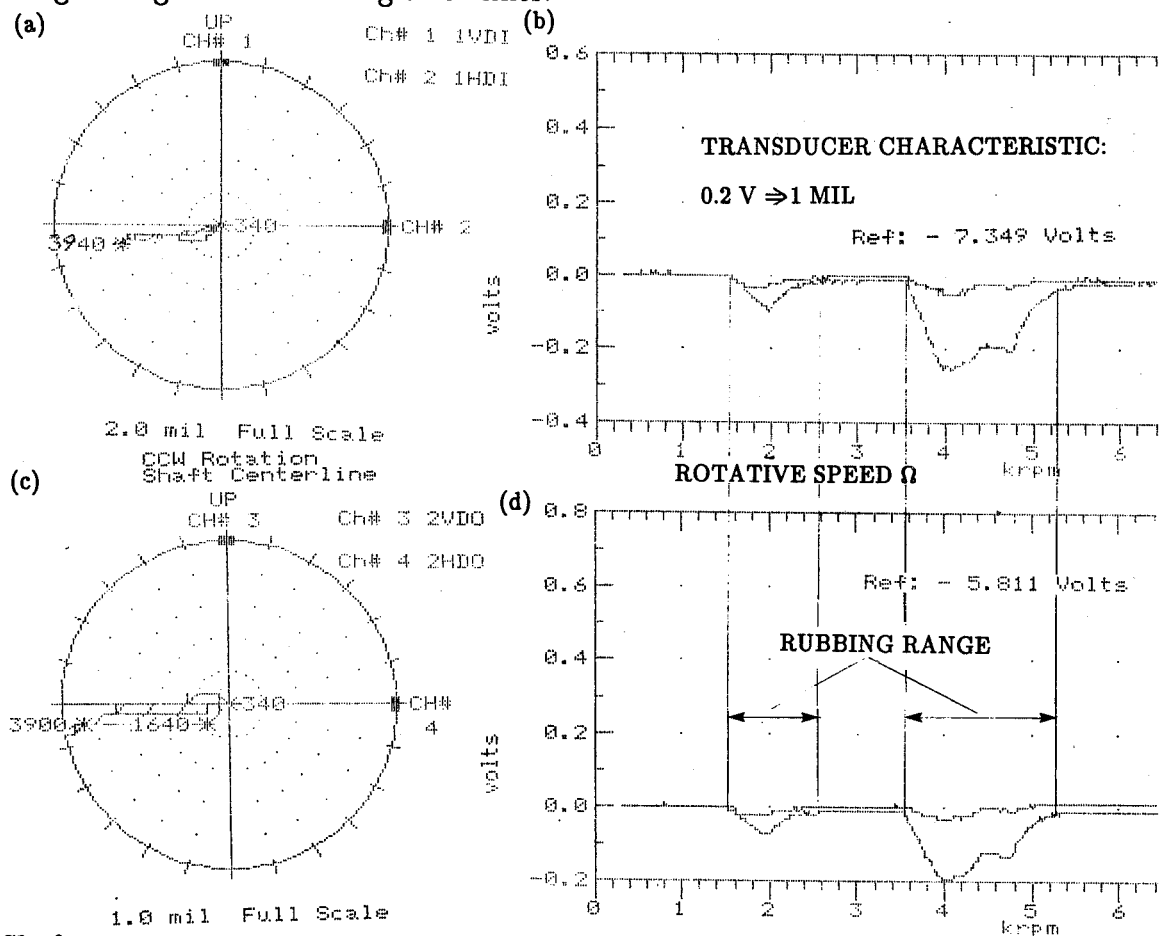
Figure 12. - Shaft centerline position at inboard (a), (b) and outboard (c), (d) locations versus rotative speed in the polar and orthogonal formats. Note significant displacements in the horizontal direction at speeds when rub occurs.

354
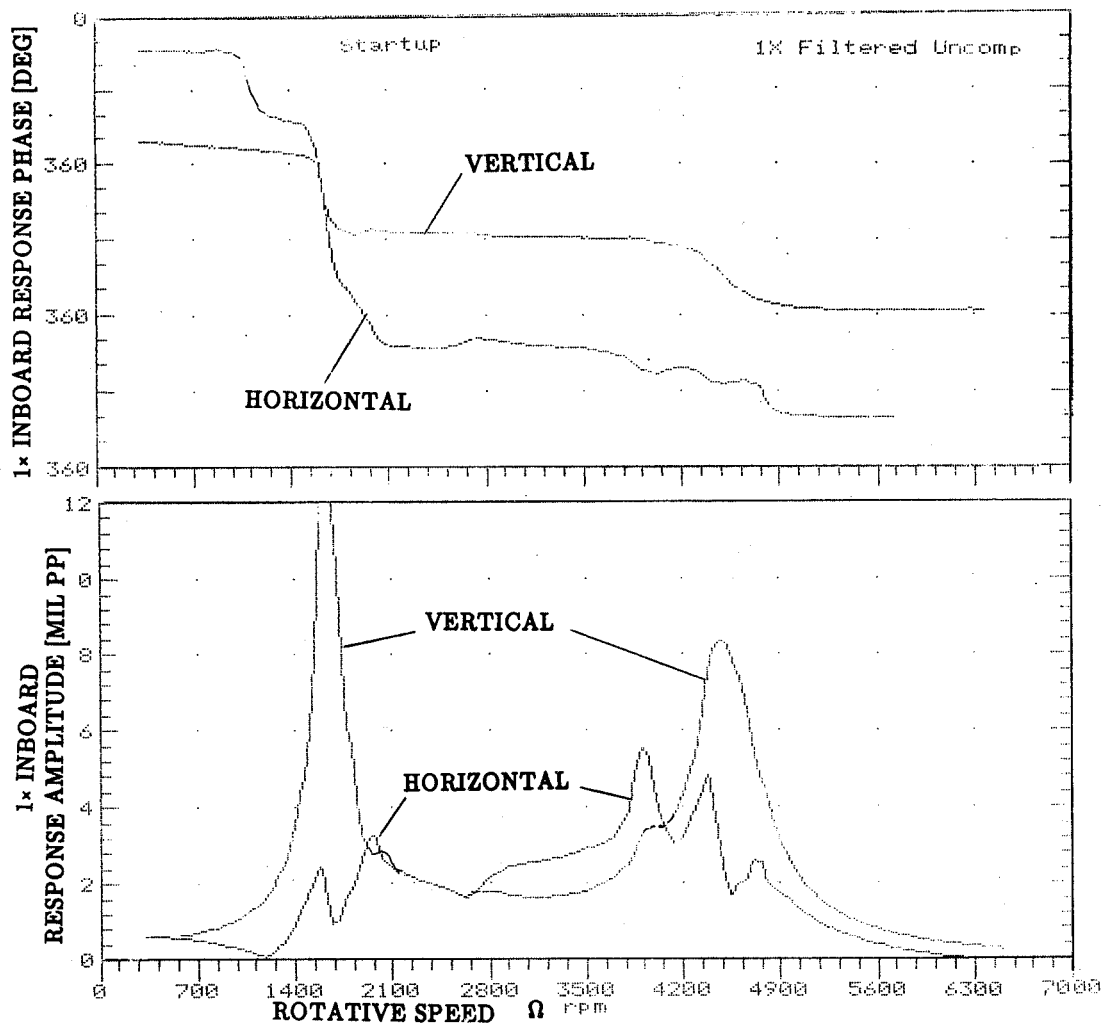
Figure 13. - Bodé plot of rubbing rotor 1× inboard vertical and horizontal responses. Note significant changes in the horizontal response, the direction where the main rubbing activity occurs.
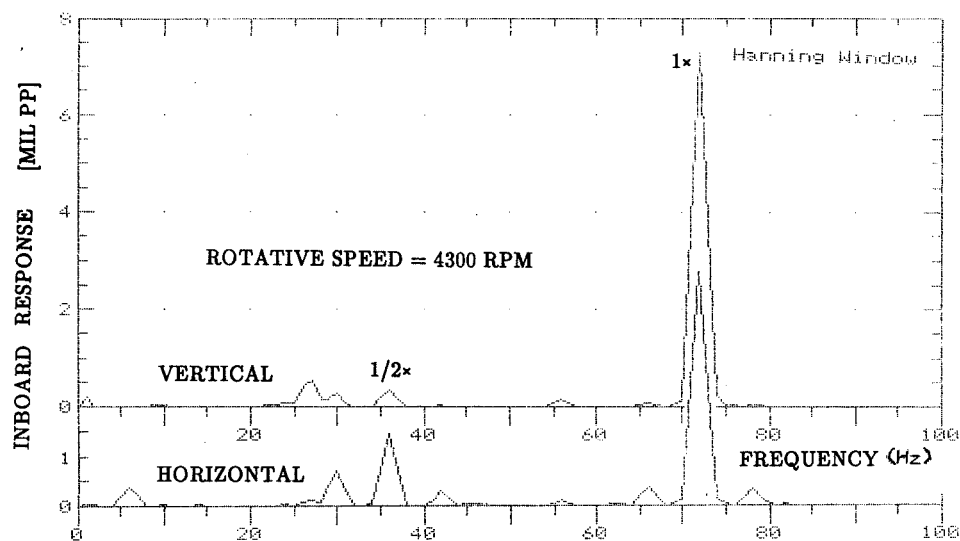
Figure 14. — Rubbing rotor vibration spectrum at 4300 rpm.

355

TEST PROCEDURE AND TRANSIENT TEST DATA

A controlled unbalance inserted at the rotor inboard disk is used to generate the required level of synchronous vibration for the rub initiation. Rotor speeds range from 0 to 6500 rpm passing through the rotor first and second balance resonances at approximately 1580 rpm and 4200 rpm respectively. It should be noted that these speeds represent the rotor's first and second balance resonances under normal operating conditions without rub.

The unbalance mass employed for this series of experiments is 0.5 grams at a radius of 30.5mm at 0 degrees (relative to the Keyphasor notch). Each rubbing rotor data run was initiated by locating the appropriate brass rub screw close to the rotor shaft. A light horizontal preload (1 to 2 lb) was then introduced at the rotor midspan.

EXPERIMENTAL RESULTS: RUB WITH PREDOMINANT
SECOND MODE 1× VIBRATION

Past experimentation [2–4,6] has focused on the rules for single point rubs occurring in rotating shafts operating in the range of predominantly first lateral mode 1× vibrations of the rotor. Vibrations were observed at the shaft axial location where the rub occurred. The rotor rig used in the present experiments allows examination of the shaft vibration pattern at several axial locations. The first two natural frequencies of the system are close enough that they fall in the range of investigated rotative speeds. The corresponding modes are bending modes of the shaft. When more than just one mode can be involved, the interpretation of the rub–related vibrations and identification of rub radial location must be done more carefully. An example is given in Figs. 11 to 15. Figure 11 presents inboard and outboard shaft vibration time base waveforms and orbits during rubbing at a constant rotative speed 4300 rpm, higher than twice first balance resonance frequency, and slightly lower than the second balance resonance frequency of the rotor. The operating speed falls into the range of the second mode, thus the basic 1× vibrations at the inboard and outboard locations are out of phase. By using information from the rotor–to–stator physical contact device, the identification of the rubbing location was not difficult: rubs occur on the inboard side at 270° where the screw is mounted. If, however, only outboard vibration data were available, the rub location might be erroneously identified on the opposite side (outboard, and at 90°).

Figure 12 presents important data which is often overlooked, namely, the shaft centerline position. When the rub occurs, the shaft is rebounding away from the contact point. Figure 13 presents the Bodé plot of the rubbing rotor synchronous (1×) response indicating significant changes in the horizontal component. The spectrum contents at 4300 rpm is given in Figure 14. Two Keyphasor dots at the orbits (Fig. 11) confirm the appearance of the 0.5× component in the rotor response. Figure 15 illustrates the rubbing shaft centerline changes.
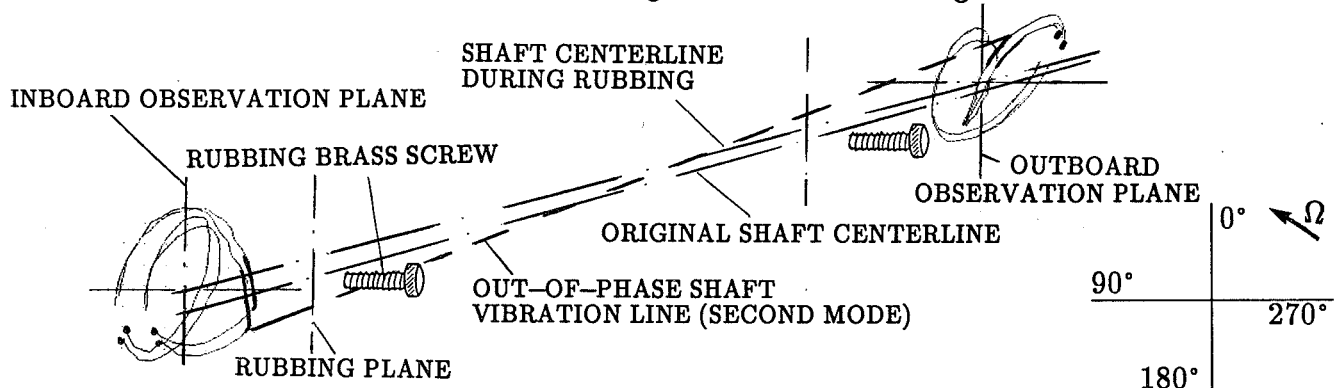
Figure 15. — Rubbing rotor centerline at 4300 rpm.

EXPERIMENTAL AND ANALYTICAL RESULTS FOR RUBBING ROTOR
AT CONSTANT ROTATIVE SPEEDS

The figures 16 to 19 illustrate the corresponding experimental and analytical results. The data in Figures 16a through 19a are the orbit/timebase waves at various operating speeds produced by the experimental rotor rig during a routine start–up. The synchronous force was generated by placing a mass unbalance in the outboard disk. The rub boundary was established by adjusting the brass rub screw next to the inboard disk until it was close to the shaft. Using the bias springs, the shaft was then preloaded toward the rub boundary enough to cause contact as the rotor synchronous vibrations increased in resonant ranges of rotative speeds. Figures 16a and 17a are the vibrational responses at a constant speed near the first balance resonance frequency, while Figures 18a and 19a are the responses near the second balance resonance frequency. Figures 16b through 19b are the simulated vibrational responses generated by the computer program for the same conditions, as the associated experimental responses. If one waveform is taken as an example, illustrated figures a and b respectively, the experimental and computer–generated responses, can be compared. The timebase waveforms in the horizontal direction where the rub occurs are almost identical. The instances of contact, indicated by the highlighted portion of the waveforms, occur at the same locations for both responses, and also have approximately the same duration. The largest difference in these two response waveforms is

Figure 16. - Rubbing rotor inboard and outboard orbits and wave-forms at 1500 rpm: (a) experimental, (b) computer-simulated.
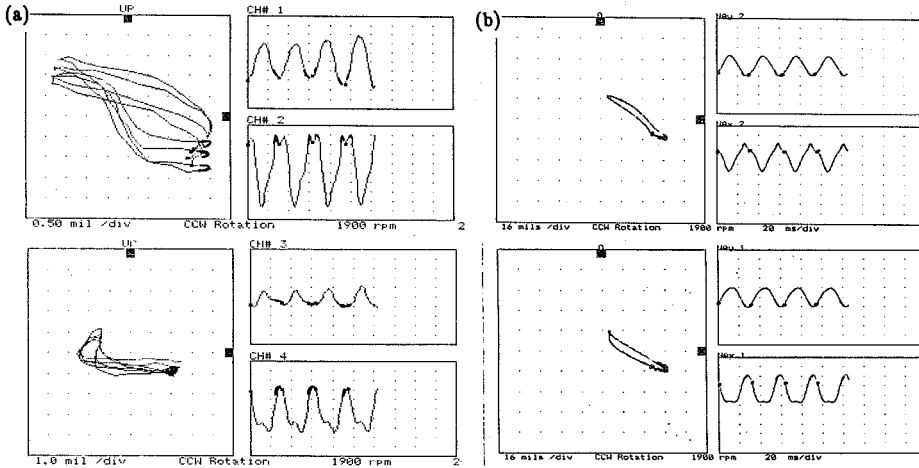
Figure 17. - Rubbing rotor inboard and outboard orbits and wave-forms at 1900 rpm: (a) experimental, (b) computer-simulated.

TABLE 1

$M_1=0.005$ lb s^2/in
$M_2=M_3=0.0025$ lb s^2/in
$K_1=K_6=182$ lb/in
$K_2=K_4=K_5=10^4$ lb/in
$K_{ri}=10^4$ lb/in
$K_3=460$ lb/in
$D_{si}=0.03$ lb s/in
$F_{u1}=2.5\cdot10^{-5}\Omega^2$ lb
$F_{u2}=F_{u3}=0$
$\varepsilon_1=90°$
$F_{p1}=F_{p2}=0$
$F_{p3}=9$ lb
$\gamma_3=0°$
$D_1=D_4=0.1$ lb s/in
$D_2=D_3=0.01$ lb s/in
$\lambda_i=0$
$K_{B1}=K_{B4}=900$ lb/in
$K_{B2}=K_{B3}=0$
$C_1=C_2=C_4=10$ in
$C_3=0.05$ in
$\mu_i=0.5$
$\kappa_i=1$ $i = 1,2,3,4$

357

the ratio of the forced vibration magnitude to the transient vibration caused by the rubbing forces. The vertical experimental and analytical response waveforms also show similar patterns. The major difference between the experimental and computed responses is related to the phases between the horizontal and vertical responses. In the experimental responses the maximum negative vertical excursion occurs at about the same time as the maximum negative excursion of the horizontal response. For the computed responses the maximum negative vertical excursion occurs when the horizontal response reaches maximum positive. This timing difference is caused by the relationship between the forced vertical response and the transient vertical response. Since the orbit format is very sensitive to the relative phases between the orthogonal waveforms, it shows the greatest difference between experimental and computed responses. Relatively large numbers of inter—related variables controlling the response and the long computational time period required to reach a steady—state solution results in an approximation to the corresponding experimental data. The two—mode rotor system modal parameters were identified prior to rubbing occurrences [5]. The identification of rub—related parameters was more difficult, and some estimation was applied (Table 1). This certainly contributes to the differences observed in the experimental versus analytical results. However, the main contributor to the differences is how the rub boundary is produced (see Figure 20). The experimental rub boundary is a flat vertical surface bounded in only one direction. The rub boundary used by the computer program is a full 360—degree circular clearance. To approximate the flat surface bounded only on one side, the computer program must use small unbalance forces combined with high preload forces and a
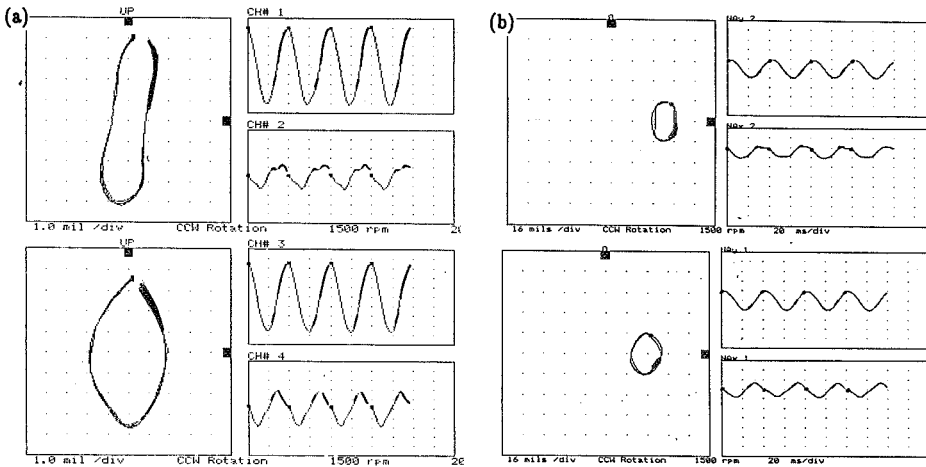

Figure 18. - Rubbing rotor inboard and outboard orbits and waveforms at 3900 rpm: (a) experimental results, (b) computer-simulated results.

Figure 19. - Rubbing rotor inboard and outboard orbits and waveforms at 4700 rpm: (a) experimental results, (b) computer-simulated results.
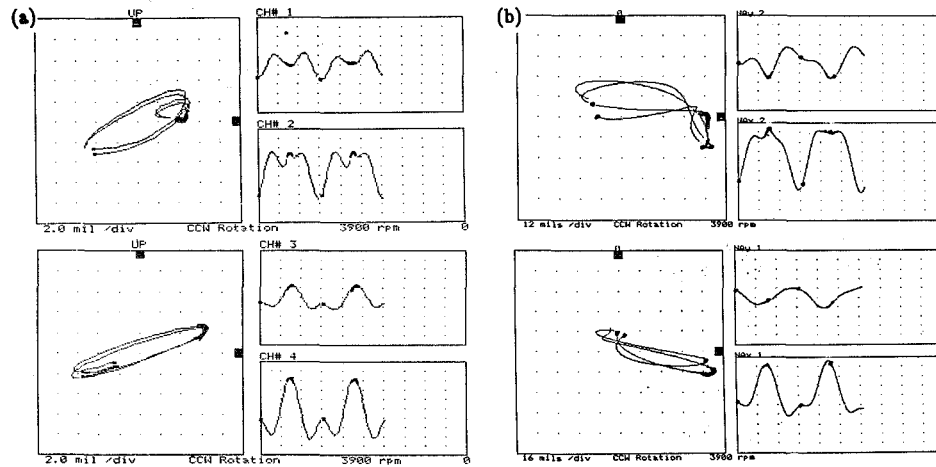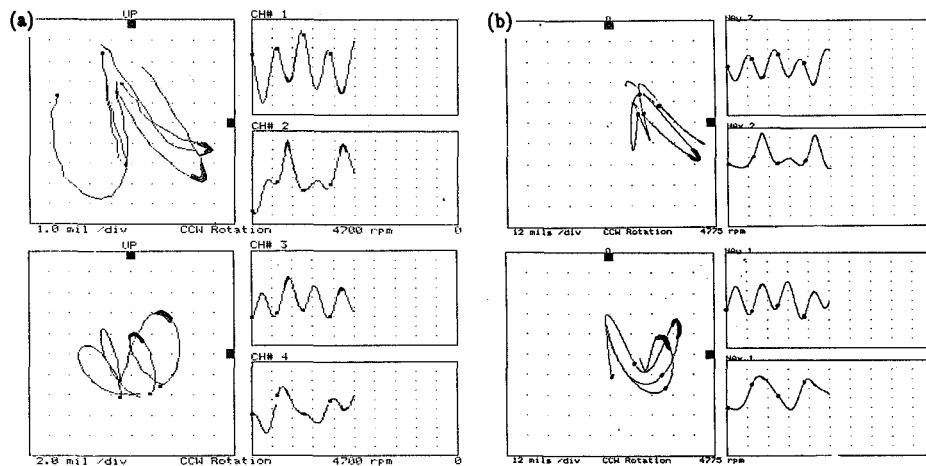
358
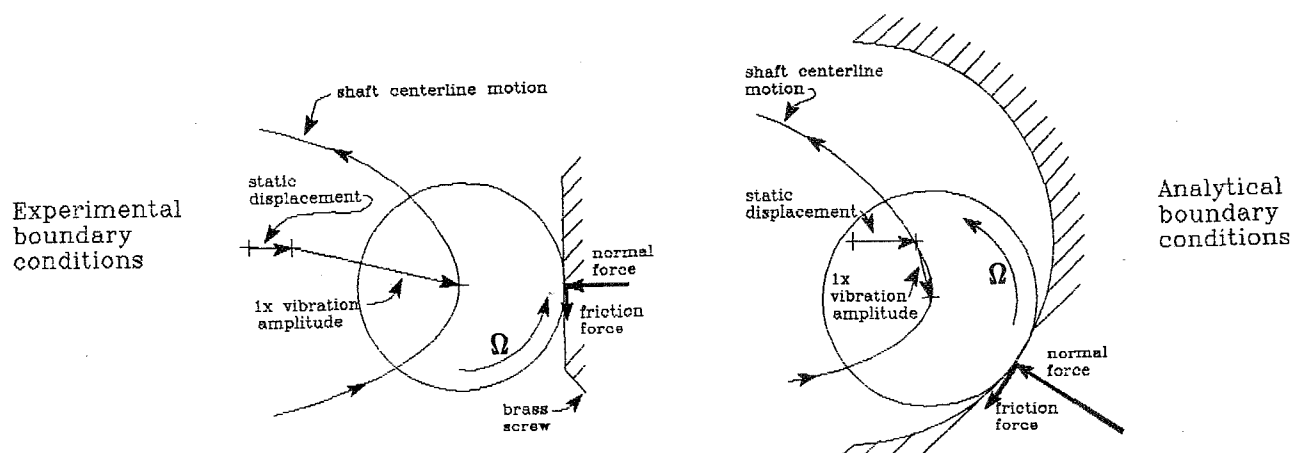
Figure 20.–Experimental and computer–simulated rubbing rotor boundaries.

relatively high clearance (Figure 6). The rotor centerline is moved away from the center of the clearance enough to allow the rebounding motion to occur within the available clearance. This process imposes limits on the ratio of unbalance to preload force. Since the impact force producing the transient motion depends on the combination of preload and unbalance forces, the unbalance response becomes a smaller part of the overall vibration. This explains the discrepancy in the ratio of forced–to–transient vibration amplitudes between the experimental and computer–generated data observed previously. The discrepancy concerning the timing relationship between the transient and unbalance responses in the vertical direction is also caused by the rub boundary configuration. When the shaft contacts the rub screw vertical surface in the experiment, there are two force components, the impact force and the tangential friction force in the downward direction for counterclockwise rotation. For counterclockwise rotation, the shaft in the computer program touches the seal simulating boundary below the clearance centerline if the combined preload and unbalance responses are greater than the clearance. The difference between this case and the experimental one is that now the impact surface is no longer vertical. Therefore, the impact force has a horizontal component similar to the experimental component, but also carries a vertical component in the up direction. If this component is higher than the friction–generated vertical down component, the net vertical force acts upward instead of downward like the experimental case. This produces the timing difference in the vertical direction noted earlier.

RUBBING ROTOR AT TWO AXIAL LOCATIONS. ADDITIONAL OBSERVATIONS

The previous experimental data have resulted in characterization of the rub phenomena by means of shaft lateral vibration frequency content. There exists some general rules that have been widely accepted. Of interest in this case is the generation of subsynchronous vibration components tied to the rotor's running speed and the rotor first natural frequency. The generation of rub–related subsynchronous components in the order of $(1/2)\times$, $(1/3)\times$, etc., necessitated the rotor speed to be at least twice, three times, and so on, the rotor's first natural frequency. Further studies relating to this concept indicate that both the generation, as well as transitions between orders of subsynchronous components, is perhaps not as clear as once believed. These general rules are true in the case of the rotor–to–stator rub at a single point; however, multiple axial points of rub occurring simultaneously involve more complex rotor responses.

During setup and adjustment of the same rotor rig for the experiment with multiple axial rub points, the existence of subsynchronous components were observed at rotative speeds below twice the rotor first natural frequency. The frequency content of the spectrum and orbit stability at various running speeds below twice first natural frequency appeared to be highly sensitive to the severity of rub, as well as the amount of radial preload applied to the rotor.

359

Data is presented in Figures 21 and 22 to illustrate these phenomena. Response orbit/timebase waves of the rubbing rotor's measured at inboard and outboard planes clearly show the presence of (1/2)× vibrations, being most predominant in the horizontal direction.

The running speed of 3143 rpm is 157 rpm lower than twice the system's "unmodified" first natural frequency of 1650 rpm. (A "modification" of system resonance occurs due to the stiffening effects of rub, and typically raises the natural frequencies.) At this time, although not quantitatively resolved, the experimental results from multi–axial rubs support to a greater extent the presence of rub–generated subsynchronous (1/2)× components occurring at rotative speeds below twice first natural frequency. These experiments do not cover the range of rotative speeds much above twice first natural frequency, nor have more than two points of rub been investigated. These topics should be addressed during further research.

ADDITIONAL EXPERIMENTAL RESULTS OF THE MULTIPLE ROTOR–TO–STATOR RADIAL RUB CONTACTS AT ONE AXIAL LOCATION

The set of tests presented below illustrates results of multiple radial rotor-to-stator contacts at one axial location. A modified rub fixture is equipped with an electric contact device and a stationary rub block (Fig. 23). The half-cylinder area of possible rotor contact simulates a seal.
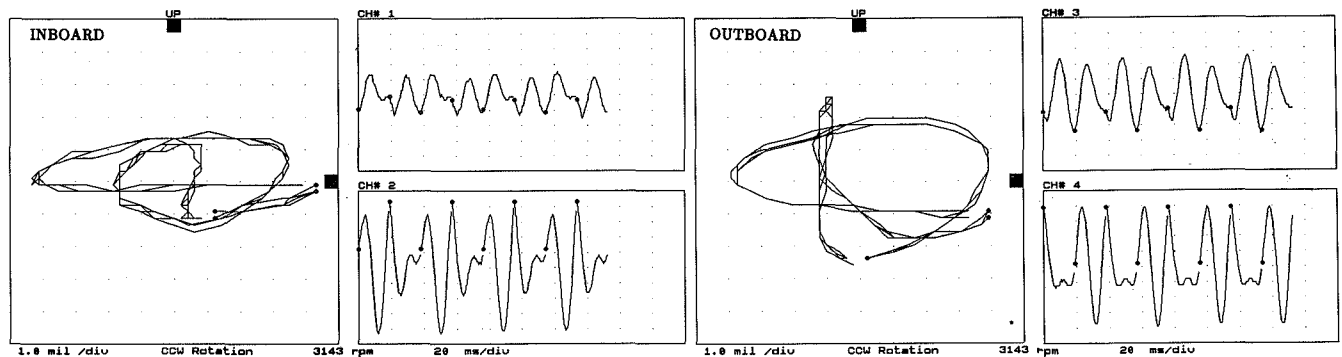
Figure 21. - Inboard and outboard rubbing rotor responses at the inboard and outboard locations at 3143 rpm. Orbits and timebase waves indicate presence of 1× plus (1/2)× components.
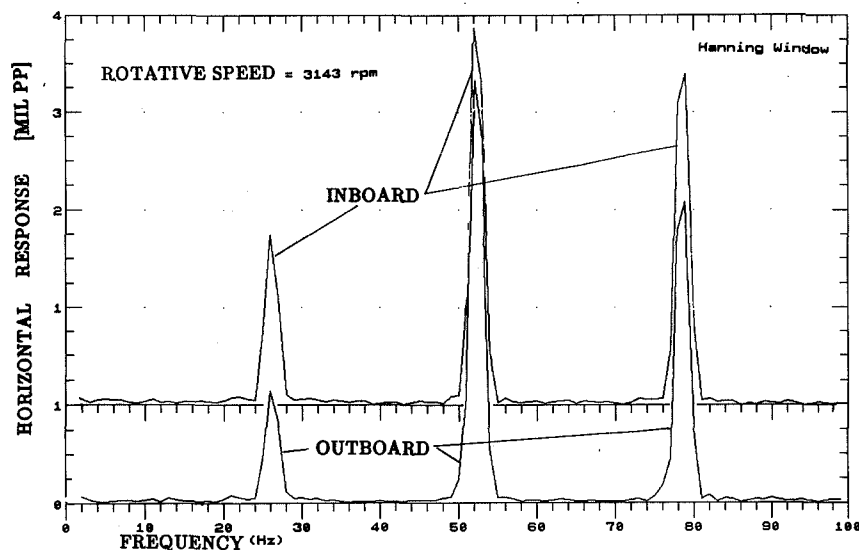
Figure 22. - Rubbing rotor vibration spectrum at 3143 rpm.

360

1.	EDDY CURRENT	5.	RUBBING SHAFT
	DISPLACEMENT PROBE	6.	TEST RUB BLOCK
2.	FIXTURE BODY	7.	ALIGNMENT PIN
3.	PLUNGER SHAFT	8.	POSITION AND PRELOAD ADJUSTERS
4.	COMPRESSION SPRING	9.	LINEAR ANTI–FRICTION BEARING
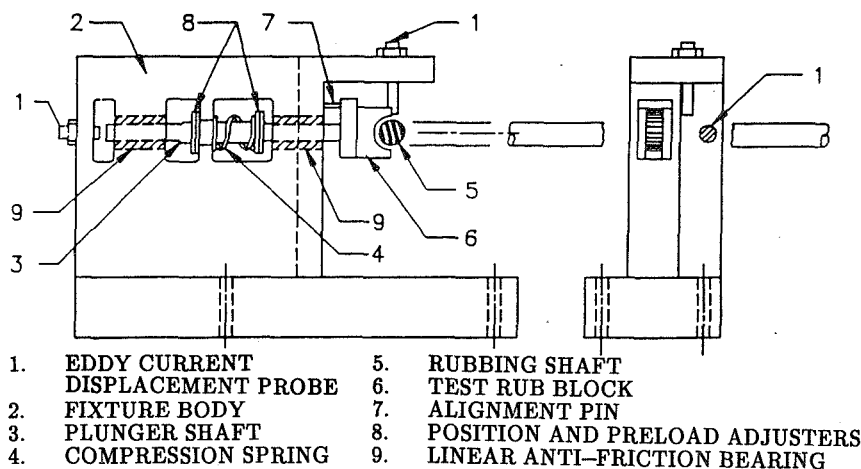
Figure 23.–Semi–circular rub fixture.

Rub may practically occur at several radial positions. Most often it occurred at two locations. The rotor–to–stator contact information during rubbing at the first balance resonance speed range has been reduced in terms of "dwelling" time ratio and contact phase ratio versus rotative speed (Fig. 24). The "ratio" was obtained by relating the actual contact time to the period of $1\times$ vibration at corresponding speeds. The $1\times$ vertical response amplitude and phase are overlayed on the graphs. Note that the rotor–to–stator contact time ratio versus rotative speed resembles in shape the $1\times$ amplitude, which suggests proportionality. Interesting is the contact phase, clearly following the $1\times$ response phase lag.

FINAL REMARKS

This paper presents experimental and computer simulated results of rotor vibrational responses during multiple partial rubbing against a stationary elements. The considered cases are characterized by "light" rub conditions for which predominant in rotor responses are impacting/rebounding phenomena. The rotor/stator contact takes a small portion of the shaft rotational period so that the system stiffness increase effect is not high. The contact normal and friction forces are also relatively low. In continuation of previously studied rotor partial rub cases [2–6], this paper illustrates the rotor dynamic behavior when rubbing occurs at multiple axial locations of the shaft. It also emphasizes the importance of taking into account the shaft centerline position, as well as modal deflection line at specific rotative speeds for adequate identification of rotor–to–stator rub occurrences.

REFERENCES

1. Muszynska, A.: Rotor–to–Stationary Element Rub–Related Vibration Phenomena in Rotating Machinery, Literature Survey, The Shock and Vibration Digest, v. 21, No. 3, March 1989.

2. Muszynska, A., Bently, D. E., Franklin, W. D., Hayashida, R. D., Kingsley, L. M., and Curry, A. E.: Influence of Rubbing on Rotor Dynamics, NASA Contract No. NAS8–36719, Final Report, Bently Nevada Corporation, March 1989.

3. Muszynska, A.: Partial Lateral Rotor–to–Stator Rub, Third International Conference on Vibrations in Rotating Machinery, C281/84, IMechE, York UK, 1984.

361
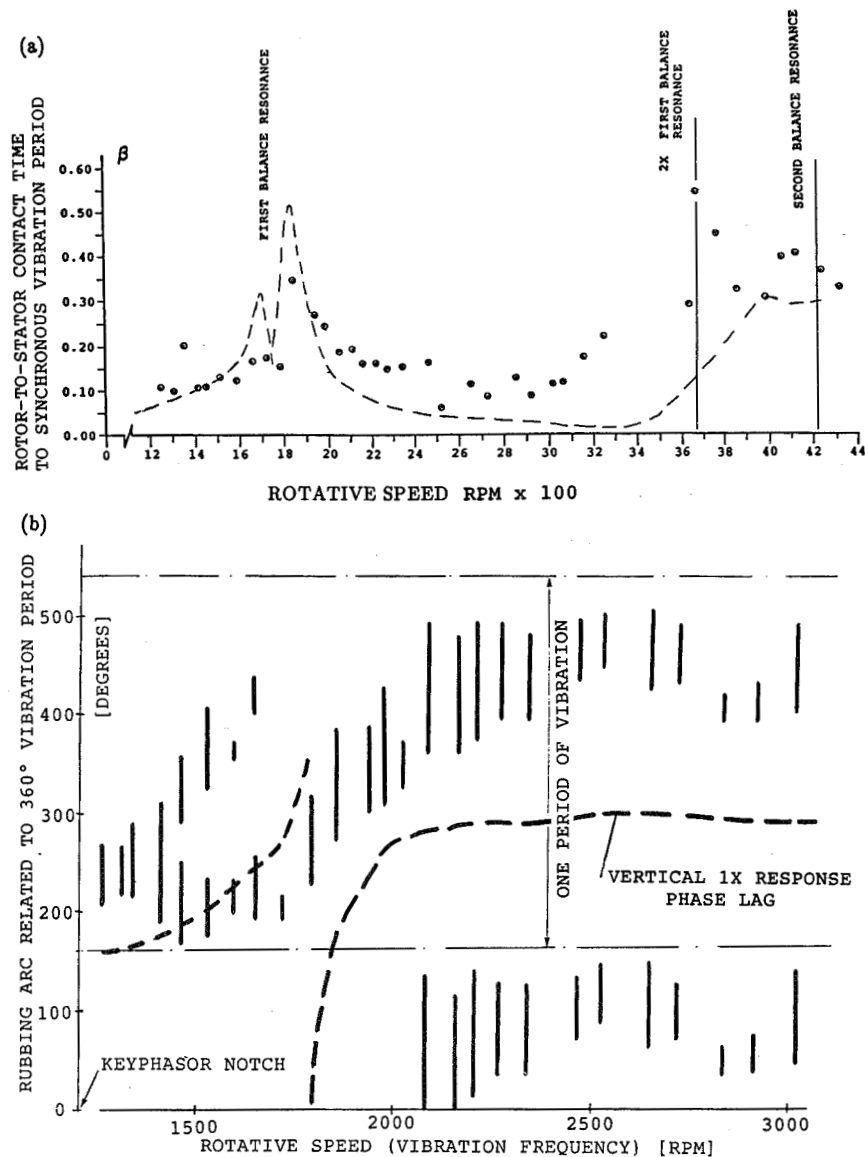
Figure 24. - (a) Rotor-to-stator contact in terms of the amount of shaft revolutions $\beta = \Omega t_c$ (t_c = contact time); (b) rub contact arc related to generalized vibration period versus rotative speed.

4. Muszynska, A.: Synchronous and Self–Excited Rotor Vibrations Caused by a Full Annular Rub, Eight Machinery Dynamics Seminar, NRC, Halifax N.S. Canada, 1984.

5. Muszynska, A., Bently, D. E., Franklin, W. D., and Hayashida, R. D.: Identification of Modal Parameters of Rotating Systems Using Perturbation Techniques, Part 1 and Part 2, Twelfth Biennial ASME Conference on Mechanical Vibration and Noise, Montreal, Canada, September 17–20, 1989.

6. Bently, D. E.: Forces Subrotative Speed Dynamic Action of Rotating Machinery, ASME Publication 74–DET–16, 1974.

THE ROCKETDYNE MULTIFUNCTION TESTER –
PART I: TEST METHOD*

B.T. Murphy, Joseph K. Scharrer, and Robert F. Sutton
Rockwell International
Canoga Park, California 91304, U.S.A.

The Rocketdyne Multifunction Tester is a general purpose test apparatus which utilizes axial and radial magnetic bearings as shaft excitation devices. The tester is modular in design so that different seal and bearing packages can be tested on the same test stand. The tester will be used for rotordynamic coefficient extraction, as well as life and fluid/material compatibility evaluations. Use of a magnetic bearing as a shaft excitation device opens up many possibilities for shaft excitation and rotordynamic coefficient extraction. In addition to describing the basic apparatus, this paper will discuss some of the excitation and extraction methods considered, and detail the chosen method. Some of the excitation methods to be discussed include random, aperiodic, harmonic, impulse and chirp.

INTRODUCTION

Recent trends in the design of high-performance turbomachinery for advanced pump-fed liquid rocket engines have moved away from rolling element bearings in favor of fluid film elements. The potential payoffs are longer life, higher admissible DN values, and more control over turbopump rotordynamics. Hydrostatic bearings and annular seals appear most promising. In effort to support the new designs, Rocketdyne has designed, and is currently fabricating, a multifunction bearing and seal tester. The goals are to measure accurate rotordynamic coefficients, conduct durability tests, and evaluate different materials, all in an environment simulating real cryogenic turbopump operating conditions. Measurement of rotordynamic coefficients is accomplished via the use of a radial magnetic bearing as a shaft motion exciter. Test bearing (or seal) reaction load is measured in the support structure. The versatility of the magnetic bearing as an exciter is the key feature of this tester.

The purpose of this article is to describe the basic methods which will be used to excite the shaft, acquire the data, and reduce the data. All three of these tasks are to be performed by a single computer. The tester is designed to run the test bearing (or seal) at a constant operating point, and use the magnetic bearing to excite the shaft in a manner suitable to permit identification of the bearing's (or seal's) complex impedance functions.

The impedance functions then yield the desired rotordynamic stiffness, damping and mass coefficients.

The application of a magnetic bearing in this manner is novel, thus there is a degree of uncertainty as to how well it will function, and what the optimum input signal will be (i.e., random, aperiodic, harmonic, swept sine, impulse, step, chirp, etc.). The versatility of having a completely arbitrary waveform generator is, therefore, most important. Also, it is desirable that the input signal delivered to the magnetic bearing be adaptive so that optimum signal to noise ratios can be achieved.

The key constraint in this test program is length of test time. Many of the tests are limited to about 5 minutes each by virtue of the blow down facility being used. In all, approximately 35 such tests are currently planned. These 35 tests are divided among different seals, different bearings, and different working fluids. Each 5 minute test must encompass a multitude of operating points (combinations of shaft speed, pressure drop, inlet swirls, eccentricities, etc.). Presently, only about 20 seconds of test time are being allotted to each operating point for measurement of rotordynamic coefficients. The chosen input signal must make optimum use of this limited amount of time.

DESCRIPTION OF APPARATUS

The multifunction tester, configured with an annular seal, is shown in figure 1. The tester consists of the basic tester and a module containing the test article. The basic tester rotor is supported on one end by a duplex ball bearing and on the other by the magnetic bearing. The module contains the test article only. When assembled, the main rotor supports are the duplex ball bearing and the test article, use of the magnetic bearing as a support is optional as discussed by Hawkins, et al. (ref. 1).

The main function of the magnetic bearing is to generate asynchronous motion of the rotor at the test article. The reaction force at the test article is measured using a calibrated cylindrical spring called a flexmount. The deflection of the flexmount under load is measured using four Bently REBAM proximity probes. The acceleration of the flexmount is measured in two orthogonal directions using PCB accelerometers. The motion of the rotor at the test article is measured using Bently proximity probes.

The initial test plan calls for testing of a 152.4 mm (6.0 inch) diameter annular seal, a 88.9 mm (3.5 inch) diameter hydrostatic bearing, and a 57 mm (2.24 inch) ball bearing in LN2 and actual cryogenic propellants. The annular seal will be tested at three different values of inlet swirl. The tester will operate at speeds up to 24,000 cpm and supply pressures to 172.4 Bar (2500 psi), for this test series. The maximum tester design speed is 30,000 cpm. The geometries for the test articles will reflect those envisioned for production rocket engine turbomachinery. This requires radial clearances in the range of 0.076-0.127 mm (0.003-0.005 inches), whereas all test results to date are for radial clearances in the range 0.254-0.508 mm (0.010-0.020 inches) and at lower shaft speeds.

FUNDAMENTALS OF ROTORDYNAMIC
COEFFICIENT MEASUREMENT

The standard relationship between bearing displacements and forces in the time domain is expressed as follows:

$$[M]\ddot{q} + [C]\dot{q} + [K]q = F \tag{1}$$

Rotors operating at steady state execute motions which are strongly periodic (i.e, harmonic). This lends itself to a frequency domain representation. Also, from a test point of view, it is more convenient to work in the frequency domain. Thus, transforming equation (1) to the frequency domain and employing complex notation (equivalent to amplitude and phase) results in

$$\begin{bmatrix} (K_{xx} + iC_{xx}\omega - M_{xx}\omega^2) & (K_{xy} + iC_{xy}\omega - M_{xy}\omega^2) \\ (K_{yx} + iC_{yx}\omega - M_{yx}\omega^2) & (K_{yy} + iC_{yy}\omega - M_{yy}\omega^2) \end{bmatrix} \begin{Bmatrix} \bar{x} \\ \bar{y} \end{Bmatrix} = \begin{Bmatrix} \bar{F}_x \\ \bar{F}_y \end{Bmatrix} \tag{2a}$$

or

$$\begin{bmatrix} Z_{xx} & Z_{xy} \\ Z_{yx} & Z_{yy} \end{bmatrix} \begin{Bmatrix} \bar{x} \\ \bar{y} \end{Bmatrix} = \begin{Bmatrix} \bar{F}_x \\ \bar{F}_y \end{Bmatrix} \tag{2b}$$

In the usual sense, the physical displacement in the x direction is the real part of the complex expression $\bar{x}e^{i\omega t}$ and similarly, for y, F_x and F_y. The complex impedances, Z, come directly from measurements of $\bar{x}$, $\bar{y}$, $\bar{F}_x$ and $\bar{F}_y$, all presumably as functions of frequency. The displacements x and y are usually obtained easily with non-contacting displacement probes. The forces F_x and F_y are more difficult, and may be measured directly with special load cells, or inferred indirectly from some other known quantities such as pressure distribution, a hammer impulse, intentional unbalance, or the snap of a suddenly released static load. Once the displacements and forces are obtained as functions of frequency, the exact procedure for obtaining the impedances Z, and in turn, the rotordynamic coefficients, depends on how the displacements and forces were generated (i.e., the overall test approach). The reduction procedures for several test approaches considered for the multifunction tester will now be described.

Single Circular Orbits - A very natural approach is to use the magnetic bearing to impart a circular whirl orbit to the rotor, and vary its frequency over the frequency range of interest (rotor speed held constant). In this case $\bar{y} = \bar{x}e^{-i\frac{\pi}{2}}$ (counterclockwise orbit) at each value of frequency giving the following:

$$Z_{xx} + Z_{xy}e^{-i\frac{\pi}{2}} = \frac{\bar{F}_x}{\bar{x}} = K_{xx} + C_{xy}\omega - M_{xx}\omega^2 - i(K_{xy} - C_{xx}\omega - M_{xy}\omega^2)$$

$$Z_{yx} + Z_{yy}e^{-i\frac{\pi}{2}} = \frac{\bar{F}_y}{\bar{x}} = K_{yx} + C_{yy}\omega - M_{yx}\omega^2 - i(K_{yy} - C_{yx}\omega - M_{yy}\omega^2) \tag{3}$$

The $\bar{x}$, $\bar{F}_x$ and $\bar{F}_y$ data obtained for a single circular orbit are not sufficient to completely determine all 4 complex Z's. However, the special shape of the orbit does permit

their partial determination by grouping of their real and imaginary components as shown. The 4 components (real and imaginary parts of $\bar{F}_x/\bar{x}$ and $\bar{F}_y/\bar{x}$) can be plotted versus frequency, and curve fits yield the 12 desired rotordynamic coefficients. Note that all 12 coefficients must be real which precludes the detection of mechanisms like hysteretic damping. Note also that there is no benefit to assuming skew symmetric stiffness, damping and mass matrices. The only information obtained as to the adequacy of the assumed KCM model is via digression from a pure quadratic. This test approach is used by Adams, et al. (ref. 2).

Dual Circular Orbits - The magnetic bearing is capable of producing either forward or backward circular whirl orbits at each frequency (not simultaneously). This forms 2 independent load cases which, when used together, completely determines all 4 complex Z's at each test frequency.

$$\begin{bmatrix} \bar{x}_f & \bar{y}_f & 0 & 0 \\ 0 & 0 & \bar{x}_f & \bar{y}_f \\ \bar{x}_b & \bar{y}_b & 0 & 0 \\ 0 & 0 & \bar{x}_b & \bar{y}_b \end{bmatrix} \begin{Bmatrix} Z_{xx} \\ Z_{xy} \\ Z_{yx} \\ Z_{yy} \end{Bmatrix} = \begin{Bmatrix} \bar{F}_{xf} \\ \bar{F}_{yf} \\ \bar{F}_{xb} \\ \bar{F}_{yb} \end{Bmatrix} \qquad \begin{array}{l} f = forward \\ b = backward \end{array} \qquad (4)$$

The 8 components are plotted versus frequency, and curve fits yield the desired rotordynamic coefficients which can now all be complex. This test approach was used by Kanki, et al. (ref. 3). Note that it is better to combine the forward and backward data to completely determine the Z's over the frequency range from f_{low} to f_{high}, rather than keeping them separate and using equation (3) to partially determine the Z's from $-f_{high}$ to $+f_{high}$ (see Ohashi, et al. (ref. 4) and Jery, et al. (ref. 5)). This same conclusion was also reached by Bolleter, et al. (ref. 6). Note also that forward and backward circular orbits taking place at the same time form an ellipse, but a single ellipse is a single load case and does not completely determine the Z's (see below).

The technique of actually plotting and inspecting the impedance functions versus frequency, followed by a curve fit, provides insight into the mechanisms at work, and also experimental scatter. The importance of this visualization apparently has been overlooked by some researchers. As opposed to plotting and curve fitting the impedance functions, the force and displacement data for some or all frequencies can be assembled into a single matrix equation as follows (i.e., rearrangement of the terms of equation (2a)):

$$[displacement\ data\ matrix]\{KCM\ vector\} = \{force\ data\} \qquad (5)$$

$$[4 * \#\ frequencies\ by\ 12]\{12\ by\ 1\} = \{4 * \#\ frequencies\ by\ 1\}$$

The 12 real rotordynamic coefficients are computed directly by either using a subset of the data to write exactly 12 equations (Adams, et al. (ref. 2)), or using all the data and performing a least squares solution (Nordman, et al. (ref. 7), Goodwin, et al. (ref. 8), and Burrows, et al. (ref. 9)). The latter approach will produce rotordynamic coefficients identical to those produced by plotting and curve fitting, but without the benefit of seeing this graphically.

366

Another approach to bypassing the impedance functions and proceeding directly to 12 unknown rotordynamic coefficients is to use a recursive estimation scheme on time domain data (Stanway (ref. 10), Sahinkaya, et al. (ref. 11), and Ellis, et al. (ref. 12)). This should yield a result similar, if not identical, to the frequency domain approach of equation (5). Among its advantages are transformation to the frequency domain with its associated windowing functions is not needed, rotordynamic coefficients can conceivably be computed on-line during test (i.e., like a filter), and it is an effective way to deal with time varying parameters (Goodwin and Payne (ref. 13)). Again, however, there is will be no graphical check on the validity of the KCM model.

Single Elliptic Orbit - The magnetic bearing can also be used to impart elliptic motion to the rotor, and vary its frequency over the frequency range of interest (rotor speed held constant). Data for a single elliptic orbit contains the same amount of information as a single circular orbit, but must be utilized differently because of its different form. For example, to use the technique of equation (3), $\bar{y}/\bar{x}$ must be constant. The displacement orbit must have a constant ratio of major to minor axis length, and must have constant orientation. It is probably not practical to satisfy these conditions. Instead, the approach of equation (5) could be used to directly compute 12 real rotordynamic coefficients. In this case it is desirable that the displacement ellipse be highly variable as a function of frequency to get the best definition of the rotordynamic coefficients. In fact, the further removed from a circle the data becomes, the more important it is that the ellipses be highly varied. It can be shown that the limiting case of a constant, purely translational orbit would render the matrix of equation (5) singular. When solving the least squares form of equation (5) it is best to use a Singular Value Decomposition (SVD) algorithm (Forsythe, et al. (ref. 14)) to get a direct indication of the quality of the solution (i.e., the matrix condition number). One can also use the statistical parameters employed by Burrows, et al. (ref. 9) to help quantify the accuracy of the least squares solution. It is interesting to note that some simple numerical experiments on equation (5) have shown that varied elliptic data can easily yield a solution twice as good as circular data. In exchange for the more precise solution, however, it is no longer possible to plot impedance functions versus frequency to provide a visual check of the validity of the KCM model.

Another approach to utilizing data for one ellipse per frequency is to assume the impedances to be skew symmetric (i.e., $Z_{xx} = Z_{yy}$ and $Z_{xy} = -Z_{yx}$). In this case equation (2b) becomes (see Bolleter, et al. (ref. 6)):

$$\begin{bmatrix} 1 & \bar{a} \\ -\bar{a} & -1 \end{bmatrix} \begin{Bmatrix} Z_{xx} \\ Z_{xy} \end{Bmatrix} = \begin{Bmatrix} \bar{F}_x/\bar{x} \\ \bar{F}_y/\bar{x} \end{Bmatrix} \qquad \bar{a} = \frac{\bar{y}}{\bar{x}} \tag{6}$$

As long as $\bar{a}$ is not $\pm i$ (i.e., not a circle), the two complex impedances can be computed using Cramer's rule, and plotted versus frequency. The plots provide a check on the KCM model, and curve fits yield 6 complex rotordynamic coefficients (K_{xx}, C_{xx}, M_{xx} and K_{xy}, C_{xy}, M_{xy}). The coefficients would be expected to be real, but need not be. For example Bolleter, et al. (ref. 6) detected hysteretic damping (complex K_{xx}) in boiler feed pump impellers using this approach. Note that the orbit must be elliptic. As $\bar{a}$ approaches $\pm i$ the solution for Z_{xx} and Z_{xy} becomes ill-defined, and is undefined when $\bar{a} = \pm i$. The following expression is an amplification factor for uncertainties in both $\bar{x}$ and $\bar{y}$:

$$f = \frac{1}{2(|a| - 1)} \tag{7}$$

If there is 5% uncertainty in $\bar{x}$ then there is f*5% uncertainty in Z_{xx} and Z_{xy}. The need to avoid circles in this case is apparent. One other potential drawback of assuming skew symmetric impedances is what happens when this assumption is violated. For example, if K_{xx} equals 90% of K_{yy} this could manifest itself as a bias in K_{xy}, or produce seemingly significant amounts of C_{xy} when in fact there is none.

Dual Elliptic Orbits- The magnetic bearing could be used to produce two different elliptic orbits at each test frequency (not at the same time). This forms two independent load cases, and is analogous to the case of forward and backward circles described earlier. In fact, the forward and backward circles is a special case of 2 ellipses. When using two ellipses it is imperative that they be independent so that the 4 Z's can be computed employing equation (4) for each frequency. The condition number (Forsythe, et al. (ref. 14)) of the matrix in equation (4) quantifies the degree of independence. The following expression due to Zhang, et al. (ref. 15) can be used to calculate the condition number at each frequency:

$$COND = \frac{B + \sqrt{B^2 - 4|\bar{x}_2\bar{y}_1 - \bar{y}_2\bar{x}_1|}}{B - \sqrt{B^2 - 4|\bar{x}_2\bar{y}_1 - \bar{y}_2\bar{x}_1|}} \tag{8}$$

where $B = |\bar{x}_1| + |\bar{x}_2| + |\bar{y}_1| + |\bar{y}_2|$. The condition number is similar to f of equation (7), and in this case is an upper limit on amplification of error. The minimum, or optimum, value is 1 which occurs only with orthogonal translational orbits of equal amplitudes. The maximum value is infinite which occurs with identical orbits (can have different sizes). A pair of forward and backward circular orbits of equal radius yields a condition number of 5.83. Adequate solutions to equation (4) can be plotted versus frequency for subsequent inspection and curve fitting. Excessive condition numbers will make the impedance curves appear "noisy" regardless of the actual signal/noise ratios. This latter fact is easily overlooked. When the condition number is too high one must resort to the techniques for single elliptic data. Numerical experiments presented by Zhang, et al. (ref. 15) dictate that a practical cutoff on condition number may be about 20 to 30.

It has been suggested that the 4 stiffness and 4 damping values (no inertia) can be obtained solely from unbalance response data at a single speed (Lund (ref. 16), Zhang, et al. (ref. 15), Lee, et al. (ref. 17) and related paper by Verhoeven (ref. 18)). This fits the two ellipse case for a single frequency. Either two identical bearings on one shaft must experience different elliptic orbits simultaneously under the action of a single unbalance distribution, or one bearing must experience different ellipses at the same speed under two different unbalance distributions. Either case can apparently be achieved in practice with a carefully designed experiment. The degree of success will depend not only on the accuracy of the bearing displacements and forces, but also on the value of the condition number of equation (8).

CURRENT TEST APPROACH

In light of the preceding discussion, it has been decided that, if possible, a test approach would be used which enables plotting of impedance functions versus frequency without assuming skew symmetry. This implies either the single circular orbit approach, or dual elliptic orbit approach. The dual elliptic approach is preferable as it completely determines the impedance functions, but may require twice the test time as the single circular approach. As mentioned earlier the length of test time is severely limited. So arbitrarily large numbers of samples will not be available for averaging out system noise. As a first step we will attempt to achieve purely translational rotor motion first in one axis and then the other. This would provide the most accurate impedance determination possible according to equation (8). The system may, however, prove to be too noisy such that there is not ample time to get enough averages when executing the two load cases sequentially. Burrows, et al. (ref. 9) and Yasuda, et al. (ref. 19) applied their load cases simultaneously via alternating harmonics and statistical independence, respectively. If necessary, we will try the method of Burrows, but at this time it is unclear whether these are viable ways to overcome a problem of insufficient averaging time. If the impedance measurements still suffer from excessive noise, we will resort to the single circular orbit approach. Should it happen that the magnetic bearing cannot satisfactorily enforce a circular orbit, we shall use the method of single elliptic data. Depending on the overall success, or lack thereof, of the current test program, future testing may employ recursive time domain methods mentioned earlier.

EXCITATION SIGNAL

The radial magnetic bearing serves as a non-contacting, dual-axis electrodynamic shaker. Its power supply has an input jack for each axis such that it can perform as 2 independent shakers. In actuality the magnetic bearing system is unproven in this regard, and at this time it still remains to be seen how well it will perform this function. Our goal is to measure the transfer functions of bearing force to bearing displacement. Since test time is at a premium, the input signal should provide a good combination of accuracy and rapidity. Another consideration is the frequency range of interest will span up to 4 system resonances which will be functions of pressure drop, shaft rpm, etc. The magnetic bearing system itself also has highly nonlinear frequency response characteristics (Hawkins, et al. (ref. 1)). It is desirable that the input signal can be spectrally shaped in an adaptive fashion so a flat displacement spectrum can be achieved on output. This will enable higher signal to noise ratios over the entire frequency range without overloading the system at the resonances. A flat displacement spectrum also makes it easier to investigate amplitude dependent nonlinearities by driving the system to progressively higher response levels.

Single frequency steady state sinusoidal testing is unquestionably the best way to fit a linear model to a real system (Herlufsen (ref. 20)), but the long test time precludes its use here. Fortunately, work by Bolleter, et al. (ref. 6), Yasuda, et al. (ref. 19) and Chang, et al. (ref. 21) indicate that a multifrequency input signal gives virtually identical results as single frequency testing. Yasuda's testing was steady state as they used random input signals. Bolleter's testing was transient as he used a rapid sine sweep, or chirp. Chang's testing was also transient as he used impact. The article by Herlufsen (ref. 20)

discusses some of the aspects, and different types, of steady state and transient testing. Since we intend to modify the input signal during test in an adaptive fashion to achieve a flat displacement spectrum, a transient signal is the logical choice.

Step (Morton (ref. 22)), impulse (Nordman, et al. (ref. 7)) and chirp (Bolleter, et al. (ref. 6)) are examples of transient input signals. Bolleter obtained excellent results using a chirp input. Also, the spectrum of a chirp can be easily shaped to virtually any desired form. Papers by White, et al. (ref. 23) and White (ref. 24) provide the technical aspects of using a chirp input signal. The chirp is thus our chosen input signal (see figure 2). Our test approach will be to input a series of chirps along one axis including the modification of each successive chirp to converge on a flat displacement spectrum. This is then repeated along the other axis. Very elongated elliptic orbits should result as long as the rotordynamic cross- coupling is not too strong. This data will then be used with the dual elliptic reduction method described earlier.

DATA ACQUISITION AND PROCESSING

A digital computer will be used to sample, and store on-line, all data channels necessary to produce rotordynamic coefficients. Prior to testing, a common broadband random signal will be input simultaneously to all channels of the data acquisition system. Interchannel transfer functions thus obtained will be used as correction factors to match the gain and phase of all channels, including filters. The same computer system will be used to compute and output the chirp signals. The computer system is capable of performing an on-line spectral analysis of the displacement response, and modifying each successive chirp accordingly.

The complex quantities $\bar{x}$, $\bar{y}$, $\bar{F}_x$ and $\bar{F}_y$ are needed for equation (4) so that the impedances can be calculated. The effects of system noise can be more effectively reduced if one works with transfer functions computed from spectral densities (see Bendat, et al. (ref. 25) or Halvorsen, et al. (ref. 26)). Thus in practice the computer will be used to compute cross and auto spectral densities from each series of chirps. These are used to compute transfer functions $\bar{F}_x/\bar{x}$, $\bar{F}_x/\bar{y}$, $\bar{F}_y/\bar{x}$ and $\bar{F}_y/\bar{y}$ as functions of frequency. For each frequency these 8 complex values (4 from the x chirps and 4 from the y chirps) are used with equation (4) to compute the complex impedances, Z. All calculations are to be done post-test by the same computer used for acquisition. Hard copy plots of the impedance functions, along with curve fits for rotordynamic coefficients, are the end product of each test.

SUMMARY

A multifunction test apparatus has been described which will be used to measure rotordynamic coefficients of bearings and seals. A radial magnetic bearing will be used to load the shaft statically and excite dynamic motion of the rotor in a controlled fashion which will enable complete definition of the test element's rotordynamic impedances as functions of frequency. Transient testing will be performed with chirp input signals being applied separately to the inertial x and y axes of the rotor. The chirp input signals will be modified on-line to achieve flat displacement spectrums at the test element. The test approach and the data reduction methodology were described in detail. The testing environment closely matches real rocket engine turbopump operating conditions in speed, pressure, clearance,

temperature, working fluid, etc. Overall, this is considered a very ambitious test program, technically. Initial testing is currently expected to take place in the summer of 1990.

NOMENCLATURE

$\bar{a}$	$\bar{y}/\bar{x}$
B	$|\bar{x}_1| + |\bar{x}_2| + |\bar{y}_1| + |\bar{y}_2|$
COND	matrix condition number
F	$\{F_x, F_y\}^T$
F_x, F_y	real test element force
$\bar{F}_x, \bar{F}_y$	complex test element force
f_{low}, f_{high}	limits of test frequency range
f	error amplification factor
K	test element stiffness matrix
C	test element damping matrix
M	test element inertia matrix
KCM	stiffness, damping and inertia
q	$\{x, y\}^T$
x,y	real displacements of test element
$\bar{x}, \bar{y}$	complex displacements of test element
Z	complex impedance of test element
i	$\sqrt{-1}$
ω	frequency of harmonic motion (rad/sec)
$|\bar{x}|$	magnitude of complex number $\bar{x}$

REFERENCES

1. Hawkins, L., Murphy, B. and Lang, K., "The Rocketdyne Multifunction Tester - Part II: Operation of a Radial Magnetic Bearing as an Excitation Source," Workshop on Rotordynamic Instability Problems in High Performance Turbomachinery, Texas A&M University, May, 1990.

2. Adams, M., Makay, E. and Diaz-Tous, I., "Measurement of Interstage Fluid-Annulus Dynamical Properties," Workshop on Rotordynamic Instability Problems in High Performance Turbomachinery, Texas A&M University, NASA CP2250, May, 1982, pp. 147-156.

3. Kanki, H. and Kawakami, T., "Experimental Study on the Static and Dynamic Characteristics of Screw Grooved Seals," ASME Publication DE-Vol. 2, *Rotating Machinery Dynamics*, Volume 1, Sept., 1987, pp. 273-278.

4. Ohashi, H. and Shoji, H., "Lateral Fluid Forces Acting on a Whirling Centrifugal Impeller in Vaneless and Vaned Diffuser," Workshop on Rotordynamic Instability Problems in High Performance Turbomachinery, Texas A&M University, NASA CP2338, May, 1984, pp. 109-122.

5. Jery, B., Acosta, A., Brennan, C. and Caughey, T., "Hydrodynamic Impeller Stiffness, Damping and Inertia in the Rotordynamics of Centrifugal Pumps," Workshop on Rotordynamic Instability Problems in High Performance Turbomachinery, Texas A&M University, NASA Conference Publication 2338, May, 1984, pp. 137- 160.

6. Bolleter, U. and Wyss, A., "Measurement of Hydrodynamic Interaction Matrices of Boiler Feed Pump Impellers," ASME Paper No. 85-DET-148, Sept., 1985.

7. Nordmann, R. and Massmann, H.,"Identification of Dynamic Coefficients of Annular Turbulent Seals," Workshop on Rotordynamic Instability Problems in High Performance Turbomachinery, Texas A&M University, NASA CP2338, May, 1984, pp. 295-311.

8. Goodwin, M. J., Penny, J. E. T. and Hooke, C. J., "Hydrostatic Supports for Rotating Machinery - Some Aspects of Oil Film Non-Linearity," ASME Paper No. 85-DET-123, Sept., 1985.

9. Burrows, C., Kucuk, N., Sahinkaya, M. and Stanway, R., "Estimation of Squeeze-Film Bearing Inertia, Damping and Stiffness Coefficients," ASME Publication DE-Vol. 2,*Rotating Machinery Dynamics*, Volume 1, Sept., 1987, pp. 109-114.

10. Stanway, R., "Journal Bearing Identification Under Operating Conditions," ASME Journal of Dynamic Systems, Measurement and Control, Vol. 106, 1984, pp. 178-182.

11. Sahinkaya, M. and Burrows, C., "Kalman Filters Applied to Time-Domain Estimation of Linearized Oil-Film Coefficients," I. Mech. E. Conference Publication 1984-10, Vibrations in Rotating Machinery, 1984, pp.109-118.

12. Ellis, J., Roberts, J. and Hosseini Sianaki, A., "A Comparison of Identification Methods for Estimating Squeeze-Film Damping Coefficients," ASME Journal of Tribology, Vol. 110, Jan., 1988, pp. 119-127.

13. Goodwin, G. and Payne, L., *Dynamic System Identification*, Academic Press, London, 1977.

14. Forsythe, G., Malcolm, M. and Moler, C., *Computer Methods for Mathematical Computations*, Prentice Hall, Englewood Cliff, New Jersey, 1977.

15. Zhang, Q., Lallement, G. and Fillod, R., "Identification of the Dynamic Characteristics of Oil Film Bearings," ASME Publication DE-Vol. 2, *Rotating Machinery Dynamics*, Volume 1, Sept., 1987, pp. 57-61.

16. Lund, J., "Evaluation of Stiffness and Damping Coefficients for Fluid-Film Bearings," *The Shock and Vibration Digest*, Vol. 11, No. 1, Jan., 1979, pp. 5-10.

17. Lee, C. and Hong, S., "Identification of Bearing Dynamic Coefficients by Unbalance Response Measurements," I. Mech. E., Part C, Vol. 203, 1989, pp. 93-101.

18. Verhoeven, J., "Excitation Force Identification of Rotating Machines Using Operational Rotor/Stator Amplitude Data and Analytical Synthesized Transfer Functions," ASME Publication DE-Vol. 2, *Rotating Machinery Dynamics*, Volume 1, Sept., 1987, pp. 207-214.

19. Yasuda, C., Kanki, H., Ozawa, Y. and Kawakami, T., "Application of Random Excitation Technique to Dynamic Characteristic Measurement of Bearing," Proceedings of the JSME, 1986, pp. 61-67.

20. Herlufsen, H., "Dual Channel FFT Analysis (Part I)," Bruel-Kjaer Technical Review No. 1-1984, 1984.

21. Chang, K., Chong, F. and Rowe, W., "Journal Bearing Vibration - a Comparison of Sinusoidal Excitation with Impact Excitation," Proceedings of the 1st European Sponsored Turbomachinery Conference, SAE No. 864965, 1986, pp. 83-89.

22. Morton, P., "The Derivation of Bearing Characteristics by Means of Transient Excitation Applied Directly to a Rotating Shaft," Dynamics of Rotors, Springer-Verlag, New York, 1975.

23. White, R. and Pinnington, R., "Practical Application of the Rapid Frequency Sweep Technique for Structural Frequency Response Measurement," Aeronautical Journal, May, 1982, pp. 179-198.

24. White, R., "Spectrally Shaped Transient Forcing Function for Frequency Response Testing," Journal of Sound and Vibration, 23(3), 1972, pp. 307-318.

25. Bendat, J. and Piersol, A., Engineering Applications of Correlation and Spectral Analysis, John Wiley and Sons, New York, 1980.

26. Halvorsen, W. and Brown, D., "Impulse Technique for Structural Frequency Response Testing," Sound and Vibration Magazine, Nov., 1977, pp. 8-21.
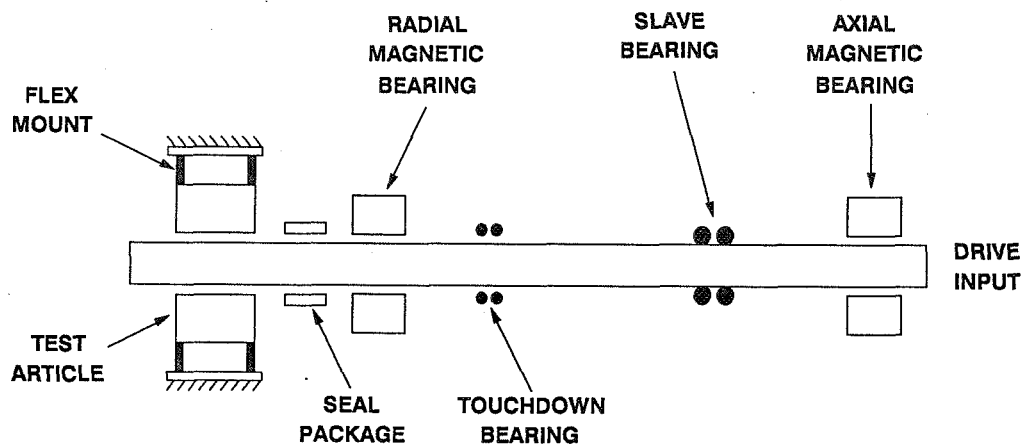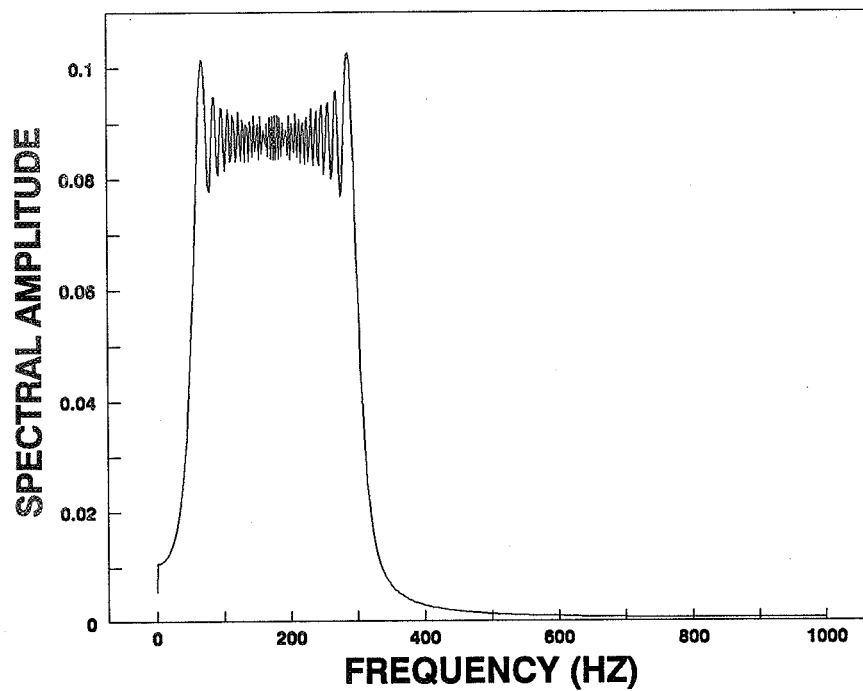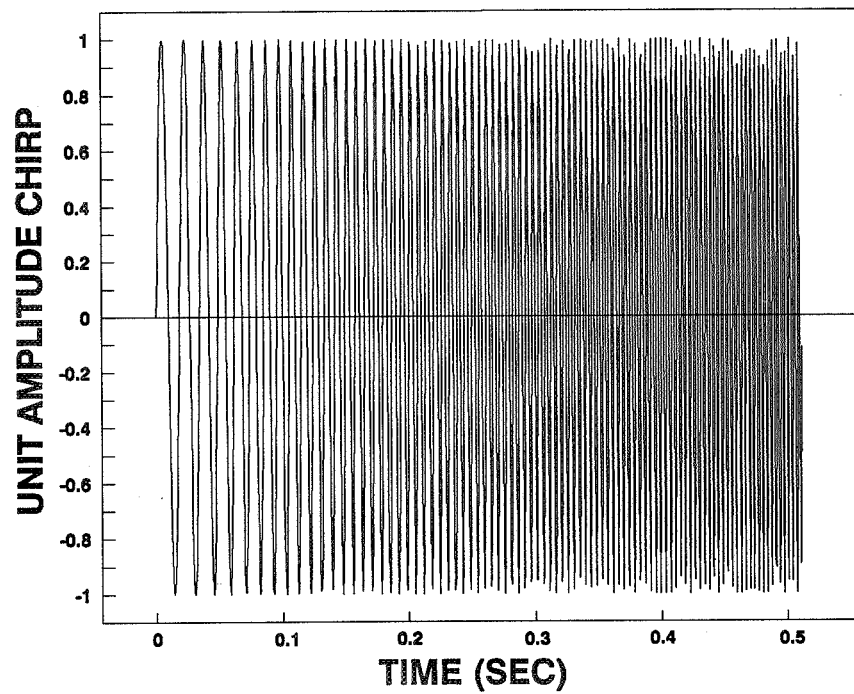
FIGURE 1) Schematic of multifunction tester.

FIGURE 2a) unit amplitude chirp, 50-350 Hz in 0.512 seconds,
2000 Hz sample rate. FIGURE 2b) amplitude spectrum of a).

THE ROCKETDYNE MULTIFUNCTION TESTER -
PART II: OPERATION OF A RADIAL MAGNETIC BEARING AS AN EXCITATION SOURCE*

L.A. Hawkins, B.T. Murphy, and K.W. Lang
Rockwell International
Canoga Park, California 91304, U.S.A.

The operation of the magnetic bearing used as an excitation source in the Rocketdyne Multifunction Tester is described. The tester is scheduled for operation during the summer of 1990. The magnetic bearing can be used in two control modes: 1) open loop mode, in which the magnetic bearing operates as a force actuator, and 2) closed loop mode, in which the magnetic bearing provides shaft support. Either control mode can be used to excite the shaft; however, response of the shaft in the two control modes is different due to the alteration of the eigenvalues by closed loop mode operation. A rotordynamic model is developed to predict the frequency response of the tester due to excitation in either control mode. Closed loop mode excitation is shown to be similar to the excitation produced by a rotating eccentricity in a conventional bearing. Predicted frequency response of the tester in the two control modes is compared, and the maximum response is shown to be the same for the two control modes when synchronous unbalance loading is not considered. The analysis shows that the response of this tester is adequate for the extraction of rotordynamic stiffness, damping, and inertia coefficients over a wide range of test article stiffnesses.

INTRODUCTION

Active magnetic bearings have been developed by numerous researchers for an increasing number of tasks. Schweitzer and Lange (ref. 1), Stanway and Burrows (ref. 2), and Salm and Schweitzer (ref. 3) have described strategies for using magnetic bearings to actively control the motion of a flexible rotor. Nikolajsen (ref. 4), Allaire (ref. 5), and Kasarda (ref. 6) have described the use of magnetic bearings as damping devices. The first commercially available magnetic bearing was introduced by Societe Europeenne de Propulsion/Societe de Mecanique Magnetique (SEP/S2M) of France in the early 1980s. Industrial applications of these bearings as primary bearings in rotating machinery have been described by Foster (ref. 7), Weise (ref. 8), and Brunet (ref. 9). Habermann and Brunet (ref. 10), Weise (ref. 11), Humphris (ref. 12), and Chen and Darlow (ref. 13) have presented details of practical magnetic bearing control systems. Chen (ref. 14) translated the parameters of a magnetic bearing control system into stiffness and damping coefficients for use in a rotordynamic analysis.

A radial magnetic bearing is used in the Rocketdyne Multifunction Tester (RMT) as

an excitation source for the identification of rotordynamic coefficients (ref. 15). The use of a magnetic bearing as an excitation source has been described by Ulbrich (ref. 16) and Wagner and Pietruszka (ref. 17). Wagner and Pietruszka used the magnetic bearing as a known force input device for the identification of rotordynamic coefficients in a test stand. In the RMT, the magnetic bearing is used as a motion input device, and test article reaction force is determined independently through a calibrated backup spring. The backup spring, or flex mount, has a stiffness of 5.25E+8 N/m (3.0 E+6 lb/in) and is instrumented with accelerometers and high resolution displacement probes. As an excitation source, the magnetic bearing must meet two requirements: 1) provide a shaft displacement at the test article of 1.25E-5 m (0.5 mils) minimum, and 2) provide a deflection of the flex mount of 1.25E-6 m (50 μin) minimum. These two requirements are necessary to provide adequate accuracy for the calculation of the rotordynamic coefficients. These requirements must be met over a large portion of the 0 – 400 Hz excitation range. The primary motivation for the study described here was to determine if the magnetic bearing would produce the necessary response at the test article.

The magnetic bearing used in the RMT can be used to excite the shaft in either of two control modes – closed loop or open loop. The response of the tester will be different in the two control modes; therefore, response to the two control modes is compared to determine which control mode produces the better response. Open loop excitation can be treated simply by applying a forcing function directly to the shaft (ref. 17). The authors are not aware of a published analysis of the magnetic bearing as an excitation source in closed loop mode. An analysis is presented here that shows closed loop excitation of a rotor to be analogous to a rotating eccentricity at a conventional bearing. The analysis is then used to predict the maximum frequency response of the RMT rotor to magnetic bearing excitation.

RADIAL MAGNETIC BEARING

A schematic for a simple magnetic bearing is shown in Figure 1. The magnetic force developed in the air gap of the magnetic bearing is given by

$$F = \mu A_p N^2 i^2 / 2h^2. \tag{1}$$

Since only the current, i, and the gap clearance, h, can change, this leads to the relation

$$\Delta F = -K_i \Delta i - K_y \Delta y \tag{2}$$

where for two pairs of magnetic poles, K_i and K_y are given by Kasarda (ref. 6) as

$$K_i = -(4\mu_0 A_p N^2 i_s)/(h_s^{\ 2}) \tag{3}$$

$$K_y = -(4\mu_0 A_p N^2 i_s^{\ 2})/(h_s^{\ 3}) \tag{4}$$

The current stiffness, K_i, is negative, indicating that an increase in current forces the mass away from its equilibrium position (toward the magnet), (ref. 12). The position stiffness, K_y, is also negative, indicating that a positive displacement toward the magnet forces the mass further from its equilibrium position. A net positive stiffness is provided in closed loop mode with proper

design of the control loop proportional gain. The radial magnetic bearing used in the RMT is an active magnetic bearing manufactured by SEP/S2M. The configuration and development testing of this magnetic bearing were described by Lang (ref. 18). The magnetic bearing is a force actuator and does not support the shaft when operated in open loop mode. When operated in closed loop mode, the magnetic bearing functions as a shaft support element that has significant stiffness and damping capability. Closed loop mode operation is required for some of the test conditions for stability reasons. The closed loop stiffness and damping coefficients of the magnetic bearing vary with frequency as given in Figures 2 and 3. These coefficients were calculated for the frequency range of interest from a transfer function provided by SEP/S2M. The position stiffness, K_y, was calculated to be $-8.76E+6$ N/m ($-50,000$ lb/in) using the nominal air gap and bias current. The maximum force that can be produced by the magnetic bearing with the rotor centered (nominal air gap) is given in Figure 4. Force capacity of the magnetic bearing is based on the maximum current that can be provided to the coils of the bearing. The force capacity is frequency dependent because the coil impedence is frequency dependent. A second constraint on magnetic bearing performance is relative rotor/housing displacement at the magnetic bearing. Maximum displacement at the magnetic bearing is 1.5E-4 m (6.0 mils) which is one-half of the air gap. The force and displacement constraints are the same for both closed loop and open loop modes.

CONTROL SYSTEM

A block diagram for the magnetic bearing controller is shown in Figure 5. In closed loop mode, the control current is determined by feedback control such that the error between a reference and actual shaft position signal is minimized. This control current is then fed to a current amplifier before going to the electromagnets of the bearing. The magnetic bearing can be used to excite the shaft by using a time varying reference signal.

Two equations that can be written from the block diagram are

$$y_c = y_a - y_o \qquad (5)$$

and

$$(F_d - y_c G(s)C_p K_i)/(ms^2 + K_y) = y_a \qquad (6)$$

It is necessary to characterize the effect of the reference signal, y_o, on the response of the rotor; therefore, let $F_d = 0$, implying no external disturbing forces such as unbalance.

Substituting Equation (6) into Equation (5) gives

$$(ms^2 + K_y + G(s)C_p K_i)y_a = G(s)C_p K_i y_o \qquad (7)$$

From Figure 5, the controlled stiffness of the bearing is

$$F_i/y_c = G(s)C_p K_i. \qquad (8)$$

This is a complex stiffness that can be represented by (ref. 13)

$$F_i/y_c = K_c + j\omega C \qquad (9)$$

377

where K_c and C are determined by the parameters of the control system, the current stiffness, and the excitation frequency. The position stiffness, K_y, is usually added to the controlled bearing stiffness so that the net stiffness of the magnetic bearing is

$$K = K_c + K_y. \tag{10}$$

The stiffness and damping coefficients given in Figures 2 and 3 are K in Equation 10 and C in Equation 9. Equation 7 may be written in terms of K and C as follows

$$(ms^2 + Cs + K)y_a = (Cs + K - K_y)y_0, \tag{11}$$

using equations 8, 9, and 10 and the substitution $j\omega = s$. If the position reference signal can be represented by

$$y_0 = Y_0 e^{j\omega t}, \tag{12}$$

then the sinusoidal component of the signal causes a shaft excitation that is similar to the shaft excitation caused by a rotating eccentricity (runout) at a conventional bearing. The position stiffness, K_y, is part of the response to the excitation but not part of the excitation; hence, it is subtracted from the total magnetic bearing stiffness, K, in the excitation term.

The feedback loop is deactivated for open loop mode operation. To excite the shaft in this mode, a control signal is fed directly to the current amplifier, C_p. The force produced is applied directly to the shaft, and no spring exists at the magnetic bearing location except for K_y.

ROTORDYNAMICS OF THE TESTER

The layout of the tester is shown in Figure 6. The shaft is supported radially by the test article, the radial magnetic bearing, and the slave bearings. In the configuration shown, the test article is a load sharing seal with stiffness variable from 0-1.75E+8 N/m (0-1,000,000 lb/in). The slave bearings form a duplex pair of angular contact ball bearings with stiffnesses of about 1.31E+8 N/m (750,000 lb/in) each as computed by the rolling element computer program of reference 19.

The mode shapes of the first three vibration modes of the tester are shown in Figure 7. A test article stiffness of 8.75E+7 N/m (500,000 lb/in) was used here, but the general character of the mode shapes is the same throughout the stiffness range to be tested. Figure 8 shows the first three forward natural frequencies of the tester as a function of test article stiffness. Results are shown for both closed loop and open loop mode operation of the magnetic bearing. These results are for a rotor speed of 20,000 cpm; however, the natural frequencies are not strongly dependent on rotor speed. The closed loop stiffness and damping coefficients of the magnetic bearing vary with the vibration mode frequency in accordance with Figures 2 and 3.

Damping for the first two vibration modes varies considerably depending on the test conditions, particularly when testing load sharing seals. Under many of the test conditions, the first two vibration modes of the tester are predicted to be unstable unless the magnetic bearing is used in closed loop mode. Therefore,

378

closed loop mode operation of the magnetic bearing is required for some of the test conditions.

TEST SIMULATION

The purpose of this analysis is to determine the response at the test article with the magnetic bearing used as an excitation source. Although closed loop mode operation must be used for some of the tests, performance of both operating modes was examined to determine if it would be advantageous to use open loop mode in some instances. In a typical test using the RMT, the rotor is driven at a constant operating speed. The desired test condition is then set for the test article. With closed loop mode operation, the rotor is excited by a frequency sweep of the reference signal, y_0. With open loop mode operation, the rotor is excited by a frequency sweep of a similar signal applied to the current amplifier of the bearing. Details of this procedure are described by Murphy (ref. 20).

The response of the rotor to closed loop mode excitation can be modelled using

$$[M]\ \ddot{q} - [G]\ \dot{\psi}\ \dot{q} + [K_r]q + [C_b]\dot{q} + [K_b]q = ([K_b] - [K_n])\ y_0 + [C_b]\ \dot{y}_0 \quad (13)$$

The matrix, $[K_n]$, has only one nonzero element -- the magnetic bearing position stiffness, K_y, which must be subtracted from the total magnetic bearing stiffness since it is not part of the excitation.

The excitation is represented by

$$y_0 = Y_0 e^{j\omega t}$$

and the response by

$$q = Q e^{j(\omega t + \phi)}.$$

As described above, the excitation signal (reference signal) forces the rotor in the same way as a rotating eccentricity at a conventional bearing. To simulate a test, the excitation is applied at the magnetic bearing degree-of-freedom to represent the dynamic reference signal, y_0, fed to the control system. The rotor spin speed, ψ, is held constant at the desired testing speed and all bearing elements other than the magnetic bearing are given constant values based on the constant rotor speed. Equation 13 is solved for various values of the excitation frequency, ω, to obtain the response of the rotor over the frequency range of interest.

Figures 9 - 12 show predicted results for a constant rotor speed of 20,000 cpm and a test article stiffness of 1.75E+7 N/m (100,000 lb/in). Figure 9 shows a comparison of predicted transfer function amplitudes at the test article for closed and open loop operation. The transfer function for the closed loop curve is calculated based on the excitation force produced by y_0. The transfer function for the open loop curve is calculated based on the forcing function applied at the magnetic bearing. The response of the first vibration mode is much lower with closed loop operation due to the higher damping.

In Figures 10-12, three constraints are placed on the system that determine the maximum response at the test article: 1) the magnetic bearing applied force, F_j,

379

cannot exceed the values given in Figure 4, 2) displacement at the magnetic bearing cannot exceed 1.5E-4 m (6.0 mils), and 3) based on clearance, the maximum allowable displacement at the test article is 1.0E-4 m (4.0 mils). The net force provided by the magnetic bearing in closed loop mode includes both the excitation force from y_0 and the reaction force due to the measured rotor motion. The force produced by the position stiffness, K_y, is not included in the constraint. The input signal varies with frequency as necessary to produce the maximum response at each frequency.

These three physical constraints serve to place an upper limit on tester response to magnetic bearing excitation. In addition, there are also two minimum conditions which must be satisfied. The two primary measured quantities of test article displacement and load must be large enough to be accurately measured with the given instrumentation. The lower limits are 1.25E-5 m (0.5 mils) of test article displacement and 1.5E-6 m (50 μin) of flex mount deflection. An appreciable range between the upper and lower operating limits is desirable so that tests on amplitude linearity could be performed.

Figure 10 is a comparison of the maximum response at the test article for closed and open loop modes. The response exceeds the requirement of 1.25E-5 m (0.5 mils) throughout the frequency range for both control modes. There appears to be only one curve in the figure because the responses are the same for the two control modes. The reason the curves are the same is that either of the first two constraints (force and displacement at the magnetic bearing) applied in the analysis serves to prescribe the rotor motion at the magnetic bearing regardless of the magnetic bearing stiffness and damping. The third constraint prescribes the motion at the test article. Since all of the constraints are the same for both control modes, the test article responses are identical.

Figure 11 shows the maximum displacement of the flex mount load sensing element. The curve is similar to that of Figure 10, and shows that the required displacement of 1.25E-6 m (50 μin) is achieved over most of the frequency range, regardless of control mode.

Figures 12 - 14 show predicted results for a constant rotor speed of 20,000 cpm and a test article stiffness of 1.3E+8 N/m (750,000 lb/in). Figure 12 shows a comparison of the predicted closed and open loop transfer function amplitudes at the test article. Again, response is lower with closed loop mode operation due to higher damping. A comparison of Figures 12 and 9 shows that test article response for a given force at the magnetic bearing is lower with the higher test article stiffness.

Figure 13 shows a comparison of the maximum response at the test article for closed and open loop modes. Again, the response is nearly the same for the two control modes, and the requirement of 1.25E-5 m (0.5 mils) displacement is met throughout most of the frequency range. A comparison of Figures 13 and 10 shows that the response at the test article is lower when the test article stiffness is higher.

Figure 14 shows the maximum displacement of the flex mount load sensing element. The required displacement of 1.25E-6 m (50 μin) is again achieved over most of the frequency range, regardless of control mode. By comparison of Figures 11 and 14, flex mount deflection is much higher with the higher test article stiffness.

Figures 10 and 13 show that the maximum response at the test article is the same for both open loop and closed loop modes. This result is due to the nature of the constraints that are placed on the analysis to determine the maximum response. This analysis does not consider the effect of synchronous loading due to unbalance. A given unbalance loading would cause a displacement response at the test article and at the magnetic bearing that would subtract directly from the allowable displacement at either location. The responses would be different for closed and open loop modes because the shaft eigenvalues are different in the two control modes. Also, a given unbalance loading would cause a reaction force at the magnetic bearing when the magnetic bearing is operated in closed loop mode. This reaction force would reduce the allowable magnetic bearing force available to excite the rotor. The net effect of unbalance is to lower the maximum achievable test article response in either control mode. This reduction in maximum test article response is minimized by operating the tester at spin speeds that are adequately distant from the rotor natural frequencies. Based on the maximum expected unbalance levels for the RMT, response due to unbalance should not exceed 1.0E-5 m (0.4 mils) at either the test article or the magnetic bearing for any of the planned test conditions with either operating mode. The closed loop reaction force at the magnetic bearing for the maximum expected unbalance force is about 330N (75 lbs), or less than 10% of the dynamic load capacity of the magnetic bearing. Therefore, the desired test article response levels should still be achieved.

CONCLUSIONS

An analysis was presented here that shows closed loop mode excitation of a rotor by a magnetic bearing to be analogous to the excitation produced by a rotating eccentricity at a conventional bearing. Open loop mode excitation can be treated simply by applying a forcing function directly to the shaft. These two methods were used to predict the maximum response of the Rocketdyne Multifunction Tester to magnetic bearing excitation in either control mode. The results show that the required response levels at the test article location are achievable over most of the frequency range. The analysis also predicts that maximum response will be the same for both open and closed loop modes. This result was due to the nature of the constraints that were used to determine maximum response. The analysis does not consider the effect of residual unbalance in the tester rotor. A synchronous unbalance loading would reduce, by differing amounts, the maximum test article response achievable in either control mode. Based on expected unbalance levels, the desired test article response levels should still be achieved.

NOMENCLATURE

A_p	=	cross section area of one pole of a magnetic bearing
C	=	magnetic bearing damping
$[C_b]$	=	bearing damping matrix
C_p	=	current amplifier gain
e	=	base of the natural logarithm
F	=	magnetic force in an air gap
F_d	=	any disturbance force, such as unbalance
F_i	=	net controlled force applied by magnetic bearing
$[G]$	=	rotor gyroscopic matrix
$G(s)$	=	controller closed loop transfer function
h	=	magnetic bearing air gap thickness
h_s	=	nominal magnetic bearing air gap thickness

381

i	=	current in magnetic bearing coil
i_c	=	control current
i_s	=	steady or bias current in magnetic bearing coil
j	=	square root of -1
K	=	net magnetic bearing stiffness
$[K_b]$	=	bearing stiffness matrix
K_c	=	magnetic bearing controlled stiffness
K_i	=	magnetic bearing current stiffness
$[K_n]$	=	magnetic bearing position stiffness matrix
$[K_r]$	=	rotor free/free stiffness matrix
K_y	=	magnetic bearing position stiffness
m	=	effective mass of the rotor
$[M]$	=	rotor mass matrix
N	=	number of turns in magnetic bearing coil
q	=	physical displacement vector
s	=	Laplace variable
t	=	time
y	=	vertical position
y_a	=	actual (measured) rotor position
y_c	=	error signal
y_o	=	position reference signal
ϕ	=	phase angle
ψ	=	rotor spin speed
μ	=	magnetic permeability
μ_o	=	magnetic permeability of free space
ω	=	excitation frequency

REFERENCES

1. Schweitzer, G. and Lange, R., "Characteristics of a Magnetic Rotor Bearing for Active Vibration Control, "First International Conference on Vibration in Rotating Machinery, I. Mech. Eng., Cambridge, September 1976, Paper No. C239/76.

2. Stanway, R. and Burrows, C.R., "Active Vibration Control of a Flexible Rotor on Flexibly-Mounted Journal Bearings," ASME J. Dynamic Systems, Measurement, and Control, Vol. 103, 1981, pp. 383-388.

3. Salm, J. and Schweitzer, G., "Modelling and Control of a Flexible Rotor with Magnetic Bearings," Third International Conference on Vibrations in Rotating Machinery, I. Mech. Eng., Cambridge, September 1984, Paper No. C277/84.

4. Nikolajsen, J.L., Holmes, R., and Gondhalekar, V., "Investigation of an Electromagnetic Damper for Vibration Control of a Transmission Shaft," Proc. Instn. Mech. Engrs., Vol. 193, 1979, pp. 331-336.

5. Allaire, P.E., Lewis, D.W., and Knight, J.D., "Active Vibration Control of a Single Mass Rotor on Flexible Supports," J. Franklin Inst., Vol 315, 1983, pp. 211-222.

6. Kasarda, M.E.F., Allaire, P.E., Humphris, R.R., and Barrett, L.E., "A Magnetic Damper for First Mode Vibration Reduction in Multimass Flexible Rotors," Gas Turbine and Aeroengine Congress and Exposition, Toronto, June 1989, ASME Paper 89-GT-213.

7. Foster, E.G., Kulle, V. and Peterson, R.A., "The Application of Active Magnetic Bearings to a Natural Gas Pipeline Compressor," ASME Paper 86-GT-61, 1986.

8. Weise, D.A., "Present Industrial Applications of Active Magnetic Bearings," 22nd Intersociety Energy Conversion Engineering Conference, Philadelphia, August 1987.

9. Brunet, M., "Practical Applications of the Active Magnetic Bearings to the Industrial World," Proc. of First International Symposium on Magnetic Bearings, Zurich, June 1988, pp. 225-244.

10. Habermann, H, and Brunet, M., "The Active Magnetic Bearing Enables Optimum Damping of Flexible Rotor," ASME Paper 84-GT-117, 1984.

11. Weise, D.A., "Active Magnetic Bearings Provide Closed Loop Servo Control for Enhanced Dynamic Response," 27th IEEE Machine Tool Conference, October 1985.

12. Humphris, R.R., Kelm, R.D., Lewis, D.W., and Allaire, P.E., "Effect of Control Algorithms on Magnetic Journal Bearing Properties," Journal of Engineering for Gas Turbines and Power, Vol. 108, No. 4, 1986, pp. 624-632.

13. Chen, H.M. and Darlow, M.S., "Design of Active Magnetic Bearings with Velocity Observer," ASME 11th Biennial Conference on Mechanical Vibration and Noise, Boston, September 1987.

14. Chen, H.M., "Magnetic Bearings and Flexible Rotor Dynamics," STLE Paper 88-AM-2D-1, 1988.

15. Sutton, R.F., "LOX/Hydrocarbon Turbomachinery Technology," JANNAF Propulsion Meeting, San Diego, 1987.

16. Ulbrich, H., "New Test Techniques Using Magnetic Bearings," Proc. of First International Symposium on Magnetic Bearings, Zurich, June 1988, pp. 281-288.

17. Wagner, N.G., and Pietruszka, W.D., "Identification of Rotordynamic Parameters on a Test Stand with Active Magnetic Bearings," Proc. of First International Symposium on Magnetic Bearings, Zurich, June 1988, pp. 289-299.

18. Lang, K.W., "Test of an Active Magnetic Bearing in Liquid Nitrogen," 12th Biennial Conference on Mechanical Vibration and Noise, Montreal, ASME Pub. DE-Vol. 18-1, 1989, pp. 321-326.

19. Jones, A.B., "A General Theory for Elastically Constrained Ball and Radial Roller Bearings Under Arbitrary Load and Speed Conditions," ASME Journal of Basic Engineering, Vol. 82, 1969, p. 309.

20. Murphy, B.T., Scharrer, J.K., and Sutton, R.F., "The Rocketdyne Multifunction Tester, Part I - Test Method," Rotor Dynamics Instability Problems in High Performance Turbomachinery, Texas A&M University, May 1990.

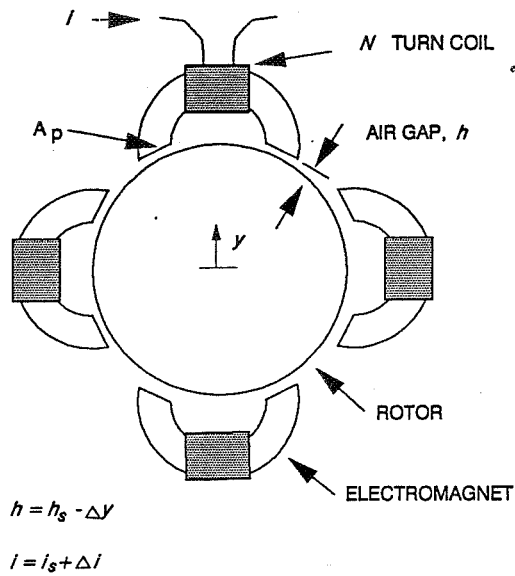$h = h_s - \Delta y$

$i = i_s + \Delta i$

Figure 1. Magnetic Bearing Schematic

Figure 2. Magnetic Bearing Stiffness Coefficient
vs. Excitation Frequency

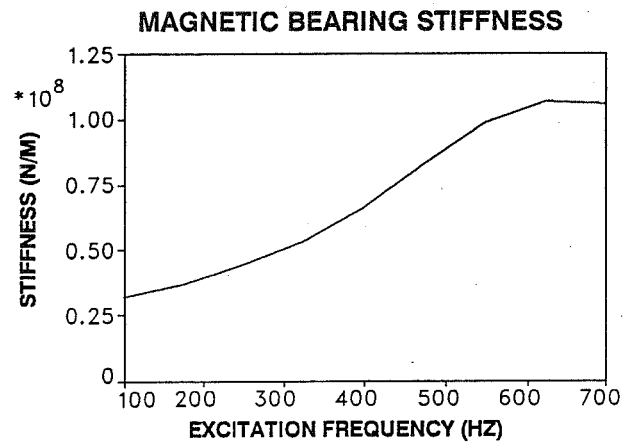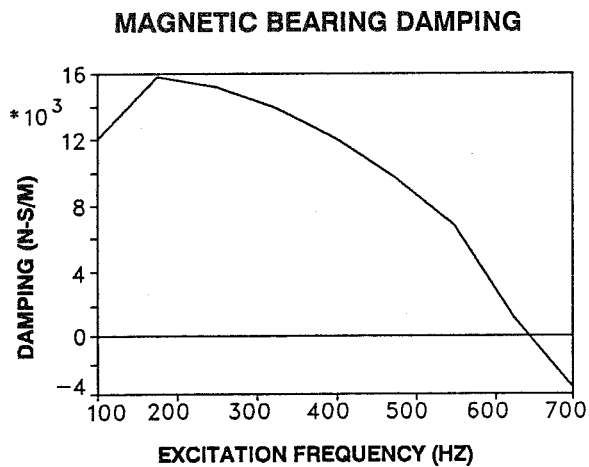Figure 3. Magnetic Bearing Damping Coefficient
vs. Excitation Frequency
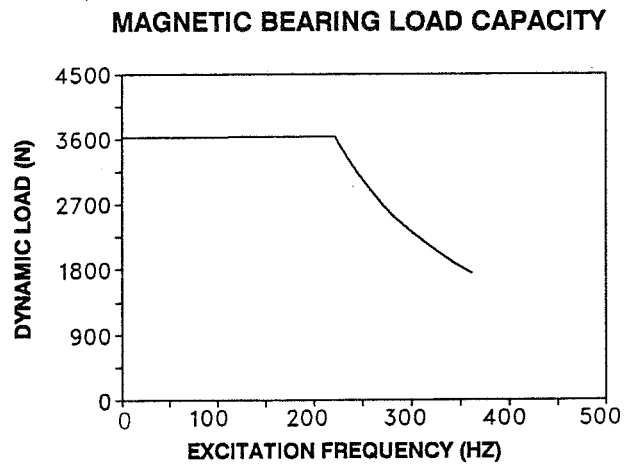
Figure 4. Magnetic Bearing Load Capacity
vs. Excitation Frequency

384
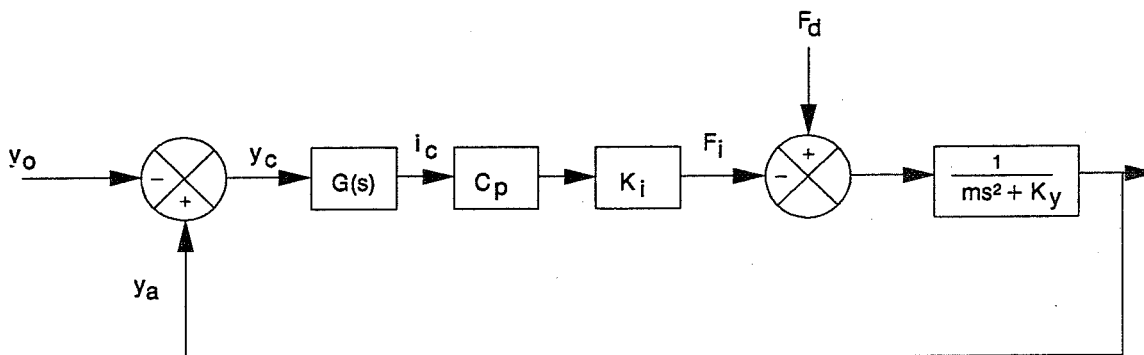
Figure 5. Magnetic Bearing Control Diagram
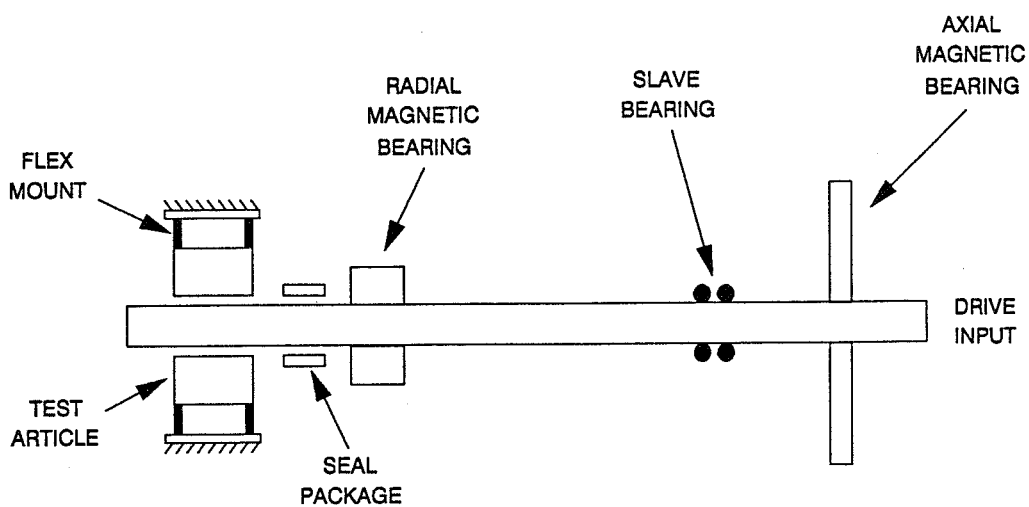
Figure 6. Schematic of Rocketdyne Multifunction Tester

385
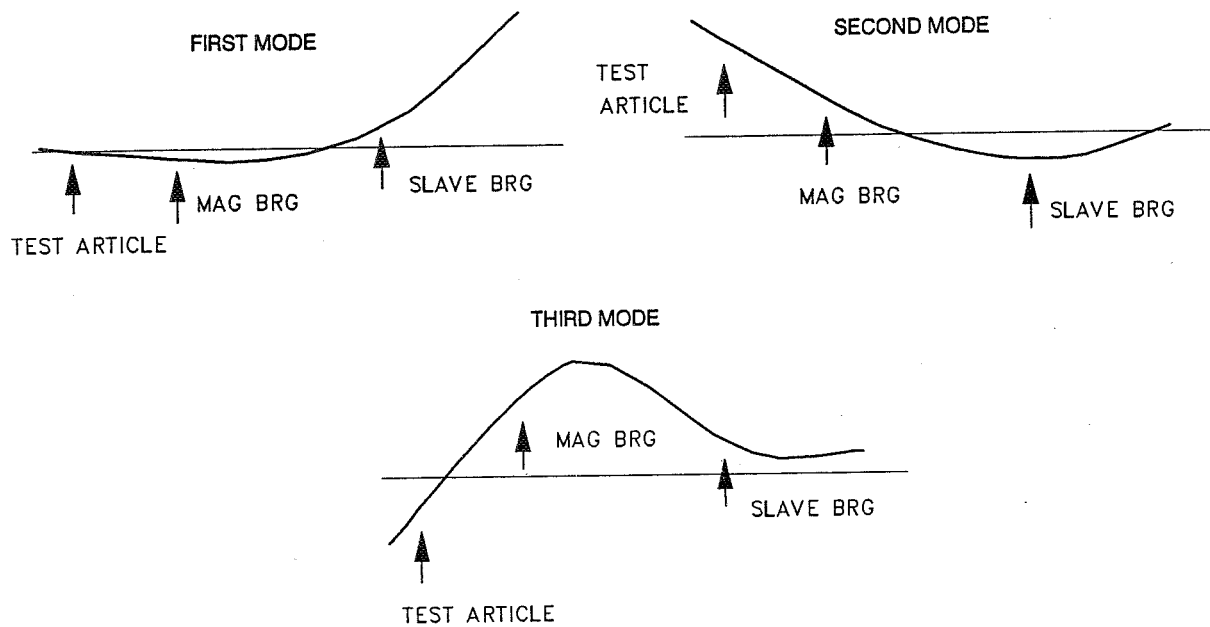
Figure 7. Mode Shapes for the First Three Vibration
Modes of the Tester
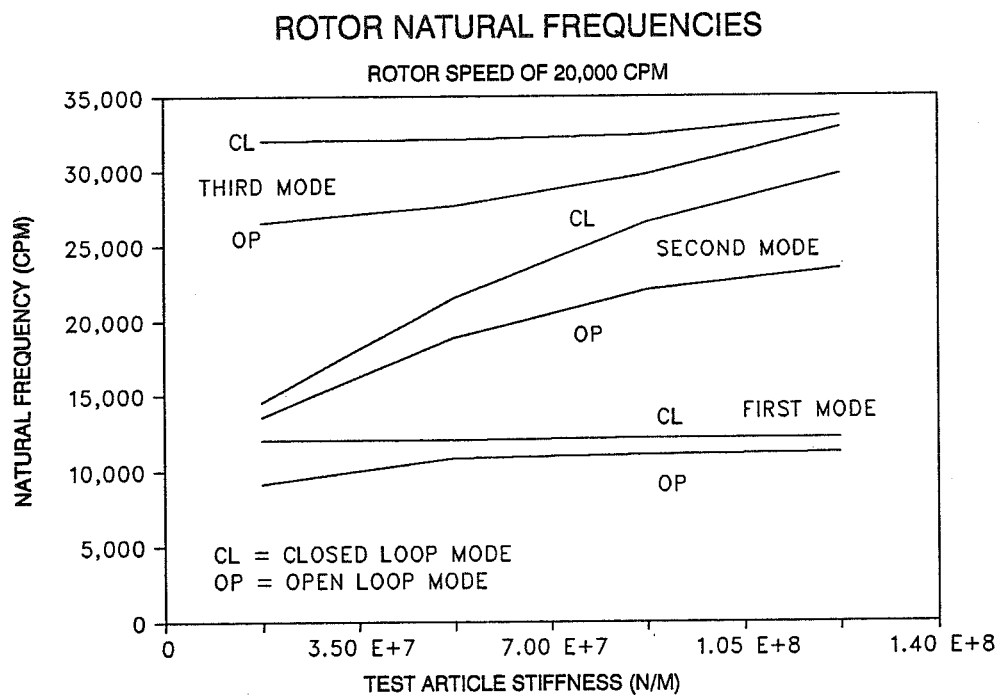
Figure 8. Natural Frequencies vs. Test Article
Stiffness for Tester

TEST ARTICLE TRANSFER FUNCTION

TEST ARTICLE STIFFNESS = 1.75E+7 N/M (100,000 LB/IN)
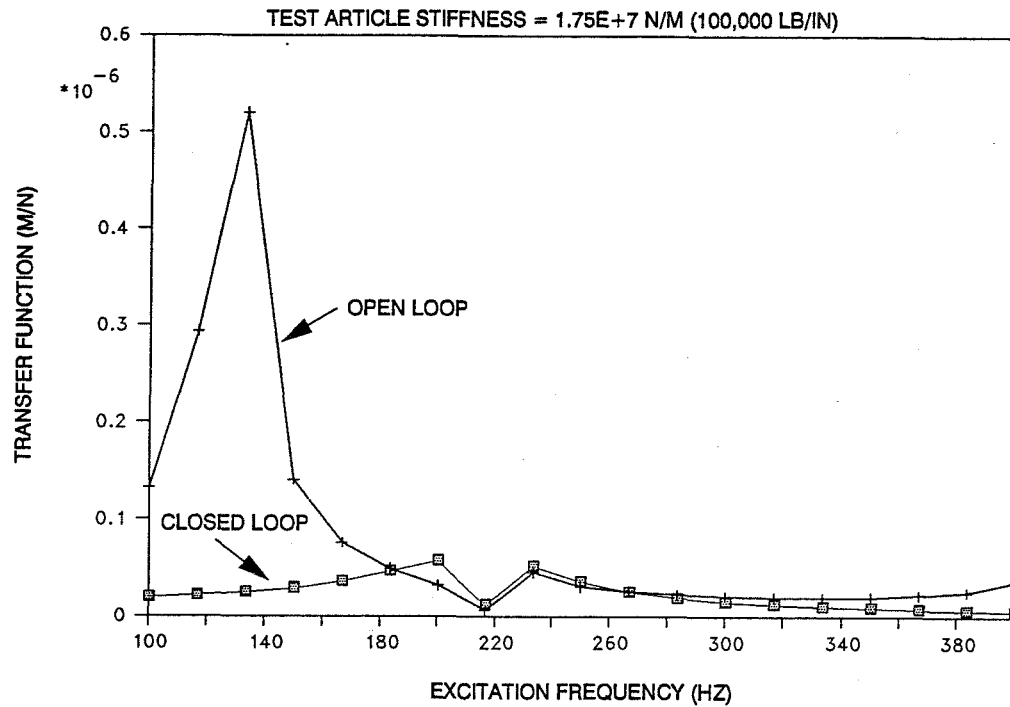
Figure 9.   Transfer Function Amplitude, Response at Test Article due to Force
at Magnetic Bearing, Test Article Stiffness = 100,000 lb/in.

MAXIMUM TEST ARTICLE RESPONSE

TEST ARTICLE STIFFNESS = 1.75E+7 N/M (100,000 LB/IN)
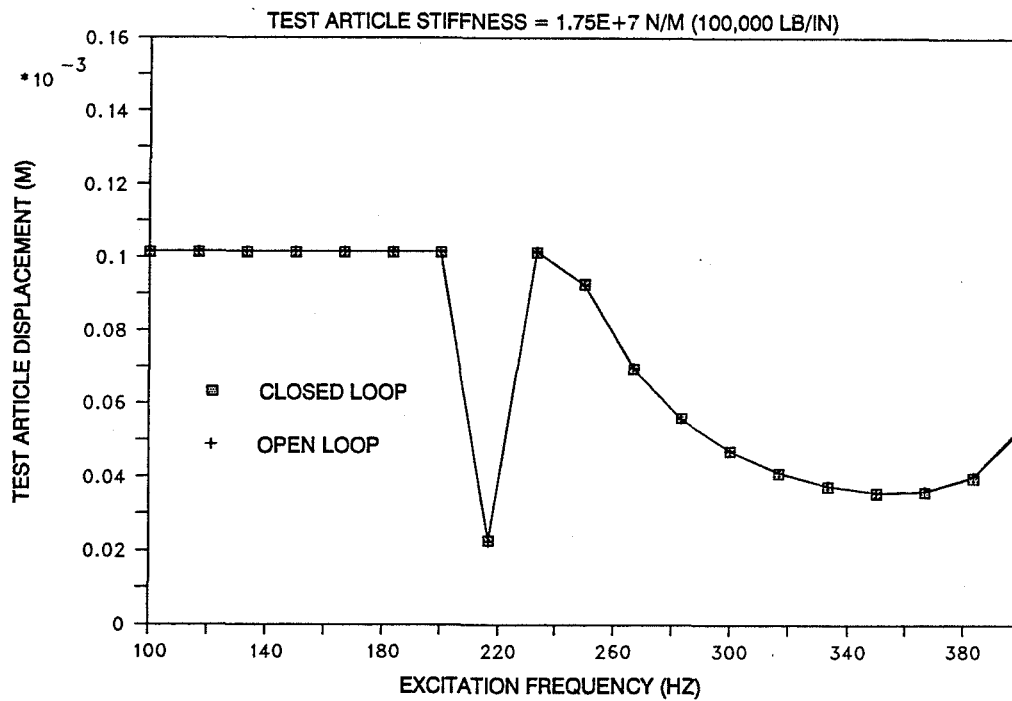
Figure 10.   Maximum Response at Test Article,
Test Article Stiffness = 100,000 lb/in.

387

MAXIMUM FLEX MOUNT RESPONSE
TEST ARTICLE STIFFNESS = 1.75E+7 N/M (100,000 LB/IN)

Figure 11.   Maximum Response at Flex Mount Load Sensing Element,
Test Article Stiffness = 100,000 lb/in.

TEST ARTICLE TRANSFER FUNCTION
TEST ARTICLE STIFFNESS = 1.31E+8 N/M (750,000 LB/IN)
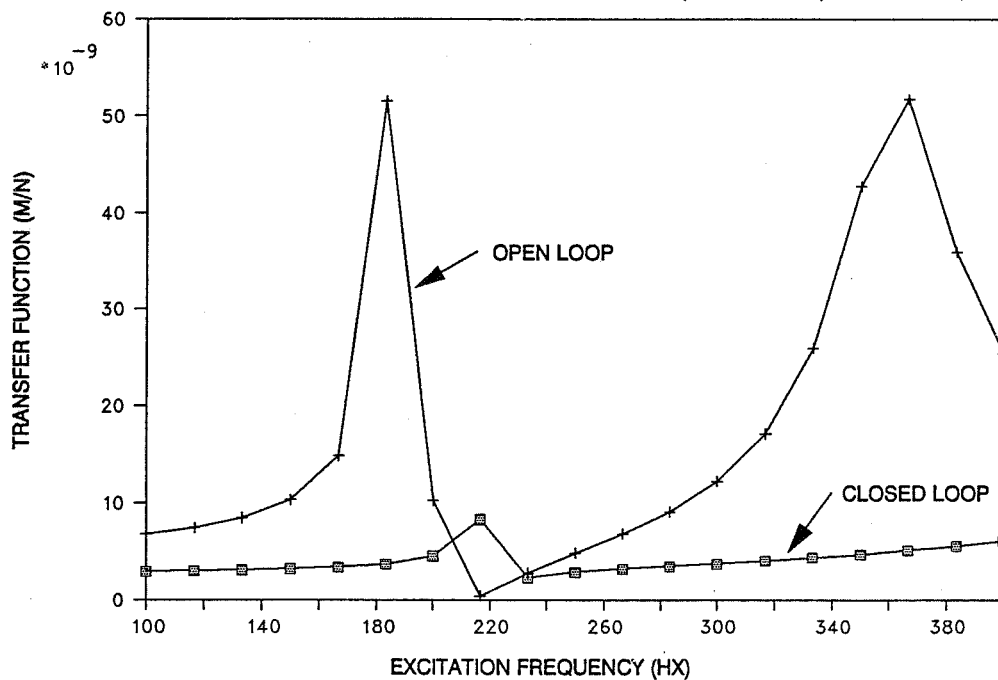
Figure 12.   Transfer Function Amplitude, Response of Test Article due to Force
at Magnetic Bearing, Test Article Stiffness = 750,000 lb/in

MAXIMUM TEST ARTICLE RESPONSE

TEST ARTICLE STIFFNESS = 1.31E+8 N/M (750,000 LB/IN)
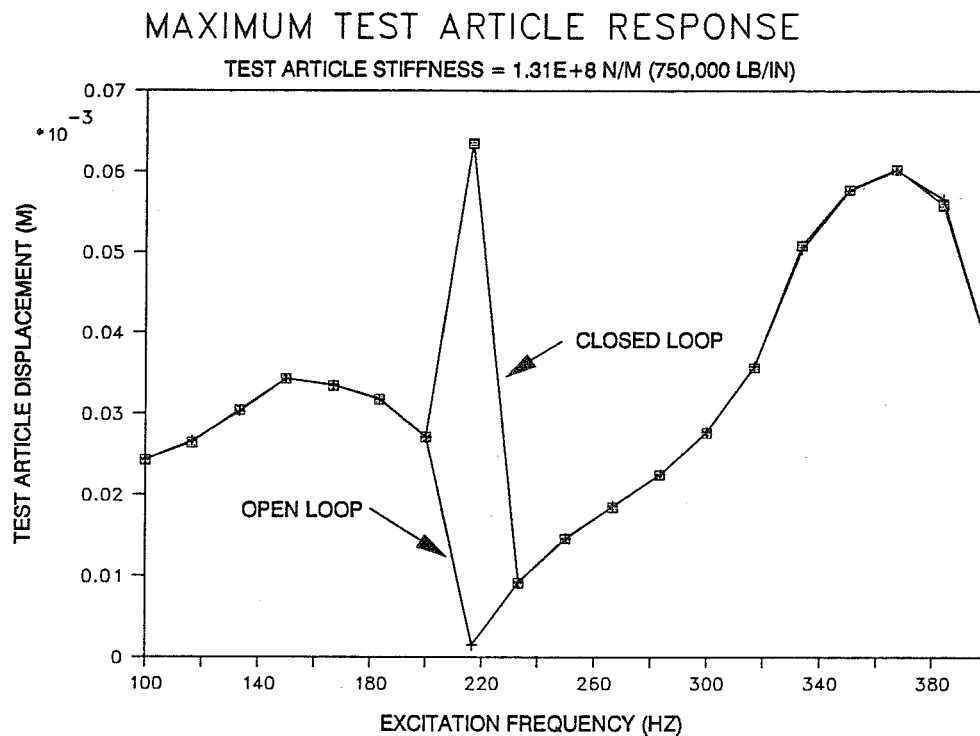
Figure 13.   Maximum Response at Test Article,
Test Article Stiffness = 750,000 lb/in.

MAXIMUM FLEX MOUNT RESPONSE

TEST ARTICLE STIFFNESS = 1.31E+8 N/M (750,000 LB/IN)

Figure 14.   Maximum Response at Flex Mount Load Sensing Element,
Test Article Stiffness = 750,000 lb/in.

389

Page intentionally left blank

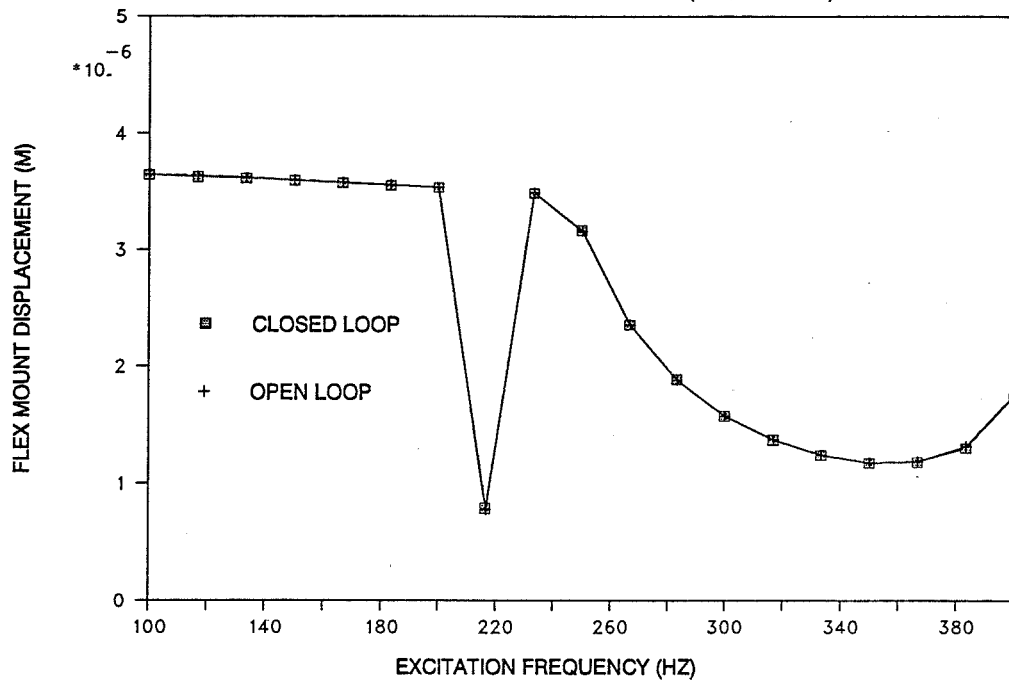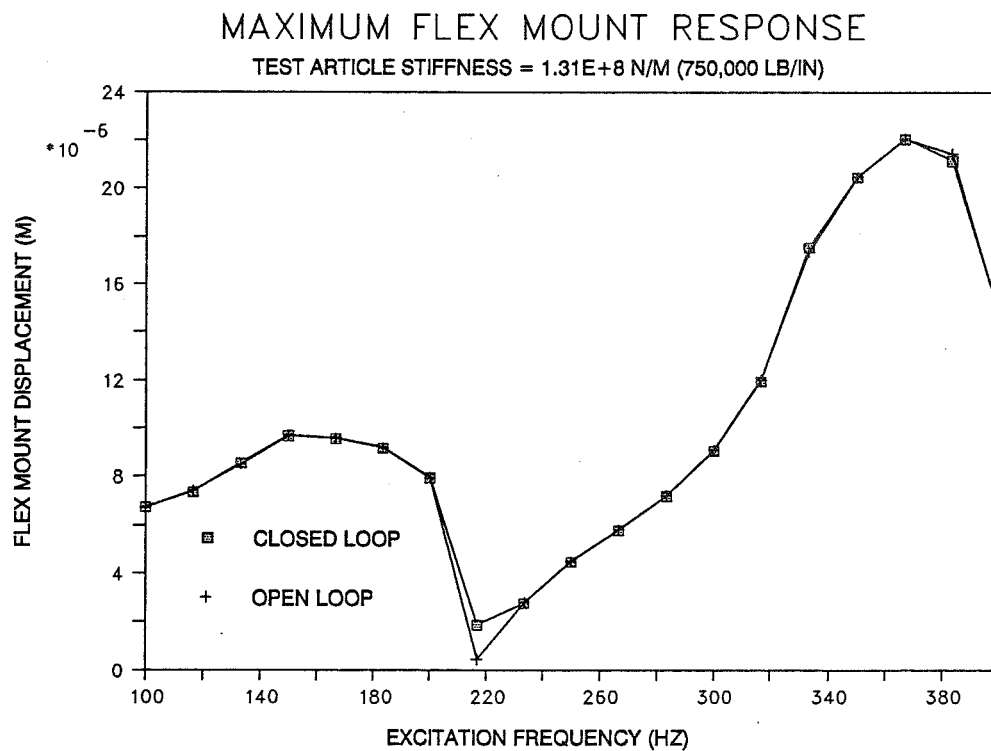# COMMENTS ON FREQUENCY SWEPT ROTATING INPUT PERTURBATION TECHNIQUES AND IDENTIFICATION OF THE FLUID FORCE MODELS IN ROTOR/ BEARING/SEAL SYSTEMS AND FLUID HANDLING MACHINES

Agnes Muszynska and Donald E. Bently
Bentley Rotor Dynamics Research Corporation
Minden, Nevada 89423, U.S.A.

The paper describes perturbation techniques used for identification of rotating system dynamic characteristics. A comparison between two periodic frequency–swept perturbation methods applied in identification of fluid forces of rotating machines is presented. The description of the fluid force model identified by inputting circular periodic frequency–swept force is given. This model is based on the existence and strength of the circumferential flow, most often generated by the shaft rotation. The application of the fluid force model in rotor dynamic analysis is presented. It is shown that the rotor stability is an entire rotating system property. Some areas for further research are discussed.

1. INTRODUCTION

Perturbation methodology is well known and widely applied in Control Theory. The main objective of perturbation is identification of the system characteristics by exciting the system with a known input function and observing (measuring) its response. The comparison between the input and output of the system gives an insight into the system characteristics, i.e., its transfer function (Fig. 1). The "system" can be a mechanical structure, or any other system, such as biological, economic, etc. When little is known about the system characteristics, the system is often referred to as a "black box." When the mathematical structure of the system characteristics is known (or rather assumed approximately known, such as, for instance linearity of the n–th order), the system is referred to as a "grey box." The identification procedure provides the parameters to the assumed mathematical structure of the system model. The transition from a "black box" to "grey box" is performed by iterative adjustments to the system model. It results from a series of perturbation tests conducted for various operating conditions.
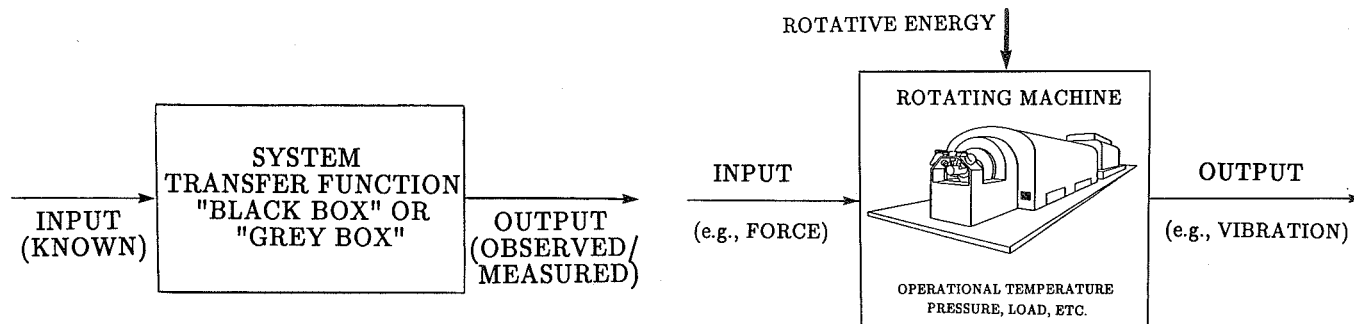

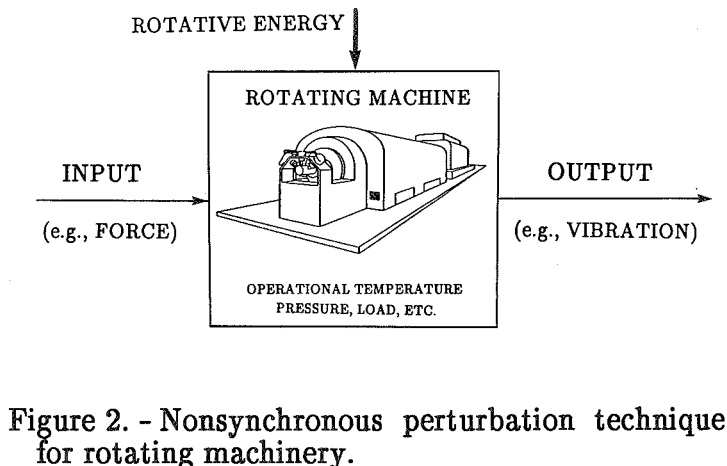Figure 1. – Identification of object characteristics by comparison of the input and output.

Figure 2. – Nonsynchronous perturbation technique for rotating machinery.

391

1.1 Perturbation Techniques in Rotating Machinery

Rotating machines are particular subjects of perturbation testing. They represent a special class of "active" mechanical structures. The main motion of a rotating machine is rotation, driven by an external energy source. In order to fully understand the rotating machine process, and identify its operational characteristics, the perturbation tests should be conducted on a machine at its operational conditions, in particular when the rotor rotates at its operating speed (Fig. 2). The rotative energy provides, therefore, an additional input to the system. Most often this input is considered uncoupled from the perturbation input/output flow. The rotating energy, as an additional input to the system has, however, a very important influence on the system: its characteristics become rotative speed dependent. The perturbation input should be entirely independent from the rotative energy input. This technique is called "nonsynchronous" perturbation [1].

There are two particular cases of the perturbation technique applied to rotating machinery. In these cases only one input is used: (i) perturbation of the rotating machine at rest (like a "passive" structure), and (ii) synchronous perturbation. In the latter technique the rotative energy represents the only input to the system. In the synchronous perturbation method a controlled unbalance transfers rotational energy into an input force [2,3]. Both these particular perturbation techniques often provide important, but also very limited, information about the rotating machine characteristics.

1.2 Characteristics of Rotating Machines

Perturbation testing of rotating machines is used for identification of their mechanical characteristics associated with modes of vibration. Shaft lateral/ bending modes attract the highest attention. In particular, the lowest lateral/ bending modes are of the greatest concern because, due to the specific role of internal damping in rotating systems, they are usually characterized by the highest vibration amplitudes, thus creating conditions for rotor failures.

In most rotating machines the shaft rotates in a fluid environment. Fluid involved in dynamic motion becomes an important part of the system. Fluid/solid interaction causes the appearance of additional modes of vibration in the system. These particular modes have been identified by nonsynchronous perturbation testing [1]. Perturbation testing is used for identification of the rotating machine characteristics at various conditions such as under steady—state or variable load, unbalance, at different rotative speeds, including operational speed and above, at various temperatures, and other conditions. The information provided from the perturbation testing is used for model adjustments; it helps to predict stability of machine operation, provides tools for malfunction diagnostics, and assists in optimization of the machine performance.

1.3 Perturbation Input

Rotating machines can be perturbed by all classical input functions used in the identification of mechanical structures. Frequency swept periodic inputs [4–27], random inputs [28], and impulse inputs [29–35] became the most popular ones. Provided that the identified system is linear, all perturbation methods should lead to the same results. Each method has, however, its own strong and weak points which result in accuracy differences in specific applications. Two methods of nonsynchronous perturbation which have several advantages in comparison with other techniques are discussed below.

1.4 Comparison of Two Frequency Swept Rotating Input Perturbation Techniques Used for Identification of Fluid Forces in Rotating Machines

There are two main perturbation techniques of nonsynchronous one—mode testing used for identification of fluid force models in rotor/bearing, rotor/seal systems, as well as in fluid handling

(a)

(b)

KNOWN
UNBALANCE
MASS

DISPLACEMENT
PROBES

PRESSURE
TRANSDUCERS

SELF ALIGNING
ROLLING ELEMENT
BEARING

Ω

$Ae^{j\omega t}$

ROTOR

FLUID

STATOR

ω
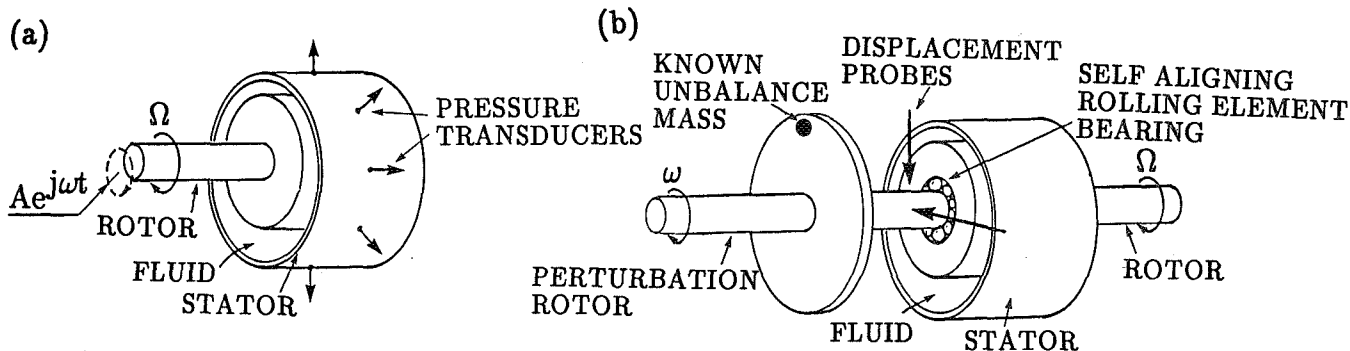
PERTURBATION
ROTOR

FLUID

STATOR

Ω

ROTOR

Figure 3. - Nonsynchronous perturbation techniques: (a) perturbation by displacement (a stationary shaft and casing displacements are also used), (b) perturbation by force.

machines (mainly pumps). The basic advantage of these methods is the rotational character of the input function in forward or reverse direction (the same or opposite to rotor rotation). This allows for independent identification of forward and backward modes of the rotating machine. These two perturbation techniques differ by the input/output functions (Fig. 3). For rotor circular orbits* they are as follows:

DISPLACEMENT: $Ae^{j\omega t}$ $\longrightarrow$ $\boxed{\bar{\kappa}(\omega) = \dfrac{1}{\bar{H}(\omega)}}$ FORCE: $(F_r + jF_t)e^{j\omega t}$ $\longrightarrow$ [Refs. 7,11,12,18-26]

FORCE: $Fe^{j\omega t}$ $\longrightarrow$ $\boxed{\bar{H}(\omega) = \dfrac{1}{\bar{\kappa}(\omega)}}$ DISPLACEMENT: $Ae^{j(\omega t + \alpha)}$ $\longrightarrow$ [Refs. 4-6,8-10,13-17]

where A is rotor displacement amplitude, α is rotor response phase (also $\alpha = \arctan(-F_t/F_r)$), ω is rotor perturbation (excitation) precessional frequency (usually varying from zero to some ω_{max}), t is time, $j = \sqrt{-1}$, F_r and F_t are radial and tangential forces respectively acting on the rotor. These forces are obtained by integrating the fluid pressure or measuring forces outside an elastically supported seal or bearing; F is the input force amplitude.

In both cases the objective is identification of the "black box," i.e., the transfer function of the system. More precisely the sought functions are $\bar{\kappa}(\omega)$ = complex dynamic stiffness, or $\bar{H}(\omega) = \dfrac{1}{\bar{\kappa}(\omega)}$ = transfer function = complex dynamic compliance of the system. The most often obtained result from either technique is the complex dynamic stiffness:

$$\bar{\kappa}(\omega) = \frac{F_r + jF_t}{A} \text{ when the input is displacement.} \qquad (1)$$

$$\bar{\kappa}(\omega) = \frac{F}{A} e^{-j\alpha} \text{ when the input is force.} \qquad (2)$$

---

*A use of noncircular forces/displacements or occurrences of noncircular response orbits/forces represent generalizations of the perturbation mehod, useful for higher eccentricities of the rotor [13]. For full identification of system parameters it requires a double number of measurements.

393

The complex dynamic stiffness components are as follows:

$$\text{Direct dynamic stiffness} \equiv \text{DDS} = \frac{F_r}{A} = \frac{F \cos \alpha}{A} \tag{3}$$

$$\text{Quadrature dynamic stiffness} \equiv \text{QDS} = \frac{F_t}{A} = -\frac{F \sin \alpha}{A} \tag{4}$$

By limiting the input to a circular periodic function, both methodologies must yield exactly the same results, provided that the system is linear, and the instrumentation yields comparable signal—to—noise ratios.

As is evident from Eqs. (3) and (4), the force—to—motion amplitude ratios F_r/A and F_t/A correspond to the direct and quadrature dynamic stiffnesses, respectively, often, in some published papers, with opposite sign convention. The authors use the notion of dynamic stiffnesses, well established in Mechanics. For a system with one complex degree of freedom (one lateral mode of the symmetric rotor with no gyroscopic effect) the Direct dynamic stiffness is composed of the static (direct) stiffness (K), minus the effect of inertia and cross damping. By definition, the static stiffness K is positive; therefore, it appears in the direct dynamic stiffness with the plus sign. The quadrature dynamic stiffness contains the product of the radial (direct) damping (D) and frequency ω, minus the constant (perturbation frequency independent) cross coupled stiffness. Since damping is positive, it is reasonable to present the corresponding straight line $D\omega$ versus perturbation frequency with a positive slope. The data from Refs. [21—23] illustrated in figures below have been presented in this unified format. The elements of the discussed above dynamic stiffnesses correspond to the standard linear bearing or seal models with isotropic properties (fluid inertia matrix with no cross terms, damping, and stiffness matrices skew symmetric).

The results of perturbation testing of rotor/fluid systems are discussed in the next section.

2. FLUID FORCE MODEL IDENTIFIED BY INPUTTING CIRCULAR

PERIODIC FREQUENCY SWEPT FORCE

As a result of over eight years of testing and identification research, the authors have proposed a fluid force model for lightly loaded bearings, seals, and fluid—handling machines, based on the significance of the steady circumferential flow [36]. The model was identified experimentally mainly by using the frequency swept circular periodic perturbation force at the input of the rotor/bearing/seal systems. A similar fluid force model was previously developed theoretically, and has existed in a simplified version in the rotordynamic literature for at least 25 years (Bolotin [37], Black [38,39]). It has not, however, been fully exploited. Following the results of the perturbation testing, the most important improvement in the model introduced by the authors was the replacement of the constant "1/2," widely used in the fluid models, by the factor "λ" (fluid circumferential average velocity ratio) as a function of fluid parameters and shaft eccentricity. This ratio has been identified for several cases of seals and bearings as a decreasing function of shaft eccentricity.

The basic fluid circumferential average velocity ratio λ is generated by the shaft rotation. Its value can, however, be strongly modified by forced fluid flow, such as preswirling and injections. Depending on the direction of the tangential preswirls and/or injections, λ can be reduced when these directions oppose shaft rotation, or increased when the preswirls/injections are in the direction of shaft rotation.

For an originally concentric shaft rotating at a constant rotative speed Ω and perturbed by an unbalanced auxiliary system providing the frequency swept rotating force with frequency ω in a range at least covering the interval $0<\omega<\Omega$ for the "whirl" mode, the plot of direct dynamic stiffness of the fluid dynamic effects (shaft and other mechanical effects excluded), versus perturbation frequency ω approximately forms a parabola (Figs. 4 and 5), and thus can be described by three parameters. By using circular input forces and maintaining isotropy of the system (rotor gravity load balanced by centering springs), so that the response orbits are circular, the authors identified the fluid force direct dynamic stiffness as [1]:

$$DDS = K_0 - M_f(\omega - \lambda\Omega)^2 \tag{5}$$

where K_0 is the fluid film static radial (direct) stiffness, M_f is the fluid inertia effect, and λ is the fluid circumferential average velocity ratio. Note that the "cross damping" (skew–symmetric terms in the damping matrix) appears in (5) as a function of the fluid inertia and Coriolis' acceleration.

The quadrature dynamic stiffness versus perturbation frequency usually forms a straight line (Figs. 6 and 7); thus, it can be described by two parameters. The authors have identified these parameters as

$$QDS = D(\omega - \lambda\Omega) \tag{6}$$

where D is the fluid film radial (direct) damping. The term $D\omega$ represents the passive effect of the shaft pushing the fluid, $-D\lambda\Omega$ is an active term transferring rotative energy into the fluid force pulling the shaft (tangential force). The quadrature dynamic stiffness (6) is the most representative and most important part of the fluid force model [40]. In spite of nonlinearities of both λ and D as functions of shaft eccentricity, QDS appears as a distinctly straight line for all tested cases except for high shaft eccentricity [1,13]. This also means that there is practically no cross inertia effect in the fluid force. Note that in the identified fluid force model the direct and quadrature dynamic stiffnesses carry the common factor λ. This means that the peak of DDS and zero of QDS occur at the same perturbation frequency (Figs. 5 and 7). The results obtained by other researchers show, however, some differences in frequency for these values (Figs. 4 and 6). This problem will be discussed in Section 7.

Figures 4 to 7 illustrate the basic results obtained by various researchers, by using nonsynchronous perturbation techniques.
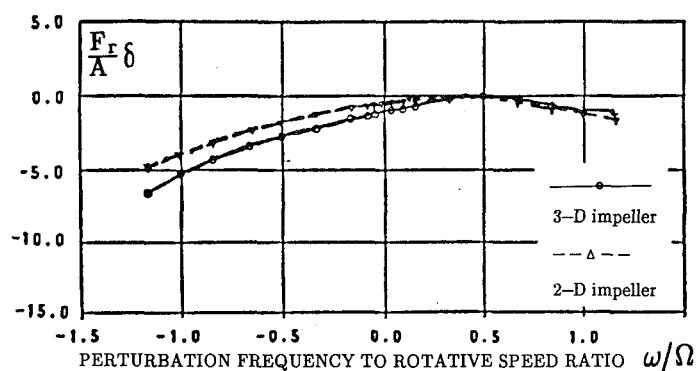
Figure 4. - Direct Dynamic Stiffness versus perturbation frequency for the system with circular displacement input, and force output. δ denotes a nondimensionalizing coefficient. Courtesy of H. Ohashi [22].

Figure 5. - Direct Dynamic Stiffness versus perturbation frequency for the system with circular force input, and displacement output [10].

395

The original response vectors versus perturbation frequency are presented in Figs. 8 and 9, in the form of Bodé plots. Note that, in the technique which uses force input, the displacement response vector has a form characteristic of responses for a one–mode system to a periodic excitation with sweep frequency (Fig. 9). The occurrence of a resonance is obvious. In comparison with the response of a classical mechanical system, the response phase is, however, ahead of the
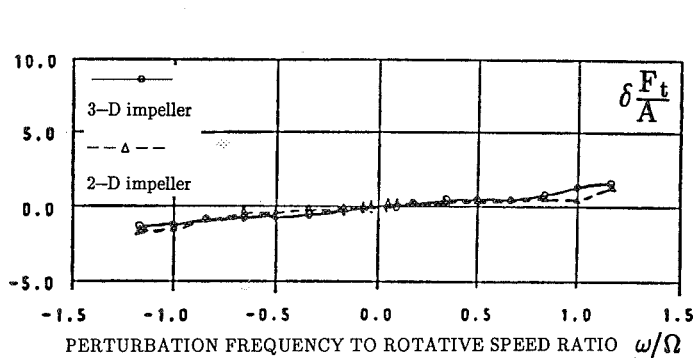
Figure 6. - Quadrature Dynamic Stiffness versus perturbation frequency for the system with circular displacement input, and force output. δ denotes a nondimensionalizing coefficient. Courtesy of H. Ohashi [22].

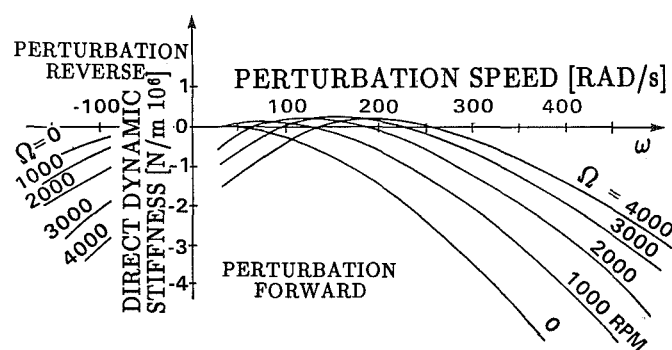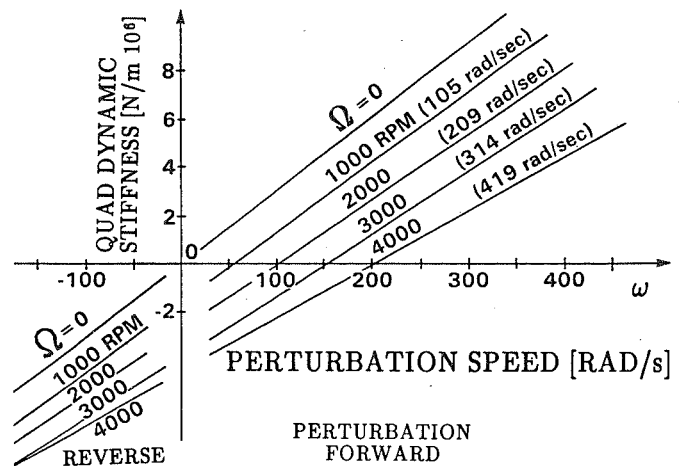Figure 7. - Quadrature Dynamic Stiffness versus perturbation frequency for the system with circular force input, and displacement output [10].
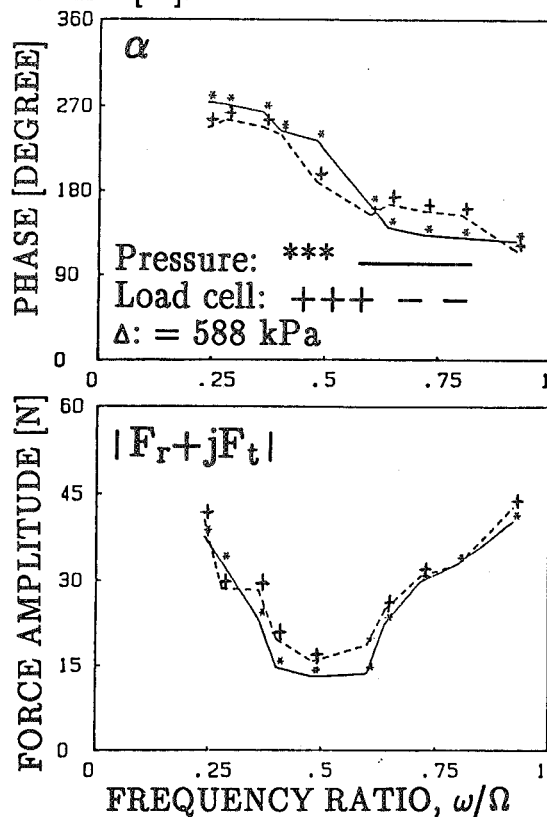
Figure 8. - Force response phase and amplitude versus perturbation frequency (perturbation by displacement. Courtesy of T. Iwatsubo [23].
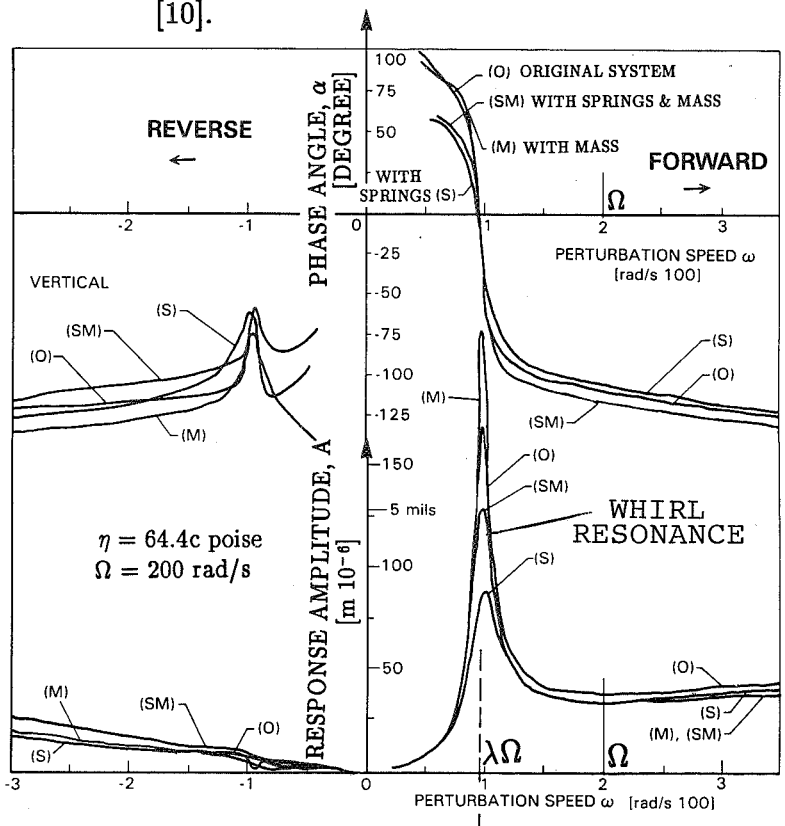
Figure 9. - Displacement response phase and amplitude versus perturbation frequency (perturbation by force) [9].

396

input force, and the phase sharply drops around 0°. This indicates the "quadrature" nature of this particular resonant phenomenon. The resonant frequency occurs at about $\lambda\Omega$, where Ω is the rotative speed. This means that $\lambda\Omega$ represents one of the system natural frequencies, which is generated purely by the fluid/solid interaction. The system QDS becomes zero. This fluid—related quadrature resonance was documented by Stone & Underwood in 1947 [4], and again by Hull in 1955 [5], but these excellent works were not immediately pursued. When the force is used as the system input, as opposed to a displacement input, the physical interpretation of the results becomes clear. The peak amplitude, which occurs when the quadrature dynamic stiffness equals zero, is of course limited by the total direct stiffness term in exactly the same fashion as the resonance at the zero of the direct stiffness, (yielding the classical stiffness—over—mass—related natural frequency) is limited by the total quadrature stiffness term (classical damping). The peak amplitudes may become very high, if the shaft rotative speed approaches the $1/\lambda$ value of the rotor system "mechanical" natural frequency, corresponding to its first bending mode [16]. (Note that the responses include rotor mechanical effects.) In fact, instability occurs when both direct and quadrature dynamic stiffnesses zero at the same frequency. This subject is discussed in Section 5.

By inputting a constant circular displacement and measuring the output in terms of forces, not only the accuracy of the results is lower, but also there is no clear physical interpretation of the results. The plot of force response amplitude versus perturbation frequency has an "anti—resonance" shape, a concave curve, a mirror image of displacement response amplitude versus frequency (Fig. 8). The phase is exactly the same in both techniques. It is obvious: by definition, the phase represents the angle between the input vector and output vector, independent of the nature of the input and output functions. Note that the dip point of the response force amplitude occurs around one half of the rotative speed, i.e., the fluid circumferential average velocity ratio λ is close to 1/2. The notion of the "force resonance," or rather "anti—resonance" is not well known in Mechanics. That is why by using the input force methodology, the authors have been more fortunate than those who used forces as outputs, to see direct physical interpretation of the results, namely that the value close to $\lambda\Omega$ is a system natural frequency.

Note the advantage of the circular perturbation, as opposed to unilateral perturbation as in impulse testing. The results of forward perturbation (rotation and precession in the same direction) and backward perturbation (opposed direction) are significantly different (Fig. 9). The resonance occurs only for the forward perturbation, i.e., the "quadrature" natural frequency $\lambda\Omega$ of the system has the plus sign only (classical "direct" natural frequencies governed by stiffness and mass have + and − signs).

3. FLUID FORCE MODEL IN DIFFERENTIAL FORM

In more general terms, the identified fluid force model can be presented as follows. In the coordinate system which rotates at an angular velocity $\lambda\Omega$ the fluid force is assumed radial, with three components (Fig. 10):

Fluid force in rotating coordinates $= M_f \ddot{z}_r + D\dot{z}_r + K_0 z_r$ (7)

where $z_r(t) = x_r(t) + jy_r(t)$ are the shaft lateral displacements in rotating coordinates; M_f, D and K_0 are the fluid inertia effect, damping and stiffness respectively.

The coordinate transformation

$$z_r = z\,e^{-j\lambda\Omega t} \quad , \quad \text{where } z(t) = x(t) + jy(t) \ , \ j = \sqrt{-1}$$ (8)

397

from rotating $z_r(t)$ to stationary coordinates $z(t)$ yields the fluid force:

Fluid force in stationary coordinates $= M_f(\ddot{z} - 2j\lambda\Omega\dot{z} - \lambda^2\Omega^2 z) + D(\dot{z} - j\lambda\Omega z) + K_0 z$ (9)

The fluid force model, in differential form (9), can be directly used in rotor dynamic analyses. In particular, for shaft periodic circular motion with a constant amplitude:

$$z = Ae^{j\omega t} \tag{10}$$

Fluid force for periodic motion $= A\{-M_f(\omega - \lambda\Omega)^2 + jD(\omega - \lambda\Omega) + K_0\}e^{j\omega t} \equiv$

$$\equiv Ae^{j\omega t}\{DDS + jQDS\} \equiv Ae^{j\omega t}\{\bar{\kappa}(\omega)\} \tag{11}$$

where $\bar{\kappa}(\omega)$ is the previously discussed complex dynamic stiffness.

4. IDENTIFICATION OF THE NONLINEAR MODEL

While determining the appropriate interpretation and use of the direct stiffness basic parabola, and the quadrature stiffness straight line, the authors are also investigating situations where the dynamic stiffness components diverge from parabolic and straight line shapes (Figs. 11 to 13). These are cases of nonlinearities, and discontinuous shifts of various basic parameters. An example is shown below.
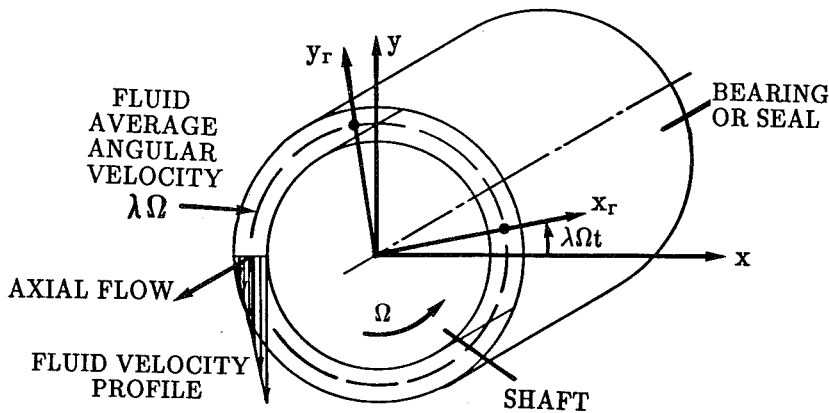
Figure 10. - Fluid force model for lightly loaded shaft.
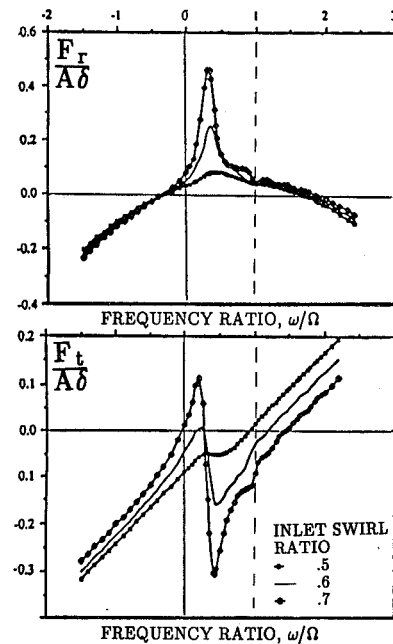
Figure 11. - Direct and Quadrature Dynamic Stiffnesses with nonlinear effects (perturbation by displacement). δ denotes a nondimensionalizing coefficient. Courtesy of D. Childs [21].

398

By inputting a force with sufficiently high amplitude $F = mr\omega^2$ (m,r are mass and radius of a controlled unbalance), the response becomes modified by system nonlinearities. The resulting dynamic stiffnesses diverge slightly from the parabolic/straight line shapes (Figs. 12 and 13). This occurs most noticeably in the range of perturbation frequency where the response amplitude is the largest (around $\omega = \lambda\Omega$) (Fig. 9). By inputting forces with sequentially increasing amplitudes, F, for each consecutive test, the nonlinear functions in the fluid force model can be identified. This identification technique is graphically presented in Fig. 14. As a first step the DDS for a linear case (when F is small) is subtracted from the DDS for a nonlinear case. The result gives the stiffness nonlinear function ψ versus perturbation frequency. Using this relationship, as well as the response amplitude versus perturbation frequency for high F, the plot of ψ versus shaft eccentricity can be
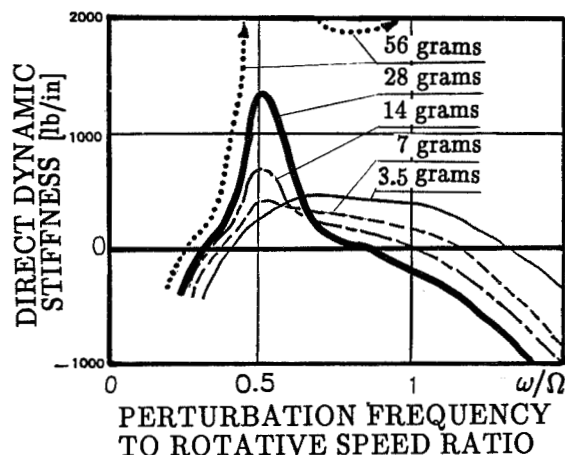
Figure 12. - Direct Dynamic Stiffnesses with nonlinear effects (perturbation by force for several cases of unbalance masses) [14].
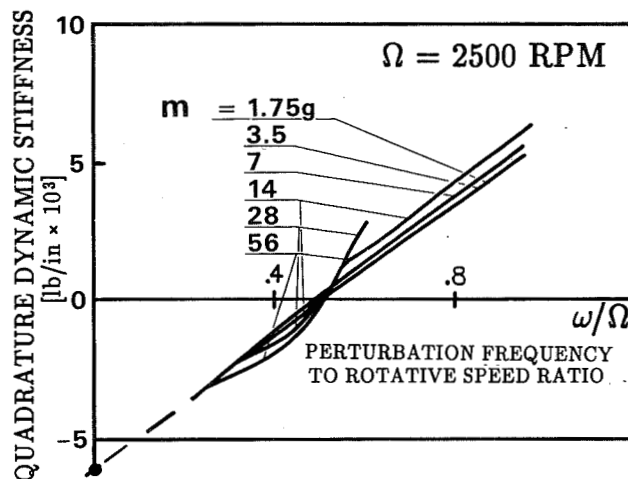
Figure 13. - Quadrature Dynamic Stiffness with nonlinear effects (perturbation by force) [17]. m denotes mass of perturbation unbalance.
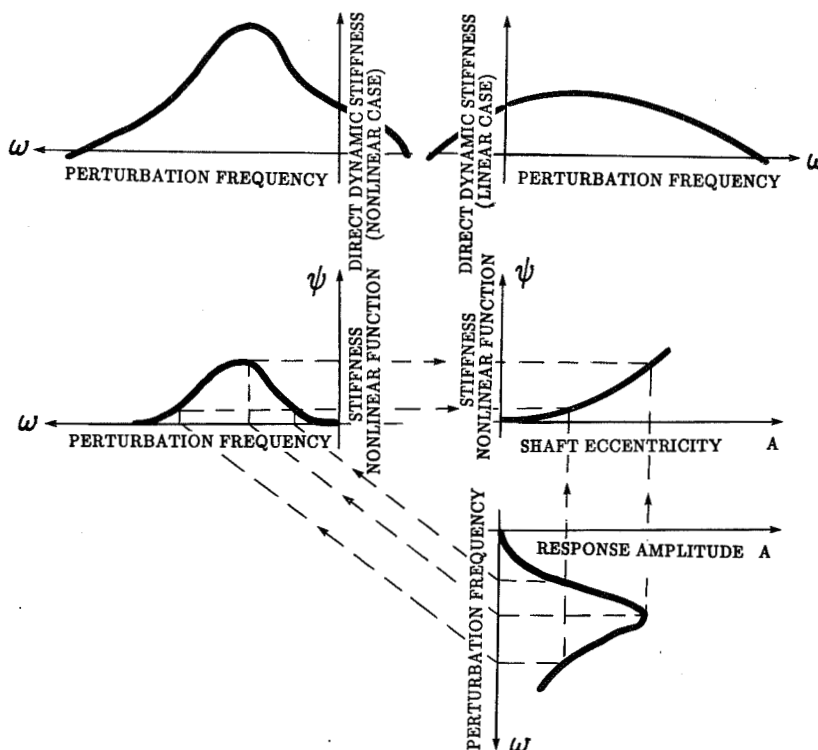
Figure 14. - Identification of fluid film stiffness nonlinearity (perturbation by force).

399

obtained. Note that the response amplitude A represents a rotating radial eccentricity of the shaft. Assuming lateral symmetry, the rotating eccentricity corresponds to the unidirectional static eccentricity of the rotor.

By a very similar method, the fluid film radial damping nonlinearity can be identified from the quadrature dynamic stiffness, provided that the nonlinearity of λ is relatively small [17].

Note that the nonlinear effects in the fluid film may be caused and/or influenced by fluid injections and preswirls [21], as well as cavitations [26].

5. ROTOR STABILITY: CRITERION AND MARGINS OF STABILITY

The rotor/fluid system dynamic stiffness components as functions of perturbation frequency can be used to predict the rotor stability and the stability margin.

In very general terms, the threshold of stability occurs when the "zeros" of the direct and quadrature dynamic stiffnesses occur at the same perturbation/precession frequency. In terms of frequency, the stability margin is the lowest difference between the zeros of the direct and quadrature dynamic stiffnesses (Fig. 15).

In actual applications, both components of the fluid force dynamic stiffness become modified by the rotor system parameters. An example is discussed below.

Consider an isotropic rotor supported in one rigid and one fluid–lubricated bearing (Fig. 16). The rotor rotates at a constant speed Ω and is perturbed by a nonsynchronous periodic circular forward (in the direction of rotation) sweep frequency force $Fe^{j\omega t}$. The model of the system is as follows:
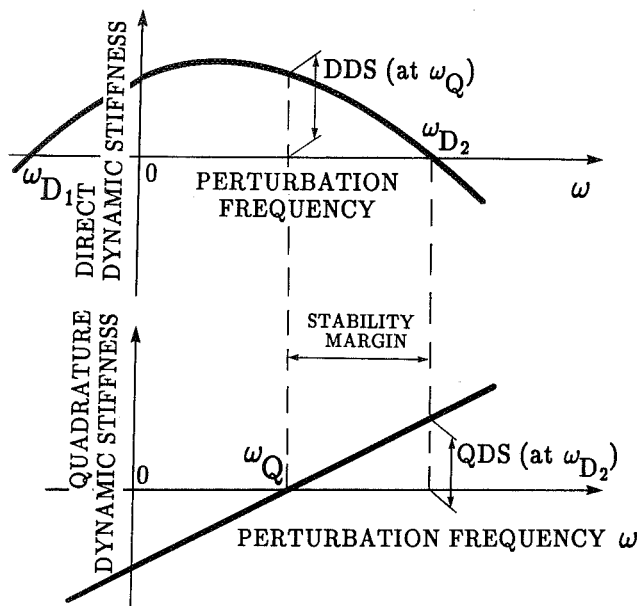
Figure 15. - Rotor stability prediction using dynamic stiffness graphs.
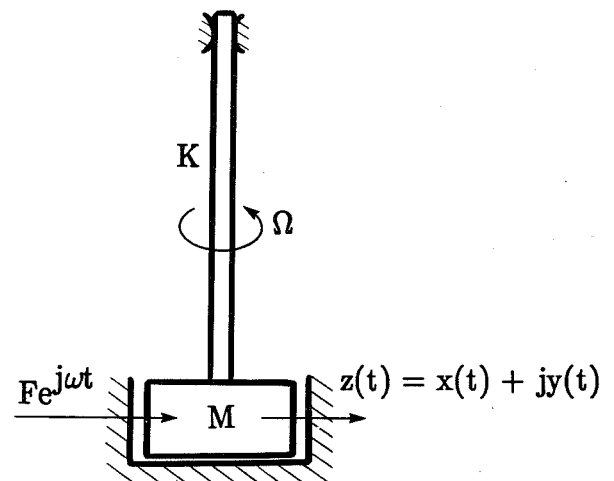
Figure 16. - Rotor/bearing system model.

400

$$M\ddot{z} + M_f(\ddot{z} - 2j\lambda\Omega\dot{z} - \lambda^2\Omega^2 z) + D_s\dot{z} + D(\dot{z} - j\lambda\Omega z) + Kz + K_0 z = Fe^{j\omega t} \qquad (12)$$

where M, D_s, K are rotor generalized (modal) mass, damping, and stiffness, for the first lateral mode respectively. The rotor system response is circular:

$$z = Ae^{j(\omega t + \alpha)} \qquad (13)$$

where the amplitude A and phase α can be calculated when Eq. (13) is substituted in Eq. (12):

$$Ae^{j\alpha}[-M\omega^2 - M_f(\omega - \lambda\Omega)^2 + D_s j\omega + Dj(\omega - \lambda\Omega) + K + K_0] = F \qquad (14)$$

From Eq. (14) the amplitude A and phase α of the forced response (13) are obtained as follows:

$$A = \frac{F}{\sqrt{[K + K_0 - M\omega^2 - M_f(\omega - \lambda\Omega)^2]^2 + [D_s\omega + D(\omega - \lambda\Omega)]^2}} \qquad (15)$$

$$\alpha = \arctan \frac{D_s\omega + D(\omega - \lambda\Omega)}{M\omega^2 + M_f(\omega - \lambda\Omega)^2 - K - K_0} \qquad (16)$$

The whirl resonance (Fig. 9) occurs when the quadrature part of the denominator of Eq. (15) is equal to zero, i.e., when

$$\omega = \frac{\lambda\Omega}{1 + D_s/D} \equiv \omega_{res} \qquad (17)$$

The resonant amplitude and phase are

$$A_{res} = \frac{F}{|K + K_0 - (M + M_f D_s^2/D^2)\lambda^2\Omega^2/(1 + D_s/D)^2|} \approx \frac{F}{|K + K_0 - M\lambda^2\Omega^2|} \ , \qquad \alpha_{res} = 0$$

The actual peak amplitude depends, however, on whether the force amplitude F is constant or dependent on frequency ω.

Eq. (16) indicates the leading–phase phenomenon for low frequency. At $\omega = 0$ the phase is

$$\alpha = \arctan \frac{D\lambda\Omega}{K + K_0} > 0$$

For $\lambda\Omega > 0$ the response is, therefore, ahead of the exciting force.

Eqs. (15) and (16) also show clearly that the whirl resonance occurs only if Ω and ω have the same rotational directions (perturbation forward). If $\omega < 0$ (perturbation backward), then the quadrature resonance does not take place (compare with experimental results, Fig. 9).

The system complex dynamic stiffness is obtained from Eq. (14) as the ratio $F/(Ae^{j\alpha})$. The dynamic stiffness components are

$$DDS = -M\omega^2 - M_f(\omega - \lambda\Omega)^2 + K + K_0 \tag{18}$$

$$QDS = D_s\omega + D(\omega - \lambda\Omega) \tag{19}$$

The system dynamic stiffness is, therefore, a combination of the rotor and fluid–related terms.

The eigenvalue problem for Eq. (12) provides the following eigenvalues:

$$s_{1,2,3,4} = \frac{1}{2(M+M_f)}(-D-D_s+2j\lambda\Omega M_f) \pm \frac{1}{\sqrt{2}}\left[\sqrt{-P+\sqrt{P^2+R^2}} \pm j\sqrt{P+\sqrt{P^2+R^2}}\right]$$

where

$$P = \frac{K+K_0-M_f\lambda^2\Omega^2}{M+M_f} - \left[\frac{D+D_s}{2(M+M_f)}\right]^2 + \left[\frac{\lambda\Omega M_f}{M+M_f}\right]^2, \qquad R = \left[\frac{M_f(D+D_s)}{(M+M_f)^2} - \frac{D}{M+M_f}\right]\lambda\Omega$$

The stability criterion, i.e., the requirement that all eigenvalues have non–positive real parts is as follows:

$$-\frac{D+D_s}{2(M+M_f)} + \frac{1}{\sqrt{2}}\sqrt{-P+\sqrt{P^2+R^2}} \leq 0 \tag{20}$$

which yields the rotative speed threshold of stability:

$$\Omega \leq \frac{1}{\lambda}\left[1+\frac{D_s}{D}\right]\sqrt{\frac{K+K_0}{M+M_f D_s^2/D^2}}$$

The natural frequency at the threshold of stability is $\sqrt{\dfrac{K+K_0}{M+M_f D_s^2/D^2}}$ (this is the imaginary part of the eigenvalue).

Inequality (20) can also be solved in another form:

$$\frac{\lambda\Omega}{1+M/M_f} - \sqrt{\frac{K+K_0}{M+M_f} - \lambda^2\Omega^2\frac{MM_f}{(M+M_f)^2}} \leq \frac{\lambda\Omega}{1+D_s/D} \leq \frac{\lambda\Omega}{1+M/M_f} + \sqrt{\frac{K+K_0}{M+M_f} - \lambda^2\Omega^2\frac{MM_f}{(M+M_f)^2}} \tag{21}$$

The direct dynamic stiffness (18) is equal to zero when

$$\omega = \omega_{D1,2} \equiv \frac{\lambda\Omega}{1+M/M_f} \pm \sqrt{\frac{K+K_0}{M+M_f} - \lambda^2\Omega^2\frac{MM_f}{(M+M_f)^2}} \tag{22}$$

The values $\omega_{D1,2}$ are called roots (zeros) of the direct dynamic stiffness. The quadrature dynamic stiffness (19) is equal to zero when

$$\omega = \omega_Q \equiv \frac{\lambda\Omega}{1+D_s/D} \tag{23}$$

402

where ω_Q is the root (zero) of the quadrature dynamic stiffness. The stability criterion (21) can, therefore, be written as

$$\omega_{D1} \leq \omega_Q \leq \omega_{D2}$$

which means, for rotor stability, the root of the system quadrature dynamic stiffness should occur between the two roots of the direct dynamic stiffness.

The <u>margin of stability</u>, in terms of frequency, is defined as a minimum distance between roots:

$$\min[(\omega_Q - \omega_{D1}), \ (\omega_{D2} - \omega_Q)] \tag{24}$$

This margin of stability is "horizontal," thus expressed in terms of frequency (Fig. 15). An additional "vertical" margin of stability can also be defined. It expresses the direct and quadrature dynamic stiffness closeness to the threshold of stability (Fig. 15):

$$\min[\text{DDS(at } \omega_Q), \ \text{QDS(at } \omega_{D1}), \ \text{QDS(at } \omega_{D2})] \tag{25}$$

The stability margin (25) indicates which parameter of the system is most likely responsible for the instability.

The <u>threshold of stability</u> occurs when both direct and quadrature dynamic stiffness have the same root, i.e., either $\omega_{D1} = \omega_Q$ or $\omega_Q = \omega_{D2}$. It means that at the precession frequency when these equalities occur, the total complex dynamic stiffness of the system equals zero (see Eq. (15) in which the denominator is zero at this case).

When the threshold of stability is exceeded, the vibration amplitude increases, most often ending up in a limit cycle self–excited vibrations, known as "whirl" and "whip," which are governed by the system nonlinearities [40, 41].

The fluid force model presented in the dynamic stiffness form provides clear suggestions for stability improvements of rotor/bearing/seal systems. Higher stability margins result when

- λ decreases (provided that $DM > D_sM_f$, which is almost always satisfied)
- K_0 increases
- D decreases (most often is, however, insensitive to stability)
- M_f decreases
- K and D_s increase
- M decreases

A higher stability margin results also when the rotative speed Ω decreases. Since variations of Ω can involve other rotor dynamic effects, such as balance resonance which may interact with fluid effects [40], Ω is not included in the above list.

The most effective parameters for rotor stability control are a decrease of the fluid circumferential velocity ratio λ and an increase of the fluid film radial stiffness K_0. The first is widely known in "anti–swirl" applications [41–51]. The second, i.e., the increase of K_0 results directly from an increase of shaft eccentricity and/or increase of the fluid pressure. The latter conclusion applies to externally pressurized ("hydrostatic") bearing and seal designs, which are widely known for their stability features. The most surprising result concerns fluid radial damping D . In most cases, an increase of D has no influence on stability, or has even a minor negative

403

effect. (This effect can be compared to destabilizing action of rotor structural/ internal friction at high rotative speeds.)

An interesting result is obtained if the classical Half Power Bandwidth method is applied to the whirl resonance. The classical amplification factor Q may be calculated as

$$Q = \frac{\omega_{res}}{\omega_2 - \omega_1}$$

where ω_{res} is given by Eq. (17) and ω_4, ω_2 are frequencies corresponding to the phases equal to $\pm 45°$ or amplitudes at $A_{res}/\sqrt{2}$ (3 dB level). For the whirl resonance the amplification becomes (Fig. 9):

$$Q \approx \frac{\sqrt{(K+K_0)M}}{D} \quad \frac{1}{\sqrt{(K+K_0)/M} \ / \lambda\Omega - 1} \tag{26}$$

The first fraction of Eq. (26) is the classical relationship of half the inverse of the damping factor. The second fraction indicates the closeness of the direct resonance (zero of DDS) to quadrature resonance. (Shaft damping and fluid inertia effect were omitted in Eq. (26) for clarity.) The whirl resonant amplitude becomes significantly magnified if the rotative speed is close to $1/\lambda$ times the rotor lateral mode natural frequency. This effect has often been observed experimentally [16].

Finally, the dynamic stiffness format can be used to successfully predict rotor instability in case of nonlinear distortions of the basic parabola/straight lines. The general idea always holds true: Instability occurs when both DDS and QDS have zeros at the same perturbation/precession frequency. Nonlinear effects may cause dramatic changes in the shape of DDS and/or QDS, including multiple zero points. Theoretical studies [52] proved, for instance, that the low frequency rotating stall instability can be predicted using the method discussed above.

Note that the relationships discussed in this chapter hold true for the considered example of one mode isotropic rotor/bearing or rotor/seal system. When more modes are taken into account, the relationships become more complex.

6. APPLICATIONS OF THE FLUID FORCE MODEL

By implementing the model identified by the authors into rotating machine dynamic equations, several significant and valuable results were obtained. The results of analysis conducted for one, two, and three mode models of rotors are very encouraging [36,40,41,42,53,54]. The model allowed for explanation of new phenomena, such as the recently observed second mode whirl [53] and second mode whip [54]. The generalization from two and three modes to "n" modes is obvious [53]. All swirl preventive measures (such as anti−swirl, preswirl, swirl brakes, fluid injections) can also be easily included in the models [41,42], and thus would give designers very good insight into the expected efficiency of such devices for stability of rotating machines.

7. FLUID FORCE MODEL ADJUSTMENTS AND GENERALIZATIONS

The model of fluid force (9) identified by the authors, using force input perturbation testing, is certainly open to further developments. One adjustment, namely the addition of nonlinear terms,

was discussed in Section 4. There exist also some other possible modifications to the model. These include:

(i) Tangential components. In the original form (7), the fluid force was assumed to have radial components only. There is a high probability, especially when the shaft eccentricity increases, that the force components are not exactly radial, but also have a tangential part. For instance the stiffness force in (7) may require an addition: the term $K_0 z_r$ should be replaced by $(K_0 - jK_t)z_r$ where K_t is tangential stiffness.

(ii) Two fluid circumferential velocity ratios. In the model (7), it was assumed that all components of the fluid force rotate at the same angular velocity $\lambda\Omega$. It might be necessary to introduce two different ratios λ_1, λ_2, one for the fluid inertia force, the other for the damping force. Thus, the adjusted model (9) will contain the terms:

$$M_f(\ddot{z} - 2j\lambda_1\Omega\dot{z} - \lambda_1^2\Omega^2 z) + D(\dot{z} - j\lambda_2\Omega z) .$$

where $\lambda_1\Omega$ and $\lambda_2\Omega$ are angular velocities at which inertia and damping forces rotate correspondingly. Two different λ ratios seem to be required in order to adequately identify the fluid force model in pumps (see Figs. 4 and 6 [22]).

(iii) Higher order terms. Some results of perturbation testing [26] suggest that the fluid force contains terms of order higher than two. In particular a third order term (jerk) should be included. With an assumed additional value of the corresponding fluid circumferential velocity ratio, λ_3, the model (9) might, therefore, be completed by the following term:

$$J(\dddot{z} - 3j\lambda_3\Omega\ddot{z} - 3\lambda_3^2\Omega^2\dot{z} + j\lambda_3^3\Omega^3 z)$$

where J can be considered as a complex parameter, containing radial and tangential components.

(iv) Nonsymmetric fluid force. Most results of the perturbation testing have been obtained for symmetric cases: perturbation around the shaft centered position. When the shaft is statically displaced to higher eccentricity, the flow conditions are certainly modified. The fluid force then contains terms of nonsymmetric nature [13,14]. In particular, the nonlinear terms identified for symmetric cases as simple functions of radial eccentricity, may require adjustments. More research is required in this area.

8. CONCLUDING REMARKS

This paper discusses the use of nonsynchronous swept frequency harmonic rotating input perturbation techniques for identification of the fluid force model in lightly loaded rotor/bearing/seal systems. Two basic methods differ by a choice of input functions: either as a force, as used by the authors and a few other researchers [1,2,4–6,8–10,13–17], or as a displacement [7,11,12,18–26]. The measured output responses are displacements or forces respectively. While both methods provide the system dynamic stiffness characteristics, the main difference between these two methods consists in data generation, acquisition, and processing; thus they provide different levels of signal–to–noise ratios. A significant contributor to noise is input/output phase readings. The first method provides a higher accuracy (around ±0.3%) than the second method, especially in phase measurements. An estimated error of the first method final results is lower than ±3%. An application of both methods to the same system (if possible) might ultimately provide the best identification data.

405

The results, in terms of the system dynamic stiffness components obtained from both methods, are very similar, as should be expected. Based on results of hundreds of tests obtained over the past eight years, the authors have provided a consistent mechanical interpretation of the results, and proposed an improved model of fluid forces in lightly loaded bearings and seals [36]. The model includes the fluid circumferential average velocity ratio as a function of shaft eccentricity, instead of a constant value 1/2 as in the classical models. (In some recent analyses the assumption about the constant 1/2 ratio starts gradually fading away.) The bearing/seal coefficients can easily be obtained from the proposed model as particular cases. The application of the improved fluid force model in rotor/bearing/seal systems yields results which stand in a very good agreement with observed and documented dynamic phenomena, such as whirl, whip, and higher mode whirl/whip vibrations [36,40,41,53,54]. The model allows for an improved prediction of the rotor stability thresholds and stability margins, as well as quantifying stability control measures. Some possible further adjustments of the fluid force model are also discussed. The latter would require more, well coordinated, experimental research.

The database resulting from different types of perturbation methodologies applied to rotor/bearing/seal/pump systems is now quite rich, including data from CalTech, Mitsubishi, Sulzer Brothers Ltd., Universities of Kobe, Tokyo, Osaka, Kaiserslautern, Texas A&M, and Case Western. It will be very useful to reduce the acquired experimental, as well as analytical/numerical, data in the form proposed in [55]. It will then become clearer what adjustments the model would require. It will also indicate directions for further research.

REFERENCES

1. Muszynska, A.: Modal Testing of Rotor/Bearing Systems, The International Journal of Analytical and Experimental Modal Analysis, July 1986, pp. 15–34.

2. Bently, D. E.; Muszynska, A. and Jones, D. I. G.: Some Aspects of the Application of Mechanical Impedance for Turbomachinery and Structural System Parameter Identification, Proc. of 3rd International Modal Analysis Conference, Orlando, Florida, January 1985, pp. 177–186.

3. Childs, D. W. and Kim, Chang–Ho: Testing for Rotordynamic Coefficients and Leakage: Circumferentially–grooved Turbulent Annular Seals, The International Conference on Rotordynamics, Tokyo, Japan, September 1986, pp. 609–618.

4. Stone, J. M. and Underwood, F. A.: Load Carrying Capacity of Journal Bearings, SAE Quart. Trans., No. 1, 1947.

5. Hull, E. H.: Journal Bearing Behavior Under Periodic Loading, G.I. Research Laboratory, Rep. No. 55–RL–1354, Schenectady, New York, 1955.

6. Bently, D. E. and Bosmans, R. F.: Oil Whirl Resonance, Fundamentals of the Design of Fluid Film Bearings, Published by ASME, 1979, pp. 131–193.

7. Iwatsubo, T.: Evaluation of Instability Forces of Labyrinth Seals in Turbines or Compressors, Rotordynamic Instability Problems in High–Performance Turbomachinery, NASA CP 2133, The First Texas A&M University Workshop, College Station, Texas, May 1980, pp. 139–168.

8. Bently, D. E. and Muszynska, A.: Stability Evaluation of Rotor/Bearing System by Perturbation Tests, Rotor Dynamic Instability Problems in High Performance Turbomachinery, NASA CP 2250, The Second Workshop at Texas A&M University, College Station, Texas, 1982, pp. 307–322.

9. Bently, D. E. and Muszynska, A.: Oil Whirl Identification by Perturbation Test, Advances in Computer–Aided Bearing Design, 82–72978, ASME/ASLE Lubrication Conference, Washington, D.C., October 1982, pp. 111–119.

10. Bently, D. E. and Muszynska, A.: Perturbation Tests of Bearing/Seal for Evaluation of Dynamic Coefficients, Symposium on Rotor Dynamical Instability, Summer Annual Conference of the ASME Applied Mechanics Division, AMD — Vol. 55, Houston, Texas, June 1983, pp. 75–88.

11. Ohashi, H. and Shoji, H.: Lateral Fluid Forces Acting on a Whirling Centrifugal Impeller in Vaneless and Vaned Diffuser, Rotordynamic Instability Problems in High–Performance Turbomachinery, NASA CP 2338, The Third Texas A&M University Workshop, College Station, Texas, May 1984, pp. 109–122.

12. Jery, B.; Acosta, A. J.; Brennen, C. E. and Caughey, T. K.: Hydrodynamic Impeller Stiffness, Damping, and Inertia, ibid., pp. 137–160.

13. Bently, D. E. and Muszynska, A.: The Dynamic Stiffness Characteristics of High Eccentricity Ratio Bearings and Seals by Perturbation Testing, ibid., pp. 481–491.

14. Bently, D. E. and Muszynska, A.: Identification of Bearing and Seal Dynamic Stiffness Parameters by Steady–State Load and Squeeze Film Tests, Proc. of BRDRC Symposium on Instability in Rotating Machinery, Carson City, Nevada, NASA CP 2409, 1985, pp. 301–316.

15. Bently, D. E. and Muszynska, A.: Measurement of Rotor System Dynamic Stiffness by Perturbation Testing, ibid., pp. 47–58.

16. Bently, D. E. and Muszynska, A.: Perturbation Study of Rotor/Bearing System: Identification of the Oil Whirl and Oil Whip Resonances, Tenth Biennial ASME Design Engineering Division Conference on Mechanical Vibration and Noise, 85–DET–142, Cincinnati, Ohio, September 1985.

17. Bently, D. E. and Muszynska, A.: Modal Testing and Parameter Identification of Rotating Shaft/Fluid Lubricated Bearing System, Proc of the 4th International Modal Analysis Conference, Los Angeles, California, February 1986, pp. 1393–1402.

18. Adkins, D. R. and Brennen, C. E.: Origins of Hydrodynamic Forces on Centrifugal Pump Impellers, Rotordynamic Instability Problems in High–Performance Turbomachinery, NASA CP 2443, The Fourth Texas A&M University Workshop, NASA CP 2443, College Station, Texas, June 1986, pp. 467–492.

19. Childs, D. W.: Force and Moment Rotordynamic Coefficients for Pump–Impeller Shroud Surfaces, ibid., pp. 503–530.

20. Kanki, H.; Fujii, H.; Hizume, A.; Ichimura, T. and Yamamoto, T.: Solving Nonsynchronous Vibration Problems of Large Rotating Machineries by Exciting Test in Actual Operating Condition, The International Conference on Rotordynamics, Tokyo, Japan, September 1986, pp. 221–226.

21. Childs, D. W.: Fluid–Structure Interaction Forces at Pump–Impeller–Shroud Surfaces for Rotordynamic Calculations, Rotating Machinery Dynamics, ASME DE–vol. 2, H0400B, Boston, Massachusetts, September 1987, pp. 581–594.

22. Ohashi, H.; Sakurai, A. and Nishihama, J.: Influence of Impeller and Diffuser Geometries on the Lateral Fluid Forces of Whirling Centrifugal Impeller, The Fifth Workshop on Rotordynamic Instability Problems in High Performance Turbomachinery, Texas A&M, NASA CP 3026, May 1988, pp. 285–306.

23. Iwatsubo, T.; Sheng, B. and Matsumoto, T.: An Experimental Study on the Static and Dynamic Characteristics of Pump Annular Seals, ibid., pp. 229–252.

24. Childs, D. W.; Elrod, D. and Hale, K.: Annular Honeycomb Seals: Test Results for Leakage and Rotordynamic Coefficients, Comparison to Labyrinth and Smooth Configurations, ibid., pp. 143–160.

25. Adams, M. L.; Yang, T. and Pace, S. E.: A Seal Test Facility for the Measurement of Isotropic and Anisotropic Linear Rotordynamic Characteristics, ibid., pp. 253–268.

26. Brennen, C. E.; Franz. R. and Arndt, N.: Effects of Cavitation on Rotordynamic Force Matrices, 1988 Conference on Advanced Earth–to–Orbit Propulsion Technology, NASA, Huntsville, Alabama, May 1988, pp. 227–239.

27. Bolleter, U.; Wyss, A.; Welte, I. and Stürchler, R.: Measurement of Hydrodynamic Interaction Matrices of Boiler Feed Pump Impellers, Trans. of the ASME, Journal of Vibration, Acoustics, Stress and Reliability in Design, v. 109, April 1987.

28. Yasuda, C.; Kanki, H.; Ozawa, T. and Kawakami, T.: Application of Random Excitation Technique to Dynamic Characteristics Measurement of Bearing, The International Conference on Rotordynamics, Tokyo, Japan, September 1986, pp. 61–68.

29. Kanki, H.; Mori, S. and Hizume, A.: Theoretical and Experimental Study on the Destabilizing Force by Labyrinth Seal, ibid., pp. 603–608.

30. Morton, P. G.: The Derivation of Bearing Characteristics by Means of Transient Excitation Applied Directly to a Rotating Shaft, Dynamics of Rotors, 1974 IUTAM Symposium, Lyngby, Denmark, Springer–Verlag, Berlin, Heidelberg, New York, 1975, pp. 350–379.

31. Nordmann, R. and Massman, H.: Identification of Dynamic Coefficients of Annular Turbulent Seals, Rotordynamic Instability Problems in High–Performance Turbomachinery, NASA CP 2338, The Third Texas A&M University Workshop, College Station, Texas, May 1984, pp. 294–312.

32. Massmann, H. and Nordmann, R.: Some New Results Concerning the Dynamic Behavior of Annular Turbulent Seals, Instability in Rotating Machinery, NASA CP 2409, Carson City, Nevada, 1985, pp. 179–194.

33. Nordmann, R.; Dietzen, F. J.; Janson, W.; Frei, A. and Florjancic, S.: Rotordynamic Coefficients and Leakage Flow for Smooth and Grooved Seals in Turbopumps, The International Conference on Rotordynamics, Tokyo, Japan, September 1986, pp. 619–628.

34. Nordmann, R. and Diewald, W.: Influence of Different Types of Seals on the Stability Behavior of Turbopumps, The Second International Symposium on Transport Phenomena, Dynamics and Design of Rotating Machinery, Honolulu, Hawaii, April 1988, pp. 351–361.

35. Diewald, W. and Nordmann, R.: Influence of Different Types of Seals on the Stability Behavior of Turbopumps, The Fifth Workshop on Rotordynamic Instability Problems in High—Performance Turbomachinery, Texas A&M University, College Station, Texas, NASA CP 3026, May 1988, pp. 197–210.

36. Muszynska, A.: Improvements in Lightly Loaded Rotor/Bearing and Rotor/Seal Models, Trans of the ASME Journal of Vibration Acoustics, Stress and Reliability in Design, v. 110, No. 2, April 1988, pp. 129–136.

37. Bolotin, V. V.: Nonconservative Problems in the Theory of Elastic Stability, The Macmillan Company, New York, 1963.

38. Black, H. F.: Effects of Hydraulic Forces in Annular Pressure Seals on the Vibrations of Centrifugal Pump Rotors, Journal of Mechanical Engineering Science, v. II, No. 2, 1969, pp. 206–213.

39. Black, H. F. and Jensen, D. N.: Dynamic Hybrid Bearing Characteristics of Annular Controlled Leakage Seals, Proceedings Journal of Mechanical Engineering, v. 184, 1970, pp. 92–100.

40. Muszynska, A.: Whirl and Whip — Rotor/Bearing Stability Problems, Journal of Sound and Vibration, v. 110, No. 3, 1986, pp. 443–462.

41. Muszynska, A. and Bently, D. E.: Anti—Swirl Arrangements Prevent Rotor/Seal Instability, Thermo—Fluid Dynamics of Rotating Machinery, Trans. of the ASME, Journal of Vibration, Acoustics, Stress and Reliability in Design, v. 111, April 1989, pp. 156–162.

42. Muszynska, A.; Franklin, W. D. and Bently, D. E.: Rotor Active "Anti—Swirl" Control, Trans of the ASME, Journal of Vibration, Acoustics, Stress and Reliability in Design, v. 110, No. 2, April 1988, pp. 143–150.

43. Jenny, R. and Wyssman, H. R.: Lateral Vibration Reduction in High Pressure Centrifugal Compressors, Proceedings of the 9th Turbomachinery Symposium, Texas A&M University, 1980, pp. 45–56.

44. Massey, I. C.: Subsynchronous Vibration Problems in High—Speed, Multistage Centrifugal Pumps, Proceedings of the 14th Turbomachinery Symposium, Texas A&M University, 1985.

45. Pace, S. E.; Florjancic, S. and Bolleter, U.: Rotordynamic Developments for High Speed Multistage Pumps, Proceedings of the 3rd International Pump Symposium, Texas A&M University, 1986.

46. Kirk, R. G. and Simpson, M.: Full Local Shop Testing of 1800 HP Gas Turbine Driven Centrifugal Compressor for Offshore Platform Service: Evaluation of Rotor Dynamics Performance, Proc. of Symp. Instability in Rotating Machinery, Carson City, Nevada, June 1985; NASA Conference Publication 2409, 1985, pp. 1–13.

47. Ambrosch, F. and Schwaebel, R.: Method of and Device for Avoiding Rotor Instability to Enhance Dynamic Power Limit of Turbines and Compressors, United States Patent, #4,273,510, June 1981.

48. Miller, E. H.: Rotor Stabilizing Labyrinth Seal for Steam Turbines, United States Patent #4,420,161, December 1983.

409

49. Wyssmann, H. R.: Theory and Measurements of Labyrinth Seal Coefficients for Rotor Stability of Turbocompressors, The Fourth Workshop on Rotordynamic Instability Problems in High Performance Turbomachinery, Texas A&M University, College Station, Texas, NASA CP 2443, June 1986, pp. 237–258.

50. Brown, R. D. and Leong, Y. M. M. S.: Experimental Measurements of Lateral Force in a Model Labyrinth and the Effect on Rotor Stability, The Third Workshop on Rotordynamic Instability Problems in High Performance Turbomachinery, NASA CP 2338, College Station, Texas, May 1989, pp. 187–210. .

51. Brown, R. D. and Hart, A.: A Novel Form of Damper for Turbomachinery, The Fourth Workshop on Rotordynamic Instability Problems in High Performance Turbomachinery, Texas A&M University, College Station, Texas, June 1986, pp. 325–348.

52. Tsujimoto, Y.; Acosta, A. J. and Yoshida, Y.: A Theoretical Study of Fluid Forces on a Centrifugal Impeller Rotating and Whirling in a Varied Diffuser, The Fifth Workshop on Rotordynamic Instability Problems in High–Performance Turbomachinery, NASA CP 3026, Texas A&M, College Station, Texas, May 1988, pp. 307–322.

53. Muszynska, A.: Multi–Mode Whirl and Whip in Rotor/Bearing Systems, Dynamics of Rotating Machinery, Ed. by J. H. Kim and W. J. Yang, Hemisphere Publ. Corp., New York; Proc. of Second International Symposium on Transport Phenomena Dynamics, and Design in Rotating Machinery, Honolulu, Hawaii, April 1988, pp. 326–340.

54. Muszynska, A. and Grant, J. W.: Stability and Instability of a Two–Mode Rotor Supported by Two Fluid–Lubricated Bearings, BRDRC Report, No. 1/90, 1990.

55. Tam, L. T.; Przekwas, A. J.; Muszynska, A.; Hendricks, R. C.; Braun M. J. and Mullen R. L.: Numerical and Analytical Study of Fluid Dynamic Forces in Seals and Bearings, Rotating Machinery Dynamics, 1987 ASME Design Technology Conference, DE–vol. 2, 1987, Trans. of the ASME, Journal of Vibration, Acoustics, Stress, and Reliability in Design, v. 110, No. 3, July 1988, pp. 315–325.

NOTATION

A	Amplitude of rotor vibration
D, K_0, M_f	Fluid radial damping, stiffness, and inertia effect respectively
D_s, K, M	Rotor generalized (modal) damping, stiffness, and mass respectively
DDS, QDS	Direct and quadrature dynamic stiffness components respectively
F	Force amplitude
F_r, F_t	Radial and tangential force components
s	Eigenvalue
t	Time
$z = x + jy$	Rotor displacement in stationary coordinates
$z_r = x_r + jy_r$	Rotor displacement in rotating coordinates
α	Force/displacement phase
$\bar{k}$	Complex dynamic stiffness
λ	Fluid circumferential average velocity ratio
ω	Perturbation/precession frequency
Ω	Rotative speed

THE APPLICATION OF A CYLINDRICAL-SPHERICAL FLOATING RING BEARING AS A DEVICE TO CONTROL STABILITY OF TURBOGENERATORS

P.S. Leung and I.A. Craighead
Newcastle Polytechnic
Newcastle upon Tyne, England

T.S. Wilkinson
NEI Parsons Ltd.
Newcastle upon Tyne, England

The development of a new device to control stability of turbogenerators is described in the present study. The device comprises a floating ring installed between the journal and bearing housing of a fluid film bearing. The journal and the inner surface of the ring are cylindrical whilst the outer surface of the ring and bearing surface are spherical providing axial location of the ring and self-alignment of the bearing. The employment of this device would lead to a consistant machine performance. System stability may be controlled by changing a number of bearing and floating ring parameters. This device also offers an additional advantage of having a very low frictional characteristics.

A feasibility study was carried out to investigate the suitability of the new device to turbogenerator applications. Both theoretical analysis and experimental observations were carried out. Initial results suggest that the new floating ring device is a competitive alternative to other conventional arrangements.

NOTATION

C	film clearance
D	diameter
G_θ, G_β	turbulent coefficients
h	film thickness
$\bar{M}_1$	non-dimensional inner film viscous moment

$$= \frac{C_1}{\mu R_1^3 L (\omega_1 + \omega_2)} M_1$$

$\bar{M}_2$	non-dimensional outer film viscous moment

$$= \frac{C_2}{\mu R_2^4 \omega_2} M_2$$

N	rotational speed in rev/s
P	pressure

R   radius
Re   Reynolds' number
S_1 inner film Sommerfeld number

$$= \frac{\mu (N_1 + N_2) L D_1}{W_1} \left(\frac{R_1}{C_1} \right)^2$$

S_2 outer film Sommerfeld number

$$= \frac{\mu N_2 L D_2}{(W_1 + W_2)} \left(\frac{R_2}{C_2} \right)^2$$

Sb   bearing Sommerfeld number

$$= \frac{\mu N_1 L D_1}{W_1} \left(\frac{R_1}{C_1 + C_2} \right)^2$$

W   loading
Z   co-ordinate in longitudinal direction
α (ring speed)/(rotor speed)
β polar co-ordinate in longitudinal direction
γ (weight of floating ring)/(bearing load)
ϵ eccentricity ratio
θ polar co-ordinate in circumferential direction
τ viscous shear stress
μ fluid viscosity
ω rotational speed in rad/s

SUBSCRIPTS

1   inner fluid film or the journal
2   outer fluid film or the ring

1.   INTRODUCTION

Modern designs of turbo-machinery usually aim at larger power output, improved
efficiency and higher running speed. These design criteria demand an improved
bearing performance. In fact, the industry is always seeking for a better bearing
design in order to achieve better control on machine performance. The development
of a new type of floating ring bearing and its potential application on turbo-
generators is described in this paper. The journal and inner surface of the ring
are cylindrical whilst the outer surface of the ring and the bearing are spherical
providing axial location of the ring and allowing self alignment of the bearing.

The idea of having a floating ring in a fluid film bearing has existed for some
time. The conventional floating ring bearing comprises an annular ring with cylin-
drical surfaces on both sides of the ring. The ring was allowed to move and rotate
freely within the space available. This bearing design is known as the plain
floating ring bearing. The earliest recorded use of this bearing can be traced back
to 1912 where such a bearing was used in Leyland's vehicles [Campbell (1)]. This
type of bearing was also used in a Parsons' steam turbine, and in the connecting rod
of Bristol aircraft engines in the 1920's [Shaw and Nussdorfer (2)]. Modifications
of the basic design also exist. A literature survey of floating ring bearings can

be found in [Leung (3)].

The new bearing design is an attempt to combine different good features found in conventional bearings into a single physical unit. The spherical outer surface of the ring would allow the bearing to tolerate large misalignments. The presence of two fluid films would possibly increase the damping of bearing. It is known that floating ring bearings usually possess low frictional characteristics. The stability of bearing may also be controlled by a variety of bearing and floating ring parameters. The purpose of the present investigation is to verify these assumptions. The behaviour of the cylindrical-spherical floating ring bearing is first analysed. The bearing performance under different working conditions is then examined and compared with those of equivalent conventional bearings. The possibility of applying the new bearing to turbo-machinery is explored through a case study.

2.   ANALYSIS

The configuration of the cylindrical-spherical floating ring bearing is illustrated in Fig 1. The inner fluid film supports the external load acting on the journal whilst the outer fluid film is required to support both the external load and the weight of the floating ring. Lubricant is supplied from the central circumferential grooves to the bearing surfaces. Hence, each fluid film may be analysed as having two shorter fluid films with the L/D ratio half the original value. The effective behaviour of each film is the sum of the shorter films.

The steady state solution of the floating ring bearing is mainly based on two equilibrium conditions,

a)   balance of forces: The sum of the hydrodynamic force of the inner film plus the weight of the floating ring should be equal to the hydrodynamic force of the outer film.

b)   balance of frictional moments on the ring: Under steady state operation, the viscous moment acting on the inside surface of the ring should be equal to the viscous moment acting on the outside surface of the ring.

In order to establish the steady state solution of the bearing, it is necessary to calculate the bearing forces of each bearing film and the viscous moments acting at both sides of the ring. The procedure is described as follows,

2.1   The Reynolds' equation and bearing forces

The Reynolds' equation for the cylindrical inner film can be written as follows,

$$\frac{1}{R_1^2} \frac{\partial}{\partial \theta_1} \left(G_{\theta_1} \frac{h_1^3}{\mu} \frac{\partial P_1}{\partial \mu_1} \right) + \frac{\partial}{\partial Z_1} \left(G_{\beta_1} \frac{h_1^3}{\mu} \frac{\partial P_1}{\partial Z_1} \right)$$

$$= \frac{(\omega_1 + \omega_2)}{2} \frac{\partial h_1}{\partial \theta_1} + \frac{\partial h_1}{\partial t} \tag{1}$$

413

and for the spherical outer film, the Reynolds' equation is,

$$\frac{1}{R_2{}^2} \frac{1}{\cos^2\beta_2} \frac{\partial}{\partial\theta_2} \left(G_{\theta_2} \frac{h_2{}^3}{\mu} \frac{\partial P_2}{\partial\theta_2} \right) + \frac{1}{R_2{}^2} \frac{\partial}{\partial\beta_2} \left(G\beta_2 \frac{h_2{}^3}{\mu} \frac{\partial P_2}{\partial\beta_2} \right)$$

$$+ \frac{1}{R_2{}^2} \theta_2 \tan\beta_2 \frac{\partial}{\partial\theta_2} \left(G\beta_2 \frac{h_2{}^3}{\mu} \frac{\partial P_2}{\partial\beta_2} \right) + \frac{1}{R_2{}^2} \frac{\partial}{\partial\beta_2} \left(G\beta_2 \frac{h_2{}^3}{\mu} \theta_2 \tan\beta_2 \frac{\partial P_2}{\partial\theta_2} \right)$$

$$+ \frac{1}{R_2{}^2} \theta_2 \tan\beta_2 \frac{\partial}{\partial\theta_2} \left(G\beta_2 \frac{h_2{}^3}{\mu} \theta_2 \tan\beta_2 \frac{\partial P_2}{\partial\theta_2} \right) = \frac{\omega_2}{2} \frac{\partial h_2}{\partial\theta_2} + \frac{\partial h_2}{\partial t} \qquad (2)$$

where G_θ and G_β are coefficients dependent on the local Reynolds' number [Constantinescu (4)], and the film thickness can be expressed as follows,

$$h_1 = C_1 (1 + \varepsilon_1 \cos \theta_1) \qquad (3)$$

$$h_2 = C_2 (1 + \varepsilon_2 \cos \theta_2 \cos \beta_2) \qquad (4)$$

Equations (1) and (2) can be normalised by using selected non-dimensional groups [Craighead (5) and Leung (3)]. For a given inner and outer eccentricity ratio, the equations can then be solved by the finite difference method. Essentially, the pressure distribution of each fluid film is described by a rectangular mesh and the pressure at each nodal point is determined iteratively. Details of the computational scheme can be found in Craighead (5). The bearing forces may then be obtained by integrating the pressure field by a numerical integration method.

2.2 Frictional moments on the ring

The frictional forces acting on the inside and outside surfaces of the ring are dependent on the viscous shear force of the lubricant in each fluid film which is in turn dependent on the relative velocities of the corresponding solid surfaces enclosing the film. From the Navier-Stokes equation, the viscous shear stresses acting on the ring can be written as,

for the inside surface,

$$\tau_1 = Q \left[\frac{h_1}{2R_1} \frac{\partial P_1}{\partial\theta_1} - \frac{\mu}{h_1} (\omega_1 - \omega_2) R_1 \right] \qquad (5)$$

and for the outside surface,

$$\tau_2 = Q \left[\frac{h_2}{2 R_2 \cos\beta_2} \frac{\partial P_2}{\partial\theta_2} + \frac{\mu}{h_2} \omega_2 R_2 \cos\beta_2 \right] \qquad (6)$$

Where Q is the ratio of turbulent friction to laminar friction, and is dependent on the mean Reynolds' number of each film. In the present study,

$Q = 0.039 \, Re^{0.57}$ for turbulent flow

$Q = 1$ for laminar flow

The frictional moments can then be obtained by integrating the corresponding shear stress so that,

for the inside surface,

$$M_1 = 2 \int_0^{L/2} \int_0^{2\pi} \tau_1 \, R_1{}^2 \, d\theta_1 \, dZ_1 \tag{7}$$

and for the outside surface,

$$M_2 = 2 \int_0^{\beta e} \int_0^{2\pi} \tau_2 \, R_2{}^3 \, \cos^2\beta_2 \, d\theta_2 \, d\beta_2 \tag{8}$$

The frictional moments may be obtained in non-dimensional form, from results of the normalised Reynolds' equation. The viscous friction in the cavitation region of the films is also included in the present study [Ruddy (6) and Leung (3)].

2.3 Calculation procedure for the steady state solution

The computational strategy to determine the steady state solution of the bearing is described in this section. From the balance of forces, the ratio of Sommerfeld number for the inner and outer fluid films can be written as,

$$\frac{S_1}{S_2} - \frac{(1 + \alpha)}{\alpha} \left(\frac{R_1}{R_2}\right)^3 \left(\frac{C_2}{C_1}\right)^2 (1 + \gamma) = 0 = G_1 \tag{9}$$

From the balance of frictional moments, the ratio of the non-dimensional moments acting at inside and outside surfaces of the ring can be written as,

$$\frac{\overline{M}_1}{\overline{M}_2} - \frac{\alpha}{(1 + \alpha)} \left(\frac{R_2}{R_1}\right)^4 \left(\frac{C_1}{C_2}\right) \left(\frac{R_1}{L}\right) = 0 = G_2 \tag{10}$$

Equations (9) and (10) determine the relationship between the inner film eccentricity ratio, the outer film eccentricity ratio, and the (ring speed/rotor speed) ratio. For a given value of inner eccentricity ratio, the equations may then be used to search for the outer film eccentricity ratio and the speed ratio. A modified form of the Newton's iteration method [Gerald (7)] was used in this study, as follows,

$$\begin{bmatrix} \varepsilon_2 \\ \\ \alpha \end{bmatrix}_{k+1} = \begin{bmatrix} \varepsilon_2 \\ \\ \alpha \end{bmatrix}_k - R_f \begin{bmatrix} \dfrac{\partial G_1}{\partial \varepsilon_2} & \dfrac{\partial G_1}{\partial \alpha} \\ \\ \dfrac{\partial G_2}{\partial \varepsilon_2} & \dfrac{\partial G_2}{\partial \alpha} \end{bmatrix}_k^{-1} \begin{bmatrix} G_1 \\ \\ G_2 \end{bmatrix}_k \tag{11}$$

where k indicates the state of successive interations and R_f is the relaxation factor.

415

The matrix containing the partial derivatives (the Jacobian matrix) is obtained by numerical perturbation of G_1 and G_2. The steady state solution is then obtained if a specified tolerance is satisfied. When R_f is equal to unity, the usual Newton's iteration method is used. It provides stable iteration for cases with laminar lubricant flow. However, the iteration may sometimes fail to converge if the lubricant flow is assumed turbulent. An under-relaxation factor of value from 0.5 to 0.75 was found satisfactory for all cases with either assumption. The application of the under-relaxation factor for laminar flow condition could reduce the computational time by up to 20% when compared with the case where R_f is equal to unity.

2.4 The dynamic characteristics of the bearing

The dynamic characteristics of the bearing are represented by a set of eight linearised force coefficients so that the bearing forces acting on the journal can be expressed by the following equations,

$$F_x = A_{xx} X + A_{xy} Y + B_{xx} \dot{X} + B_{xy} \dot{Y}$$

$$F_y = A_{yx} X + A_{yy} Y + B_{yx} \dot{X} + B_{yy} \dot{Y}$$
(12)

The displacement coefficients, A's, are obtained by perturbing the displacement of the journal centre from its steady state position. The velocity coefficients, B's, are obtained by perturbing the velocity of the journal centre. These coefficients may then be used to study the stability and response characteristics of the bearing applied to different rotor systems.

3. PARAMETRIC INVESTIGATION OF BEARING PERFORMANCE

To ensure good design and reliable service it is necessary to determine the behaviour of the new bearing under different working conditions. In this study, six bearing parameters were investigated. A bearing with typical parameter values was first selected as the reference case. Each parameter was then varied about the reference conditions and any changes in bearing characteristics have been noted. The results are desctibed as follows.

3.1 The clearance ratio (C2/C1)

The ratio of the outer film clearance to the inner film clearance was found to be significant in determining many bearing characteristics. Design charts are given in this case as examples. In the present study, it is assumed that the total clearance of the inner and outer films is constant. Variation of C2/C1 is achieved by changing the inner film and outer film clearances at the same time.

For a given operating condition, it was found that increasing C2/C1 would cause a reduction in inner film eccentricity ratio, but an increase in outer film eccentricity ratio. As a result, the overall bearing eccentricity ratio, which is defined as the ratio of the journal displacement to the total clearance, is reduced (Fig 2). This implies that the load carrying capacity of the bearing is increased by an increase of clearance ratio. The bearing attitude angle, however, is reduced (Fig 3). Increasing the value of C2/C1 will also increase the (ring speed)/ (rotor speed) ratio (Fig 4). Consider that the inner film clearance is reduced as C2/C1 is increased, the shear force acting at the inside surface of the ring will then be increased. The speed ratio is therefore increased.

The journal frictional loss (usually indicated by the friction factor) is also increased for a similar reason (Fig 5).

The dynamic coefficients of the bearing are shown in Figs 6 and 7. These coefficients are used to calculate the limit of stability [Craighead (5)] of the bearing (Fig 8). The effect of the clearance ratio on the dynamic stability can be divided into two regions : for low Sommerfeld numbers, the stability is reduced by increasing value of the clearance ratio; for high Sommerfeld numbers, increasing the value of the clearance ratio will increase the limit of stability. Large values of clearance ratio is therefore beneficial in high speed or light load operations. The ratio of the (whirl speed)/(rotor speed + ring speed) was found to be about 0.5 as expected (Fig 9) [Orcutt and Ng (8)]. However, it is common to calculate the (whirl speed/ rotor speed) for bearings with a single film. For the floating ring bearing, the value of this ratio will be higher than 0.5 and within the range of 0.6 to 0.7 (Fig 10).

3.2 The ratio of the ring radii (R2/R1)

The ratio of the ring outside radius to inside radius also affects the performance of the floating ring bearing. For an increasing value of R2/R1, the frictional moment acting at the outside surface of the ring will be increased. This reduces the (ring/rotor) speed ratio and hence reduces the load carrying capacity of the outer film. As a result, the overall load carrying capacity and attitude angle of the bearing is reduced. The frictional power loss, however, is increased because the reduction of ring speed will increase the frictional force acting at the journal surface. In terms of dynamic characteristics, increasing the value of R2/R1 increases the limit of stability of the bearing for the range of Sommerfeld Number examined.

3.3 The (L/D1) ratio

The effects of varying the L/D1 ratio on the floating ring bearing are similar to those found in conventional bearings. Increasing the value of L/D1 ratio will cause an increase in load carrying capacity and attitude angle of the bearing. However, for a given Sommerfeld Number, both the speed ratio and friction factor are not seriously affected by the change in L/D1 ratio. It should be noted that, if the variation of L/D1 ratio is achieved by simply varying the length of the bearing, a smaller L/D1 ratio will result in a smaller Sommerfeld number. In this case, reduction of L/D1 ratio will cause a slight reduction of the speed ratio and a significant reduction in frictional loss. In terms of dynamic behaviour, a reduction of L/D1 ratio will increase the limit of stability of the bearing. Hence, a bearing with a small value of L/D1 ratio is often preferred.

3.4 The mean bearing Reynolds' number

There are two fluid films in a floating ring bearing. The Reynolds' numbers are usually different for each film. In order to ensure comparable results, the mean bearing Reynolds' number of the floating ring bearing is defined herein to indicate the Reynolds' number of an equivalent single film bearing. In the present study, the bearing clearance of the single film bearing is equal to the total clearance of the floating ring bearing. The actual Reynolds' number for the inner and outer films is therefore less than the mean bearing Reynolds' number due to the existence of a rotating ring and a smaller clearance for each film.

417

The effects of increasing the bearing Reynolds' number on the floating ring bearing are quite similar to those found in single film bearings. However, the floating ring bearing is less sensitive to the change of bearing Reynolds' number, as would be expected. Increasing the value of bearing Reynolds' number will increase the load carrying capacity and the attitude angle of the bearing. The frictional loss is also increased as expected. It should be pointed out that the bearing Reynolds' number has a significant effect on the ring speed ratio. The ring speed is dependent on the viscous friction of the fluid films and the bearing Reynolds' number affects the viscous friction considerably. An increase in Reynolds' number will cause an increase in speed ratio. Also, increasing the value of the bearing Reynolds' number reduces the limit of stability of the bearing.

3.5 The supply pressure

The lubricant supply may sometimes be pressurised, for example, to increase the lubricant flow rate. It was found in this study that pressurising the lubricant increased the load carrying capacity and attitude angle of the floating ring bearing. This was achieved at the cost of reducing bearing stability. It is generally known that the existence of a cavitation region in a bearing may have a stabilising effect on the bearing performance. Pressurising the lubricant, however, will reduce the cavitation region of the bearing.

3.6 The weight of the floating ring

The weight of the floating ring is usually small compared with the loading on the bearing (ie. less than 5%), and is neglected in most analyses. The effect of the loading due to the ring was examined in this study. It was found that the weight of the floating ring had very little effect on both the steady state and the limit of stability of the floating ring bearing. The bearing performance was practically unchanged even when the weight of the ring was increased up to 10% of the bearing loading. This result indicates that the weight of the ring may be neglected without significant loss of accuracy. It also allows more flexibility in selecting the ring material without affecting the bearing performance.

4. COMPARISON WITH OTHER BEARINGS

The steady state and dynamic performance of the cylindrical-spherical floating ring bearing have been compared with an equivalent plain floating ring bearing, a conventional cylindrical bearing and an elliptical bearing. In order to ensure comparable results, all bearing parameters such as the L/D1 ratio, Reynolds' number, C2/C1 ratio and R2/R1 ratio, where applicable, are kept identical to those of the cylindrical-spherical floating ring bearing. For the single film bearings, the bearing clearance was equal to the total clearance of the inner and outer fluid films of the floating ring bearing. All bearings studied were analysed by the finite difference technique for finite bearings.

It was found that the behaviour of the cylindrical-spherical floating ring bearing is very similar to that found in a plain floating ring bearing. The load carrying capacity of the spherical outer film of the new bearing is slightly lower than that of the cylindrical outer film of the plain bearing [Leung (9)]. Despite some minor differences, the characteristics of the two floating ring bearings are so close that, for practical purposes, the differences may be ignored. The new floating ring bearing, hence, has the advantage over the plain floating ring bearing of being self aligning.

The load carrying capacity of the floating ring bearing was found to be higher than the cylindrical bearing but lower than the elliptical bearing. The separation of a single fluid film into two thinner films is thought to be reasonable for the increase of the load carrying capacity of the floating ring bearing over the cylindrical bearing. However, the frictional power loss of the floating ring bearing, with laminar lubricant flow, is slightly higher than the loss of the cylindrical bearing but very close to that of the elliptical bearing. For similar reasons as above, the reduction of film thickness will increase the viscous friction in the bearing films and hence increase the frictional loss when compared with the cylindrical bearing. The geometry of the elliptical bearing is responsible for the high load carrying capacity and high frictional loss of the bearing.

The real advantage of the floating ring bearing in terms of energy reduction is its ability to reduce film turbulence when compared to a single film bearing. For a given operating condition (ie. a given Sommerfeld Number), the degree of turbulence in the inner and outer films of the floating ring bearing is less than that of an equivalent cylindrical or elliptical bearing, especially with high Reynolds' numbers. As an example, when the bearing Reynolds' number is increased from laminar to about 3000, the power loss of the single film bearings is increased by 3 to 4 times the original value. The power loss of the floating ring bearing, however, is only increased by about 50% of the original value. As a result, the frictional loss of the floating ring bearing is only about 30 to 40% of that of the single film bearings. Potentially, a considerable amount of energy can be saved.

Stability analyses of the bearings with a rigid rotor show that the limit of stability of the floating ring bearing examined is higher than that of the cylindrical bearing but lower than that of the particular elliptical bearing. It should be pointed out that the ellipticity of the elliptical bearing studied is relatively high (ellipticity = 0.4), which makes the bearing more stable. Although the behaviour of the reference floating ring bearing does reflect the general behaviour of this type of bearing, it is not optimised for high stability. More favourable results could be obtained with suitable selection of bearing parameters.

4.1 An alternative means of comparison

The results reported so far were concerned with a floating ring bearing having a total inner and outer film clearance equal to the clearance of the equivalent single film bearing : the total clearance was kept constant even when the C2/C1 ratio was varied. However, it is also possible to construct a floating ring bearing with the inner film clearance equal to that of the single film bearing. The inner film clearance can be kept unchanged and variation of C2/C1 achieved by varying the size of the outer film clearance. The total film clearance of the floating ring bearing is hence larger than that of the equivalent conventional bearing. Most early studies of the floating ring bearing are, in fact, concerned with this second arrangement. The performance of these two arrangements of the cylindrical-spherical floating ring bearing has also been examined in this study.

The first bearing, in which the total clearance of the bearing was kept constant, was found to have a higher load carrying capacity and higher limit of stability when compared with the second arrangement. However, the frictional loss of the second bearing was lower than that of the first arrangement. Because of the larger total clearance, the lubricant flowrate of the second bearing should be larger than the first bearing. Compared to conventional bearings, the load carrying capacity, frictional loss and limit of stability of the second bearing are all lower than those of the particular cylindrical bearing.

The first arrangement is more favourable when load carrying capacity and dynamic stability are important, which is the case for most turbo-machines. The second arrangement is favourable when frictional losses and lubricant overheating are serious problems.

5.   A CASE STUDY WITH A SCALED LP TURBINE ROTOR

The application of the cylindrical-spherical floating ring bearing to turbo-machinery has been examined by a case study. The floating ring bearing was used to support a scaled LP turbine rotor. The dynamic behaviour of the system was examined and the performance of the floating ring bearing has been compared with other bearings.

The scaled flexible rotor system constitutes to part of a long term research pro-gramme and is dynamically similar to a steam turbine for a 660 MW power plant [Leung (3)]. The bearing loading of a steam turbine is considered relatively high when compared to a fast speed gas turbine. The rotor was originally supported by a pair of elliptical bearings and the bearing Reynolds' number at operating speed was estimated to be about 3500.

The frictional loss of the cylindrical-spherical floating ring bearing at operating speed was found to be only 27% of the loss for elliptical bearings, and 40% of the loss for cylindrical bearings. Hence, considerable amount of energy could be saved by using the floating ring bearing.

The stability of the rotor system was examined by eigen value analysis [ie. Craighead (5)]. Rigid foundation was first assumed. The real and imaginary parts of the eigen values indicate the stability and the system (damped) natural frequencies. Results of the study showed that the highest threshold speed was achieved when the rotor was supported by the elliptical bearing. The threshold speed was about 1.75 times the operating speed. The floating ring bearing came second. The threshold speed was found to be 1.5 times the operating speed. The threshold speed of the rotor with cylindrical bearing was below the operating speed. The cylindrical bearing would hence be unsuitable for this application. At the operating speed, the equivalent damping ratio for the lowest system frequency was 0.26 for the elliptical bearing, and 0.22 for the floating ring bearing. Despite a lower value of damping ratio, the damping in the floating ring bearing is sufficient to ensure safe and stable operation.

System response to mass unbalance was also investigated. It was found that least force was transmitted through the cylindrical bearing to ground. The elliptical bearing came second whilst the force transmitted through the floating ring bearing was the highest among the bearings examined. This result indicates that more attention is required for the supporting foundation if the floating ring bearing is to be employed. Damped flexible foundations are usually used in modern power plants. Results indicate that the forces transmitted to the ground were reduced by the introduction of a flexible foundation. The differences among the bearings in response analysis were also reduced to be very small.

A limited amount of experiments were performed on a rig (Fig 11) to verify the corresponding analysis. Generally the experimental results confirmed the theoretical results [Leung (3)]. It may be interesting to point out that many earlier investigators reported the difficulty to make the floating ring start to rotate.

In the case of turbogenerators, the machines are usually started by using the oil jacking technique. The floating ring would therefore be lifted up initially by hydrostatic pressure. With careful operations, the ring starting problem could be eliminated in turbogenerator applications.

It is worthwhile to point out that instability problems may not necessary be recognised during the design stage of a machine. Sometimes, dynamic problems only surface after the machine is commissioned and expensive remedy action is necessary. Since the dynamic properties of the floating ring bearing can be controlled by a variety of parameters, the bearing offers more choices (and hence a better chance) to correct the performance of machine.

The results of this case study suggest that each of the bearings examined offers some advantages over the others. The elliptical bearing is slightly favourable in terms of dynamic characteristics. However, the cylindrical-spherical floating ring bearing offers considerable energy saving and it is self aligning. The dynamic characteristics of the bearing is satisfactory, especially with damped flexible foundations. The overall performance of the cylindrical-spherical floating ring bearing makes it competitive with the elliptical bearing. Despite good response characteristics and simple geometry, the cylindrical bearing is not favourable in this application.

6. CONCLUSIONS

The development of the cylindrical-spherical floating ring bearing is described. With considerations of the ability to handle misalignment, low frictional characteristics, steady state and dynamic properties, the new bearing has shown favourable performance in turbogenerator applications. The development of this bearing is still in its early stage. The present study, however, demonstrates that the new bearing is an alternative and competitive design which is worthy of consideration.

REFERENCES

1) Campbell C
   Floating bush bearings
   Chartered Mechanical Engineers, March 1987, pp 14.

2) Shaw M C and Nussdorfer T J
   An analysis of the full-floating journal bearing
   NACA Report No 866, 1947.

3) Leung P S
   An investigation of the dynamic behaviour of floating ring bearing systems and their application to turbogenerators
   PhD Thesis, Dept of Mechanical Engineering, Newcastle Polytechnic, 1988.

4) Constantinescu V N
   Basic relationships in turbulent lubrication and their extensions to include thermal effects
   Transaction of A.S.M.E., Paper No 72-Lub-16.

Craighead I A
A study of the dynamics of rotor-bearing systems and related fluid-film bearing characteristics.
PhD Thesis, Dept of Mechanical Engineering, University of Leeds, 1976.

6)   Ruddy A V
The dynamics of rotor bearing systems with particular reference to the influence of fluid film journal bearings and the modelling of flexible rotors.
PhD Thesis, Dept of Mechanical Eng, University of Leeds, 1973.

7)   Gerald C F
Applied numerical analysis.
Addison-Wesley, 1980.

8)   Orcutt F K and Ng C W
Steady-state and dynamic properties of journal bearing in laminar and super-laminar flow regimes.
NASA Report CR-733, June 1967.

9)   Leung P S, Craighead I A and Wilkinson T S
An analysis of the steady state and dynamic characteristics of a spherical hydrodynamic journal bearing.
Journal of Tribology, A.S.M.E., July 1989, pp 459-467.

10) Leung P S, Craighead I A and Wilkinson T S
An analysis of the steady state and dynamic characteristics of a cylindrical-spherical floating ring bearing.
IMechE Conference C242, 1988, pp 349-357.

11) Kettleborough C F
Frictional experiments on lightly-loaded fully floating journal bearings.
Australian Journal of Applied Science, 1955, pp 211-220.

12) Hill H C
Slipper bearings and vibration control in small gas turbines.
Transaction of A.S.M.E., 1958, Vol 80, pp 1756-1764.

13) Dworski J
High speed rotor suspension formed by fully floating hydrodynamic radical and thrust bearings.
Transaction of A.S.M.E., Journal of Engineering for Power, 1964, Vol 86.

14) Kahle G W
Analytical and experimental investigation of a full floating journal bearing.
PhD Thesis, University of Illinois, January 1971.

15) Tanaka M and Hori Y
Stability characteristics of floating bush bearings.
ASLE-ASME Joint Lubrication Conference, October 1971.

16) Nakagawa E and Hiroshi A
Unbalance vibration of a rotor-bearing system supported by floating ring
bearing.
Bulletin of J.S.M.E., March 1973, Vol 16, pp 503-512.

17) Nikolajsen J L
The effect of variable viscosity on the stability of plain journal bearings
and floating ring journal bearings.
Journal of Lubrication Technology, October 1973, pp 447-1973.

18) Li C H and Rohde S M
On the steady state and dynamic performance characteristics of floating ring
bearings.
Journal of Lubrication Technology, July 1981, pp 389-397.

19) Tondl A
Some problems of rotor dynamics.
Chapman and Hall, 1965.

20) Lund J W
Rotor-bearing dynamics design technology part VII : the three lobe bearing
and floating ring bearing.
Mechanical Technology Inc., February 1968.

21) Howarth R B
A theoretical analysis of the floating pad journal bearing.
Tribology Convention, 1970.

22) Chow C Y
Dynamic characteristics and stability of a helical-grooves floating ring
bearing.
Transaction of A.S.L.E., April 1983, Vol 27, pp 154-163.
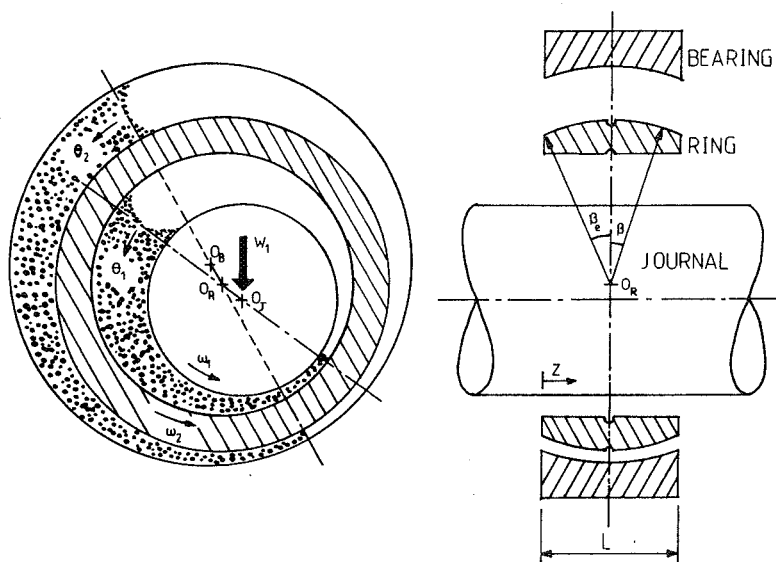
Fig 1   Configuration of the cylindrical-spherical
        floating ring bearing

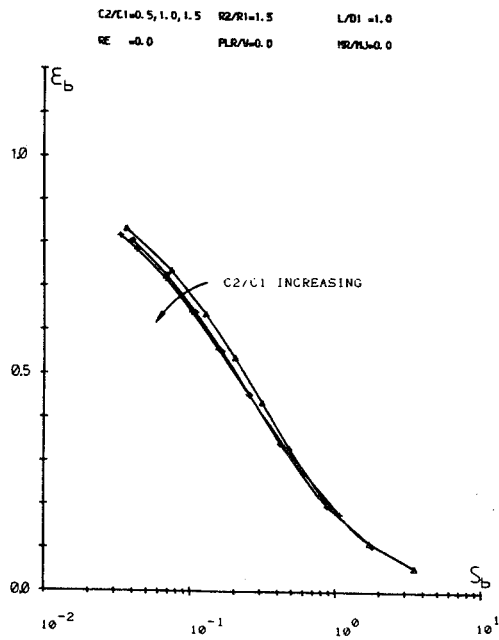Fig 2   Bearing eccentricity ratio vs
        Sommerfeld number
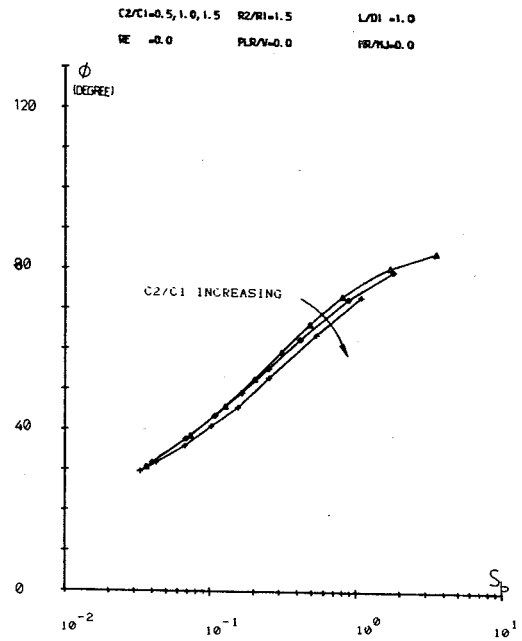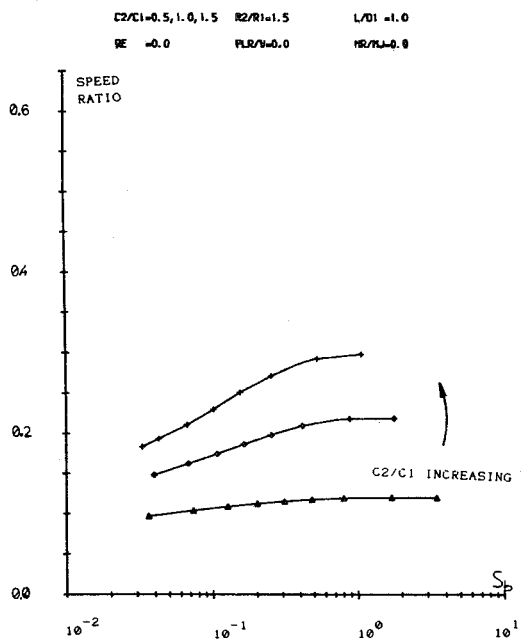
Fig 3   Attitude angle vs Sommerfeld
        number

Fig 4   Speed ratio vs Sommerfeld
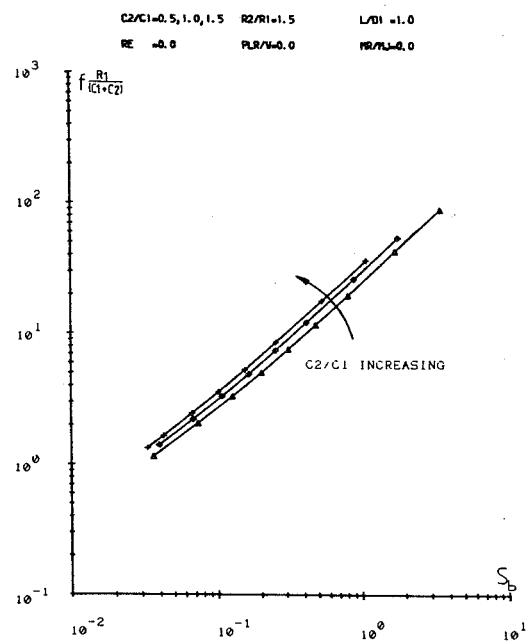   number

Fig 5   Friction factor vs Sommerfeld
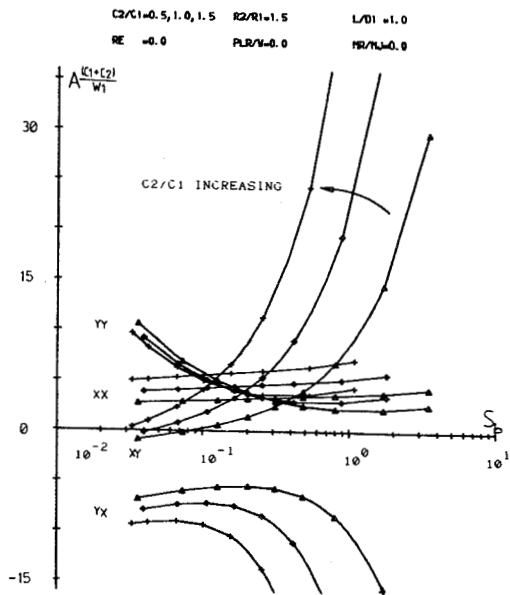   number

424

Fig 6   Displacement coefficients vs
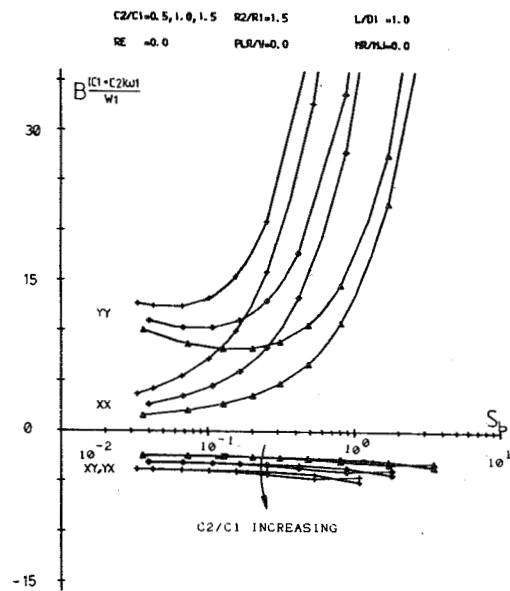   Sommerfeld number

Fig 7   Velocity coefficients vs
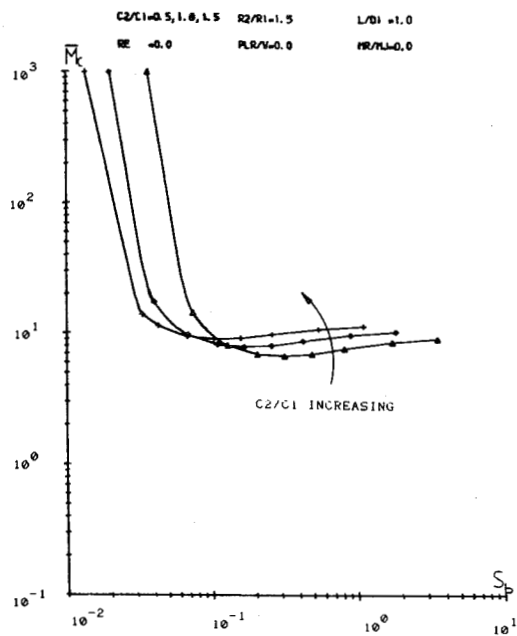   Sommerfeld number
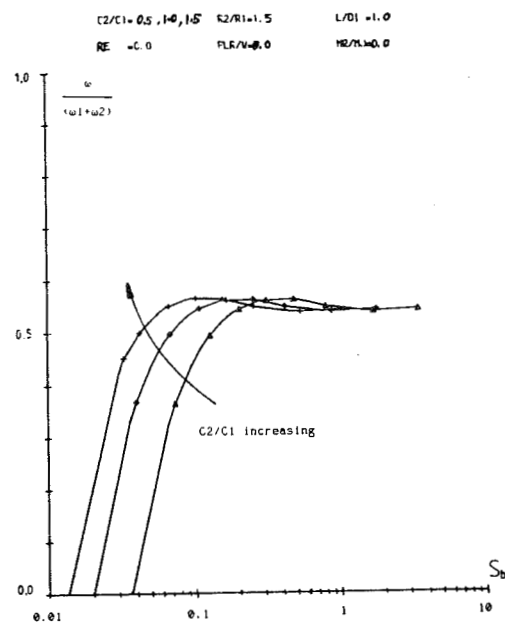

Fig 8   Critical mass vs Sommerfeld
        number

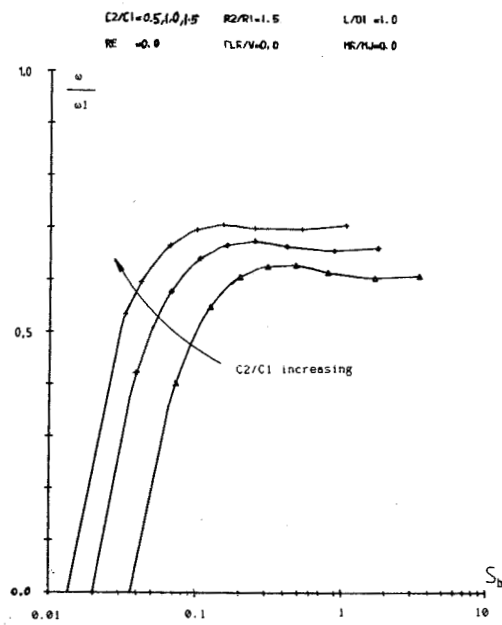Fig 9 $\omega/(\omega_J + \omega_R)$ vs Sommerfeld
        number

425

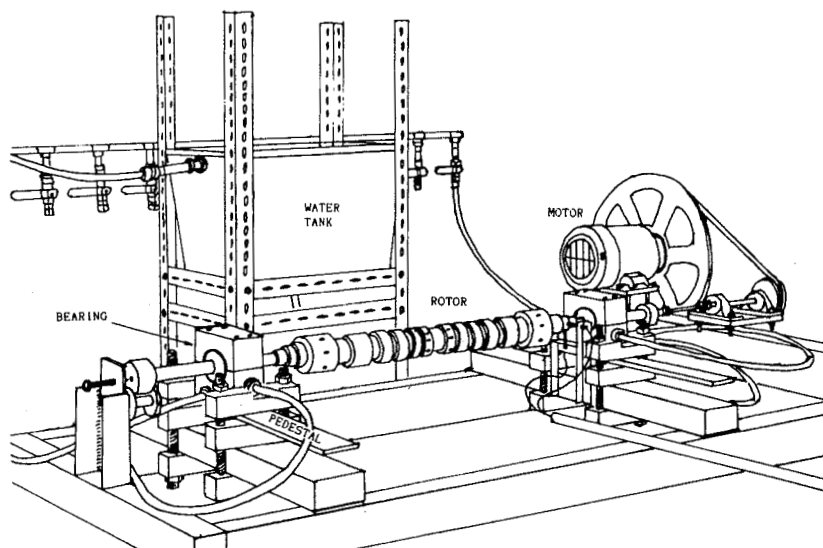Fig 10 ω/ω_J vs Sommerfeld number

Fig 11 Layout of test rig

426

FLUID COMPRESSIBILITY EFFECTS ON THE DYNAMIC RESPONSE OF HYDROSTATIC JOURNAL BEARINGS

Luis A. San Andres
Mechanical Engineering Department
Texas A&M University
College Station, Texas 77843-3123, U.S.A.

A theoretical analysis for the dynamic performance characteristics of laminar flow, capillar/orifice compensated hydrostatic journal bearings is presented. The analysis considers in detail the effect of fluid compressibility in the bearing recesses. At high frequency excitations beyond a break frequency, the bearing hydrostatic stiffness increases sharply and it is accompanied by a rapid decrease in direct damping. Also, the potential of pneumatic hammer instability (negative damping) at low frequencies is likely to occur in hydrostatic bearing applications handling highly compressible fluids. Useful design criteria to avoid undesirable dynamic operating conditions at low and high frequencies are determined. The effect of fluid recess compressibility is brought into perspective, and found to be of utmost importance on the entire frequency spectrum response and stability characteristics of hydrostatic/hybrid journal bearings.

INTRODUCTION

The dynamic performance of hydrostatic and hybrid journal bearings (HJBs) has been a subject of growing theoretical interest. In the past, conventional applications of HJBs were restricted to support heavy loads at zero or low speeds and also to low operating eccentricities required for precise machine tools. However, industry's expanding demands for higher speed applications and the ability of bearings to support dynamic loads have brought the need to consider and study in detail the dynamic performance of these type of bearings.

Davies and Leonard (1969) first studied the dynamic behavior of HJBs, and derived under restricted conditions closed form solutions for small motions about the concentric position. The limited stability characteristics of hybrid bearings have been confirmed experimentally by Davies and Leonard (1970, 1971), and Leonard and Rowe(1973). M.K. Ghosh (1979) and V.N. Singh(1979) have also presented numerical analyses for the static and dynamic performance characteristics of HJBs. For best dynamic performance, the analyses show that optimum direct damping is attained at low recess pressure ratios and reduced recess to bearing area ratios. Based on the concentric thin land theory, Rowe (1980) presented coefficients for hydrostatic and hydrodynamic stiffness and squeeze damping for capillary, orifice and constant flow control HJBs. The mechanism of whirl instability for hybrid operation is explained, and

427

A	$\pi\, d^2/4$. Orifice area $[m^2]$
b	Recess circumferential length [m].
c	radial clearance [m]
$C_{XX}, C_{XY}, C_{YX}, C_{YY}$	damping coefficients [Ns/m]
C_d	Orifice discharge coefficient
D	2 R . Bearing diameter [m].
d_o, d_c	Orifice and capillary diameter [m]
f	ω/ω_B. dynamic frequency ratio.
h	$H/c = 1 + \Delta\varepsilon_x\cos\Theta + \Delta\varepsilon_y\sin\Theta$ Dimensionless film thickness.
h_x, h_y	$\cos\Theta$, $\sin\Theta$
H_r	Recess depth [m].
$K_{XX}, K_{XY}, K_{YX}, K_{YY}$	Stiffness coefficients [N/m]
L, l	Bearing axial width, recess axial length [m].
N	Number of recesses on bearing.
P	Fluid pressure $[N/m^2]$.
P_a, P_s	Ambient and external supply pressures $[N/m^2]$
P_r	$(P_r - P_a)/(P_s - P_a)$. recess pressure ratio.
q_r	$Q_r\, \mu/c^3(P_s - P_a)$ Dimensionless recess flow rate into film lands
v_o	$\sqrt{2(P_s - P_r)/\rho}$. Fluid speed through orifice [m/s].
v_{so}	$\sqrt{1/(\beta\rho)}$. Orifice Fluid speed at sonic conditions [m/s]
v_{sc}	$\sqrt{A_c/(\beta\,8\pi\mu l_c)}$. Capillar fluid speed at sonic conditions
V_r, V_s	$(H_r + H)lb + V_s$ Total recess volume, volume of orifice supply line [m^3].
{X,Y}	Inertial coordinate system.
z	restrictor control parameter.
α_c	reduced damping factor due to compressibility, eqn. (14)
β	Fluid compressibility factor $[m^2/N]$.

δ_o	$A_o \mu \sqrt{2}/c^3/\sqrt{\rho(P_s-P_a)}$	Design Orifice parameter.
δ_c	$A_c^2/(8\pi\, l_c\, c^3)$.	Design capillary parameter.
λ_1	$\mu\omega A_r/c^2(P_s-P_a)$	Recess frequency parameter
λ_2	$V_r \beta(P_s-P_a)/clb$.	Compressibility parameter
Λ	$\mu\Omega R^2/c^2(P_s-P_a)$	Rotational speed parameter.
σ	$\mu\omega R^2/c^2(P_s-P_a)$	Frequency parameter at film lands.
ω	Excitation or whirling frequency [1/sec]	
ω_B	Break frequency [1/s], eqn. (15).	
Ω	Rotational speed of journal [1/s]	
ϕ	$K_{xy}/\Omega C_{xx}$. Whirl frequency ratio.	
$\Delta\varepsilon_x$, $\Delta\varepsilon_y$	Dimensionless perturbed eccentricities	
$\delta\Theta, \delta\phi$	$2\pi/N$; b/R	
$\Delta\Theta, \Delta\xi$	$\delta\Theta-\delta\phi$; $(L-1)/D$	
τ	ωt Dimensionless time coordinate	
Θ, ξ	$(x,y)/R$. Dimesionless circumferential and axial coordinate	
γ	$\dfrac{2\Delta\xi L}{\delta\Theta\,\Delta\Theta\,D}$ Circumferential flow factor	

Subscripts:

o	refers to zeroth order solution or no compressibility solution.
r	refers to bearing recesses
α	refers to first order solution

Superscripts:

n	refers to n-th recess

it is shown that the whirl frequency ratio is equal to 0.5. Nonetheless, the introduction of hydrostatic stiffness into the rotor-bearing system raises the frequency of whirl onset.

Rohde and Ezzat (1976) presented an analysis which accounts for the lubricant compressibility in the bearing recesses and supply line. The results, also supported by the analysis of Ghosh and Viswanath (1987) and Ghosh et al. (1989), show that when the journal is subjected to high frequency excitations the bearing stiffness and damping characteristics can change drastically. The behavior is determined by a "break" frequency beyond which the bearing direct stiffness increases sharply and it is accompanied by a rapid decrease in direct damping. The analyses cited are based on full numerical solutions to the Reynolds equations, and thus, their results can not be easily used in practice.

The present work introduces a theoretical analysis for the dynamic performance characteristics of capillar/orifice compensated centered hydrostatic journal bearings. The analysis considers in detail the effect of fluid recess compressibility. Useful design criteria to avoid undesirable dynamic operating conditions at low and high frequencies are determined. Conditions to avoid complete loss of damping at small frequencies are also presented.
The relevance of the analysis is immediately recognized since the performance characteristics of HJBs are relatively independent of the static journal center displacement for small to moderate values of the eccentricity vector.

ANALYSIS

The geometry of a hydrostatic bearing and reference coordinate systems are shown in Figure 1. A lubricant at external pressure P_s is supplied through either a capillary or orifice to each recess, flows into the film lands, and then exits the bearing. The performance characteristics of HJBs are governed by momentum and continuity considerations at the film lands as well as flow continuity through the recesses. The former define the pressure and flow fields over the thin film region, whereas the latter provides values for the pressure in the recesses.

The continuity equation at each recess determines the global flow balance between the flow through the orifice (Q_o) or capillary (Q_c) restrictors, the recess outflow into the film lands (Q_r), and the time change of fluid mass within the recess volume. The recess continuity equation is then given as

$$Q_i = Q_r + \frac{\partial V_r}{\partial t} + V_r \beta \frac{\partial P_r}{\partial t} \qquad (1)$$

where β represents the fluid compressibility factor. The inlet flow (Q_i) through the external restrictor depends on the nature of the control device, i.e.

for orifice:

$$Q_i = Q_o = C_d \frac{\pi d_o^2}{4} \sqrt{2\,(P_s - P_r)/\rho} \qquad (2a)$$

430

for capillar:

$$Q_i = Q_c = \frac{\pi d_c^4}{128 \mu l_c} (P_s - P_r) \qquad (2b)$$

For small amplitude motions of frequency ω about the concentric position, the land film thickness is described by the real part of the expression:

$$h = H/c = 1 + e^{i\tau} (\Delta\varepsilon_x h_x + \Delta\varepsilon_y h_y) \qquad (3)$$

$$h_x = \cos \Theta , \quad h_y = \sin \Theta$$

$$\tau = \omega t, \quad \Delta\varepsilon_x, \; \Delta\varepsilon_y \ll 1$$

The film land and recess pressures are expressed as the sum of a zeroth and first order complex fields describing the equilibrium centered position and the perturbed dynamic motion, respectively. Hence, in dimensionless form

$$p = p_o + e^{i\tau} (\Delta\varepsilon_x p_x + \Delta\varepsilon_y p_y) \qquad (4)$$

$$P_r = P_{ro} + e^{i\tau} (\Delta\varepsilon_x p_{rx} + \Delta\varepsilon_y p_{ry})$$

The linear perturbation method used determines the recess continuity equation to be accordingly divided into zeroth and first order expressions as

zeroth order recess continuity equation:

a)capillary:
$$\delta_c (1 - p_{ro}) = q_{ro} \qquad (5a)$$

b) orifice:
$$\delta_o \sqrt{(1-p_{ro})} = q_{ro} \qquad (5b)$$

and the dimensionless film flow into the lands is given by (Davies, 1969, Rowe, 1980) as

$$q_{ro} = \frac{\delta\Theta}{12\Delta\xi} p_{ro} \qquad (6)$$

δ_c and δ_o are the capillary and orifice design parameters that help to determine the restrictor geometry for the desired operating pressure ratio.

first order recess continuity equation at nth recess:

a)capillary:
$$-p_{r\alpha}^n [\delta_c + i \lambda_1 \lambda_2] = q_{r\alpha}^n \qquad (7a)$$

b)orifice:
$$-p_{r\alpha}^n [\frac{\delta_o^2}{2q_{ro}} + i \lambda_1 \lambda_2] = q_{r\alpha}^n \qquad (7b)$$

$$\alpha = x,y; \quad n=1,2,\ldots,N$$

431

and $q_{r\alpha}{}^n$ is the perturbed land flow on the closure surrounding the nth recess. For laminar flow, the film flow is equal to (Rowe, 1980, SanAndres, 1989a)

$$q_{r\alpha}{}^n = \frac{p_{ro}}{2\Delta\xi} \int_{\theta_n}^{\theta_{n+1}} h_\alpha \, d\theta + \frac{2\delta\theta}{12\Delta\xi} \, p_{r\alpha}{}^n \qquad \ldots\ldots \text{hydrostatic axial flow}$$

$$+ \frac{L/D}{6\;\Delta\theta} \, [\; 2\; p_{r\alpha}{}^n - p_{r\alpha}{}^{n+1} - p_{r\alpha}{}^{n-1} \;] \qquad \ldots\ldots \text{hydrostatic circ. flow}$$

$$(8)$$

$$+ 2 \, \frac{L}{D} \, \frac{\Lambda}{2} \; h_\alpha \; \Big|_{\theta_n}^{\theta_{n+1}} \qquad \ldots\ldots \text{hydrodynamic flow}$$

$$+ i \; \sigma \, \frac{L}{D} \int_{\theta_n}^{\theta_{n+1}} h_\alpha \, d\theta \qquad \ldots\ldots \text{squeeze film flow}$$

$$\theta_n = n\delta\theta$$

Collecting similar terms, equations (7) are reduced to

$$\frac{\gamma}{2} (\; p_{r\alpha}{}^{n+1} - p_{r\alpha}{}^{n-1}) - (\; z+1+\gamma + i \; \lambda_1\lambda_2 \, \frac{6\Delta\xi}{\delta\theta} \;) \; p_{r\alpha}{}^n =$$

$$(9)$$

$$= \frac{3p_{ro}}{\delta\theta} \int_{\theta_n}^{\theta_{n+1}} h_\alpha \, d\theta + 12 \, \frac{L\Delta\xi}{D\delta\theta} \left[\frac{\Lambda}{2} \, h_\alpha \; \Big|_{\theta_n}^{\theta_{n+1}} + i \; \sigma \int_{\theta_n}^{\theta_{n+1}} h_\alpha \, d\theta \right]$$

$$n=1,2,\ldots. N$$

where z is a control parameter, first introduced by Rowe (1980), and given as

$$z = z_0 = \frac{p_{ro}}{2(1-p_{ro})} \; ; \; z = z_c = \frac{p_{ro}}{1-p_{ro}}$$

for orifice and capillary restrictors, respectively. Analytical solution to the system of equations (9) is easily accomplished(see Davies and Leonard, 1969). The resulting dynamic recess pressures are equal to

$$P_{r\alpha}^n = - \frac{\frac{3 p_{ro}}{\delta\theta} \int_{\theta_n}^{\theta_{n+1}} h_\alpha \, d\theta + 12 \frac{L\Delta\xi}{D\delta\theta} \left[\frac{\Lambda}{2} - h_\alpha \Big|_{\theta_n}^{\theta_{n+1}} + i \, \sigma \int_{\theta_n}^{\Theta_{n+1}} h_\alpha \, d\theta \right]}{[\, z+1+ 2\gamma \sin^2(\pi/N)] \, (1 + i \, f)} \tag{10}$$

$$\alpha = x,y; \quad n=1,2,..N$$

where $f=\omega/\omega_B$ is a frequency ratio. ω_B is named a "break" frequency, and its relevance on the bearing dynamic force response will be discussed latter. The break frequency is given by the expression:

$$\omega_B = \frac{\pi D c^3}{3N(L-1)\mu\beta V_r} (z+1+2\gamma\sin^2(\pi/N)) \tag{11}$$

Dynamic force coefficients are calculated by integration of the first order pressure field over the journal surface,

$$\frac{K_{\alpha\beta} + i\omega \, C_{\alpha\beta}}{LD(P_s-P_a)/c} = - \frac{D}{L} \int_0^{L/D} \int_0^{2\pi} p_\beta \, h_\alpha \, d\theta \, d\xi \tag{12}$$

$$\alpha, \ \beta = x, \ y$$

and it is recalled that $h_x=\cos\theta$ and $h_y=\sin\theta$, respectively. After some algebraic manipulations, it is found that the stiffness and damping coefficients are given by

$$K_{xx} = K_{yy} = K_{xxo} \frac{(1+f^2/\alpha_c)}{1+f^2} \tag{13a}$$

$$C_{xx} = C_{yy} = C_{xxo} \frac{(1-\alpha_c)}{1+f^2} \tag{13b}$$

$$K_{xy} = -K_{yx} = \frac{K_{xyo}}{1+f^2} \tag{13c}$$

$$C_{xy} = -C_{yx} = - \frac{K_{xyo}}{\omega_B(1+f^2)} \tag{13d}$$

433

where K_{xxo}, C_{xxo}, K_{xyo} are the dynamic force coefficients in the absence of the fluid compressibility effect. These coefficients are identical to those presented by Rowe (1980) and presented in Table 1.

The parameter α_c is denoted as a reduced damping factor due to compressibility at zero frequency and given by

$$\alpha_c = \frac{3 \, N \, V_r \, (P_r - P_a) \, \beta}{\pi L D c \, [z + 1 + 2\gamma \sin^2(\pi/N)]} \tag{14}$$

The dynamic force coefficients given in equations (13) depend strongly on the frequency ratio $f = \omega/\omega_B$. Dynamic operation at $f=1$ results in a reduction of 50% in direct damping and a considerable increase in hydrostatic stiffness. The "break" frequency ω_B, equation (12), is rewritten in terms of the restrictor characteristics as

a) orifice HJB:

$$\omega_B = \frac{A_o \, v_{so}^2}{V_r \, v_o \, z_o} \, (z_o + 1 + 2\gamma \sin^2(\pi/N)) \tag{15a}$$

b) capillary HJB:

$$\omega_B = \frac{A_c \, v_{sc}}{V_r \, z_c} \, (z_c + 1 + 2\gamma \sin^2(\pi/N)) \tag{15b}$$

where v_s is the fluid velocity at sonic conditions across the orifice or capillar, and v_o is the fluid speed through the orifice restrictor. Appropriate design of HJBs requires the bearing to operate under dynamic conditions well below the break frequency ω_B. As a rule of thumb, it is suggested that operation above $f=0.01$ should be avoided. High break frequencies can only be achieved on HJBs with shallow recesses (small overall recess plus supply line volumes) and large diameters for the orifice and capillars. For orifice compensated HJBs, a large ratio of sonic speed to fluid orifice speed is desired; while for capillar HJBs, the restrictor length should be kept to a minimum. Of course a negligible value of the fluid compressibility factor β is sufficient to insure adequate dynamic operation without stiffness hardening and reduced damping. It is mentioned that fluids of large viscosity and HJBs with small axial recess lengths are more likely to present low values of the break frequency ω_B.

Dynamic operation at very high frequencies determines a complete loss of damping while the hydrostatic stiffness attains its limiting value. As $\omega \to \infty$, from equation (13a) we obtain

$$K_{xx} \to K_{xx\infty} = \frac{K_{xxo}}{\alpha_c} = \omega_B \, C_{xxo} = N \, \sin^2(\pi/N) \, \frac{(L+1) \, L R^2}{V_r \, \beta} \tag{16}$$

Note that the asymptotic value of direct stiffness depends solely on the

434

compressibility factor β and the recess volume, and it is independent of the fluid properties or external supply conditions.

Although dynamic operation at frequencies well below ω_B is highly desired, the possibility of "pneumatic hammer instability" in a HJB should be carefully analyzed. This phenomenon characteristic of highly compressible fluids such as in gas-lubricated hydrostatic bearings (Lund, 1965) occurs at low frequencies and determines negative values of the direct damping coefficients. At zero frequency, from equation (12b), the value of direct damping is given as $C_{xx} = C_{xxo} (1-\alpha_c)$. Thus, null or negative damping is avoided if the reduced damping factor is small, $\alpha_c \ll 1$, or from equation (14), if

$$\frac{N\, V_r\, (P_r-P_a)\, \beta}{\pi\, LDc} \ll \frac{1}{3}\, [z+1+2\gamma\, \sin^2(\pi/N)] \qquad (17)$$

which requires a low ratio of recess volume to film land volume, and small products of recess pressure and compressibility factor β. This condition possesses a severe restriction on the recess volume and the maximum allowed recess pressure for highly compressible fluids such as liquid hydrogen. Redecliff and Vohr (1969) have recommended that the total volume in the feeding recesses be less than 5% the total volume in the bearing film in order to avoid pneumatic hammer effects. The relation derived in the present analysis gives a better though more stringent criteria. Equation (17) requires the recess volume to be low, and thus, the recess depth must be kept to a minimum consistent with providing uniformity of pressure over the recess.

For hybrid operation, the whirl frequency ratio is a fundamental property of the bearing(independent of the rotor system) which determines the maximum shaft operating speed before whirl instability occurs. The whirl ratio ϕ is defined as

$$\phi = \frac{K_{xy}}{\Omega\, C_{xx}} = \frac{1}{2\, (1-\alpha_c)} \qquad (18)$$

Thus, in a centered HJB the whirl ratio ϕ is at most equal to 0.50, and it is substantially increased if the reduced damping factor α_c is large. From a rotordynamics point of view, hybrid bearings offer no advantage in relation to plain journal bearings. Additionally, if fluid recess compressibility is large, it causes the limited applicability of hybrid bearings to be further restricted.

The conditions stated are of considerable importance in HJBs used for cryogenic applications such as those handling liquid hydrogen. For LH2, the compressibility factor β is rather large while its viscosity is very small. Typical bearing supply pressures exceed 6.9MPa(1000 psig) in order to attain the required levels of load capacity. In this case, even if recesses of low depth are designed, it is very likely that the reduction in damping due to the fluid compressibility is large.

EXAMPLES

The following sample case serves to show the effect of recess compressibility on the dynamic force coefficients of a typical capillary HJB.

The example has been taken from an application presented by Rhode(1976). The geometric and operating parameters for the bearing are as follows:

$N=8$, $L=35.56$ mm(1.4in), $D=71.12$ mm(2.8in),
   $l=30.48$ mm(1.2in), $b=22.84$ mm(0.9in),
   $c=0.0254$mm(0.001in), $Hr/c=10,30,50$,
   $d_c=0.325$mm, $l_c=19.1$mm,

   $\mu=0.0345$ Ns/m^2, $\beta=5.8\ 10^{-10}$ m^2/N,

   $P_s-P_a = 689.5$ KPa(1000 psig), $p_{ro}=0.3$
   $\Omega = 1000$ rpm (16.66 Hz),

For the sample bearing, the static direct stiffness and damping coefficients at zero frequency and no compressibility are equal to $K_{xxo}=5.20\ 10^7$ N/m and $C_{xxo}=2.5\ 10^6$ Ns/m, respectively. For 3 different values of the recess depth, Figures 2 and 3 show the variation of K_{xx} and C_{xx} for increasing values of the frequency ratio f. The calculated values of the break frequency and reduced damping factor are given by

$Hr/c=10$; $\lambda_2^2=0.0044$, $\omega_B=2281$ Hz, $\alpha_c=0.001448$,
$Hr/c=30$; $\lambda_2^2=0.0124$, $\omega_B= 809$ Hz, $\alpha_c=0.004081$,
$Hr/c=50$; $\lambda_2^2=0.0204$, $\omega_B= 492$ Hz, $\alpha_c=0.006710$,

Figure 2 shows that the direct stiffness increases dramatically as the excitation frequency grows. Note that the greater the break frequency(smaller recess depth), the greater is the asymptotic value of the stiffness coefficient. Figure 3 shows the damping coefficient to decrease as the excitation frequency increases. Note that the damping curves are almost identical due to the smallness of the reduced damping factor α_c. The whirl frequency ratio for synchronous excitation at 1000 rpm is very close to 0.5 due to the smallness of the factor α_c. No significant reduction in damping is found at low frequencies due to the low product of recess pressure and compressibility parameter β.

The effect of a large compressibility factor β on a shallow recess, orifice compensated HJB has been considered. The sample bearing is typical of a current cryogenic application with liquid hydrogen as the working fluid. The geometric and operational parameters for the bearing are given as follows:

$N=8$, $L=62.58$mm(2.463in), $D=84.43$ mm(3.32in),
   $l=b=22.776$mm(0.896mm)
   $c=0.0254$mm(0.001in), $Hr/c=5,10,15$
   $d_o=0.779$mm,

   $\mu=6.279\ 10^{-6}$ Ns/m^2, $\rho=51.11$ kg/m3, $\beta=8.86\ 10^{-9}$ m^2/N,

   $P_s-P_a = 20.684$ MPa (3000 psig), $p_{ro}=0.5$

   $\Omega = 25000$ rpm (416.6 Hz)

The operating parameters determine the flow regime in the bearing to be turbulent, and thus, the results of the present analysis are not valid. However, the author (SanAndres,1989a) has presented a similar analysis for turbulent HJBs

with inertia effects. This analysis is more complex and does not provide closed form formulae for direct evidence of the compressibility effect on the dynamic force coefficients.

Figures 4 and 5 show the synchronous ($\omega=\Omega$) stiffness and damping coefficients for increasing recess depths and as a function of the compressibility parameter β. For the value of β corresponding to liquid hydrogen, the calculated break frequency ω_B is well above 10^3 Hz and thus, fluid compressibility does not affect greatly the direct stiffness coefficients. Figure 2 shows the stiffness coefficients to be constant since essentially the frequency ratio f is almost zero for the application considered. Figure 5 shows the direct damping coefficient to be greatly affected by the compressibility parameter β and the recess depth. The loss in damping at the operation point for LH2 is larger for the largest recess depth considered.

Figure 6 shows the whirl frequency ratio ϕ to approach a value equal to 0.5 as the compressibility parameter tends to zero(incompressible, $\beta \rightarrow 0$). As β increases, the whirl ratio ϕ also increases denoting a substantial reduction in available direct damping. At a value of $\beta=8.88 \ 10^{-8} \ m^2/N$ typical for LH2, the whirl ratio ϕ raises from 0.554 to 0.651 as the recess depth increases from 5 to 15 times the bearing clearance.

The results presented clearly show the inconvenience of the proposed HJB since the stability characteristics of the bearing are worse than those of a plain journal bearing. Further reduction of the recess depth will certainly reduce the whirl frequency ratio but will convert the HJB into a plain journal bearing and cause a drastic reduction in direct hydrostatic stiffness. Suggested fixes that can substantially improve the stability characteristics of the bearing are

a) to reduce the axial extent of the recess so as to reduce the recess volume and provide more space for development of the squeeze film damping effect. However, shorter recess axial lengths will determine reduced hydrostatic stiffness. To reduce the recess circumferential extent is not recommended since then the mean flow circumferential velocity will grow rapidly and it may determine and effective increase in the whirl ratio.

b) A roughened bearing surface will reduce substantially the cross coupled stiffness coefficient and reduce the whirl ratio ϕ well below 0.5 (SanAndres, 1989b). Fluid injection opposite to shaft rotation may also reduce the cross-coupled effects, although a quantitative analysis is not yet available.

CONCLUSIONS

The dynamic behavior of externally pressurized bearings has been shown to be highly dependent on the fluid compressibility at the bearing recesses. At high frequency excitations beyond a break frequency, the bearing hydrostatic stiffness increases sharply and it is accompanied by a rapid decrease in direct damping. Also, the potential of pneumatic hammer instability (negative damping) at low frequencies seems to be certain in hydrostatic bearing applications handling highly compressible fluids.

The analysis presented has shown that the bearing dynamic force response

437

for the entire frequency spectrum is determined by just 2 parameters, the break frequency ω_B and the reduced damping factor α_c. Criteria to avoid stiffness hardening and damping reduction by removing the break frequency well above the desired operating frequency are derived and discussed. At low frequencies, the dynamic performance of the bearing is substantially degraded if the reduced damping factor is large. Furthermore, the limited stability characteristics of hybrid bearings are severely restricted. To avoid this effect it is required for the recess volumes(recess depth) to be small. However, for highly compressible fluids, improved bearing stability characteristics may demand a reduced limit on the maximum external supply pressure to the bearing. Consequently, reduced load capacity and stiffness are to be tradedoff for stability. HJBs with a roughened bearing surface could be an appropriate alternative for better bearing stability and dynamic performance.

REFERENCES

Davies, P.B., and Leonard, R., 1969, "The Dynamic Behavior of Multi-Recess Hydrostatic Journal Bearings," Proc. Instn. Mech. Engnrs., Vol. 184, Part 3L, pp. 139-144.

Davies, P.B., and Leonard R., 1970, "Stability of Multirecess Hydrostatic Journal Bearings," Journal of Mechanical Engineering Science, Vol. 12, 2, pp. 150-152.

Ghosh, M.K. , Majumdar B.C., and J.S. Rao, 1979, "Steady State and Dynamic Behavior of Multirecess Hybrid Journal Bearings," Journal of Mechanical Engineering Science, Vol. 21, 5, pp. 345-351.

Ghosh, M.K, and N.S. Viswanath, 1987, "Recess Volume Fluid Compressibility Effect on the Dynamic Characteristics of Multirecess Hydrostatic Journal Bearings," ASME Journal of Tribology, Vol. 109, pp. 417-426.

Ghosh, M.K., S.K. Guha, and B.C. Majumdar, 1989, "Rotordynamic Coefficients of Multirecess Hybrid Journal Bearings," WEAR, Vol. 129, pp. 245-259.

Leonard, R., and W.B. Rowe, 1973, "Dynamic Force Coefficients and the Mechanism of Instability in Hydrostatic Journal Bearings," WEAR, Vol. 23, pp. 277-282.

Lund, J.W., 1965, "A Theoretical Analysis of Whirl Instability and Pneumatic Hammer for a Rigid Rotor in Pressurized Gas Journal Bearings," ASME Paper 65-Lub-12.

Redecliff, J.M., and J.H. Vohr, 1969, "Hydrostatic Bearings for Cryogenic Rocket Engine Pumps," ASME Journal of Lubrication Technology, pp. 557-575.

Rhode, S.M., and H.A. Ezzat, 1976, "On the Dynamic Behavior of Hybrid Journal Bearings," ASME Journal of Lubrication Technology, pp. 557-575.

Rowe, W.B., 1980, "Dynamic and Static Properties of Recessed Hydrostatic Journal Bearings by Small Displacement Analysis," ASME Journal of Lubrication Technology, Vol. 102, pp. 71-79.

San Andres, L.A., 1989a, "Approximate Analysis of Turbulent Hybrid Bearings. Static and Dynamic performance for Centered Operation," submitted for review to

ASME Journal of Tribology.

San Andres L.A., 1989b, "Turbulent Hybrid Bearings with Fluid Inertia Effects, I-Analysis and Numerical Model, II-Results and Discussion," submitted for review to ASME Journal of Tribology.

Singh, D.V., R. Sinhasan, and R.C. Ghai, 1979, "Static and Dynamic Characteristics of an Orifice Compensated Hydrostatic Journal Bearing," ASLE Transactions, Vol. 22, 2, pp. 162-170.

TABLE 1

Dynamic Force Coefficients for Laminar Flow Hydrostatic Journal Bearings

no fluid compressibility effects

$$K_{xxo} = K_{yyo} = \frac{3N^2}{4\pi} \sin^2 (\pi/N) \ \frac{(1 + 1/L)}{(z+1+2\gamma\sin^2(\pi/N))} \ P_{ro} \ \frac{(P_s - P_a)LD}{c}$$

$$C_{xxo} = C_{yyo} = \frac{3N^2}{4\pi} \sin^2 (\pi/N) \ \frac{(1 + 1/L)(1 - 1/L)}{(z+1+2\gamma\sin^2(\pi/N))} \ \frac{\mu L^3 D}{c^3}$$

$$K_{yxo} = -K_{xyo} = \frac{3N^2}{8\pi} \sin^2 (\pi/N) \ \frac{(1 + 1/L)(1 - 1/L)}{(z+1+2\gamma\sin^2(\pi/N))} \ \frac{\mu \Omega L^3 D}{c^3}$$

$$C_{yxo} = C_{xyo} = 0$$

where $\quad z_o = \dfrac{P_{ro}}{2(1-P_{ro})}; \quad z_c = \dfrac{P_{ro}}{1-P_{ro}}$

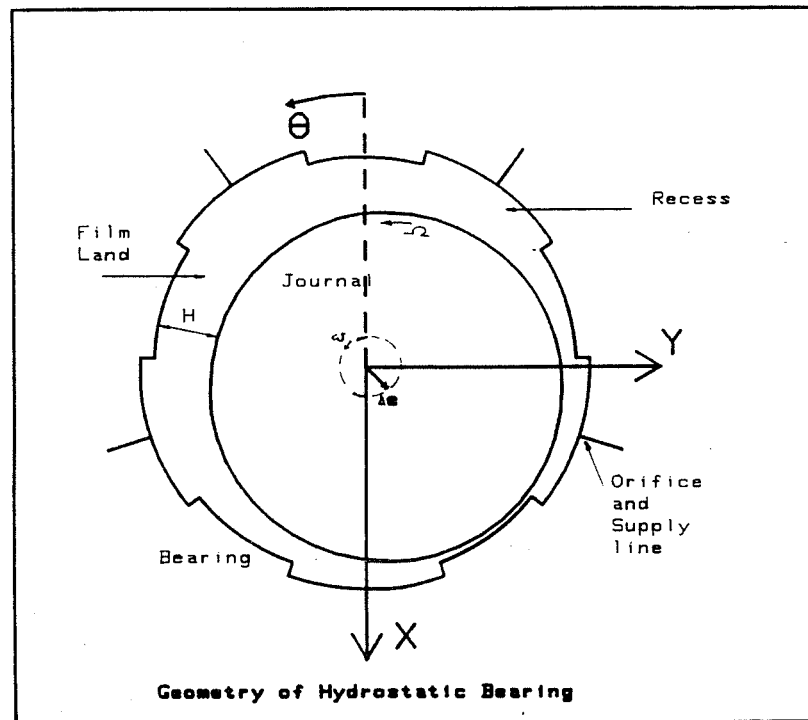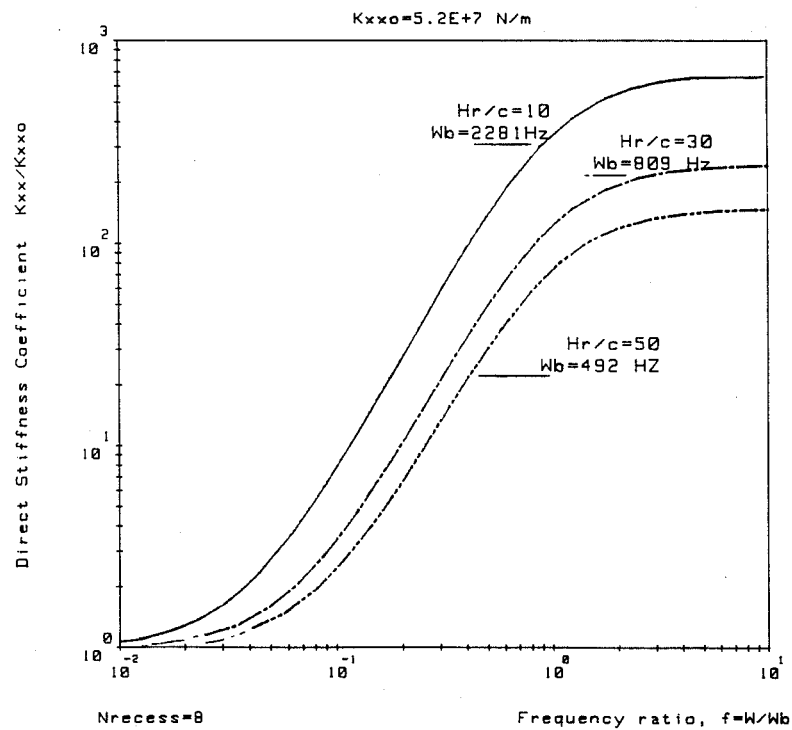$$\gamma = \frac{2 \ \Delta\xi \ L}{\delta\theta \ \Delta\theta \ D}$$

439

Figure 1. Geometry of a hydrostatic journal bearing and description of coordinate systems.

Figure 2. Effect of excitation frequency on direct stiffness for a capillary hydrostatic journal bearing with increasing recess depths.
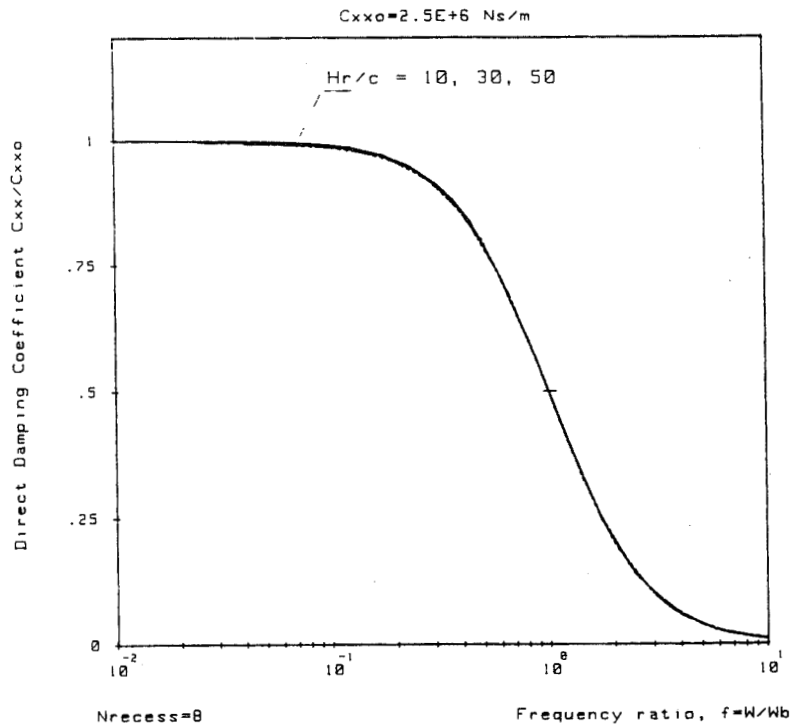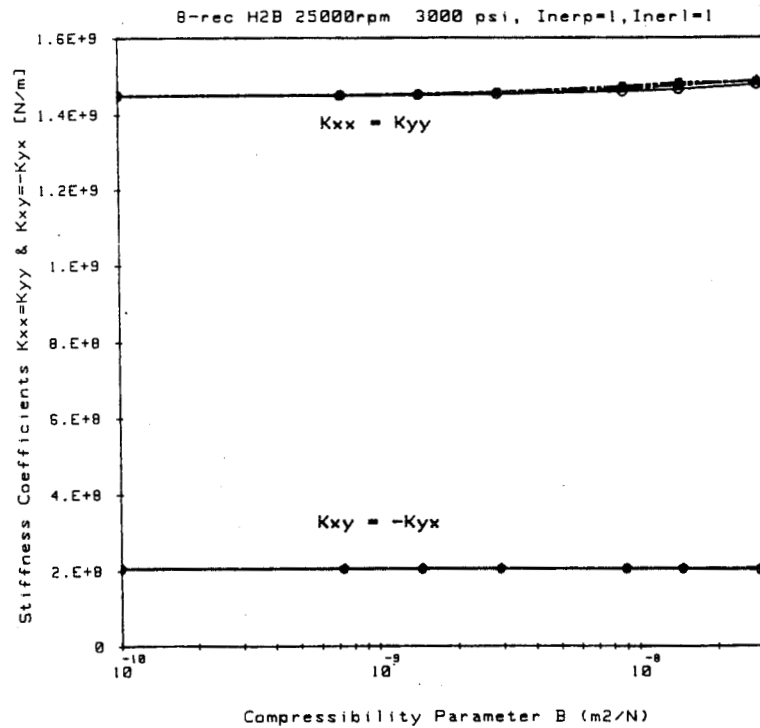
Cxxo=2.5E+6 Ns/m

Figure 3. Effect of excitation frequency on direct damping for a capillary
hydrostatic journal bearing with increasing recess depths.

Capillar HJB: L/D=.5, 1000rpm, Ps=689500Pa, c=2.54E-5m

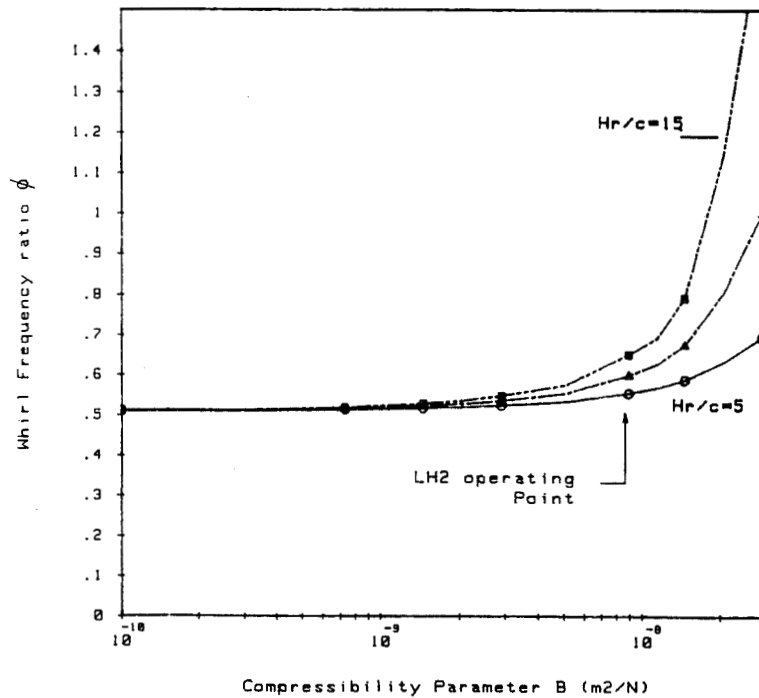Figure 4. Effect of fluid compressibility factor β and recess depth on
synchronous stiffness coefficients for a liquid hydrogen, orifice
compensated, hybrid bearing.

441
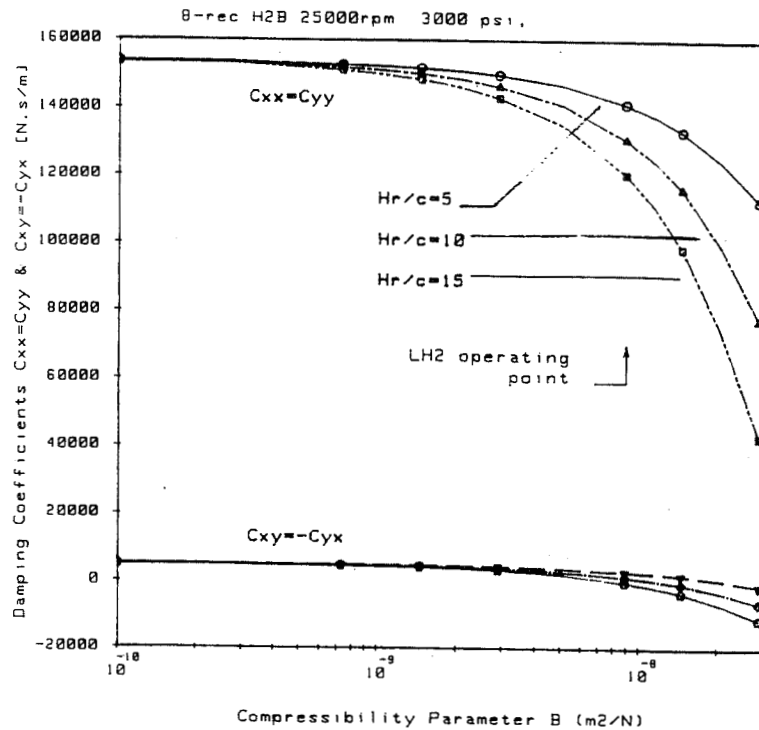
Figure 5. Effect of fluid compressibility factor β and recess depth on the synchronous damping coefficients for a liquid hydrogen, orifice compensated, hybrid bearing.

Figure 6. Whirl Frequency ratio φ for a LH2 hybrid bearing. Combined effect of fluid compressibility and recess depth.

442

EFFECT OF ECCENTRICITY ON THE STATIC AND DYNAMIC PERFORMANCE OF A TURBULENT HYBRID BEARING*

Luis A. San Andres
Mechanical Engineering Department
Texas A&M University
College Station, Texas 77843-3123, U.S.A.

The effect of journal eccentricity on the static and dynamic performance of a water lubricated, 5-recess hybrid bearing is presented in detail. The hydrostatic bearing has been designed to operate at a high speed and with a large level of external pressurization. The operating conditions determine the flow in the bearing to be highly turbulent and strongly dominated by fluid inertia effects. The analysis covers the spectrum of journal center displacements directed towards the middle of a recess and towards the mid-land portion between 2 consecutive recesses. Predicted dynamic force coefficients are uniform for small to moderate eccentricities. For large journal center displacements, fluid cavitation and recess position determine large changes in the bearing dynamic performance. The effect of fluid inertia force coefficients on the threshold speed of instability and whirl ratio of a single mass flexible rotor is discussed.

INTRODUCTION

Hydrostatic and hybrid(combined hydrostatic and hydrodynamic) journal bearings (HJBs) have recently been the subject of increased attention because of their potential applications as support elements in cryogenic high speed turbomachinery. These bearings have been proposed because of their high radial stiffness, accuracy of positioning and good vibration damping characteristics. Despite these attractive features, the hydrodynamic action at high speeds may bring the potential of half speed whirl instability. Thus, it is of importance to determine the limits of safe operation for such bearing applications

To provide the levels of load support needed in high speed machinery operating with cryogenic fluids requires large external pressure supplies. These unique operating conditions give rise to large film Reynolds numbers, and cause the flow within the bearing film to be highly turbulent and strongly dominated by fluid inertia effects both at the recess edges and in the thin film land regions. Conventional analytical treatments are confined to the numerical solution of the Reynolds equation for turbulent flow, and thus, can not interpret correctly the actual complex phenomena occuring in HJBs.

b   Recess circumferential length [m].

c   radial clearance [m]

$C_{XX}, C_{XY}, C_{YX}, C_{YY}$ damping coefficients [Ns/m]

C_d Orifice discharge coefficient

D   2 R . Bearing diameter [m].

d_o Orifice diameter [m]

F_x, F_y Fluid film forces in X and Y directions [N].

$$f_J = 0.001375 \left[1 + \left(\frac{5 \times 10^5}{R_J} \right)^{1/2.65} \right]$$ Turbulent friction factor at journal surface

$$f_B = 0.001375 \left[1 + \left(\frac{5 \times 10^5}{R_B} \right)^{1/2.65} \right]$$ Turbulent friction factor at bearing surface

h $H/c = 1 + \varepsilon_x \cos\theta + \varepsilon_y \sin\theta$ Dimensionless film thickness.

H_r Recess depth [m].

I_1, I_2, I_4 Inertia coefficients for stability analysis.

$K_{XX}, K_{XY}, K_{YX}, K_{YY}$ Stiffness coefficients [N/m]

K_{eq} Equivalent bearing stiffness coefficient [N/m].

K_r Half of rotor stiffness [N/m].

k_x, k_y $(1/2)(k_J + k_B)$ dimensionless shear parameters in circumferential and axial directions

k_J, k_B $f_J R_J$, $f_B R_B$. Turbulent shear parameters at journal and bearing surfaces.

L   Bearing axial width [m].

l   Recess axial length [m].

N_{rec} Number of recesses on bearing.

$M_{XX}, M_{XY}, M_{YX}, M_{YY}$ Inertia or added mass coefficients [Kg].

M_r Half of rotor mass [Kg].

P   Fluid pressure [N/m^2].

444

P_s External supply pressure [N/m^2].

Qr $\int H (V.n) d\Gamma_r$. Recess flow into film lands [m3/s]

Re $\rho\Omega cR/\mu$ Nominal circumferential flow Reynolds number.

Re_p $\rho c^3(P_s-P_a)/\mu^2 R$ Pressure flow Reynolds number.

Re_p^* (Re_p) (c/R) Modified pressure flow Reynolds number.

R_J, R_B $(\rho/\mu)H[(U-\Omega R)^2+V^2]^{1/2}$, $(\rho/\mu)H[U^2+V^2]^{1/2}$.
Reynolds numbers at journal and bearing surfaces.

To   Fluid film resistance torque [Nm]

U,V   mean flow velocities in circumferential and axial dirs.

V_r $(H_r+H)A_r+V_s$ Total recess volume [m^3] .

V_s Volume of orifice supply line [m^3].

{X,Y}   Inertial coordinate system.

α_i relative effective fluid inertia mass at support.

β Fluid compressibility factor [m^2/N].

$\varepsilon_x, \varepsilon_y$ (e_x,e_y)/c. Dimensionless journal eccentricities in X & Y directions

Λ $\mu\Omega R^2/c^2(Ps-Pa)$. Rotational speed parameter.

ϕ ω_s/Ω_s. Whirl frequency ratio.

ϕ_0 Whirl frequency ratio without fluid inertia effects.

ω Excitation or whirling frequency [1/sec]

ω_s Whirl frequency at instability threshold [1/sec].

Ω Rotational speed of journal [1/s]

Ω_s Threshold speed of instability [1/s].

Redecliff and Vohr (1969), Heller (1974), and Deguerce et al. (1975) have presented finite difference solutions to the turbulent flow Reynolds equation. Reported numerical flow rates and hydrodynamic forces are lower than experimental measurements but considered satisfactory. Artiles, Walowit, and Shapiro (1982) presented a well documented numerical method for prediction of the static and dynamic performance characteristics of turbulent HJBs. The analysis includes the local effect of fluid inertia at the recess edges, but the fluid compressibility effect at the recess volumes is neglected. The turbulence model employed by Artiles seems to give inconsistant results in the transition

from pressure dominated flow to pure shear flow at high speed operation.

The influence of fluid inertia at the recess edges and hydrodynamic pressure generation within the recess for high rotational speeds have been shown and discussed in detail in the experimental work of Chaomleffel and Nicholas (1986). The magnitude of the measured edge pressure drop appears to be dependent on the journal rotational speed and the recess depth. Comparisons of the experiments with predictions based on a finite difference solution to the turbulent Reynolds equation with fluid inertia effects are also included in the same reference. The numerical calculations for load and flow rate were found to be always greater than the measurements, and predicted edge pressure drops were determined to be smaller than those observed.

SanAndres(1989a) has developed a full inertial numerical analysis for accurate prediction of the performance characteristics of orifice compensated turbulent HJBs. The analysis departs from the mean flow Navier-Stokes equations and includes the effect of recess volume fluid compressibility. The numerical results presented by SanAndres (1989b) indicate that fluid inertia at the film lands acts as an additional flow resistance, and thus, causes reduced flow rates and greater hydrodynamic effects when compared to an inertialess solution. Inertia force coefficients of large magnitude in bearings handling large density fluids and with low values of the clearance ratio (c/R) are reported. The full inertial analysis developed by the author shows a considerable improvement over conventional analyses based on the classical Reynolds equation.

The present paper introduces further numerical predictions for a high speed HJB currently under testing. The effect of journal eccentricity on the static and dynamic performance of the sample bearing are throughly detailed. A simple analysis to determine the influence of fluid inertia on the threshold speed of instability for a simple flexible rotor supported on hybrid bearings is presented.

ANALYSIS

Figure 1 presents the geometry of a hydrostatic journal bearing. Fluid passes across a restrictor orifice and a recess area of relatively large clearance, and then flows through the film lands to the bearing discharge. The performance characteristics of the bearing are governed by momentum and continuity considerations in the fluid film lands as well as flow continuity through the bearing recesses. The former defines the pressure and velocity fields over the bearing lands, whereas the latter provides values for the pressure in the recesses.

San Andres (1989a) presented a derivation of the appropriate equations for fully turbulent flow in hybrid bearings. The analysis considers the effect of fluid inertia (advection and temporal terms) at the film lands and a local Bernoulli type inertia effect at the recess edges. For an isoviscous incompressible fluid, the continuity and momentum equations for the turbulent bulk flow on the film lands are given as

$$\frac{\partial}{\partial x}(UH) + \frac{\partial}{\partial y}(VH) + \frac{\partial H}{\partial t} = 0 \tag{1}$$

$$-H\frac{\partial P}{\partial x} = \frac{\mu}{H}(k_x U - k_J \frac{R\Omega}{2}) + \rho \left\{ \frac{\partial}{\partial t}(HU) + \frac{\partial}{\partial x}(HU^2) + \frac{\partial}{\partial y}(HUV) \right\} \tag{2}$$

$$-H\frac{\partial P}{\partial y} = \frac{\mu}{H}k_y V + \rho \left\{ \frac{\partial}{\partial t}(HV) + \frac{\partial}{\partial x}(HUV) + \frac{\partial}{\partial y}(HV^2) \right\} \tag{3}$$

The turbulent shear parameters k_x and k_y are taken as local functions of the friction factors relative to the journal and bearing surfaces (Hirs, 1973, Nelson, 1987).

The continuity equation at the recess is defined by the global balance between the flow through the orifice restrictor, the recess outflow into the film lands, and the temporal change of fluid mass in the recess volume. The recess continuity equation is then given by

$$C_d \frac{\pi d_o^2}{4} \left[\frac{2(P_s - P_r)}{\rho} \right]^{1/2} = Q_r + \frac{\partial V_r}{\partial t} + V_r \beta \frac{\partial P_r}{\partial t} \tag{4}$$

where β represents the fluid compressibility factor at the recess volume. The recess outflow into the film lands, Q_r, is determined by integration of the mean flow velocity vector along a closed path Γ_r encompassing the recess boundary.

For hybrid operation a pressure rise occurs within the downstream portion of the recess (Chaomleffel et al.,1985). This region is considered as a one-dimensional step bearing. The local acceleration of fluid from relatively stagnant conditions at the recess to a high velocity at the film lands causes a sudden pressure drop at the recess boundary. The pressure at the entrance to the film lands is modeled by simple Bernoulli type relations based on the theory developed by Constantinescu (1975).

San Andres (1989a) presented a numerical procedure for effective solution of the nonlinear governing equations (1) through (5). The numerical method is based on the SIMPLEC algorithm of Van Doormal & Raithby (1984) for iterative solution of the film land equations, and it is combined with a Newton-Raphson algorithm for estimation of recess pressures and satisfaction of the recess flow constraints. The flow field is divided into a zero-th and first order fields describing the equilibrium condition and perturbed dynamic motion, respectively. Solution of the zero-th order field gives the steady state bearing characteristics such as flow, load and friction torque. The first order field determines the dynamic force coefficients for the excitation frequency of interest.

447

<u>RESULTS</u>

A Hydrostatic-Hybrid Bearing Test program is under development at Texas A&M University. The purpose of the program is to develop an experimental data base and analytical capabilities for turbulent flow hydrostatic bearings. The objectives of the program are to design and build a test apparatus, systematically test the bearings, and develop an analysis to predict the bearing characteristics and anchor it to the test data.

The hydrostatic bearing test apparatus has been designed and is currently under preliminary testing. Table 1 presents a description of the 5 recess test hydrostatic bearing considered as a test case. The working fluid is hot water at a temperature of 71.1C(160F), and the maximum rated inlet supply fluid pressure is 7.23 MPa(1050 psi). The rotor speed ranges from 0 to 500Hz(30000 rpm), and the bearing and journal surfaces are considered perfectly smooth. For the conditions shown in Table 1, the flow within the bearing is highly turbulent with dominance of hydrodynamic effects at the highest rotational speed. The large value of the modified Reynolds number, Re_p^x , shows that fluid inertia at film lands will have a considerable influence on the test bearing static and dynamic performance characteristics.

The orifices of the test bearing have been sized for a concentric pressure ratio equal to 0.5 at the maximum operating speed of 30000 rpm. This condition implies that the predicted pressure drop between the supply and recess pressures is equal to the pressure drop between the recess and the outside of the bearing. The selected concentric pressure ratio is not necessarily an optimum for the present bearing configuration but was chosen on the grounds of common practice for establishing bearing stiffnesses which are not too far from optimum. For an orifice discharge coefficient equal to one, the present full inertial analysis predicted an orifice diameter equal to 1.496mm.

A complete analysis has been carried out to determine the effects of journal center eccentricity on the static and dynamic performance characteristics of the test bearing at 30000 rpm and an external supply pressure equal to 6.54 Mpa(950psi). The journal center displacements ranged from the concentric position to eccentricity radii equal to 90% of the film clearance in the directions toward the middle of a recess and toward the mid-point in the lands between two consecutive recesses. Figure 2 shows the predicted bearing flow rate and the film friction torque for the range of journal displacements considered. The flow rate is a maximum at the concentric position and decreases as the eccentricity increases. The friction torque is a minimum at the centered position and increases rapidly as the journal center displacement approaches the bearing clearance. The increment in torque and reduction in flow rate are due to increased flow resistance for growing eccentricities. The results show the flow and the torque to appear closely as even functions of the eccentricity. The maximum reduction in flow rate at the largest eccentricity considered, (e/c)=0.9, is approximately equal to 22% of the flow at the centered position, while the increment in torque is about 30%.

Figure 3 shows the calculated recess pressures for different values of the static journal eccentricity. Negative eccentricities, ε_x, denote journal displacements to the midland between recesses 1 and 5 located at 36° and 324°, respectively. Positive eccentricities, ε_x, denote journal displacements toward the middle of recess 3 located at 180°. Figure 4 shows the entire pressure field

448

over the journal surface for selected values of the journal center displacement. At the concentric position the recess pressures are identical and the bearing has null load capacity. The pressure field for null eccentricity is depicted in Figure 4(c).

For displacements toward the middle of a recess, Figure 3 shows that maximum recess pressures are attained at recesses 2 and 3 located in the converging portion of the film thickness. The large pressures attained at the second recess are caused by the effect of journal rotation and will generate a substantial film force normal to the journal displacement. For eccentricity radii larger than 0.5, cavitation was found to appear in the land region around recess 4 where the film thicknesses is diverging. Figures 4(d) and 4(f) show the pressure field for eccentricities ε_x equal to 0.4 and 0.7, respectively; note that for large journal displacements there is a significant hydrodynamic effect between recesses 2 and 3.

For displacements toward the midland between recesses 1 and 5, Figure 3 shows that maximum recess pressures are located at recess 5 in the convergent portion of the film thickness while low recess pressures are attained at recesses 2 and 3 in the divergent film thickness region. Fluid cavitation is predicted to occur for eccentricities larger than 0.6. Figures 4(a) and 4(b) show the pressure field for eccentricities ε_x equal to -0.7 and -0.4, respectively. Note from Figure 3 that for large journal displacements toward the land between the recesses, the pressure at recess 5 exceeds the supply pressure indicating that there is backflow through the orifice. These results are to be taken with caution, since the analysis presumes the flow-orifice relation to be valid for any flow direction. However, experimental evidence presented by Redecliff and Vohr (1969) shows that, for high eccentricity operation, recess pressures larger than the external supply pressure are indeed possible.

Figure 5 shows the predicted film forces, $-F_x$ and F_y, parallel and normal to the static journal displacement, respectively. For the journal speed considered, 500 Hz(30000 rpm), the hydrodynamic effects are dominant and determine a normal force F_y larger than the hydrostatic force F_x. The angle between the resultant load and the eccentricity vector is equal to 56° and remains relatively constant for the entire range of eccentricity radii considered. For small to moderate eccentricities, the film forces are linear with the static displacement and will determine constant stiffness coefficients. For large static displacements toward the middle of a recess, the curvature of the film forces is upward due to fluid cavitation. However, for displacements toward the mid-land, the film forces curvature is first inward reducing the film forces and then, outwards increasing the forces. This seemingly strange effect is explained in terms of the pressure field not being able to develop substantially in the convergent portion of the film thickness due to the presence of recess 5, and thus pushing water back-flow through the orifice.

Figures 6 through 8 show the calculated synchronous stiffness, damping, and inertia coefficients for the hydrostatic bearing operating at 30000 rpm. The rotordynamic coefficients are uniform for small to moderate journal eccentricity radii. The cross-coupled stiffness coefficients shown in Figure 6 are substantially larger than the direct coefficients and demonstrate the dominance of hydrodynamic effects on the bearing dynamic performance. For large static journal displacements, the bearing direct stiffness (K_{xx}) increases dramatically due mainly to the effect of fluid film cavitation. Figures 7 and 8 show the

direct damping and inertia coefficients to be one order of magnitude larger than the cross coupled damping and inertia coefficients. The magnitude of the direct inertia coefficients is large due to the large density of the fluid and the low clearance to bearing radius ratio. At the concentric position, the direct inertia coefficient is equal to 17.9 Kg and determines for synchronous excitation at 500 Hz(30000 rpm) a reduction of almost 88.3% in the dynamic stiffness ($K_{xx}-\omega^2 M_{xx}$). This result proves that fluid inertia is of utmost importance in the dynamic performance of hydrostatic bearings handling fluids of large density.

The calculated rotordynamic coefficients for an excitation frequency equal to the rotating speed are not affected by the compressibility of the fluid at the recess volume due to the low recess depth to clearance ratio of the designed test bearing. However, for supersynchronous excitations well above the rated journal rotational speed, compressibility effects become important and may cause significant losses in damping and increased values of direct stiffness.

The results obtained for the test bearing dynamic coefficients prompted the question of the test rotor-bearing stability characteristics. Appendix A presents the criteria derived for the threshold speed of instability and whirl frequency ratio of a simple flexible rotor supported on identical bearings and includes the effect of the inertia force coefficients. This effect is significant in the present application.

Figure 9 presents the calculated whirl frequency ratio (ϕ) versus the journal eccentricity for the rotor-bearing system studied. The calculated results show that the whirl ratio is independent of the rotor flexibility and equal to 0.492 for small to moderate static journal center displacements. For the largest positive eccentricities (journal displacement towards the middle of a recess), the whirl ratio drops sharply to a value equal to 0.36. However, for large displacements toward the middle of a land (negative eccentricity ε_x) the whirl ratio increases well above 0.5. This abnormal effect is due to the loss in direct stiffness and the inability of the bearing to attain high pressures at the film lands due to orifice backflow. The results presented clearly show that the dynamic characteristics of the test hybrid bearing are no better than for a plain journal bearing.

Figure 10 presents the threshold speed of instability for the test rotor-bearing system. The rotor mass is equal to 30.84 Kg and the shaft is considered as rigid. The figure includes the predicted onset speed Ω_s if fluid inertia effects are neglected. A net reduction in critical speed of almost 25% is observed to occur due to the large influence of the inertia force coefficients on the stability response of the test system.

CONCLUSIONS

The effect of journal eccentricity on the static and dynamic performance of a water lubricated, 5-recess hybrid bearing is presented in detail. The hydrostatic bearing has been designed to operate at a speed of 30Krpm and a large level of external pressurization(6.64MPa). These operating conditions determine the flow in the bearing to be highly turbulent and strongly dominated by fluid inertia effects.

450

The numerical predictions are based on the full turbulence-inertial analysis of SanAndres(1989a). The analysis covers the spectrum of journal center displacements directed towards the middle of a recess and towards the mid-land portion between 2 consecutive recesses. Bearing flow rate decreases and friction torque increases as the eccentricity increases. Film forces are linear with the eccentricity for small to moderate static journal center displacements. For large eccentricities, film forces are affected by fluid cavitation and present some unusual features. For large static displacements towards the mid-land it is observed that back flow through the orifices occurs. This unexpected behavior degrades considerably the static as well as the dynamic performance of the bearing.

The dynamic force coefficients for the test bearing are predicted to be constant for small to moderate values of the journal eccentricity. However, for large static displacements toward the mid-land it is observed that the direct force coefficients are substantially reduced. Direct inertia force coefficients of substantial magnitude are predicted in the present application. The levels obtained are a direct consequence of the large density of the fluid considered.

Hydrostatic bearings operating in hybrid mode at high rotational speeds present similar stability characteristics as plain journal bearings. For a single mass flexible rotor supported on HJBs, the threshold speed of instability is reduced by the rotor flexibility and the fluid inertia effect. The cross-coupled inertia coefficients are shown to degrade the stability response of the bearing by reducing the whirl frequency ratio.

APPENDIX A
Linear Stability Analysis

Criteria for the threshold speed of instability and whirl frequency ratio of simple rotor-bearing systems are well known in the literature (Lund, 1965, Chen et al., 1985). These analyses usually consider a rigid or flexible, single mass rotor supported in bearings which possess stiffness and damping characteristics. The influence of inertia force coefficients in the stability of these rotor-bearing systems has not been accounted due presumably to the general assumption that these coefficients are negligible in most circumstances. However, the calculated inertia force coefficients for the present application are rather large compared to the mass of the test rotor, and thus, their effect on the stability of the system is regarded as important.

Consider a single rotor of mass $2M_r$ supported on a pair of identical bearings by a massless shaft of stiffness $2K_r$. Instability sets in at a rotational speed Ω_s when the journal starts a forward precessional motion at the whirl frequency $\omega_s = \phi \, \Omega_s$. From the solution of the homogeneous system of equations for the motion of the rotor and bearing supports, it is determined that the whirl speed ω_s and the whirl frequency ratio ϕ are easily obtained from the following quartic equations:

$$\frac{M_r}{K_r} \alpha_i \, \omega_s^{\,4} - \left[1 + \alpha_i + \frac{K_{eq}}{K_r} \right] \omega_s^{\,2} + \frac{K_{eq}}{M_r} = 0 \qquad (A.1)$$

and

$$\phi^4 I_4 + \phi^2 (I_2 - 1) + \phi_o^{\,2} = 0 \qquad (A.2)$$

where

$$\alpha_i = \frac{(M_{xx} + M_{yy}) - 2I_1}{2M_r}$$

$$K_{eq} = \frac{K_{xx}C_{yy} + C_{xx}K_{yy} - C_{yx}K_{xy} - C_{xy}K_{yx}}{Cxx + Cyy}$$

$$I_1 = \frac{C_{yx}M_{xy} + C_{xy}M_{yx}}{C_{xx} + C_{yy}} \qquad (A.3)$$

$$I_2 = \frac{K_{xy}M_{yx} + K_{yx}M_{xy} - I_1(K_{xx} + K_{yy}) + 2K_{eq}I_1}{C_{xx}C_{yy} - C_{xy}C_{yx}}$$

$$I_4 = \Omega_s^{\,2} \frac{I_1^{\,2} - M_{xy}M_{yx}}{C_{xx}C_{yy} - C_{xy}C_{yx}}$$

and

$$\phi_o^{\,2} = \frac{(K_{eq} - K_{xx})(K_{eq} - K_{yy}) - K_{xy}K_{yx}}{\Omega_s^{\,2} (C_{xx}C_{yy} - C_{xy}C_{yx})} \qquad (A.4)$$

If fluid inertia effects are eliminated, then the coefficients α_i, I_1, I_2 and I_4 are equal to zero, and the stability formulae derived are identical to the criteria presented by Lund (1965) and Chen(1985). From equation (A.1) it is determined that the fundamental effect of fluid inertia is to reduce the threshold speed of instability if the ratio of masses α_i is large.

For operation at the concentric position ($\varepsilon_x = \varepsilon_y = 0$), the direct dynamic coefficients are identical and the cross-coupled coefficients differ in sign. At this condition, the whirl frequency ratio is obtained from the expression:

$$\phi^2 \Omega_s^{\,2} M_{xy} + \phi \Omega_s C_{xx} - K_{xy} = 0 \qquad (A.5)$$

where it is noted that the whirl ratio is reduced if the cross-coupled inertia coefficient Mxy is negative.

REFERENCES

Artiles, A., Walowit J., and W. Shapiro, 1982, "Analysis of Hybrid Fluid Film Journal Bearings with Turbulence and Inertial Effects," Advances in Computer Aided Bearing Design, ASME Publication G00220, pp. 25-52.

Chaomleffel J.P. and D. Nicholas, 1986, "Experimental Investigation of Hybrid Journal Bearings," Tribology International, Vol. 19, No 5, pp.253-259.

Chen, Y.S., H.Y. Wu, and P.L. Xie, 1985, "Stability of Multirecess Hybrid Operating Oil Journal Bearings," ASME Journal of Tribology, Vol. 107, pp. 116-121.

Constantinescu, V.N. and S. Galetuse, 1975, "Pressure Drop Due to Inertia Forces in Step Bearings," ASME Paper 75-Lub-34.

Deguerce B., and D. Nicholas, 1975, "Turbulent Externally Pressurized Bearings – Analytical and Experimental Results," Conference on Hybrid Bearings, Proc. Instn. Mech. Engnrs., paper XII(ii), pp. 228-233.

Heller, S., 1974,"Static and Dynamic Performance of Externally Pressurized Fluid Film Bearings in the Turbulent Regime," ASME Journal of Lubrication Technology, pp. 381-389.

Hirs G.G., 1973, "A Bulk Flow Theory for Turbulence in Lubricant Films," ASME Journal of Lubrication Technology, pp. 173-146.

Lund, J.W., 1965, "The Stability of an Elastic Rotor in Journal Bearings with Flexible, Damped Supports," ASME Journal of Applied Mechanics, pp. 911-920.

Nelson C.C., and D.T. Nguyen, 1987, "Comparison of Hir's equation with Moody's equation for Determining Rotordynamic Coefficients of Annular Pressure Seals," ASME Journal of Lubrication Technology, Vol. 109, pp. 144-148.

Redecliff, J.M. and J.H. Vohr, 1969, "Hydrostatic Bearings for Cryogenic Rocket Engine Pumps," ASME Journal of Lubrication Technology, pp. 557-575.

San Andres, L., 1989a, "Turbulent Hybrid Bearings with Fluid Inertia Effects, Part 1: Analysis," submitted for review to ASME Journal of Tribology.

San Andres, L., 1989b, "Turbulent Hybrid Bearings with Fluid Inertia Effects, Part 2: Results," submitted for review to ASME Journal of Tribology.

Van Doormaal J.P., and G.D. Raithby, 1984, "Enhancements of the SIMPLE Method for predicting Incompressible Fluid Flows," Numerical Heat Transfer, Vol. 7, pp. 147-163.

Figure 1. Geometry of a Hydrostatic Journal Bearing and description of coordinate systems.
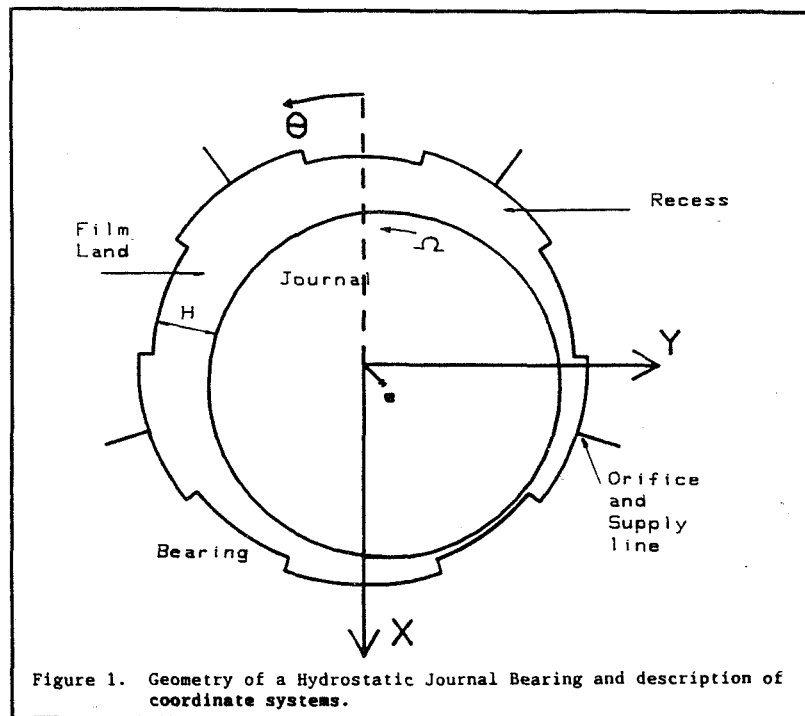
5 Recess Hydrostatic Water Bearing
TAMU Experimental Program (1989)
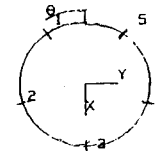
Geometry:
Diameter = 76.2mm(3.00 in)
Length = 76.2mm(3.00 in)
Recess lxb = 27mm x 27mm

Clearance = 0.0762mm(0.003in)

Recess depth Hr = 0.457mm(0.018in)

Orifice diameter = 1.496mm

Fluid: Water at 71.1C(160F)
        Viscosity, 3.98E-4 Pa sec
        Density: 977 Kg/m3

Pressure Supply:6.54MPa(950psi)

Journal speed: 0 to 30000 rpm

Dimensionless Parameters

Reynolds Numbers: Rep=467000,Re*=935.0
Speed ParameterΛ: 0 to 0.04783
Rotation Reynolds Number: 0 to 22360

L/D=1, l/L=.354, N·b/πD=.113
c/R=0.002, Hr/c=6

Table 1. Description of 5 recess hydrostatic water bearing under development for TAMU Hybrid Bearing Research program (1989) Bearing geometry and operating conditions.

454
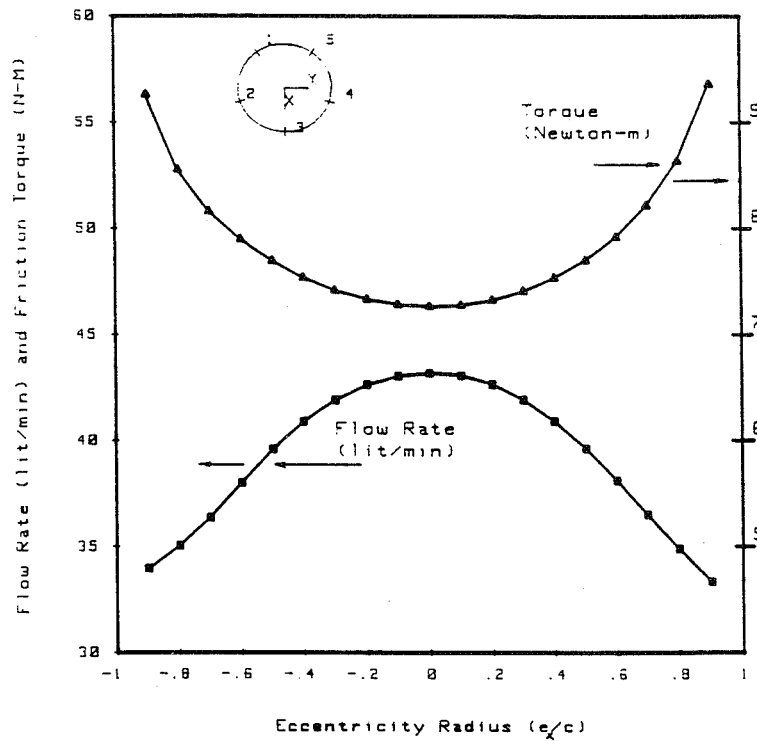
Figure 2. Predicted flow rate and friction torque for test hydrostatic water bearing as a function of static journal eccentricity. Pressure supply equal to 6.54MPa(950psi) and journal speed equal to 500Hz(30000 rpm). Orifice diameter equal to 1.496 mm.
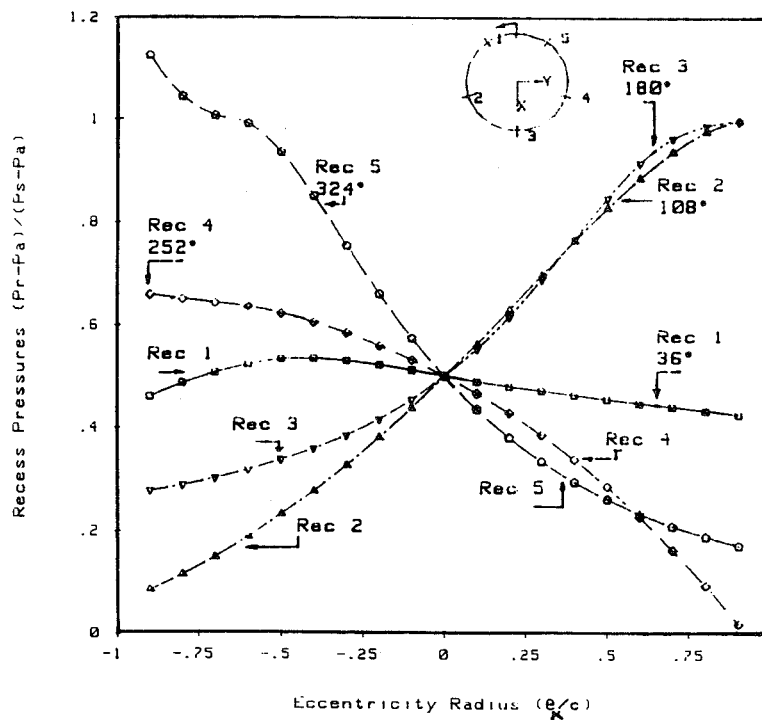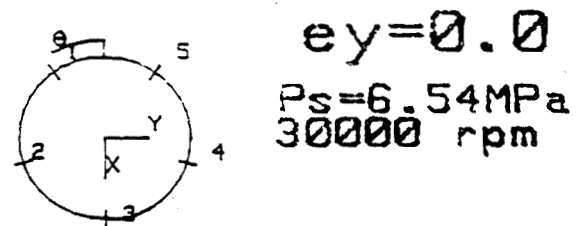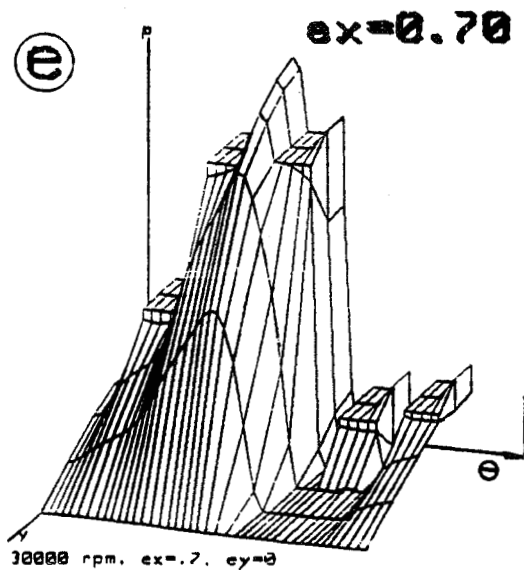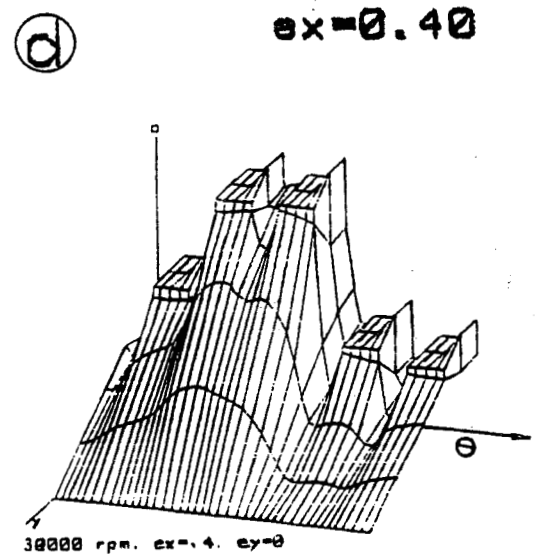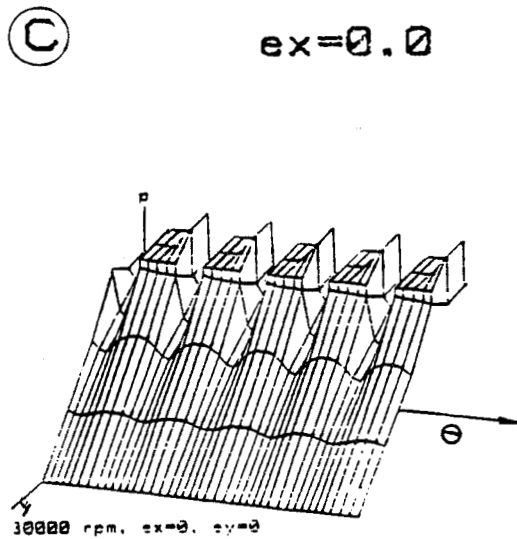

Figure 3. Predicted dimensionless recess pressure for test hydrostatic water bearing as a function of static journal eccentricity. Pressure supply equal to 6.54MPa(950psi) and journal speed equal to 500Hz(30000 rpm). Orifice diameter equal to 1.496 mm.

455

(a) ex=-0.70

(b) ex=-0.40

30000 rpm. ex=-.7, ey=0

30000 rpm. ex=-.4, ey=0

(c) ex=0.0

(d) ex=0.40

30000 rpm. ex=0, ey=0

30000 rpm. ex=-.4, ey=0

(e) ex=0.70

30000 rpm. ex=-.7, ey=0
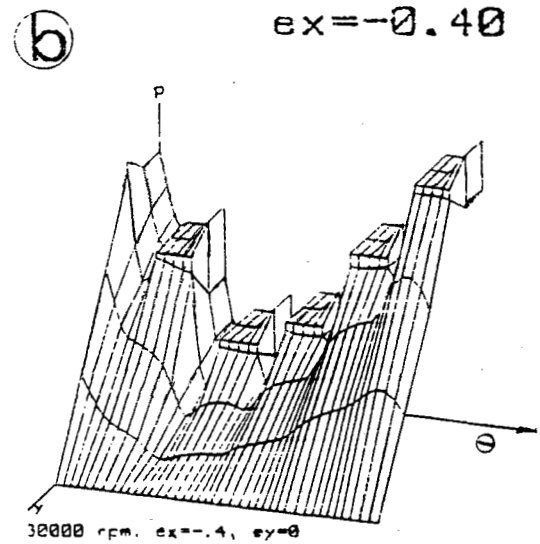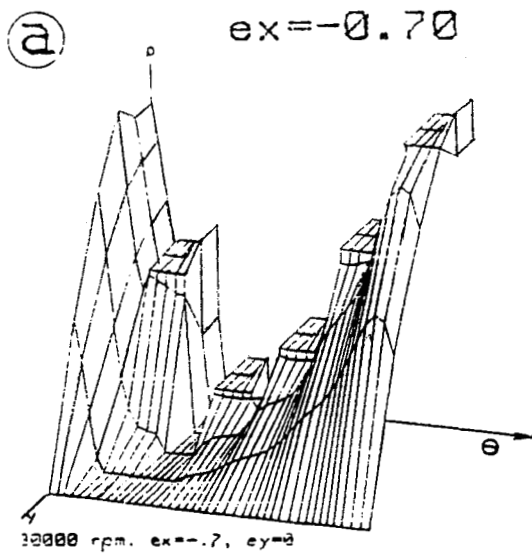
ey=0.0
Ps=6.54MPa
30000 rpm

Figure 4.

Pressure fields for selected values of
journal static eccentricity. Circumferential
coordinate and recess number designation
increase from left to right.
Orifice do=1.496mm

456

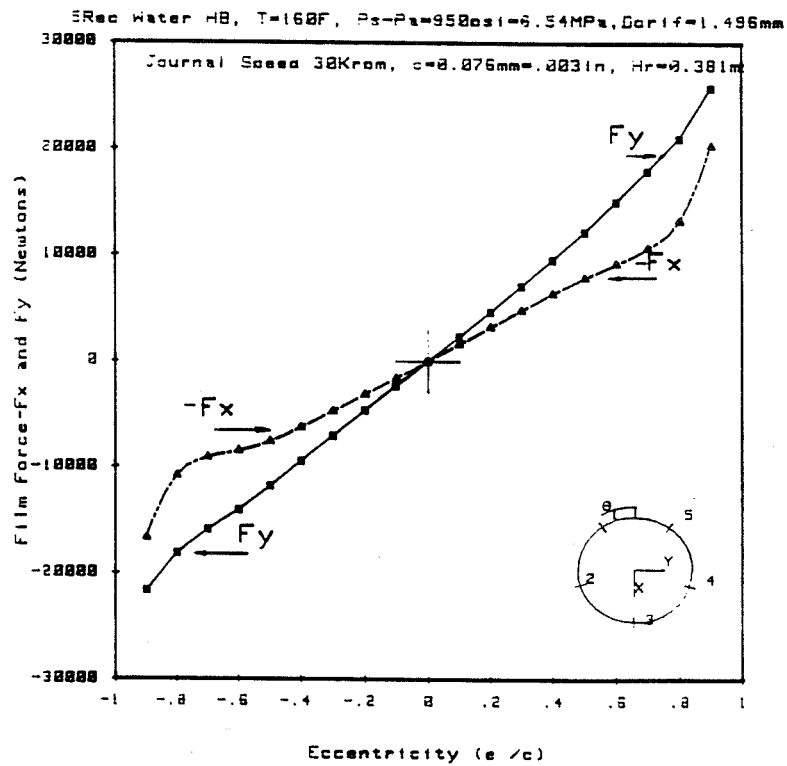ERec Water HB, T=160F, Ps-Pa=950psi=6.54MPa,Dorif=1.496mm

Journal Speed 30Krpm, c=0.076mm=.003in, Hr=0.381m

Figure 5. Film forces parallel(-F$_x$) and normal(F$_y$) to journal static displacements for test hydrostatic water bearing. Ps=6.54 MPa, 30000 rpm, orifice diameter=1.496 mm.

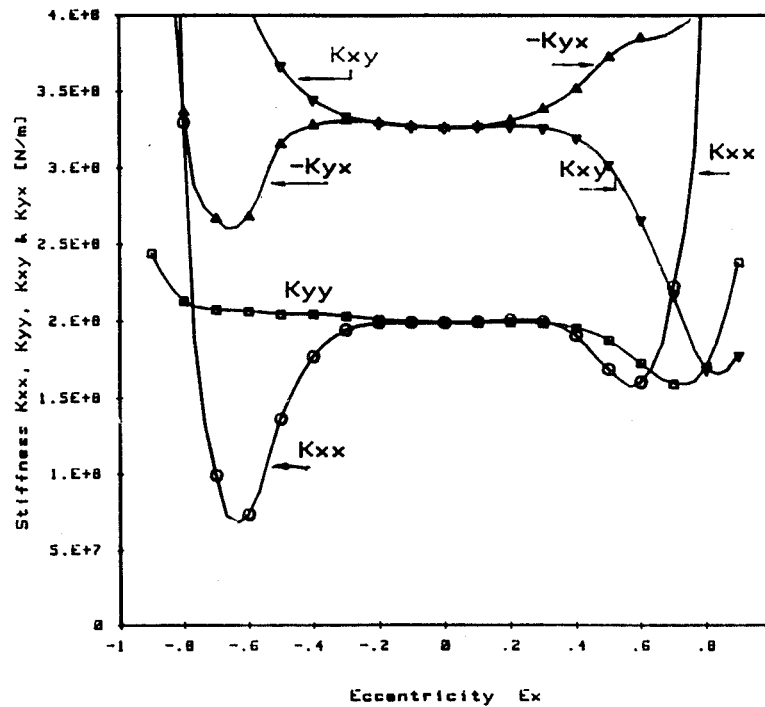**Figure 6.** Predicted stiffness coefficients for test hydrostatic water bearing versus journal static eccentricity. Ps=6.54 MPa, 30000 rpm, orifice diameter=1.496 mm.

457
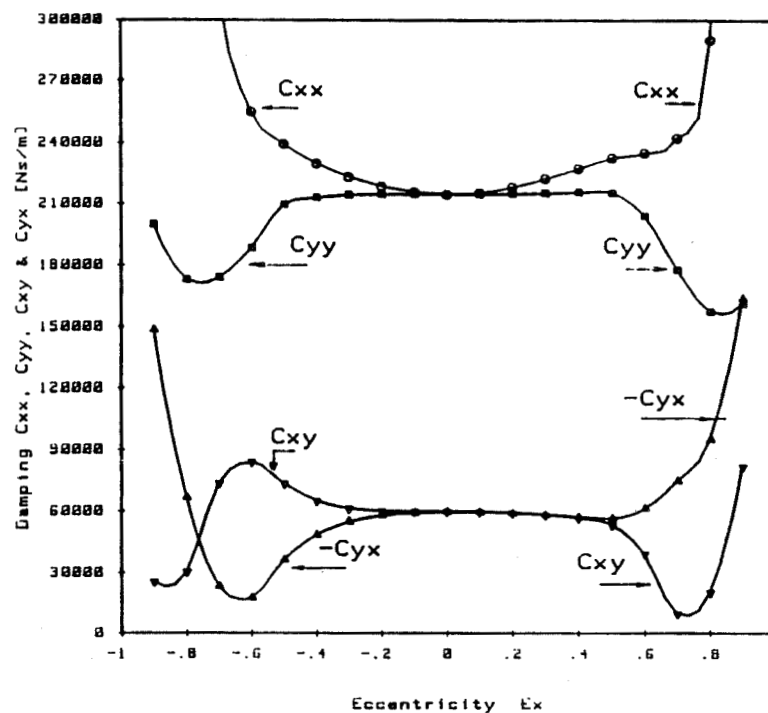
Figure 7. Predicted damping coefficients for test hydrostatic water
bearing versus journal static eccentricity. Ps=6.54 MPa, 30000
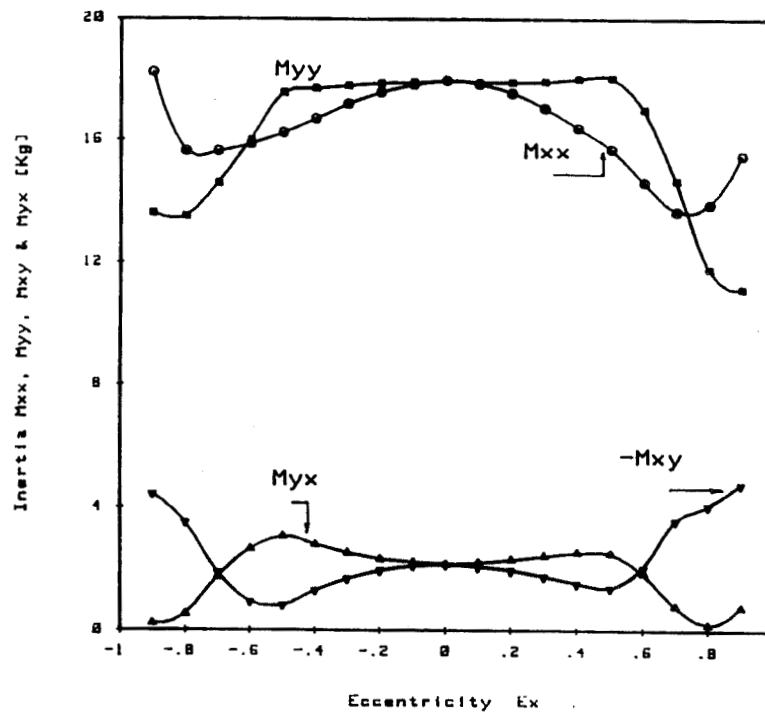rpm, orifice diameter=1.496 mm.

Figure 8. Predicted inertia force coefficients for test hydrostatic
water bearing versus journal static eccentricity. Ps=6.54 MPa,
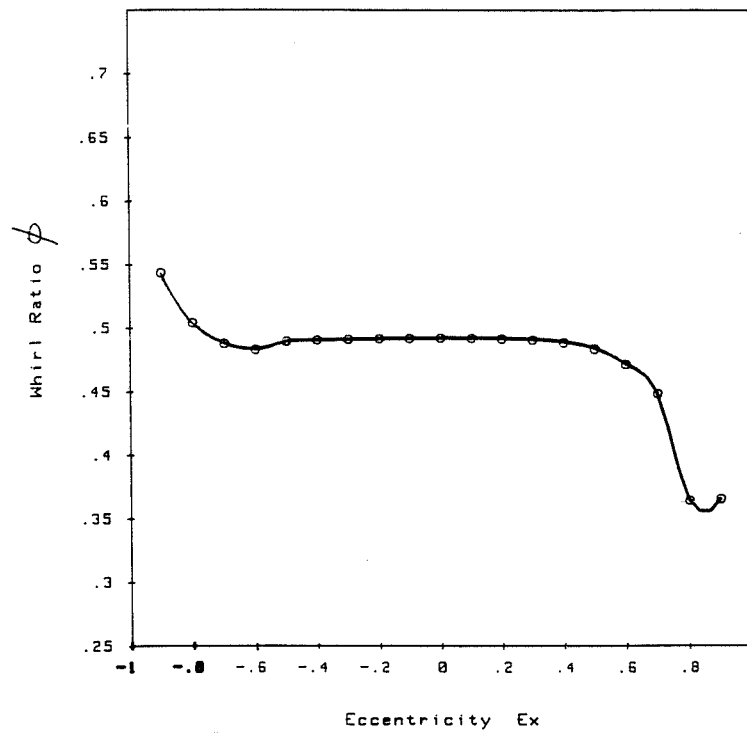30000 rpm, orifice diameter=1.496 mm.

Figure 9. Whirl frequency ratio ϕ for test rotor-hybrid bearing system versus journal static eccentricity.
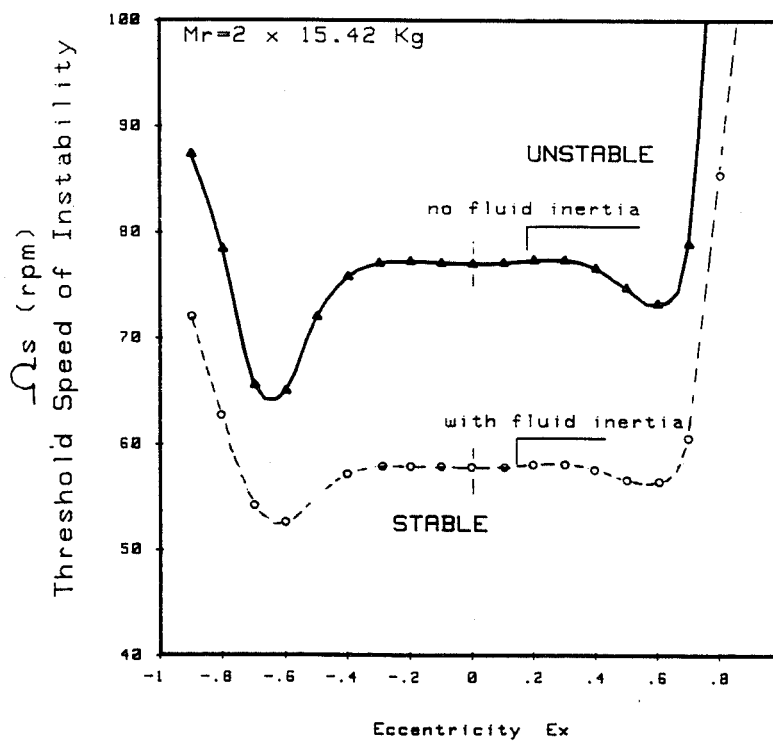

Figure 10. Threshold speed of instability Ω_s for test rotor-hybrid bearing system versus journal static eccentricity.

459

NASA
National Aeronautics and
Space Administration

Report Documentation Page

1. Report No. NASA CP-3122	2. Government Accession No.	3. Recipient's Catalog No.

4. Title and Subtitle	5. Report Date
Rotordynamic Instability Problems in High-Performance Turbomachinery—1990	October 1991
	6. Performing Organization Code 553-13-00

7. Author(s)	8. Performing Organization Report No. E-5628
	10. Work Unit No.

9. Performing Organization Name and Address National Aeronautics and Space Administration Lewis Research Center Cleveland, Ohio 44135 - 3191	11. Contract or Grant No.
	13. Type of Report and Period Covered

12. Sponsoring Agency Name and Address National Aeronautics and Space Administration Washington, D.C. 20546 - 0001	Conference Publication
	14. Sponsoring Agency Code

15. Supplementary Notes

The workshop was sponsored by Texas A&M University, College Station, Texas 77843-3123, and NASA Lewis Research Center. The workshop was held at Texas A&M University on May 21-23, 1990.

16. Abstract

The first rotordynamics workshop proceedings (NASA CP-2133, 1980) emphasized a feeling of uncertainty in predicting the stability of characteristics of high-performance turbomachinery. In the second workshop proceedings (NASA CP-2250, 1982) these uncertainties were reduced through programs established to systematically resolve problems, with emphasis on experimental validation of the forces that influence rotordynamics. In the third proceedings (NASA CP-2338, 1984) many programs for predicting or measuring forces and force coefficients in high-performance turbomachinery produced results. Data became available for designing new machines with enhanced stability characteristics or for upgrading existing machines. In the fourth proceedings (NASA CP-2443, 1986) there emerged trend toward a more unified view of rotordynamic instability problems and several encouraging new analytical developments. The fifth workshop (NASA CP-3026, 1989) supported the continuing trend toward a unified view with several new developments in the design and manufacture of new turbomachineries with enhanced stability characteristics along with new data and associated numerical/theoretical results. The present workshop continues to report field experience and experimental results, and it expands the use of computational and control techniques with integration of damper, bearing, and eccentric seal operation results. The intent of the workshop and this proceedings is to provide a continuing impetus for an understanding and resolution of these problems.

17. Key Words (Suggested by Author(s)) Instabilities; Rotordyamics; Turbomachinery; Seals; Bearings	18. Distribution Statement Unclassified - Unlimited Subject Category 37

19. Security Classif. (of the report) Unclassified	20. Security Classif. (of this page) Unclassified	21. No. of pages 460	22. Price* A21

NASA FORM 1626 OCT 86   *For sale by the National Technical Information Service, Springfield, Virginia 22161

NASA-Langley, 1991